Purinergic Receptor Modulators and the Effect on Microglial Function

A thesis submitted to fulfil the requirements

of the degree of

Doctor of Philosophy

by

Chianna Maeve Dane

2026

The University of Sydney

Faculty of Science

School of Chemistry

Contents

Statement of Originality

This is to certify that, to the best of my knowledge, the content of this thesis is my own work. This thesis has not been submitted for any degree or other purposes. I certify that the intellectual content of this thesis is the product of my own work and that all the assistance received in preparing this thesis and sources have been acknowledged.

Chianna Dane

Author Attribution Statement

This thesis describes work performed by the author in the School of Chemistry at the University of Sydney, under the supervision of Professor Michael Kassiou between March 2022 and September 2025. The main body of this thesis contains less than 80,000 words.

The *in silico* studies described in Chapters 2 and 5 was guided by Dr Jonathan Du and software was provided by the In Silico Drug Design Facility, CDDI. Crystal structures were elucidated by Professor David Hibbs at the Sydney University School of Pharmacy. Biological assays, and accompanying experimental, were provided by Mr André McKenzie within the Faculty of Medicine and Health at the University of Sydney.

This research was supported by an Australian Government Research Training Program (RTP) Scholarship.

No content produced by generative AI tools has been used in the preparation of this thesis.

Chianna Dane

As the supervisor for the candidate upon which this thesis is based, I can confirm that the authorship statements above are correct.

Professor Michael Kassiou

Acknowledgments

First and foremost, I would like to express my sincere gratitude to my supervisor, Professor Michael Kassiou, for their invaluable guidance and leadership over the years. Thank you for fostering an environment that inspires both critical thinking and curiosity. It has been a real privilege to be part of your group, and I'm incredibly proud to now count myself among the Kassiou alumni.

This thesis would not have been possible without the generous support and guidance of Dr. Andrew Montgomery and Dr. Jakob Lane. Thank you for your continued support throughout my time as both an honours and PhD student, both in the lab and out. I am deeply grateful for the countless times you've taken time out of your busy schedules to proofread my work, troubleshoot chemistry problems, watch practice presentations, and help keep the lab running smoothly. To Dr. Jonathon Danon, thank you for your guidance and support over the years. Your wealth of knowledge and passion for science is truly infectious.

To Dr. Wendy Tran, thank you for being my emotional support chemist over the past three years. Your constant willingness to help, no matter how big or small the task, has never gone unnoticed and is deeply appreciated. I've learned so much from you, and I'm incredibly grateful for your friendship. It's been an absolute pleasure working alongside you (in silence of course) down in Cornforth.

To the entire Kassiou and Danon groups, both past and present, thank you for making my PhD experience so memorable. I am extremely grateful to have had the opportunity to work and learn from you all. To Taylor, Dane and Nick, thank you all for being so generous with your time whether it was troubleshooting chemistry, proofreading this thesis or enabling (and encouraging) my coffee addiction. It has been a pleasure to work and teach alongside you all. I will always remember to keep the flow rates high and songs going 'on & on'.

I would also like to acknowledge and thank Dr. Eryn Werry and André McKenzie, from the Kassiou group, who were crucial in establishing and performing biological assays to evaluate

compounds in this work. To Dr Jonathan Du, thank you for all your guidance and assistance with the *in silico* studies.

To Nick Proschogo, thank you for giving me the opportunity to be a part of the mass spectrometry team. Working with you has truly been a pleasure, I've learned a great deal and really valued the experience. My appreciation also goes out to the other brilliant technical staff at the School of Chemistry. To Ian Luck, Paige Hawkins, Cody Szczepina and Dennis Cheng, your assistance has been invaluable. The research reported in this thesis was supported by the award of a Research Training Program scholarship.

To my friends and family, thank you for providing both distractions and encouragement when needed. I couldn't have done it without the constant support and endless motivation you have provided. To my Mum, thank you for teaching me to approach challenges head on, with both an open heart and mind. Without your endless love and encouragement, I wouldn't be where I am today.

Finally, to my partner Xavier. Words cannot begin to describe how thankful I am for your unwavering love, support and patience over the past few years. Thank you for constantly believing in me and celebrating my wins with the same enthusiasm as if they are your own. Without your unfailing belief in me none of this would have been possible. Thank you.

Abstract

Purinergic receptors, particularly those expressed on microglia, have emerged as key modulators of neuroinflammation and neurodegeneration. Within the P2 subfamily, the P2X4 and P2Y6 receptors both play an essential role in microglia-mediated immune responses. Upon activation, the P2X4 and P2Y6 receptors release a range of pro-inflammatory cytokines and induce microglial phagocytosis, respectively. With both pathways shown to underlie the pathogenesis of several inflammatory conditions, targeting the P2X4 and P2Y6 receptors therapeutically presents an exciting opportunity to deepen our understanding of microglial function and address an unmet clinical need.

Inhibition of the P2X4 receptor has been highlighted as a potential therapeutic target for chronic pain states and traumatic brain injury and therefore has been the focus of both pharmaceutical and academic groups. However, current ligands suffer from poor selectivity amongst P2X subtypes and unfavourable pharmacokinetic properties. Through the incorporation of adamantane, this exploratory study aims to enhance our understanding of the binding domains of both the P2X4 and P2X7 receptors, whilst providing a predictive framework for the design of selective purinergic antagonists. Patent literature compounds spanning a diverse range of steric and electronic features which exhibit varying levels of functional activity were selected for diversification, thus enabling a comprehensive structure activity relationship assessment. Assays to assess hP2X4R functional activity have not currently been undertaken, but *in silico* evaluation of the compound library has suggested detrimental steric clashes between the adamantane and surrounding proteins/ligands.

Pharmacological inhibition of the P2Y6 receptor has been shown to prevent neuronal loss and cognitive deficits in *in vivo* models of acute amyloid pathology, highlighting its therapeutic potential in conditions such as Alzheimer's disease. However, targeting the P2Y6 receptor therapeutically has remained elusive due to a lack of drug-like molecules available. In the absence of P2Y6 receptor structural data, structure activity relationship studies such as this one, aim to identify key pharmacophoric features for potent and selective P2Y6 receptor inhibition. Diversification of the reported P2Y6 receptor antagonist **37** failed to yield any novel lead compounds. The exploration of **37** and other reported inhibitors has highlighted potential discrepancies in the reported literature further emphasising the importance of intra-laboratory

validation and the methodological inconsistencies that can arise when assessing P2Y6 receptor functional activity. Therefore, highlighting the urgent need for robust and reproducible functional assays.

This thesis has explored both the P2X4 and P2Y6 receptor subtypes, both of which are primarily located on the microglia. Through the exploration of pharmacophores, the work described has contributed to the development of selective and potent purinergic receptor modulators. Advancing drug discovery efforts toward purinergic targets like the P2X4 and P2Y6 receptors represents an exciting opportunity to address a critical gap in the treatment of neurodegenerative diseases.

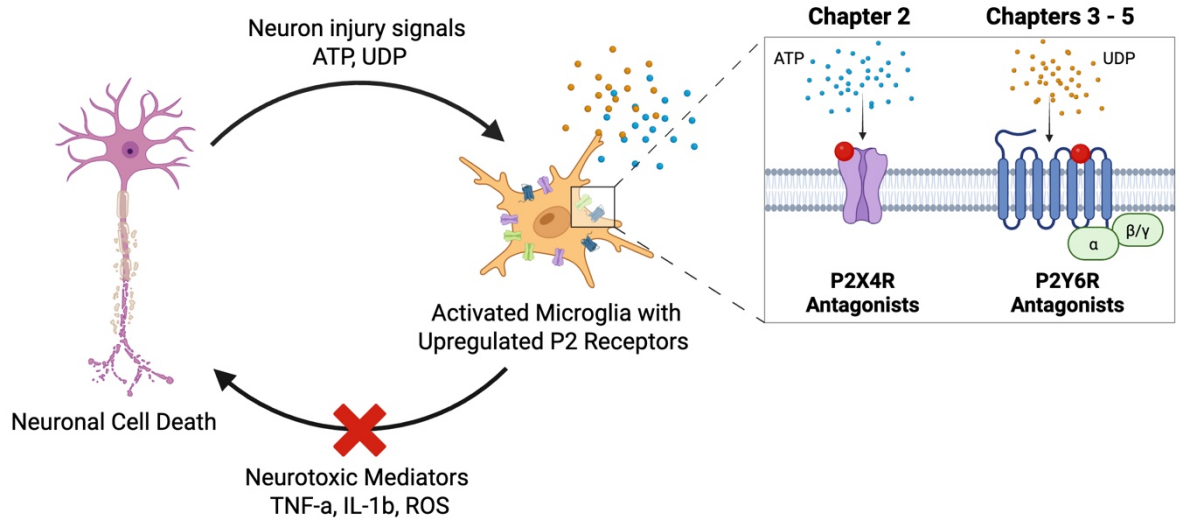

Abbreviations

Å	Angstrom
°C	Degrees Celsius
δ	Chemical Shift (ppm)
µ	Micro
µM	Micromolar concentration
AcOH	Acetic Acid
AD	Alzheimer's Disease
ADME	Absorption, Distribution, Elimination and Metabolism
ADP	Adenosine Diphosphate
anhy.	Anhydrous
APCI	Atmospheric Pressure Chemical Ionisation
aq.	Aqueous
ATP	Adenosine 5'-Triphosphate
BBB	Blood-Brain Barrier
BDNF	Brain-Derived Neurotrophic Factor
BINAP	2,2′-Bis(diphenylphosphino)-1,1′-binaphthalene
$BocNH_2$	*tert*-Butyl carbamate
Boc_2O	di-*tert*-Butyl decarbonate
BuLi	Butyllithium
cat.	Catalytic Amount
CDI	1,1'-Carbonyldiimidazole
cLogD	Calculated Octanol/Buffer Partition Coefficient
CNS	Central Nervous System
conc.	Concentrated
COSY	Homonuclear Correlation Spectroscopy
COX	Cyclooxygenase
Cs_2CO_3	Caesium Carbonate
CuI	Copper(I) Iodide
CYP	Cytochrome P450
d	Doublet
DABCO	1,4-Diazabicyclo[2.2.2]octane
DBM	Dibromomethane
DBU	1,8-Diazabicyclo[5.40]undec-7-ene

DCDMH	1,3-Dichloro-5,5-dimethylhydantoin
DCE	1,2-Dichloroethane
DDQ	2,3-Dichloro-5,6-dicyano-1,4-benzoquinone
DMA	*N*,*N*-Dimethylacetamide
DMAP	4-Dimethylaminopyridine
DMB	2,4-Dimethoxybenzyl
DMF	*N*,*N*-Dimethylformamide
DMF-DMA	*N,N*-Dimethylformamide Dimethyl Acetal
DMI	*N*,*N*-Dimethylformimidamide
DMP	Dess–Martin Periodinane
DMSO	Dimethylsulfoxide
DPPA	Diphenylphosphoryl Azide
EC_{50}	Half Maximal Effective Concentration
EDC.HCl	1-Ethyl-3-(3-dimethylaminopropyl)carbodiimide hydrochloride
eq.	Molar Equivalent(s)
ESI	Electron Spray Ionisation
Et_3N	Triethylamine
EtOAc	Ethyl Acetate
EtOH	Ethanol
FDA	Food and Drug Administration
$Fe(OTs)_3$	Iron(III) Tosylate
FGI	Functional Group Interconversion
g	Gram(s)
GABA	Gamma-Aminobutyric Acid
GPCR	G-Protein Coupled Receptors
h	Hour(s)
H_2SO_4	Sulfuric Acid
HATU	1-[Bis(dimethylamino)methylene]-1*H*-1,2,3-triazolo[4,5-*B*]pyridinium 3-oxide hexafluorophosphate
HBTU	*N,N,N′,N′*-Tetramethyl-*O*-(1*H*-benzotriazol-1-yl)uronium hexafluorophosphate
HCl	Hydrogen Chloride
HEK	Human Embryonic Kidney
Hex	*n*-Hexanes
HFIP	1,1,1,3,3,3-Hexafluoro-2-propanol

HMBC	Heteronuclear Multiple Bond Correlation
HOBt.H_2O	1-Hydroxybenzotriazole hydrate
HOMO	Highest Occupied Molecular Orbital
HPLC	High-Performance Liquid Chromatography
HRMS	High-Resolution Mass Spectrometry
HSQC	Heteronuclear Single Quantum Coherence
HTS	High-Throughput Screening
Hz	Hertz
IC_{50}	Ligand Concentration Required to Inhibit Biological Effect by 50% Relative to a Control.
IFD	Induced-Fit Docking
IL-1β	Interleukin-1β
IP	Inositol Phosphates
IP_3	Inositol Triphosphate
^{i}Pr	Isopropyl
^{i}PrMgCl	Isopropylmagnesium chloride
$^{i}Pr_2$NEt	*N,N*-Diisopropylethylamine
^{i}PrOBPin	Isopropoxyboronic acid pinacol ester
J	Coupling Constant
KCC2	Potassium-Chloride Cotransporter 2
KO	Knock-Out
KOH	Potassium Hydroxide
LDA	Lithium diisopropylamide
LGIC	Ligand-Gated Ion Channel
LHMDS	Lithium bis(trimethylsilyl)amide
$LiAlH_4$	Lithium Aluminium Hydride
LiHMDS	Lithium hexamethyldisilazide
LiTMP	Lithium tetramethylpiperidine
logP	Partition Coefficient, Indicator of Compound Lipophilicity
LPS	Lipopolysaccharide
LRMS	Low-Resolution Mass Spectrometry
m-	*Meta* Substitution
m	Multiplet
M	Molar Concentration
m/z	Mass to Charge Ratio

mAbs	Monoclonal Antibodies
MAPK	Mitogen-Activated Protein Kinase
MEC	Minimum Efficacious Concentration
MeOH	Methanol
$MeSO_3H$	Methanesulfonic Acid
mg	Milligram(s)
$MgSO_4$	Magnesium Sulfate, Anhydrous
MHz	Megahertz
MIDA	*N*-Methyl iminodiacetic acid
min	Minute(s)
ML	Machine Learning
mL	Millilitre
mol	Mole(s)
MS	Multiple Sclerosis
MW	Microwave Irradiation
NaH	Sodium Hydride, 60% Dispersion in mineral oil
$NaHCO_3$	Sodium Hydrogen Carbonate
$NaHSO_3$	Sodium Bisulfite
NaOH	Sodium Hydroxide
NAM	Negative Allosteric Modulator
NBS	*N*-Bromosuccinimide
NCS	*N*-Chlorosuccinimide
NIS	*N*-Iodosuccinimide
NLRP3	(NOD)-Like Receptor Protein 3
nM	Nanomolar Concentration
NMO	*N*-Methylmorpholine-*N*-oxide
NMR	Nuclear Magnetic Resonance
NOE	Nuclear Overhauser Effect
NOESY	Nuclear Overhauser Effect Spectroscopy
NP	Neuropathic Pain
o-	*Ortho* Substitution
p-	*Para* Substitution
p-$MePhSO_3H$	*p*-Toluenesulfonic acid
P(*t*-Bu)$_3$	Tri-*tert*-butylphosphine
P2X4R	P2X4 Receptor

P2X7R	P2X7 Receptor
P2XR	P2X Receptors
P2YR	P2Y Receptors
P2Y6R	P2Y6 Receptor
PAM	Positive Allosteric Modulator
PBS	Dulbecco's Phosphate Buffered Saline
PCC	Pyridinium Chlorochromate
PD	Parkinson's Disease
$Pd(amphos)Cl_2$	Bis(di-*tert*-butyl(4-dimethylaminophenyl)phosphine)dichloropalladium(II)
$Pd(dba)_2$	Palladium(0) Bis(dibenzylideneacetone)
$Pd(dppf)Cl_2$	[1,1′-bis(diphenylphosphino)ferrocene]dichloropalladium(II)
$Pd(OAc)_2$	Palladium(II) Acetate
$Pd(PPh_3)_4$	Palladium-tetrakis(triphenylphosphine)
$Pd(PtBu_3)_2$	Bis(tri-*tert*-butylphosphine)palladium(0)
$Pd_2(dba)_3$	Tris(dibenzylideneacetone)dipalladium(0)
PET	Positron Emission Tomography
PGE2	Prostaglandin E2
pH	Potential of Hydrogen
$PhSO_2Cl$	Benzenesulfonyl Chloride
PIFA	Phenyliodonium Bis(trifluoroacetate)
PK	Pharmacokinetic
pK_a	Acid Dissociation Constant
PLC	Phospholipase C
PNS	Peripheral Nervous System
$POCl_3$	Phosphorus Oxychloride
PPA	Polyphosphoric Acid
PPh_3	Triphenylphosphine
ppm	Parts Per Million, Chemical Shift
PXR	Pregnane X Receptor
quant.	Quantitative Yield, > 98%
rac	Racemic Mixture
RMSD	Root Mean Square Deviation
ROS	Reactive Oxygen Species
R_T	Retention Time

rt	Room Temperature
RTD	Rigid-Target Docking
SAR	Structure-Activity Relationship
sat.	Saturated Solution
$Sc(OTf)_3$	Scandium(III) Triflate
S_EAr	Electrophilic Aromatic Substitution Reaction
SEM	2-(Trimethylsilyl)ethoxymethyl
S_N1	Unimolecular Nucleophilic Substitution
S_N2	Biomolecular Nucleophilic Substitution
S_NAr	Nucleophilic Aromatic Substitution
$SOCl_2$	Thionyl Chloride
SSRI	Selective Serotonin Reuptake Inhibitor
STD-NMR	Saturation-Transfer Difference NMR Experiments
t	triplet
t-BuBrettphos	2-(di-*tert*-Butylphosphino)-2′,4′,6′- triisopropyl-3,6-dimethoxy-1,1′-biphenyl
t-BuOH	*tert*-Butanol
t-BuOK	Potassium *tert*-Butoxide
T_3P	Polyphosphoric Anhydride
TBAB	Tetrabutylammonium Bromide
TBAF	Tetrabutylammonium Fluoride
TBD	1,5,7-Triazabicyclo[4.4.0]dec-5-ene
TBHP	*tert*-Butyl hydroperoxide
TBI	Traumatic Brain Injury
TCT	Trichloro Triazine
TFA	Trifluoroacetic Acid
THF	Tetrahydrofuran
TLC	Thin Layer Chromatography
TLR	Toll-Like Receptor
TMP	2,2,6,6-Tetramethylpiperidine
TMSOTf	Trimethylsilyl Trifluoromethanesulfonate
TNF-α	Tumor Necrosis Factor-α
TOF	Triethylorthoformate
TPAP	Tetrapropylammonium Perruthenate
UDP	Uridine Diphosphate

UTP	Uracil Triphosphate
VT	Variable Temperature
v/v	Volume to volume
WLSTD	Wuhan LL Science and Technology Development Co
Xantphos	4,5-Bis(diphenylphosphino)-9,9-dimethylxanthene
XP	Extra Precision
XPhos	2-Dicyclohexylphosphino-2′,4′,6′-triisopropylbiphenyl
zP2X4R	Zebrafish P2X4 Receptor

Chapter 1. Introduction

1.1 Purinergic Signalling

Purine nucleosides and nucleotides such as adenosine and adenosine 5'-triphosphate (ATP) coordinate the function of almost all cells in the human body.[1] Collectively, these molecules and processes form a network of cellular communication termed purinergic signalling. Purinergic signalling, and therefore purinergic receptors (P1 or P2 receptors), has been described as a primitive evolutionary system involved in both neuronal and non-neuronal mechanisms.[2] Challenging the initial belief that ATP was purely a source of intracellular energy, in 1972 Burnstock proposed its role as a transmitter responsible for non-adrenergic, non-cholinergic transmission.[3,4] The concept of purinergic neurotransmission is now widely accepted to play a role in immune responses, exocrine and endocrine secretion, inflammation, pain, platelet aggregation and endothelial-mediated vasodilation.[1] Furthermore, purinergic receptors have similarly been identified to mediate cellular functions such as cell proliferation, differentiation and phagocytosis.[1]

Integral to neurotransmission and neuromodulation within the central nervous system (CNS), purinergic receptors are instrumental in facilitating cognition, memory and movement.[2] However, chronic activation or defective purinergic receptors can also be causative factors of a broad scope of pathological conditions, including neurodegenerative diseases.[5] This therefore emphasises the regulatory importance of the "purinome" (comprising endogenous agonists, receptors, and enzymes participating in purinergic signalling) – a fascinating complex system that is involved in countless (patho)physiological processes.[5]

1.2 Purinergic Receptors

Receptors to purines and pyrimidines have been cloned and characterised into two distinct protein families of G-protein coupled receptors (GPCR) (P1 and P2Y) and ligand-gated ion channels (LGIC) (P2X) (Figure 1.1).[1] Categorised by their endogenous ligand, the P2 receptor family recognise extracellular purine and pyrimidine nucleotides, such as ATP and uracil triphosphate (UTP). Whereas, P1 receptors are activated by adenosine, the breakdown product of ATP. The P1 receptors include four different subtypes of GPCR (A_1, A_{2A}, A_{2B}, and A_3) that

couple to adenylate cyclase to mediate physiological effects such as cardiovascular, immune and CNS activities (Figure 1.1).[1,2]

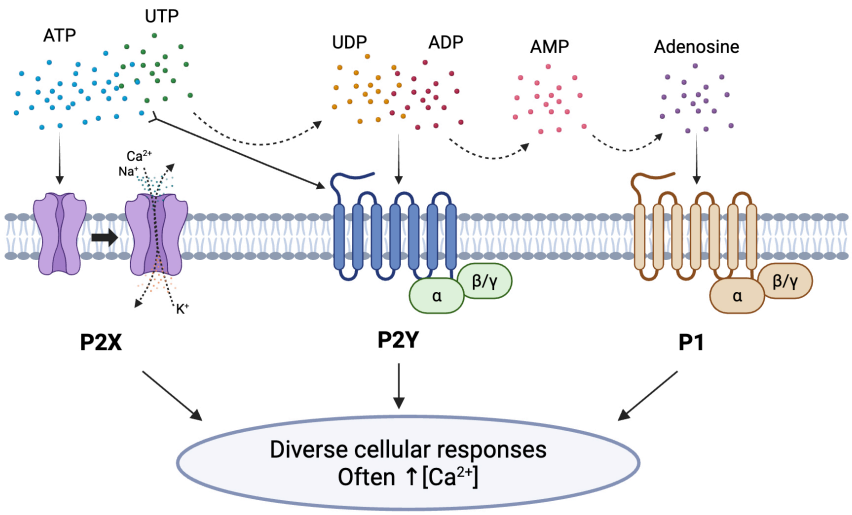

Figure 1.1 Purinergic receptor subtypes. Adapted from Woods *et al*.[6] Created with BioRender.com.

1.2.1 P2X Receptors

The P2X receptors (P2XR) are comprised of seven subclasses of LGIC, which allow for the non-selective influx of cations (Ca^{2+}, Na^{+}, and K^{+}) into the cell.[2] Located throughout both the peripheral nervous system (PNS) and CNS the P2X receptors cover a broad range of functional and clinical significance. Although all exclusively recognise ATP as their endogenous ligand, each subclass is activated by a distinct concentration, ranging from high nanomolar to low millimolar.[7] Moreover, the P2XR subtypes display variation in their kinetics of channel gating, encompassing rates of desensitisation timescales from milli-seconds (P2X1 and P2X3), to seconds (P2X2, P2X4 and P2X5) and to receptors that show minimal desensitisation (P2X7).[8] This, in conjunction with being expressed on diverse cell types, accounts for their expansive involvement in pathological conditions.[7]

Stoichiometrically, P2XR generally adopt either a homotrimeric configuration of three identical subunits or a hexamer of two conjoined trimers (Figure 1.2A).[7,9] However, as our knowledge of purinergic signalling improves, an increasing number of heteromultimers (a mixture of subunits e.g. P2X2/3) have been reported, thereby contributing to the diversity of the P2X receptor family.[2] Structurally, each subunit shares a common topology, consisting of

two transmembrane regions, connected by a large cysteine rich extracellular loop, and an intracellular amino- and carboxy-termini (Figure 1.2B).[7] Each subunit also contains a variety of consensus binding motifs for protein kinases and lipid binding regions. Amongst the P2X1-6 receptors, the transmembrane domains and cysteine loop are largely conserved, with the carboxyl-terminus being the most structurally divergent between subtypes.[7] Most notably, the P2X7 receptor (P2X7R) contains a highly extended carboxyl terminus, giving rise to its divergent functionality (Figure 1.2B).[7]

Insights into the molecular mechanisms of channel gating by ATP were revealed by the elucidation of a 'cytoplasmic cap' within the ATP-bound open-state conformation of the human P2X3 receptor. The cytoplasmic cap describes the domain formed through an interaction between cytoplasmic residues in the N- and C-termini.[8] Serving as a source of stability for the open pore once ATP has bound, the stability of the cytoplasmic cap is thus directly related to the rate and extent of receptor desensitisation, thought to only form transiently in fast desensitisers.[8] However, in slow desensitisers, such as the P2X4 receptor (P2X4R), it has been shown to also be present in the apo closed state structure.[8] Within the rat P2X7R the cytoplasmic cap was found to be permanently stabilised by a series of palmitoylated residues within the extended cysteine termini thereby accounting for its distinct kinetics.[8,10]

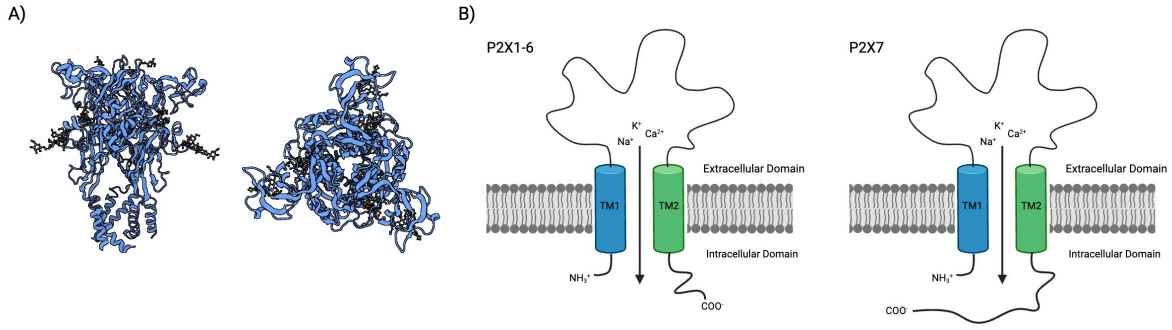

Figure 1.2 Structural characteristics of the P2X receptors. A) Trimeric structure of the gated zebrafish P2X4 receptor channel in the CTP-bond, open state. Structure was reproduced from the RSCB Protein Data Bank file 5WZY. B) Membrane topology of the P2X receptor subunits, illustrating the extended 242 amino acid residue carboxyl terminus of the P2X7R responsible for its divergent functionality. Created with BioRender.com.

To date, structures have been published for only three of the seven homotrimeric receptor subtypes, and for none of the eight heterotrimeric human receptors. Structures of animal

receptor orthologs have been solved, revealing a largely conserved overall architecture in the apo closed state.[7] However, variation in small molecule functional activity has been observed among mammalian receptors, suggesting key pharmacological differences between P2X receptors from different species.[11–13] Additionally, the P2X7R exists as multiple isoforms due to alternative splicing mechanisms or single-nucleotide polymorphisms.[14] Although these crystallographic studies provided a foundational understanding of P2XR structure and function, the required truncation of the cytoplasmic N- and C-termini for crystallization limited insights into the full biological complexity of P2XRs.[7] Therefore highlighting caution when selecting tools for *in silico* structure based drug design and *in vivo* animal studies ascribing cellular responses.[13]

Pharmacologically, the P2X receptors have been demonstrated to participate in both physiological and pathological processes.[2] Serving as an acute 'danger signal', ATP behaves as a mediator of inflammation and immunity. Following inflammation or metabolic stress, ATP is released into the extracellular media *via* both autocrine and paracrine signalling channels.[9,15] During the course of inflammation, P2X receptors are upregulated on immune cells. In turn, the increased concentration of extracellular ATP promotes systemic inflammation through elevated activation of purinergic signalling pathways. Within the CNS, microglia are the primary immune cells that mediate neuroinflammatory responses to insult following a change in the homeostasis.[15] The function of microglia is regulated by a large array of purinergic receptors, including receptors from all three subtypes. Across the P2X subtype, the P2X4 and P2X7 receptors have been highlighted to play an essential role in microglia-mediated immune responses and therefore were the subject of this study.

1.2.1.1 The P2X4 Receptor

The P2X4R is a non-selective LGIC, expressed primarily on immune and endothelial cells in both the PNS and CNS.[16,17] In primary cells such as microglia, macrophages and endothelial cells, the P2X4R localises predominantly in lysosomes, where it is protected from proteolysis by its glycosylation.[18,19] It has also been shown to localise on the plasma membrane and other intracellular compartments such as vesicles and vacuoles.[18] Recognised for its involvement in fast neurotransmission within the PNS and modulation of neuronal-glial interactions in the CNS, the P2X4R has been implicated in a multitude of pathological states.[20] Upon activation by ATP, the P2X4R facilitates an influx of cations into the cell, resulting in a variety of

downstream signalling events. Within immune cells, the corresponding signalling events include release of prostaglandin E2 (PGE2) from macrophages, the brain-derived neurotrophic factor (BDNF) from microglia and blood flow-dependent Ca^{2+} signalling in endothelial cells (Figure 1.3).[21,22] As such, changes in P2X4R expression and function have been linked to inflammatory and neuropathic chronic pain (Figure 1.3), synaptic dysfunction and neuroinflammation.[5] Additionally, together with the P2Y12 receptor, the P2X4R regulates microglial chemotaxis, an early response observed in Alzheimer's disease (AD) brains in reaction to amyloid deposition.[23]

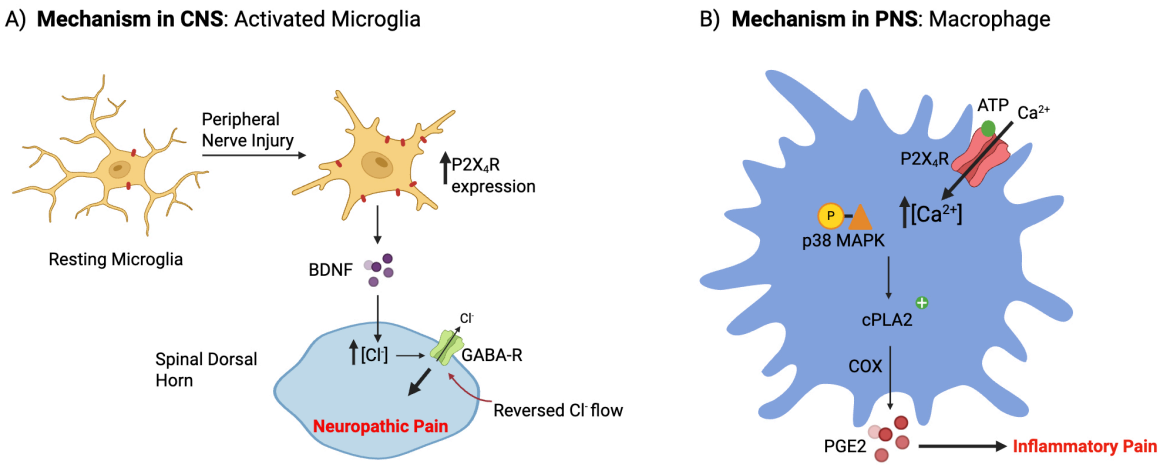

Figure 1.3 Involvement of the P2X4R in inflammation pathways in both the PNS and CNS demonstrated through chronic pain states. A) Following peripheral nerve injury, microglia are activated and P2X4R expression increases. Activation of P2X4Rs by ATP leads to the release of BDNF, and thereby the increase of intracellular chloride concentration. Consequently, the chloride ion flow is reversed, and inhibitory effect of GABA is reduced, resulting in neuron hyperexcitability. B) Activation of P2X4R on peripheral macrophages induces calcium influx and phosphorylation of p38 MAPK, stimulating activation of cPLA2 and COX-dependent release of PGE2. Created with BioRender.com

The crystal structures of the zebrafish P2X4 receptor (zP2X4R) in the ATP-unbound, closed and ATP-bound, open states were first reported in 2009.[24,25] Resembling a 'dolphin-like' shape, the P2X4 monomeric structure confirmed the three-fold symmetry for the homotrimeric assembly.[24] However, truncated forms, lacking the N- and C-terminus, were utilised thereby limiting our understanding of the receptor for many years.[17] In 2025, Shi *et al.* published the cryo-EM structures of the full-length wild-type human P2X4R in apo closed, antagonist-bound inhibited and ATP-bound desensitised states.[8] The report provided crucial information about the structural and sequence similarity between the two P2X4R orthologs (Figure 1.4A). The

hydrophobic extracellular domain demonstrated a high degree of similarity, although the transmembrane domains exhibited different orientations between the two orthologs (Figure 1.4A).[8] Critically, the P2X4R antagonist BAY-1797, was shown to bind in the canonical allosteric binding site located in the extracellular domain near the top of the receptor (Figure 1.4B).[8] Within the homotrimer, three molecules of BAY-1797 were shown to bind in close proximity – within 3.3 Å of each neighbouring, symmetry-related molecule (Figure 1.4C).[8] Key ligand binding interactions observed will be discussed further in section **1.4.5**. The model will provide a useful aid for future structure-based drug design, however, unfortunately was unavailable prior to conducting the synthetic component described in this dissertation.

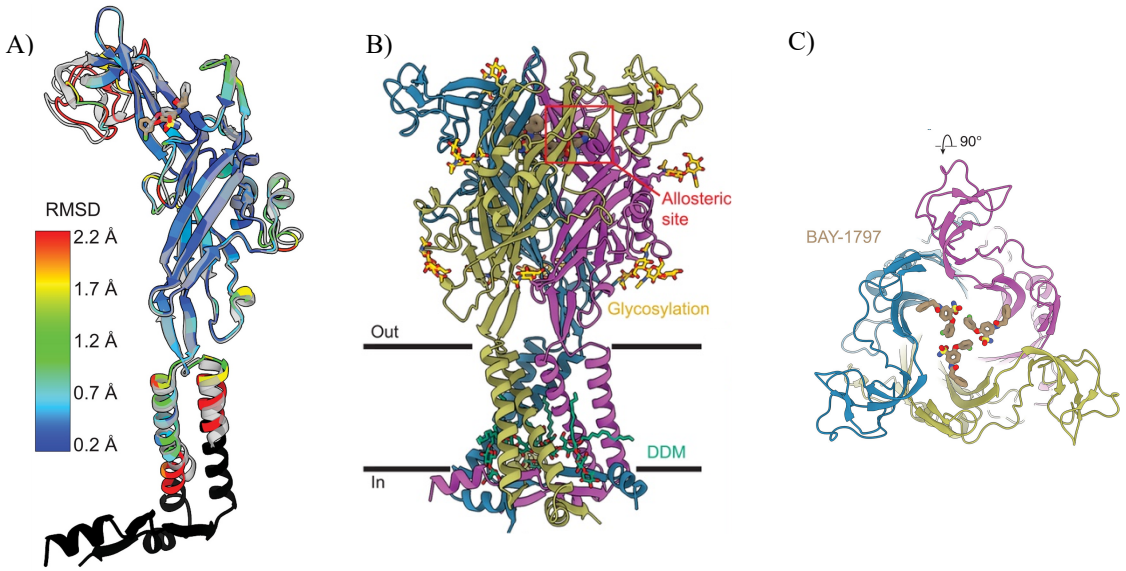

Figure 1.4 BAY-1797 binds to hP2X4 in the allosteric binding site. A) Structural alignment of hP2X4 (ligand in tan, peptide coloured by RMSD, with null values in black; PDB ID: 9BQI) and zP2X4R (transparent grey; PDB ID: 8JV6) in complex with BAY-1797. A smaller RMSD indicates greater similarity between the structures. B) BAY-1797 bound to full-length wild-type hP2X4 receptor. The allosteric binding site is highlighted with a red box. C) The top-down view of BAY-1797 bound to hP2X4R, highlighting the threefold symmetric binding mode of BAY-1797. Each molecule of BAY-1797 binds in close proximity (3.3 Å apart), near the axis of symmetry of the receptor. Reprinted (adapted) with permission from *Sci. Adv.* **2025**, 11, *3*. DOI: 10.1126/sciadv.adr3315 Copyright 2025 The American Association for the Advancement of Science.

Moreover, the P2X4R has been reported to form two heteromultimers with the P2X1 and P2X6 receptors.[26,27] Despite having similar desensitisation kinetics and structure to the homomeric P2X4R, neither heteromultimer has been identified to play a role in pathological states and will therefore not be discussed further.[2,26,27]

1.2.1.2 The P2X7 Receptor

The cytoplasmic termini play a critical role in receptor desensitisation, trafficking, and signalling.[28] Unique for its extended carboxyl terminus, the P2X7R demonstrates bifunctionality depending on the length of agonist exposure.[29] Brief activation by high concentrations of ATP (100 μM) forms a non-selective cation channel, allowing the influx of both monovalent and divalent cations leading to inward current depolarisation at the resting membrane potential.[30,31] However, following sustained activation, a large, non-selective pore is formed, facilitating the passage of organic ions.[29] Widely expressed across diverse cell types in both the peripheral and central nervous systems, and exhibiting distinct cell-specific properties and functions, the P2X7R has been implicated in a broad range of physiological and pathophysiological processes.[30] Ranging from immune responses, cell proliferation and death, metabolic events and phagocytosis, the P2X7R has been highlighted as a major driver of inflammation.[32]

1.2.1.3 Relationship Between the P2X4 and P2X7 Receptors

The close relationship between the P2X4R and P2X7R has been a key area of focus over recent years.[33] As both the P2X4 and P2X7 receptor modulators are active components in alleviating microglia-dependent pathological processes, understanding this interaction is therapeutically relevant.

Studies have suggested a structural and functional interaction between the two receptors due to their co-expression on immune and endothelial cells.[2,33,34] In addition, the two receptors have the highest degree of amino acid similarity (48.6% in humans, and 49.8% for rat) in comparison to other P2X receptors, with their respective genes located nearby on chromosome 12.[9,33] Indication of a functional interaction between the two has been reported in airway ciliated cells, dendritic cells, gingival epithelial cells and macrophages.[35–38] For example, in immune cells it was found that normal P2X7 receptor-dependent functions, such as cell death and release of inflammatory chemokines, were altered when P2X4R expression levels were reduced.[33] However, evidence of P2X4/P2X7 heteromerization is a point of contention, with the leading hypothesis suggesting a cooperative mechanism as separate, but physically interacting homotrimeric receptors.[33,39–41] Currently, limited data has been provided for the potential functional interaction between microglia P2X4 and P2X7 receptors, however selectivity of

potential therapeutics must be assessed at both receptors to confirm causation of functional activity.

1.2.2 P2Y Receptors

The metabotropic P2Y family of receptors is comprised of eight mammalian subtypes each encoded by distinct genes.[42,43] The GPCRs can then be further divided into two groups based on their primary signalling transduction pathway and protein sequence similarity.[42] Coined after the two human P2Y receptors that have been successfully co-crystallised and characterised; they are commonly referred to as the 'P2Y1-like' and 'P2Y12-like' receptor classes. The P2Y1-like subgroup (consisting of the P2Y1, P2Y2, P2Y4, P2Y6 and P2Y11 receptors) signals *via* $G_{q/11}$ proteins producing an increase in phospholipase C (PLC) production and corresponding increase in inositol phosphates (IP) and intracellular Ca^{2+} concentration (Figure 1.5).[44] The P2Y11 receptor is also able to couple to G_s proteins thereby increasing adenylate cyclase activity.[42] In contrast, the P2Y12-like subfamily (P2Y12, P2Y13 and P2Y14) couples to $G_{i/o}$ proteins to produce their pharmacological effect (Figure 1.5).[44,45] By activating $G_{i/o}$ proteins, adenylate cyclase activity is inhibited (Figure 1.5).[45] The non-consecutive numbering of mammalian P2Y receptors is due to the misassignment of species homologues or proteins. For example, originally assigned the P2Y5 receptor, the lysophosphatidic acid receptor LPAR6 was renamed following radioligand binding experiments.[46,47]

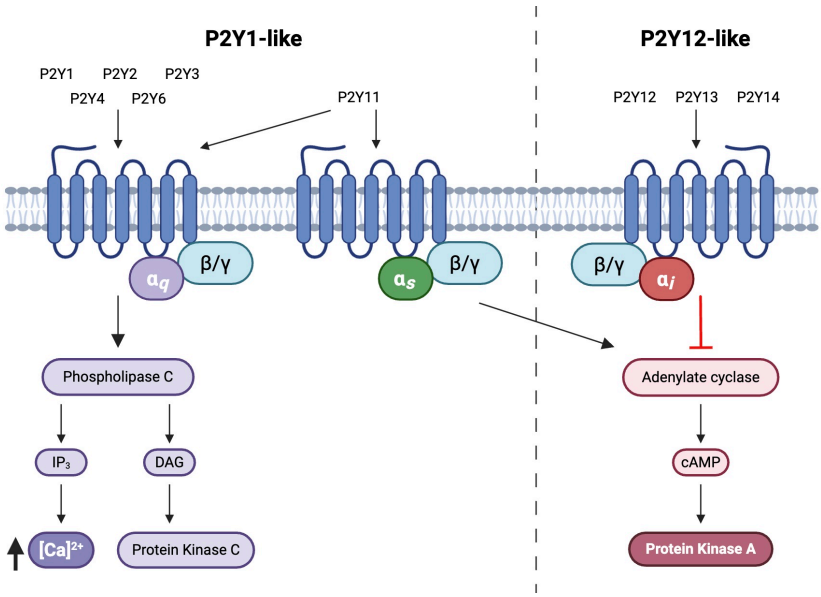

Figure 1.5 P2Y receptor subtypes and their primary signalling transduction pathways. Figure adapted from Muller *et al.*[45] Created with BioRender.com

The membrane-bound proteins adopt the characteristic GPCR molecular topology (Figure 1.5). P2Y receptors belong to the δ-branch of the rhodopsin-like receptor family and are composed of seven transmembrane domains, with an extracellular N-terminus and an intracellular C-terminus.[42] Unlike other G-protein families, the P2Y receptors exhibit limited sequence homology.[43] This is evident as each receptor has different selectivity and affinity for individual nucleotides and G-protein signalling pathways.[42] Located throughout the entire body, P2Y receptors therefore participate in a wide variety of biological functions. Such include immune regulation, platelet aggregation and smooth muscle cell proliferation.[48] A summary of the pharmacology and therapeutic indication for each P2Y receptor is provided in table 1.1.[42–44,48]

Despite a growing interest in the potential therapeutic role of P2Y receptors, limited small molecule modulators with favourable physicochemical and pharmacokinetic properties have been reported.[49–54] Of the P2Y receptors, development of P2Y12R ligands has been the most successful with four FDA-approved antagonists for thrombosis.[43] With the development of P2Y receptor homology models, the development of new selective antagonists is expected to increase over the coming years.

Table 1.1 P2Y Receptor endogenous ligand and distribution in the body.[48]

Receptor	G Protein	Agonist	Distribution	Biological function
P2Y1	$G_{q/11}$	ADP	Platelets, CNS, heart, skeletal muscle, GI tract	Blood coagulation, haemostasis, synaptic plasticity and pain transmission
P2Y2	$G_{q/11}$	ATP UTP	Lung, skeletal and cardiac muscle, kidney, brain	Mediate inflammatory response
P2Y4	$G_{q/11}$	UTP	Placenta, brain, vascular smooth muscle, lung	Regulation of microglial pinocytosis and eosinophil activation
P2Y6	$G_{q/11}$	UDP	Brain, placenta, thymus, spleen, kidney, lung, intestine	Mediate inflammatory response

P2Y11	$G_{q/11} + G_s$	ATP	Spleen, intestine, dendritic cells	Granulocyte activation Dendritic cell maturation
P2Y12	$G_{i/o}$	ADP	Platelets, brain	Blood coagulation Mediate inflammatory response
P2Y13	$G_{i/o}$	ADP	Brain, spleen	Regulation of cholesterol and glucose metabolism
P2Y14	$G_{i/o}$	UDP UDP-glucose	Brain, heart, adipose tissue, placenta, intestine, hematopoietic cells	Mediate inflammatory response

1.2.2.1 The P2Y6 Receptor

The P2Y6 receptor (P2Y6R) is a membrane bound, G_q-protein coupled receptor, expressed on multiple different cell types in the PNS and CNS.[55] Accounting for its diverse role in both physiological and pathological conditions, the P2Y6R has been shown to regulate cellular responses in both immune and non-immune cells.[56] The P2Y6R is activated by its endogenous ligand, extracellular uridine diphosphate (UDP, EC_{50} = 50 – 300 nM), and to a lesser extent UTP (EC_{50} = 6 μM), adenosine diphosphate (ADP, EC_{50} = 30 μM), and ATP (EC_{50} = 3 mM).[56] Found on the plasma membrane, the P2Y6R has also been shown to be internalised by a clarithin-dependent pathway to regulate activity.[57]

Following activation by UDP, the P2Y6R increases the production of inositol triphosphate (IP_3) and initiates the PLC signalling pathway resulting in a persistent increase in intracellular Ca^{2+} levels (Figure 1.6).[56,58] This triggers the production and release of pro-inflammatory cytokines and chemokines. It also functions as a sensor for phagocytosis, thereby playing an essential role in inflammation in both the peripheral and central nervous systems (Figure 1.6).[58,59]

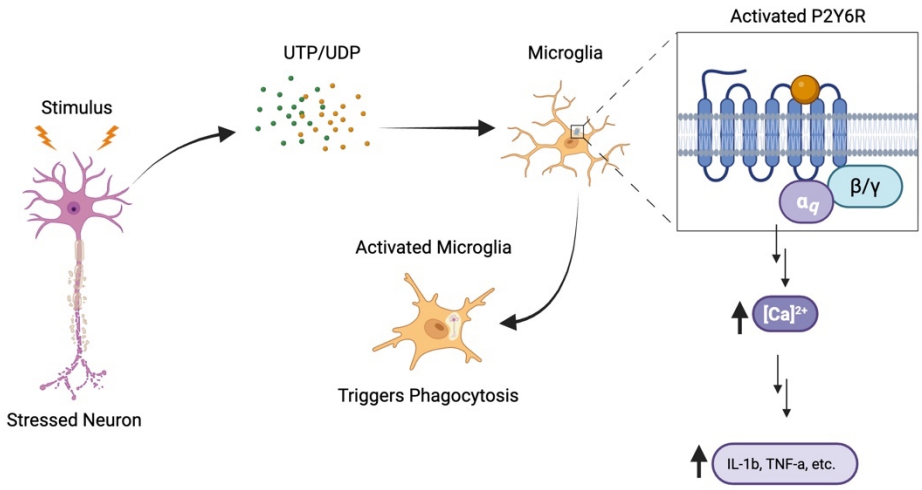

Figure 1.6 The microglial P2Y6R, activated by extracellular UDP released by stressed neurons, plays an important role in inflammation through production of proinflammatory mediators and facilitation of microglial phagocytosis of neurons. Adapted from Puigdellivol *et al*.[58] Created with BioRender.com

To date, the structure of the P2Y6R is unsolved. However, homology models based on the hP2Y1R have suggested a nucleotide binding site between the seven transmembrane alpha helices.[60] Therefore, current P2Y6R investigative ligands are generally broad-spectrum P2 agonists and antagonists. However, the P2Y6R, and thus selective P2Y6 antagonists, remain of prominent interest with growing evidence for its role in neurodegenerative disorders.[56]

1.3 Microglia and Neuroinflammation

Dynamic cross-talk between the CNS and the immune system is required to maintain CNS homeostasis.[61] Microglia are non-neuronal cells that serve as the primary immune cells within the CNS.[62] Functionally, microglia play a pivotal role in CNS development, immune surveillance and have evidently been implicated in pathological conditions stemming from neuroinflammation.[61,63–65] Throughout CNS development, microglia have been shown to modulate synaptic remodelling, migration and differentiation of cells, and formation of the blood vessel and neural networks.[66] Whereas in the adult brain, microglia continuously survey the brain parenchyma, serving as the first line of defence in the CNS.[66,67] Consequently, microglia are required to be highly motile in order to successfully execute their function.

Microglia motility refers to the change of morphology for a respective process.[66] Previously thought to exist in a dichotomy between the relaxed and activated state, it is now well

documented that microglia can exist as a continuum of subtypes based on their morphological characteristics and location within the brain (Figure 1.7).[64,68] Microglia in their surveillance state resemble a ramified structure and exhibit weak phagocytic activity (Figure 1.7).[68] Upon recognition of an inflammatory stimulus, the resting microglia entrap damaged cells through microglia chemotaxis.[69] Extension of the ramified structure surrounds dead cells, then retract to adopt an ameboid morphology with the depletion of chemotaxin.[69] Polarisation into this activated swollen-like shape results in increased production of pro-inflammatory cytokine, chemokines and free radicals, such as tumor necrosis factor-α (TNF-α), interleukin-1β (IL-1β), and nitric oxide. Immune activated microglia also produce enhanced immune responses such as phagocytosis, proliferation, migration and antigen presentation.[66]

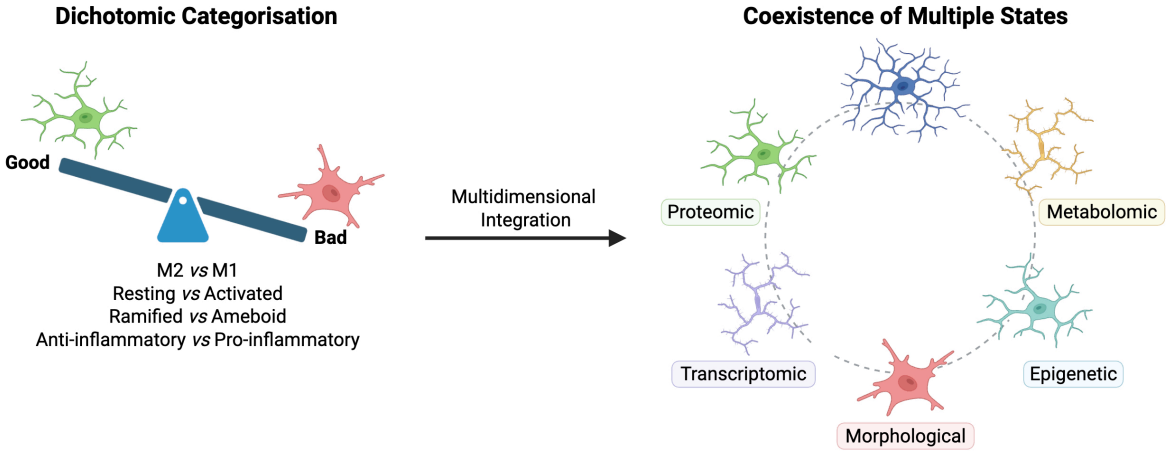

Figure 1.7 Redefined view of microglia states. Previously considered in dichotomic categories, microglia are now believed to exist as a multidimensional model of coexisting states. Adapted from Paolicelli *et al.*[68] Created with BioRender.com

Microglial phagocytosis can exert both a protective and detrimental function within the brain. During development, microglia assist in shaping neuronal networks and removing apoptotic neurons, excess live neurons or neuronal precursors and protein aggregates through microglial phagocytosis.[56,70,71] However, excessive uptake of protein aggregates, can lead to neuroinflammation and eventually neurodegeneration. Although the exact mechanism by which neurodegeneration originates is still poorly understood, there is increasing evidence that apoptosis of neurons and extensive synaptic loss are key contributors.[56] Within an animal model of AD, microglial phagocytosis has been demonstrated to contribute to synaptic loss.[72] This is further supported by the correlation between genes associated with AD risk and those

associated with microglial phagocytosis.[73] This correlation is similarly observed when analysing Parkinson's disease (PD) risk-associated genes.[56] PD is characterised by motor deficits, Lewy bodies and progressive loss of midbrain dopaminergic neurons.[56] Extracellular neuromelanin, a protein expressed in high levels in dopaminergic neurons of the substantia nigra, has been shown to activate microglia causing neuronal loss.[74] Neuronal loss was attenuated by knockout of the microglial phagocytotic receptor CR3 in mice, further highlighting its role in neurodegeneration.[74]

In addition to this, microglia regulate the innate immune function of astrocytes, determining whether a neuroprotective or neurotoxic response is employed.[9] However, prolonged activation of the immune system leads to a dysregulated response, whereby inflammatory factors become toxic for neurons.[75] Chronic activation of microglia can thereby both initiate and progress a series of neurodegenerative diseases including AD, PD disease, multiple sclerosis (MS), stroke and retinal degeneration.[61,63] Microglia's role in neurodegenerative disorders is further implicated through the presence of a plethora of purinergic receptors both intracellularly and on the cell surface which are upregulated following activation.[65] Numerous reports suggest that the neurotoxic responses mediated by activated microglia can also be induced by activation of the purinergic receptors, thus creating a chronic self-perpetuating cycle of inflammation.[9,65,76–79]

1.3.1 Microglia and the P2X Receptors

Within the P2X family, the P2X4 and P2X7 receptors both play an essential role in microglia-mediated immune responses and therefore are tightly linked to neurodegenerative diseases. In disease states, the P2X4 and P2X7 receptors are shown to be upregulated in inflammatory foci and microglia.[75] Despite their general overexpression in most neurological conditions, the role played in the inflammatory cascades and in secondary brain damage is different in each condition.[80] Therapeutic intervention through targeting either receptor has demonstrated great promise in reducing excessive initiation of pro-inflammatory signalling.[81–84] However, conflicting reports have been released suggesting that the P2X4R and P2X7R can exert both beneficial and harmful effects during disease progression.[75,85–93] Suspected to be due to the diverse range of roles each takes in immune responses, further research is required to understand their full role in inflammation.

The P2X4R is a key modulator of glia and neurons in both physiological and inflammatory responses in the CNS.[94] Within microglia-related associated neural diseases, the expression and motility of P2X4 receptors on microglia fluctuates consistently. Toulme *et al*, demonstrated through single-molecule imaging that P2X4Rs travelled passively throughout resting microglia and were dynamically regulated following a change in extracellular ATP concentration.[95] Activation of microglial P2X4R by ATP, and the consequential intracellular Ca^{2+} increase, induces microglial motility and chemotaxis, *via* the phosphoinositide 3-kinase pathway. The P2X4Rs involvement in microglia chemotaxis, has since further been supported through animal models involving pharmacological blockade or knockdown of the P2X4R.[96,97] For example, within a lipopolysaccharide (LPS) initiated model of neuroinflammation, rats that were treated with a P2X4R antagonist demonstrated a reduction in microglial morphological changes as well as an overall decrease in microglia apoptosis.[94]

Generally, following an inflammatory stimulus the P2X4R promotes microglial release of pro-inflammatory cytokines, such as TNF-α and IL-1β, and BDNF. BDNF then binds to transmembrane tyrosine kinase B in secondary sensory neurons triggering a downregulation of the potassium-chloride cotransporter 2 (KCC2), increasing the intracellular chloride concentration (Figure 1.3).[23] Consequently, the chloride ion flow is reversed, making GABA and glycine less hyperpolarising and in some cases depolarising (Figure 1.3).[23] Direct evidence for the release of BDNF from activated microglia following P2X4R stimulation was provided in a neuropathic pain (NP) animal model. Following peripheral nerve injury, P2X4R knock-out (KO) mice were shown to have a significant reduction in hyperalgesia and displayed impaired BDNF signalling.[22] A similar observation was made in an AD model, where decreased KCC2 expression corresponded to increased BDNF and TNF-α.[23]

Therefore, within pathological states indicative of chronic inflammation, such as NP and traumatic brain injury (TBI), P2X4R activation generally promotes detrimental effects.[22,83] Within a TBI animal model, inhibition of the signalling pathways associated with microglial P2X4R saw a reduction in inflammation and apoptosis of microglia.[83] Therefore demonstrating the potential neuroprotective effects of P2X4R antagonists. However, contradictory data were found in a MS model in which the potentiation of P2X4R signalling favoured an immunosuppressive phenotype of microglia.[88,98] This promotes the remyelination response and ameliorated neurological symptoms in animal models of MS.[88]

Similarly, the dysregulated expression and activation of microglia P2X7Rs contribute to the pathogenesis of inflammation and thus neurodegenerative diseases. Due to its bifunctional nature, the P2X7R contributes both to the initiation of an inflammatory response and promotes chronic inflammatory signalling.[99] Within pathological conditions, sustained activation of microglia P2X7 receptors results in a cascade of pro-inflammatory mediators (e.g. IL-1β, TNF-α, reactive oxygen species (ROS)) and pro-apoptotic events, culminating in cell death (Figure 1.8).[100] This is then perpetuated through glutamate and ATP efflux from glia *via* the P2X7R large pore. Upon cell death, further ATP is released thereby generating a self-perpetuating cycle of inflammation.[99]

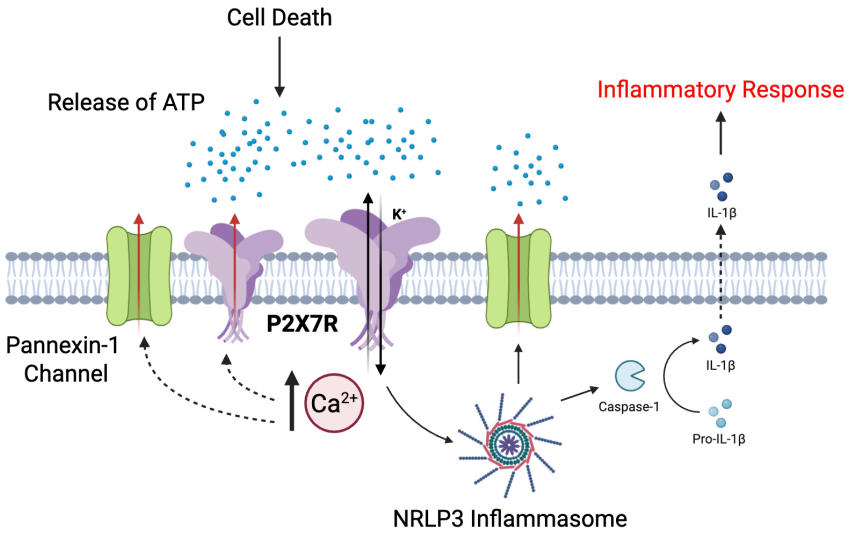

Figure 1.8 NLRP3 inflammasome activation by P2X7 receptor. Extracellular ATP binds and activates P2X7 receptors, which induces Ca^{2+} influx and K^{+} efflux. Augmented extracellular ATP concentration initiates opening of the large conductance P2X7R pore, thus amplifying the signal. K^{+} efflux induces NLRP3 inflammasome assembly and the formation of more pannexin-1 channels. NLRP3 inflammasome assembly activates caspase-1, which cleaves pro-IL-1β into IL-1β and promotes its release, thereby producing an inflammatory response. Adapted from Oliveira-Giacomelli *et al.*[100] Created with BioRender.com

A close relationship between microglia P2X7R and the nucleotide-binding oligomerization domain (NOD)-like receptor protein 3 (NLRP3) has been documented (Figure 1.8).[101] NLRP3 plays a significant role in regulating innate immunity within the CNS. Forming an NLRP3 inflammasome, the complex activates pro-caspase 1, which cleaves the inactive IL-1β precursor to thereby mediate inflammation (Figure 1.8).[100] Within a spinal cord injury animal model, upregulation of the P2X7R on the cell surface of microglia was shown to be coincident

with an increase in neuroinflammation.[101] Both the concentration of inflammatory cytokines around the lesion and the expression of NLRP3 inflammasome were upregulated by P2X7R agonists and downregulated by P2X7R antagonists.[101] These findings suggest that microglia P2X7Rs participate in spinal-cord mediated neuroinflammation *via* regulation of the NLRP3 inflammasome-dependent pathway. The role of the P2X7R in neuroinflammation has been more broadly supported by several P2X7R KO animal studies, demonstrating a significant role in mediating microglial cell death and cytokine release.[32,102,103]

The P2X4 and P2X7 receptors undoubtedly play key roles in the formation, maintenance and pathology of the CNS. However, despite the growing evidence, our understanding of how this neuromodulation and consequent neurodegeneration occurs is still not completely understood. P2X receptors make a complex contribution to microglial function, and further experimentation investigating microglial heterogeneity and dynamics during the progression of disease is required.

1.3.2 Microglia and the P2Y6 Receptor

Upregulated on microglia following neuronal damage, the P2Y6R is known as an essential regulator of inflammation and phagocytosis.[55] Through detection of diffusible UDP signals, the P2Y6R acts as a sensor for microglial phagocytosis and modulates the innate immune reaction by recruiting monocytes and macrophages to the area of concern.[55] Activation of the P2Y6R by UDP was shown to induce microglial migration and motility, two key functions necessary for phagocytosis.[59,104–106]

Within an acute amyloid model of AD, excessive microglial phagocytosis is observed following injection of amyloid beta.[55,58] However, within P2Y6 KO mice, no increase in microglia phagocytosis was observed. Comparatively, a threefold increase was detected in the wild-type mice.[58] Importantly, P2Y6 KO mice also exhibited physiological inflammation, suggesting that P2Y6R antagonists may be a viable therapeutic to prevent memory deficit and neuronal loss in AD and other brain pathologies.[55,58]

Microglia activated through Toll-like receptor (TLR)-2 or -4 can cause neuronal death by phagocytosing otherwise viable neurons. Activation of microglia by LPS *via* the TLR-4

resulted in an increase in P2Y6 expression.[107] Within PD animal models, LPS has been implicated in causing loss of dopaminergic neurons, a key characteristic of PD.[108] A study by Neher *et al*. demonstrated that neuronal loss induced by LPS was prevented when in the presence of MRS2578, a known P2Y6R inhibitor.[108] Although inflammatory activation of microglia was not affected. Additionally, P2Y6R expression is increased in the peripheral monocytes of PD patients compared to healthy controls, identifying it as a potential biomarker for the disease.[107]

Overall, UDP-P2Y6 signalling in the context of CNS disorders plays a dual role in immunity: promoting inflammation and modulating adaptive immune responses.[55] Therefore, depending on the disease state, P2Y6R activation can lead to both beneficial and harmful outcomes. Although within neurodegenerative disorders specifically, there is growing evidence that inhibiting the P2Y6R may be beneficial in reducing microglial recruitment, activation and phagocytosis.[56] However, progress in this area is significantly hampered by the lack of potent and selective P2Y6R drug-like molecules.

1.4 Modulating the Purinergic Receptors

Evidently, the relationship between microglia and the purinergic system is complex and highly dependent on the pathology at play. Both beneficial and detrimental effects within neurodegenerative diseases have been reported due to the interaction of purinergic receptors and microglia. Targeting these receptors through therapeutics remains an attractive approach to regulate immune responses occurring during neurodegeneration. However, validation of the receptors as a target is hindered by a lack of selective and potent agonists and antagonists.[28,42] The therapeutic potential of purinergic receptor antagonists is highlighted by the myriad of pharmaceutical companies and academic research groups focused on this area.[45,109] Yet, it similarly highlights the difficulties associated, as only limited clinical advancements have been made in the 21st century despite the advancement in both crystallography and chemical biology.

1.4.1 Allosteric Modulation

Due to the high level of structural similarity amongst P2X orthosteric binding sites, the design of selective orthosteric agonists and antagonists is hard to achieve. Consequently, many have adopted an allosteric drug design approach in which small-molecule drugs are designed to bind

to secondary binding sites on the targeted biomolecule.[110] Allosteric sites are generally not as conserved amongst subtypes thereby providing a plausible alternative to grant higher selectivity.[110] Binding of the allosteric ligand stabilises a conformation of the target receptor that affects either the binding affinity or efficacy of the endogenous orthosteric ligand. The allosteric modulation may result in either an enhancement (positive allosteric modulator; PAM) or inhibition (negative allosteric modulator; NAM) of the resulting activity. In the absence of the endogenous ligand, a true allosteric modulator will therefore have no functional activity.[110] However, it should be noted that the selectivity of allosteric modulators may be probe-dependent and thus should be characterised with the physiological agonist ATP.[111]

Allosteric sites on P2X receptors have been confirmed and shown to be modulated by ions (e.g. Mg^{2+}, Ca^{2+}, and Zn^{2+}), lipids (e.g. phosphatidylinositol polyphosphates), and steroids.[111,112] Of particular relevance to the current study, NAMs have been reported for the P2X4 and P2X7 receptors, and have shown particular promise in improving toxicity profiles due to less off-target binding.[112]

1.4.2 Orthosteric and Allosteric Agonists of the P2X Receptors

ATP (**1**) is the endogenous ligand for all P2X receptors, with many chemically derived analogues mimicking it structurally (**2** – **4**, Figure 1.9).[28,111] Despite the orthosteric binding site being highly conserved amongst subtypes, there is substantial variation in ATP potency. Developed analogues have thereby strived to improve on metabolic stability (e.g. 2-Methylthio-ATP, **2**), subtype selectivity (e.g. a,b-Methylene ATP, **3** – preference for P2X1 and P2X3) and toxicity (e.g. BzATP, **4**) (Figure 1.9).[111]

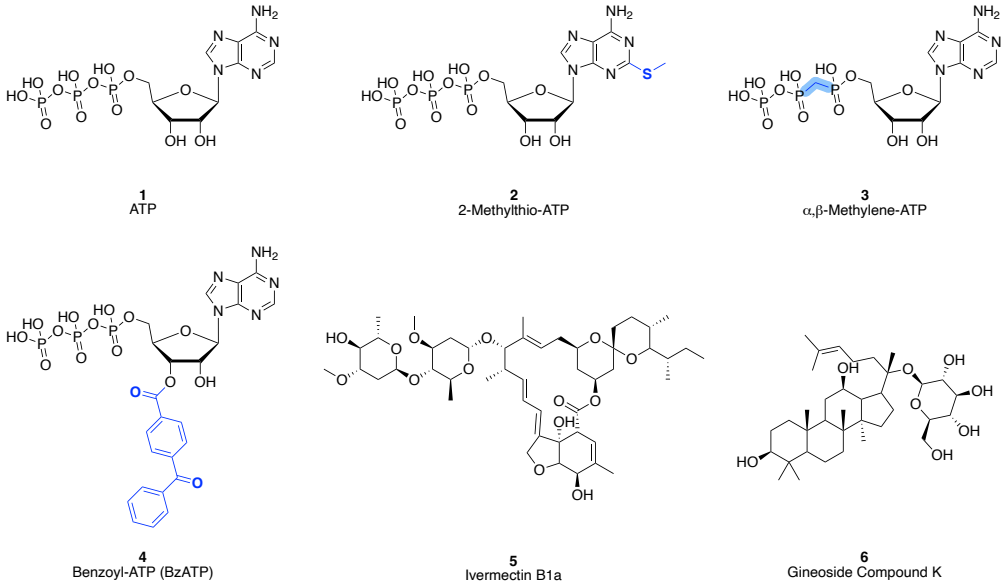

Figure 1.9 Select agonists and PAMs of P2X receptors. Structural differences between ATP analogues and ATP are highlighted in blue.

In light of the previously described chronic cycle of inflammation, enhancing the activity of the 'danger' sensing P2X7 receptor seems counterintuitive. However, there is growing evidence for the use of P2X7R PAMs as therapeutic probes beyond validation for *in vitro* assay development and pharmacological assessment.[112] Ivermectin (**5**, Figure 1.9), is a macrocyclic lactone that has been shown to be a PAM of both the P2X4 and P2X7R.[111,113,114] Most commonly known as a broad-spectrum anti-parasitic agent, Ivermectin has demonstrated utility in bacterial mouse models and cancer immunotherapy.[112,115–118] Potentiation of either receptor by Ivermectin was shown to increase bacterial killing in macrophages and improve bacterial control in a mouse model of sepsis.[116,117] Whilst mediation of purinergic signalling *via* the P2X4/P2X7/Pannexin-1 system promoted a novel form of cancer cell death in human breast cancer cells.[118]

Shown to provide immune protection against viral (dengue), bacterial (tuberculosis) and parasitic (malaria) infections, P2X7R PAMs provide an interesting alternative to traditional antimicrobials.[112] Ginsenoside compound K (**6**, Figure 1.9) was found to bind at a novel binding site in the central vestibule region of the human P2X7R, also shared by the P2X4R, and potentiate ATP activity. Accordingly, apoptotic pathways were favoured over lytic cell death pathways, a beneficial strategy in the removal of pathogens.[112,119]

1.4.3 Orthosteric and Allosteric Antagonists of the P2X7 Receptor and the Role of Adamantane

The role of P2X7R activation in the production of pro-inflammatory cytokines has encouraged an intensive pursuit for the development of P2X7R antagonists from both industry and academic institutions.[113] Encompassing a broad range of chemotypes (Figure 1.10) the NAMs boast potent and selective activity for the P2X7R.[113,120] Developed specifically to penetrate the CNS, JNJ-54175446 (**7**, Phase 2) and GSK1482160 (**8**, Phase 1) both entered clinical trials for depression and rheumatoid arthritis respectively (Figure 1.10).[121,122] Unfortunately, GSK1482160 was abandoned following a first-in-human evaluation, due to insufficient results from a pharmacokinetic (PK) and pharmacodynamic model.[121] Preliminary simulations of various dose regimens found that GSK1482160 would be unable to confer an adequate safety profile and produce the pharmacological response (> 90% inhibition of IL-1β release throughout entire dosing interval) deemed necessary to sufficiently test the P2X7 mechanism.[121] Therefore, leaving the therapeutic relevance of the P2X7R for rheumatoid arthritis a point of contention.[121]

Furthermore, P2X7R activation has been identified as a potential biomarker for the pro-inflammatory phenotype of microglia within the CNS.[123,124] Development of a P2X7R positron emission tomography (PET) radioligand provides a potential method of imaging inflammation within CNS diseases. Adaptation of reported P2X7R antagonist chemotypes have resulted in the development of numerous PET radioligands, with ^{3}H, ^{11}C (**9**) and ^{18}F (**10**) PET imaging agents described (Figure 1.10).[124,125] To date, [^{11}C]SMW139 (**9**), [^{18}F]JNJ-64413739 (**10**) and [^{3}H]JNJ-64413739 PET tracers been utilised in *in vivo* quantification of the P2X7R expression in human brain tissue.[126] P2X7R PET ligands such as **9** and **10** have demonstrated promising results as prospective tools in studying neuroinflammatory diseases such as MS and AD.[124–129] However, study sample sizes have been limited to a few individuals with the radioligands expressing variable kinetics and specificity.[126] Data from larger cohorts to understand variations in expression in the population, and a larger analysis of patients is still required before potential translation into the clinic.[126] Nevertheless, additional studies are warranted for further clinical evaluation of these P2X7R PET tracers.

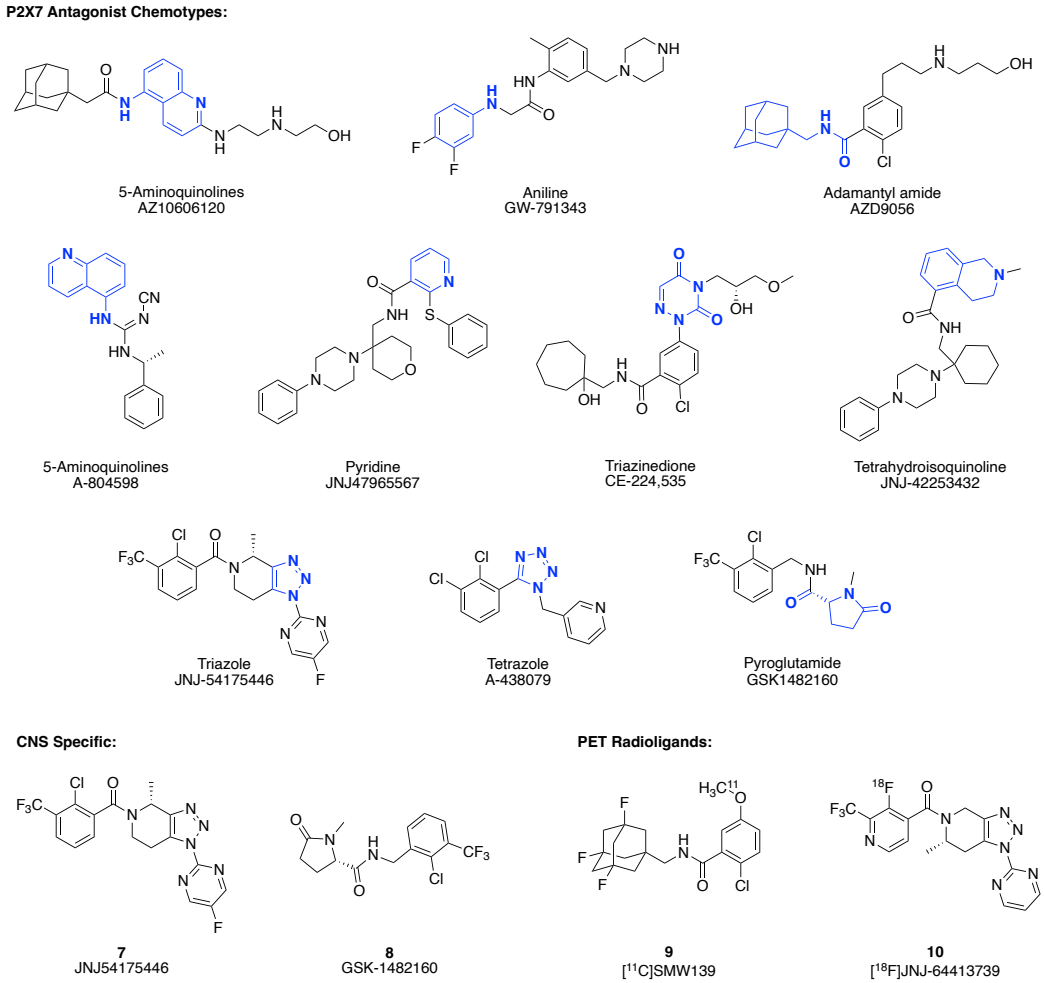

Figure 1.10 Selection of structurally diverse P2X7R antagonists and negative allosteric modulators reported as pharmacological tools or therapeutics. Compounds are arranged according to structural class (highlighted in blue).

The adamantane amides (**11**, **12** and **14**, Figure 1.11) were first reported by AstraZeneca in 2003 following a high-throughput screening (HTS) assay.[130] The initial hit (**11**) reported an acceptable potency (pIC_{50} = 6.9), although the molecular weight (MW = 540 g/mol) and lipophilicity (cLogP = 6.2) were appreciably outside the lead criteria limits.[130] However, it still provided a good starting point for a drug discovery campaign. Consequently, later iterations of this scaffold successfully demonstrated that a similar potency against P2X7 was maintained with only one amide chain (**12**) as opposed to two as seen in compound **11** (Figure 1.11).[130] This modification reduced the overall molecular weight of the analogue however, the inclusion of an aryl halide group resulted in high rates of *in vitro* rat hepatocyte intrinsic clearance (> 100).[130] In an effort to alleviate these issues, O'Brien-Brown *et al.* developed a series of novel P2X7R antagonists (**13**) entailing a hybrid scaffold between the adamantyl benzamides (**14**) and cyanoguanidine chemotype (**15**) reported by Abbott Laboratories (Figure 1.11).[131,132]

Within the adamantyl-cyanoguanidine library, the adamantyl moiety remained as the hydrophobic portion connected to various substituted aryl groups *via* a cyanoguanidine linker. Structure-activity relationship (SAR) studies around this hybrid chemotype have spanned multiple years and remain under investigation in the Kassiou group (Figure 1.11).[133]

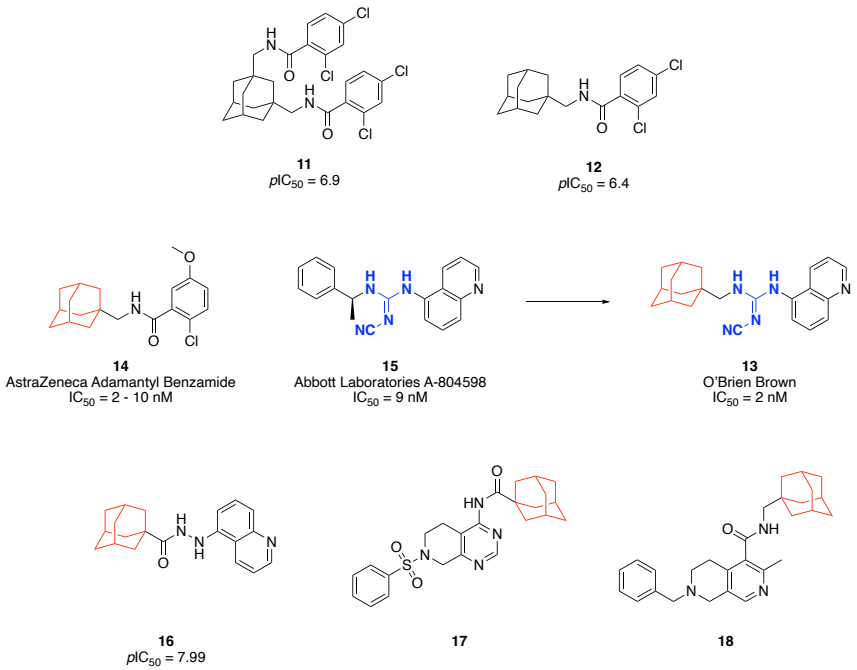

Figure 1.11 P2X7R antagonists containing adamantane. IC_{50} data reported from *in vitro* cellular assays with hP2X7R. Data extracted from Baxter, A. *et al*. **2003** (**11**, **12**, and **14**); Donnelly-Roberts, D. *et al*. **2009** (**15**); O'Brien-Brown, J. *et al*. **2017** (**13**); Nelson, D. *et al*. **2008** (**16**).

Incorporation of the adamantyl moiety in P2X7R antagonists has demonstrated enhanced efficacy across diverse chemotypes (**14, 16 – 18**, Figure 1.11).[130,134,135] By inclusion of the hydrophobic group, potency and blood-brain barrier (BBB) permeability have increased for polar compounds.[131,136,137] The adamantane functional group has been a consistent feature in new analogues and has thus been identified as a privileged structure for the P2X7R. More broadly, adamantane has also shown utility as a suitable polycyclic replacement of phenyl rings to escape the 'flat land' of modern drug discovery.[133] Drug discovery programs targeting ion channels, such as the P2X receptors, have exploited the three-dimensional space occupied by the adamantyl group to control the precise orientation of functional groups. Purposefully exploiting the unique electronic and steric characteristics of adamantane derivatives may provide a novel approach to overcome physicochemical or bioactivity challenges.[138]

1.4.4 Orthosteric and Allosteric Antagonists of the P2X4 Receptor

With the growing evidence for the active role that the P2X4R plays in coordinating the microglial response to cellular injuries and/or diseases, there has been a large incentive to develop selective antagonists as potential therapeutics.

Previous attempts to identify potent and selective P2X4R antagonists have provided allosteric ligands with poor pharmacokinetic properties and low potency. 5-BDBD (**19**, Figure 1.12), a benzodiazepine derivative, and the urea analogue BX430 (**20**, Figure 1.12) were both reported to display NAM activity with antagonistic properties at the hP2X4R.[111,123] Although comparable to the non-selective P2X antagonist TNP-ATP (**21**), they suffered from poor potency.[123] Furthermore, BX-430's functional activity was not found to translate to rat or mouse P2X4Rs making *in vivo* assays challenging.[139]

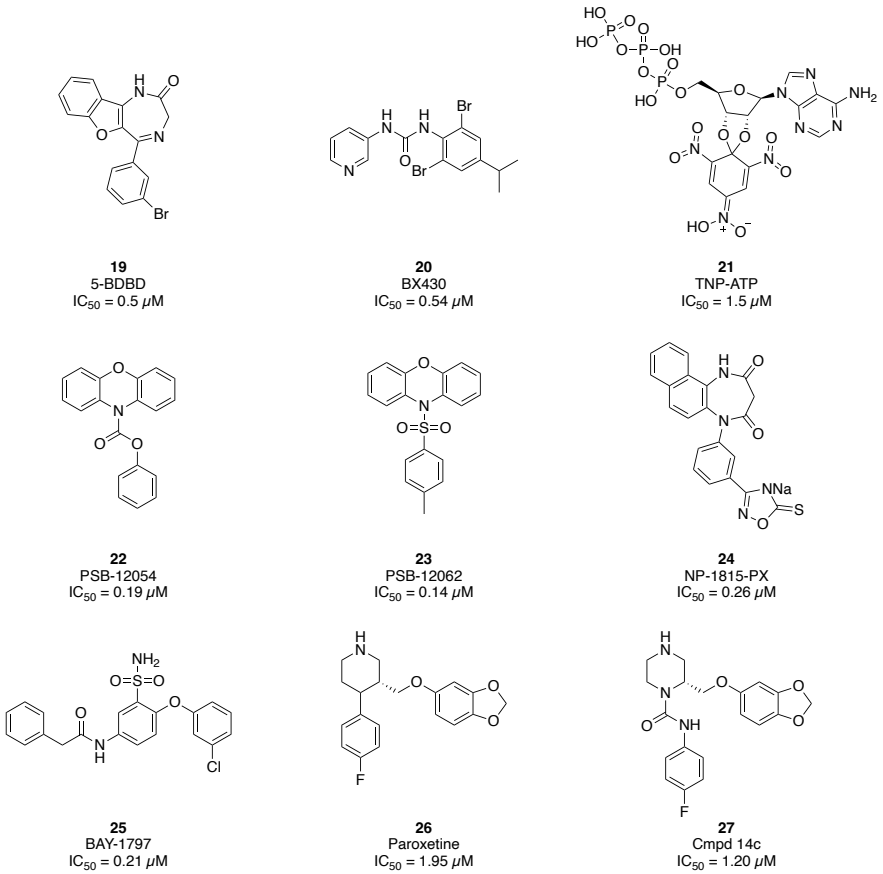

Figure 1.12 Select orthosteric and allosteric P2X4R antagonists, with reported hP2X4R IC_{50} values. Data extracted from Zarrinmayeh, H. *et al*. **2020** (**19 – 21**); Sophocleous, R. *et al*. **2022** (**22**, **23**), Matsumura, Y. *et al*. **2016** (**24**); Werner, S. *et al*. **2019** (**25**); Erlitz, K. *et al*. **2025** (**26**, **27**).

In an effort to increase potency and overcome solubility issues, two *N*-substituted phenoxazines, PSB-12054 (**22**) and PSB-12062 (**23**) were proposed (Figure 1.12).[17,123] Despite improving on potency, their highly lipophilic character resulted in low water solubility.[17] Mitigating the solubility issues faced by previous antagonists, NP-1815-PX (**24**, Figure 1.12), a carbamazepine derivative was first proposed following a chemical library screen by Matsumura *et al.* in 2016.[140] Demonstrating promising results within an NP animal pain model, **24** was also reported to have reasonable potency and selectivity amongst P2X subtypes.[140] However, it did not enter clinical development due to poor BBB permeability and poor oral absorption.[140]

Following a promising hit in a HTS assay, Bayer published BAY-1797 (**25**, Figure 1.12).[141] The arylsulfonamide derivative was reported to have an IC_{50} of 0.21 μM at the hP2X4R and demonstrated promising anti-inflammatory and anti-nociceptive events in a mouse model of inflammatory pain.[141] Despite its selectivity among P2X ion channel subtypes, BAY-1797 (**25**) exhibited a large binding affinity to the pregnane X receptor resulting in hazardous cytochrome P450s (CYP) induction.[141] In response to these findings, Bayer conducted a structure-guided optimisation study, retaining this chemotype within their later patent literature.[142–146]

Most recently, derivatives of the selective serotonin reuptake inhibitor (SSRI) paroxetine (**26**) have been reported as selective piperazine-based P2X4R antagonists (**27**, Figure 1.12).[147] Whilst reporting moderate potency, the study highlighted that increasing lipophilicity tended to improve antagonistic P2X4R activity.[147] However, the analogues similarly suffered from poor pharmacokinetic properties, with undesirable protein plasma binding and metabolic stability.[147]

While relatively little peer-reviewed literature describing novel P2X4R antagonists has been published over recent years, there has been a significant amount of patent literature produced by pharmaceutical companies. Several patents from Bayer Pharmaceuticals, Nippon Chemiphar and Wuhan LL Science and Technology Development Co (WLSTD) have been filed, presenting further P2X4R antagonists (Figure 1.13).[109,142–146,148–153]

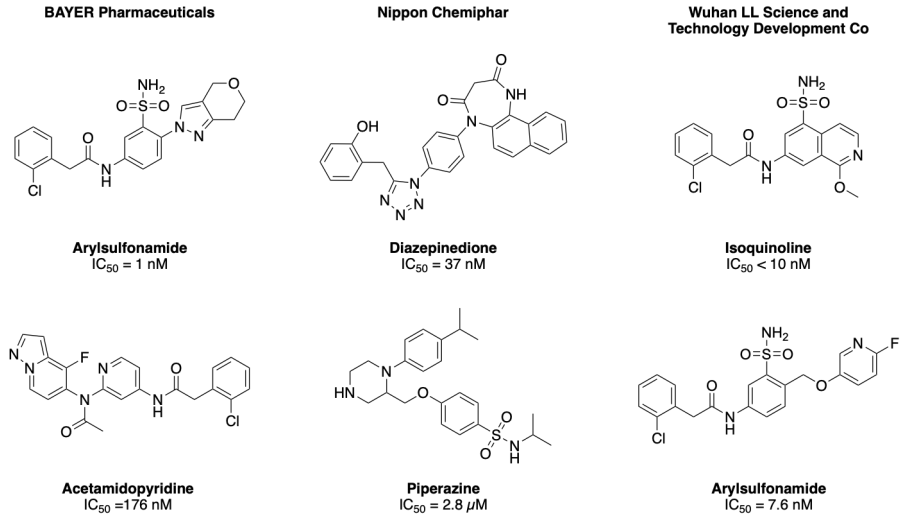

Figure 1.13 Select P2X4R antagonists filed in patent literature. Data extracted from ref.[146,149,152–155]

Earlier this year, the cryo-EM crystal structure of BAY-1797 (**25**) bound to the hP2X4R was published, providing key information about the ligand binding interactions.[8] Three molecules of BAY-1797 (**25**, Figure 1.12) were found to bind in close proximity within individual canonical allosteric binding sites located in each subunit (Figure 1.14).[8] Hydrogen bonding interactions with several adjacent residues was identified to highlight ligand binding (Figure 1.14 B and C). Of note, the sulfonamide nitrogen forms two key hydrogen bonds with the backbone carbonyl oxygen Arg87 and Val90 (Figure 1.14B). Additionally, the benzyl group forms an edge-to-face aromatic interaction with Trp84 (Figure 1.14C).[8] Orientation of BAY-1797 (**25**, Figure 1.14) was revealed to have the phenylacetamide moiety pointing outwards from the receptor, with suggestion of additional space around the motif to accommodate substitution of the phenylacetamide ring.[8]

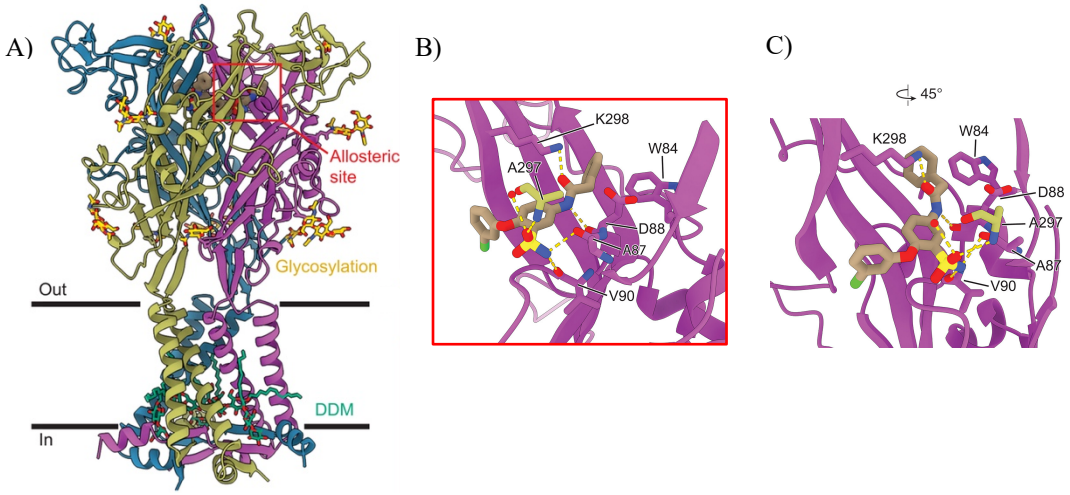

Figure 1.14 BAY-1797 binds to the allosteric site of hP2X4R. A) Ribbon representation of BAY-1797 bound to full-length wild-type hP2X4 receptor. Allosteric binding site is highlighted in red. B) Magnified view of the allosteric binding site (red box) occupied by BAY-1797. Hydrogen bonds are shown with yellow dotted lines. C) Magnified view of the allosteric site rotated by 45°, highlighting an edge-to-face interaction between Trp84 and BAY-1797. Reprinted (adapted) with permission from *Sci. Adv.* **2025**, 11, *3*. DOI: 10.1126/sciadv.adr3315 Copyright 2025 The American Association for the Advancement of Science.

Throughout the current landscape of P2X4R antagonists – including both patent and academic/scientific literature structures – extensive SAR of substituted aryl motifs within this part of the molecule has been explored. However, SAR analyses have frequently omitted sterically complex hydrophobic motifs, such as adamantane, thereby limiting insight into the steric and electronic tolerance of the P2X4 binding pocket. Given the close relationship between the P2X4 and P2X7 receptors in mind, and the corresponding correlation between successful P2X7 antagonism and the introduction of adamantane, the effect of adamantane within P2X4R antagonists can be explored.

1.4.5 P2Y6 Agonists

Unlike their P2X receptor counterpart, the P2Y receptors show limited sequence homology and have variation in endogenous ligand recognition.[43] The current landscape of P2Y6R agonists is strictly limited to pyrimidine-based nucleotide derivatives.[156,157] Ligands **28** and **29** are potent hP2Y6R agonists, predominantly used experimentally to validate the role of the P2Y6R in peripheral indications (Figure 1.15).[43,158,159] Of note, 5-OMe-UDP(α-β)-R_p isomer (**28**) has been highlighted as a potential drug for P2Y6 receptor-linked diseases such as inflammatory bowel disease, glaucoma, or cell protection post ischemic events.[159–161]

However, some have suggested that oral drug design has been hampered by the importance of retaining the negatively charged phosphates of nucleotides for their interaction with the P2Y receptors.[43] Therefore, identification of new scaffolds is imperative. High-throughput screening or machine learning could provide efficient avenues to identify new fragments in the space.

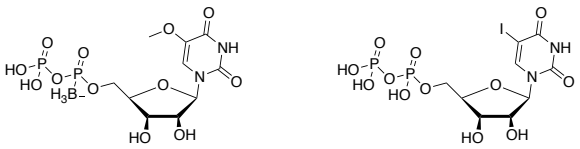

28
5-OMe-UDP(α-β)-R*p*
EC_{50} = 0.008 μM

29
5-I-UDP
EC_{50} = 0.015 μM

Figure 1.15 Pyrimidine ribonucleotides derivatives as potent hP2Y6R agonists. Data extracted from Ginsburg-Shmuel, T. *et al*. **2012** (**28**); Maruoka, H. *et al*. **2010** (**29**).

1.4.6 P2Y6 Antagonists

Selective and potent drug-like antagonists of the P2Y6R are limited. Nucleotide derivatives of UDP (**30**, Figure 1.16) have been reported, however possess low affinity and selectivity issues amongst the P2Y subfamily.[111,162,163] Currently the gold standard for *in vitro* and *in vivo* studies is the isocyanato-substituted dimeric thiourea derivative, MRS2578 (**31**, Figure 1.16). Although beneficial for evaluating the pharmacological role of the P2Y6R, it cannot be translated clinically due to its low water solubility and high reactivity.[164] The diisothiocyanate derivative is a potent (hP2Y6R IC_{50} = 37 nM), insurmountable antagonist thought to bind covalently to the receptor.[164] SAR studies identified that a longer chain length and both isothiocyanate groups were beneficial for activity.[164]

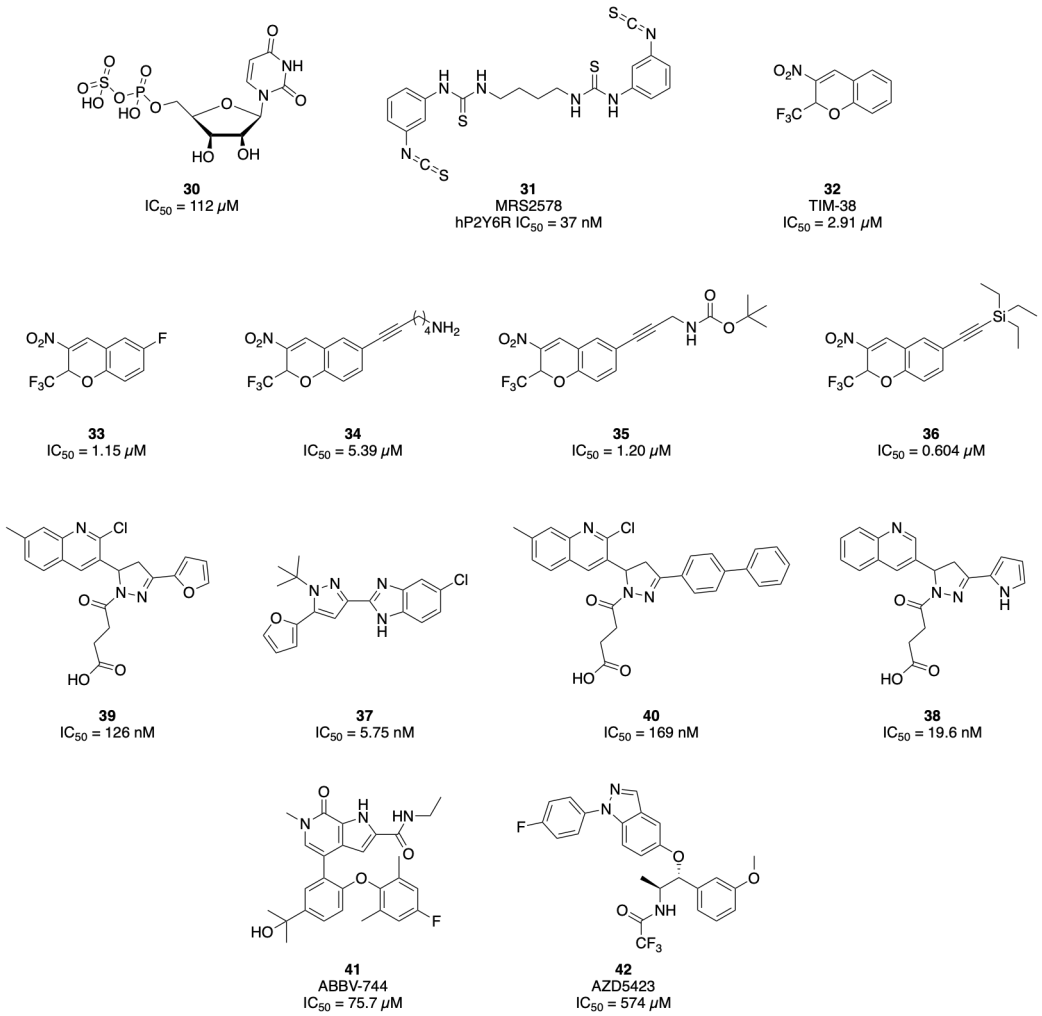

Figure 1.16 Select P2Y6R antagonists with reported activities at the hP2Y6R. Data extracted from Meltzer, D. *et al*. **2015** (**30**); Mamedova, L. *et al*. **2004** (**31**); Jung, Y. *et al*. **2021** (**32**, **35**); Jung, Y. *et al*. **2022** (**33**, **36**); Oliva, P. *et al*. **2024** (**34**); Zhu, Y. *et al*. **2023** (**37**, **39**); Zhao, Y. *et al*. **2024** (**37**, **40**); Puhl, A. *et al*. **2024** (**41**, **42**).

Another chemotype of P2Y6R antagonists are the *2H*-chromene analogues reported by Jacobson and colleagues. Initially identified following an HTS, the racemic antagonist TIM-38 (**32**, IC_{50} = 2.91 μM, Figure 1.16) was found to be selective for the P2Y6R, indicating that the activity of these compounds was not due to the general reactivity of the electrophilic nitro-group.[165] Retaining the core TIM-38 scaffold, they have continued their exploration of the scaffold by investigating substitution positioning on the unsaturated ring.[166–168] Substitution with halogens (**33**), and larger appendments linked *via* an alkyne motif (**34** and **35**) all generally resulted in decreased activity (Figure 1.16).[166–168] Introduction of silyl derivatives (**36**) was the most successful, resulting in a 5-fold increase in inhibitory activity and low cell toxicity (Figure 1.16).[167] However, despite identification of the nitro pharmacophore, the series displayed a

largely flat SAR profile, with no clear preference of positioning, chain length and terminal functionality of the ethynyl-linked substituent.[165–168] Furthermore, the 2H-chromene analogues have been reported to have off-target inhibition at adrenergic and dopamine receptors, further reinforcing the demand for novel scaffolds for P2Y6R antagonists.[168]

Recently, two novel classes of P2Y6R antagonists featuring a benzimidazole (**37**, reported in 2023) and quinoline (**38**, reported in 2024) chemotype respectively, were described independently of one another (Figure 1.16).[169,170] However, the two chemotypes reported similarities in compound design, key pharmacophores and pharmacological indication. In both studies, a structure-based virtual screening pipeline was employed utilising a P2Y6 homology model (based on the P2Y1R; PDB ID: 4XNV) constructed by Li and coworkers.[169] On the basis of speculated conformation and binding determinants, hit compounds **39** (hP2Y6R IC_{50} = 126 nM) and **40** (hP2Y6R IC_{50} = 169 nM) were reported containing identical dihydropyrazole and quinoline pharmacophores.[169,170] Optimisation of **39** by traditional SAR methods led to the lead benzimidazole compound **37** (hP2Y6R IC_{50} = 5.75 nM, Figure 1.16).[169] The dihydropyrazole motif was replaced with the generally more stable pyrazole ring, producing only a small change in bond angle of the pharmacophore.[169] Additionally, the long-chain carboxyl group was replaced by the *tert*-butyl functional group due to concerns with deprotonation of the carboxyl group at physiological pH and corresponding bioavailability challenges.[169] In contrast, Zhao *et al.*, performed SAR on hit compound **40 (**hP2Y6R IC_{50} = 168.5 nM, Figure 1.16) retaining the dihydropyrazole and quinoline pharmacophores.[170] Substitution of the biphenyl motif for smaller electron rich aromatic rings was favourable for functional activity.[170] Exploration of the chloroquinoline revealed that methyl substitution at the 7- or 8-position was well tolerated however increased activity was observed for the quinoline analogue, leading to the hit compound **38** (hP2Y6R IC_{50} = 19.6 nM, Figure 1.16).[170] Compound **37** and **38** demonstrated potent activity and selectivity, although no information was provided about toxicity and BBB permeability.[169,170] Notably, **37** and **38** were shown to effectively suppress the activation of the NLRP3 inflammasome in colon and lung tissue, respectively.[169,170] These findings highlight P2Y6R as a potential target for inflammatory diseases such as ulcerative colitis and LPS-induced lung injury.

To aid the discovery of novel P2Y6R antagonist chemotypes, Jacobson and coworkers established a machine learning model.[162] Machine learning (ML) and other computational

approaches, have demonstrated great utility for GPCR ligand discovery and have been suggested to be more efficient than HTS of assembled compound library.[162,171,172] Through various in-built algorithms, ML techniques can analyse SAR datasets, recognise patterns and infer activity based on learned molecular features. The interactions of 21 diverse structures were then evaluated at three P2YR subtypes, the P2Y6R, P2Y14R and P2Y1R.[162] All three subtypes recognise nucleoside 5'-diphosphates as their endogenous ligand and have been implicated in inflammatory pathways.[42] ABBV-744 (**41**, hP2Y6R IC_{50} = 75.7 μM, Figure 1.16), an experimental anticancer drug that acts as an epigenetic reader domain inhibitor, was identified to have a diverse range of interactions with the P2YR family.[162] ABBV-744 (**41**) was identified to inhibit the hP2Y6R in a non-surmountable fashion, suggesting a competitive antagonist mode of action.[162] However, further studies are required to confirm the exact mechanism of inhibition. Additionally, AZD5423 (**42**, Figure 1.16) was identified to weakly inhibit the hP2Y6R (hP2Y6R IC_{50} = 574 μM).[162] Possessing no clinical similarity to ABBV-744, AZD5423 (**42**) is a non-steroidal glucocorticoid receptor modulator and clinical candidate for mild allergic asthma and COPD.[173] Interestingly, the two compounds possess no structural similarity, providing two unique scaffolds for further diversification. However, both scaffolds are likely to exhibit inherent off-target activity that warrant careful consideration.

Antibodies and related biologics have provided a unique method of targeting GPCRs.[175] Currently, three monoclonal antibodies (mAbs) are commercially available for P2Y6R; however, their utility is limited by insufficient specificity and the need for rigorous controls to obtain valid and meaningful data.[175] This was evident as both western blot and immunohistochemistry experiments in wild type and P2Y6R KO tissue produced similar results for all three mAbs.[175]

Building on this foundation, further work to expand our knowledge of key pharmacophoric features is required. The development of P2Y6R antagonists will expand our understanding of the mechanisms underlying neurodegenerative diseases, thereby reducing the gap towards an effective therapeutic.

1.5 Project Aims

This dissertation focuses on the exploration, validation and diversification of purinergic receptor modulators and their corresponding effects on microglial function within a pathological state. The work presented utilised classical drug-discovery approaches to expand the pharmacophore models targeting the P2X and P2Y receptors. Following synthesis and characterisation, the compound library was assessed in appropriate *in vitro* models for the selected receptors. The results of these assays were envisioned to direct further pharmacophore exploration and lead optimisation.

1.5.1 Investigating the Effect of Adamantane Derivatives on P2X4 and P2X7 Receptor Activity and Subtype Selectivity

(Chapter 2)

The generation of compound libraries is fundamental to medicinal chemistry and plays a key role in the development and optimisation of lead candidates. **Chapter 2** investigates the impact of adamantane derivatives on P2X4 and P2X7 receptor activity and subtype selectivity. A selection of P2X4R antagonist chemotypes reported in patent literature were synthesised and diversified to include the adamantane motif. Using a range of analogues with varying functional activity enabled a comprehensive analysis of how the adamantane motif affects both potency and selectivity at the P2X4R, providing critical insights into ligand-receptor interactions.

1.5.2 Identifying Key Pharmacophores for Potent and Selective P2Y6 Antagonists

(Chapters 3 – 5)

The drug discovery pipeline of small molecules targeting the P2Y6R is limited. In the absence of P2Y6R structural data, SAR studies such as this one aim to identify key pharmacophoric features for potent and selective P2Y6R antagonists. The work in **Chapters 3 – 5** explored the diversification of the reported benzimidazole analogue **37** through traditional medicinal chemistry techniques, and a subsequent hybridisation strategy with compound **38**. A combination of both approaches has provided a strategy for compound library design that can simultaneously explore small structural changes whilst reducing potential pharmacokinetic liabilities of the lead candidate.

Chapter 2. Investigating the Effect of Adamantane Derivatives on P2X4 and P2X7 Receptor Activity and Subtype Selectivity

2.1 Introductory Remarks

Inhibition of the P2X4R *via* small molecules is well regarded as a potential solution for reducing the overactivation of microglia and the imminent pathological conditions.[17,87,176,177] Despite this, there is still a significant lack of potent and selective P2X4R inhibitors on the market, highlighting the difficulties associated with their clinical development. The arylsulfonamide antagonist, BAY-1797 (**25**) is widely used for validation of *in vivo* studies although its clinical progression is hindered by its poor pharmacokinetic profile.[141] Despite an extensive chemotype exploration conducted by Bayer, non-aromatic functionalities are often omitted from P2X4R antagonist patent literature, leaving critical pharmacophoric insights unknown. Adamantane derivatives have shown great promise in the development of novel P2X7R antagonists, improving both the potency and pharmacokinetic properties for CNS permeability.[133] With many considering the adamantane motif a privileged structure for the P2X7R, the translatability of these trends to P2X4R antagonists is of great interest.

2.1.1 Chapter Aims

The work described in this chapter aimed to explore the structural motifs influencing activity at the P2X4 receptor. Initially, the effect of the hydrophobic moieties on selectivity and potency of known P2X4R antagonist scaffolds was examined through the introduction of adamantane. This approach was intended to be further extended through the incorporation of 1,3,5-trifluoroadamantane. The highly electronegative fluorine atom forms strong, polar covalent bonds with carbon, thereby reducing the lipophilicity and blocking metabolically labile sites.

Upon successful synthesis, these candidates were to be evaluated and assessed in both P2X4 and P2X7 *in vitro* assays. The following exploratory study therefore aimed to deepen our understanding of both receptor binding domains to provide a more predictive framework for designing selective purinergic antagonists. This will therefore provide a more accurate evaluation of the effect of purinergic receptor antagonists on the modulation of microglial function within a pathological state. The outcomes of the biological evaluation of these compounds will direct further investigations.

2.2 Identification and Synthesis of P2X4 Chemotypes

Three structurally distinct P2X4R antagonist scaffolds reported in patent literature were selected for investigation (Figure 2.1 A – C).[142,148,149] Across all three scaffolds, SAR analysis of the chlorophenyl motif was limited, restricting analogues to aromatic substitutions. Previous work by the Jorgensen group on the arylsulfonamide scaffold (Figure 2.1A) suggested that aromatic interactions are not critical for P2X4R inhibition, as the adamantane analogue exhibited potency comparable to the lead compound BAY-1797 (**25**).[178] To determine whether this effect is chemotype-specific or generalisable across P2X4R antagonists, modifications of the chlorophenyl motif were kept constant (Figure 2.1D). Incorporation of adamantane allowed direct assessment of its impact on functional activity, providing insights into receptor-ligand interactions and potential strategies to achieve selectivity between P2X4 and P2X7 receptors.

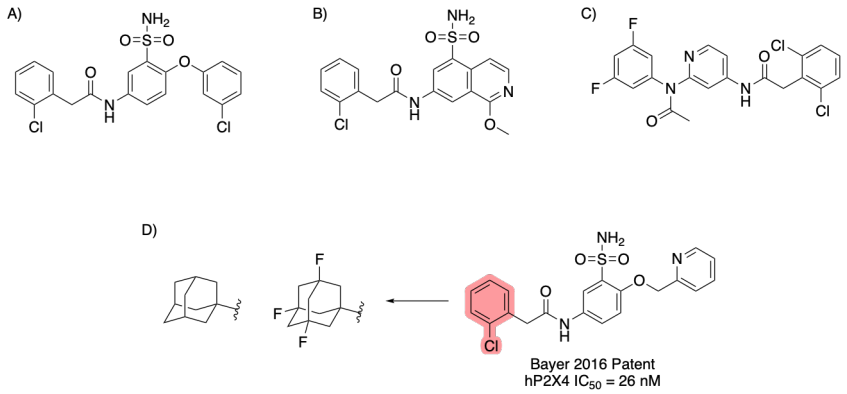

Figure 2.1 A) – C) Structurally diverse P2X4R antagonist leads sourced from patent literature. Compounds A and C were both sourced from Bayer pharmaceutical patents in 2016 and 2022 respectively. Compound B was sourced from the 2021 patent by WLSTD.[142,148,149] D) Example substitution to explore the effects of adamantane. Pictured here is an analogue selected from the Bayer 2016 patent describing arylsulfonamides.[142]

2.2.1 Arylsulfonamide Derivatives

The arylsulfonamide motif is a key reoccurring functionality amongst P2X4R antagonists. Bayer pharmaceuticals has saturated the patent space with six patents exploring the SAR surrounding the right-hand side of the molecule with substitution at both the 3 and 4 position (Figure 2.2).[142–146,179] However, despite this, very limited exploration has been made to the phenylacetamide component, with only aromatic moieties explored.

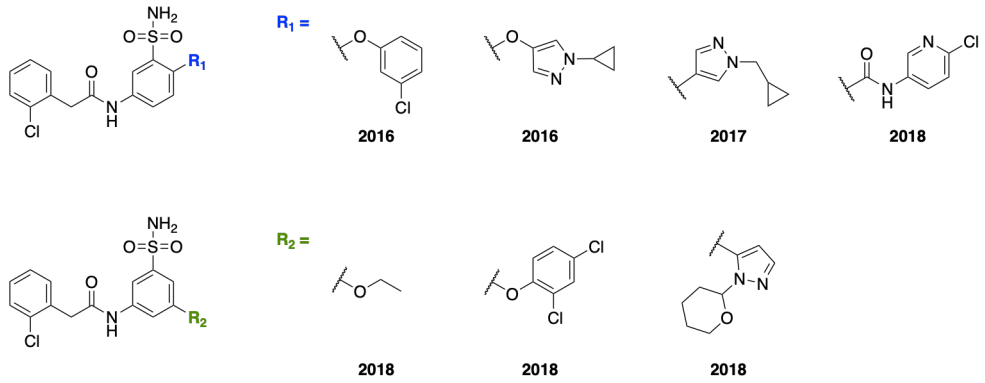

Figure 2.2 Substitution patterns explored within the arylsulfonamide chemotype described by Bayer in their patents ranging from 2016 to 2018.[142–146]

To explore the effects of adamantane thoroughly, five analogues from the 2016 patent were selected for modification (Figure 2.3).[142] The compounds were selected to encompass a range of functionalities and electronics reporting a range of functional activities from the lead compound BAY-1797 (**25**, Figure 1.12), to the most potent reported, the 4-fluoro analogue (Figure 2.3).[141,142]

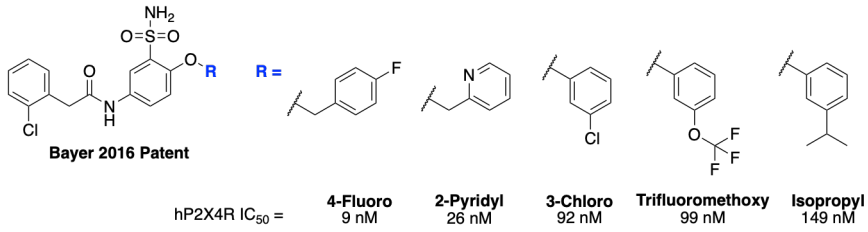

Figure 2.3 Proposed aryl sulfonamide derivatives obtained from the Bayer Pharmaceuticals 2016 patent.[142]

Two distinct pathways were utilised within the synthesis of the arylsulfonamide derivatives. Within this dissertation the synthetic pathways used will be designated the 'chlorosulfonic acid' or the 'benzyl thiol' routes, in relation to the method of installation of the sulfonyl chloride moiety. Similarly, derivatives will be referred to by their corresponding aryl ether subclasses. Aryl ether subclasses have been coined as the abbreviation signifying their key functional group distinction. For example, the 3-(trifluoromethoxy)phenyl analogues will be referred to as trifluoromethoxy analogues. A full list of subclass abbreviations is provided in figure 2.3.

2.2.1.1 Chlorosulfonic Acid Route

The 3-chloro analogues were accessed *via* a six-step synthetic approach described in scheme 2.1. The synthesis began with the installation of the sulfonyl chloride motif (**43**) through an electrophilic aromatic substitution reaction (S_EAr) between 1-fluoro-4-nitrobenzene (**44**) and chlorosulfonic acid (Scheme 2.1). The sulfonyl chloride **43** was then reacted with 2,4-dimethoxybenzylamine and subsequently treated with 3-chlorophenol to yield the aryl ether intermediate **46**. Deviating away from the reported method, the nitroarene **46** was then reduced to the corresponding aniline **47** *via* a Béchamp reduction with elemental iron in an acidic media. Traditional hydrogenation conditions of H_2/Pd were deemed not suitable for the current example due to the presence of the arylhalide and potential for Pd-halogen exchange.[180] To increase the synthetic pathways efficiency a late-stage divergent synthesis was employed through a series of amide couplings followed by the acid-mediated cleavage of the 2,4-dimethoxybenzyl (DMB) functional group to yield the final analogues (**25**, **51**, **52**) in moderate yields (Scheme 2.1).

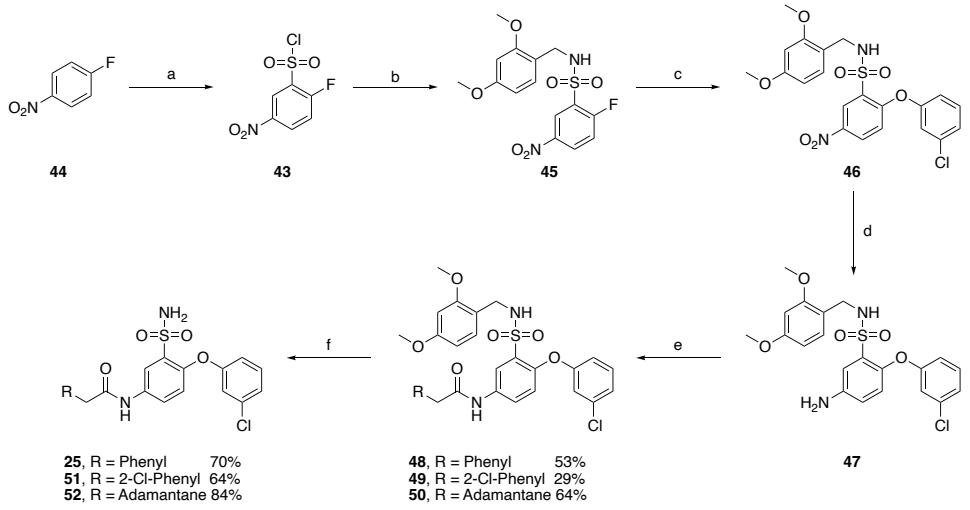

Scheme 2.1 Synthetic pathway to access 3-chlorophenol derivatives *via* installation of the sulfonyl chloride moiety by chlorosulfonic acid. *Reagents and Conditions* (a) HSO_3Cl, reflux, 48 h, 47% (b) 2,4-dimethoxybenzylamine, $NaHCO_3$, CH_2Cl_2, rt, 6 h, 34% (c) 3-chlorophenol, Cs_2CO_3, CH_3CN, reflux, 6 h, 90% (d) $Fe_{(s)}$, $NH_4Cl_{(aq)}$, EtOH, 75 °C, 3 h, 89% (e) 1. RCH_2COOH, $(COCl)_2$, cat. DMF, CH_2Cl_2, 0 °C - rt, 2 h; 2. $^iPr_2NEt$, CH_2Cl_2, rt, 3 h (f) TFA, CH_2Cl_2, rt, 1 h.

Due to the deactivating nitro group present on the 1-fluoro-4-nitrobenzene (**44**, Scheme 2.1), a large excess of chlorosulfonic acid was required to install the sulfonyl chloride moiety. Therefore, to improve the overall safety of the pathway, an alternative route to install the primary sulfonamide was required.

2.2.1.2 Benzyl Thiol Route

To overcome the above safety concerns, a benzyl thiol precursor was proposed to install the primary sulfonamide for the remaining four aryl ether subclasses (Figure 2.3). The retrosynthetic analysis of the remaining aryl ether subclasses is illustrated in figure 2.4. The primary sulfonamide **53** was envisaged to be accessed *via* an S_N2 reaction with the sulfonyl chloride, which in turn could be achieved *via* a chloro-oxidation of the benzylthiol **54**. Like the initial route, amide coupling reactions could be conducted using the aryl ether aniline **55**, which in turn could be afforded from the nitroarene **56** under Béchamp conditions. A variation to the Buchwald-Hartwig reaction could be utilised to instate the benzyl thiol (**56** and **57**) moiety to the nitroarene (**58** and **59**) which could be achieved *via* a nucleophilic aromatic substitution (S_NAr) or S_N2 depending on commercially available materials (**59** or **60**). The order of the former two steps was found to be interchangeable and assigned based on commercial availability of starting materials.

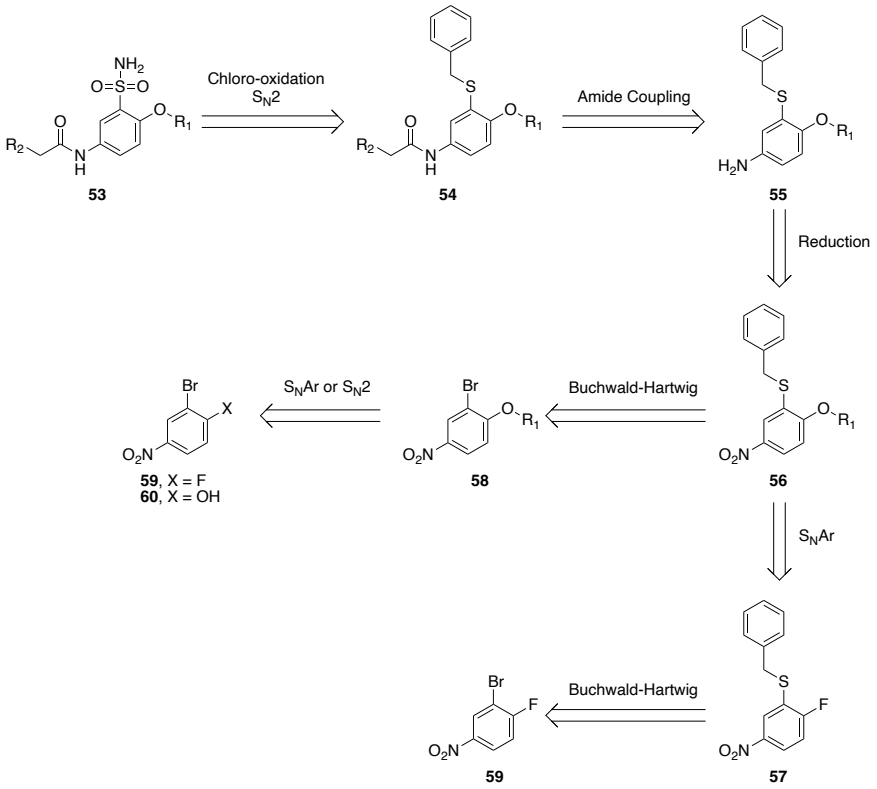

Figure 2.4 Retrosynthetic approach of accessing arylsulfonamide analogues *via* the benzyl thiol intermediate.

In order to avoid toxicity concerns and enable a more divergent synthesis, a large-scale Buchwald-Hartwig cross-coupling reaction between 2-bromo-1-fluoro-4-nitrobenzene (**59**) and benzyl mercaptan was performed (Scheme 2.2A). Facilitating the formation of the carbon-

sulfur bond, this variation of the Buchwald-Hartwig reaction employs similar conditions to that of a traditional Buchwald-Hartwig reaction, utilising $Pd_2(dba)_3$ and Xantphos as the Pd(0) source and catalyst, respectively.[181] Using these standard conditions, the desired benzyl thiol **57** was afforded in moderate yield.

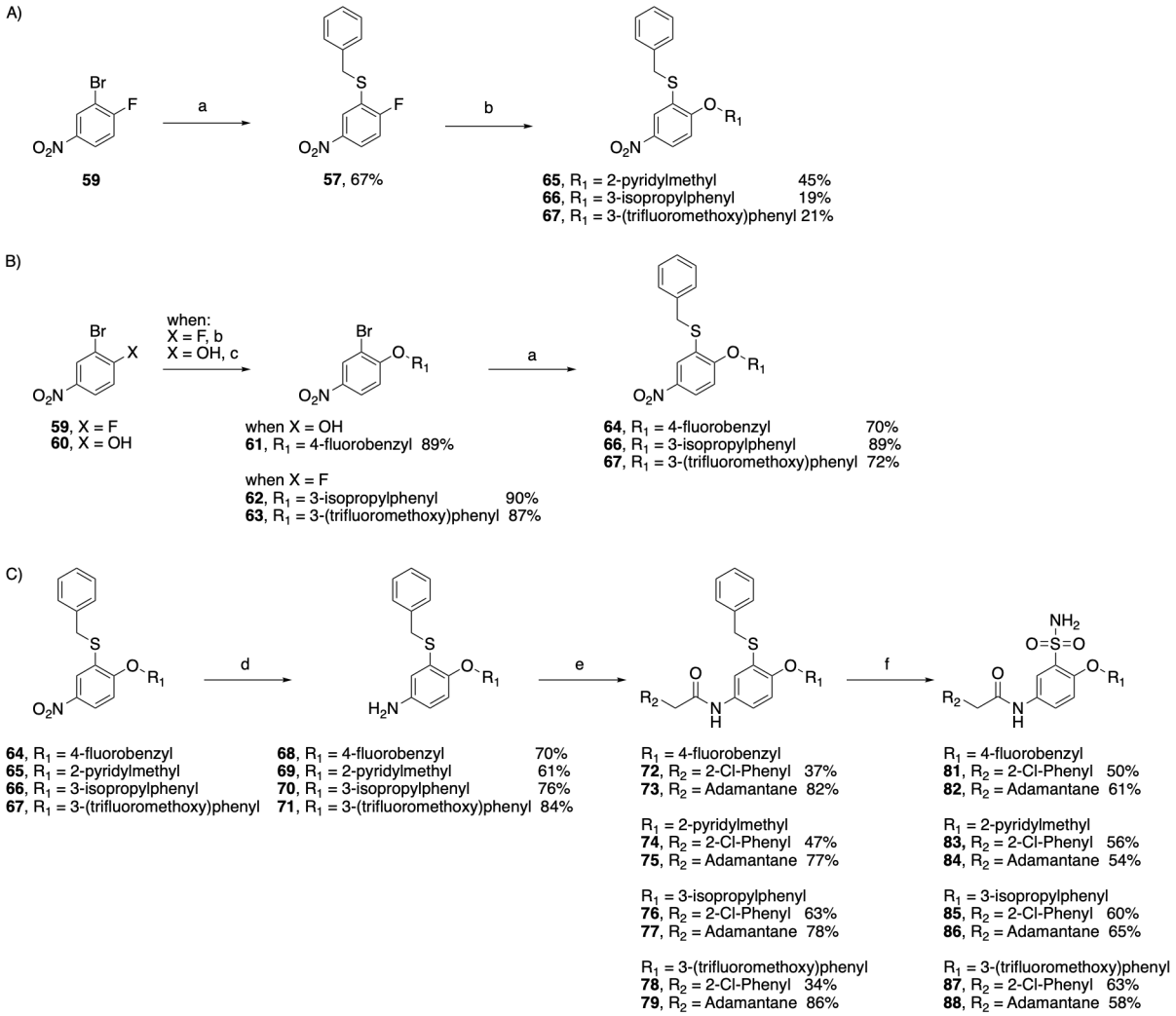

Scheme 2.2 Synthetic pathway to access various aryl ether subclasses *via* the benzyl thiol intermediate. *Reagents and Conditions* (a) Benzyl mercaptan, $Pd_2(dba)_3$, Xantphos, $^iPr_2NEt$, 1,4-dioxane, 80 °C, 18 h (b) R_1OH, Cs_2CO_3, CH_3CN, reflux, 6 h (c) 1-(bromomethyl)-4-fluorobenzene, Cs_2CO_3, CH_3CN, reflux, 6 h (d) $Fe_{(s)}$, $NH_4Cl_{(aq)}$, MeOH/THF, 75 °C, 3 h (e) 1. R_2CH_2COOH, $(COCl)_2$, cat. DMF, CH_2Cl_2, 0 °C – rt, 2 h; 2. $^iPr_2NEt$, CH_2Cl_2, rt, 3 h (f) 1. DCDMH, CH_3CN/THF/AcOH/H_2O (80:15:3:2), 0 – 5 °C, 2 h; 2. $NH_4OH_{(aq)}$, 50 °C, 2 h.

The synthetic pathway to install the aryl ether motif was largely dependent on the commercial accessibility of the relevant starting materials (Scheme 2.2). Phenol derivatives of the 2-pyridyl, isopropyl, and trifluoromethoxy allowed for a S_NAr reaction to be trialled. Standard S_NAr conditions with the benzyl thiol intermediate **57** and Cs_2CO_3 as the base, saw poor yields

across the board (Scheme 2.2A). The order of the reaction sequence was therefore reversed and installation of the aryl ether moiety prior to the Buchwald-Hartwig cross-coupling was trialled (Scheme 2.2B). Accordingly, 2-bromo-4-nitrophenol (**60**) was reacted with 1-(bromomethyl)-4-fluorobenzene under basic conditions to afford the 4-fluorobenzyl aryl ether intermediate **61** in an excellent yield (Scheme 2.2B). Aryl ethers **61** – **63** were then subsequently treated under the Buchwald-Hartwig conditions described earlier, which afforded the desired benzyl thiols (**64**, **66** and **67**, Scheme 2.2B) in substantially better yields to that of the initial reaction sequence (Scheme 2.2 A and B).

With the aryl ether intermediates **64** – **67** in hand, a functional group interconversion (FGI) of the nitro group under Béchamp conditions yielded the respective anilines **68** – **71** in excellent yields (Scheme 2.2C). The amide derivatives **72** – **79** were achieved *via* an acid chloride mediated amide coupling reaction. The acid chloride intermediate of both the 2-(2-chlorophenyl)acetic acid and 1-adamantaneacetic acid were first synthesised independently with oxalyl chloride and catalytic DMF, followed by coupling with the aryl ethers **64 – 67** (Scheme 2.2C) to yield the amide products (**72** – **79**).

The transformation of benzyl thiol into the corresponding primary sulfonamide (**81** – **88**) was initially explored using a sequential chloro-oxidation/S_N2 approach reported by Veisi *et al*.[182] The direct oxidative conversion to the arenesulfonyl chloride is accomplished using 1,3-dichloro-5,5-dimethylhydantoin (DCDMH**, 80**, Figure 2.5A) as the chlorine source.[182,183] The proposed mechanism describes the reaction proceeding *via* the formation of the sulfoxide (**I**, Figure 2.5A) and a chlorosulfoxonium cation (**II**, Figure 2.5A) as key intermediates. Following an S_N1-like mechanism, oxidative cleavage of the benzylic C-S bond is facilitated due to the resonance stabilised benzylic carbocation (Figure 2.5B).[183] It is proposed that DCDMH (**80**) serves as the direct source of chlorine, rather than generating chlorine gas *in situ*. This was supported through experimentation as no formation of gas was observed within the reaction. Due to the instability of the sulfonyl chloride, an aqueous workup performed at temperatures cooler than 10 °C is necessary prior to conversion to the primary sulfonamide to remove 5,5-dimethylhydantoin and any benzylic by-product formed. Finally, treatment of the sulfonyl chloride with ammonium hydroxide results in the formation of the target primary sulfonamide (**81** – **88**, Scheme 2.2C).

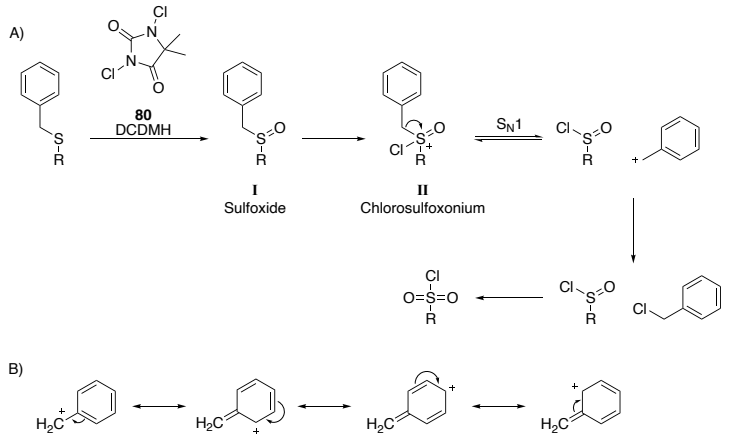

Figure 2.5 Proposed mechanism (A) of chloro-oxidation to yield the sulfonyl chloride facilitated by the resonance stabilised benzylic carbocation (B).[183]

Although successful for the 4-fluoro and 2-pyridyl analogues, over reaction was observed amongst the isopropyl, and to a minor extent the trifluoromethoxy derivatives (Table 2.1). Over-chlorination was observed ortho to the isopropyl and para to the ethoxy bridge on the isopropylbenzene (**89** and **90**, Figure 2.6A), and was fully characterised by mass spectrometry, NMR and X-ray crystallography (Appendix 1). DCDMH (**80**) is considered an alternative N-Cl reagent to *N*-chlorosuccinimide (NCS) and can act as a source of electrophilic and radical chlorine.[184–186] A plausible mechanism for its formation is shown in figure 2.6; in which the electron-donating nature of both the isopropyl and ethoxy functional groups direct a S_EAr like mechanism to allow for the excess DCDMH to chlorinate the aryl ring. The proposed mechanism was supported by the observed correlation between DCDMH equivalents and yield of over-chlorinated product (Table 2.1). As the equivalence of DCDMH was reduced, a concurrent reduction in the over-chlorinated product was also observed by high performance liquid chromatography (HPLC). Although reducing the equivalence of DCMDH circumvented the formation of the undesired by-product, it also slowed the reaction considerably, resulting in residual starting material after prolonged reaction times. The over-chlorinated product for the trifluoromethoxy derivative was only observed in trace amounts and therefore the substitution pattern was unable to be confirmed.

Table 2.1 Analysis of relative ratio of over-reacted product with varying equivalents of DCDMH.

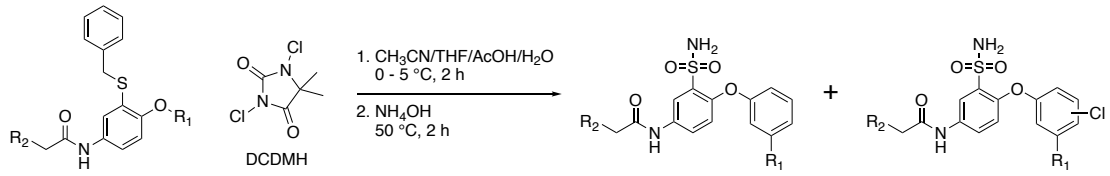

SM	R_2 Group	Aryl Ether (R_1)	DCDMH (eq)	Product : Over-reacted[a]
77	Adamantane	^{i}Pr	3	0 : 98
77	Adamantane	^{i}Pr	2	59 : 39
76	2-Chlorophenyl	^{i}Pr	2	52 : 45
79	Adamantane	OCF_3	2	98 : 0
78	2-Chlorophenyl	OCF_3	2	91 : 6
78	2-Chlorophenyl	OCF_3	1	98 : 0

[a]Ratio of product to over-reacted compound is represented %Area as per HPLC data acquired from 1 mg/mL of compound at 254 nM (methods provided in **7.1**). Remaining % is attributed to other impurities.

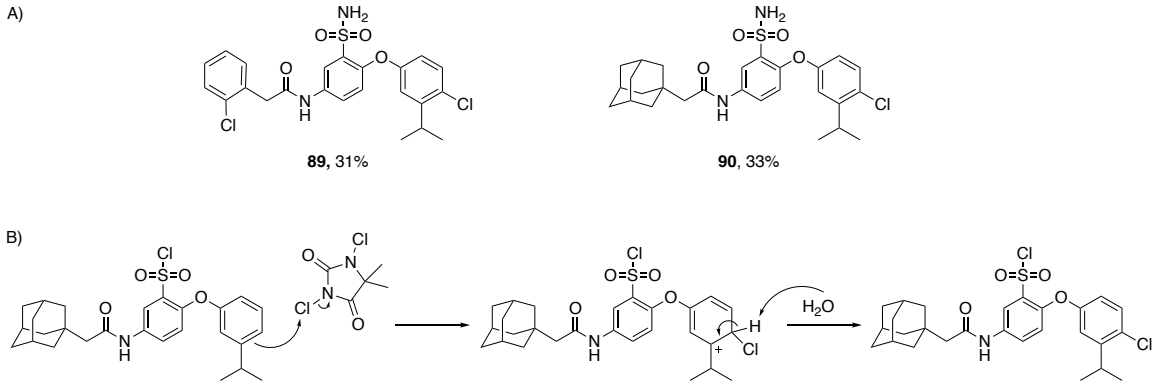

Figure 2.6 A) Over chlorinated products **89** and **90** isolated. B) Proposed reaction mechanism of over-chlorinated product. Excess DCDMH promoted a S_EAr like mechanism to form the over-reacted product.

Although the mixture of the over-reacted by-product (**89** and **90**) and the desired primary sulfonamide (**85** and **86**) could be separated by semi-preparative HPLC, the relatively low yield amongst all the isopropyl derivatives warranted further investigation into alternate reaction conditions. Consequently, an alternative method utilising NCS was explored for the 2-chlorophenyl isopropyl analogue (Scheme 2.3).[187–189] Employing NCS as an oxyhalogenation reagent allowed for a milder and more practical method of accessing the sulfonyl chloride *via* a radical mechanism. Able to be performed at room temperature the new protocol circumvented the need for the workup to be carried out at cold temperature. Utilising

recrystallised NCS the reaction proceeded cleanly in 42% yield with no signs of over-chlorination (Scheme 2.3). Therefore, the following method should be utilised within future work to improve reaction efficiency and reduce the potential of over-reaction.

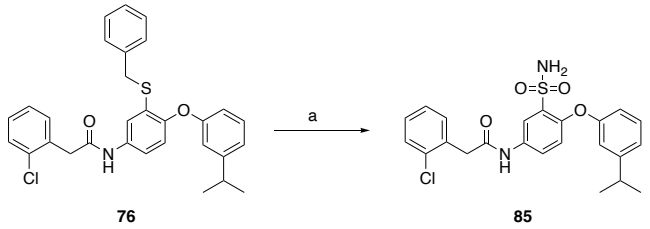

Scheme 2.3 Conversion of benzyl thiol (**76**) to primary sulfonamide (**85**) by NCS. *Reagents and Conditions* (a) 1. NCS, CH_3CN/THF/AcOH/H_2O (80:15:3:2), rt, 2 h; 2. THF, $NH_4OH_{(aq)}$, rt, 1 h, 42%

2.2.2 Isoquinoline Derivatives

Fused ring systems were also explored through the WLSTD 2021 series of isoquinoline structures (Figure 2.7).[149] WLSTD presented a series of isoquinoline, quinoline and tetrahydroisoquinoline core structures each containing the characteristic sulfonamide motif, with the patent claiming 'high antagonist activity, excellent selectivity, low toxicity and excellent metabolic stability'.[149] Analysis of the provided structures showed increased activity when substituting at the C1 position of the isoquinoline motifs. Accordingly, three analogues were chosen, limiting the minimum functional activity to an IC_{50} of 200 nM. Within this dissertation the isoquinoline derivatives will be named in reference to the C1 substitution, i.e. chloro, methoxy and isopentyloxy (Figure 2.7).

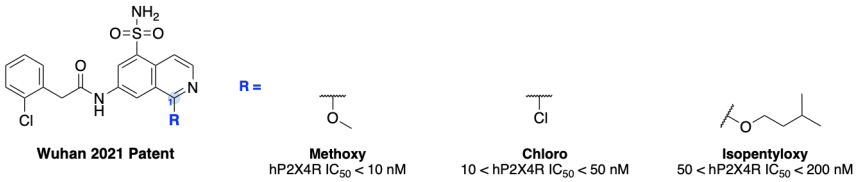

Figure 2.7 Selected isoquinoline analogues for future modification. Analogues were selected from each of the reported functional activities ranges within the WLSTD 2021 patent.[149] The C1 position of the isoquinoline is highlighted in blue.

2.2.2.1 Retrosynthesis of Isoquinoline Derivatives

Access to the final isoquinoline series (**91**) was envisioned to be achieved *via* a 7-step synthetic approach shown in Figure 2.8. For each of the analogue families (i.e. substitution at C1) slight variation to the order of synthesis is required. A late stage deprotection/S_NAr reaction of **92**

with sodium methoxide allows for the divergent synthesis of both the chloro and methoxy analogues. Whereas for the isopentyloxy analogues the isopentyloxy moiety was introduced earlier through a S_NAr reaction. By incorporating a late-stage divergent step, such as the amide coupling (**92**), efficiency of the synthetic pathway is increased allowing for a more diverse library. A Buchwald-Hartwig reaction was initially proposed to instate the *tert*-butyl carbamate (**93**), which is then deprotected to afford the required aniline **94**. The protected 7-bromo-1-chloroisoquinoline-5-sulfonamide (**95**) was anticipated to be formed *via* a S_EAr reaction (**96**) and successive amination (**97**) and sulfonamide coupling, from commercially available 7-bromo-1-chloroisoquinoline (**98**). A *N,N*-dimethylformimidamide (DMI) protecting group was initially utilised to mirror the synthetic pathway featured in the patent.[149]

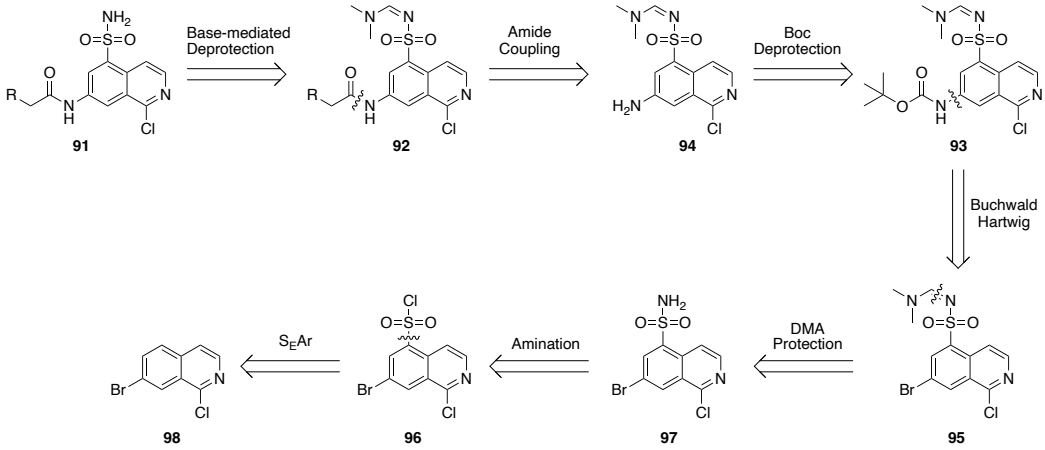

Figure 2.8 Retrosynthetic pathway for the isoquinoline derivatives presented in the WLSTD 2021 patent.[149]

2.2.2.2 Synthesis of Sulfonamide Protected Intermediates

7-Bromo-1-chloroisoquinoline (**98**) was treated with excess chlorosulfonic acid at elevated temperatures to yield the sulfonyl chloride **96** (Scheme 2.4). Due to the electron deficient nature of the pyridinyl ring in the isoquinoline, S_EAr favours the benzenoid ring.[190] Regioselective substitution at the C5 position predominated with no C8 substituted regioisomers isolated. Substitution at the C5 position was consistent with the *J*-coupling values observed and 2D NMR data (Appendix 2).

The DMI protected sulfonamide (**95**) was accessed *via* a nucleophilic addition with *N,N*-dimethylformamide dimethyl acetal (DMF-DMA) succeeding amination of the sulfonyl

chloride **96** with ammonium hydroxide (Scheme 2.4). With the protected sulfonyl isoquinolines in hand a C–N cross-coupling reaction was proposed at the aryl-bromide to introduce an aniline handle.

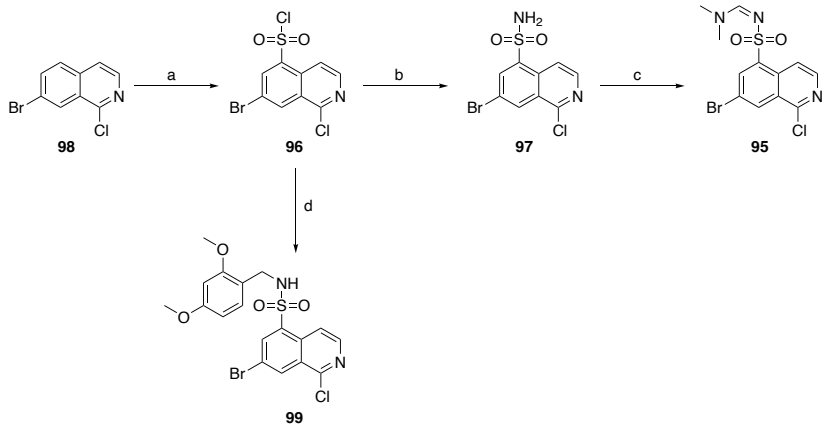

Scheme 2.4 Synthesis of protected sulfonamide intermediates **95** and **99**. *Reagents and Conditions* (a) HSO_3Cl, reflux, 120 h, 46 – 51% (b) NH_4OH, 50 °C, 3 h, 80% (c) DMF-DMA, DMF, 70 °C, 3 h, 90% (d) 2,4-dimethoxybenzylamine, $NaHCO_3$, CH_2Cl_2, rt, 6 h, 60 – 65%.

2.2.2.3 Pd-Catalysed Aminations

The Buchwald-Hartwig amination is a common strategy incorporated in drug discovery to access C–N bonds *via* a palladium catalysed cross-coupling.[181] Despite the extensive literature precedence for a broad-range of NH-containing substrates, several challenges still exist for the direct amination of heteroaryl halides with ammonia.[191,192] Productive catalysis is hindered by ammonia displacing the ancillary ligands to form unreactive ammonia complexes of palladium.[192] In addition, utilising ammonia gas as a coupling partner is not feasible due to the inherent safety and handling risks, coupled with the potential to generate polyarylated side products.[192] Consequently, ammonia surrogates are employed to install the primary aniline motif.[192] Of these, *tert*-butyl carbamate is most frequently used as an ammonia equivalent as it is readily available and has a facile deprotection method. In general, however, Buchwald-Hartwig methodology for carbamates is limited, and mirror those employed for amide-type nucleophile coupling.[192]

Conditions reported in the parent patent were initially trialled (Table 2.2, entry 1), utilising $Pd(dppf)Cl_2$ and Xantphos as the Pd-catalyst and ligand respectively.[149] It was initially trialled with the chelating ligand Xantphos in an effort to prevent the formation of unwanted κ2

interactions between the amide and Pd centre.[193] After 24 hours, TLC analysis and mass spectrometry of the reaction mixture showed a complex reaction mixture consisting predominantly of starting material. As starting material was being recovered, it was postulated that oxidative addition of the Pd(0) source into the C-X bond was not occurring sufficiently. Therefore, the palladium catalyst was substituted for $Pd(dba)_2$, a Pd(0) species (Table 2.2, entry 2). Although more unstable, Pd(0) sources are more reactive as they do not require to be first reduced to the active form.[192] Unfortunately, this too resulted in a complex reaction mixture with no presence of product by crude ESI-MS analysis. Solubility concerns were addressed by employing biphasic conditions utilising tetrabutylammonium as a phase transfer catalyst (Table 2.2, entry 3).[181] However, the reaction produced a complex reaction mixture containing starting material and trace amounts of deprotected sulfonamide. Deprotection of the sulfonamide was postulated to be due to the presence of sodium hydroxide.

Table 2.2 Buchwald-Hartwig conditions for the synthesis *tert*-butyl carbamate isoquinolines (**93** and **99**), from protected sulfonamide intermediates **95** and **99**.

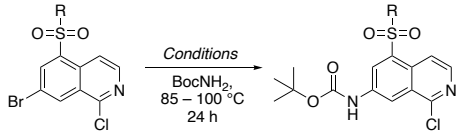

Entry	SM	Conditions	Yield
1	**95**	$Pd(dppf)Cl_2$, Xantphos, Cs_2CO_3, 1,4-dioxane	— [a]
2	**95**	$Pd(dba)_2$, Xantphos, Cs_2CO_3, 1,4-dioxane	— [a]
3	**95**	$Pd(dba)_2$, Xantphos, TBAB, toluene/NaOH (2M)	— [a]
4	**99**	$Pd(dba)_2$, Xantphos, TBAB, toluene/NaOH (2M)	— [a]
5	**99**	$Pd(dppf)Cl_2$, Xantphos, Cs_2CO_3, DMF	— [a]
6	**99**	$Pd(dba)_2$, Xantphos, Cs_2CO_3, 1,4-dioxane	— [a]
7	**99**	$Pd(dba)_2$, XPhos, Cs_2CO_3, *t*-BuOH	— [a]

[a] Complex reaction mixture as indicated by TLC analysis.

Reported conditions for the Buchwald-Hartwig of carbamates utilise a strong non-nucleophilic base like sodium *tert*-butoxide.[194,195] Due to the similar pK_a of NaOH and NaOtBu, the synthetic route was redirected and a base stable sulfonamide protecting group, of DMB (**99**) was trialled instead (Scheme 2.4). However, this proved equally unsuccessful with a complex

reaction mixture being produced (Table 2.2, entry 4). Subsequent Buchwald-Hartwig trials with **99** were attempted using caesium carbonate as a base, as there was literature precedence.[193,194] Disappointingly, complex reaction mixtures were also experienced when utilising both a Pd(0) and Pd(II) catalyst as reported in the patent (Table 2.2, entries 5 and 6).

Dialkylbiaryl phosphone ligands, such as XPhos, have been shown to be more effective with unactivated arylhalides, or weak-nucleophile coupling partners.[194,196] By increasing the steric bulk and strong electron-donor ability of the ligand, XPhos, acts to promote formation of the active [L_1Pd^0] complex and reductive elimination.[196] However, within this system substitution of Xantphos for XPhos (Table 2.2, entry 6) was not successful and similarly resulted in a complex reaction mixture.

Substitution of coupling partners was also explored through the introduction of an alternative aniline surrogate, di-*tert*-butyl-iminodicarboxylate (Boc_2NH, Table 2.3, entry 1). The enhanced N-H acidity of the secondary amine (pK_a = 9.4, predicted by MarvinSketch) relative to the primary amine (pK_a = 15.9, predicted by MarvinSketch) has been suggested to be advantageous when using standard carbonate bases (pK_a ≈ 10).[192] Unfortunately, these conditions failed to yield the desired product, resulting only in the recovery of starting materials (Table 2.3, entry 1). Additional efforts utilising similar Buchwald-Hartwig conditions, with 2-((3*r*,5*r*,7*r*)-adamantan-1-yl)acetamide (**101**) as the nucleophile, proved equally unsuccessful (Table 2.3, entry 2).[192]

Benzophenone imine is an attractive alternative ammonia equivalent used for the generation of primary anilines.[197,198] It provides a practical nucleophile in C–N cross-coupling reactions due to its inability to form diarylated side products and low steric hindrance.[198] Additionally, the resulting *N*-aryl imine provides a stable protecting group with facile removal methods accommodating for a broad scope of neighbouring functional groups.[193,196,199] Compound **99** was treated with freshly distilled benzophenone imine, $Pd(OAc)_2$ and *(rac)*-BINAP (Table 2.3, entry 3). A complex reaction mixture was indicated by TLC analysis, with no indication of product formation by mass spectrometry.

Table 2.3 Variation of amine surrogates within Buchwald-Hartwig conditions.

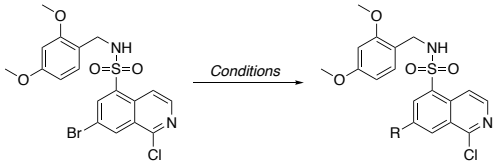

Entry	R	Conditions	Yield
1	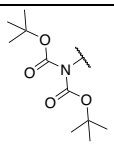	Boc_2NH, $Pd(dba)_2$, Xantphos, Cs_2CO_3, 1,4-dioxane, 85 °C, 48 h	S.M.[a]
2	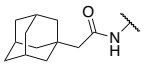	**101**, $Pd(dba)_2$, Xantphos, Cs_2CO_3, 1,4-dioxane, 85 °C, 24 h	S.M.[a]
3	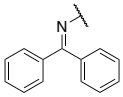	Benzophenone imine, $Pd(OAc)_2$, *(rac)*-BINAP, Cs_2CO_3, toluene, 100 °C, 24 h	___ [b]

[a] S.M. represents recovered starting material, as no reaction occurred. [b] Complex reaction mixture as indicated by TLC analysis.

Further optimisation of the Buchwald-Hartwig conditions could potentially overcome these limitations. Such optimisation might involve exploring multiple ligand systems (Pd_2dba_3 in combination with P(*t*-Bu)$_3$, or *t*-BuBrettPhos), stronger bases (sodium *tert*-butoxide) and different ammonia surrogates (LHMDS).[192] However, the decision was made to redirect efforts towards Ullman coupling methodologies, given their reported success with weakly nucleophilic substrates.[192]

2.2.2.4 Cu-Catalysed Aminations

The unsuccessful optimisation of Buchwald-Hartwig conditions necessitated a shift toward copper-catalysed amination methodologies. Ullmann couplings have demonstrated great utility in expanding the scope of weakly nucleophilic amines compatible with C–N bond-forming reactions.[192,200] Cu-catalysed reactions have been found to be advantageous when using amidic substrates due to their propensity to form bidentate complexes with the copper catalyst.[192] Consequently, the concentration of the active copper species is increased, promoting the forward reaction. Moreover, chelating ligands such as amino acids and 1,2-diamines, have accelerated the reaction rate of Ullmann couplings whilst circumventing the traditionally harsh conditions.[200,201]

Efforts to utilise Ullmann-type couplings for the synthesis of **93** or **100** encountered significant challenges (Table 2.4). Initial attempts employed cuprous iodide as the catalyst, in conjunction with the amino acid ligand L-proline and caesium carbonate as the base. Both *tert*-butyl carbamate and ammonium hydroxide (Table 2.4, entries 1–3) failed to yield the desired product, resulting only in the recovery of starting materials. Additional attempts utilising similar copper-catalysed systems, with varying ligands (Table 2.4, entry 4) and copper catalysts (Table 2.4, entry 5), proved equally unsuccessful.[202,203] Finally, the combination of cuprous iodide and 4-hydroxy-L-proline at elevated temperatures within a sealed tube yielded the desired aniline (**102**) in moderate yields (Table 2.4, entry 6).[204] Notably, these optimised conditions were able to be translated amongst the methoxy and isopentyloxy analogues in higher yields (Scheme 2.5).

Table 2.4 Ullmann conditions for the synthesis of amino-isoquinoline intermediates.

Entry	SM	Conditions	Yield
1	**95**	$BocNH_2$, CuI, L-proline, Cs_2CO_3, DMSO, 80 °C, 24 h	S.M.[a]
2	**99**	$BocNH_2$, CuI, L-proline, Cs_2CO_3, DMSO, 80 °C, 24 h	S.M.[a]
3	**99**	NH_4OH, CuI, L-proline, Cs_2CO_3, DMSO, 80 °C, 24 h	S.M.[a]
4	**99**	NH_4OH, CuI, DMEDA, DMSO, 100 °C, 16 h	S.M.[a]
5	**99**	NH_4OH, Cu_2O, NMP/H_2O (1:1, v/v), 80 °C, 24 h	—[b]
6	**99**	NH_4OH, CuI, 4-OH-L-proline, Cs_2CO_3, DMSO, 140 °C, Sealed, 18 h	40%

[a]S.M. represents recovered starting material, as no reaction occurred. [b] Complex reaction mixture as indicated by TLC analysis.

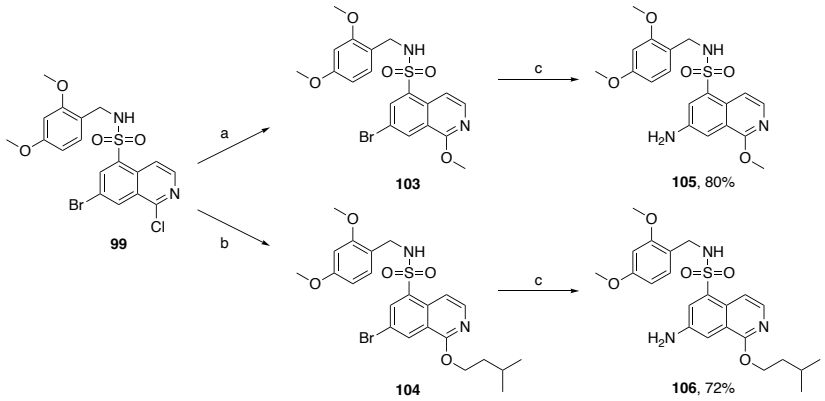

Scheme 2.5 Synthesis of methoxy (**105**) and isopentyloxy aniline (**106**) derivatives. *Reagents and Conditions* (a) NaOMe, MeOH, reflux, 16 h, 72% (b) isoamyl alcohol, NaH, DMF, 90 °C, 6 h, 74% (Table 2.5, entry 3) (c) NH_4OH, 4-OH-L-proline, CuI, Cs_2CO_3, DMSO, 140 °C, sealed tube, 18 h.

Modification of the chloro motif to the corresponding methoxy and isopentyloxy analogues occurred *via* a S_NAr of the protected sulfonamide intermediate **99** prior to amination (Scheme 2.5). Treating **99** with a large excess of sodium methoxide in anhydrous methanol afforded the methoxy-bromo analogue (**103**) in moderate yields (Scheme 2.5). In contrast, reaction of **99** with isoamyl alcohol in the presence of sodium hydride (NaH) at ambient temperature was unsuccessful, with only starting material recovered (Table 2.5, entry 1). Heating the reaction to reflux (Table 2.5, entry 2), was also unsuccessful. Stringent anhydrous conditions were found to be crucial for the success of this reaction. Incomplete conversion was observed when a greater excess of both base and anhydrous alcohol was utilised at elevated temperature (Table 2.5, entry 3), resulting in both product and starting material. Interestingly, the yield suffered when the reaction was conducted in an isoamyl alcohol (anhy.)/*N,N*-dimethylformamide solvent mix (7:2) (Table 2.5, entry 4). Anilines **105** and **106** were achieved *via* the optimised Ullman Coupling conditions described in table 2.4, entry 6 (Scheme 2.5).

Table 2.5 S_NAr conditions to access isopentyloxy bromo intermediate **104**.

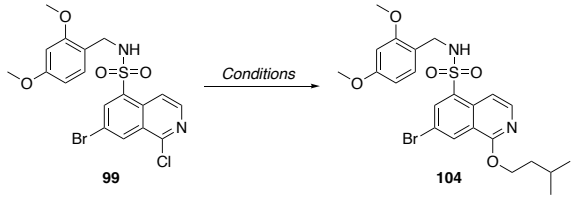

Entry	Conditions	Yield
1	Isoamyl alcohol (1.2 eq), NaH (1.5 eq), DMF, rt, 16 h	S.M.[a]
2	Isoamyl alcohol (1.2 eq), NaH (1.5 eq), anhy. DMF, reflux, 16 h	S.M.[a]
3	anhy. Isoamyl alcohol (2.4 eq), NaH (3 eq), anhy. DMF, reflux, 16 h	74%
4	NaH (3 eq), anhy. isoamyl alcohol:DMF (7:2), reflux, 24 h	26%

[a]S.M. represents recovered starting material, as no reaction occurred.

Amide derivatives **107** – **112** were synthesised *via* an amide coupling reaction with the appropriate acetic acid. A range of coupling agents (HATU, HBTU, EDC/HOBt and T_3P) were trialled, with polyphosphoric anhydride (T_3P) reporting the most consistent yields (Scheme 2.6). Treating compounds **107** – **112** with trifluoroacetic acid furnished the desired final compounds (**113 – 118**) in good yields.

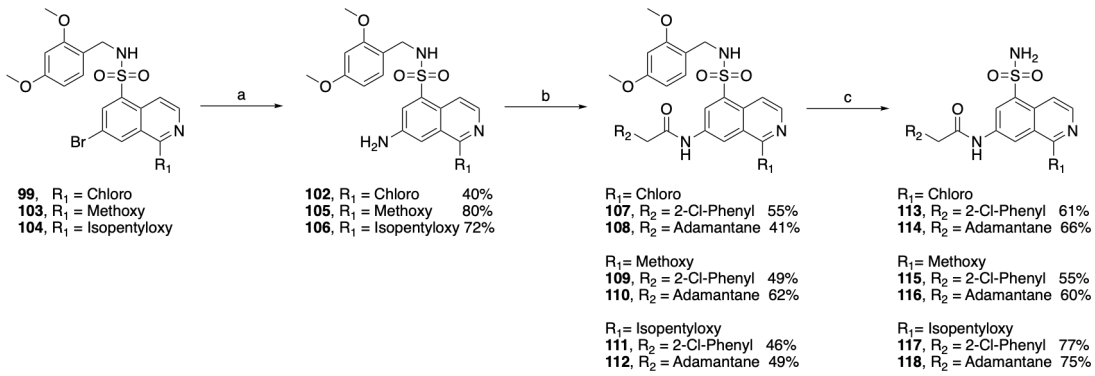

Scheme 2.6 Synthesis of final primary sulfonamide isoquinoline anaolgues **113** – **118**. *Reagents and Conditions* (a) NH_4OH, 4-OH-L-proline, CuI, Cs_2CO_3, DMSO, 140 °C, Sealed, 18 h (b) R_2CH_2COOH, T_3P, Et_3N, DMF, rt, 2 h (c) TFA, CH_2Cl_2, rt, 1 h.

2.2.3 Acetamidopyridine Derivatives

In 2022, Bayer Pharmaceuticals filed a patent describing a range of acetamidopyridines (Figure 2.9) as P2X4R antagonists.[148] Unlike many P2X4R antagonists, these compounds don't include a primary sulfonamide functional group. The compounds reported in the patent mostly possessed poor IC_{50} values (> 250 nM).[149] As such, rather than selecting the most potent analogue for further scaffold elaboration, the difluorophenyl and phenyl analogues were chosen as they had the most extensive SAR presented within the patent. Thus, the effect of introducing adamantane could be analysed amongst a broader range of substituents with varying electronics. Throughout the following discussion the acetamidopyridines will be referred to by the functionality on the left-hand side of the molecule, i.e. difluoro or phenyl (Figure 2.9).

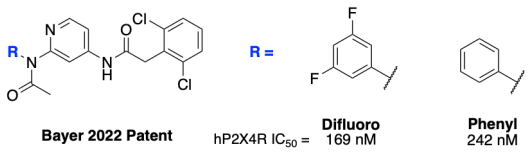

Figure 2.9 Proposed acetamidopyridines derivatives obtained from the Bayer Pharmaceuticals 2022 patent. Only two analogues were chosen due to the poor IC_{50}'s reported.[148]

2.2.3.1 Retrosynthesis of Acetamidopyridine Derivatives

The acetoamidopyridine series (**119**) can be disconnected to provide the aminopyridyl acetamide **120** with the appropriate acid as shown in figure 2.10. Aminopyridyl acetamides could be afforded from a FGI of the nitroarene **121** which could be afforded through an acetylation of the nitropyridine-2-amine **122** with acetic anhydride. A Buchwald-Hartwig reaction between commercially available aniline and 2-bromo-5-nitropryidine (**123**) affords the nitropyridine-2-amine (**122**).

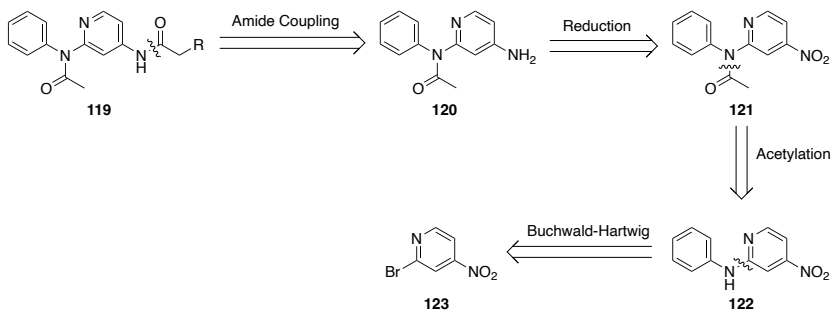

Figure 2.10 Retrosynthetic pathway for the acetamidopyridine derivatives presented in the Bayer 2022 patent.[148] An identical strategy is followed for the synthesis of the 3,5-difluoro analogues.

2.2.3.2 Synthesis of Acetamidopyridine Derivatives

The synthesis of compounds **124** – **127** is shown in scheme 2.7 and followed a similar approach to that reported in the 2022 patent.[119] Firstly, a Buchwald-Hartwig reaction forms the C–N bond between the respective aromatic amine (**128** and **129**) and 2-bromo-4-nitropyridine (**123**). $Pd(dba)_2$ and Xantphos were utilised as the Pd(0) source and ligand, respectively, with caesium carbonate as the base. The bisarylamines **130** and **122** (Scheme 2.7) were then dissolved in acetic anhydride, with catalytic DMAP, to form the corresponding acetamide (**131** and **121**) in near quantitative yields. Nitro compounds **131** and **121** were then reduced under Béchamp conditions in neat acetic acid. When traditional Béchamp conditions were utilised with stoichiometric acid, significant cleavage of the acetamide was observed. Therefore, by conducting the reaction in neat acetic acid, this was able to outcompete the unwanted side reaction (Scheme 2.7; conditions c). The desired aniline product **132** was therefore isolated as the acetate salt. However, when trialling neat acetic acid for the phenyl derivative **121**, cleavage of the acetamide was still observed, producing a 50:50 ratio of the acetamide aniline **120** and deacetylated product. Hydrogenation with Pd/C was therefore employed, resulting in the desired aniline **120** in quantitative yield (Scheme 2.7; conditions d).

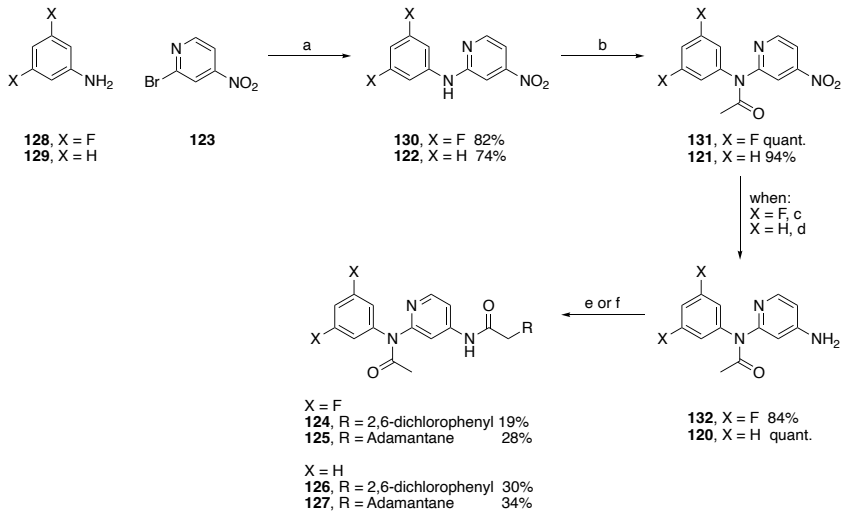

Scheme 2.7 Synthesis of the acetamidopyridine derivatives. *Reagents and Conditions* (a) $Pd(dba)_2$, Xantphos, Cs_2CO_3, 1,4-dioxane, 80 °C, 18 h (b) Ac_2O, DMAP, 110 °C, 4 h (c) $Fe_{(s)}$, AcOH, rt, 3 h (d) Pd/C, H_2, EtOAc, rt, 12 h (e) 1. RCH_2COOH, $(COCl)_2$, cat. DMF, CH_2Cl_2, 0 °C – rt, 2 h; 2. $^{i}Pr_2NEt$, CH_2Cl_2, rt, 3 h (f) 2-(2,6-dichlorophenyl)acetic acid, T_3P, Et_3N, DMF, rt, 2 h – *See table 2.6 for further discussion.*

Under acid chloride amide coupling conditions, the target amides (**124 – 127**) could be obtained by coupling with the previously synthesised anilines **132** and **120**, in moderate yields (Scheme 2.7). However, for compound **124**, this method saw an unexpected side product (**133**) to form, with no product formation (Table 2.6, entry 1). Full characterisation, including X-ray crystallography (Appendix 3), was conducted on the unknown and was concluded to be the enaminoketone product (**133**), as shown in figure 2.11A.

It is postulated that the excess oxalyl chloride and DMF were not removed entirely from the system upon addition of the amine. Therefore, following keto-enol tautomerisation, attack of the chloromethyleneiminium salt (**I**) lead to the formation of the enaminoketone (**II**, Figure 2.11B).[205,206] Evidence for this transformation is found in Bergman and Stalhandske's 1996 paper outlining the cyclisation of *N*-acylathranilic acids with Vilsmeier reagents.[206] The synthesis was rationalised by an initial cyclisation of the phenylacetylated anthranilic acid, with subsequent attack of the active methylene site to the electrophilic Vielsmier-Haack reagent.[206] A similar reaction was also described by Thomas and Asokan for the formation of enaminoketones.[205]

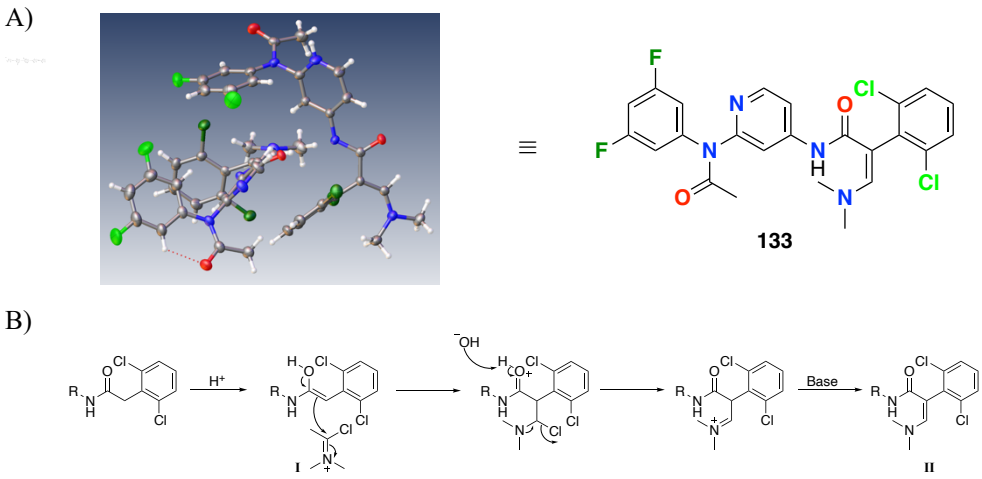

Figure 2.11 A) X-ray crystal structure of enaminoketone side product (**133**) from oxalyl chloride amide coupling reaction. Heteroatoms colours are represented in the corresponding structure. B) Proposed mechanism for side product formation.

A selection of conditions was trialled for the amidation of **132** (Scheme 2.7) with 1-adamantaneacetic acid to furnish **124**. Both HATU (Table 2.6, entries 2 and 3) and EDC/HOBt (Table 2.6, entry 4) mediated amide couplings saw no conversion to the desired

product **124** (by TLC and mass spectrometry analysis) after 24 h, with only starting material isolated. Finally, T_3P was employed as an amide coupling reagent in the presence of triethylamine (Table 2.6, entry 5). These conditions saw an incomplete reaction with conversion to the desired amide **124** in poor yield. The mechanism is shown in figure 2.12, where the acetate (**I**) attacks one of the phosphorus atoms to form the ring open active ester form (**II**).[207] This increases the electrophilicity of the carbonyl, promoting attack of the aniline to form the amide. The by-product (**III**, Figure 2.12) is water soluble and is therefore removed easily within the aqueous work up.[207]

Table 2.6 Amide coupling conditions trialled for the formation of the 2,6-dichloro 2,5-difluoro analogue **124**.

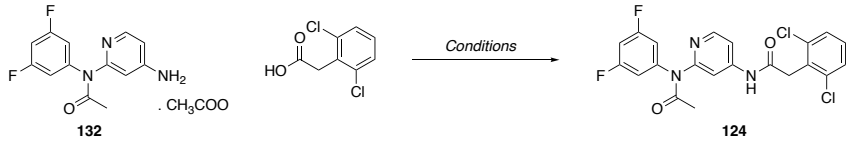

132 **124**

Entry	Conditions	Yield
1	a. $(COCl)_2$, cat. DMF, CH_2Cl_2, 0 °C – rt, 2 h b. $^iPr_2NEt$, CH_2Cl_2, rt, 3 h.	**133** (16%)[a]
2	HATU, $^iPr_2NEt$, DMF, rt, 5 h	S.M.[b]
3	HATU, Et_3N, cat. DMAP, DMF, rt, 18 h	S.M.[b]
4	EDC.HCl, HOBt.H_2O, $^iPr_2NEt$, CH_2Cl_2, rt 24 h	S.M.[b]
5	T_3P, Et_3N, DMF, rt, 2 h	23%

[a] See previous discussion and figure 2.11 for proposed mechanism; [b] S.M. represents recovered starting material, as no reaction occurred.

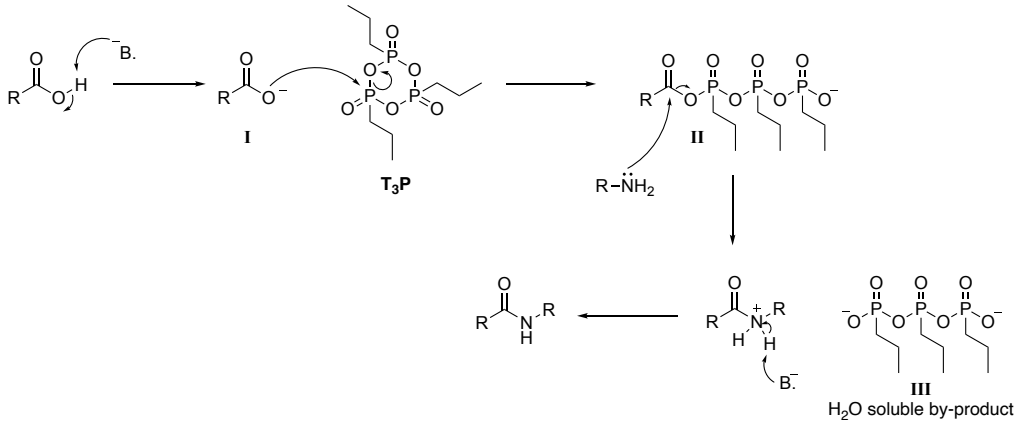

Figure 2.12 T_3P amide coupling reaction mechanism.

2.3 Synthesis of Trifluoroadamantane Acetic Acid

Inclusion of adamantane in drug scaffolds has been shown to improve pharmacological activity and physicochemical properties across a multitude of drug targets.[138,208] Although the 'lipophilic bullet' is burdened by the metabolic lability of its bridgehead carbons being prone to oxidation.[209] A hydrogen-to-fluorine bioisosteric replacement strategy of the bridgehead hydrogens ensures that beneficial physicochemical properties are retained whilst removing the metabolic soft spots. This monovalent isosteric substitution with fluorine can influence a compound's pharmacological profile due to fluorine's distinct electronic characteristics.[210] Owing to its high electronegativity, the carbon-fluorine bond is inherently stronger and more polar than a typical carbon-hydrogen bond.[210] Due to the commercial cost ($488 USD for 50 mg – 08/08/25 AmBeed), 2-(3,5,7-trifluoroadamantan-1-yl)acetic acid (**134**) was attempted to be synthesised in house.[211]

2.3.1 Retrosynthesis of Trifluoroadamantane Acetic Acid

The retrosynthetic strategy for synthesising 2-(3,5,7-trifluoroadamantan-1-yl)acetic acid (**134**) is presented in figure 2.13. The acetic acid **134** was envisioned to be accessible by oxidation of the acetaldehyde **135** under Pinnick conditions. A one-carbon homologation of aldehyde **136** could yield the acetaldehyde **135**. The aldehyde **136** could be obtained through oxidation of the primary alcohol **137** following reduction of the ethyl ester **138**. The ethyl ester **138** could be synthesised *via* a Fischer esterification of the commercially available 3,5,7-trifluoroadamantane-1-carboxylic acid (**139**).

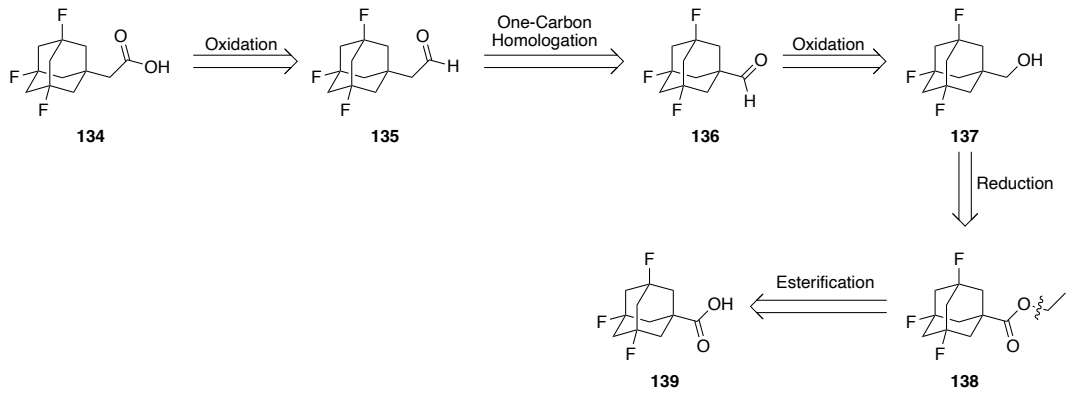

Figure 2.13 Retrosynthetic strategy to access 2-(3,5,7-trifluoroadamantan-1-yl)acetic acid (**134**).

2.3.2 Synthesis of Trifluoroadamantane-1-carbaldehyde Intermediate

Synthesis of ethyl ester **138** was achieved in good yields *via* a Fischer esterification with ethanol and catalytic sulfuric acid (Scheme 2.8). The ester was then reduced to the corresponding primary alcohol **137** with $LiAlH_4$. Multiple oxidation conditions were trialled to convert the primary alcohol to the corresponding aldehyde **136** (Table 2.7). Oxidation by pyridinium chlorochromate (PCC) was shown to be the most efficient (Table 2.7, entry 1). Additionally, difficulty removing the Dess-Martin periodinane (DMP) by-product from the product provided further rationale to utilise PCC, despite the corresponding safety concerns. With the aldehyde intermediate **136** in hand, a series of one-carbon homologation reactions were attempted to yield the acetaldehyde **135**.

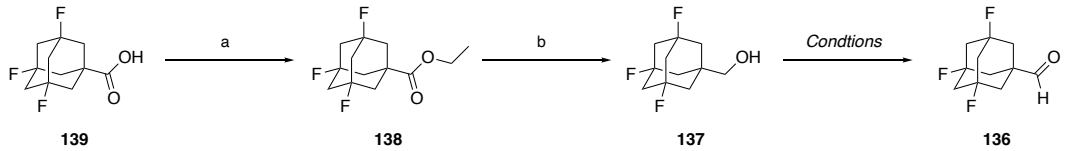

Scheme 2.8 Synthesis of key intermediate, (3*s*,5*s*,7*s*)-3,5,7-trifluoroadamantane-1-carbaldehyde **136**. *Reagents and Conditions* (a) H_2SO_4, EtOH, reflux, 2 h, 75% (b) $LiAlH_4$, THF, reflux, 4 h, 93% (c) Conditions provided in Table 2.7.

Table 2.7 Oxidation conditions explored to synthesis (3*s*,5*s*,7*s*)-3,5,7-trifluoroadamantane-1-carbaldehyde **136**.

Entry	Conditions	Yield
1	PCC, CH_2Cl_2, rt, 4 h	68%
2	DMP, $NaHCO_3$, CH_2Cl_2, rt, 2 h	49%
3	NMO, TPAP, CH_2Cl_2, rt, 4 h	31%

PCC: pyridinium chlorochromate; DMP: Dess-Martin periodinane; NMO: *N*-methylmorpholine-*N*-oxide; TPAP: tetrapropylammonium perruthenate

2.3.3 One-Carbon Homologations

One-carbon homologation strategies of carboxylic acids have been demonstrated to be a valuable transformation in organic chemistry. However, many processes require two to five sequential steps, making it a challenging task in terms of atom economy, yield and ease of

reaction.[212] Consequently, efforts have turned to utilising the extensive knowledge around carbonyl chemistry, in particular aldehydes due to their increased reactivity compared to other carbonyl moieties.[212] Despite many strategies existing, limited experimental data is available for the one-carbon homologation of saturated polycycles such as adamantane.

Throughout the following homologation attempts, trial reactions were often first performed with intermediates synthesised from 1-adamantanecarboxylic acid to reduce the commercial expense ($10 vs $90 USD for 5 g – 08/08/25 AmBeed).[213,214] Previous work in the group has commonly reported trifluoroadamantane analogues to be largely unreactive, often resulting in incomplete consumption of starting material and lower yields compared with their adamantane counterpart.[215]

2.3.3.1 Wittig Olefination

A Wittig olefination was initially attempted due to the previous success experienced in our group when synthesising 3-(1-adamantyl)propanoic acid.[216] The Wittig reaction describes the reaction between an aldehyde (**I**) and phosphonium ylide (**II**) to form the desired alkene (**III**) *via* a reverse [2+2] cycloaddition (Figure 2.14). Hydrolysis of the respective alkene (**III**) forms the desired acetaldehyde (**IV**, Figure 2.14). Utilising (methoxymethyl)triphenylphosphonium chloride (**140**, Figure 2.14) as the Wittig reagent, trace amounts of product were observed by crude NMR on a 100 mg test scale (Scheme 2.9, Table 2.8, entry 1). However, this was not translated when the reaction was scaled up to 500 mg (Table 2.8, entry 2), with only starting material isolated. Similarly, increasing the equivalents of potassium *tert*-butoxide (*t*-BuOK) (entry 3), and switching to a stronger base in NaH (entry 4) failed to furnish the desired product (Table 2.8).

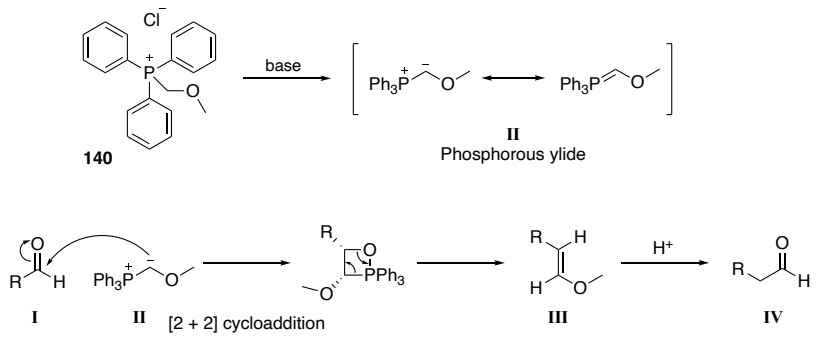

Figure 2.14 Wittig olefination mechanism. The phosphonium ylide (**II**) reacts with the aldehyde (**I**) to form the desired alkene (**III**) *via* a reverse [2+2] cycloaddition.

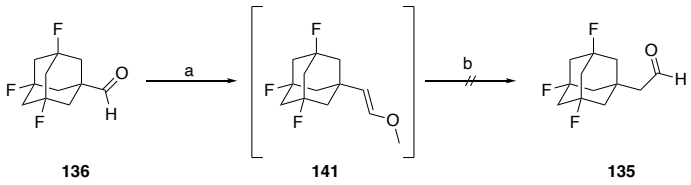

Scheme 2.9 Attempted one-pot Wittig olefination of trifluoroadamantane carbaldehyde (**136**) to yield the corresponding acetaldehyde. *Reagents and Conditions* (a) (methoxymethyl)triphenylphosphonium chloride, *t*-BuOK, THF, 0 °C – rt, 16 h, not isolated (b) 6M HCl, H_2O, $(CH_3)_2CO$, reflux, 12 h.

Table 2.8 Wittig olefination conditions trialled within the synthesis of 2-((3*s*,5*s*,7*s*)-3,5,7-trifluoroadamantan-1-yl)acetaldehyde (**135**).

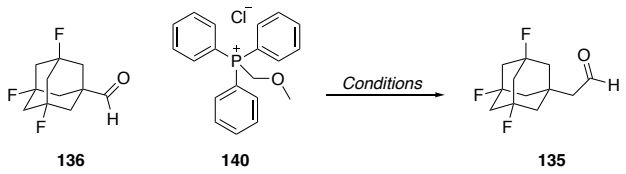

Entry	Scale (mg)	**140** (eq)	Base	Yield
1	100	2	*t*-BuOK (2 eq)	trace
2	500	2	*t*-BuOK (2 eq)	S.M.[a]
3	100	2	*t*-BuOK (3 eq)	S.M.[a]
4	60	2	NaH (2 eq)	S.M.[a]

[a]S.M. represents recovered starting material, as no reaction occurred

2.3.3.2 Corey-Fuch Homologation

Taking inspiration from the Corey-Fuch homologation, Huh *et al*. described a synthetic strategy to yield one-carbon extended aryl acetic acids through reaction of their dibromoalkene derivatives with pyrrolidine under mild conditions (Scheme 2.10).[217] Aldehyde **142** was treated with carbon tetrabromide and triphenylphosphine. Generating the phosphine-dibromomethylene ylide *in situ*, a Wittig-type dibromoolefination of aldehyde **142** successfully formed the dibromoalkene **143** in 65% yield (Scheme 2.10). To overcome stability concerns of the dibromoalkene the isolated compound was stored at 4 °C in the absence of direct light. Compound **143** was then stirred in a pyrrolidine/water solvent mix (10:1) at room temperature. The reported method boasted excellent yields after 1 h, however after 24 h only starting material was retrieved.[217] Dipolar aprotic solvents have been suggested to increases the reaction rate between dibromoalkenes and amines.[218] The solvent system was therefore substituted to a DMF/H_2O (3:1) mixture, and elevated temperatures were attempted to no avail (Scheme 2.10). [219]

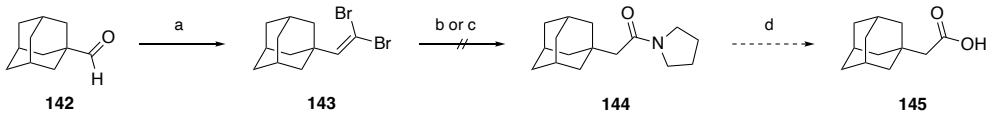

Scheme 2.10 Attempted synthesis of 1-adamantaneacetic acid (**145**) *via* tertiary amide intermediate **144**. *Reagents and Conditions* (a) PPh_3, CBr_4, CH_2Cl_2, 0 °C – rt, 2 h, 65% (b) Pyrrolidine/H_2O (10:1), rt, 24 h (c) Pyrrolidine, DMF/H_2O (3:1), 80 °C, 24 h (d) 1M HCl, 1,4-dioxane, reflux, 12 h.

Building off the successful isolation of the dibromoalkene intermediate, a true Corey-Fuch homologation was attempted. The Corey-Fuch homologation has provided considerable synthetic utility in the preparation of terminal alkynes by one-carbon homologation of an aldehyde (Figure 2.15).[212] Hydration of the alkyne then yields the desired homologated carboxylic acid product.[212] In 2021, Tao *et al*. described the synthesis of carboxylic acids *via* the oxidation of alkynyl boronate (**I**) intermediates (Figure 2.15).[219] The alkynyl boronate **I** is generated from the respective dibromoalkene **II** in the presence of *n*-BuLi and isopropoxyboronic acid pinacol ester (^{i}PrOBPin) at 0 °C. Next, the alkynyl boronate C(sp)-B bond is oxidised by Oxone®, followed by hydrolysis and tautomerisation of the alkyne to yield the ketene intermediate **III** (Figure 2.15).[219–221] Ketene **III** then undergoes nucleophilic attack by water to produce the desired acetic acid **IV** (Figure 2.15). The reported procedure covered a broad substrate scope, notably reporting the formation of adamantane and cycloalkane acetic acids in excellent yields.

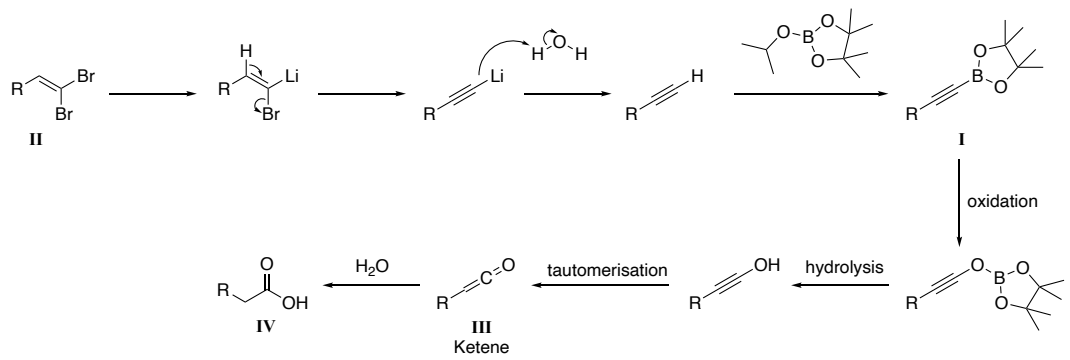

Figure 2.15 Corey-Fuch homologation of dibromoalkene *via* the oxidation of alkynyl boronate intermediates.

Under the former conditions, 1-adamantaneacetic acid (**145**) was successfully synthesised, albeit in substantially lower yields (45%) than that reported by Tao *et al.* (Scheme 2.11) (Paper yield 77%).[219] Trifluoroadamantyl dibromide alkene (**146**) was similarly prepared with carbon tetrabromide and triphenylposphine *via* a Wittig reaction (Scheme 2.11). By TLC analysis

consumption of alkene **146** was observed, although following oxidation a complex reaction mixture was observed with no sign of product formation.

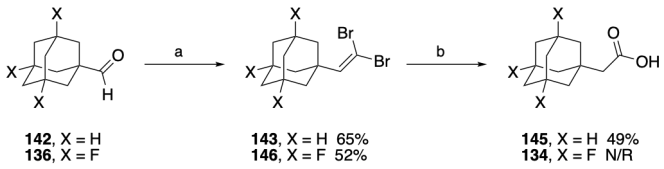

Scheme 2.11 Corey-Fuch homologation trials to yield acetic acid product. *Reagents and Conditions* (a) PPh_3, CBr_4, CH_2Cl_2, 0 °C – rt, 2 h (b) 1. *n*-BuLi, ^{i}PrOBpin, 4M HCl in 1,4-dioxane, THF, 0 °C – rt, 4 h; 2. Oxone®, $(CH_3)_2CO/H_2O$, 50 °C, 12 h. ^{i}PrOBpin: 2-Isopropoxy-4,4,5,5-tetramethyl-1,3,2-dioxaborolane

2.3.3.3 Jocic-Reeve Homologation

In an effort to increase the reactivity of the adamantyl motif, Jocic-Reeve homologation conditions were trialled. Generating the highly reactive *gem*-dichloroepoxide intermediate (**I**, Figure 2.16A) *in situ*, Jocic-Reeve homologations have been described for a broad scope of substrates including conversion of aldehydes to homologated carboxylic acids.[212] The reaction first requires the synthesis of the respective trichloromethyl carbinol (**II**, Figure 2.16).[212] Treating the former with base affords the α-trichloromethyl tertiary alkoxide ion (**III**), which reacts intramolecularly to form the epoxide intermediate (**I**) *in situ* (Figure 2.16A).[212] Nucleophilic attack occurs regioselectively at the alpha-carbon producing the alpha-substituted acid chloride (**IV**) which can then be subject to a variety of conditions (Figure 2.16A).[212]

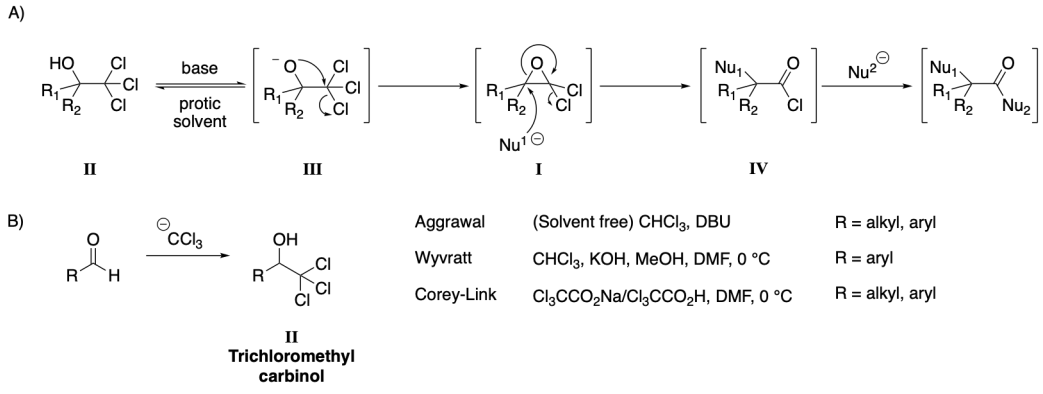

Figure 2.16 A) Jocic-Reeves homologation mechanism proceeds *via* the reactive *gem*-dichloroepoxide intermediate (**III**). B) Common methods of synthesising trichloromethyl carbinols (**II**).[212]

The three most commonly used procedures to access trichloromethyl carbinols are shown in figure 2.16B.[212] The condensation of chloroform under basic conditions is often used for addition to sterically hindered or non-enolizable aldehydes.[212] Aggrawal *et al.* described the formation of carbinols promoted under milder conditions using cyclic amidines bases.[222] The amidine promoted addition of chloroform occurred under solvent free conditions with stoichiometric amounts of base.[222,223] Trial reactions with **142** were conducted in an effort to synthesise adamantane trichloromethyl carbinol **147**. A range of bases and reaction mixture concentrations were screened and are presented in table 2.9. Using one equivalent of the amidine base 1,8-diazabicyclo[5.40]undec-7-ene (DBU), with a slight excess of chloroform saw no consumption of starting material (Table 2.9, entry 1). The lack of reactivity was suspected to be due to the insufficient amount of solvent. Therefore, DBU was substituted for the cyclic guanidine 1,5,7-triazabicyclo[4.4.0]dec-5-ene (TBD) due to its increased basicity and greater compatibility to more dilute solutions.[222,224,225] Unfortunately, no product formation was observed in either case with only starting material recovered (Table 2.9, entries 2 and 3).

Table 2.9 Attempted synthesis of trichloromethyl carbinol intermediate utilising cyclic amidine bases.

142 **147**

Entry	Conditions	Yield
1	DBU, $CHCl_3$ (2 eq), rt, 24 h	S.M.[a]
2	TBD, $CHCl_3$ (2 eq), rt, 24 h	S.M.[a]
3	TBD, $CHCl_3$ (4 eq), rt, 24 h	S.M.[a]

[a]S.M. represents recovered starting material, as no reaction occurred. DBU: 1,8-diazabicyclo[5.40]undec-7-ene; TBD: 1,5,7-triazabicyclo[4.4.0]dec-5-ene

As the primary alcohol, a common side-product derived from the Cannizzaro reaction, was not observed, more forcing conditions with different chlorine sources (sodium trichloroacetate) and stronger bases (KOH) could be explored (Figure 2.16B).[212] However, as the reported substrate scope had broadly been limited to aryl motifs, it was decided to pivot to other homologation techniques.

2.3.3.4 Kowalski Ester Homologation

The Kowalski ester homologation describes the one-carbon elongation of an ester with methylene dibromide.[212] Heralded as a safer alternative to the Arndt-Eistert synthesis it has been shown to have utility on both alkyl and aryl substituents.[226] Precedent for its efficacy on other saturated polycyclic frameworks, including adamantane and cubane, has been established by previous group members, thereby presenting it as a viable option for the current scaffold.[227–229]

Dibromoketone **148** is obtained from the ethyl ester **138** by addition of dibromomethyllithium; formed *in situ* from lithium tetramethylpiperidine (LiTMP) and dibromomethane (DBM) (Scheme 2.12). The reaction was performed under strict anhydrous conditions with freshly distilled 2,2,6,6-tetramethylpiperidine (TMP). Following previous efforts in the group on the cubane structure, preparation of dibromomethyllithium from TMP and *n*-BuLi was performed at 0 °C over 5 min.[229] Subsequent cooling to -78 °C prior to addition of the ethyl ester **138** afforded the α,α-dibromoketone **148** in moderate yields after quenching in aqueous hydrochloric acid (Scheme 2.12).[226] Diverging from the original Kowalski procedure, the α,α-dibromoketone **148** was isolated and purified prior to the subsequent homologation step.

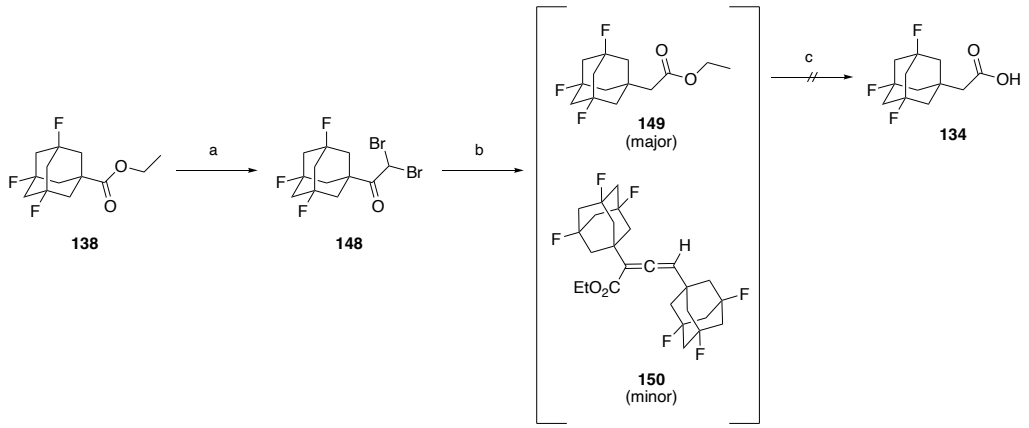

Scheme 2.12 Attempted Kowalski homologation of ethyl 2-((3*s*,5*s*,7*s*)-3,5,7-trifluoroadamantan-1-yl)acetate (**149**). Crude mixture of the homologated ester was telescoped through to hydrolysis reaction to improve ease of purification. *Reagents and Conditions* (a) 1. TMP, *n*-BuLi, THF, 0 °C, 5 min; 2. DBM, THF, -78 °C, 1 h, 44% (b) 1. LiHMDS, THF, -78 °C, 20 min; 2. *n*-BuLi, -78 °C, 15 min; 3. AcCl, EtOH, rt, 15 min, not isolated (c) LiOH.H_2O, MeOH/H_2O (3:1), reflux, 5 h. TMP: 2,2,6,6-tetramethylpiperidine; *n*-BuLi: n-butyllithium; LiHMDS: lithium hexamethyldisilazide

The dibromoketone **148** was then subjected to a three step, one-pot reaction to form the homologated ester *via* the ketene intermediate (**I**, Figure 2.17). Compound **148** is initially treated with lithium hexamethyldisilazide (LiHMDS) to form the corresponding enolate **II**, which then undergoes a lithium-halogen exchange (**III**) upon addition of *n*-BuLi (Figure 2.17). The carbenoid intermediate (**IV**) rearranges to give the ynolate (**V**) *via* a Fritsch-Buttenberg-Weichell rearrangement (Figure 2.17).[230] Quenching with acidic ethanol therefore forms the homologated ester (**VI**, Figure 2.17).

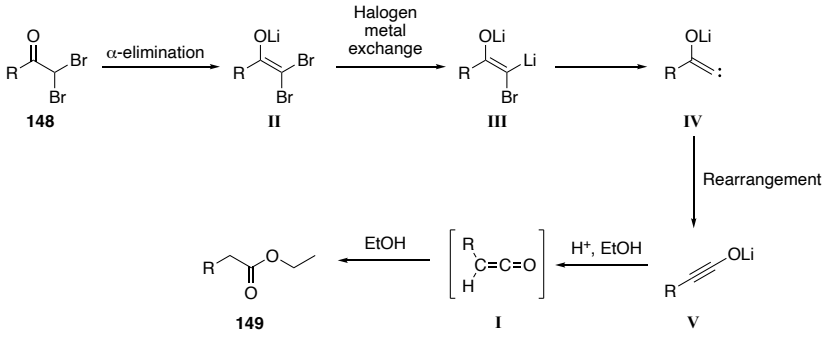

Figure 2.17 Kowalski homologation mechanism. The dibromoketone (**148**) is treated with LiHMDS and *n*-BuLi to form the homologated ester (**149**) product *via* the ketene intermediate (**I**).

It had previously been reported that a difficult separation of the homologated ester **149** and minor allene by-product (**150**) was experienced for the adamantane derivative (Scheme 2.12).[228] As such, following mass spectrometry analysis of the reaction, it was telescoped through to a basic hydrolysis, followed by acidification in an effort to yield the desired homologated acid (Scheme 2.12). Unfortunately, a complex reaction mixture was observed following the homologation conditions, and no product was identified post hydrolysis. Characterisation of the crude reaction mixture identified the mass corresponding to the acetic acid (*m/z* 247 $[M\text{-}H]^-$), however no carbonyl carbon was observed by NMR. Additionally, unidentifiable proton and carbon signals were observed, suggestive of an adamantane with a different chemical environment. Thus, the reaction was deemed unsuccessful with only the possibility of trace quantities of desired product observed.

Despite the unsuccessful synthesis, additional optimisation of the homologation parameters may be explored. Future attempts for the formation of **149** should consider the use of *sec*-BuLi prior to *n*-BuLi as it has been demonstrated to promote the key metal-halogen exchange/rearrangement (Figure 2.17) more efficiently.[226] This hybrid approach was also

reported by Kowalski to reduce the formation of *n*-butyl bromide in the low-temperature metal-halogen exchange step, as well as the α-keto dianion formed in the deprotonation step.[226]

2.3.4 Future Directions

Within the discussed retrosynthetic strategy to access 2-(3,5,7-trifluoroadamantan-1-yl)acetic acid, a significant bottle neck was experienced within the one-carbon homologation step. Future work in this area should initially focus on the retrial of the Kowalski and Corey-Fuch methodology as they showed the most promise. Initial attempts were conducted on a small scale and may benefit from scaling up. Advantages include easier handling and enable full analysis of side product for effective troubleshooting.

Notably, the synthesis of 2-(3,5,7-trifluoroadamantan-1-yl)acetic acid was reported by Liu *et al.* in 2018 (Scheme 2.13).[231] The synthetic strategy described the reduction of the carboxylic acid **139** to the primary alcohol **137** (step a), which was then treated with thionyl chloride to yield the alkyl chloride **151** (step b) (Scheme 2.13). Nucleophilic substitution (S_N2) of the cyanide ion affords the alkyl nitrile **152** (Scheme 2.13, step c). The nitrile **152** then undergoes a base-catalysed hydrolysis reaction and subsequent acidic work up to afford the desired acetic acid **134** (Scheme 2.13, step d). Initially, this synthetic pathway was disregarded due to scalability issues. The method involved the use of 11 equivalents of sodium cyanide and had a reported overall yield of 0.59% over four steps.[231] Due to the safety concerns and atom efficiency of the reported pathway it was not attempted in the initial trials. However, future work towards the synthesis of 2-(3,5,7-trifluoroadamantan-1-yl)acetic acid would benefit from the exploration of alternative methods to access the alkyl nitrile intermediate. Viable alternatives include direct oxidative conversion and carbon-carbon bond cleavage.[232,233]

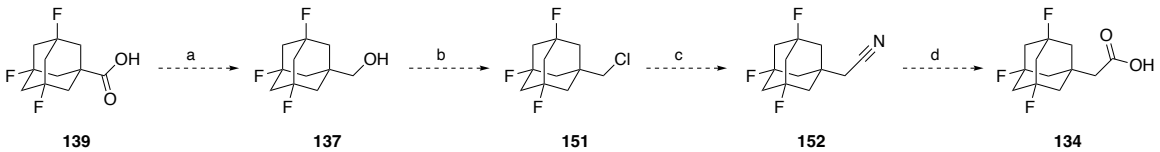

Scheme 2.13 Reported synthetic pathway to access 2-(3,5,7-trifluoroadamantan-1-yl)acetic acid.[231]

Additionally, other homologation methods such as the Arndt-Eistert should be explored. Eaton and colleagues successfully applied this transformation to the cubane scaffold, therefore

demonstrating its utility amongst saturated carbocycles.[234] Mechanistically, the acetic acid is achieved from the α-diazoketone *via* a Wolff rearrangement in the presence of catalytic silver (or irradiation, step c) and subsequent hydrolysis (Scheme 2.14, step d).[234] However, there are also considerable shortcomings to the former method with many citing the substantial hazards associated with diazomethane.[235]

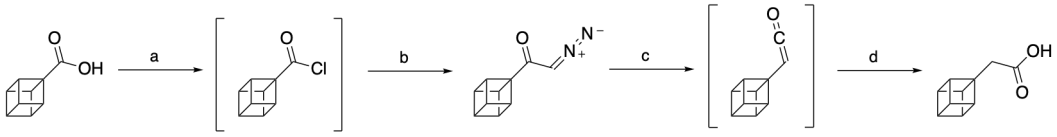

Scheme 2.14 Ardnt-Eistert synthesis reported for the one-carbon homologation to yield cubane acetic acid.[234]

Future efforts towards the synthesis of 2-(3,5,7-trifluoroadamantan-1-yl)acetic acid should be directed towards the aforementioned protocols. However, given the synthetic difficulty in obtaining **134**, efforts were diverted to more pertinent scaffolds whilst awaiting biological and metabolism data on the corresponding adamantane analogues.

2.4 Molecular Docking Studies in the hP2X4R

The *in silico* docking study performed and presented within **Chapters 2** and **5** were performed with the assistance of Dr Jonathon Du from the Faculty of Medicine and Health, Sydney Pharmacy School at the University of Sydney.

2.4.1 Introduction to Molecular Docking Studies

Molecular docking is a well-established structure-based computational technique commonly used in drug discovery. By predicting and analysing the presence, or lack thereof, of covalent and non-covalent binding between a ligand and receptor, molecular docking enables the identification of novel compounds of therapeutic interest.[236] Furthermore, docking can provide rationale for particular SAR trends and ligand-target interactions at a molecular level.[236] This process typically involves first predicting how a ligand is oriented within a receptor, followed by estimating their compatibility using a scoring function. Although the accuracy of molecular docking methods are ever improving, all molecular docking studies are accompanied by approximations.[237] For example, scoring functions provide insight into the relative orientation

or conformation binding tightness of a ligand within a protein; however, they are not universally accurate.[238] The effects of receptor flexibility and explicit solvation on binding affinity are often neglected in force field algorithms.[239] In addition, conformational changes in protein side chains and the backbone that occur upon ligand binding are typically ignored, which can lead to inaccurate or misleading predictions.[237] As a result, extensive validation against experimental data is essential to evaluate the reliability of docking outcomes and ensure that the predicted binding modes are biologically relevant.

Within this dissertation, the *in silico* study was used solely for the purpose of analysing non-covalent binding of ligands, and all future references herein will be based on this use. Data will be used to further investigate the SAR surrounding key interactions for recognition by the hP2X4R (PDB ID: 9BQI) and propose a potential triage strategy to make future workflows more efficient.

2.4.2 *In Silico* Docking Study of Reference and the Synthesised Compound Libraries

2.4.2.1 Validation of *In Silico* Model

The cryo-EM structures of the full-length wild-type human P2X4R in apo closed, antagonist-bound inhibited and ATP-bound desensitised states were published in 2025.[8] The study confirmed that BAY-1797 (**25**) bound in the canonical allosteric binding site, located within the extracellular domain near the top of the receptor. However, more significantly, three molecules of BAY-1797 were demonstrated to bind within close proximity (3.3 Å apart) near the axis of symmetry of the receptor.[8] Therefore, locating the ligands in close enough proximity for intermolecular bonding interactions and detrimental steric clashes to occur.[240,241] Consequently, single ligand molecular docking experiments into an individual subunit would not suffice. The methodology developed described the sequential docking of an individual ligand into the three protein chains. To avoid inaccuracies and bias within the results no constraints were applied.[242] Furthermore, Glide XP docking methods were used as they have shown to be the most accurate when reproducing docking results.[237]

Firstly, to demonstrate that the selected protein structure and employed methodology was reliable for cross-docking experiments (docking of non-native ligands) the co-crystallised ligand (**25**) was docked within the minimised protein structure to ensure the same interaction

and orientation could be reproduced with the proposed methodologies; this will be referred to as 'self-docking'. The self-docking experiment successfully emulated the co-crystallised structures (Figure 2.18). Characteristic hydrogen bonding interactions between the sulfonamide and the side chains of Val90, Ala93 and Ala87 were replicated. The reported aromatic interactions between the benzyl group and Trp84 were also observed.

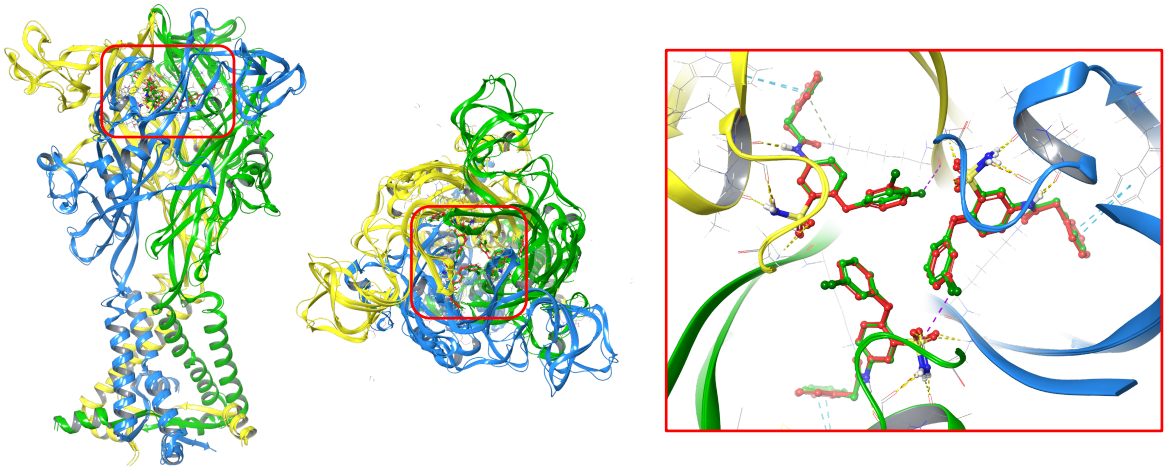

Figure 2.18 Self-docking of BAY-1797 in the hP2X4R allosteric binding pocket (PDB ID: 9BQI). Self-docking experiment (green) is superimposed with the co-crystallised ligand (red) to validate the *in silico* methodology adopted. The allosteric antagonist binding pocket is highlighted by the red box, and dashed lines represent predicted binding interactions.

2.4.2.2 Adamantyl Compound Library

Within the original crystal structure, BAY-1797 was found to be oriented so that the chlorophenoxy group pointed inwards toward the centre of the receptor and the phenylacetamide moiety is pointed outwards from the receptor (Figure 2.18).[8] Analysis by Shi *et al.* concluded that there was space for *meta*-substitution of the phenyl group, therefore highlighting the motif as a key area to probe.[8] Interestingly, within the original SAR analysis conducted by Werner *et al*. only one analogue was included with a *meta*-substitution at the phenylacetamide motif.[141] The 3-methylphenyl derivative was shown to have improved antagonistic activity to BAY-1797 (hP2X4R IC_{50} = 52 nM), although tight off-target binding to the xenobiotic sensor, the pregnane X receptor (PXR) (PXR Binding MEC = 0.21 μM; MEC: minimum efficacious concentration) was observed as well. Activation of the pregnane X receptor results in the upregulation of liver enzymes including the cytochrome P450 enzyme family.[243] Predominantly involved in phase 1 metabolism, increasing CYP enzyme activity can lead to undesired off-target effects.[244]

The study also demonstrated that halogen substitution in the *ortho*-position was well tolerated at the hP2X4R.[141] Conversely, *para*-substitutions diminished P2X4R activity.[141] Expanding on this, the Jorgensen group (unpublished work) identified that aromatic interactions are not crucial for antagonism of the hP2X4R with the cubane and adamantane derivative well tolerated.[178,245] The synthesised compound library described herein investigates the effect of adamantane in three unique P2X4R antagonist chemotypes. The caged polycycle system of adamantane is often utilised within drug discovery campaigns as an outer benchmark of steric allowance and tolerance of hydrophobic motifs.[138]

A sub-group of compounds from the synthesised compound library were selected for rigid target docking (RTD) (Figure 2.19). The compound sub-library represents examples from each chemotype, composed of the outer limits of functional activity (IC_{50} of patent leads = 9 – 242 nM). By including examples with reported poor activity, the results from the molecular model could infer if there was a correlation between binding affinity and functional activity.

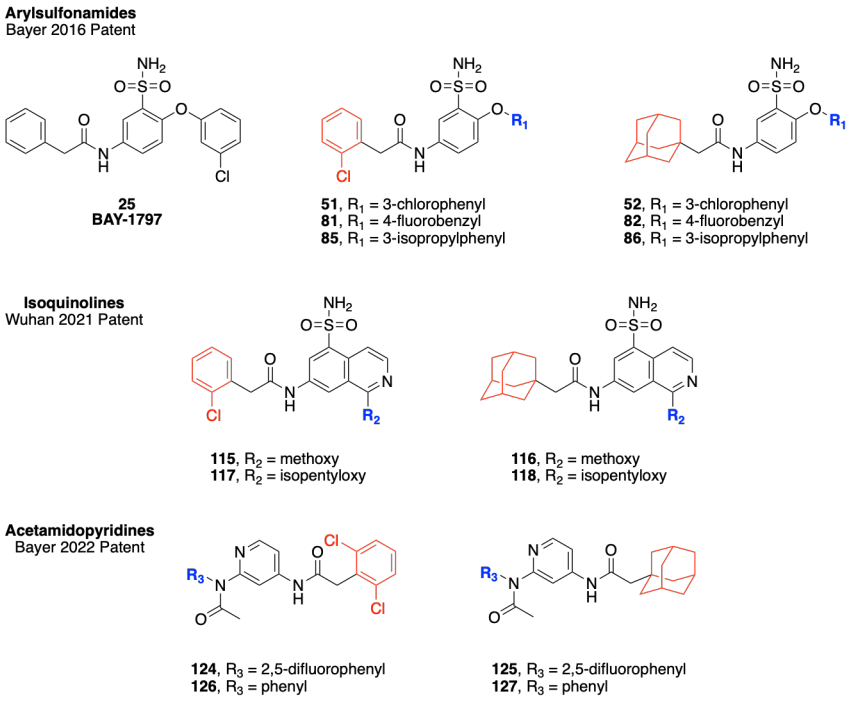

Figure 2.19 Selected compounds from the synthesised compound library for RTD experiments.

The RTD experiments determined key binding interactions and predicted steric clashes within the allosteric site. The impact of occupation of space within the outer hydrophobic region was examined through the analysis of adamantane derivatives. Introduction of adamantane within

the arylsulfonamide chemotype caused moderate steric clashing between the vicinal ligands and surrounding protein (Figure 2.20A). Orientated in the reverse direction to their 2-chlorophenyl counterpart, the adamantane analogues adopted a variety of orientations to accommodate the larger polycycle. Therefore, the analogues failed to adopt the triangular like positioning seen for 2-chlorophenyl arylsulfonamides and BAY-1797 (Figure 2.20 and 2.19). This was appropriately translated by the poor docking scores (Appendix 4). In particular, the adamantane isopropyl derivative **86** was unable to successfully dock all three ligands, reporting no docking poses for chain C. This suggests that flat saturated aromatic rings are better suited to the three-ligand model. This notion was further supported by the docking results seen in the isoquinoline and acetamidopyridine scaffolds. Large flexible alkyl chains, as seen in isopentyloxy derivatives **117** and **118**, similarly caused moderate steric clashing with the surrounding protein (Figure 2.20B). This was further exacerbated with the introduction of the adamantyl motif **118**, with clashing observed between the three ligands (Figure 2.20B).

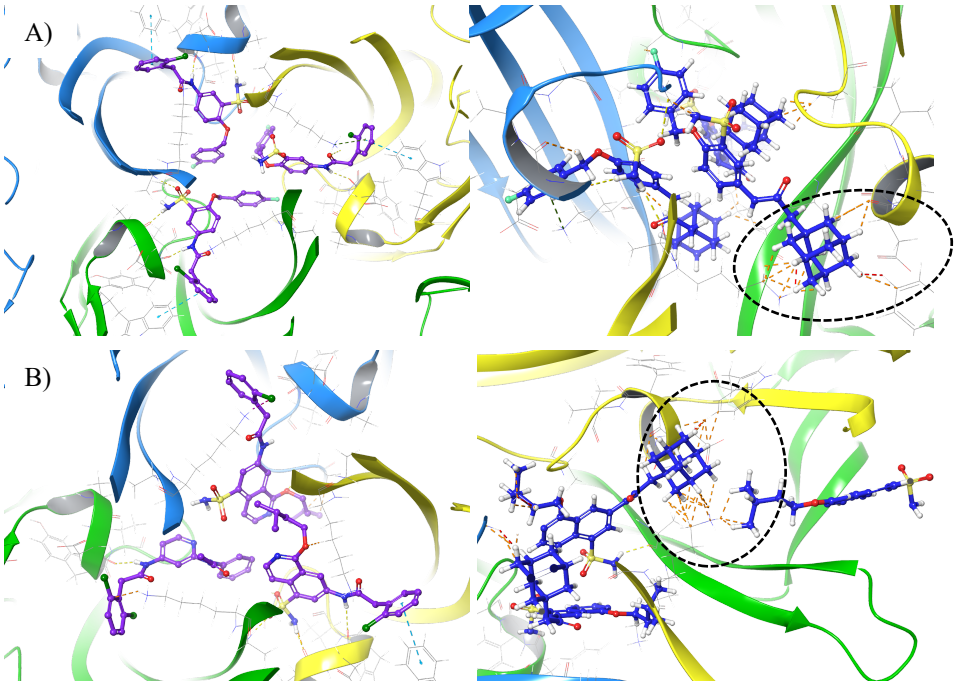

Figure 2.20 Adamantane analogues failed to adopt trimer ligand conformation due to steric clashing. Rigid-target docking of 4-fluorobenzyl arylsulfonamide analogues (A; **81:** purple and **82**: blue), and isopentyloxy isoqinoline derivatives (B; **117**: purple and **118**: blue) viewed from the top-down. Introduction of adamantane (**82** and **118**) disrupts the threefold symmetric binding observed for the chlorophenyl analogues (**81** and **117**) with significant steric clashing predicted with the surrounding protein (dashed line circle). Binding interactions such as hydrogen bonds (yellow dotted lines), π-π aromatic (blue dotted lines), and steric clashes (orange dotted lines) are shown.

Hydrogen bonding interactions with the sulfonamide motif were identified to be a principal binding interaction within the canonical P2X4R allosteric sites (Figure 2.21). Literature compounds of the arylsulfonamide and isoquinoline chemotypes were observed to be well tolerated all demonstrating the reported hydrogen bonding between the sulfonamide and Ala87 and Ala93 (Figure 2.21A). In the absence of the sulfonamide motif, literature acetamidopyridine compounds (**124** and **126**) reported poorer docking scores, with only a singular hydrogen bond between the amide NH and Asp88 predicted (Figure 2.21B).

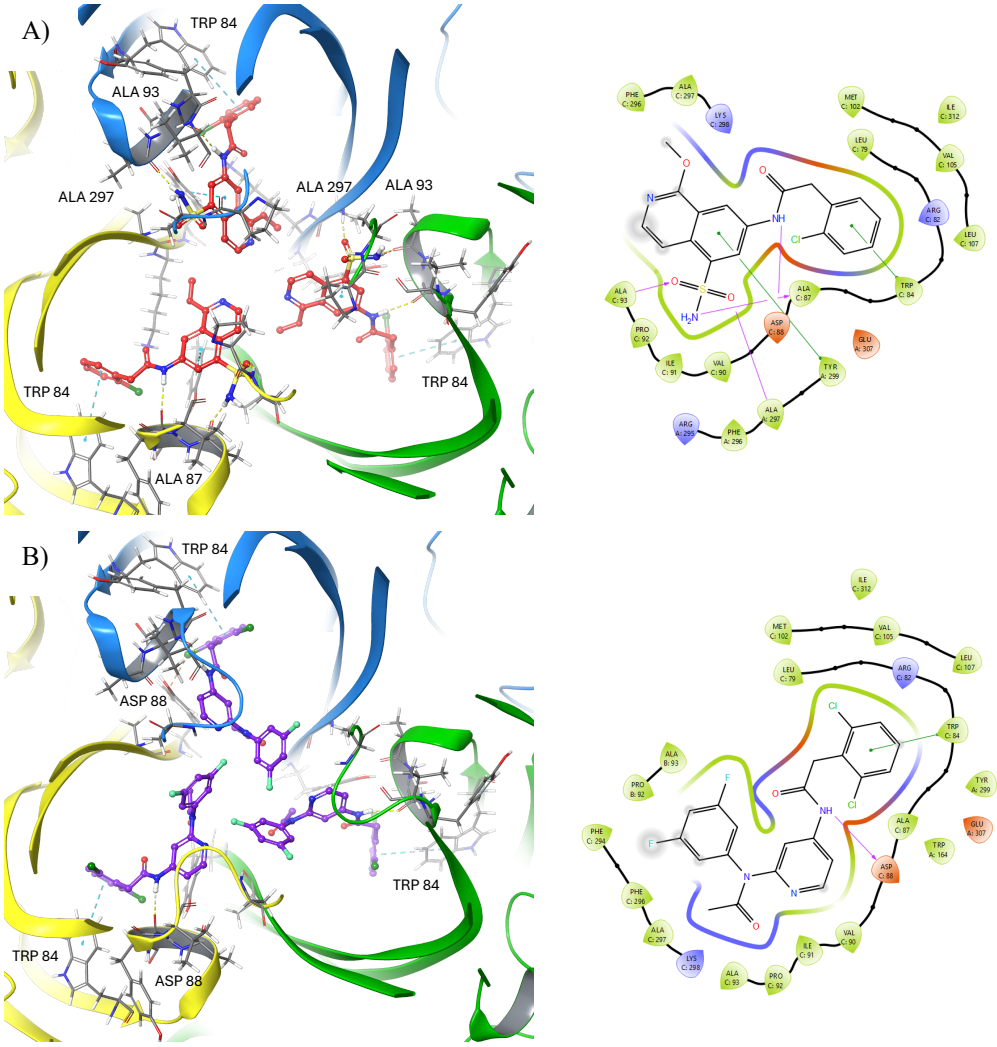

Figure 2.21 Rigid-target docking experiments demonstrated the importance of hydrogen-bond interactions within the P2X4 allosteric site. The sulfonamide functionality (A – **115**, red structure) forms a stable interaction with Ala87 and Ala93. Acetamidopyridine derivatives (B – **124**, purple structure) forms a singular hydrogen bond with Asp88. 2D representations of the ligand binding interactions are provided for further clarity. Hydrogen bonds are indicated by yellow dotted lines, and purple arrows in the 2D representation.

At biological pH the acetamidopyridine chemotype are predicted to be protonated. Overall, the protonated species exhibited larger docking scores in comparison to their neutral analogues indicating that they are not well tolerated within the P2X4R allosteric sites.

2.4.2.3 Future Directions and Conclusions

The *in silico* model described herein, successfully recreated the trimeric binding mode of the co-crystallised structure reported by Shi *et al*.[8] However, despite this, analysis of the arylsulfonamide literature compounds identified that no correlation between docking score (Appendix 4) and reported functional activity was observed, with the selected negative controls reporting similar or better docking scores to their respective positive control (Appendix 4). Furthermore, the current *in silico* model assumes that all three chemotypes are allosteric inhibitors of the hP2X4R. No data on the binding mode of the isoquinoline and acetamidopyridine analogues were provided within the corresponding patent literature.[148,149] Therefore, the trends observed for the isoquinoline and acetamidopyridine derivatives can only be used as a guide, and no definitive assertions can be made about the *in vitro* P2X4R binding affinity of the aforementioned compounds in the absence of biological data.

With the previous points considered, RTD studies of the synthesised compound library suggest that replacement of aromatic motifs for adamantane is detrimental to binding within the homotrimeric hP2X4R. Preliminary results implied that bulky caged carbocycles are not sterically allowed to adopt the advantageous orientation seen by the co-crystalised BAY-1797. The docking study predicts two ligands bind tightly within the allosteric sites, while a third is positioned further into the extracellular domain. This spatial arrangement likely accounts for the poor docking scores observed for the adamantyl derivatives (Figure 2.22, Appendix 4).

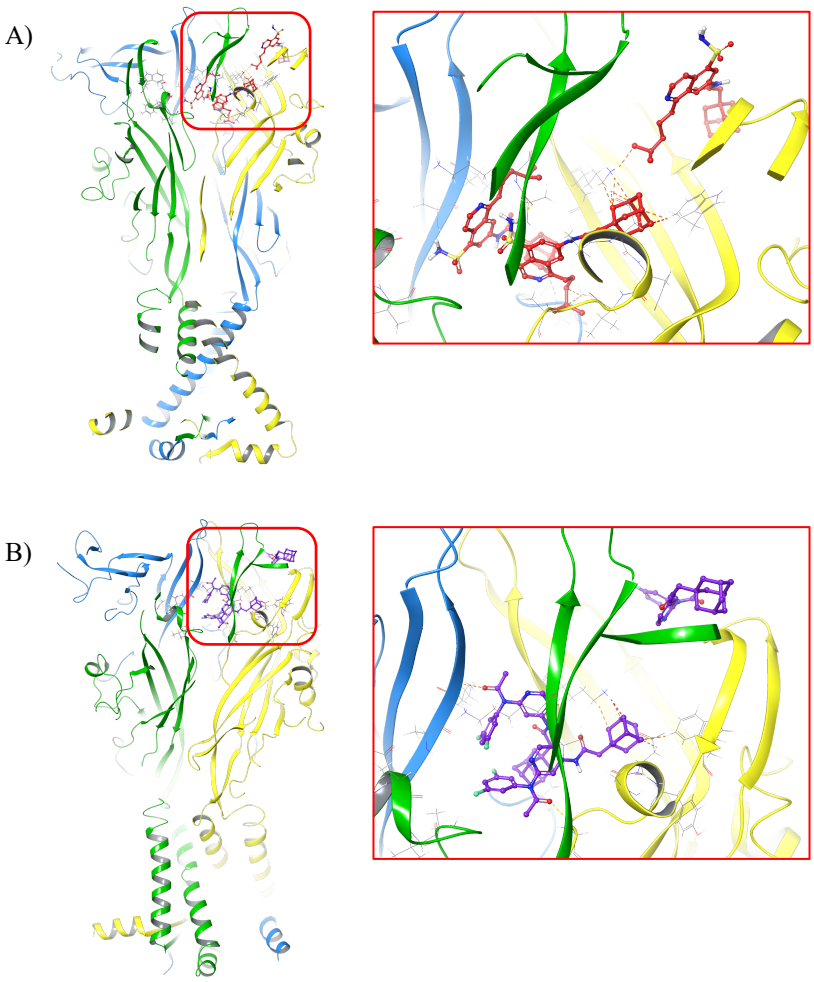

Figure 2.22 Adamantane analogues of the isoquinoline (A) and acetamidopyridine (B) chemotypes failed to adopt the threefold symmetric binding mode seen for the arylsulfonamide derivatives, suggestive that RTD experiments have significant limitations of cross-docking in the homotrimeric system.

Cross-docking within rigid-target frameworks can often yield misleading results, as these methods do not account for conformational changes in protein side-chains or the backbone upon ligand binding.[237] This limitation becomes particularly evident when dealing with structurally diverse chemotypes, as observed with compounds **115 – 118** and **124 – 127** (Figure 2.22). Induced-fit docking (IFD) addresses this issue by incorporating receptor flexibility, offering a more realistic representation of ligand-protein interactions.[237,246] By allowing the protein to adapt to the ligand, IFD improves accuracy and reduces the likelihood of false negatives (i.e. poorly scored true binders).[246] However, the computational demands of IFD are significantly higher, making it unsuitable for inclusion in this initial study, though it should be considered in future analyses.[237]

2.5 Biological Evaluation

The *in vitro* evaluations performed and presented throughout **Chapter 2** were performed by André McKenzie with the Faculty of Medicine and Health at the University of Sydney. Synthesised derivatives were intended to be evaluated for functional activity at both the hP2X4 and hP2X7 receptors. At the time of writing all derivatives discussed and synthesised throughout this chapter have not been evaluated at the hP2X4R. *In vitro* data for the hP2X7R has been provided and will therefore be discussed independently.

2.5.1 P2X4 *In Vitro* Photoscreen Assay

Initially, an *in vitro* photoscreen assay was trialled for the assessment of P2X4 inhibition. The luminescence assay provides an alternative method to fluorescent dyes, reporting less false positives due to the large robust signal produced. The photoscreen used HEK-293 cells stably expressing hP2X4R, and the Ca^{2+} regulated photoprotein, Photina. In the presence of coelenterazine and P2X4R-stimulated Ca^{2+} influx, Photina emits light which is then quantified *via* a luminescence-capable reader. However, equipment limitations rendered this methodology unreliable. Upon exposure to the reference agonist CTP, the signal occurred too rapidly to be recorded reproducibly due to the reader's short acquisition interval. This therefore led to intra-assay variability of raw signals, which only increased with larger plate layouts.[247] Consequently, alternative assay approaches were investigated.

2.5.2 P2X4 *In Vitro* Fluo-4 Dye Uptake Assay

To overcome the above limitations, an alternative assay approach was utilised still harnessing the P2X4R's role facilitating Ca^{2+} influx. Antagonistic effects of the synthesised compound library will be evaluated in an *in vitro* Fluo-4 dye uptake assay in HEK-239 cells stably transfected with hP2X4R. P2X4 ion channel activity in immune cells, such as microglia, are commonly assessed by Ca^{2+} flux assays utilising cell permeable Ca^{2+}-sensitive dyes in conjunction with fluorescence spectrophotometry.[1] Utilising the downstream accumulation of Ca^{2+} following P2X4R activation, the Fluo-4 dye binds to Ca^{2+} producing its 'active' form. Following activation the Fluo-4 dye fluorescence emission shifts from the excitation maxima to a longer wavelength (λ_{max} (excitation) (ion bound) = 494 nm; λ_{max} (emission) (ion bound) = 516 nm).[249,250] The change in fluorescence intensity is measured for a single wavelength and normalised against the basal signal. Fluo-4 is the most commonly used calcium indicator due

to its low affinity to Ca^{2+}, thereby enabling it to measure much higher concentrations of Ca^{2+} before saturation.[250] Following the differentiation of HEK-hP2X4R cells, the cells were pre-incubated with a buffer solution containing Fluo-4 NW dye. Subsequent stimulation with agonist ATP and test compounds facilitates a response. Assay details are provided in **Chapter 7.7.3**.

2.5.3 P2X7 *In Vitro* YO-PRO®-1 Dye Uptake Assay

Functional activity of the synthesised compounds at the P2X7R was evaluated through *in vitro* YO-PRO® dye uptake assay in THP-1 cells stably transfected with hP2X7R. The YO-PRO®-1 dye uptake assay provides a quantitative estimation of P2X7R activity through measuring changes in membrane permeability. Indicative of sustained P2X7R activation, the P2X7R forms a large transmembrane domain which allows for cellular uptake of cations. YO-PRO®-1, a cationic dye typically cell membrane-impermeant, is thus able to permeate through the transmembrane pore and binds to nucleic acids within the cell. Upon binding, the intensity of the YO-PRO®-1's fluorescence emission increases, thus providing evidence of P2X7R activation.

After THP-1 cell differentiation, cells were treated with a buffer solution containing YO-PRO®-1, BzATP and test compounds. P2X7R activation is simulated through the administration of BzATP, a potent P2X7 agonist. Antagonism of the P2X7R is indicated through a reduction of BzATP-induced dye uptake into the cells and consequently reduced fluorescence intensity. The magnitude of inhibition is quantitatively determined by a fluorescent plate reader. Compounds were initially screened at 10 μM in technical duplicate with a minimum of three independent repetitions completed. Compounds reported to have a BzATP-induced dye uptake fluorescence intensity less than 30% of the control at 10 μM were subject to dose-response experiments. The activity data were reported as the IC_{50} value – the drug concentration required to inhibit dye uptake by 50% relative to the control. Therefore, smaller IC_{50} values indicate more potent inhibition. Assay details and methods are available in **Chapter 7.7.5**.

2.5.4 Biological Results and Discussion

Validation of the hP2X4R antagonist assay was attempted with two distinct known antagonists; BX430 (**20**) and BAY-1797 (**25**). Utilising ATP (**1**, EC_{60} = 1 μM) as the agonist, the compounds were reported to have comparable IC_{50} values to that in literature.[13,141,251] However, a large degree of intra-assay variability, and insurmountable ATP agonism by BX430 was experienced. Moreover, BAY-1797 demonstrated incomplete antagonism not able to reduce ATP-induced Ca^{2+} influx down to basal levels. These results differed greatly to the original publications in which complete antagonism and low variability was reported despite utilising two distinct approaches.[141,251] However, literature following a similar protocol to that reported here (chapter **7.7.3**) similarly noted non-traditional concentration response curves.[13,178,245,252] Due to this level of variability, optimisation of the P2X4R antagonist assay developed is required prior to screening of novel candidates.

Selectivity amongst P2X receptors is an important yet often overlooked *in vitro* assessment. Homomeric P2X4R and P2X7R are known to be involved in a number of the same pathologies and have been postulated to physically interact.[33,36,39,40,253] For example, within a chronic pain state both P2X4 and P2X7 receptors are upregulated on microglia to result in a cascade of inflammatory mediators.[123] Therefore, the synthesised compound library were also tested for an inhibitory effect within a THP-1/hP2X7R cell line (assay details available in chapter **7.7.5**).

The inhibitory data of the synthesised compound library (Figure 2.23) at the hP2X7R in the YO-PRO®-1 dye uptake assay are presented in figure 2.24 and table 2.10. Cells were initially treated with compounds at 10 μM concentration, with analogues reporting a decrease in BzATP-induced dye uptake of less than 50% deemed inactive (Figure 2.24). Of the compound library only six compounds were found to be P2X7R inhibitors (**84**, **86**, **113**, **125 – 127**). However, compounds **113** and **126** were found to be insoluble above 10 μM impeding further dose-response experiments. Although limited, these data provide important insights into selectivity and offer further evidence supporting adamantane as a privileged structure for P2X7R.

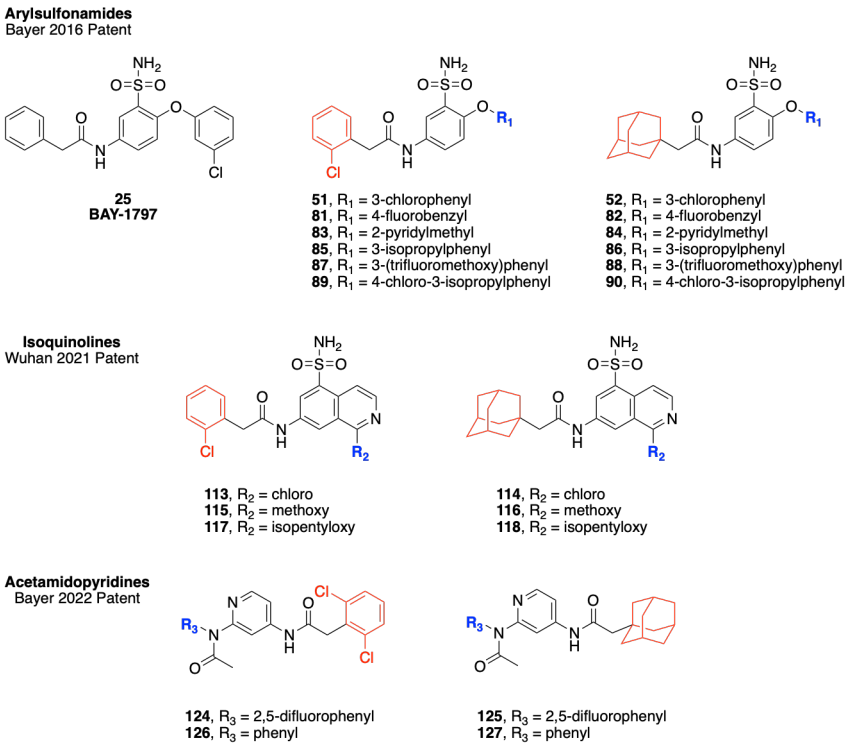

Figure 2.23 Synthesised compound library assessed for antagonistic activity at the hP2X7R.

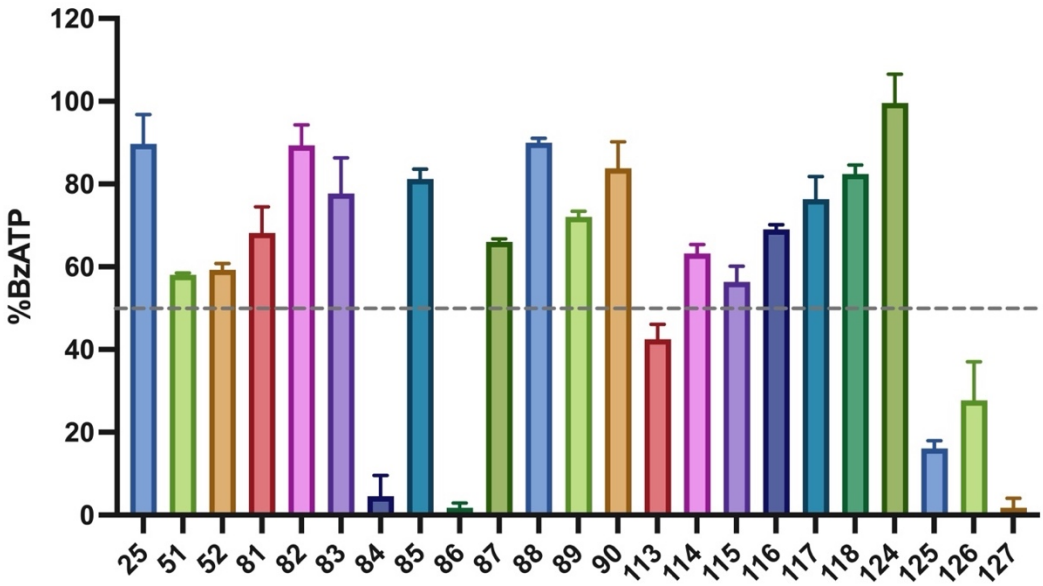

Figure 2.24 Percentage of BzATP induced dye uptake fluorescence of THP-1 cells stably expressing hP2X7R in response to addition of buffer and the compound library at 10 μM. Experiments were performed in duplicate, and data is the mean percentage of the positive control ± SD ($n \geq 3$ experiments). Lower %BzATP indicates less P2X7R activity. Compounds with %BzATP over 50% (dotted line) were deemed inactive.

Across the acetamidopyridine chemotype (**125** and **127**), incorporation of an adamantane motif was consistently beneficial for P2X7R inhibition (Figure 2.24, Table 2.10). In contrast, no clear trend was observed among the arylsulfonamide series, suggesting that inclusion of an adamantane motif alone may not be sufficient to confer P2X7R antagonist activity. Similarly, substitution with the fused isoquinoline ring system, as seen in the WTSDL compounds, appeared to abolish antagonist activity, suggesting a degree of structural flexibility may be required for effective binding at the P2X7R active site. However, considering the reported hP2X4R IC_{50} values for the lead chlorophenyl analogues, these findings suggest a strong potential for selective hP2X4R inhibition. However, such conclusions remain speculative pending further biological evaluation at the hP2X4R.

Table 2.10 *In vitro* IC_{50} values of select compounds at the hP2X7R. Functional dye uptake assay performed using YO-PRO®-1 and human THP-1 cells.

Cmpd	Structure	%BzATP at 10 μM	IC_{50} mean ± SD (nM)[b]	pIC_{50}[c]
84	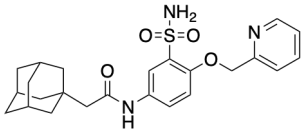	4.46	3010 ± 366	5.5
86	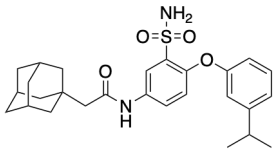	1.76	1160 ± 54	5.9
125	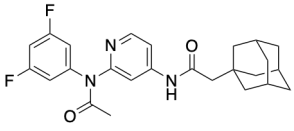	16.12	3720 ± 338	5.5
127	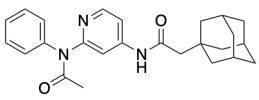	1.76	957 ± 170	6.0

[a]Assay methods used are included in **Chapter 7.7.5**. [b]IC_{50} reported as mean of 3 repetitions, uncertainty reported as standard deviation. [c] negative logarithm (base 10) of the IC_{50} value.

2.6 Concluding Remarks

This chapter has outlined the successful synthesis of three distinct P2X4R antagonist chemotypes and their corresponding adamantane analogues, yielding a total of 23 ligands for *in vitro* evaluation (Figure 2.23). Lead structures were chosen from a range of reported functional activities to enable a robust assessment of the effect of adamantane on both functional activity and selectivity for the P2X4 or P2X7 receptors. *In silico* analysis in the hP2X4R suggests that incorporation of adamantane may result in unfavourable steric clashes with the surrounding protein, correlating with poorer docking scores across all chemotypes (Appendix 4). However, there are limitations in the current methodology, and thus no reliable assertions can be made about the *in vitro* P2X4R binding affinity, or functional activity of these compounds in the absence of biological data.

The P2X4R antagonist assay developed lacked robust reproducibility and failed to replicate the expected effects of known antagonists. Further optimisation of the current assay is required before it can be used for screening of the described compound library. Therefore, as only a limited number of biological results are available for the compound library, no extensive conclusions have been made. Unfortunately, without P2X4R *in vitro* data we are unable to evaluate the effects of adamantane on P2X4R antagonism. However, further support for the correlation between adamantyl-containing ligands and ability to convey P2X7R antagonism has been provided throughout the acetamidopyridine chemotype. Of the synthesised compound library, no analogue reported improved potency to those reported in literature.[254] Therefore, they do not warrant further exploration as novel P2X7 antagonist chemotypes.

The attempted synthesis of trifluoroadamantane acetic acid is also described within **Chapter 2**. The synthetic difficulty experienced in accessing the acetic acid may rationalise the low occurrence of similar analogues in literature and the corresponding commercial price. Although not successfully synthesised, the trifluoroadamantane derivatives will provide valuable data determining the effect of the hydrophobic interaction.[255] By increasing the electron density in the outermost potion of the polycycle through hydrogen-to-fluorine replacement we can assess whether the binding site preference is affected by the strength of the resulting hydrophobic interactions.[255,256] Additionally, the trifluoro analogue is an important comparative structure within metabolic evaluation and other pharmacokinetic studies.

Further conclusions assessing the impact of adamantane will be made as more biological results become available. From these, structure-based drug design can be implemented to investigate the binding pocket and design further optimised drug candidates.

Chapter 3. Diversification of the Benzimidazole Scaffold

3.1 Introductory Remarks

Understanding the relationship between different pharmacophores and the corresponding impact on biological activity lies at the heart of medicinal chemistry. Within drug discovery campaigns, various strategies are employed to create an extensive overview of critical ligand-receptor interactions, which are then used to direct optimisation of lead compounds. Standard approaches include SAR, structure-based ligand design and scaffold hopping techniques.

The current landscape of small-molecule P2Y6 inhibitors is relatively scarce, limited to the three known chemotypes previously discussed in **1.4.6** (Figure 1.15).[164,168,257] As interest in the role of the P2Y6R in pathological states continues to grow, there is an increasing need for potent and selective antagonists to validate animal models and support potential clinical development. In the absence of human P2Y6R structural data, SAR studies such as this one aim to identify key pharmacophoric features for potent and selective P2Y6R antagonists. In 2023, Zhu *et al.* described a series of benzimidazole based P2Y6R antagonists reporting potent activity, with biological in relevance in an inflammatory bowel disease model.[257] However, minimal structural modifications were performed on the original scaffold therefore limiting our knowledge of receptor-ligand interactions within the P2Y6R binding site. The benzimidazole scaffold was identified to have three main moieties that could be subjected to diversification (Figure 3.1). **Chapter 3** describes modifications to the 5,6-heterocycle, and pyrazole motif through traditional SAR approaches (Figure 3.1). Replacement of the metabolic soft spot, as identified by computational methods (Appendix 10), will be discussed in **Chapter 4**.

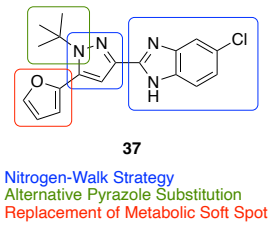

Figure 3.1 Proposed modifications of the benzimidazole chemotype reported by Zhu *et al.*

3.1.1 Chapter Aims

The work described in this chapter aimed to synthesise a series of small-molecule drug candidates with reported activity at the P2Y6 receptor for *in vitro* assay validation. Diversification of the reported benzimidazole scaffold generated analogues designed to probe the electronic and steric allowances of the P2Y6 binding site, revealing key pharmacophoric features for potent and selective antagonism.

3.2 Synthesis of Validation Compounds

To begin the investigation into identifying key pharmacophoric features for potent and selective P2Y6 antagonists, a range of structures from the original patents were chosen as validation tools. The three structures chosen, **37, 153** and **154**, and their reported IC_{50} values are shown in figure 3.2.[257–259] The selected analogues included compounds exhibiting low nanomolar activity as well as approximately thirty-fold weaker activity, serving as positive and 'negative' controls to support validation of the *in vitro* assay being developed concurrently with this study.

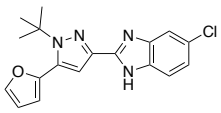

37

Patent:
hP2Y6R IC_{50} = 5.75 nM
% inhib. at 10 μM = 132.71%

Paper:
hP2Y6R IC_{50} = 5.914 nM

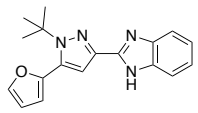

153

Patent:
hP2Y6R IC_{50} = 878.54 nM
% inhib. at 10 μM = 69.12%

Paper:
hP2Y6R IC_{50} = 159.24 nM

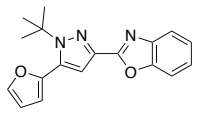

154

Patent:
hP2Y6R IC_{50} = 0.64 nM
% inhib. at 10 μM = 118.06%

Paper:
hP2Y6R IC_{50} = 30.81 nM

Figure 3.2 Reference compounds sourced from the two original patents were synthesised to validate our *in vitro* assay. Data extracted from Li, H. *et al*. **2022** (**37, 153**); Hu, Q. *et al*. **2022** (**154**); Zhu, Y. *et al.* **2023** (**37, 153, 154**).[257–259]

At the time this work was initially undertaken, only patent literature describing these analogues was available.[258,259] Subsequent publication of the corresponding study by Zhu *et al.* revealed discrepancies in the reported IC_{50} values for compounds **37**, **153** and **154** (Figure 3.2).[257] These inconsistencies further underscore the need for validation of the *in vitro* results, which will be discussed in **Chapter 5**.

3.2.1 Synthesis of Benzimidazole Derivatives 37 and 153

The benzimidazole analogues **37** and **153** were synthesised from the common aldehyde intermediate **155**, according to the patent procedure (Scheme 3.1).[258] The synthesis began with a Claisen condensation between 2-acetylfuran (**156**) and diethyl oxalate to form the diketone **157** (Scheme 3.1). The β-diketone intermediate was observed to exist as the enol-tautomer *via* NMR analysis. β-diketones are known to undergo keto-enol tautomerisation, producing two tautomeric forms (**158** and **159**) existing in a relative equilibrium according to the electronics of the substituents (Figure 3.3). The interconversion can be studied relative to NMR timescales.[260] Slow exchange will exhibit separate signals for the keto and enol forms, whereas if interconversion is fast the signals will coalesce to produce a single averaged signal.[260] Within the NMR of compound **157,** only one average structure of the enol form **159** was detected. This phenomenon is common with β-diketones due to the intramolecular hydrogen-bonds formed in the enol form making it highly stabilised.[261,262] The observed ^{1}H and ^{13}C resonances (δ = 6.93 and 99.1 ppm respectively) occur within the expected range of alkenyl -CH groups and are suggested to originate from conjugation-stabilised enolate **159**. A ^{1}H-^{13}C heteronuclear Single Quantum Coherence (HSQC) and heteronuclear multiple bond correlation (HMBC) spectrum was obtained to establish multiple-bond correlation between the observed alkenyl -CH resonance and the corresponding alkene and carbonyl carbons respectively, confirming the enolate **159** structure (Figure 3.3).

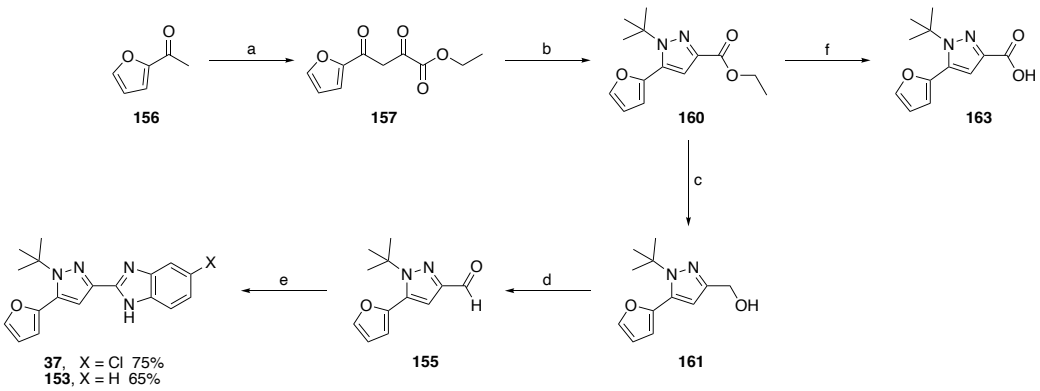

Scheme 3.1 Synthesis of benzimidazole validation compounds **37** and **153**. *Reagents and Conditions* (a) diethyl oxalate, *t*-BuOK, ethylene glycol dimethyl ether, THF, 0 – 25 °C, 1 h, 63 – 83% (b) *tert*-butylhydrazine hydrochloride, EtOH, rt, 8 h, 94% (c) $LiAlH_4$, THF, reflux, 2 h, 86 – 96% (d) DMP, CH_2Cl_2, rt, 2 h, 60 – 94% (e) 4-chlorobenzene-1,2-diamine or benzene-1,2-diamine, $NaHSO_3$, EtOH:H_2O (2:1), reflux, 2 h; (f) LiOH.H_2O, MeOH/H_2O (3:1), reflux, 1 h, quant.

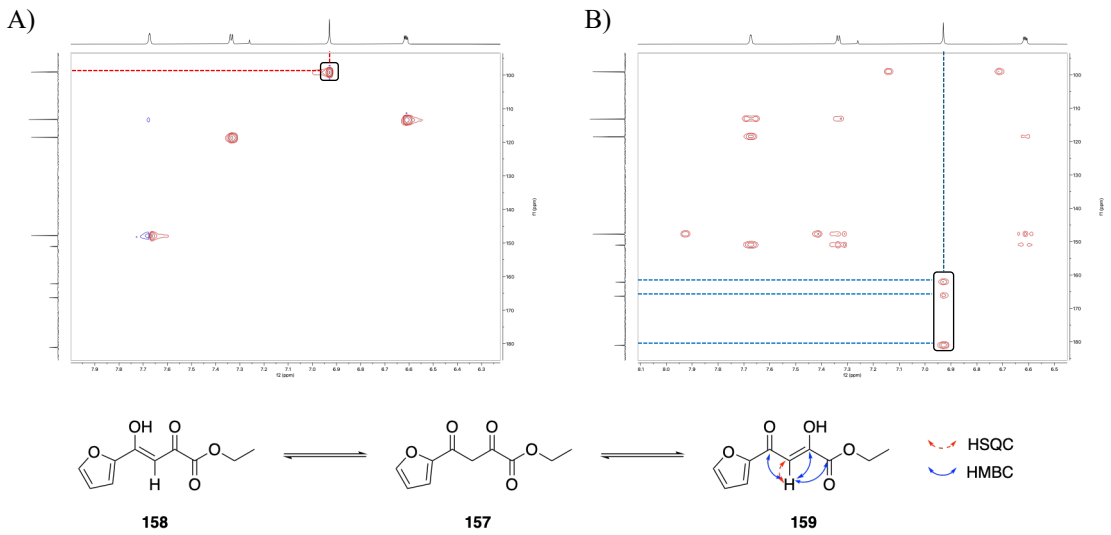

Figure 3.3 ^{1}H – ^{13}C HSQC (A, red dashed arrow) and HMBC (B, blue solid arrow) correlation of *β*-diketone **157** and associated enolate forms ($CDCl_3$, 400 MHz, 298 K).

A Paal-Knorr synthesis of **157** and *tert*-butylhydrazine hydrochloride rendered the desired 1,3,5-trisubstituted pyrazole (**160**). Traditionally, the condensation of hydrazines with 1,3-dicarbonyl compounds suffers from poor regio-selectivity.[263] However, the former reaction was found to be regio-specific to the desired 5-furan regioisomer. Although lacking the expected nuclear Overhauser effect (NOE) correlation between the 2H of the furan and the *tert*-butyl, the produced NMR spectra matched supporting literature.[263] The regio-specificity was similarly observed by Ruatta *et al.* when using *tert*-butylhydrazine compared to less sterically hindered hydrazines, suggesting that steric interactions between the bulky *tert*-butyl group and the furyl moiety play a crucial role in directing the reaction.[263] The aldehyde intermediate **155** was then achieved through reduction of the ester (**160**) to the primary alcohol **161** with $LiAlH_4$ and subsequent oxidation with DMP (Scheme 3.1). Condensation of the appropriate diamine and **155** in the presence of sodium bisulfite afforded the two analogues **37** and **153** in moderate yields (Scheme 3.1). Characterisation of **37** demonstrated tautomerism to occur in solution.

Existing in dynamic equilibrium with one another, tautomerism is facilitated by low energy barriers between the molecule's energy minima.[264] The corresponding effect can alter the positioning of hydrogen bond donors and acceptors, and therefore structure orientation in the binding pocket. Additionally, small changes in molecular structure or solvent environment can dramatically change the ratio of tautomers.[265] Characterisation of tautomers *via* NMR is either

simplified or complicated depending on the relative time scale of proton exchange and interaction with the solvent.[260] Furthermore, the tautomeric equilibrium is largely influenced by the dielectric constant of the medium and the ability of solvents to form hydrogen bonds with the tautomer.[266] Tautomerism within benzimidazole scaffolds is well reported, however elucidation of the corresponding NMR spectra is often overlooked with most studies merely aiming to obtain a better spectra for publication.[266,267]

Compound **37** exhibits the [1,3]H-shift based annular tautomerism characteristic of the benzo[*d*]imidazaoles.[268] Within unsubstituted or symmetrically substituted benzimidazole derivatives the N1(H)/N3(H) prototropic equilibria are energetically degenerate.[268] However, due to the positioning of the chlorine functional group, a non-degenerate pair of tautomers results, producing unique chemical environments within NMR spectroscopy. This was posited due to the presence of the two singlets representing the benzimidazole NH (δ = 12.94 – 12.70 (m, 1H) ppm) of **37** (Figure 3.4A). This was later confirmed through saturation-transfer and elevated temperature (343 K) experiments where the two singlets were observed to decrease in intensity and converge respectively (Figure 3.4). Saturation-transfer difference NMR experiments (STD-NMR) are often utilised to identify ligand-receptor binding interactions.[269,270] However, the approach has since been adapted to probe chemical exchange processes such as tautomerism.[271,272] In these experiments, spectra are recorded with off-resonance irradiation (reference spectra) and on-resonance irradiation, where radiofrequency pulses are applied to a single proton resonance.[269] Continuous irradiation leads to saturation of the targeted nucleus, and if chemical exchange is present, this saturation is transferred to the exchanging species.[272] This transfer of magnetization in the on-resonance experiment leads to a significant reduction in signal intensities for the ligand.[270] For tautomeric systems undergoing dynamic exchange, selective irradiation of a resonance corresponding to one tautomer (e.g. NH singlet at 12.77 ppm, Figure 3.4A) results in attenuation or disappearance of the irradiated signal.[270] Simultaneously, the corresponding resonance of the exchanging tautomer (e.g. NH singlet at 12.83 ppm, Figure 3.4A) is reduced in intensity due to saturation transfer mediated by chemical exchange. All other resonances that do not participate in the exchange process remain unaffected, producing a spectrum depicting a mixture of tautomers minus the irradiated peak.[270]

Furthermore, during the NMR analysis of **37**, it was noticed that some signals of the benzimidazole ring in the ^{1}H and ^{13}C NMR spectra broadened and their intensity dropped at ambient temperature in $CDCl_3$. Exploring alternative deuterated protic- and aprotic solvents (CD_3OD, CD_3CN, Acetone-d_6, DMSO-d_6) identified significant solvent effects on the resonance lines as well as the ^{1}H and ^{13}C NMR chemical shifts observed. Within the ^{13}C spectra (300 K, DMSO-d_6), duplicated signals of some carbon atoms located in the neighbourhood of the tautomeric interconversion sites were clearly observed. The formation of intermolecular hydrogen bonds could decrease the rate of interconversion between the two tautomers when DMSO-d_6 was used as a solvent (Appendix 5). Therefore, due to the strong solute-solvent interaction, two sets of carbon signals were observed. To investigate this further, high-temperature experiments at 343 K were performed with the hope that introducing energy to the system, **37** would converge. However, we failed to see the signals coalesce and rather the intensity of the quaternary carbons dropped significantly, appearing as part of the baseline (Figure 3.4B). As the rate of inter-conversion between tautomer's decreases in correlation with reduction of temperature, **37** was also analysed in acetone-d_6 at 203 K, in an effort to intensify the two sets of ^{1}H signals of the benzimidazole ring. It was observed that cooling to 203 K only resulted in further broadening (Figure 3.4B). Crystallography techniques were next explored to confirm the hypothesised molecule structure by X-ray crystallography. Multiple attempts utilising a variety of crystallography techniques – e.g. slow evaporation, vapour diffusion and layer diffusion in a variety of solvents – were conducted to no avail.[273] This phenomenon will be further discussed in **Chapter 4** in relation to the compound library of furan-substituted derivatives.

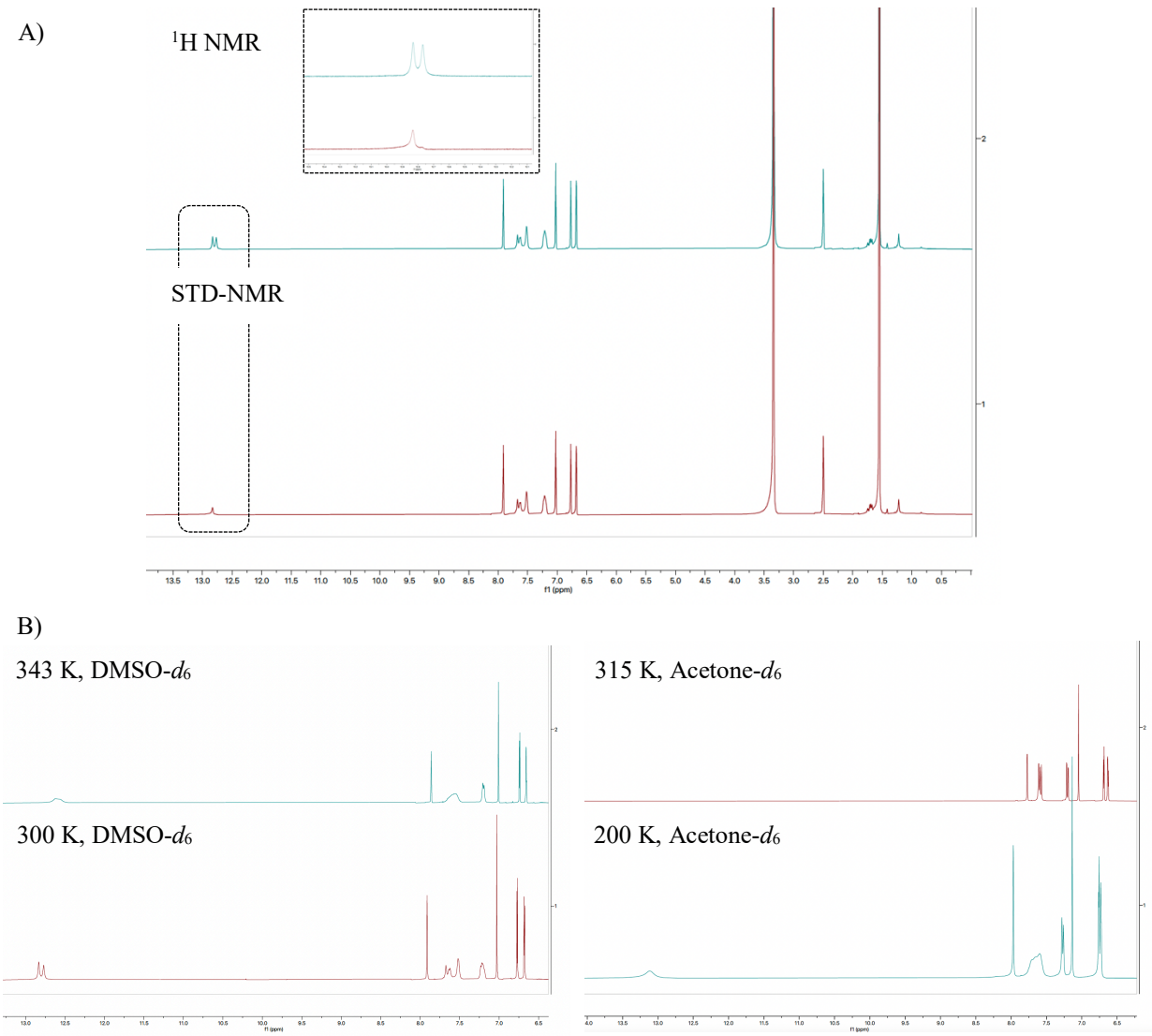

Figure 3.4 ^{1}H NMR (400 MHz) analysis of **37** tautomers by STD-NMR (A) and variable temperature (VT) NMR (B).

3.2.2 Synthesis of Benzoxazole Derivative 154

It was initially envisioned that the benzoxazole derivative **154** could be accessed *via* a one-pot cyclocondensation reaction between **155** and 2-aminophenol as described in scheme 3.1 (Table 3.1, entry 1).[259] However, following prolonged heating and addition of an excess of 2-aminophenol no product formation was observed. Mass spectrometry analysis of the crude reaction mixture suggested that the reaction was stalling at the imine intermediate. Magnesium sulfate was added to the reaction mixture to act as a water scavenger and drive the equilibrium in the forward direction (Table 3.1, entry 2). However, this also failed to yield the desired product.

Table 3.1 Cyclocondensation conditions for the synthesis of **154** from aldehyde intermediate **155**.

155 **154**

Entry	Conditions	Yield
1	2-aminophenol, $NaHSO_3$, EtOH:H_2O (2:1), reflux, 48 h	S.M. [a]
2	2-aminophenol, $NaHSO_3$, $MgSO_4$, EtOH, reflux, 48 h	S.M. [a]
3	2-aminophenol, MeOH/Glycerol (1:5), 90 °C, 16 h	S.M. [a]
4	2-aminophenol, $Na_2S_2O_5$, EtOH, 140 °C, MW, 1 h	S.M. [a]
5	2-aminophenol, PIFA, EtOH, 140 °C, MW, 2 h	—[b]

[a] S.M. represents recovered starting material, as no reaction occurred. [b] Complex reaction mixture as indicated by TLC analysis. MW represents reactions performed inside a microwave reactor. PIFA: Phenyliodonium bis(trifluoroacetate)

An alternative reaction media of glycerol/methanol was trialled to accommodate higher reaction temperatures (Table 3.1, entry 3). Glycerol has shown great utility as an alternative green reaction medium in base- and acid-promoted condensations, Pd-catalysed cross-coupling reactions and catalytic hydrogenation.[274] Although reported to include both electron withdrawing and donating derivatives in the reaction scope, the protocol was similarly unsuccessful with only starting material isolated.[274]

Sodium metabisulfite, $Na_2S_2O_5$, has been shown to effectively promote the oxidative cyclisation of the imine intermediate.[275] However, under microwave-assisted conditions sodium metabisulfite, proved equally unsuccessful (Table 3.1, entry 4).[275] Phenyliodonium bis(trifluoroacetate) (PIFA, **162**) was also trialled as an alternative oxidant (Table 3.1, entry 5).[276] In the presence of PIFA (**162**), the imino nitrogen (**I**, Figure 3.5) can attack the trivalent iodine, making the adjacent carbon more electrophilic.[276] This activation facilitates nucleophilic attack by the oxygen lone pair, leading to formation of the benzoxazoline intermediate **I** (Figure 3.5). The benzoxazole is formed following subsequent dehydrogenation with iodobenzene and trifluoroacetic acid as by-products (Figure 3.5).[276] Although, the one-pot cyclocondensation under microwave irradiation resulted in a complex reaction mixture, with no sign of product formation by mass spectrometry.

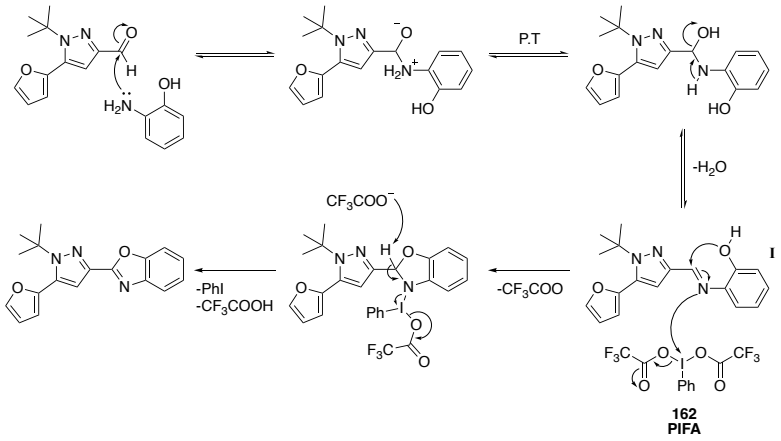

Figure 3.5 Reaction mechanism for the formation of benzoxazoles with phenyliodonium bis(trifluoroacetate) as the oxidant.[276]

Conventionally, condensation reactions to yield benzoxazoles require the carboxylic acid derivative in the presence of a strong acid at high temperature.[277–279] Due to the susceptibility of the *tert*-butyl group present in the starting material to undergo cleavage under analogous conditions these methods were initially avoided. The transformation in polyphosphoric acid (PPA) was therefore undertaken cautiously. Firstly, the carboxylic acid intermediate **163** was achieved *via* the ester hydrolysis of **160** (Scheme 3.1). Under solvent free conditions, **163** was treated with PPA. Pre-heating the PPA at 80 °C aided the transfer of the reagent.[279,280] Following heating at 100 °C for several hours (Table 3.2, entry 1), only starting material was recovered. Although unsuccessful, the reaction demonstrated that the *tert*-butyl group could withstand relatively harsh conditions and thus validated future attempts utilising sulfonic acid catalysts.

Table 3.2 Amide coupling and subsequent cyclisation conditions trialled to synthesis **154** from carboxylic acid intermediate **163**.

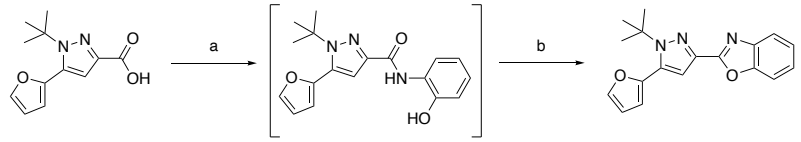

163 **164** **154**

Entry	Conditions	Yield
1	2-aminophenol, PPA, 100 °C, 18 h	S.M. [a]
2	a. 2-aminophenol, HATU, $^{i}Pr_2NEt$, DMF, rt, 6 h b. *p*-$MePhSO_3H.H_2O$, toluene, reflux, 24 h	8%
3	a. 2-aminophenol, HATU, $^{i}Pr_2NEt$, DMF, rt, 6 h b. *p*-$MePhSO_3H.H_2O$, toluene, 110 °C, MW, 1 h	—[b]
4	a. $(COCl)_2$, cat. DMF, CH_2Cl_2, rt, 1 h b. 2-aminophenol, $MeSO_3H$, 1,4-dioxane, reflux, 24 h	—[c]

[a] S.M. represents recovered starting material, as no reaction occurred. [b]Complex reaction mixture as indicated by TLC analysis. [c]Reaction didn't proceed past amide formation. MW represents reactions performed inside a microwave reactor.

Cyclisation of complex phenyl groups with sulfonic acid catalysts (i.e. *p*-$MePhSO_3H$ or $MeSO_3H$) to form benzoxazoles is reported.[278,281] Amidation with 2-aminophenol under HATU coupling conditions yielded the amide derivative (**164**) (Table 3.2, entries 2 and 3). The cyclisation of **164** to the desired benzoxazole **154** was achieved by heating with *p*-$MePhSO_3H$.[281] However, the reaction suffered from poor yields due to a challenging purification. In addition, amide starting material and the free pyrazole derivatives of both starting material and product were isolated (Table 3.2, entry 2). In an effort to reduce *tert*-butyl cleavage the cyclisation reaction was trialled under microwave irradiation. However, no reaction was observed with reduced reaction times (Table 3.2, entry 3). To increase the electrophilicity of the carbonyl carbon for nucleophilic attack the acid chloride was first formed.[278] The one-pot approach sees addition of 2-aminophenol in the presence of $MeSO_3H$ to the corresponding acid chloride of **163**. Unfortunately, this approach furnished a worse result and saw a complex reaction mixture form (Table 3.2, entry 4).

Following these unsuccessful attempts to yield **154**, the corresponding paper describing the patented compounds was published.[257] Within the paper, the synthesis of the 2-arylbenzoxazoles was disclosed to have been synthesised *via* 2,3-dichloro-5,6-dicyano-1,4-benzoquinone (DDQ) promoted oxidative cyclisation of the corresponding Schiff base.[257]

Formation of benzoxazoles *via* DDQ promoted oxidative cyclisation has been shown to be successful for a broad range of aldehydes with both electron donating and electron-withdrawing groups.[282] The Schiff base (imine intermediate) was generated *in situ* upon treating aldehyde **155** with 2-aminophenol in methanol overnight (Scheme 3.2). Subsequent oxidation by DDQ yielded the desired benzoxazole **154** in low yields.

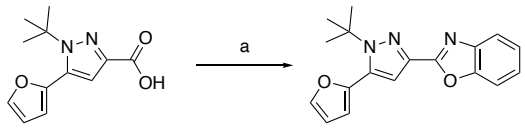

163 **154**

Scheme 3.2 Synthesis of the benzoxazole validation compound by oxidation by DDQ. *Reagents and Conditions* (a) 1. 2-aminophenol, MeOH, 45 °C, 12 h; 2. DDQ, CH_2Cl_2, rt, 24 h, 23%. DDQ: 2,3-dichloro-5,6-dicyano-1,4-benzoquinone.

3.3 Nitrogen Walk Approach to Explore Bioisosteric Replacement of the 5,6-Heterocycle

Heteroaromatic nitrogen compounds were identified among the most significant structural components of pharmaceuticals by a retrospective analysis of FDA-approved drugs.[283] A common strategy in modern drug design, known as the 'nitrogen-walk', involves replacing a CH group with a nitrogen atom within aromatic or heteroaromatic rings. This subtle modification is frequently employed during lead identification and optimisation to preserve or enhance key physicochemical and pharmacological properties.[284–287] Such effects generally occur due to changes in ligand-receptor interactions around critical hydrogen bonding and electrostatic interactions with important residues within the binding site.[284] As a result, this approach has been implicated in library design for ligands targeting GPCRs with varying degrees of success.[284–287] However, application of this approach within the infancy stage of SAR studies proves extremely beneficial in identifying key ligand-receptor binding interactions. As such, a nitrogen-walk around the 5,6-heterocycle motif (Figure 3.6) was proposed to gain a greater understanding about the electronics and favourable binding interactions within the P2Y6 binding site. The target compound library (**165** – **181**) is displayed in figure 3.6. Particular interest surrounds the purine (**167**) analogue due its shared features with endogenous nucleotides. In addition, the imidazo[1,2-*a*]pyridine (**169**) moiety is commonly recognised as a 'drug prejudice' scaffold due to its wide applications in medicinal chemistry.[288–290]

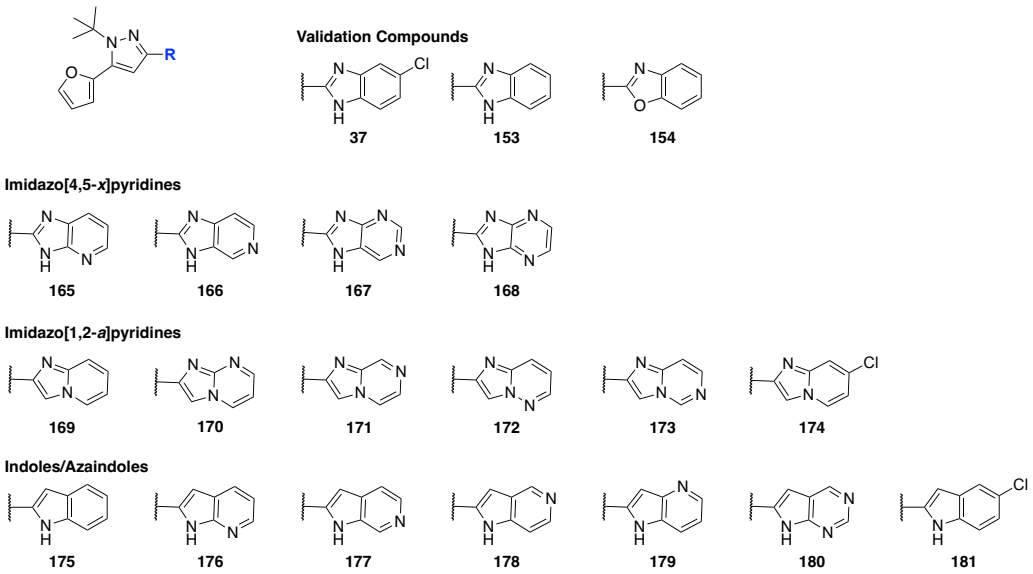

Figure 3.6 Proposed compound library illustrating diversification of the 5,6-heterocycle pharmacophore through a nitrogen-walk strategy.

3.3.1 Synthesis of the Imidazo[4,5-*x*]pyridine and Purine Analogues

The initial synthetic route used to access the imidazo[4,5-*x*]pyridine and purine analogues (**165** – **168**) is shown in scheme 3.3A. The condensation of *ortho*-phenylenediamine derivatives with carboxylic acids is a common protocol employed to synthesise 2-substituted benzimidazole analogues, with multiple catalytic partners reported.[291,292] Mechanistically, the reaction proceeds *via* the amide intermediate, and therefore has been reported as both a one- and two-step process.[291,293,294] Amidation conditions were trialled concurrently with the two diamine reagents (**182** and **183**, Scheme 3.3A). 1,1'-Carbonyldiimidazole (CDI) and 1-ethyl-3-(3-dimethylaminopropyl)carbodiimide hydrochloride (EDC.HCl) mediated couplings both successfully formed the respective amides as confirmed by mass spectrometry (Table 3.3, entries 1 – 4).[293,294] It was then proposed that the respective amides could be cyclised to form the desired imidazo-pyridine derivatives without prior isolation. Cyclisation conditions encompassing both acid free (Table 3.3, entry 1) and a spectrum of acids varying strength (*p*-$MePhSO_3H.H_2O$, AcOH) in elevated temperatures (Table 3.3, entries 2 – 4) were conducted to no avail.[293–296]

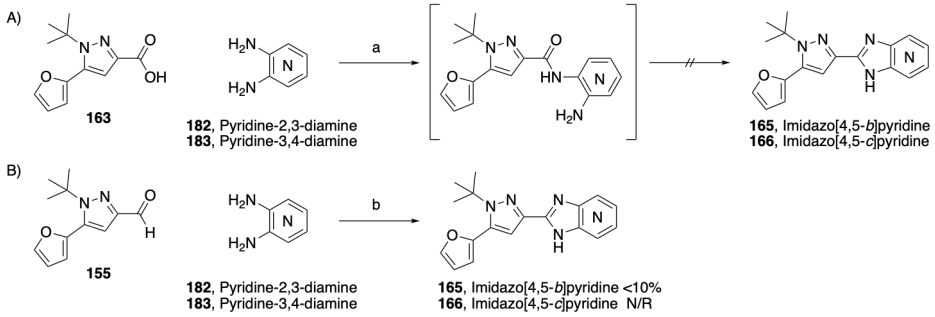

Scheme 3.3 Synthesis of imidazo[4,5-*x*]pyridine derivatives from the respective diamine and carboxylic acid (A) and aldehyde (B) starting materials. *Reagents and Conditions* (a) provided in Table 3.3 (b) appropriate diamine, $NaHSO_3$, EtOH:H_2O (2:1), reflux, 2 h. N/R: no reaction.

Table 3.3 Amide coupling and cyclisation conditions trialled in the synthesis of imidazo[4,5-*x*]pyridine derivatives.

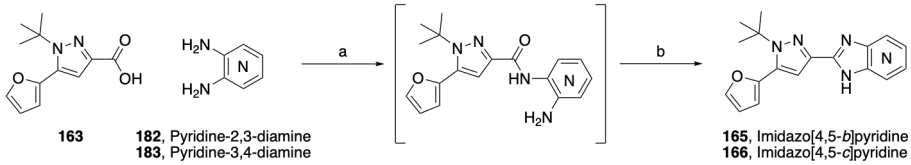

Entry	No.	Pyridine Diamine	Conditions	Yield
1	**165**	**182**	a. CDI, THF, 60 °C, 12 h b. 60 °C, 12 h	— [a]
2	**165**	**182**	a. CDI, THF, 60 °C, 12 h b. *p*-$MePhSO_3H.H_2O$, toluene, 130 °C, sealed tube, 16 h	— [b]
3	**166**	**183**	a. EDC.HCl, $HOBt.H_2O$, Et_3N, DMF, 60 °C, 12 h b. *p*-$MePhSO_3H.H_2O$, toluene, reflux, 24 h	— [a]
4	**166**	**183**	a. EDC.HCl, $HOBt.H_2O$, Et_3N, DMF, 60 °C, 12 h b. AcOH (0.1 M), reflux, 12 h	— [a]

[a] Reaction didn't proceed past amide formation. [b] Complex reaction mixture as indicated by TLC analysis. CDI: 1,1'-Carbonyldiimidazole; $HOBt.H_2O$; 1-Hydroxybenzotriazole hydrate. EDC.HCl: 1-Ethyl-3-(3-dimethylaminopropyl)carbodiimide hydrochloride.

Following the success of the benzimidazole derivatives (chapter **3.2.1**) it was envisioned that a late-stage cyclocondensation reaction could be performed on the aldehyde intermediate **155** and the respective diamine. Compound **155** was treated with the respective diamine in the presence of sodium bisulfite in an EtOH/H_2O solvent mixture. Unfortunately, this approach afforded **165** in very low yields (< 10%), with no product formation observed for the pyridine-3,4-diamine analogue (Scheme 3.3B). To overcome this, sodium metabisulfite, $Na_2S_2O_5$, was

introduced to the reaction as a reducing agent.[292] $Na_2S_2O_5$ first reacts with the aldehyde by donating electrons to form a metabisulfite adduct of aldehyde **155**.[297] The diamine, then readily condenses with this reactive adduct to form the 2-substituted imidazo-pyridine and purine analogues (**165 – 168**) in moderate yields (Table 3.4).[275,297–299]

Table 3.4 Synthesis of imidazo[4,5-*x*]pyridine derivatives *via* the condensation of **155** with $Na_2S_2O_5$ as an oxidant.

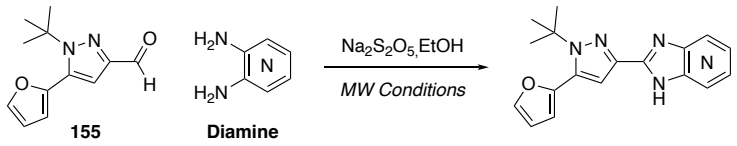

Entry	No.	Diamine	Product	MW Conditions	Yield
1	**166**	Pyridine-3,4-diamine	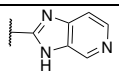	15 min, 80 °C; 5 min, 100 °C	—[a]
2	**166**	Pyridine-3,4-diamine	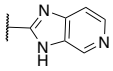	5 min, 80 °C; 5 min, 140 °C	35%
3	**165**	Pyridine-2,3-diamine	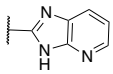	5 min, 140 °C (x4)	32%
4	**167**	Pyrimidine-3,4-diamine	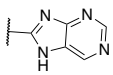	5 min, 140 °C (x4)	25%
5	**168**	Pyrazine-2,3-diamine	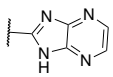	5 min, 140 °C (x4)	30%

[a] Reaction stalled at imine intermediate. No product was formed. MW represents reactions performed inside a microwave reactor.

3.3.2 Synthesis of Imidazo[1,2-*a*]pyridine Analogues

Access to the final imidazo[1,2-*a*]pyridine analogues (**169** – **174**) was envisioned to be achieved *via* the three-step retrosynthetic approach shown in figure 3.7. The final analogues would be afforded from an Ortoleva-King type reaction with the respective aniline derivative and ketone intermediate **184**. A Claisen condensation (**185**) and subsequent Paal-Knorr pyrazole formation could be employed to yield ketone **184**.

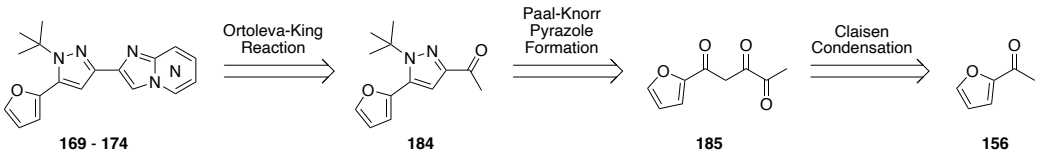

Figure 3.7 Retrosynthetic approach of accessing the imidazo[1,2-*a*]pyridine derivatives (**169** – **174**).

3.3.2.1 Synthesis of Ketone Intermediate

Initial attempts to synthesise the β-ketone (**185**) included a Claisen condensation of 2-acetylfuran (**156**) with ethyl pyruvate (**186**). Three distinct attempts were conducted to yield the β-ketone product (Table 3.5, entries 1 – 3). These conditions encompassed a range of bases varying in strength and nature (*t*-BuOK, NaH and NaOMe), both aprotic and protic solvents (THF, MeOH) and temperatures.[257,300] The mechanism involves abstraction of an α-hydrogen from the carbonyl compound to form the resonance-stabilised enolate.[301] Thus, the success of the reaction largely relies on the alkoxide source. Unfortunately, product formation was still not observed when a 1M solution of NaOMe was freshly prepared in house (Table 3.5, entry 4). Therefore, the negative results were postulated to be due to the poor reactivity of ethyl pyruvate.

Table 3.5 Claisen condensation attempts to synthesise the β-ketone (**185**).

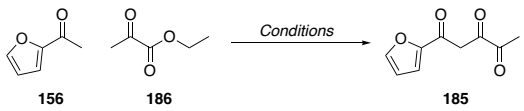

156 **186** **185**

Entry	Conditions	Yield
1	*t*-BuOK, THF, 0 – 25 °C, 16 h	S.M. [a]
2	NaH, THF, 50 °C, 3 h	— [b]
3	NaOMe, MeOH, reflux, 16 h	S.M. [a]
4	NaOMe (1M prepared in house), MeOH, reflux, 16 h	S.M. [a]

[a] S.M. represents recovered starting material, as no reaction occurred. [b] Complex reaction mixture as indicated by TLC analysis.

To overcome the issues associated with the synthesis shown in figure 3.7, a slightly altered synthesis of **184** was undertaken. The adjusted synthesis is shown in scheme 3.4 and focused on construction of the ketone functionality *via* a Weinreb ketone synthesis. The corresponding Weinreb amide **187** was synthesised *via* a HATU-mediated amide coupling of the previously synthesised carboxylic acid **163** with *N,O*-dimethylhydroxylamine hydrochloride (Scheme 3.4). Alkylation of **187** with methylmagnesium bromide (MeMgBr) proceeded in excellent yields to form the desired ketone **184** (Scheme 3.4).

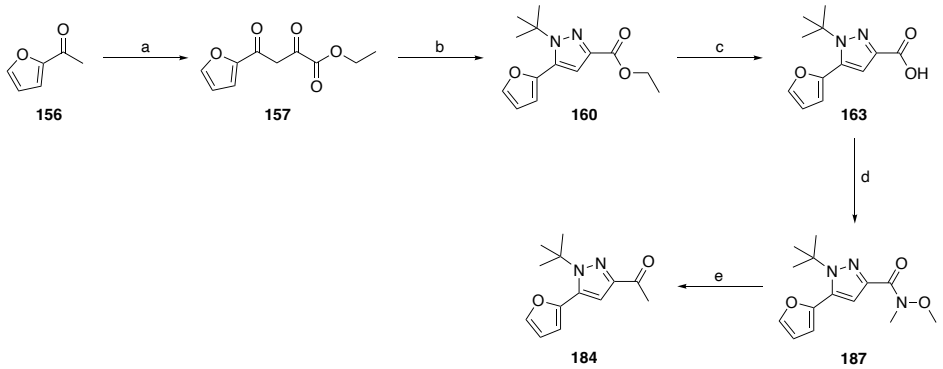

Scheme 3.4 Synthesis of key ketone intermediate **184** *via* a Weinreb amide. *Reagents and Conditions* (a) diethyl oxalate, *t*-BuOK, ethylene glycol dimethyl ether, THF, 0 – 25 °C, 1 h, 63 – 83% (b) *tert*-butylhydrazine hydrochloride, EtOH, rt, 8 h, 94% (c) LiOH.H_2O, MeOH/H_2O (3:1), reflux, 1 h, quant. (d) *N*,*O*-dimethylhydroxylamine hydrochloride, HATU, $^{i}Pr_2NEt$, DMF, rt, 4 h, 85–94% (e) MeMgBr (3M in diethyl ether), THF, 0 – 25 °C, 2 h, 74–96%.

3.3.2.2 Ortoleva-King Type Reaction

The imidazo[1,2-*a*]pyridine scaffold has shown to be beneficial in both drug design and materials chemistry. Recognised as a 'drug prejudice' scaffold, the motif has been heralded as one of the most versatile building blocks in organic chemistry.[288–290] Consequently, methods to synthesise and diversify the imidazo[1,2-*a*]pyridines scaffold are expansive.[290] The Ortoleva-King type imidazo[1,2-*a*]pyridine synthesis describes the reaction of active methylene compounds with stoichiometric amounts of molecular iodine and 2-aminopyridine (Scheme 3.5).[302] A one-pot method was undertaken in which an Ortoleva-King intermediate (pyridinium iodide **I**, Figure 3.8) is generated *in situ*, followed by I_2–NH_4OAc assisted cyclisation.[290] Mechanistically, α-iodination of the aryl ketone first occurs generating the iodoketone **II** (Figure 3.8). The lone pair of the pyridine endocyclic nitrogen attacks the α-carbon to produce the pyridinium salt **I** (Figure 3.8). Deprotonation of **III** by NH_4OAc, forms the corresponding imine **IV** which undergoes an intramolecular cyclisation to from the tetrahydro imidazo[1,2-*a*]pyridin-2-ol (**V**, Figure 3.8). Aromaticity is then regained *via* the condensation of **V** to form the imidazo[1,2-*a*]pyridine product **169**.[290] Performing the reaction with 2-aminopyridine at room temperature under an inert atmosphere resulted in poor yields and an arduous purification (Table 3.6, entry 1). Yields were increased slightly when performed at elevated temperature (Table 3.6, entry 2) and under an aerobic atmosphere (Table 3.6, entries 3 and 5), however the reaction still suffered from purification issues. Complex separation is often observed when using stoichiometric amounts of iodine due to the formation of iodide by-products. An alternative source of iodine in *N*-iodosuccinimide (NIS) was utilised as the

succinimide by-product could easily be removed *via* a basic workup procedure (Table 3.6, entry 4).[303] Unfortunately, it failed to furnish the desired product.

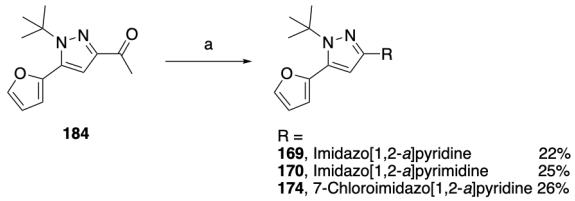

Scheme 3.5 Synthesis of imidazo[1,2–*a*]pyridine derivatives (**169**, **170**, **174**) from **184** under Ortoleva-King like conditions. *Reagents and Conditions* (a) appropriate amino pyridine, I_2, NH_4OAc, EtOH, reflux, air, 24 h.

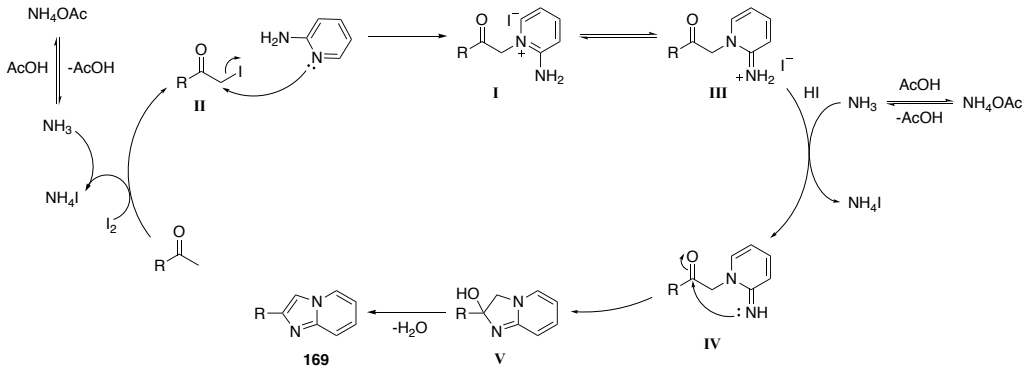

Figure 3.8 Proposed mechanism for the synthesis of imidazo[1,2-a]pyridine *via* an Ortoleva-King like reaction.

Table 3.6 Ortoleva-King like conditions for the synthesis of imidazo[1,2–*a*]pyridine derivatives.

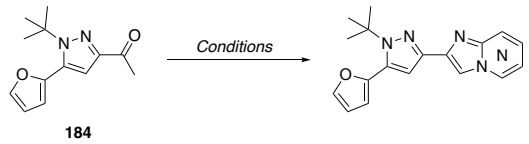

Entry	No.	Aniline	Product	Conditions	Yield
1	**169**	2-Aminopyridine	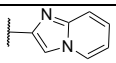	I_2, NH_4OAc, EtOH, rt, N_2, 24 h	15%
2	**169**	2-Aminopyridine	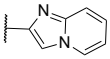	I_2, NH_4OAc, EtOH, reflux, N_2, 24 h	19%
3	**170**	2-Aminopyrimidine	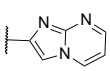	I_2, NH_4OAc, EtOH, reflux, air, 24 h	22%
4	**170**	2-Aminopyrimidine	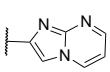	NIS, H_2O, 80 °C, air, 6 h	S.M.[a]
5	**174**	4-Cl-pyridin-2-amine	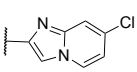	I_2, NH_4OAc, EtOH, reflux, air, 24 h	26%

[a] S.M. represents recovered starting material, as no reaction occurred

To overcome the poor yields experienced, an alternative strategy was employed involving the α-bromoketone derivative **188**. The α-bromoketone was first synthesised by way of a silyl enol ether intermediate. Silyl enol ether **189** was prepared by treatment of **184** with trimethylsilyl trifluoromethanesulfonate (TMSOTf) under basic conditions. The desired α-bromoketone **188** was then isolated following α-bromination of **189** with *N*-bromosuccinimide (NBS) under basic conditions (Scheme 3.6). To avoid potential decomposition the α-bromoketone was stored under nitrogen at -20 °C.

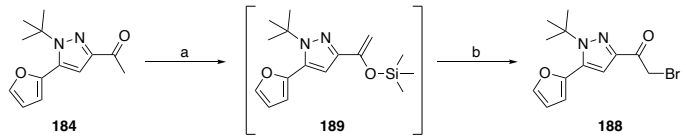

Scheme 3.6 Synthesis of α-bromoketone intermediate **188** *via* a silyl enol ether (**189**). *Reagents and Conditions* (a) TMSOTf, $^{i}Pr_2NEt$, CH_2Cl_2, 0 – 25 °C, 5 h, not isolated (b) NBS, THF, 0 – 25 °C, 6 h, 53%.

The desired imidazo[1,2-*a*]pyridine analogues (**169 – 172**) were successfully synthesised by treating **188** with the respective anilines (Table 3.7, entries 1 – 5). Following an analogous pathway to the Ortoleva-King like reaction, catalytic DBU (**190**) was trialled to promote imine formation (Table 3.7, entry 1).[304] DBU (**190**) is a sterically hindered amidine base, introduced to abstract a proton from the amine group of the pyridinium salt (**I**, Figure 3.9). The inclusion of base was reported to enable the reaction to be performed at ambient temperature, a valuable parameter when in the presence of labile motifs such as the *tert*-butyl.[304] Following 12 h, the reaction mixture was deemed to be mainly starting material by TLC analysis. Heating the reaction mixture to reflux afforded the desired product in a higher yield than the iodo-trial (Table 3.7, entry 1), albeit with challenging purification. A control experiment in the absence of base (Table 3.7, entry 2) identified that the α-bromoketone **188** readily reacted with the desired anilines in moderate yields (Scheme 3.6).[305] Performing the reaction in a sealed vessel at elevated temperatures improved the yields further and was thereby identified as the optimal conditions for further diversification (Table 3.7, entries 3 – 5).[305] The optimised conditions demonstrated a broad substrate amongst various heterocycles (Table 3.7, entry 6), with the exception of 4-aminopyrimidine (**173**). Crude analysis of the 4-aminopyrimidine reaction mixture by mass spectrometry suggested successful formation of the imine intermediate (*m/z*

326 $[M+H]^+$). It is postulated that due to the arrangement of nitrogens in the ring, the imine intermediate is highly stabilised through resonance, thereby cyclisation is not favoured.[306]

Table 3.7 Conditions for the synthesis of imidazo[1,2-*a*]pyridine derivatives from α-bromoketone **188** starting material.

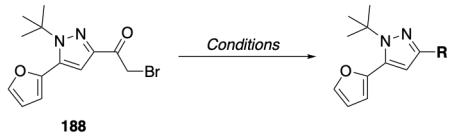

188

Entry	No.	Aniline	R	Conditions	Yield
1	**169**	2-Aminopyridine	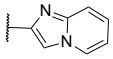	DBU, EtOH/H_2O, rt – reflux, 20 h	36%
2	**172**	3-Aminopyridazine	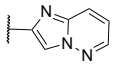	EtOH, reflux, 48 h	70%
3	**172**	3-Aminopyridazine	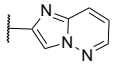	EtOH, 100 °C, sealed tube, 24 h	73%
4	**170**	2-Aminopyrimidine	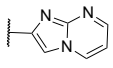	EtOH, 100 °C, sealed tube, 24 h	62%
5	**171**	2-Aminopyrazine	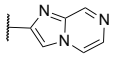	EtOH, 100 °C, sealed tube, 24 h	57%
6	**173**	4-Aminopyrimdine	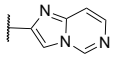	EtOH, 100 °C, sealed tube, 24 h	— [a]

[a] Complex reaction mixture as indicated by TLC analysis. No sign of product formation by mass spectrometry analysis. DBU: 1,8-Diazabicyclo[5.4.0]undec-7-ene.

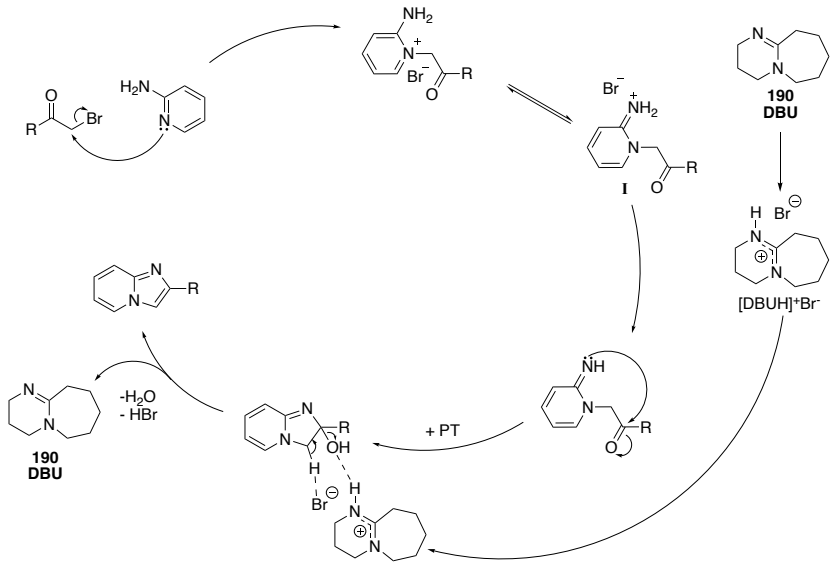

Figure 3.9 DBU promotes imine formation and through abstracting the amine proton of the pyridinium salt, thereby allowing for the reaction to occur under more mild conditions.

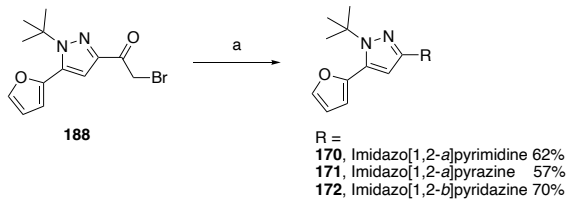

Scheme 3.6 Synthesis of imidazo[1,2-*a*]pyridine derivatives (**170 – 172**) from α-bromoketone **188** starting material.

The attempted synthetic pathways to access the imidazo[1,2-*c*]pyrimidine analogue **173** are summarised in table 3.8. Attempts presented in entries 1 – 3 have previously been described in this chapter (see **3.3.2.2**). The cyclocondensation reaction between 4-aminopyrimidine (**191**) and α-bromoketone **188** was observed to stall at the imine intermediate (identified *via* mass spectrometry and TLC analysis) (Table 3.8, entry 3). To promote the intramolecular attack of the imine nitrogen into the carbonyl, catalytic DMAP was added, and the reaction was transferred to a sealed tube to enable higher reaction temperatures. DMAP is a commonly used catalyst in acylation reactions as it forms a stable reactive intermediate with the carbonyl group (in this case of the starting material) that lowers the overall energy barrier.[307] Alternatively, reaction conditions were trialled in which the α-bromoketone **188** could be generated *in situ*, utilising NBS as the brominating agent, and *p*-$MePhSO_3H$ as a catalyst (Table 3.8, entry 4).[308] Unfortunately, these conditions failed to yield the α-bromoketone **188** analogue, instead brominating on the 2-position of the furan (**192**, confirmed by NMR: Appendix 6).

Table 3.8 Synthetic attempts to access the imidazo[1,2-*c*]pyrimidine (**173**) analogue.

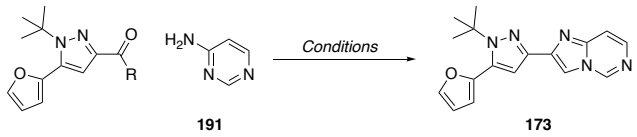

191 **173**

Entry	SM	R	Conditions	Outcome
1	**184**	CH_3	I_2, NH_4OAc, EtOH, reflux, air, 72 h	—[a]
2	**184**	CH_3	I_2, NH_4OAc, EtOH, 120 °C, air, MW, 2 h	—[a]
3	**188**	CH_2Br	EtOH, DMAP, 100 °C, sealed tube, 24 h	—[b]
4	**184**	CH_3	1. NBS, *p*-$MePhSO_3H$, CH_2Cl_2, 50 °C, MW, 1 h 2. $NaHCO_3$, MeOH, 80 °C, MW, 5 min	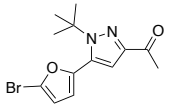 **192**
5	**155**	H	$FeCl_3$, $MeNO_2$/DMF (2:1), 110 °C, air, 24 h	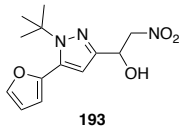 **193**
6	**155**	H	$FeCl_3$, $MeNO_2$ (1 eq), DMF, 110 °C, air, 24 h	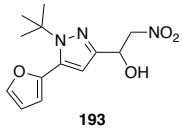 **193**

[a] Complex reaction mixture as indicated by TLC analysis. [b] Reaction stalled at imine intermediate. No product was formed. MW represents reactions performed inside a microwave reactor. Characterisation of side products **192** and **193** is presented in Appendix 6.

Iron(III)-catalysed, one-pot, three-component cross-coupling nitration reactions have been reported to successfully synthesis a range of imidazo[1,2-*a*]pyridine derivatives.[309] Although demonstrated to have good functional-group tolerance around the aromatic ring, this method has not been translated to pyrimidine reagents.[309] Mechanistically, the reaction utilises iron(III) chloride as a Lewis acid to promote the reaction by increasing the electrophilicity of both the aldehyde and the imine (Figure 3.10). First, imine **I** (Figure 3.10) is formed through the condensation of the aniline and aldehyde reagents. Imine **I** then reacts with nitromethane *via* a Michael addition to form the aza-Henry product **II** (Figure 3.10).[309] Intermediate **II** then undergoes tautomerisation to give **III**, which enables a 5-*exo*-*trig* intramolecular cyclisation to give **IV** (Figure 3.10). The imidazo-pyridine product (**V**) is subsequently formed through elimination of both water and nitroxyl (Figure 3.10). Unfortunately, the reaction conditions failed to provide the desired imidazo-pyrimidine **173**, rather the nitroethanol (**193**) derivative was formed when nitroethanol was utilised in excess and stoichiometrically (Table 3.8, entries 5 and 6). Formation of the nitroethanol **193** can be justified through analysis of the traditional

Henry reaction – or nitroaldol condensation – between an aldehyde and nitromethane. Therefore, producing this side-product even following pre-stirring of aldehyde **155** and aniline **191** as conducted in entry 6, further highlights the poor nucleophilicity of 4-aminopyrimidine (**191**).

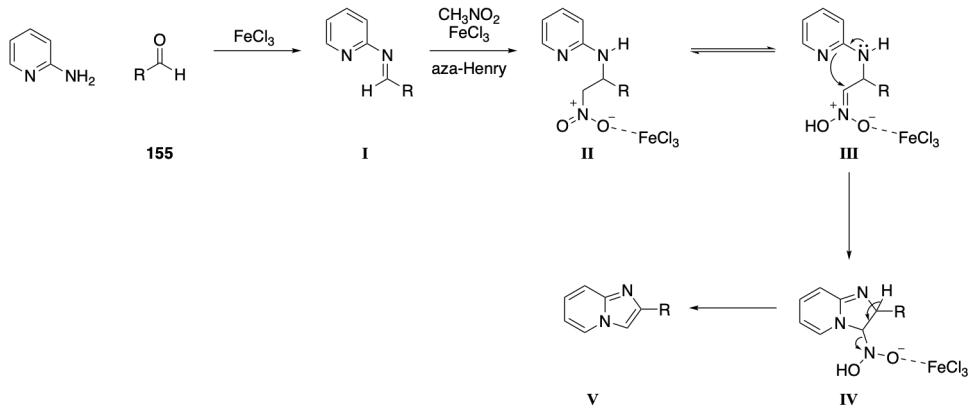

Figure 3.10 Synthesising imidazo[1,2-*a*]pyridine derivatives *via* the aza-Henry intermediate (**II**).

It was postulated that the synthetic difficulty could be ascribed to the poor reactivity of 4-aminopyrimidine. Within diazines, the effects of additional nitrogen atoms are roughly additive.[310] Therefore, having a nitrogen both *para*- and *ortho*-substituted in relation to the amine, the negative charge is highly stabilised as both can draw electron density away forming a highly conjugated system.[310] Given the synthetic difficulty in obtaining **173**, efforts were diverted to more pertinent scaffolds. Future effects towards the synthesis of imidazo[1,2-*c*]pyrimidine **173** should be directed towards alternative methods. Synthetic pathways to access imidazo[1,2-*a*]pyridine derivatives have been reviewed extensively, however 4-aminopyrimidine (**191**) is rarely included in the substrate scope.[288–290] McDonald and coworkers reported a general method for the preparation of electron-deficient imidazo[1,2-*a*]pyridine like ring systems (Scheme 3.7).[311] The approach described treatment of the aniline with dimethyl ketal tosylate in acetonitrile at elevated temperature in the presence of catalytic scandium(III) triflate ($Sc(OTf)_3$) (Scheme 3.7).[311] Reported to proceed *via* an acid catalysed imine formation, the methodology was applied to a large scope of pyridine derivatives. As trace amounts of imine were observed within the Ortoleva-King attempt (Table 3.8, entry 1) the aforementioned method could be a viable option to explore.

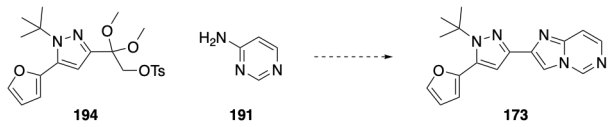

Scheme 3.7 Alternative pathway to access the imidazo[1,2-*c*]pyrimidine **173** analogue *via* the dimethyl ketal tosylate intermediate **194**.[311]

3.3.3 Synthesis of Indole Analogues

The indole functional group is ubiquitous in nature and modern drug scaffolds. Evidently, synthetic approaches to access the heterocycle are expansive with no general rules identified for reaction success.[312–314] The retrosynthetic strategy to access the indole derivatives (**175** – **181**) was proposed to stem from the common ketone intermediate (**184**) described in **3.3.2.1** (Figure 3.11).

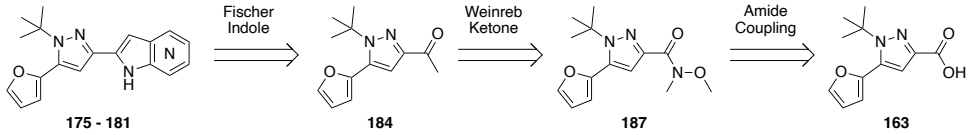

Figure 3.11 Retrosynthetic strategy to access indole and azaindole derivatives.

3.3.3.1 Fischer Indole Synthesis

The Fischer indole synthesis describes the acid mediated condensation of an arylhydrazine with an enolizable ketone.[312] Mechanistically, the Fischer indole cyclisation involves the acid catalysed [3,3]-sigmatropic rearrangement of the aryl hydrazine tautomer (**I**) to form the bisiminobenzylketone product **II** (Figure 3.12).[312] Elimination of ammonia, and corresponding cyclisation and aromatisation of compound **III** forms the desired indole (**175**, Figure 3.12). Limitations to the current methodology include a large excess of reagents, strong acidic media and often prolonged reaction times at elevated temperatures making it incompatible with some functional groups.[313]

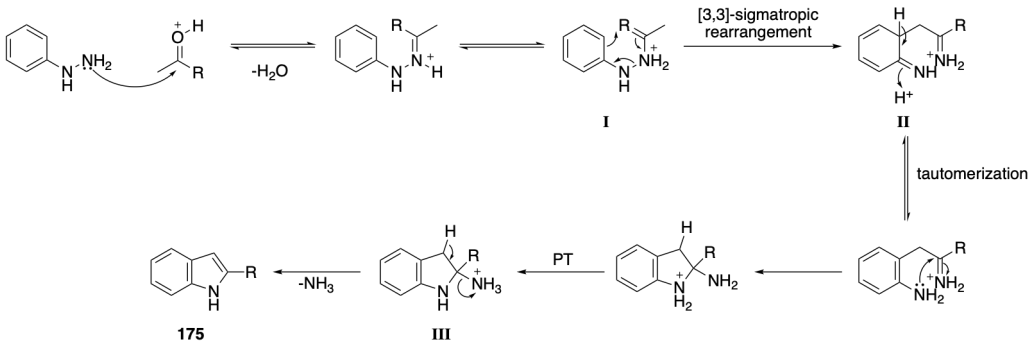

Figure 3.12 Fischer indole mechanism.

Due to the presence of the acid labile *tert*-butyl functionality present on our target molecule, a mild protocol was investigated. Siddalingamurthy and co-workers reported the successful synthesis of indoles *via* Fischer indolization utilising the mild and inexpensive catalyst of trichloro triazine (TCT, **195**).[315] Performing as a HCl surrogate, ethanol reacts with TCT to displace chloride ions (Figure 3.13).[315] Therefore, TCT promotes the reaction through the slow liberation of nascent HCl (Figure 3.13). Unwanted side products (e.g. hydrolysis of hydrazones) are also circumvented using an organic solvent rather than aqueous acidic media as seen in traditional protocols.[315] Unfortunately, within the current system, no product was formed under the mild TCT conditions (Table 3.9, entry 1). Formation of the hydrazone intermediate was identified by mass spectrometry (*m/z* 323 $[M+H]^+$) and TLC, although it was efficiently hydrolysed upon aqueous work up to produce recovered starting material.

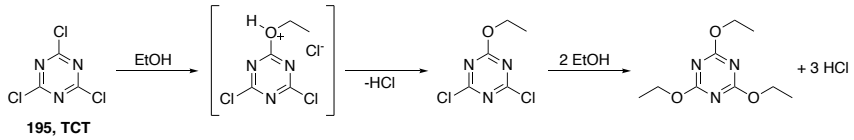

Figure 3.13 Nascent release of HCl by the reaction of ethanol and TCT.

Table 3.9 Fischer indole conditions trialled for the synthesis of indole derivative **175**.

184 175

Entry	Conditions	Yield
1	TCT (0.1 eq), EtOH, 80 °C, 24 h	S.M. [a]
2	1M HCl (cat.), EtOH, 80 °C, 6 h	— [b]
3	TFA (8 eq), 1,2-DCE, 40 °C, 6 h	— [b]
4	H_2SO_4 (4%), H_2O, 100 °C, 24 h	S.M. [a]
5	H_2SO_4 (4%), H_2O, 120 °C, MW, 20 min	S.M. [a]
6	*p*-$MePhSO_3H.H_2O$ (1.1 eq), toluene, 90 °C, Ar, 48 h	S.M. [a]
7	1. AcOH (cat.), EtOH, reflux, 6 h 2. $ZnCl_2$, DMF, 100 °C, MW, 1 h	S.M. [a]

[a] Starting material isolated. Hydrazone observed by mass spectrometry and TLC, although hydrolysed post aqueous work up. [b] Complex reaction mixture as indicated by TLC analysis. MW represents reactions performed inside a microwave reactor.

More traditional Fischer indolizations were similarly trialled to no avail utilising a range of acids with varying strengths and temperatures (Table 3.9, entries 2 – 6). Furthermore, the Lewis acid zinc chloride was also trialled in a two-step reaction scheme (Table 3.9, entry 7).[316] Reported to accommodate and improve yields in normally difficult Fischer indolization processes, the hydrazone is first formed using an acid mediated system, with the subsequent cyclisation promoted by the Lewis acid in microwave-assisted conditions. A complex reaction mixture was indicated by TLC analysis, with no indication of product formation by mass spectrometry. Therefore, following the unsuccessful attempts *via* the forcing conditions in Fischer indole protocols, an alternative strategy was devised to access the indole analogues.

3.3.3.2 Madelung Indole Synthesis

The Madelung indole synthesis describes the cyclisation of *ortho*-alkylamides with alkoxy bases or organolithium reagents (Figure 3.14).[317,318] Amidation with *o*-toluidine (**196**) under HATU coupling conditions yielded the amide derivative **197** in 87% yield (Scheme 3.8). Treating **197** with 3 equivalents of *n*-BuLi under inert conditions failed to see conversion with only starting material isolated. Increasing the reaction equivalents of base to 6, was similarly

unsuccessful with the reaction observed to halt at the proposed formation of the saturated hydroxy-indoline intermediate **198** (suggested by the observed mass spectra - *m/z* 346 $[M+Na]^+$) (Figure 3.14). To promote the dehydration of **198** to **175**, the hydroxyl group was activated with thionyl chloride ($SOCl_2$), in an effort to lower the energy barrier (Scheme 3.8). Addition of pyridine ensures that the chlorination occurs *via* an S_N2 mechanism.[319] Subsequent aromatisation was postulated to occur more easily due to the presence of a better leaving group, however a complex reaction mixture resulted. Due to time constraints, accessing the indole analogues *via* a Madelung indole synthesis was halted, however future attempts should consider attempting the dehydration with $SOCl_2$ in the absence of pyridine.[314] Removing pyridine could allow for either a β-elimination pathway or conventional S_Ni pathway to occur. Within a series of 3-hydroxyindanones, $SOCl_2$ was shown to form a six-membered transition state that effectively affiliated the dehydration to the desired indenones.[314]

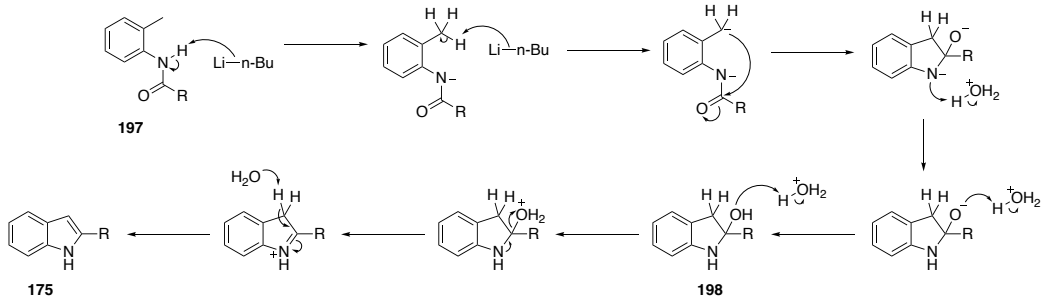

Figure 3.14 Proposed mechanism for the Madelung indole synthesis with *n*-BuLi *via* hydroxy-indoline intermediate **198**.

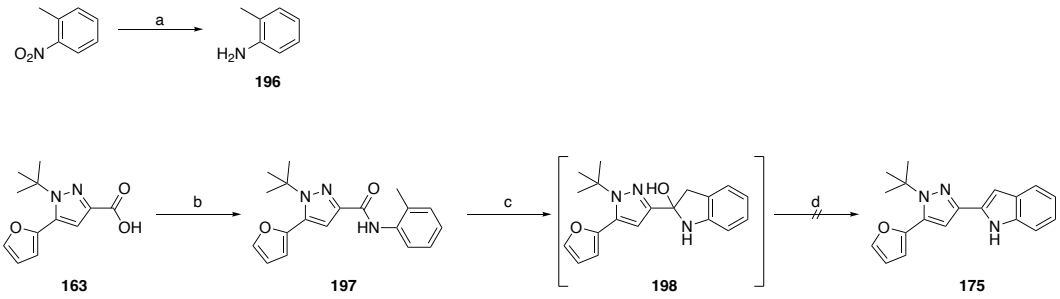

Scheme 3.8 Attempted synthesis of indole derivative **175** *via* Madelung conditions. *Reagents and Conditions* (a) 4,4'-bipyridine, $B_2(OH)_4$, DMF, rt, 1 h, 65% (b) **196**, HATU, $^iPr_2NEt$, DMF, rt, 12 h, 87% (c) *n*-BuLi, THF, -20 – 25 °C, 72 h (d) $SOCl_2$, Pyridine, CH_2Cl_2, 0 – 25 °C, 5 h.

3.3.3.3 Intramolecular Heck Reactions

The intramolecular Heck reaction has shown utility in the synthesis of indole, carbazoles and indolines.[312] Protocols describing the palladium-catalysed annulation of *ortho*-haloanilines and

ketones/aldehydes have been developed.[320,321] Firstly, the enamine is formed, followed by an intramolecular Heck reaction to provide the indole. Choice of base and solvent were highlighted to be critical to the success of the reaction and minimisation of by-product formation.[320] To avoid amine-derived by-products, the base must not be able to be oxidised by palladium. Therefore, by selecting a bicyclic tertiary amine base like 1,4-diazabicyclo[2.2.2]octane (DABCO), this issue was resolved.[320] Diverting slightly from the original methodology the *ortho*-bromoaniline was selected for the initial trials. This decision was justified as the corresponding starting materials for the proposed azaindole analogues are commercially available. 2-Bromoaniline (**199**) was treated with ketone **184**, DABCO and $Pd(OAc)_2$ in DMF under inert conditions (Table 3.10, entry 1). Following heating for 24 h, the reaction failed to show any sign of reaction progression with only starting material recovered.

Building off the former work, Jia and co-workers extended the methodology of one-pot palladium catalysed annulations to accommodate both *ortho*-chloroanilines, *ortho*-bromoanilines and aldehyde coupling partners.[321] The reaction utilised $Pd(dba)_2$ and XPhos as the Pd-catalyst and ligand respectively. Both ketone (**184**) and aldehyde **(155**) coupling partners were trialled (Table 3.10, entries 2 and 3). *N,N*-Dimethylacetamide (DMA) was used within the aldehyde trial to circumvent the possibility of DMF out competing. After 24 hours, TLC analysis and mass spectrometry of both trials showed a complex reaction mixture consisting predominantly of starting material.

Table 3.10 Pd-catalysed annulation conditions.

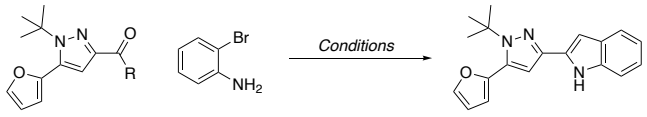

155, R = H
184, R = CH_3 **199** **175**

Entry	SM	Conditions	Yield
1	**184**	$Pd(OAc)_2$, DABCO, DMF, 110 °C, 24 h	S.M. [a]
2	**184**	$Pd(dba)_2$, XPhos, KOAc, DMF, 85 °C, 24 h	— [b]
3	**155**	$Pd(dba)_2$, XPhos, KOAc, DMA, 110 °C, 24 h	S.M. [a]

[a] S.M. represents recovered starting material, as no reaction occurred. [b] Complex reaction mixture as indicated by TLC analysis.

3.3.3.4 Suzuki Cross-Coupling Reactions

Within the current scaffold, constructing the indole ring system had proved synthetically difficult. Therefore, efforts turned to the direct functionalisation of the furan-pyrazole core structure through carbon-carbon bond formation. The retrosynthetic analysis of the Suzuki-type cross-coupling reaction to form the sulfonyl-indole derivative **200** is illustrated in Figure 3.15. The boronic ester (**201**) and haloindole intermediates (**202**) were synthesised in parallel to allow for a late-stage convergent coupling reaction (Figure 3.15). The boronic ester could be accessed from the halo-intermediate **203** through a Miyaura borylation reaction. Cyclisation of the β-enaminones (**204**) and succeeding halogenation yields compound **205** (Figure 3.15). β-enaminones **204** is afforded by a condensation reaction of 2-acetylfuran (**156**) with the DMF-DMA reagent (Figure 3.15).[322] Additionally, the haloindole intermediate **202** was envisioned to be afforded by the halogenation of the phenylsulfonylindole derivative **206** (Figure 3.15). Compound **206** is achieved through the reaction of the respective indole (**207**) and benzyl sulfonyl chloride (Figure 3.15).

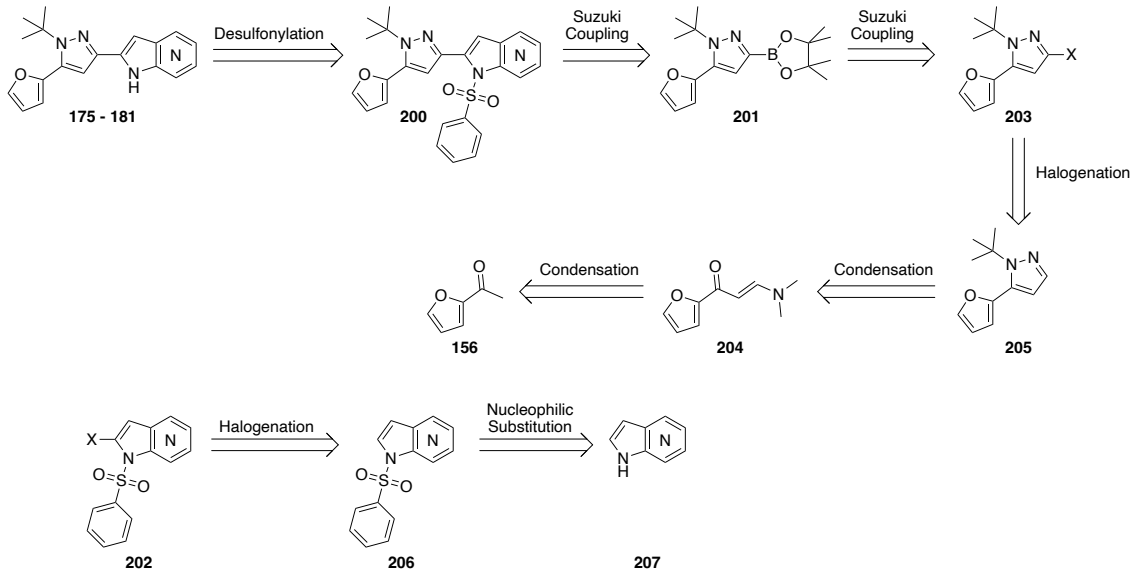

Figure 3.15 Retrosynthetic pathway to access indole and azaindole derivatives *via* a Suzuki cross-coupling reaction with the protected halo-indole derivative.

Halogenation of indoles preferentially occurs at the 3-position, with 1-*H*-2-halogenated indoles being reported as unstable.[323] To overcome these shortcomings introduction of an *N*-electron withdrawing protecting group (such as Boc or phenyl sulfonyl group) has been shown to increase stability, and promote regioselectivity through the neighbouring group participation

effect.[324] Nucleophilic substitution of the indole (**208** and **209**) nitrogen with benzenesulfonyl chloride ($PhSO_2Cl$) gave the phenylsulfonyl indole (**210**) and azaindole (**211**) derivatives in excellent yields (Scheme 3.9). Iodination was initially approached through lithiation reactions with lithium diisopropylamide (LDA) prepared *in situ* (Scheme 3.9). Although product was isolated, separation from unreactive starting material and di-iodinated species by chromatography was insurmountable. Hauser bases, or magnesium amide bases, are a great alternative to organolithium reagents when tight chemoselective control needs to be achieved.[325] Hauser type bases obtain good functional group tolerance and chemoselectivity due to the magnesium producing more covalent, and thereby less reactive, metal-ligand bonds.[325] Magnesiation of **210** and **211** was achieved through *in situ* preparation of *i*-PrMgCl to diisopropylamine, followed by addition of iodine to the magnesioindole to give the desired iodo-indole derivative (**212** and **213**). Distillation of the diisopropylamine from calcium hydride was found to be fundamental to the success of the reaction (Scheme 3.9, Table 3.11, entries 1 – 5). The azaindole analogue **213**, similarly, produced a mixture of product, starting material and over-reacted species (confirmed by mass spectrometry) when two equivalents of base were used (Scheme 3.9, Table 3.12, entry 3). Decreasing the equivalents of base under this value however resulted only in trace amounts of product formation (Table 3.11, entries 4 and 5). This outcome was not surprising as a major disadvantage of Hauser bases are their poor solubility in THF, thus requiring a large excess of base.[325] Although inseparable, it was anticipated that the three products could successfully be telescoped through to the Suzuki coupling as a crude mixture.

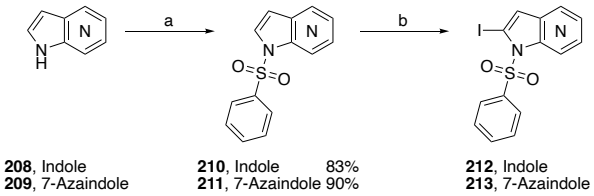

Scheme 3.9 Synthesis of iodo-indole derivatives for the subsequent Suzuki reaction. *Reagents and Conditions* (a) NaH, $PhSO_2Cl$, DMF, 0 – 25 °C, 5 h (b) 1. *i*-PrMgCl (2M in THF), diisopropylamine, THF, rt, 3 h; 2. I_2, THF, rt, 1 h – *See table 3.11 for further discussion.*

Table 3.11 Iodination conditions trialled for the iodination of phenylsulfonyl indole derivatives **210** and **211**.

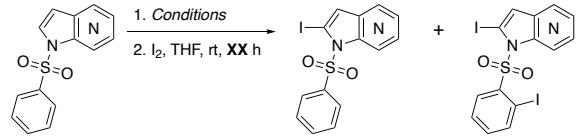

210, Indole
211, 7-Azaindole

212, Indole
213, 7-Azaindole

214, Indole
215, 7-Azaindole

Entry	Indole	*i*-PrMgCl (eq)	*i*-Pr$_2$NH (eq)	Time	Outcome
1	**210**	2	4	3	S.M.[a]
2	**210**	2	4 (distilled)	3	**210** + **212**
3	**211**	2	4 (distilled)	3	**211**, **213** + **215**
4	**211**	1.2	2.4 (distilled)	24	**211** + **213** (trace)
5	**211**	1.6	3.2 (distilled)	24	**211** + **213** (trace)

[a] S.M. represents recovered starting material, as no reaction occurred

Synthesis of the boronic ester coupling partner **201**, started with the condensation reaction of the carbonyl methyl group of 2-acetylfuran (**156**) and the DMF-DMA reagent to form the β-enaminones **204** (Scheme 3.10).[326] Analysis of ^{1}H NMR data confirmed the formation of the *E*-isomer ($^3J_{HH}$ = 12.5 Hz). Cyclocondensation of **204** with *tert*-butylhydrazine hydrochloride in ethanol at reflux constructed pyrazole **205** (Scheme 3.10).[327] The reaction was found to be regioselective for the 1,5-pyrazole isomer (regioisomer confirmed by NMR analysis and supporting literature).[327] The reaction follows attack of the more reactive amino group of the hydrazine at the β-carbon atom of the β-enaminone.[326,328] This then undergoes elimination of dimethylamine to form the β-hydrazino unsaturated ketone. Heterocyclisation is then attained from the attack of the second amino group of the hydrazine to the carbonylic carbon.[326,328]

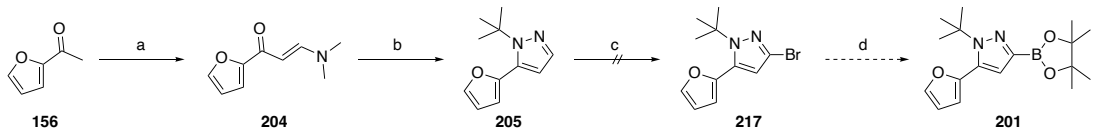

156 **204** **205** **217** **201**

Scheme 3.10 Synthesis of boronic ester intermediate for Suzuki coupling. *Reagents and Conditions* (a) DMF-DMA, DMF, 80 °C, 2 h, 50% (b) *tert*-butylhydrazine hydrochloride, EtOH, reflux, 2 h, 65% (c) 1. *n*-BuLi, THF, -78 °C, 2 h; 2. CBr_4, THF, -78 – 25 °C, 2 h (d) Bis(pinacolato)diborane, KOAc, Pd(dppf)Cl_2, DMF, 80 °C, 16 h.

Compound **205** was treated with *n*-BuLi and then carbon tetrabromide to install the bromo-group in 53% yield (Figure 3.16).[329] However, upon ^{1}H NMR analysis and further evaluation of the relative pK_a*'s* (predicted by MarvinSketch) throughout the molecule it was identified that bromination had occurred at the 5-position of the furan (**216**), rather than the pyrazole (**217**) (Figure 3.16, Appendix 7).[330] Anticipating that this issue would persist in subsequent halogenation attempts, the synthetic strategy was redirected towards an alternative functional handle.

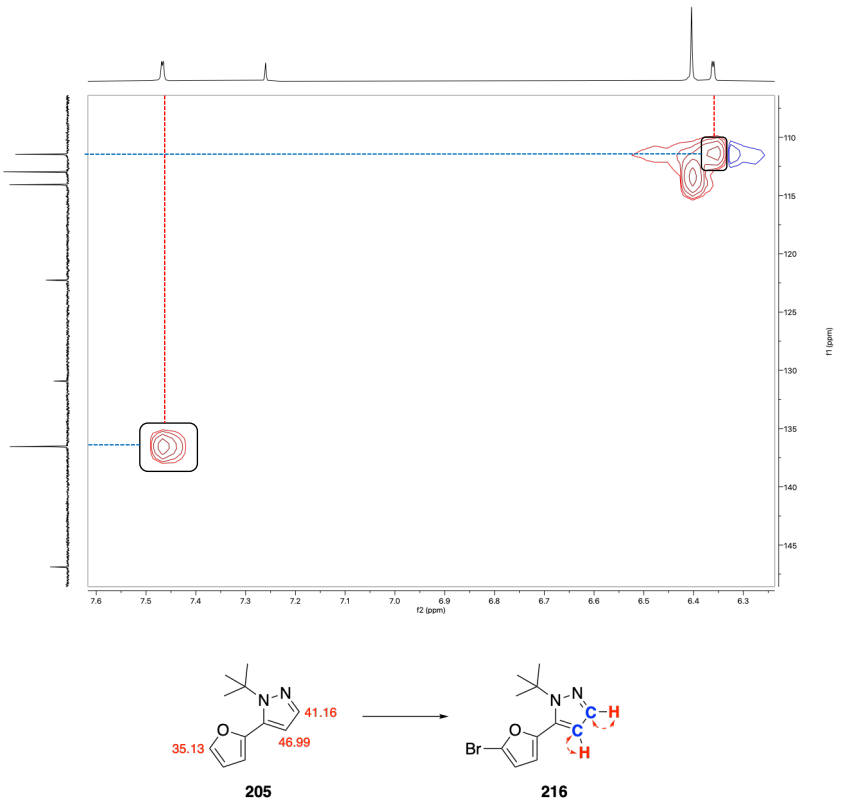

Figure 3.16 Bromination of **205** with *n*-BuLi and CBr_4 resulted in the incorrect product, with bromination occurring at the 5-position of the furan (**216**). ^{1}H (red) – ^{13}C (blue) HSQC correlation (red dashed arrow) of 1,5-substituted pyrazole ($CDCl_3$, 500 MHz, 298 K). Analysis supported by relative pK_a predicted by MarvinSketch (numbers in red).

Arylamines are readily functionalised to arylhalides or arylboronates through Sandmeyer-type reactions making it a viable handle for further attempts (Scheme 3.11).[331,332] Advantageous due to the lack of expensive ligands and catalysts required, and consequential heavy metal contamination, direct borylation reactions of arylamines boast a wide substrate scope under mild conditions.[331,332] Synthesis of the 3-aminopyrazole intermediate **218** was initially explored through the addition and cyclisation between *tert*-butylhydrazine and β-ketonitrile

219 (Scheme 3.11), introducing the NH_2 group from synthons rather than through functionalisation of the pre-built pyrazole.[302]

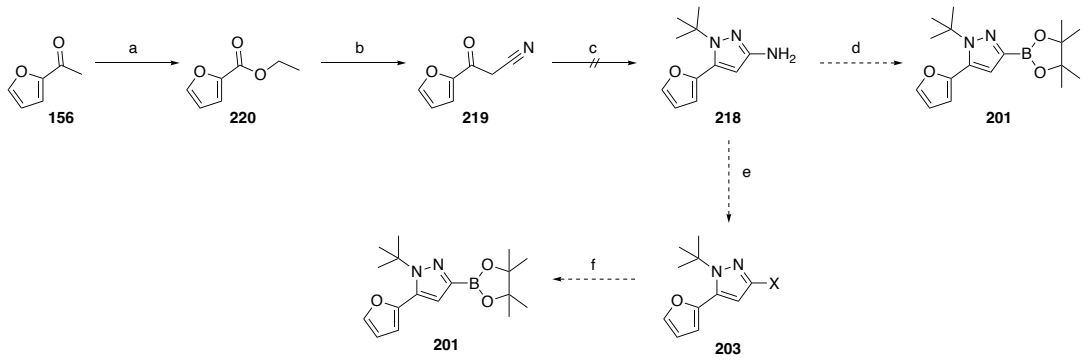

Scheme 3.11 Synthesis of alternative amine handle *via* nitrile intermediate. *Reagents and Conditions* (a) EtOH, H_2SO_4 (cat.), reflux, 2 h, 74% (b) NaH, CH_3CN, THF, reflux, 5 h, 53% (c) *tert*-butylhydrazine hydrochloride, NaOH, EtOH, 0 – 25 °C, 24 h (d) Bis(pinacolato)diboron, *t*-BuONO, CH_3CN, 80 °C, 2 h (e) $NaNO_2$, KI, 2.5 M HCl/H_2O, 0 °C, 3 h (f) Bis(pinacolato)diboron, Cs_2CO_3, DMF, 85 °C, 16 h. *t*-BuONO: *tert*-butyl nitrite.

Treating furan ethyl ester (**220**) with NaH, enabled a Claisen condensation with acetonitrile to access the β-ketonitrile **219** (Scheme 3.11).[334] A mix of aminopyrazole regioisomers was expected from the ensuing condensation reaction.[335,336] Generally, the regioselectivity is controlled by the nucleophilicity of the hydrazine nitrogen atoms, and subsequent nucleophilic attack to either the nitrile or activated olefin (Figure 3.17A). The reaction therefore either proceeds under thermodynamic (primary amino group attacking) or kinetic (secondary amine group attacking) conditions to produce the 5-amino (**221**) and 3-amino (**218**) pyrazole respectively.[335] For simple alkyl hydrazines, kinetic control was observed when in the presence of base at low temperatures.[335] β-ketonitrile (**219**) and sodium hydroxide was added to a stirring solution of *tert*-butylhydrazine hydrochloride at 0 °C. Unfortunately, the 5-aminopyrazole (**221**) was formed selectively, as confirmed by a selective NOESY correlation between the *tert*-butyl protons and amine (Figure 3.17B). Upon revisiting the mechanism (Figure 3.17A), it was considered unlikely that the secondary amine could effectively compete in the initial nucleophilic attack due to the steric hindrance of the *tert*-butyl group. Consequently, the formation of the desired regioisomer in appreciable amounts was deemed improbable.

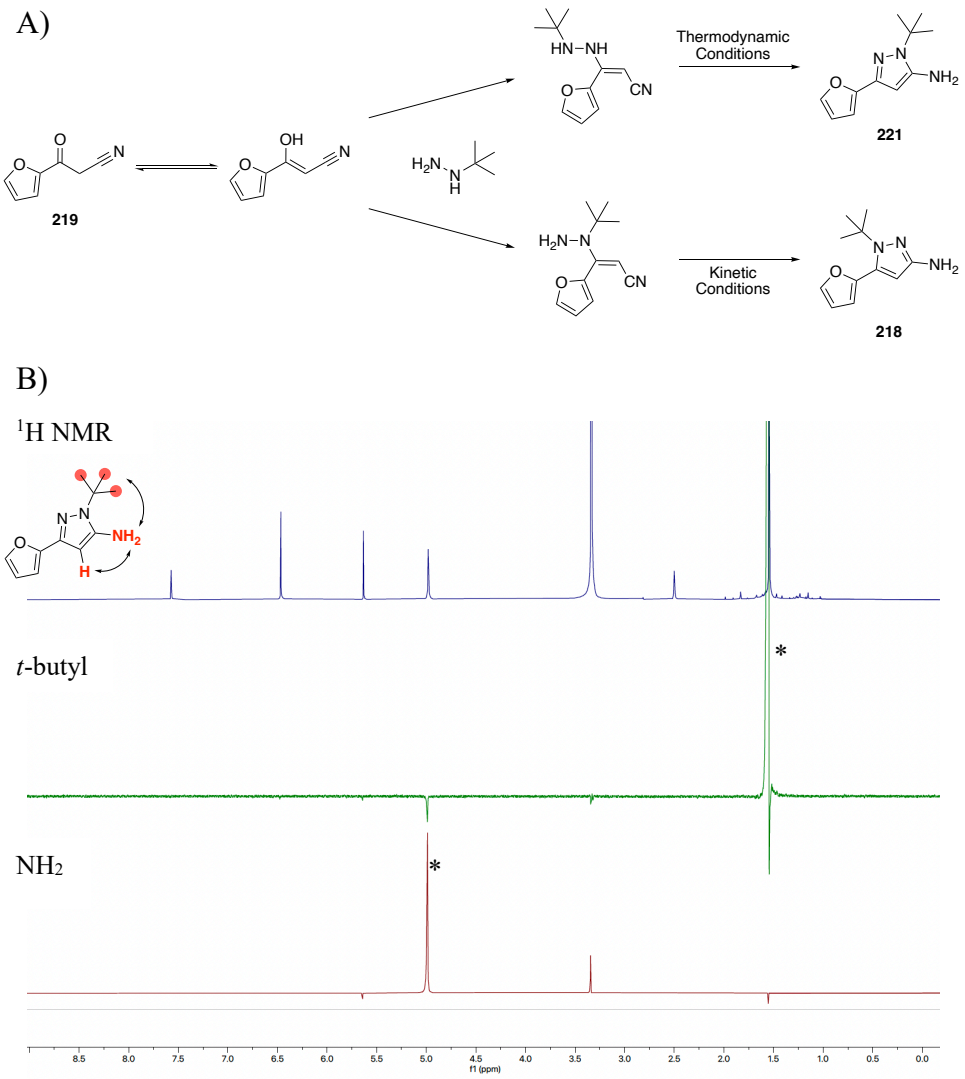

Figure 3.17 A) Pathway to yield the 3- and 5-aminopyrazole regioisomers (**218** and **221**, respectively). B) ^{1}H NMR (DMSO-d_6, 500 MHz, 298 K) of isolated amino-pyrazole regioisomer **221**. Selective 1D NOESY irradiating the *tert*-butyl (green) and amino protons (red). * denotes peak irradiated.

The Curtius rearrangement is frequently used throughout synthetic chemistry to convert carboxylic acids to amines and their derivatives.[337] Involving the thermal decomposition of an acyl azide **222** to produce the isocyanate **223** intermediate, the Curtius rearrangement offers a broad substrate scope and complete retention of stereochemistry.[337] Consequently, a one-pot procedure was proposed describing the direct conversion of carboxylic acid **163** to the corresponding carbamates **224** and **225** with diphenylphosphoryl azide (DPPA) and the respective alcohol (Scheme 3.12). This method is beneficial as it removes the need to isolate the potentially explosive acyl azide **222** derivative and produces the more stable carbamate protected amine (Scheme 3.12). Conditions to yield both the *tert*-butyl (**224**, Scheme 3.12) and ethyl carbamate (**225**, Scheme 3.12) were trialled.[337,338] In both cases, formation of the acyl

azide (**222**) was confirmed by mass spectrometry and TLC analysis. Unfortunately, upon heating, a complex reaction resulted in both cases with no sign of product formation.

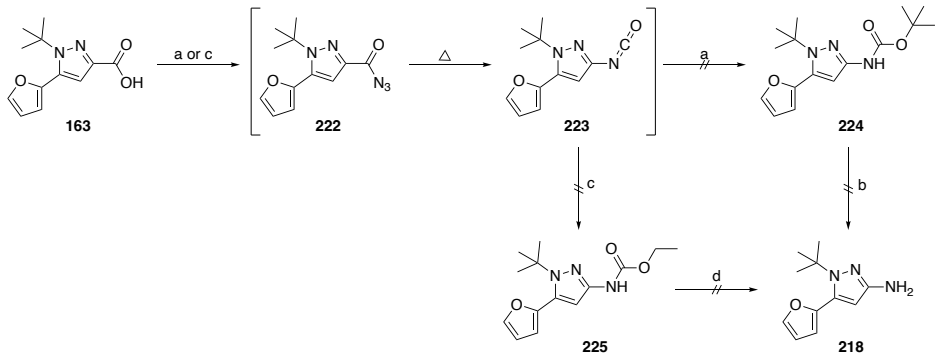

Scheme 3.12 Conversion of the carboxylic acid derivative **163** to the amine intermediate *via* a one-pot Curtius rearrangement reaction with DPPA. *Reagents and Conditions* (a) DPPA, Et_3N, *t*-BuOH, 50 °C, 6 h (b) 4M HCl in 1,4-dioxane, rt, 2 h (c) DPPA, Et_3N, EtOH/1,4-dioxane, reflux, 16 h (d) 10% NaOH, EtOH, reflux, 5 h. DPPA: diphenylphosphoryl azide.

Due to time constraints, work on this scaffold disappointedly had to be ceased, although future iterations to yield **218** would benefit from a step-wise protocol starting from the carboxylic acid **163** (Scheme 3.13A).[300] The carboxylic acid **163** is first treated with oxalyl chloride to afford the corresponding acid chloride. The acyl chloride then reacts with sodium azide to affect azido substitution to the acyl azide (**222**, Scheme 3.13A). Upon heating the acyl azide will undergo rearrangement to the isocyanate (**223**, Scheme 3.13A) which undergoes nucleophilic attack of the alcohol to yield the respective carbamate compound (**224**, Scheme 3.13A). Alternatively, Curtius rearrangements have been shown to occur under a zinc-mediated mechanism at lower temperatures.[339] The reaction utilises di-*tert*-butyl decarbonate (Boc_2O) as the Boc source and tetrabutylammonium bromide (TBAB) as a phase-transfer catalyst (Scheme 3.13B).[339]

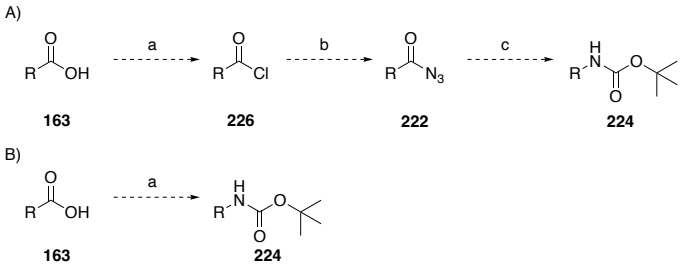

Scheme 3.13 Proposed alternative pathways to access the *Boc*-protected amine intermediate (**224**). A) Step-wise approach. B) One-pot procedure utilising TBAB and $Zn(OTf)_2$.

3.3.3.5 Future Directions

Future efforts towards the construction of the indole and azaindole heterocycles (**175** – **181**) should initially involve addressing the suggestions proposed for the Madelung synthesis (chapter **3.3.3.2**) and Suzuki coupling pathway (chapter **3.3.3.4**). Additionally, a novel approach to access the indole analogues through a linear synthetic pathway is proposed in scheme 3.14. Following the successful synthesis of the quinoline analogues in chapter **4.3.2.2.3**, a similar pathway could be adapted for the indole derivatives. The synthetic pathways describes the deprotection and selective alkylation of the pyrazole **227** (Scheme 3.14, step e and f).[340,341] Pyrazole **227** could be accessed from the cyclisation and subsequent oxidation of the α,β-unsaturated ketone **228** (Scheme 3.14, step c and d).[342] A base catalysed Claisen-Schmidt reaction between the respective indole-carbaldehydes (**229**) and 2-acetylfuran (**156**) was projected to form **228** (Scheme 3.14, step b).[170]

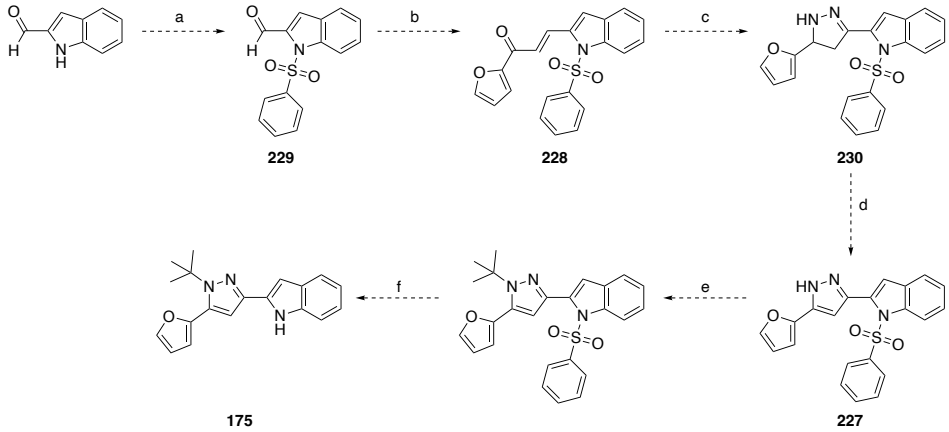

Scheme 3.14 Proposed synthetic pathway to access the indole and azaindole derivatives *via* the dihydropyrazole intermediate (**230**).

3.4 Diversification of the Pyrazole Motif

The pyrazole motif was a key pharmacophore of interest for further diversification. Minimal structural modifications were performed on this section of the molecule within the original SAR exploration, with those limited to diversification of the alkyl group.

The electronic character and overall reactivity of nitrogen containing five-membered rings (azoles) is vastly different.[343,344] Azole nitrogens can adopt one of two electronic types: pyrrole-like, which are acidic and electron-releasing (often lone pair is involved in aromaticity), or pyridine-like, and therefore basic sp^2-hybridised.[343] The number of electronegative nitrogens within the ring greatly affects the reactivity of the heterocycle. For

example, 1,2,4-triazoles are virtually unreactive towards electrophiles due to the decrease in electron density at the carbon atoms.[345] Within diazole heterocycles the basicity is largely affected by the mesomeric effect.[344] Whilst in heterocycles with more than two heteroatoms, the lower basicity reported is attributed to the inductive electron withdrawing effect of the pyridine-type nitrogen atoms.[345] Within drug discovery, azoles have been noted as a key pharmacophoric feature with a broad spectrum of biological activities.

The target compound library (**231** – **235**, Figure 3.18) features variation to the *tert*-butyl alkyl chain as well as a range of azole derivatives. Both strategies are commonly employed to aid pharmacokinetic challenges and often utilised to tailor the lipophilicity, solubility and metabolic viability of drug scaffolds. The pyrrole analogue was not included in the compound library due to its inherent susceptibility to oxidative metabolism.[346,347]

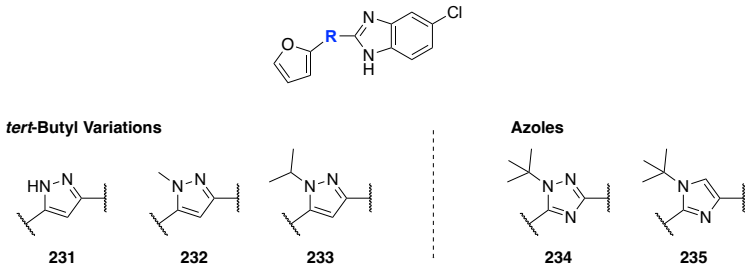

Figure 3.18 Compound library investigating the pyrazole pharmacophore, through substitution of the *tert*-butyl motif and various azoles.

3.4.1 Variation to the *t*-Butyl Moiety

Within the original virtual structure-based drug design reported by Zhu *et al.* the long-chain carboxyl group was substituted for the *tert*-butyl group to mitigate potential bioavailability issues.[257] SAR analysis of the *tert*-butyl moiety was limited however, to further simplified alkyl chains such as isopropyl and methyl derivatives. Better inhibitory activity was found to occur with substitution of *tert*-butyl groups and furanyl-substituted derivatives (Figure 3.19).[257] However, this initial analysis was conducted on the less potent phenyl-substituted derivatives with no *tert*-butyl replacements explored for furanyl-substituted analogues (Figure 3.19). Consequently, the isopropyl-, methyl-substituted and 1-*H*-pyrazole derivatives of compound **37** were synthesised to evaluate whether the decrease in activity observed is attributed to the decrease in alkyl chain and corresponding sterics.

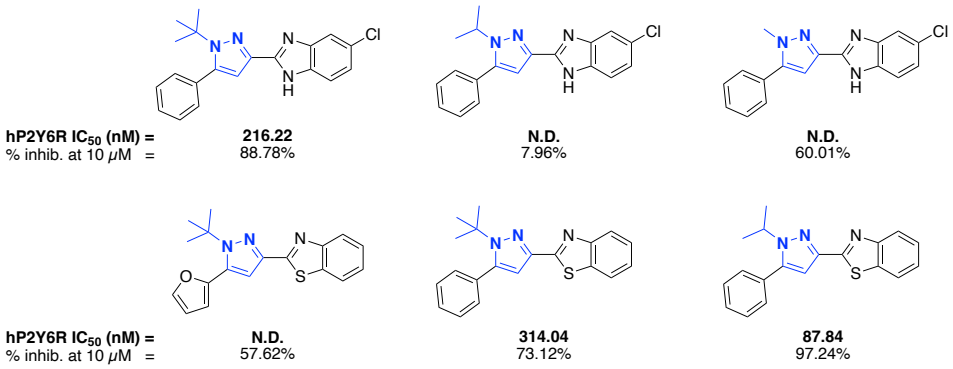

Figure 3.19 Analogues exploring the SAR of the various *N*-substituted pyrazoles. Data extracted from Zhu, Y. *et al*. **2023**.[169] N.D. = not determined

3.4.1.1 Synthesis of *N*-H-Pyrazole Derivative

Numerous studies have demonstrated that the *tert*-butyl group becomes labile under acidic conditions at elevated temperatures.[263,348] Therefore it was envisioned that the free *N*-H-pyrazole derivative **231** could easily be achieved from compound **37**. However, the *tert*-butyl group appeared more stable than originally believed with no reaction occurring in aqueous acid solutions (Table 3.12, entries 1 – 3).[263,348] Suspected to be due to the poor solubility of compound **37** in aqueous media, switching solvent systems to toluene furnished the desired product in good yields (Table 3.12, entry 4). The yield was able to be further improved upon by conducting the reaction in the presence of microwave irradiation (Table 3.12, entry 5).

Table 3.12 Cleavage of the *tert*-butyl group under acidic conditions to result in the *N*-H-pyrazole analogue (**231**).

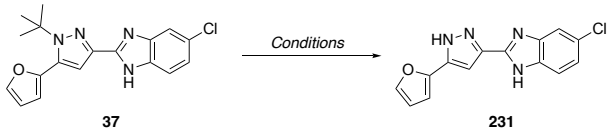

Entry	Conditions	Yield
1	Formic acid, 80 °C, 20 h	S.M. [a]
2	1M HCl /$CHCl_3$ (10:1), 50 °C, 4 h	S.M. [a]
3	TFA, H_2O, 120 °C, sealed tube, 16 h	S.M. [a]
4	TFA, toluene, 120 °C, sealed tube, 16 h	52%
5	TFA, toluene, 160 °C, MW, 30 min	70%

[a] S.M. represents recovered starting material, as no reaction occurred. MW represents reactions performed inside a microwave reactor.

Characterisation of **231** proved difficult due to the four potential tautomeric forms (Figure 3.20). The annular tautomerism of *N*-unsubstituted pyrazoles is a well-known issue in heterocyclic chemistry.[349] As discussed in chapter **3.2.1** the rate of conversion between the forms and their ability to interact with the solvent/each other greatly effects the resolution of the produced NMR spectra. Adding to the complexity, *N*-unsubstituted pyrazoles can form intermolecular hydrogen bonds with one another creating a lattice like structure.[349] The compound was first characterised in DMSO-d_6 following the successful resolution of previous analogues. A clear mixture of tautomers was observed within the ^{1}H NMR, however many carbons were unable to be resolved with many observed to be merged in with the noise signals. Switching solvents to DMF-d_7, produced sharp distinct signals corresponding to average resonances in the ^{1}H NMR, although did not resolve the corresponding carbon spectra. Additionally, degradation occurred quickly at room temperature, making it extremely difficult to obtain accurate 2D data. Consequently, the analogue was stored under inert conditions at 4 °C.

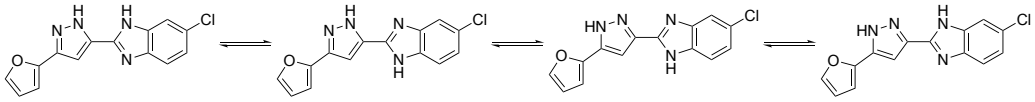

Figure 3.20 Possible tautomeric states of *N*-H-pyrazole analogue (**231**).

3.4.1.2 Synthesis of Methyl- and Isopropyl-Pyrazole Derivatives

The methyl- and isopropyl-pyrazole derivatives were accessed *via* a four-step linear synthetic approach illustrated in scheme 3.15. The diketone **157** was synthesised in an analogous manner to that described in **3.2.1** (Scheme 3.15). Condensation of the appropriate hydrazine with **157** yields the desired 1,3,5-trisubstituted pyrazoles (**236** and **237**) (Scheme 3.15). In principle, the condensation of a monosubstituted hydrazine with a non-symmetrical 1,3-diketone can lead to the formation of a mixture of two pyrazole regioisomers. As such, both regioisomers (**236** and **238**) were observed for the methyl-pyrazole derivative in a 1:1 ratio when conducted in ethanol (Scheme 3.15A and Table 3.13, entry 1). Substituting ethanol for 1,1,1,3,3,3-hexafluoro-2-propanol (HFIP, **239**) dramatically favoured the formation of the desired 5-regioisomer (**236**) (Table 3.13, entry 2).[350] Whereas, similar to the *tert*-butyl derivative, only one regioisomer (**237**) was formed in isolable quantities, from isopropylhydrazine in ethanol (Scheme 3.15B and Table 3.13, entry 3). 2D-NMR of the compound failed to provide a NOE correlation between the isopropyl and furan hydrogens. However, comparison to literature data confirmed that the 5-furan regioisomer had been formed.[351]

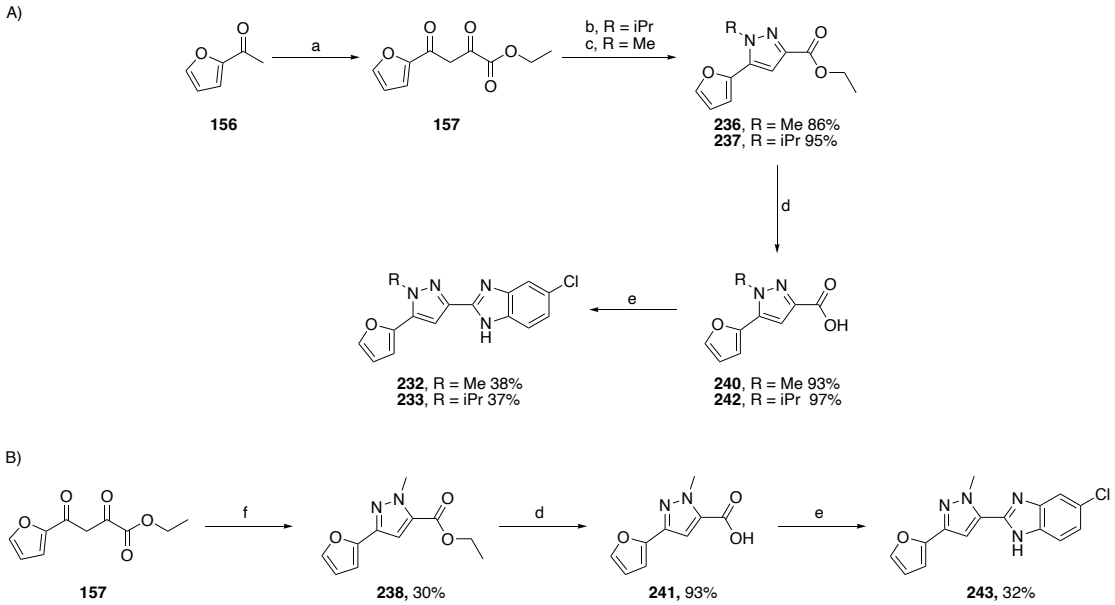

Scheme 3.15 Synthetic pathway to access *N*-alkyl-pyrazole derivatives. A) methyl 5-furan regioisomer (**232**) and isopropyl derivative (**233**), B) methyl 3-furan regioisomer (**243**). *Reagents and Conditions* (a) diethyl oxalate, *t*-BuOK, ethylene glycol dimethyl ether, THF, 0 – 25 °C, 1 h, 63 – 83% (b) methyl hydrazine, HFIP, rt, 1 h (c) isopropyl hydrazine, EtOH, rt, 8 h (d) $LiOH.H_2O$, $MeOH/H_2O$ (3:1), reflux, 1 h (e) 1. 4-chlorobenzene-1,2-diamine, HATU, $^{i}Pr_2NEt$, DMF, rt, 16 h; 2. AcOH/toluene (10:1), 75 °C, 24 h (f) methyl hydrazine, EtOH, rt, 8 h.

Table 3.13 Effect of solvent on regioselectivity of Paal-Knorr pyrazole formation.

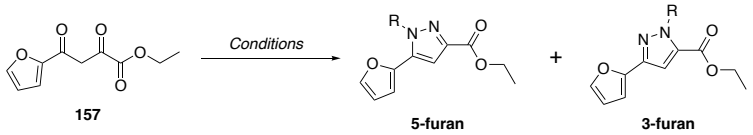

Entry	R	Conditions	5-regio : 3-regio
1	Me	EtOH, rt, 16 h	1 : 1
2	Me	HFIP, rt, 1 h	6 : 1
3	^{i}Pr	EtOH, rt, 16 h	1 : 0[a]

[a] Trace amounts of the isopropyl 3-furan regioisomer were detected by mass spectrometry analysis.

Fluorinated alcohols, such as HFIP (**239**), exhibit distinct characteristics (high hydrogen bonding donor ability, low nucleophilicity, high ionizing power and ability to solvate water) that have been shown to dramatically influence the outcomes of chemical reactions.[352] Exhibiting distinctive reactivity in comparison to their nonfluorinated counterparts, fluorinated alcohols have therefore become utilised as solvents, cosolvents and additives in synthetic chemistry.[350,352] Demonstrating utility throughout a broad range of transformations, evaluation of the cost/benefit ratio of using HFIP must be considered due to its corresponding toxicity

profile.[352] Within the current mechanism, the enhanced regioselectivity induced using HFIP was attributed to its non-nucleophilic character.[350] When ethanol is used, it may compete with the hydrazine nucleophile for attack at the more reactive carbonyl group, thereby producing low regioselectivity. However, as HFIP is a very poor nucleophile, this competition is circumvented (Figure 3.21).[350] Coordination of the fluorinated solvent to the carbonyl groups increases the electrophilic character, promoting the reaction and accounting for the faster reaction times observed experimentally (Figure 3.21, Scheme 3.15). Furthermore, formation of the hydrazone (**I**, Figure 3.21) intermediate sees the loss of a water molecule which could be facilitated by both the strong ionising power and ability to solvate water.[350] The 3-regioisomer (**238**) was identified to share similarity with the initial hit compound **39** in Zhu *et al.*, and therefore was decided to be progressed through to the benzimidazole product.

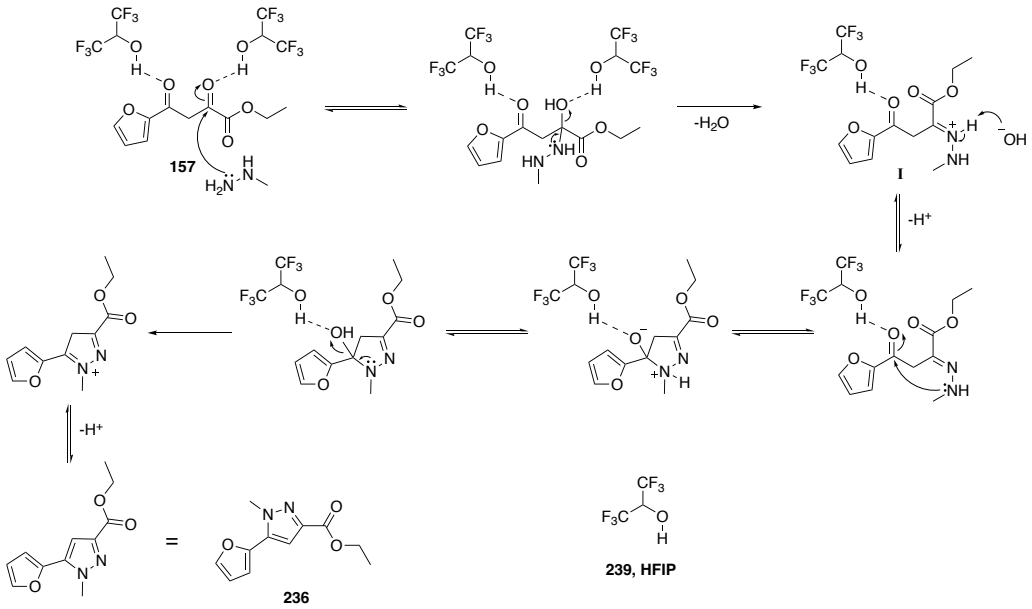

Figure 3.21 Plausible mechanism for the formation and relative bias to the 5-furan regioisomer (**236**) when fluorinated alcohols such as HFIP are used as solvents

Basic hydrolysis of the ethyl esters (**236 – 238**) with lithium hydroxide furnished the respective carboxylic acid (**240 – 242**) compounds in excellent yields (Scheme 3.15). A one-pot HATU-mediated amide coupling and subsequent cyclocondensation was performed with 4-chlorobenzene-1,2-diamine to yield the final benzimidazole products (**232, 233** and **243**, Scheme 3.15).

3.4.2 Synthesis of Triazole Analogue

3.4.2.1 Retrosynthesis of Triazole Analogue

The retrosynthetic strategy for synthesising the 1,2,4-triazole derivative (**234**) is presented in figure 3.22. The final benzimidazole scaffold could be accessed from the carboxylic acid (**244**) through a one-pot amide coupling and cyclocondensation with 4-chlorobenzene-1,2-diamine. Hydrolysis of the ethyl ester **245** provides the carboxylic acid **244**. The 1,2,4-triazole ethyl ester **245** could be obtained from the hydrazone **246** and furfurylamine under oxidative conditions. Reaction of ethyl 2-oxoacetate (**247**) with *tert*-butylhydrazine hydrochloride gives hydrazone **246**.

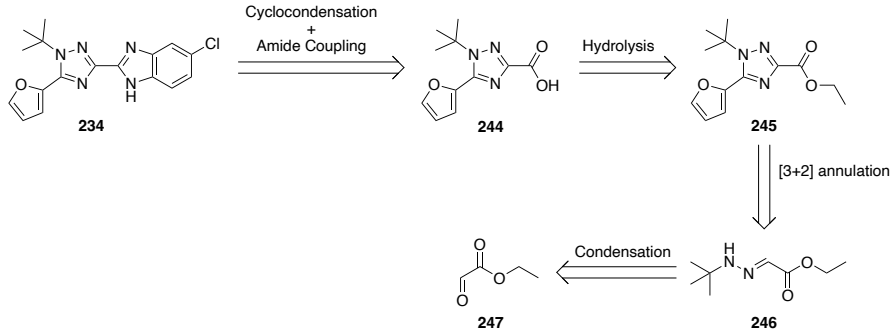

Figure 3.22 Retrosynthetic pathway to access the triazole derivative **234** from a hydrazone starting material.

3.4.2.2 Hydrazone Pathway

Hydrazone **246** was formed through the reaction between ethyl 2-oxoacetate (**247**) and *tert*-butylhydrazine hydrochloride in the presence of base (Scheme 3.16).[353] The reaction was found to be very low yielding due to suspected volatility issues, and therefore telescoped through to the subsequent step. Molecular iodine and *tert*-butyl hydroperoxide (TBHP) were added to a stirring solution of **246** and freshly distilled furfurylamine in acetonitrile.[354,355] Formation of the corresponding 1,2,4-triazole (**245**) occurred under oxidative conditions *via* a cascade C-H functionalisation, double C–N bond formation, and oxidative aromatisation sequence in the presence of iodine as a catalyst.[355] Within the reaction, iodine and TBHP act as the oxidant and *tert*-butyl source respectively. The conditions successfully synthesised the triazole ester **245**, albeit in very low yields following a tedious purification process. As a result of the overall synthetic challenges of the synthetic plan, it was decided that an alternative route would be devised.

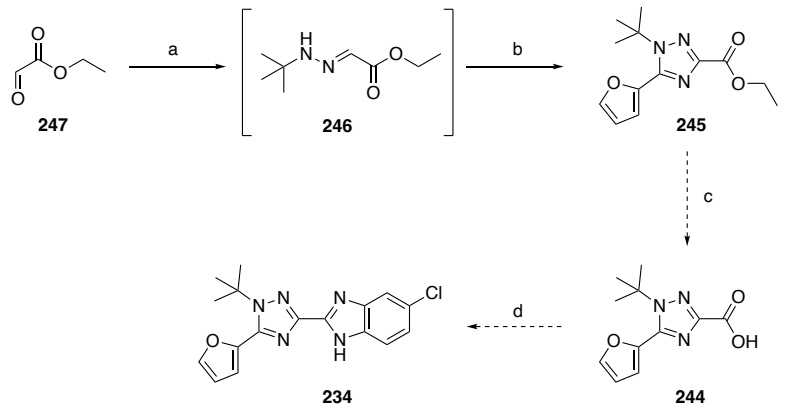

Scheme 3.16 Synthetic conditions to access **234** *via* formation of a hydrazone (**246**) starting material. *Reagents and Conditions* (a) *tert*-butylhydrazine hydrochloride, Et_3N, THF, reflux, 7 h, not isolated (b) furfurylamine, I_2, TBHP, CH_3CN, 90 °C, 4 h, 17% over two steps (c) $LiOH.H_2O$, $MeOH/H_2O$ (3:1), rt, 12 h (d) 1. 4-chlorobenzene-1,2-diamine, HATU, $^iPr_2NEt$, DMF, rt, 16 h; 2. AcOH/toluene (10:1), 75 °C, 24 h. TBHP: *tert*-butyl hydroperoxide.

3.4.2.3 Amidine Pathway

Owing to the high reactivity of their nucleophilic nitrogen atoms, amidines have been extensively utilised as organic catalysts and ligands in the formation of nitrogen-carbon bonds.[356,357] To address the difficulties in accessing non-symmetrical 1,3,5-substituted 1,2,4-triazoles Castanedo and coworkers developed a one-pot, two-step reaction of carboxylic acids, primary amidines and monosubstituted hydrazines (Scheme 3.17).[357] Starting with the *in situ* formation of the amide **248** from 2-furoic acid (**249**) and methyl 2-amino-2-iminoacetate (**250**), amide **248** then reacts with *tert*-butylhydrazine hydrochloride and cyclises to form the desired triazole (**251**, Scheme 3.17). Ester hydrolysis under basic conditions yielded the corresponding carboxylic acid **244** (Scheme 3.17). A HATU-mediated amide coupling with 4-chlorobenzene-1,2-diamine, followed by the acid catalysed cyclocondensation yielded the triazole analogue **234** in 35% yield (Scheme 3.17).

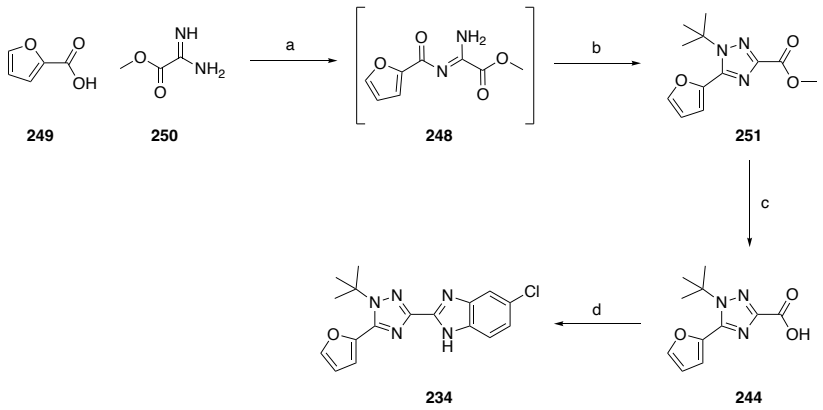

Scheme 3.17 Synthesis of the triazole derivative **234** *via* amidine **248** intermediate. *Reagents and Conditions* (a) HATU, $^{i}Pr_2NEt$, DMF, rt, 12 h, not isolated (b) *tert*-butylhydrazine hydrochloride, AcOH, 80 °C, 6 h, 40% c) $LiOH.H_2O$, $MeOH/H_2O$ (3:1), rt, 12 h, 80% (d) 1. 4-chlorobenzene-1,2-diamine, HATU, $^{i}Pr_2NEt$, DMF, rt, 16 h; 2. AcOH/toluene (10:1), 75 °C, 24 h, 35%

3.4.3 Synthesis of Imidazole Analogue

3.4.3.1 Retrosynthesis of Imidazole Analogue

Synthetic protocols to access unsymmetrical 1,2,4-imidazole cores are limited. The synthetic pathway to access the imidazole analogue **235** consisted of a six-step pathway in which the imidazole core (**252**) would be formed from a one-pot reduction and cyclisation of the enamine intermediate **253** (Figure 3.23). The benzimidazole motif was constructed last through an amide coupling between 4-chlorobenzene-1,2-diamine and the carboxylic acid (**254**) and acid mediated cyclocondensation, analogous to that of the triazole and *tert*-butyl variations (chapter **3.4.2.3** and **3.4.1.2**). A Suzuki coupling to the halo-imidazole species **255** would instate the furan motif to form the imidazole carboxylate **256**.

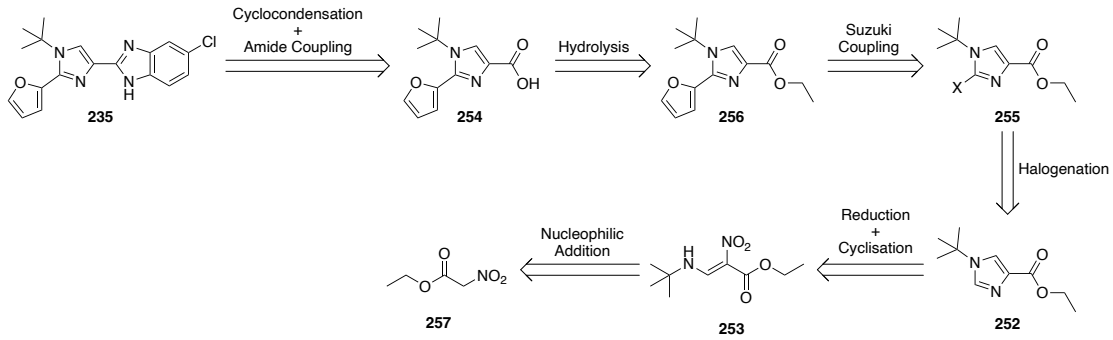

Figure 3.23 Retrosynthetic strategy to access the imidazole derivative (**235**)

3.4.3.2 Cross-Coupling Pathway

3.4.3.2.1 Synthesis of Ethyl 1-(*tert*-Butyl)-1*H*-imidazole-4-carboxylate

To construct the imidazole core, the enamine intermediate **253** was first synthesised from *tert*-butylamine, ethyl 2-nitroacetate (**257**) and triethylorthoformate (TOF) in an acetic acid/ethanol solvent system (Scheme 3.18).[358] **253** was achieved in low yields as the *E*-isomer ($^3J_{HH}$ = 15.1 Hz observed). **253** was then treated with elemental iron and TOF in acetic acid.[358] Emulating the Béchamp reduction, the resulting amine cyclises with TOF to form the corresponding imidazole carboxylate (**252**) in good yields (Scheme 3.18).

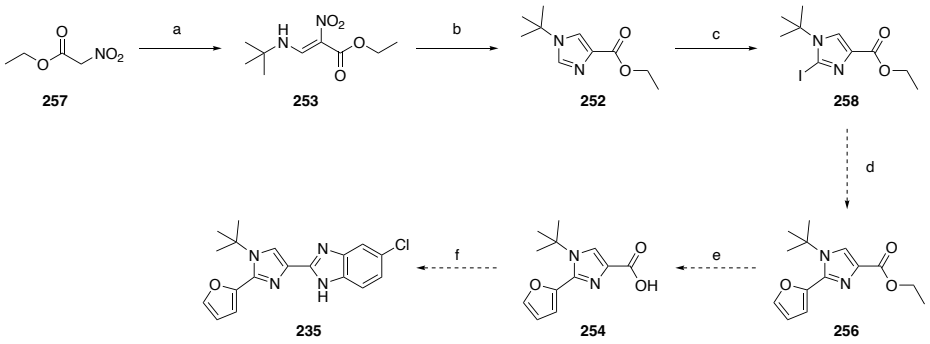

Scheme 3.18 Synthesis of imidazole intermediate **252**. *Reagents and Conditions* (a) *tert*-butylamine, TOF, AcOH, EtOH, 90 °C, 5 h, 25 – 32% (b) TOF, $Fe_{(s)}$, AcOH, 85 °C, 5 h, 64 – 75% (c) Conditions discussed in **3.4.3.2.2** (d) Conditions discussed in **3.4.3.2.3**. (e) $LiOH.H_2O$, $MeOH/H_2O$ (3:1), rt, 12 h (d) 1. 4-chlorobenzene-1,2-diamine, HATU, $^iPr_2NEt$, DMF, rt, 16 h; 2. AcOH/toluene (10:1), 75 °C, 24 h. TOF: triethylorthoformate

3.4.3.2.2 Synthesis of Halo-Imidazole Intermediate

In preparation for the Suzuki cross-coupling reaction the halo-handle needed to be installed on **252**. Initiation of the catalytic cycle of Pd-cross-coupling reactions occurs from oxidative addition of the Pd(0) into the C–X bond of the aryl halide.[359] Therefore the relative rate of oxidative addition is influenced by the strength of the C–X bond, with aryl-iodides being generally the most reactive. The regioselectivity for the corresponding halogenation was a point of concern. Electrophilic aromatic substitution of imidazole is favoured at the C4 and C5 position due to the electron withdrawing nature of the two nitrogens. However, in the case that positions 4 and 5 are blocked, substitution will take place in position 2.[360] Within the current scaffold it was postulated that a mixture of C5 and C2 halogenation would occur due to the presence of the electron withdrawing ester at C4.[361]

Within the imidazole scaffold, the C–H bond at the 2-position (between the two nitrogens) is the most acidic, thereby making it susceptible to halogenation by organolithium reagents.[362] Lithiation of **252** with *n*-BuLi followed by an electrophilic quench with iodine was attempted (Table 3.14, entry 1).[361–363]

Table 3.14 Iodination attempts on **252**.

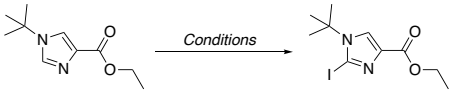

252 **258**

Entry	Scale (mg)	Conditions	Yield
1	50	*n*-BuLi, I_2, THF, -78 – 0 °C, 12 h	—[a]
2	40	NIS (2 eq, incremental), THF, reflux, 24 h	14%
3	100	NIS (2 eq, incremental) THF, reflux, 24 h	7%
4	100	NIS (1.5 eq), DMF, 60 °C, 24 h	1%
5	30	NIS (2 eq, incremental), HFIP, 25 °C, 16 h	S.M. [b]

[a] Complex reaction mixture as indicated by TLC analysis. [b] S.M. represents recovered starting material, as no reaction occurred.

Reported methods for the electrophilic halogenation of imidazoles generally demonstrate that selective monohalogenation is rarely achieved, with reactions typically yielding mixtures of mono- and poly-halogenated isomers.[364] Efforts were therefore pivoted to the use of succinimide reagents (Table 3.14, entries 2 – 5) as they allow for stricter stoichiometric control, thereby reducing the risk of over-reaction. Monoiodination of **252** was successfully achieved upon stirring with NIS in refluxing THF (Table 3.14, entry 2). However, the reaction was observed to be sluggish, with no improvement following incremental addition of NIS.[365,366] Furthermore, the reaction proved to not be scalable, with the yield decreasing by half upon scaling it up 2-fold (Table 3.14, entry 3). Therefore, a preliminary screen of suitable reaction solvents was conducted in an effort to increase the yield (Table 3.14, entries 3 – 5). Considerably worse yields were experienced when the solvent was switched to DMF (Table 3.14, entry 4) and HFIP (Table 3.15, entry 5).[367]

Due to the poor yields and scalability issues faced, bromination methods were explored. It was envisioned that a similar metalation approach would permit bromination of **252**. Treating **252**

with NBS in THF at room temperature gave the monobrominated product (**259**) in poor yields (Table 3.15, entry 1).[368] Conducting an analogous solvent screen to the iodination attempts provided a significant improvement in yields (Table 3.15, entries 1 – 4).[365,367–369] Changing the solvent system to DMF proved highly effective, demonstrating moderate yields throughout upscaling (Table 3.15, entry 4).[369] 2D-NMR analysis, for example the $^{3}J_{CH}$ correlation between the imidazole proton and the carbonyl carbon, was consistent with mono-bromination occurring at the C-2 position.

Table 3.15 Solvent screen within the bromination of **252** with NBS.

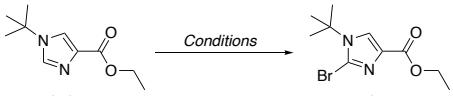

Entry	NBS (eq)	Solvent	Yield
1	1.1 – 1.6	THF	10%
2	1.1	CH_3CN/H_2O (1:1 v/v)	36%
3	1.1 – 2.2	HFIP	42%
4	1.1	DMF	55 – 60%

3.4.3.2.3 Suzuki Cross-Coupling

With the brominated species **259** in hand, a range of Suzuki cross-coupling methodologies were explored to synthesise **256** (Table 3.16). The initial attempt utilised $Pd(PPh_3)_4$ as the catalyst with potassium phosphate in a biphasic 1,4-dioxane/water system (Table 3.16, entry 1).[368] The reaction was conducted with degassed solvent, under argon in a sealed tube at elevated temperatures. After 24 h, no reaction had been observed to have proceeded by TLC or mass spectrometry analysis. Transitioning to a bidentate ligand, such as $Pd(dppf)Cl_2$, aimed to alter the electronic and steric environment around the palladium centre to promote oxidative insertion.[192] This modification proved ineffective, resulting only in the recovering of starting material (Table 3.16, entry 2).

Table 3.16 Suzuki coupling conditions trialled within the synthesis of **256**.

Entry	Conditions	Yield
1	$Pd(PPh_3)_4$ (10%), K_3PO_4, 1,4-dioxane/H_2O (4:1 v/v), 100 °C, 24 h	S.M. [a]
2	$Pd(dppf)Cl_2$ (10%), Cs_2CO_3, 1,4-dioxane/H_2O (4:1 v/v), 80 °C, 24 h	S.M. [a]
3	$Pd(dppf)Cl_2$ (10%), Cs_2CO_3, 1,4-dioxane, 80 °C, 24 h	S.M. [a]
4	$Pd(amphos)Cl_2$ (10%), Cs_2CO_3, 1,4-dioxane, 80 °C, 24 h	S.M. [a]
5	$Pd(amphos)Cl_2$ (10%), Cs_2CO_3, 1,4-dioxane, 180 °C, MW, 24 h	S.M. [a]
6	$Pd(amphos)Cl_2$ (20%), Cs_2CO_3, 1,4-dioxane, 80 °C - reflux, 24 h	S.M. [a]
7	$Pd(OAc)_2$ (10%), XPhos, Cs_2CO_3, toluene, reflux, 24 h	S.M. [a]
8	$Pd(OAc)_2$ (3%), DABCO, Cs_2CO_3, DMF, 110 °C, 24 h	S.M. [a]

[a] S.M. represents recovered starting material, as no reaction occurred. MW represents reactions performed inside a microwave reactor.

Multiple reports have identified 2-furyl boronic acids to have stability issues and be disposed to undergo protodeboronation.[359] Protodeboronation (Ar–B → Ar–H) describes the cleavage of the boronic acid by water to result in a carbon-hydrogen bond (Figure 3.24A).[359] To reduce formation of protodehalogenation and protodeborylation side products, water was removed from the system. $Pd(dppf)Cl_2$ remained as the Pd-catalyst, as a highly active catalyst system has been suggested to be effective in avoiding side-product formation. Additionally, $Pd(dppf)Cl_2$ has also been shown to drive effective reductive elimination due to its wide bite-angle.[359] As a result of the wide bite-angle, the two aryl groups are situated closer together and therefore have a larger orbital overlap, thus promoting reductive elimination.[359] However, no reaction was observed under these revised conditions (Table 3.16, entry 3).

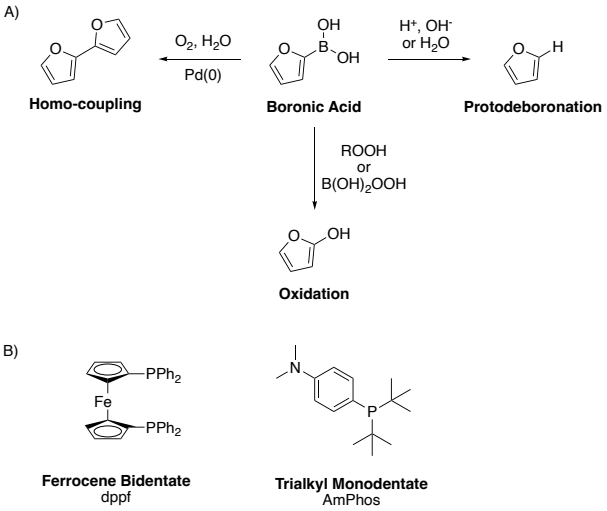

Figure 3.24 A) Side reactions of the Suzuki reaction. B) Highly effective ligands utilised in Suzuki reactions.

Following the unsuccessful attempts with Pd(dppf)Cl_2 and Pd(PPh_3)$_4$, it was postulated that the imidazole species may be too electron donating making oxidative addition difficult to achieve. Therefore, a more sterically hindered, electron rich system such as Pd(amphos)Cl_2 was introduced (Figure 3.24B). Known for being effective in coupling challenging heterocyclic halides, Pd(amphos)Cl_2 is growing in popularity.[359] Unfortunately, under standard coupling conditions, microwave assisted, and with increased catalyst loading no reaction was observed to occur when utilising Pd(amphos)Cl_2 in the present system (Table 3.16, entries 4 – 6).

Polarity of solvent has been shown to have a significant effect on the outcome of Suzuki reactions.[359] Non-polar and polar solvents were investigated in entries 7 and 8 (Table 3.16). Substitution for an alternative Pd(II)-source and electron rich ligand in Pd(OAc)$_2$ and XPhos respectively, similarly furnished no product formation (Table 3.16, entry 7). DABCO provides an alternative to the air and moisture sensitive bulky trialkylphosphine ligands.[370] Utilising Pd(OAc)$_2$ as the palladium source, and DABCO as the ligand in DMF, proved equally unsuccessful (Table 3.16, entry 8).

The issues experienced in the former Suzuki cross-coupling attempts were ascribed to the stability of 2-furan boronic acid. Unlike the side-reactions driven by oxidative processes (e.g. homo-coupling and oxidation to the phenol, Figure 3.24A) strategies to prevent the formation of the protodeboronated species are limited.[359] Inherent to the boronic acid itself,

protodeboronation causes an ongoing challenge in synthetic chemistry when using specific heterocyclic boronic acids.[359] Therefore rendering some boronic acids or esters impractical within Suzuki cross-couplings. Alternative approaches to incorporating unstable motifs such as 2-furan boronic acid include exploring other C–C cross-coupling reactions such as Negishi and Hiyama reactions, due to increased stability of the arylzinc or arylsilane species.[359] Additionally, decarboxylative cross-couplings offer an attractive alternative. Messina *et al.* described a robust decarboxylative cross-coupling route for the effective coupling of heterocycle functionalities prone to be unstable under Suzuki conditions.[371] However, an initial attempt utilising $Pd(P\textit{t}Bu_3)_2$ as the catalyst with caesium carbonate in DMF under microwave irradiation also failed to furnish the desired product (Scheme 3.19).[371] Although this pathway was abandoned, future attempts of the decarboxylative cross-coupling would benefit from exploring other bases such as KOH and Na_2CO_3 and the addition of $\textit{n}Bu_4NCl$ as an additive.[371]

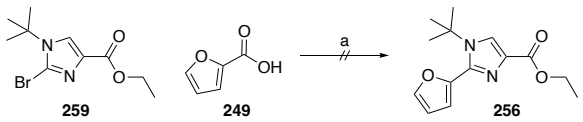

Scheme 3.19 Decarboxylative cross-coupling to yield **256**. *Reagents and Conditions* (a) $Pd(P\textit{t}Bu_3)_2$, Cs_2CO_3, DMF, 170 °C, MW, 40 min.

To overcome the issues associated with the previously described cross-coupling reactions, an alternative route describing a palladium-catalysed direct arylation of methyl 5-bromofuran-2-carboxylate was devised (Scheme 3.20). C–H activation methods describe the coupling of an arylhalide, under palladium catalysed conditions. Due to the inherent safety and handling concerns of 2-halofurans, methyl 5-bromofuran-2-carboxylate (**260**) was utilised to provide a more stable coupling partner. Hydrolysis of the methyl ester **261** to the carboxylic acid **262**, meant **262** could then be subjected to a decarboxylative cross-coupling reaction to yield the imidazole derivative (**235**, Scheme 3.20).[372] In order to control selectivity of the methyl carboxylate cleavage, the benzimidazole pharmacophore would be constructed prior (Scheme 3.20). In preparation for the direct arylation, **252** was hydrolysed to yield the carboxylic acid **263**. Compound **263** was then treated with 4-chlorobenzene-1,2-diamine under HATU amide coupling conditions and subsequent acid catalysed cyclocondensation to yield the imidazole-benzimdazole derivative **264**.

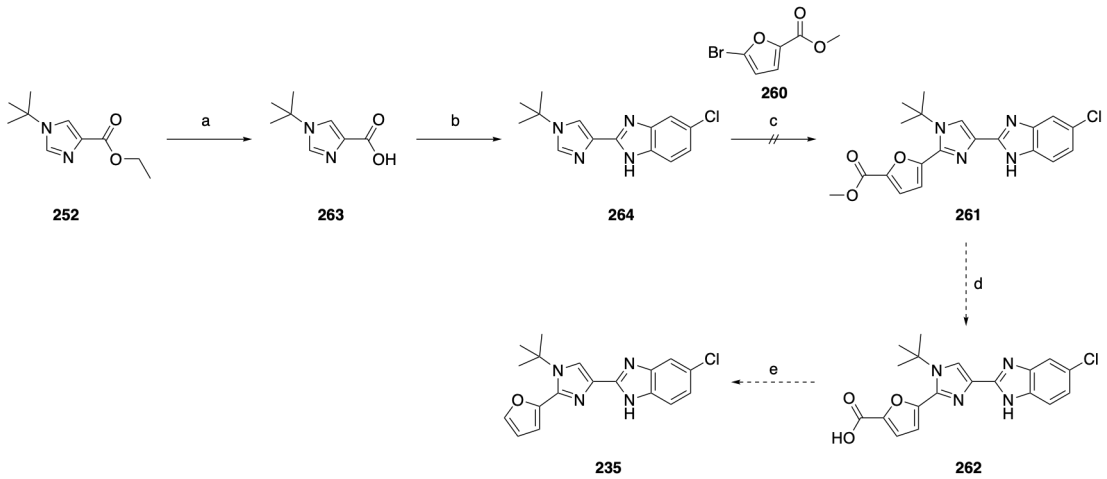

Scheme 3.20 Synthetic pathway describing the direct arylation of **264** and subsequent decarboxylation to yield the final imidazole analogue **235**. *Reagents and Conditions* (a) $LiOH.H_2O$, $MeOH/H_2O$ (3:1), rt, 12 h, 99% (b) 1. 4-chlorobenzene-1,2-diamine, HATU, $^{i}Pr_2NEt$, DMF, rt, 16 h; 2. AcOH/toluene (10:1), 75 °C, 24 h, 33% (c) Conditions discussed in Table 3.18 (d) $LiOH.H_2O$, $MeOH/H_2O$ (3:1), rt, 12 h (e) Ag_2CO_3, AcOH, DMSO, 120 °C, 16 h.

Direct C–H activation provides an exciting approach to access a variety of coupled or substituted products that are otherwise difficult to achieve.[373] However, inducing functionality can be difficult due to the high bond dissociation energy, making C–H bonds usually less reactive. Consequently, methods utilising conventional heating require elevated temperatures for long reaction times, thereby making these methods unsuitable for labile functional groups.[373] Microwave irradiation, provides an efficient source of heating by utilizing radiation rather than conduction.[373] Therefore, microwave assisted C–H activation methods boast reduced reaction times at elevated temperatures. Using $Pd(OAc)_2$ and Xantphos as the palladium catalyst and ligand respectively, the coupling of methyl 5-bromofuran-2-carboxylate (**260**) with **264** was conducted in 1,4-dioxane under microwave assisted heating (Table 3.17, entry 1).[374] Following 3 hours at 150 °C a complex reaction mixture was produced with no sign of product formation by mass spectrometry.

Table 3.17 C-H activation methods trialled for the coupling of methyl 5-bromofuran-2-carboxylate (**260**) with **264**.

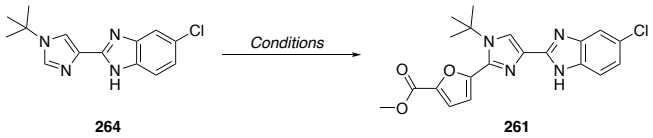

Entry	Conditions	Yield
1	**260**, $Pd(OAc)_2$, Xantphos, Cs_2CO_3, 1,4-dioxane, 150 °C, MW, 30 min	—[a]
2	**260**, $Pd(OAc)_2$, CuI, KI, DMF, 140 °C, Ar, 52 h	—[a]

[a] Complex reaction mixture as indicated by TLC analysis. MW represents reactions performed inside a microwave reactor.

Bellina *et al.* reported the selective C-2 arylation of azoles (including imidazoles) with arylbromides under base-free and ligandless conditions *via* a one-pot domino halogen exchange and Pd- and Cu-mediated arylation reaction (Table 3.17, entry 2).[375] Utilising the two catalyst system, C-2 arylation proceeds *via* the formation of an organocopper(I) derivative (**I**), followed by a transmetallation reaction with an arylpalladium(II) halide species (**II**) and a reductive elimination (Figure 3.25).[375] Potassium iodide is utilised within the reaction to promote the halogen exchange of unreactive aryl bromides to their aryl iodide form (Figure 3.25).[375] Analysis of the crude reaction mixture following heating in DMF at 140 °C for 52 hours showed no product formation.

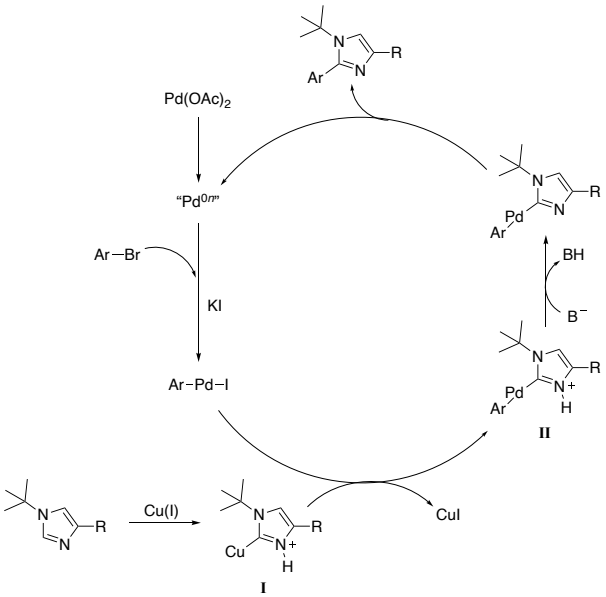

Figure 3.25 One-pot domino halogen exchange and Pd- and Cu-mediated arylation reaction catalytic cycle.

Further optimisation of the C–C bond formation coupling could potentially overcome the limitations experienced and are therefore discussed further in section **3.4.3.5**. However, due to the innate instability and reactivity of many furan coupling partners the decision was made to redirect efforts to alternative pathways.

3.4.3.3 Amidine Pathway

Following the unsuccessful attempts at coupling the furan motif, a synthetic pathway building up from the furan functional group was developed (Scheme 3.21). Firstly, freshly distilled furfural (**265**) was treated with hydroxylamine hydrochloride in the presence of sodium hydroxide to yield the corresponding oxime (**266**, Scheme 3.21).[376] **266** was isolated as a mixture of stereoisomers, with both the *E*- and *Z*-isomer seen in the NMR spectra.[377] Treating **266** with acetonitrile and catalytic cupric acetate successfully dehydrated the oxime to the corresponding nitrile in 40% yield (**267**, Scheme 3.21). In agreement to the literature, the corresponding amide was also isolated in comparative yields.[377]

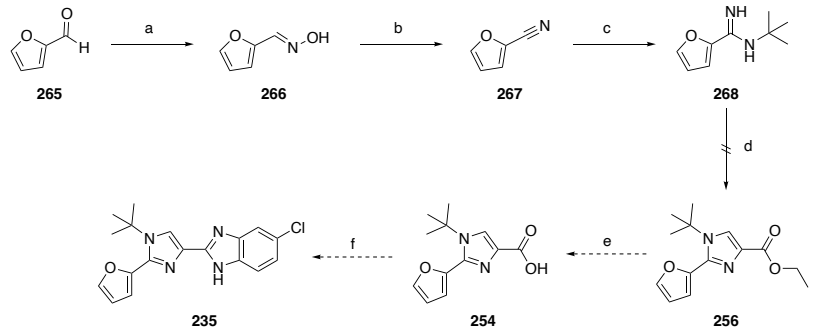

Scheme 3.21 Proposed synthesis of imidazole derivative **235** from amidine intermediate **268**. *Reagents and Conditions* (a) $NH_2OH.HCl$, NaOH, H_2O/EtOH (2:1), rt, 1 h, 80% (b) $Cu(OAc)_2$, CH_3CN, reflux, 1 h, 40% (c) *tert*-butylamine, $AlCl_3$, rt, 1 h, 33% (d) ethyl bromopyruvate, $KHCO_3$, THF/H_2O (1:1, v/v), 50 °C, 48 h (e) $LiOH.H_2O$, MeOH/H_2O (3:1), reflux, 1 h (e) 1. 4-chlorobenzene-1,2-diamine, HATU, $^{i}Pr_2NEt$, DMF, rt, 12 h; 2. AcOH/toluene (10:1), 75 °C, 48 h.

The *N*-substituted amidine motif **268** was constructed *via* an alkyl amine (**269**) and aryl nitrile (**267**) using the Lewis acid $AlCl_3$ (**270**).[378,379] The reaction was conducted at elevated temperatures of 140 °C within a sealed tube. Mechanistically, the Lewis acid serves to activate the nitrile *via* an aluminium amine intermediate (**I**, Figure 3.26).[379,380] Nucleophilic attack of the Lewis acid by the alkyl amine (**269**) results in a negatively charge aluminium ion. Following this the corresponding aluminium amine (**I**, Figure 3.26) is formed *via* the loss of HCl. The nitrile (**267**) then coordinates to the dichloro-aluminium amine (**II**) to form the

activated Lewis acid-base complex (**II**). Attack of the nitrile from the amine lone pair forms **III**, which forms the desired amidine upon regeneration of $AlCl_3$.[380]

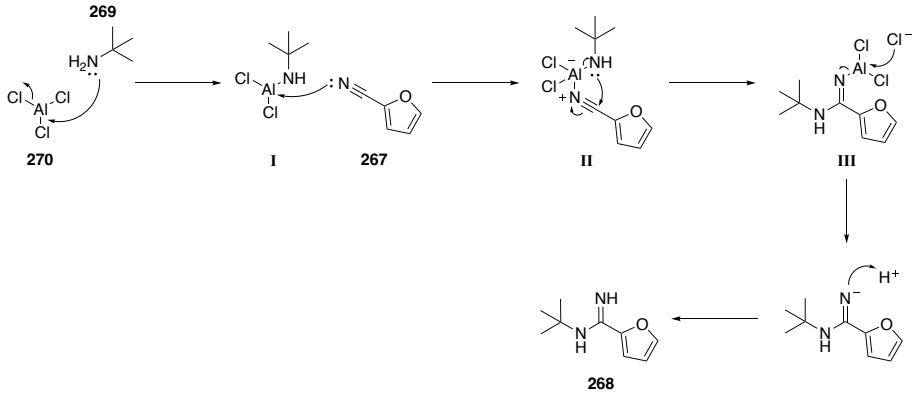

Figure 3.26 Proposed mechanism for the formation of amidine **268** *via* an $AlCl_3$ mediated pathway.

Condensation of amidine **268** with ethyl bromopyruvate failed to yield the desired imidazole (**235**, Scheme 3.21). In order for the reaction to proceed the condensation rate of α-bromoketone with the amidine needs to outcompete the decomposition rate of the bromoketone in water.[381] Additionally, bicarbonates were identified as the optimal base as it only serves a proton scavenger pushing the equilibrium forward.[381] Thus, sodium bicarbonate and 1,4-dioxane were initially trialled as the base and solvent respectively (Scheme 3.21).[382] To overcome the poor solubility observed in the previous conditions, a biphasic system of THF and water, with potassium bicarbonate as the base was also explored however it too proved equally unsuccessful (Scheme 3.21). Unfortunately, due to time constraints this pathway was abandoned. However, future iterations would benefit from a series of reactions screening different bases (e.g. potassium carbonate, *t*-BuOK), solvents (e.g. THF, DMF, CH_3CN) and elevated temperatures.[381]

3.4.3.4 Enamine Pathway

Working in parallel to the previously described amidine pathway, an alternative approach initialised from the enamine intermediate described in scheme 3.18 (chapter **3.4.3.2.1**) was also explored. Taking inspiration from the initial synthetic pathway (chapter **3.4.3.2.1**), it was envisioned that the furan motif could be installed during the one-pot reduction and cyclisation of the enamine intermediate **253** (Scheme 3.22).[383] Furan diethylacetal **271** was successfully synthesised from furfural (**265)** with TOF in the presence of iron(III) tosylate ($Fe(OTs)_3$) in

ethanol (Scheme 3.22). Within the reaction $Fe(OTs)_3$ acts as a Lewis acid catalyst, and orthoformate as a water scavenger.[383] The success of the reaction was largely dependent on the fresh distillation of furfural.

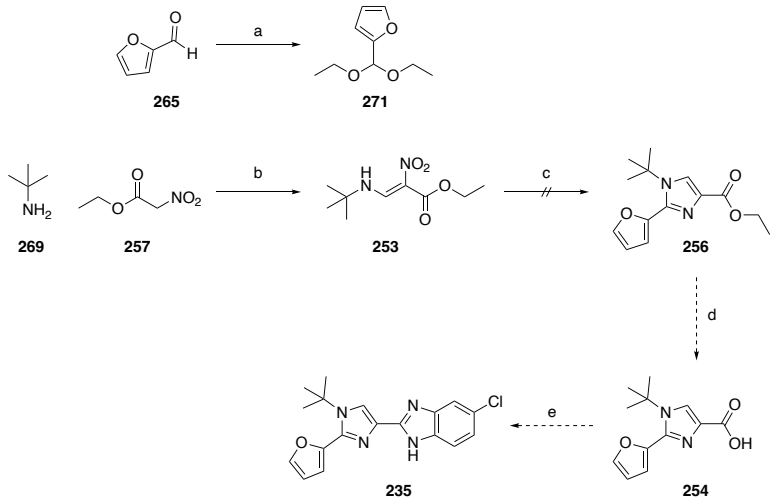

Scheme 3.22 Proposed synthesis of imidazole analogue **235** from enamine starting material **253**. *Reagents and Conditions* (a) TOF, $Fe(OTs)_3$, EtOH, rt, 4 h, 70% (b) TOF, AcOH, EtOH, 90 °C, 5 h, 25 – 32% (c) **271**, $Fe_{(s)}$, AcOH, 85 °C, 5 h (d) $LiOH.H_2O$, $MeOH/H_2O$ (3:1), reflux, 1 h (e) 1. 4-chlorobenzene-1,2-diamine, HATU, $^iPr_2NEt$, DMF, rt, 12 h; 2. AcOH/toluene (10:1), 75 °C, 48 h.

The one-pot reduction and cyclisation of enamine **253** with **271** resulted in a complex reaction mixture, with trace product formation observed by mass spectrometry (APCI *m/z* 263 $[M+H]^+$). Due to time constraints, further exploration of the current pathway was halted, however should be explored in future attempts.

3.4.3.5 Future Directions

Within the discussed synthetic approach to access the imidazole analogue, the cross-coupling reaction to amend the furan motif to the pyrazole scaffold provided a significant synthetic challenge. The difficulty experienced was accredited to the instability of the furan coupling partners and inefficient oxidative addition. Future efforts should therefore initially be directed towards the latter two pathways discussed, in which the furan motif is incorporated into the scaffold earlier. Suggestions include trialling different base sources to promote the condensation between amidine **268** and the α-bromoketone. Additionally, alternative Béchamp reduction conditions, such as varied electron sources in zinc or tin, should be employed in the one-pot reduction/cyclisation of enamine **253** with diacetyl **271**.

Finally, C–C cross-coupling methodology could be revisited in the form of Negishi and Hiyama cross-couplings, and direct C2-arylation. Direct C2-arylation methods reported in literature are restricted to aryl iodides and aryl bromides at high temperatures.[362,363] Selective C2-arylation of SEM-imidazoles was achieved when employing strong alkoxide bases such as sodium *tert*-butoxide in a nonpolar solvent (Scheme 3.23A, step a).[362] Additionally, the addition of copper(I) salts generates a bias towards the C-2 position (Scheme 3.23B, step d).[384] Due to the commercial cost and relative safety concerns surrounding 2-halofurans these methods were not explored within the initial study, although may provide a future avenue to explore.

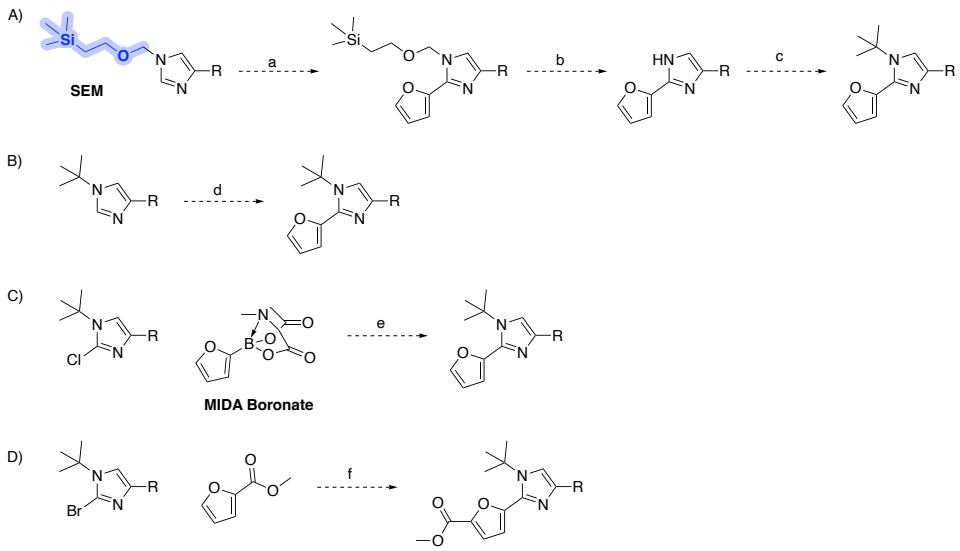

Scheme 3.23 Proposed avenues to access the imidazole derivative. Direct arylation methods incorporating SEM-imidazole (A) and copper salts (B) to promote selective C-2 arylation.[328,350] MIDA boronate (C) species have been demonstrated to have increased stability to boronic acids.[385] Methyl 2-furoate (D) obtains superior physicochemical properties to furan for direct arylation.[386]

2-furanylboronic acid has been reported to lose 90% of its activity after 15 days storage at ambient temperature.[387,388] However alternative boronate sources have provided more stable options that are additionally resistant to protodeboronation (Figure 3.27). Examples include the (MIDA) triisopropyl borate, and trifluoroborates (Figure 3.27).[359,388] These masked boronate species generate the boronic acid *in situ* during the Suzuki coupling reaction. Therefore, protodeboronation can still occur *in situ* due to the prolonged reaction times often required for Suzuki reactions. To overcome this, Knapp *et al.* reported methodology in which the choice of base could control the rate of hydrolysis of MIDA boronates and therefore the *in situ* rate of

release of unstable boronic acids (Scheme 3.23C, step e). [369] Within C-H direct arylation reactions, methyl 2-furoate provides a beneficial starting material. Advantageous over furan itself, methyl 2-furoate provides a viable option for the synthesis of 2-arylfurans due to a range of physicochemical properties (Scheme 3.23D, step f).[386] Examples include a higher boiling point, lower toxicity profile and mitigated risk of overreaction. Decarboxylation methods of furan derivatives have been reported extensively in literature.

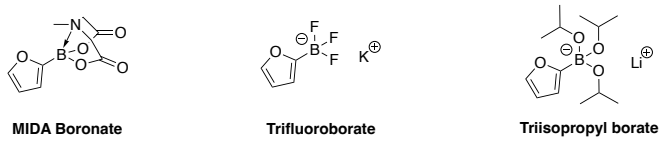

Figure 3.27 Alternate borate species.

3.5 Analogues with Increased Rotational Freedom

Creating a comprehensive view of the binding pocket for drug design requires a deep understanding of the subtleties and boundaries of receptor and ligand flexibility.[389] Although restricting conformational rotation of a ligand has its benefits (decreasing the entropic penalty and stabilizing a favorable binding conformation for better potency) in drug design, it is entirely target dependent. [352–354] In the absence of structural data, as experienced in P2Y6R drug design, analogues of varying degrees of flexibility should be explored to broadly investigate the binding domain. The proposed compound library (**272** – **275**, Figure 3.28) contribute an element of rotational freedom through decyclisation and introduction of methylene spacers.

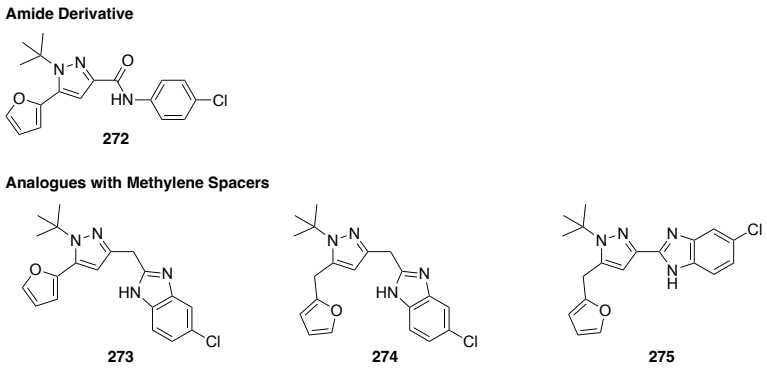

Figure 3.28 Derivatives introducing a degree of conformational freedom.

3.5.1 Synthesis of Amide Analogue

A common strategy to reduce conformational freedom of a molecule around an amide bond, is the isosteric replacement to azole derivatives such as imidazole.[393] Therefore, in the case of phenyl amide moieties, replacement for benzimidazole has been demonstrated to reduce free rotation and alter physicochemical properties. This replacement has thereby demonstrated beneficial properties within multiple drug discovery campaigns.[394–396] Therefore, the *p*-chlorophenyl amide analogue was presented as an obvious choice to explore the effects of rotational freedom. The overlay of the two compounds within the P2Y6 homology and AlphaFold molecular models (details of which will be discussed further in **Chapter 5**) is presented in Appendix 8. Analysis of the two predicted binding modes demonstrated close pose alignment in the AlphaFold model, with equivalent binding interactions with Arg266 and Tyr20 residues (Appendix 8). On the contrary, the two compounds were predicted to exist in reversed orientation to each other within the template homology model (Appendix 8).

Starting from the common carboxylic intermediate **163** previously synthesised in **3.2.1**, a HATU mediated amide coupling was conducted with 4-chloroaniline to achieve the desired amide **272** in 82% yield (Scheme 3.24).

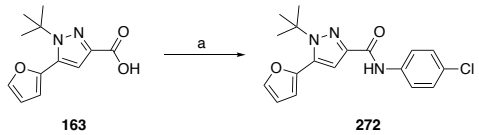

163 **272**

Scheme 3.24 HATU mediated amide coupling to access amide derivative **272.** *Reagents and Conditions* (a) HATU, $^{i}Pr_2NEt$, DMF, rt, 12 h, 82%.

3.5.2 Analogues with Methylene Spacers

3.5.2.1 Synthesis of Methyl Benzimidazole Analogue

Synthesis of the methyl benzimidazole analogue (**273**) started with the formation of the Weinreb amide **276**. A HATU mediated amide coupling reaction between 2-furoic acid (**249**) and *N,O*-dimethylhydroxylamine hydrochloride furnished the **276** in 71% yield (Scheme 3.25). The β,γ-diketo ester **277** is formed through the γ-acylation of the dianion (**I**, Figure 3.29) by the Weinreb amide **276**.[376,397–399] NaH first deprotonates the alpha-proton of ethyl acetoacetate (**278**) to form the mono-anion **II** (Figure 3.29). Treatment of this monoanion (**II**) with *n*-BuLi gave the dianion **I** (Figure 3.29). Theoretically, NaH can deprotonate both hydrogens, however

after the second deprotonation the two negative charges will repel each other therefore destabilising the double-deprotonated product. Therefore, a stronger base in *n*-BuLi is required to initiate the second deprotonation. This consecutive nature must occur, as using *n*-BuLi initially has been shown to undergo an addition reaction with the carbonyl group rather than conducting the desired deprotonation.[398] Stability of the β,γ-diketo ester **277** was a point of concern and was therefore telescoped through to the subsequent Paal-Knorr pyrazole formation following partial purification. However, stability of similar derivatives has been achieved by converting them to the bispotassium salt, and thereby provides a useful alternative if larger quantities are required. [392]

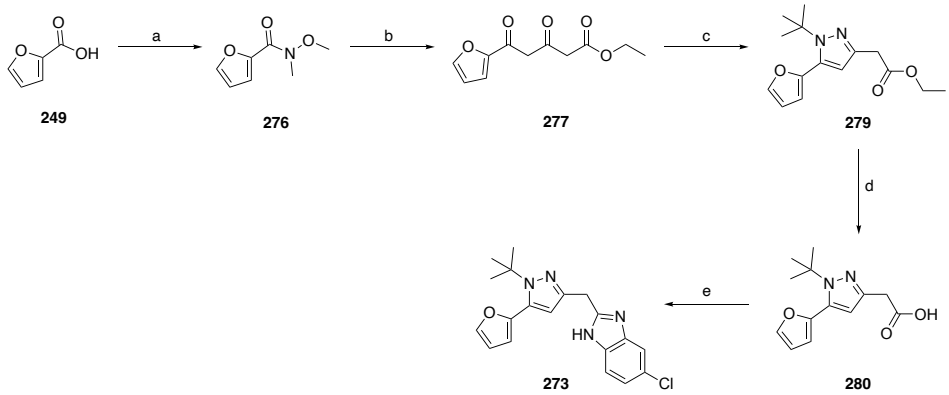

Scheme 3.25 Synthesis of the methyl-benzimidazole analogue **273**. *Reagents and Conditions* (a) *N*,*O*-Dimethylhydroxylamine hydrochloride, HATU, $^{i}Pr_2NEt$, DMF, rt, 12 h, 71% (b) 1. ethyl acetoacetate, NaH, THF, 0 °C; 2. *n*-BuLi, -78 °C, 3 h, 30% (c) *tert*-butylhydrazine hydrochloride, EtOH, rt, 8 h, 46% (d) $LiOH.H_2O$, $MeOH/H_2O$ (3:1), reflux, 1 h, 72% (e) 1. 4-chlorobenzene-1,2-diamine, HATU, $^{i}Pr_2NEt$, DMF, rt, 12 h; 2. AcOH/toluene (10:1), 75 °C, 48 h, 28%

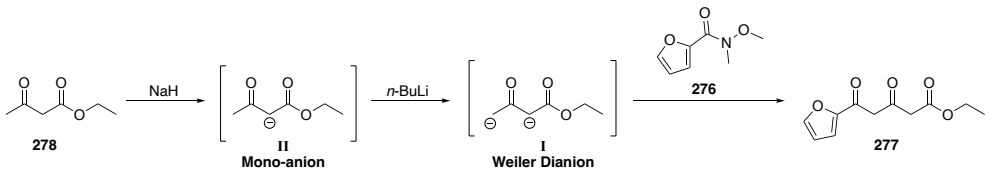

Figure 3.29 Synthesis of β,γ-diketo ester **277** *via* the Weiler dianion (**II**).

Compound **276** was immediately treated with *tert*-butylhydrazine hydrochloride in ethanol at room temperature overnight to form the 5-furan regioisomer (**279**) selectively. Support for the assignment was provided by the lack of NOE correlation between the methylene CH_2 and *tert*-butyl (Appendix 9). The ethyl ester **279** was hydrolysed to yield the corresponding carboxylic acid (**280**) in 78% yield. An amide coupling and subsequent acid mediated cyclocondensation

reaction of **280** and 4-chlorobenzene-1,2-diamine yielded the final methyl benzimidazole finale analogue **273**.

3.5.2.2 Future Directions

Due to time constraints the remaining two analogues proposed in the compound library presented in figure 3.28 were not attempted. A retrosynthetic pathway to access the remaining analogues is featured in figure 3.30 and should be attempted following analysis of the biological data provided by the previously discussed analogues. Drawing inspiration from the previously discussed routes, it was envisioned that the di-methylene spaced (**274**, Figure 3.30A) and the methyl furan (**275**, Figure 3.30B) derivatives could be accessed *via* a Claisen condensation and γ-acylation respectively.

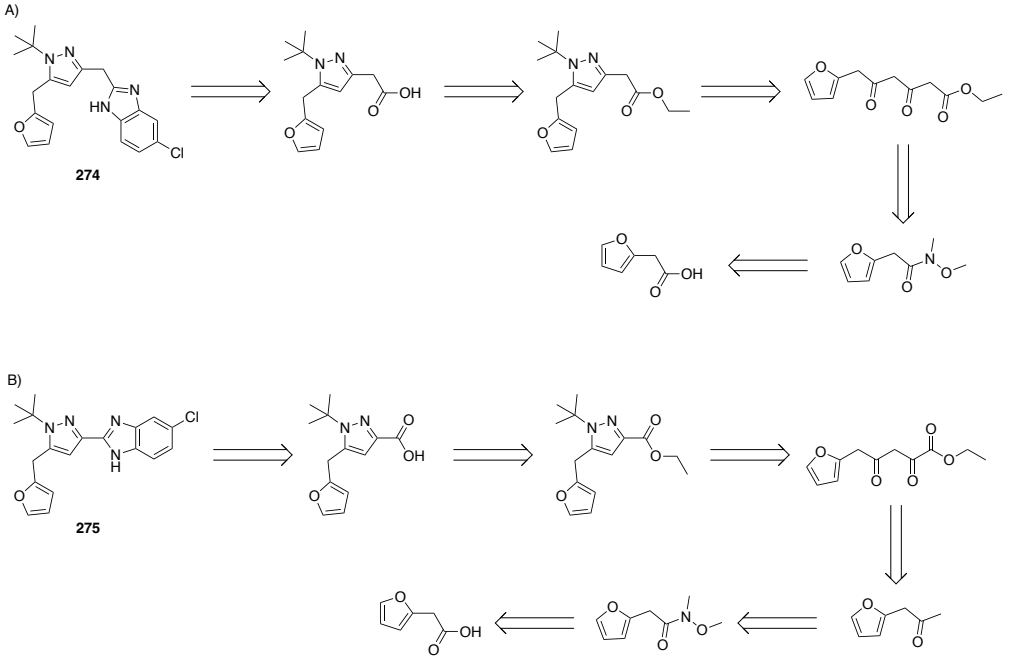

Figure 3.30 Retrosynthetic pathways to access the methyl-furan methyl-benzimidazole (A, **274**) and methyl-furan (B, **275**) analogues within the methylene spacer library.

3.6 Concluding Remarks

This chapter has described the successful synthesis and diversification of lead candidate **37** through traditional SAR approaches. The constructed compound library, consisting of 15 novel ligands, will expand the SAR knowledge of the P2Y6 benzimidazole antagonist chemotype therefore providing critical information about key binding interactions within the ligand-

binding domain. Exploration of the 5,6-heterocycle and pyrazole motifs of **37**, included a nitrogen-walk strategy, substitution and isosteric replacements. These investigations have studied the effect of varying H-bond donors/acceptors, flexibility, steric and electronic characters. The biological results and corresponding conclusions of the compound library described in this chapter will be discussed in detail in **Chapter 5**.

Chapter 4. Structural Hybridisation of Compound 37 with Quinoline Chemotype

4.1 Introductory Remarks

Within the drug discovery process, clinical development of small molecules is often ceased due to a lack of appropriate PK properties.[400–402] Heralded as a strategic necessity, integration of PK modelling within the early stages of the drug discovery pipeline enhances the lead optimisation process significantly.[400,401] Preliminary analysis of the benzimidazole lead compound **37** *via* computational metabolism predictors (e.g. BioTransformer3, FAME3, GloryX and XenoSite) identified the furan and benzimidazole (to a lesser extent) motifs to be metabolic soft spots (Figure 4.1, Appendix 10).[403–408] Therefore, identifying two key moieties that would benefit from diversification.

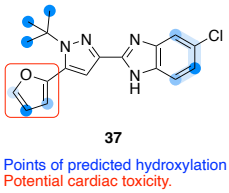

Figure 4.1 Metabolic soft spots on **37** identified *via* computational methods.

Structural hybridisation describes the strategy of incorporating beneficial components from two distinct chemotypes to make a novel compound with superior characteristics.[409] Within drug design, the strategy provides an attractive opportunity for lead optimisation or to evade patent space, and has shown to be effective across a broad range of targets.[131,409] Within the infancy stage of lead identification, structural hybridisation can provide an efficient strategy to expand the existing ligand compound library and develop a new generation of safe and effective drug candidates. By taking key motifs, the strategy promotes a thorough analysis of key pharmacophoric features required for selectivity, and potency. Additionally, structural hybridisation can be utilised to optimise absorption, distribution, elimination and metabolism (ADME) factors, resulting in new entities less toxic in comparison to the original drug leads.[409] The hybrid compound can be composed of elements from two or more partners assembled covalently with or without a linker.[409] Therefore, depending on the mode of hybridisation, there are multiple permutations and combinations of how the two partners can be assembled.[409] One such example, includes the Kassiou group's work surrounding P2X7 antagonists in which the

hybridised adamantyl cyanoguanidine compound **13** displayed a four-fold greater inhibitory potency than the lead compound **15**, whilst improving the PK properties of lead **14** (Figure 4.2).[131]

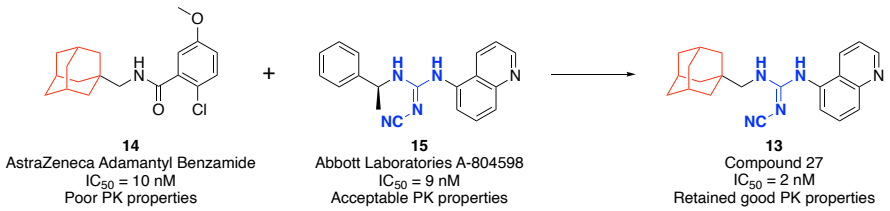

Figure 4.2 Structural hybridisation of the adamantyl amide (**14**) scaffold reported by AstraZeneca and cyanoguanidine (**15**) scaffold reported by Abbott Laboratories produced compound 27 (**13**), which displayed good potency and PK properties within a hP2X7 *in vitro* assay. Data extracted from O'Brien-Brown, J. *et al*. **2017**.

In 2024, Zhao *et al.* reported a series of quinoline-dihydropyrazole analogues as potent, highly selective P2Y6R antagonists with activity in an *in vivo* anti-inflammatory model.[170] Pre-existing structural similarities between the quinoline and benzimidazole chemotypes made them an appropriate selection for the corresponding complementary partner in the hybridised structures. A preliminary screen of 300 in house compounds identified **40** as the study's hit compound (Figure 4.3). Utilising the homology model developed by Li and coworkers, binding interactions of **40** were suggested, which were utilised to drive future optimisation attempts.[170] Compound **40** was sectioned into three key components for diversification. Optimisation of the biphenyl motif identified that six-membered rings generally increased potency (Figure 4.3).[170] Substitution of electron-donating groups were well tolerated at both *meta*- and *para*-positions.[170] Similarly, electron-rich heterocycles provided good pharmacological activity (Figure 4.3).[170] SAR analysis of the quinoline pharmacophore identified that substitution of the methyl group at the 7- or 8-position on the chloroquinoline reported good activity regardless of the presence of an aromatic ring on the right-hand side of the molecule (Figure 4.3).[170] Inhibitory activity was further improved by removal of both the methyl and chloro-functional groups leaving the bare quinoline.

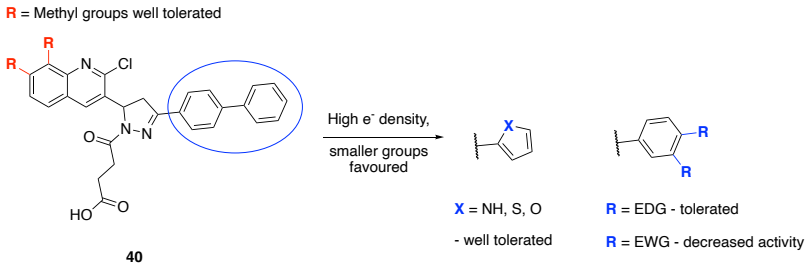

Figure 4.3 Summary of SAR findings during the optimisation of **40** by Zhao *et al.* Substitution at the 7- or 8-position of a methyl group on the chloroquinoline (red) were best tolerated and high electron density, smaller groups were favoured in place of the biphenyl (blue).

4.1.1 Chapter Aims

This chapter continues the exploration of the benzimidazole chemotype through a structural hybridisation approach. Computational analyses identified potential metabolic soft spots on lead compound **37** (Figure 4.1), highlighting key motifs for modification. By utilising a structural hybridisation-like approach a series of novel compounds were synthesised that are predicted to be less susceptible to oxidation. The analogues synthesised will therefore provide valuable information regarding structural features required to elicit biological activity.

4.2 Quinoline Validation Compounds

Prior to applying structural hybridisation between the two chemotypes, validation compounds (**38**, **40** and **281**) from the quinoline chemotype were synthesised. Analogous to the approach in **Chapter 3**, three structures – including the hit (**40**) and lead (**38**) compound – with a range of reported functional activity were chosen (Figure 4.4). These structures will provide further validation of both the *in vitro* assay employed in this work and the SAR described herein.

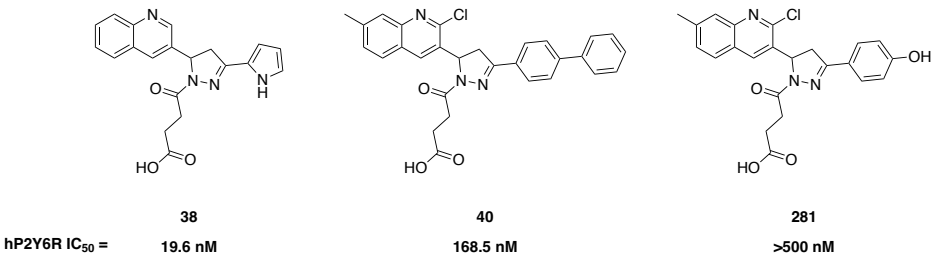

Figure 4.4 Validation compounds (**38**, **40** and **281**) sourced from Zhao *et al.*, with corresponding IC_{50} data. Data extracted from Zhao, Y. *et al*. **2024**.

4.2.1 Synthesis of Quinoline Validation Compounds

Compounds **38, 40** and **281** were synthesised *via* a three-step linear procedure as per the corresponding paper (Scheme 4.1).[170] Formation of the α,β-unsaturated diketones (**282 – 284**) was achieved through a Claisen-Schmidt condensation of the respective quinoline carboxyaldehyde (**285** and **286**) with acetyl compounds under basic conditions (Scheme 4.1). Compounds **282** and **283** were then reacted with hydrazine monohydrate in ethanol to furnish the dihydropyrazole intermediate (**287** and **288**, Scheme 4.1). Refluxing in ethanol with succinic anhydride obtained the target compounds **38** and **40** in moderate yields (Scheme 4.1). Succinic anhydride reacts with the primary amine in a ring-opening process to create an amide bond and terminal carboxylate.

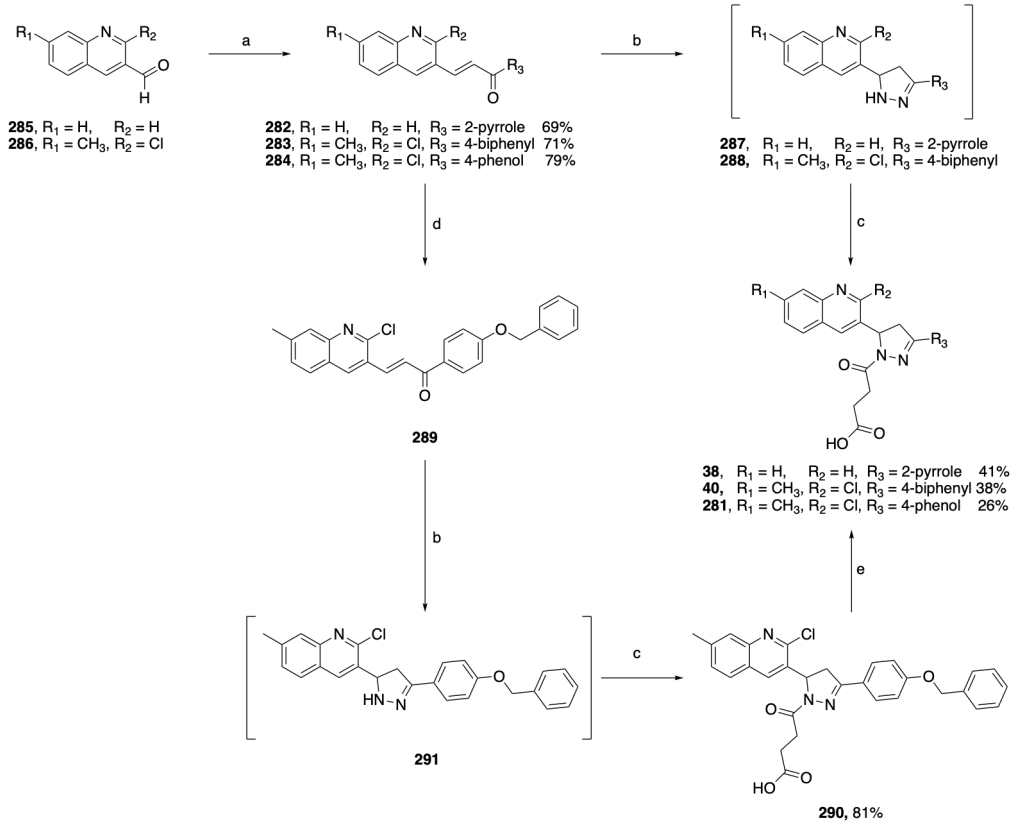

Scheme 4.1 Synthesis of quinoline-dihydropyrazole validation compounds. *Reagents and Conditions* (a) appropriate acetyl compound, 2.5 M NaOH, EtOH, rt, 1 h (b) hydrazine monohydrate, EtOH, reflux, 1 h, not isolated (c) succinic anhydride, CH_2Cl_2, reflux, 2 h (d) benzyl bromide, NaH, DMF:THF (2:1) rt, 3 h, 90% (e) 1M BBr_3, CH_2Cl_2, 0 – 25 °C, 1 h, 26% (f) Ac_2O, 80 °C, 3 h, 82%

The free phenol motif on **284** proved troublesome, causing side product formation and challenging purification of later intermediates. To overcome these issues, a benzyl protecting

group was introduced. Compound **284** was treated with benzyl bromide at 0 °C following deprotonation with NaH (Scheme 4.1). The benzyl protected α,β-unsaturated diketone **289** was achieved in 90% yield, following a simple purification (Scheme 4.1). The benzyl protected final product **290** was then prepared through cyclisation with hydrazine monohydrate to yield **291** and subsequent addition and ring-opening of succinic anhydride. The target compound **281** was achieved through a benzyl deprotection with boron tribromide (Scheme 4.1). Purification of **281** was achieved through reverse phase flash chromatography with TFA as an additive. Therefore, the corresponding di-TFA salt was isolated.

4.3 Structural Hybridisation Library

Structural hybridisation of the benzimidazole and quinoline P2Y6R antagonist chemotypes was investigated to overcome the predicted metabolic liabilities of **37**. Throughout the multiple PK modelling tools utilised to assess **37**, the furan and benzimidazole motif were consistently forecasted to be prone to metabolism *via* oxidation. Oxidative metabolism of electron rich functional groups – such as five-membered heterocycles – by CYP enzymes is a widely reported issue in drug scaffolds.[346,404] Correlated with the electronic structure, the metabolic stability of heterocycles and thus likelihood to undergo oxidation, is often biased towards the molecule with the higher-energy highest occupied molecular orbital (HOMO).[346,410] It should be noted that the electronic structure is not the only parameter that affects susceptibility to oxidation but also steric effects and substrate recognition. Comparison amongst commonly utilised heterocycles in drug discovery, five-membered heterocycles with one heteroatom have higher HOMO energy than six-membered counterparts.[344] Substitution of electron-rich aromatic rings (Furan HOMO eV = -9.32) with electron-poor heterocycles, such as pyridine (HOMO eV = -9.93), is a common strategy utilised within medicinal chemistry to mitigate oxidative metabolism.[346]

The resulting compound library (**292 – 301**) of structurally hybridised molecules is presented in figure 4.4. To provide a closer comparison to the benzimidazole analogues and therefore allow for a deeper SAR analysis, a merged (chimeric) hybrid approach was utilised in which one component of the benzimidazole scaffold was manipulated at a time. Evaluation of the quinoline chemotypes SAR reported in Zhao *et al.*, provided clear major pharmacophores for hybridisation.[170] In an effort to maintain potency, furan modifications were limited to

functional groups reporting an IC_{50} of less than 200 nM in the original scaffold. Aromatic motifs included in the original SAR conducted by Zhu *et al.* were thereby removed, resulting in the seven modifications pictured (Figure 4.4).[257] Analogously, only top scoring (IC_{50} < 100 nM) quinoline motifs were synthesised (Figure 4.4).

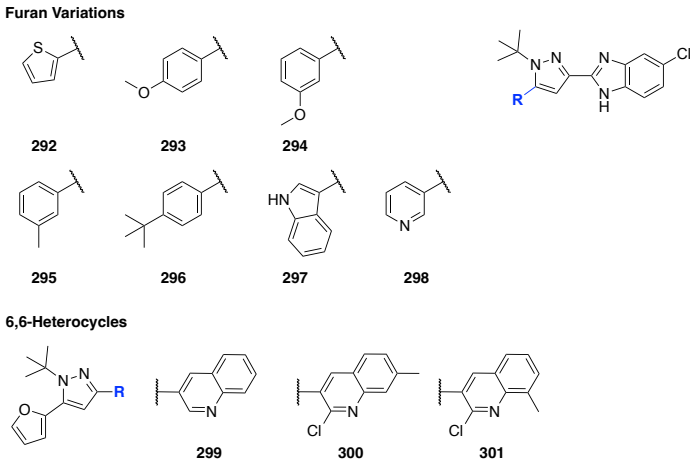

Figure 4.4 Compound library (**292 – 301**) derived from structural hybridisation.

4.3.1 Modification of the Furan Motif

Synthesis of analogues **292** – **297** were accessed *via* a four-step linear synthetic pathway, incorporating the furan variation in the initial Claisen condensation. The pathway presented an alternative to the synthetic procedure described in chapter **3.3.1**, optimising the methodology to be overall more efficient reducing the total synthetic steps by one.

The synthesis began with a Claisen condensation between the respective ketone (**302 – 307**) and diethyl oxalate (Scheme 4.2). Substituting the base for NaH and heating at 50 °C resulted in the respective β-diketones in moderate yields.[376] Treating the β-diketones **308 – 313** with *tert*-butylhydrazine in ethanol at room temperature formed the 3-pyrazole carboxylate regioisomers **314 – 319** selectively as confirmed by NOE correlations. Subsequent ester hydrolysis in basic conditions yielded the corresponding carboxylic acids **320 – 325** (Scheme 4.2). Treating **320** – **325** with 4-chlorobenzene-1,2-diamine under HATU-mediated amide coupling conditions furnished the corresponding amides. Following partial purification, acid mediated cyclocondensation of the corresponding amides produced the final benzimidazole products **292** – **297** (Scheme 4.2).

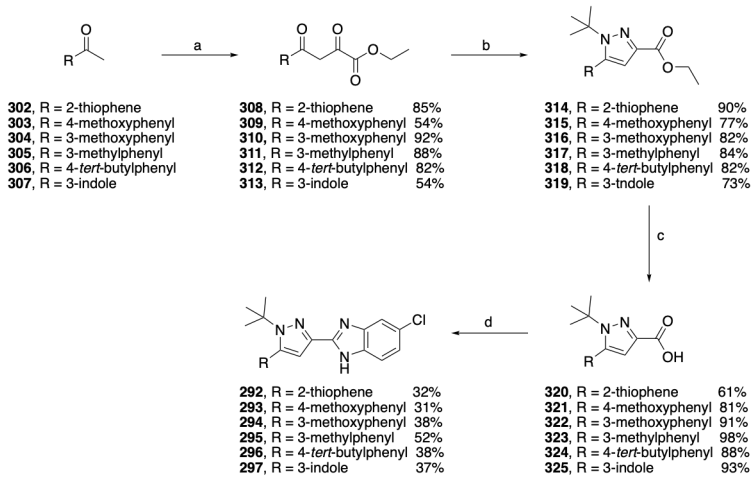

Scheme 4.2 Synthesis of furan modified analogues **292 – 297**. *Reagents and Conditions* (a) diethyl oxalate, NaH, toluene, 50 °C, 1 h; (b) *tert*-butylhydrazine hydrochloride, EtOH, rt, 12 h (c) $LiOH.H_2O$, $MeOH/H_2O$ (3:1), reflux, 1 h (d) 1. 4-chlorobenzene-1,2-diamine, HATU, $^{i}Pr_2NEt$, DMF, rt, 16 h; 2. AcOH/toluene (10:1), 75 °C, 24 h.

The additional protonation state of the 3-pyridyl nitrogen rendered this analogue not suitable for the carboxylic acid route described in scheme 4.2. Due to conflicting pK_a values predicted for the 3-pyridyl carboxylic acid derivative, low yields were anticipated due to an arduous aqueous work up. Consequently, the 3-pyridyl analogue **298** was synthesised *via* the route described by the parent paper Zhu *et al.* (Scheme 4.3). The 3-pyridinyl pyrazole derivative **326** was furnished *via* the Claisen condensation between 3-acetylpyridine (**327**) and diethyl oxalate, followed by a Paal-Knorr pyrazole formation between **328** and *tert*-butylhydrazine hydrochloride (Scheme 4.3). Reduction of the ester functional group of **326** to the primary alcohol **329** was achieved by treating with $LiAlH_4$ at reflux (Scheme 4.3). The primary alcohol was then oxidised to the corresponding aldehyde **330** *via* a DMP oxidation. Condensation of **330** with 4-chlorobenzene-1,2-diamine and sodium bisulfite yields the final benzimidazole analogue **298** in 74% yield (Scheme 4.3).

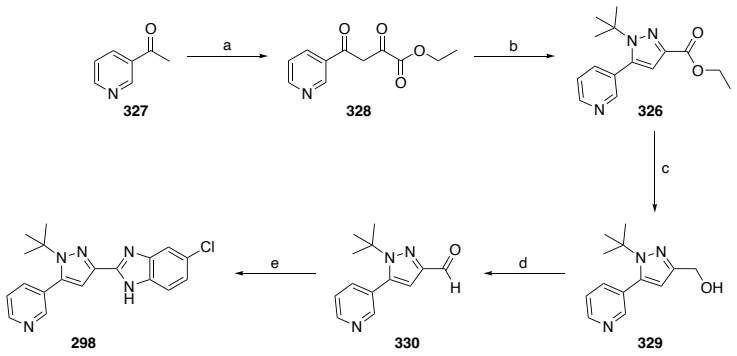

Scheme 4.3 Synthesis of 3-pyridyl analogue **298**. *Reagents and Conditions* (a) diethyl oxalate, NaH, THF, reflux, 1 h, 37% (b) *tert*-butylhydrazine hydrochloride, EtOH, rt, 8 h, 67% (c) $LiAlH_4$, THF, reflux, 2 h, 79% (d) DMP, CH_2Cl_2, rt, 2 h, 68% (e) 4-chlorobenzene-1,2-diamine, $NaHSO_3$, EtOH:H_2O (2:1), reflux, 2 h, 75%.

Compounds **292 – 298**, similarly all afforded a pair of non-degenerate tautomers, and thus suffered from poor resolution of quaternary carbons in ^{13}C NMR experiments. Generally, heterocyclic compounds exhibiting prototropic tautomerism, as seen here, exist as a mixture of tautomers in solution. [260,265,349] However, the type of NMR spectra observed is contingent on the difference between the activation energy separating the tautomers, which thereby determines the lifetimes of the states, and the chemical shift difference, Δw, between tautomeric states.[260] For long lifetimes compared with $1/\Delta w$ conditions of slow exchange produce individual sets of signals for the tautomeric states. However, when lifetimes are shorter, this condition of slow exchange is not fulfilled resulting in line broadening.[260] Variable temperature (VT) NMR experiments provide a useful avenue to explore the thermodynamic activation characteristics of dynamic processes such as tautomerism.[411] The coalescence temperature describes the minimum temperature at which the two distinct coalescing signals merge into a single peak.[260,411] At lower temperatures, the rate of proton exchange between the two tautomers is slowed making both of them visible within the NMR spectrum (Figure 4.5 A and B).[260] In contrast to **37** (discussed in chapter **3.3.1**), the pyridyl analogue **298** NMR spectra became sharper with colder temperatures, resolving both sets of ^{13}C signals (Figure 4.5B). It was hypothesised that the corresponding ^{13}C pairs, were the peaks adjacent to one another. However, a coalescence temperature was failed to be determined, as the ^{13}C peaks were observed to broaden so intensely that they disappeared into the baseline upon warming (Figure 4.5B). Increasing the sample concentration as well as extending the ^{13}C experiment time failed to resolve all broad peaks.

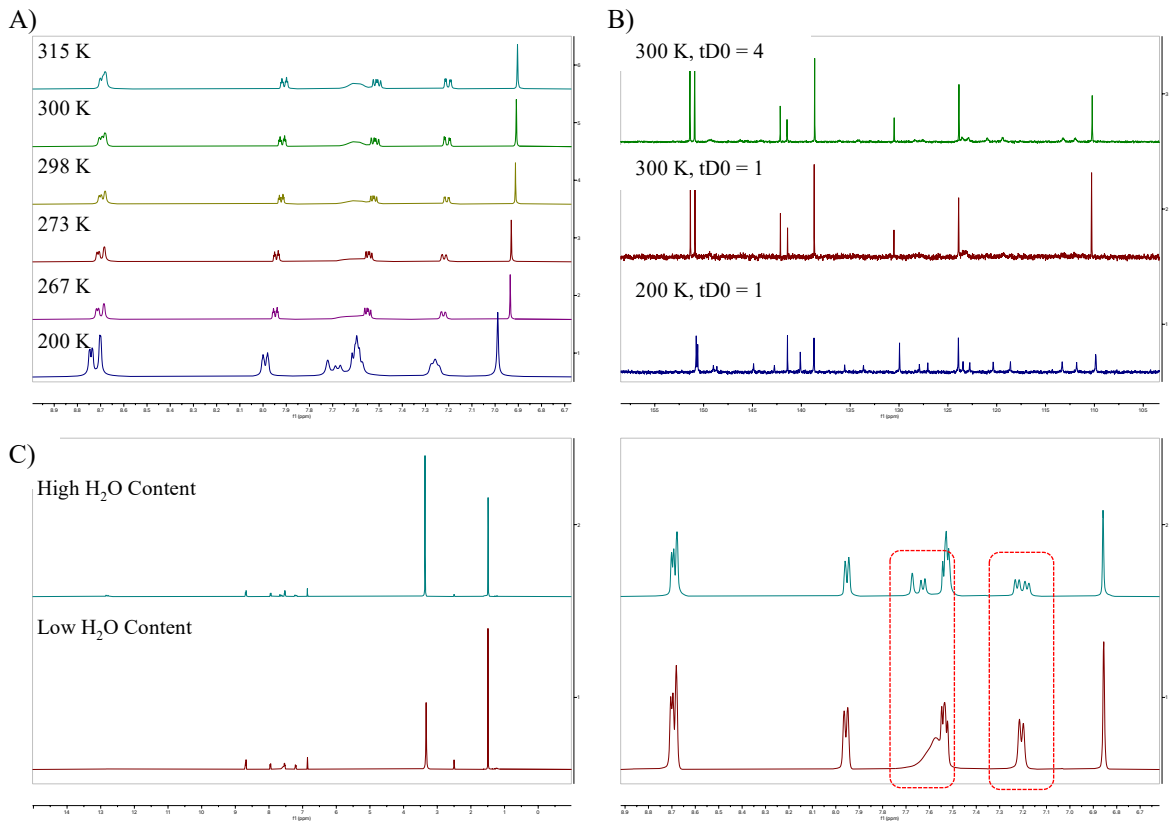

Figure 4.5 Investigating the conversion rate between the two tautomers of **298** through variable temperature ^{1}H (A: δ = 8.9 – 6.7 ppm) and ^{13}C (B: δ = 155 – 105 ppm) experiments (Acetone-d_6, 400 MHz) and water concentration (C: DMSO-d_6, 400 MHz, 298 K).

Unfortunately, for the modified furan derivatives (**292 – 298**) no common solvent or VT-NMR experiment was found to optimise the NMR spectra. As a result, each sample was characterised in DMSO-d_6 at room temperature. Variation in NMR DMSO-d_6 samples were observed depending on the "open-life" of the solvent. Due to the inherent hygroscopicity of DMSO, acquiring a spectra in complete anhydrous solvent is tedious and can be challenging. When a higher water content was present, it appeared to cause come of the tautomeric peaks to resolve suggesting a slower exchange rate between tautomeric forms (Figure 4.5C). A similar observation was made by Kaufman and colleagues in their investigation of triclabendazole and its tautomeric forms by NMR.[411] Mechanistically, Kaufman and colleagues proposed that the rate of the tautomerization process was dependent on the nature and degree of the intermolecular aggregation (Figure 4.6A) and the equilibria between self-associated tautomer-solvent complexes (Figure 4.6B).[411] Following a similar phenomenon to that observed in benzimidazole-based anion receptors, a further degree of complexity is added with additional hydrogen-bond acceptors or donors in neighbouring functional groups as they may rearrange

to form oligomeric aggregates (Figure 4.6C).[349,412,413] In order to confirm the presence of self-aggregates, concentration dependent experiments would need to be conducted. Due to the disparities already observed amongst the different analogues, and literature support for tautomerisation to occur between two or more benzimidazole units it was concluded that these experiments were not required purely for characterisation purposes. However, the proposed mechanism provides further justification for the poor resolution of ^{13}C signals. Despite incomplete assignment, and failure to produce a suitable crystal sample, the molecular structure of analogues **292** – **298** was concluded with a high degree of confidence to be the 5-aryl pyrazole regioisomer (Appendix 11).

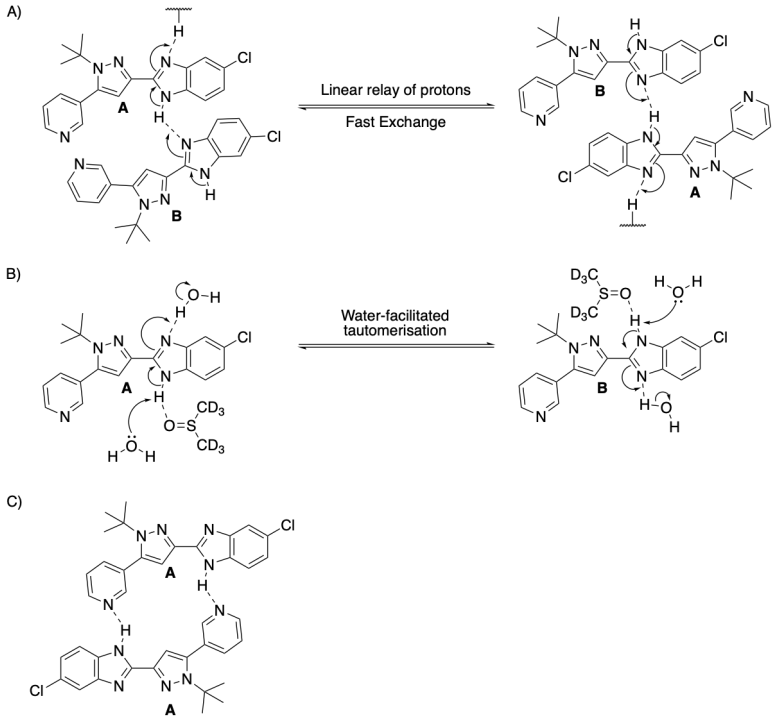

Figure 4.6 Benzimidazole tautomerism within DMSO-d_6. A) Linear intermolecular movement of protons. B) Water-facilitated tautomerisation facilitated by coordination to DMSO-d_6. C) Hydrogen bonding can be facilitated between conjugates to afford oligomeric aggregates. Tautomers were denoted **A** and **B** for visualisation purposes.

4.3.2 Synthesis of 6,6-Heterocycle Derivatives

4.3.2.1 Synthesis of Quinoline Analogue

The synthesis of the quinoline analogue **299** was achieved through a cyclocondensaton of 2-(aminophenyl)methanol (**331**) with **155** (synthesis discussed in chapter **3.3.1**) in DMSO (Scheme 4.4).[414] Within the procedure, DMSO acts not only as the solvent but also as the C1

source which gets incorporated into the 2-position of the quinoline ring (Figure 4.7). Promoted by *t*-BuOK, the mechanism follows the deprotonation of DMSO to form the methylsulfinyl (dimsyl) anion (**I**, Figure 4.7). Reacting with the aldehyde derivative forms the key styryl sulfoxide intermediate (**II**, Figure 4.7). *Ipso*-substitution of the amine anion (**III**) with the styryl sulfoxide **II** produces **IV**, following elimination of the [MeSO]$^-$ species (Figure 4.7).[414] Intermediate **IV** then undergoes oxidation of the benzyl alcohol group to the corresponding aldehyde, and subsequent *C*-nucleophilic addition to afford the cyclised **V** intermediate (Figure 4.7). Dehydration of **V** yields the final quinoline product **299**. Trace quantities of product were formed, however due to an insurmountable purification process an alternative pathway was required.

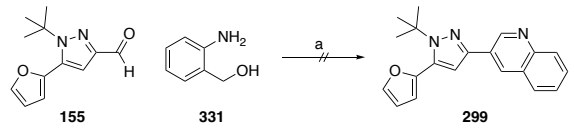

Scheme 4.4 Synthesis of quinoline analogue **299** *via* the base promoted mechanism utilising DMSO as the C1 source. *Reagents and Conditions* (a) *t*-BuOK, DMSO, air, 90 °C, 16 h.

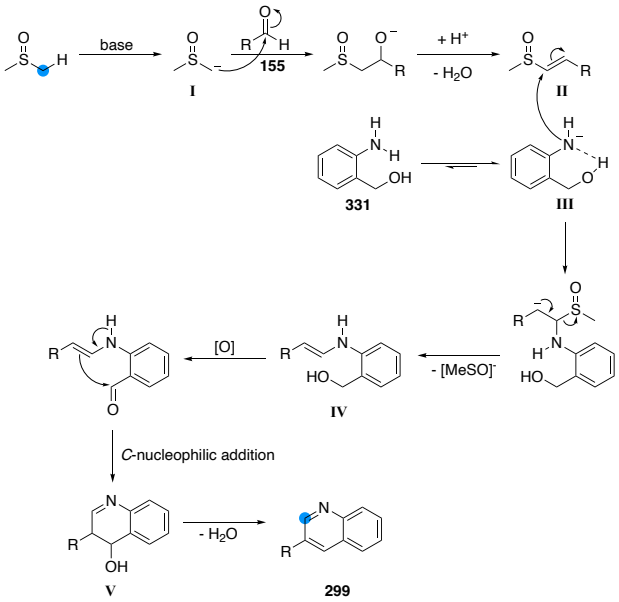

Figure 4.7 Proposed mechanism for quinoline formation through a cyclocondensation of 2-(aminophenyl)methanol (**331**) with aldehyde **155**.

Alternatively, a Claisen condensation promoted by NaH, between 2-acetylfuran (**156**) and ethyl 3-quinoline carboxylate (**332**) was conducted to yield the diketone **333** (Scheme 4.5). Compound **333** was then treated with *tert*-butylhydrazine hydrochloride to form the desired *tert*-butyl pyrazole **299** *via* a Paal-Knorr pyrazole formation (Scheme 4.5). Elevated

temperatures for a prolonged period, with incremental addition of further equivalents of hydrazine, failed to see complete consumption of starting material. Despite the low yields (23%, Scheme 4.5) a sufficient amount of quinoline derivative **299** was isolated for *in vitro* testing. The reaction produced a single regioisomer, with NMR spectra consistent with that expected for the 5-furan pyrazole isomer (Appendix 12).

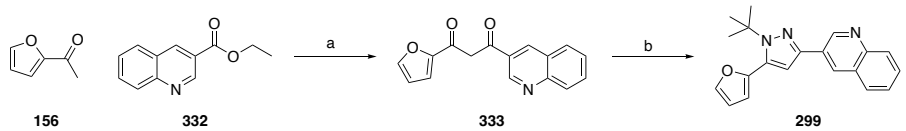

Scheme 4.5 Synthesis of quinoline analogue **299** from ethyl 3-quinoline carboxylate. *Reagents and Conditions* (a) NaH, THF, 65 °C, 3 h, 49% (b) *tert*-butylhydrazine hydrochloride, EtOH/THF (2:1), rt – reflux, 48 h, 23%.

4.3.2.2 Synthesis of Chloro-methylquinoline Analogues

4.3.2.2.1 Retrosynthesis of Chloro-methylquinoline Analogues

The retrosynthetic strategy for synthesising the chloro-methylquinoline analogues **230** and **231** is presented in figure 4.8. The pathway involves a four-step procedure in which the quinoline (**230** and **231**) was formed through a one-pot chlorination and cyclisation of the pyrazole intermediate **334** with phosphorus oxychloride ($POCl_3$). Pyrazole **334** was accessed through a Claisen condensation and subsequent pyrazole formation from **335**. Compound **336** was achieved from the amide coupling of 3-ethoxy-3-oxopropanoic acid (**337**) and the appropriate toluidine.

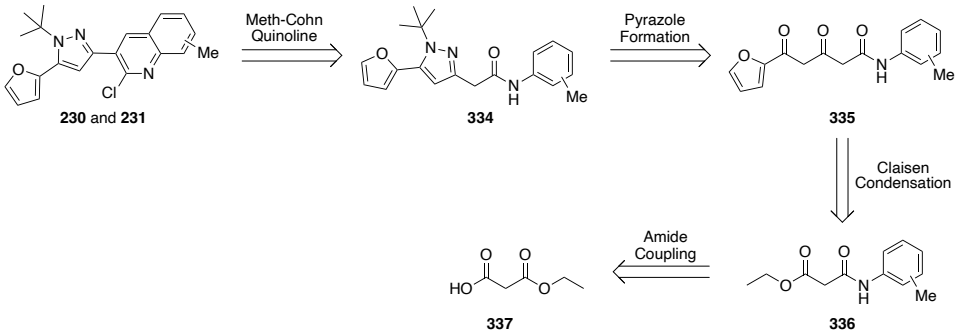

Figure 4.8 Retrosynthetic pathway to access the chloro-methylquinoline analogues.

4.3.2.2.2 Claisen Condensation Pathway

Firstly, 3-ethoxy-3-oxopropanoic acid (**337**) was treated with oxalyl chloride and catalytic DMF to form the acid chloride intermediate. Compound **338** was then achieved by coupling with *m*-toluidine in the presence of base (Scheme 4.6). Initial attempts to synthesise the β-ketone (**339**) included a Claisen condensation of 2-acetylfuran (**156**) with **338**. A series of attempts were conducted, utilising a range of bases varying in strength and nature (NaH and *t*-BuOK), both polar and non-polar solvents (toluene, THF, DME) and temperatures (Table 4.1, entries 1 – 5). Additionally, stoichiometric ratio of reagents and order of addition were altered in an effort to promote the forward reaction (Table 4.1, entries 3 – 5). However, all efforts resulted in no product formation.

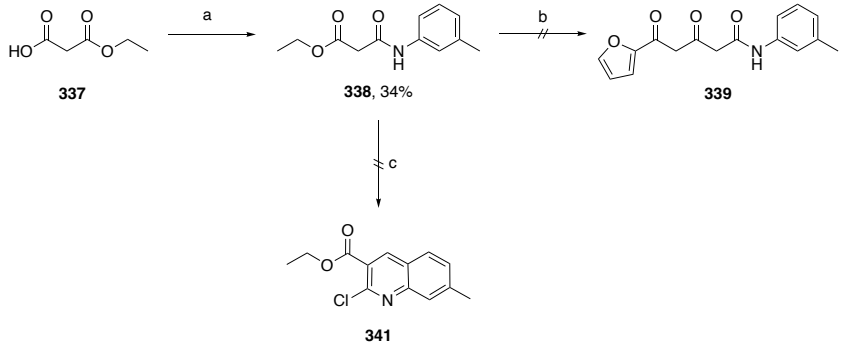

Scheme 4.6 Synthesis of chloro-methylquinoline analogues. *Reagents and Conditions* (a) 1. $(COCl)_2$, cat. DMF, CH_2Cl_2, rt, 1 h; 2. *m*-toluidine, Et_3N, CH_2Cl_2, rt, 2 h, 52% (b) Conditions discussed in Table 4.1 (c) $POCl_3$, DMF, 100 °C, 4 h.

Table 4.1 Claisen condensation conditions trialled for the formation of **339**.

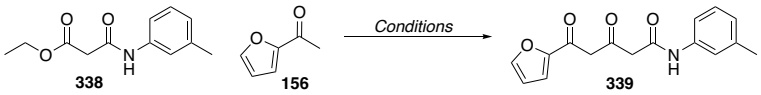

Entry	**338** (eq)	**156** (eq)	Base	Conditions	Yield
1	1	2	NaH (3 eq)	toluene, 50 – 90 °C, 6 h	S.M. [a]
2	1	2	NaH (6 eq)	toluene, 50 °C, 6 h	—[b]
3	2	1	*t*-BuOK (2 eq)	THF/DME (1:1), rt, 5 h	—[b]
4	1	1	*t*-BuOK (2 eq)	THF, rt, 5 h	—[b]
5	1	2	*t*-BuOK (2 eq)	THF, rt, 5 h	—[b]

[a] S.M. represents recovered starting material, as no reaction occurred. [b] Complex reaction mixture as indicated by TLC analysis.

Accordingly, an alternative synthetic route was sought. Given that we were able to successfully synthesise the quinoline analogue **299** *via* a Claisen condensation of a quinoline carboxylate (chapter **4.4.2.1)**, a similar strategy was adopted for the target chloro-methylquinoline analogues. Firstly, the respective quinoline carboxylates were prepared. The Meth-Cohn quinoline synthesis describes the conversion of acylanilidies into 2-chloro-3-substitued quinolines by the action of the Vilsmeier reagent in $POCl_3$. First, DMF reacts with $POCl_3$ *via* an S_N2 mechanism to form the Vilsmeier-Haack reagent (**340**, Figure 4.9). The acylanilide (**I**) is then converted to the β-chloroenamine **(II**) by the action of $POCl_3$, which is then formylated with the Vilsmeier reagent to give **III** (Figure 4.9). Compound **III** then undergoes an electrocyclic reaction to form the pyrido-ring (**IV**) (Figure 4.9). Therefore, within the reaction the acylanilide provides the framework of the quinoline and the 4-carbon is supplied by the Vilsmeier reagent.

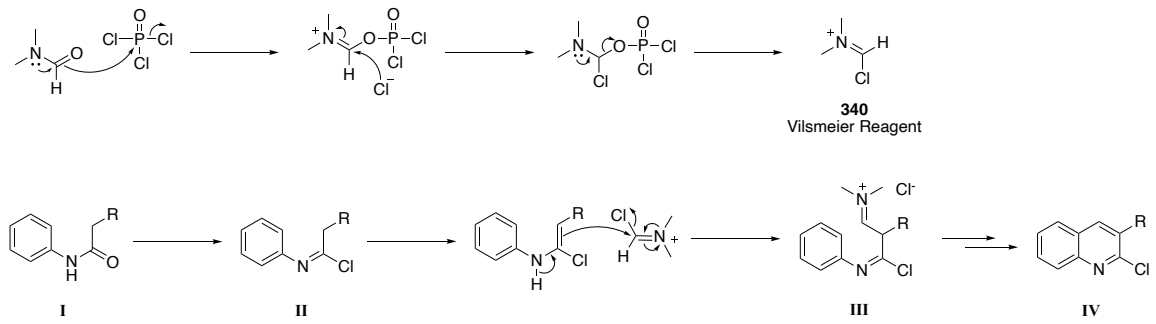

Figure 4.9 Mechanism of the Meth-Cohn Quinoline Synthesis.

Compound **338** was added to a stirring solution of $POCl_3$ and DMF and heated to 100 °C for 4 hours.[415] TLC and mass spectrometry analysis of the reaction mixture showed complete reaction degradation with no sign of product (**341**) formation. It was postulated that the presence of the ester group may be inhibiting the cyclisation due to its electron-withdrawing nature.[416] Similar issues were previously reported by Meth-Cohn *et al.* whilst conducting mechanistic studies of a similar transformation.[416]

Therefore, the respective chloro-methylquinoline carboxaldehyde **342** and **343** were sourced commercially. Oxidation of the two quinoline carboxaldehydes (**342** and **343**) to the corresponding carboxylic acids (**344** and **345**) was achieved *via* a Pinnick oxidation with 2-methylbut-2-ene and an aqueous solution of sodium chlorite and sodium dihydrogen

phosphate (Scheme 4.7). With the acids in hand, **344** and **345** were subjected to standard Fischer esterification conditions to yield the corresponding ethyl esters (**341** and **346**), albeit in poor yields along with formation of the respective ethoxy S_NAr side-product (**347** and **348**, Scheme 4.7, Appendix 13) in comparable yields (Table 4.2, entry 1). Activating the carboxylic acid **344** through formation of the acyl chloride improved yields, however similarly resulted in side-product formation (**347**, Table 4.2, entry 2). Formation of the ethoxy side products **347** and **348** was successfully eliminated *via* Steglich esterification conditions in which ethanol is used stoichiometrically (Table 4.2, entries 3 and 4).

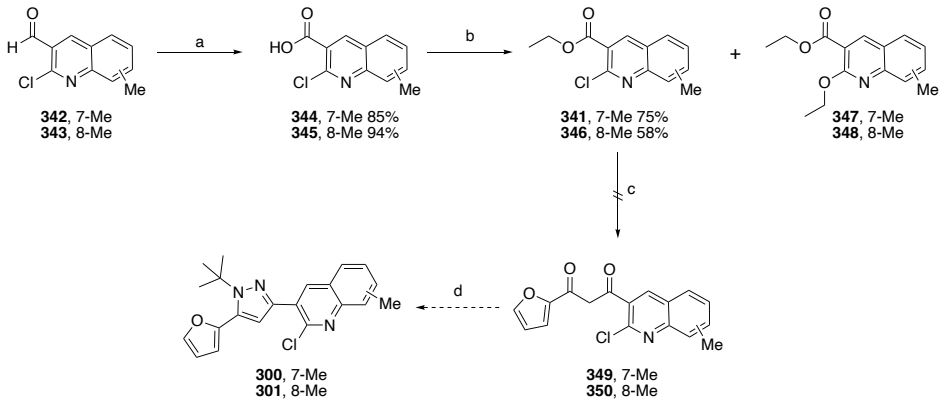

Scheme 4.7 Alternative route to access chloro-methylquinoline analogues. *Reagents and Conditions* (a) 2-methylbut-2-ene, $NaClO_2$, NaH_2PO_4, *t*-BuOH/H_2O (2:1), rt, 5 h (b) Conditions discussed in Table 4.2 (c) Conditions discussed in Table 4.3 (d) *tert*-butylhydrazine hydrochloride, EtOH, rt, 12 h.

Table 4.2 Esterification conditions to synthesis compounds **341** and **346**.

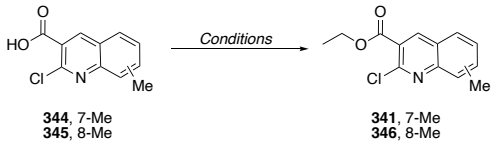

Entry	SM	Conditions	Yield
1	**345**	H_2SO_4 cat., EtOH, reflux, 4 h	21%
2	**344**	1. $(COCl)_2$, CH_2Cl_2, rt, 1h 2. EtOH, rt, 3 h	59%
3	**344**	EtOH, EDC.HCl, DMAP, CH_2Cl_2, rt, 4 h	75%
4	**345**	EtOH, EDC.HCl, DMAP, CH_2Cl_2, rt, 4 h	58%

With the quinoline carboxylates (**341** and **346**) in hand, a Claisen condensation with 2-acetylfuran (**156**) was trialled to yield the respective diketone product (**349** and **350**, Scheme

4.7). Identical conditions to those utilised in the synthesis of **333** (chapter **4.4.2.1**) were initially used (Table 4.3, entries 1 and 2). However, for both the 7-methyl (**341**) and 8-methyl (**346**) analogues, only a complex mixture was observed, and no desired product could be isolated. A similar result was observed when the equivalents of base were reduced to 1.1 (Table 4.3, entry 3). Transitioning to a weaker base (e.g. *t*-BuOK) was equally unsuccessful with only starting material isolated (Table 4.3, entries 4 and 5).

Table 4.3 Claisen condensation conditions trialled to form the chloro-methylquinoline diketones **349** and **350**.

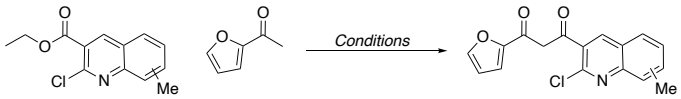

341, 7-Me
346, 8-Me

156

349, 7-Me
350, 8-Me

Entry	SM	Conditions	Yield
1	**341**	NaH (5 eq), THF, 65 °C, 3 h	—[a]
2	**346**	NaH (5 eq), THF, 65 °C, 3 h	—[a]
3	**346**	NaH (1.1 eq), THF, 65 °C, 3 h	—[a]
4	**341**	*t*-BuOK (2 eq), THF, rt, 5 h	S.M.[b]
5	**346**	*t*-BuOK (2 eq), THF, rt, 5 h	S.M.[b]

[a] Complex reaction mixture as indicated by TLC analysis. [b] S.M. represents recovered starting material, as no reaction occurred.

The Claisen coupling partners were then reversed. This required the preparation of 1-(2-chloro-8-methylquinolin-3-yl)ethenone (**351**) and ethyl 2-furancarboxylate (**220**), both of which could be easily accessed *via* a Weinreb ketone synthesis and Steglich esterification, respectively (Scheme 4.8). Weinreb amide **352** was synthesised *via* a HATU-mediated amide coupling of the previously synthesised carboxylic acid **345** and *N,O*-dimethylhydroxylamine hydrochloride (Scheme 4.8). Treating **352** with MeMgBr furnished the ketone **351** in moderate yields (Scheme 4.8). Unfortunately, repeating the Claisen procedure using the "reversed" coupling partners with NaH was equally unsuccessful resulting in recovery of only starting material (Scheme 4.8). Consequently, the present pathway was abandoned and an alternate route to access the chloro-methylquinoline analogues was developed.

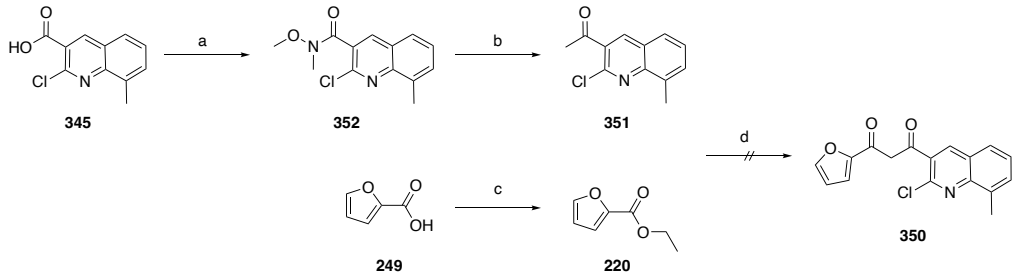

Scheme 4.8 Synthesis of alternative coupling partners **351** and **220**. *Reagents and Conditions* (a) *N*,*O*-Dimethylhydroxylamine hydrochloride, HATU, $^{i}Pr_2NEt$, DMF, 78% (b) MeMgBr (3M in diethyl ether), THF, 0 – 25 °C, 2 h, 57% (c) EtOH, EDC.HCl, DMAP, CH_2Cl_2, rt, 4 h, 80% (d) NaH, THF, 65 °C, 24 h.

4.3.2.2.3 Dihydropyrazole Pathway

Adapting the literature procedure for the quinoline validation compounds (chapter **4.3**) it was postulated that the chloro-methylquinoline analogues could be accessed from the successive oxidation and alkylation of the respective dihydropyrazole derivatives. The α,β-unsaturated diketones **353** and **354** were achieved through a Claisen-Schmidt condensation between the commercially sourced chloro-methylquinoline carboxaldehydes (**342** and **343**) and 2-acetylfuran (**156**) in good yields (Scheme 4.9).[170]

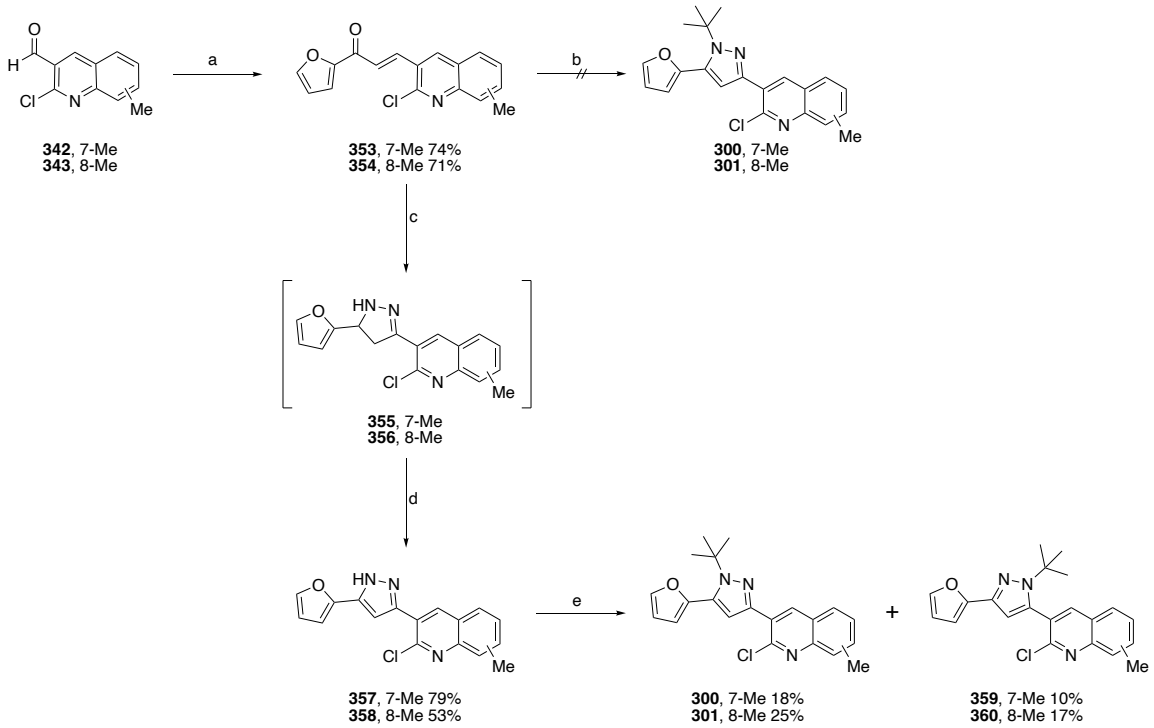

Scheme 4.9 Synthesis of chloro-methylquinoline analogues (**300** and **301**) *via* an oxidative dehydrogenation of the pyrazoline ring system. *Reagents and Conditions* (a) 2-acetylfuran, NaOH 2.5 M, EtOH, rt, 2 h (b) 1. *tert*-butylhydrazine hydrochloride, DMSO, Ar, 85 °C, 16 h; 2. DDQ, toluene,

reflux, 16 h (c) hydrazine monohydrate, EtOH, reflux, 1 h, not isolated (d) I_2, DMSO, 140 °C, 2 h (e) *t*-butyl 2,2,2-trichloroacetimidate, $Cu(OTf)_2$, CH_2Cl_2, rt, 24 h.

Formation of the pyrazole ring system was then envisioned to be achieved through a one-pot condensation and oxidation with *tert*-butylhydrazine hydrochloride in aerobic conditions. Although the α,β-unsaturated diketones **353** and **354** condensed smoothly to afford the dihydropyrazole analogues **355** and **356** (confirmed by TLC and mass spectrometry) the prolonged heating times failed to furnish the desired pyrazole product (Scheme 4.9).[417,418] DDQ was introduced as a more efficient oxidant to mediate the aromatization (Scheme 4.9).[417,418] Unfortunately, this approach only furnished a complex reaction mixture.

A stepwise approach was therefore implemented in which the pyrazole motif would be formed first, then followed by subsequent alkylation (Scheme 4.9). The pyrazoline ring system (**357** and **358**) was introduced by refluxing diketones **353** and **354** with hydrazine monohydrate. Oxidative dehydrogenation of the dihydropyrazole **355** and **356** intermediates to the *N*-H-pyrazole (**357** and **358**) was achieved with iodine in DMSO at elevated temperatures (Scheme 4.9).[342] Alkylation attempts of the *N*-H-pyrazole (**357** and **358**) are summarised in table 4.4. *tert*-Butanol (*t*-BuOH) is a commonly used alkylating agent for aromatic compounds. Proceeding *via* an S_N1 mechanism, *t*-BuOH reacts with the acid source to form isobutylene and then the corresponding *tert*-butyl carbocation intermediate. Heating **357** and **358** in *t*-BuOH with stoichiometric H_2SO_4, resulted in complete degradation of starting material and a complex reaction mixture (Table 4.4, entries 1 and 2).[419] Substituting the acid for TFA, resulted in a similar outcome (Table 4.4, entry 3).[420]

Table 4.4 *tert*-Butyl alkylation conditions

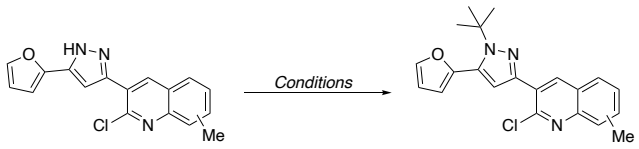

357, 7-Me
358, 8-Me

300, 7-Me
301, 8-Me

Entry	SM	Conditions	Yield
1	**357**	*t*-BuOH, H_2SO_4, reflux, 5 h	—[a]
2	**358**	*t*-BuOH, H_2SO_4, reflux, 5 h	—[a]
3	**357**	*t*-BuOH, TFA, 80 °C, 5 h	—[a]
4	**357**	*t*-butyl bromide, K_2CO_3, DMSO, rt, 84 h	—[a]
5	**357**	*t*-butyl 2,2,2-trichloroacetimidate, $Cu(OTf)_2$, CH_2Cl_2, rt, 24 h	18%
6	**358**	*t*-butyl 2,2,2-trichloroacetimidate, $Cu(OTf)_2$, CH_2Cl_2, rt, 24 h	25%

[a] Complex reaction mixture as indicated by TLC analysis.

Alkylation of pyrazoles with primary or alkyl halides is commonly reported in literature.[421] However, there is limited methodology for secondary and tertiary halides. Although pyrazoles readily participate in nucleophilic substitution reactions, when secondary halides are employed as electrophiles, elimination and rearrangement of the halide dominates.[421] In order to increase the nucleophilicity of the pyrazole the reaction was conducted in a 'superbasic media', comprised of a mixture of an alkali metal base and DMSO.[421] DMSO is an excellent metal-coordinating solvent, therefore weakening the electrostatic interactions between metal cations and anions. As a result, both the alkali metal base becomes more basic, and the resulting pyrazolate anion becomes more nucleophilic.[421] Pyrazole **357** was treated with *tert*-butyl bromide under basic conditions and following prolonged reaction times (84 h) and incremental addition of *tert*-butyl bromide, a complex reaction mixture was produced with no trace of product formation (Table 4.4, entry 4).

Alkylation of **357** and **358** was finally achieved through the substitution reaction with *tert*-butyl 2,2,2-trichloroacetimidate (Table 4.4, entries 5 and 6).[341,422,423] Promoted by copper triflate, the reaction proceeds *via* the decomposition of the imidate to produce the *tert*-butyl carbocation (**I**, Figure 4.10).[422,423] The cation is subsequently captured by the pyrazole and following proton transfer, yields the alkylated pyrazole (**II**, Figure 4.10). Intermediate **II** then reacts with a further equivalent of imidate to provide the alkylated pyrazole (**III**, Figure 4.10).[422,423] The

reaction proceeded in moderate yields at room temperature producing a mixture of the two regiosiomers (7-Me: **300** and **359**; 8-Me: **301** and **360**, Scheme 4.9). The two regioisomers were successfully separated by column chromatography and characterised through the presence and corresponding absence of the NOE correlation between the 3H-furan and *tert*-butyl hydrogens (Appendix 15). Due to the structural similarities of the 3-furan regioisomers **359** and **360** to the validation dihydropyrazole compounds **38**, **40** and **281** they will also be tested for activity at the hP2Y6R.

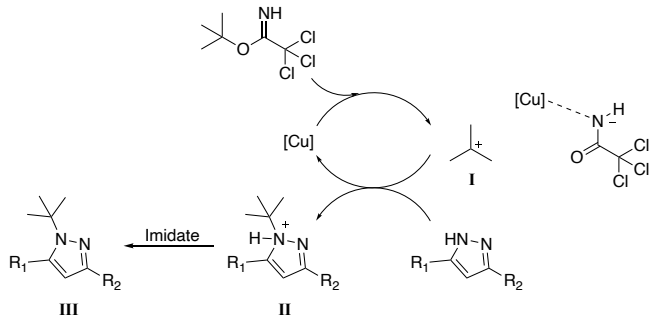

Figure 4.10 Proposed mechanism of copper-catalysed *N*-alkylation with *tert*-butyl 2,2,2-trichloroacetimidate.

4.4 Concluding Remarks

This chapter has demonstrated how structural hybridization can diversify an existing scaffold to produce novel candidates that evade potential metabolic soft spots. Structural hybridisation of the benzimidazole scaffold **37** with the quinoline chemotype **38** produced a compound library of 12 compounds, that has replaced the furan metabolic soft spot and further expanded the diversification of the 5,6-heterocyclic motif. Furthermore, additional validation compounds have been synthesised to further support the validity of our *in vitro* assay. The biological results and corresponding conclusions of the compound library described in this chapter will be discussed in detail in **Chapter 5**.

Chapter 5. Validation and *In Vitro* Evaluation of P2Y6 Ligands

The *in vitro* evaluations performed and presented throughout **Chapter 5** were conducted by André McKenzie within the Faculty of Medicine and Health at the University of Sydney. Synthesised derivatives were evaluated for functional activity at the human P2Y6 receptor.[247] At the time of writing all derivatives discussed and synthesised throughout **Chapters 3** and **4**, have not been evaluated at the hP2Y6R.

5.1 Introductory Remarks

A fundamental role of medicinal chemistry is to design small molecules that ensure reliable preclinical target validation. Regardless of how substantiated a drug program is, the ability to measure and quantify modulation of the biological target is essential for further progression.[424]

The P2Y6 receptor, has been highlighted as a promising therapeutic target for inflammatory, neurodegenerative and metabolic disorders.[42] However, despite the previous evidence, modulation of the P2Y6R can yield distinct responses depending on the type and stage of the disease.[56] Further validation of its role in disease models is required, although has remained elusive due to a lack of drug-like molecules available.[56] Additionally, with the crystal structure yet to be elucidated, targeting the P2Y6R therapeutically is largely considered to be in its early stages of the drug discovery pipeline. Biological evaluation of literature compounds and modified derivatives will therefore provide both validation and SAR analysis of the described chemotypes, progressing the field closer to therapeutically relevant molecules.

5.1.1 Chapter Aims

Interest in the P2Y6R as a potential therapeutic target is reinforced by the recent patents and complementary papers by three independent research groups.[168,170,257] The papers by Zhu *et al.* and Zhao *et al*. described a structure-based virtual screening pipeline that identified a benzimidazole and quinoline chemotype, respectively, as potent and selective P2Y6R antagonists. **Chapters 3** and **4** aimed to expand on the current SAR of these scaffolds through both traditional SAR (**Chapter 3**) and hybrid (**Chapter 4**) strategies. The following chapter will therefore focus on evaluation of these compounds at the P2Y6R. Achieved through the

development of tools to probe P2Y6 activity, modifications to the 5,6-heterocycle and pyrazole motif will therefore be indexed against lead compounds to identify essential pharmacophores for potent activity.

Establishing our own *in vitro* assay was fundamental to the strength of our medicinal chemistry campaign. Validation of such was aimed to be achieved through assessment of reported inhibitors with a range of functional activities. The compound library selected included both positive and negative controls from two distinct peer-reviewed articles. The synthesis of these compounds has been described in **Chapters 3** and **4**.

5.2 *In Vitro* Evaluation

5.2.1 *In Vitro* Assay Development

The net pharmacological response of microglial P2Y6R activation is the increase in intracellular Ca^{2+} levels.[56] Following a PLC signalling pathway, activation of the P2Y6R triggers IP_3 which then induces a steady accumulation intracellular Ca^{2+} levels before rapidly degrading to IP_2 and then IP_1.[55,425] *In vitro* assays for agonist and antagonist screening at the P2Y6R have been reported for both quantification of intracellular Ca^{2+} levels and IP_3 production (Appendix 15).[167,168,170,257] Both methodologies have reported benefits and limitations. Detection of intracellular Ca^{2+} levels by fluorescent dyes has demonstrated utility as a robust and reliable method within HTS assays.[425] However, calcium flux can be rapid and transient, failing to detect constitutive activity (or inverse agonism) and subject to interference from fluorescent compounds.[425] Quantification of IP_3 production occurs either directly or indirectly through IP_1 concentration. Generally, IP_3 accumulation assays require radioactive sensors, and therefore are expensive and hazardous to run. Additionally, IP_3 rapidly metabolises (mean IP_3 lifetime = 9 sec) to its metabolites IP_2 and then IP_1, making readings difficult.[425,426] It was therefore decided to not emulate the IP_3 *in vitro* assay described in the reference paper by Zhu *et al.* (Appendix 15).[257]

Functional activity of the synthesised compounds at the hP2Y6R was initially explored through an IP_1 G_q detection assay. The IP-One HTRF assay provides a promising alternative for the direct quantification of IP_1 (and thereby indirectly IP_3) in cultured cells.[425,427] The assay describes a competitive immunoassay amenable to large compound libraries.[427] Screening tools

must first be validated with known P2Y6R agonists. In line with the cell manufacturer protocol, quantification of the downstream production of IP_1 following P2Y6R activation was first attempted. However, the approach was abandoned due to high levels of intra-assay variability reflected in poor R^2 values, coupled with large error bars for each concentration point.[247]

Within literature, P2Y6R *in vitro* assays are commonly centred around the downstream mobilisation of Ca^{2+}.[168] The Ca^{2+} flux assay successfully passed agonist validation, reporting an EC_{50} value for UDP (EC_{50} = 22.8 ± 7.7 nM) comparable to literature values with limited variability between repeats.[166–168] Validation of the antagonist assay was initially attempted with the known P2Y6R antagonist, MRS2578 (**31**). However, the compound suffered from solubility limitations, with the maximum achievable concentration to be 10 μM. Antagonism of each compound was assessed by its ability to reduce the response of P2Y6R (i.e. intracellular Ca^{2+} flux) when in the presence of EC_{80} UDP levels. At 10 μM MRS2578 produced no significant difference and was therefore deemed to not produce any antagonism. The poor solubility and stability of MRS2578 has been reported in literature.[164,428,429] Stability issues of MRS2578 in DMSO-d_6 were similarly observed throughout our own analytical stability investigation (Appendix 16). Significant decomposition was observed when stored in DMSO-d_6 at room temperature over 7 days (Appendix 16). Degradation was similarly observed when stored at -8 °C (Appendix 16). Isothiocyanate functional groups are strong electrophiles prone to undergo hydrolysis to the corresponding amine when in the presence of water (Figure 5.1).[430,431] This was supported by mass spectrometry analysis, in which the corresponding mass of the *N*-alkythiocarbamic acid and amine were observed (Appendix 16). Water was not excluded from the system throughout the stability studies so to emulate the assay conditions.

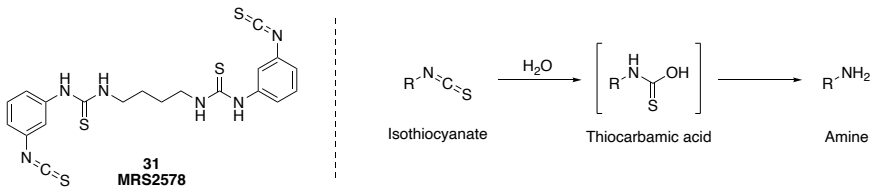

Figure 5.1 Degradation of isothiocyanate compounds when in the presence of water.

Validation of the hP2Y6R Ca^{2+} flux antagonist assay was later achieved with PPADS, a broad spectrum P2 antagonist. Although PPADS produced a significant reduction in UDP-induced Ca^{2+} flux (44.8%) at 100 μM, it failed to produce an antagonist response at lower

concentrations. Despite this, the antagonist assay was deemed valid based on the comparable values of PPADS inhibition with those reported in literature (31% at 100 μM), and therefore was progressed to screening of the synthesised compound library.[432] Furthermore, adequate P2Y6R expression on the 132-1N1-hP2Y6R cells was confirmed *via* western blot methods.[247] Assay details are provided in **Chapter 7.7.8**.

5.2.2 *In Vitro* Evaluation of Literature Compounds

Inter-assay variability of functional activity is commonly observed in medicinal chemistry campaigns.[424,433,434] Paralleled with the relative infancy of the reported P2Y6R antagonist landscape, screening of literature compounds is essential to confirming *a priori* results and thus future SAR analysis. Proprietary compounds from both the benzimidazole (**Chapter 3: 37**, **153**, **154**) and quinoline (**Chapter 4: 38**, **40**, **281**) scaffolds were therefore initially screened for inhibitory activity (Figure 5.2).

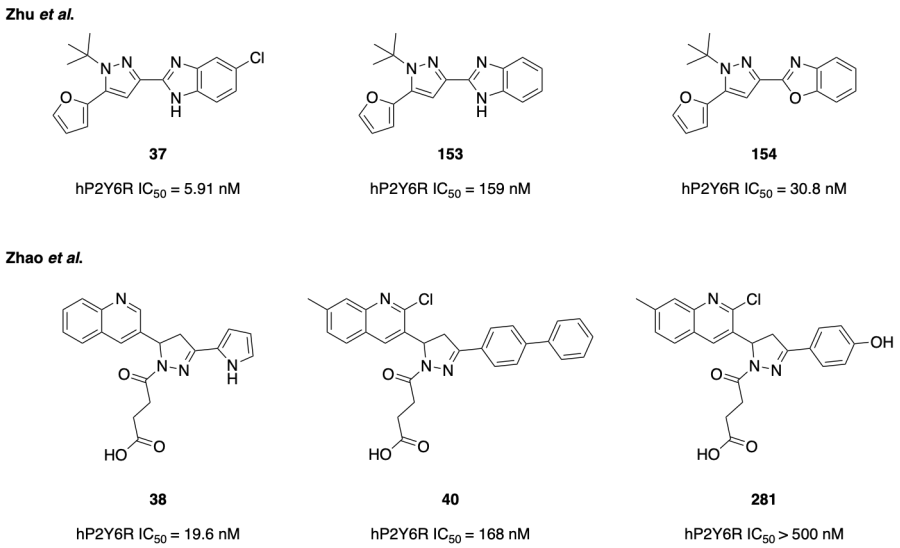

Figure 5.2 Literature compounds used for validation of *in vitro* and *in silico* studies. Data extracted from Zhu, Y. *et al.* **2023** (**37, 153, 154**) and Zhao, Y. *et al*. **2024** (**38, 40, 281**).[170,257]

Compounds **37**, **38**, **153** and **154** were all screened at 10 μM. Antagonism was defined as inhibition of UDP-stimulated F/F_0 that produced a statistically significant reduction from UDP-only conditions (100%) *via* one-way ANOVA. The benzimidazole compound **153** exhibited the greatest reduction of UDP-stimulated Ca^{2+} influx with 79.2 ± 14.7% UDP-only F/F_0 (Figure 5.3). However, all compounds (**37**, **38**, **153** and **154**) failed to significantly decrease F/F_0 levels,

suggesting that they were unable to produce antagonism of the P2Y6R in a Ca^{2+} flux assay (Figure 5.3). At the time of writing, *in vitro* data for compounds **40** and **281** within the Ca^{2+} flux assay by McKenzie were not available.[247]

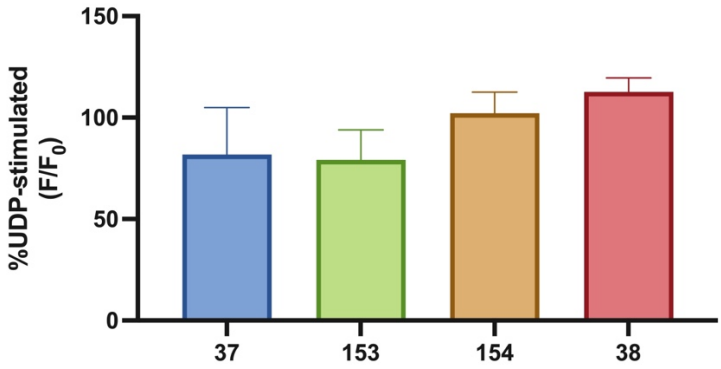

Figure 5.3 Literature compounds demonstrated no antagonism of the hP2Y6R. Percentage of UDP-stimulated Ca^{2+} flux in 132-1N1 cells stably expressing hP2Y6R in response to 10 μM of compound. Positive control represents UDP (EC_{80})-only conditions (100%). Data represented as the mean percentage of the positive control ± SD of n ≥ 3 independent runs performed in duplicate.

Due to the conflicting results with previous reports, literature compounds were also assessed for antagonism by the third-party commercial provider, Eurofins Scientific. Similarly, compounds **37**, **38**, **153** and **281** were found to be inactive in their own P2Y6R antagonist Ca^{2+} flux assay (Table 5.1).[247] These results were similarly reported by Jacobson and coworkers in their latest publication describing P2Y6R chromene antagonists, declaring compound **37** to only be a weak hP2Y6R antagonist (18.9 ± 8.5% inhibition at 100 μM, Table 5.1).[168] Jacobson and coworkers did not screen any of the other literature compounds discussed herein.

Further variability in reported functional activity is present within the patent containing **37** and the subsequent publication (Table 5.1).[258] Between the two sources, the data for lead compound **37** demonstrated a lack of concentration-response relationship. Despite data points reporting different concentrations (10 vs 1 μM), an identical percentage inhibition (132%) was reported (Table 5.1).[257,258] Similarly, this also transpired for compound **153** (69.1% at 10 and 1 μM). Potential variability between the patent and publication was further insinuated by the corresponding IC_{50} value of **153** to vary by over 700 nM (Table 5.1).[257,258]

Table 5.1 Summary of experimental results for published P2Y6R antagonists.

	37		**153**		**38**	
Source	% Inhibition[a]	IC_{50} (nM)	% Inhibition[a]	IC_{50} (nM)	% Inhibition[a]	IC_{50} (nM)
McKenzie[b]	18.1% (10 μM)	-	20.7% (10 μM)	-	-12.6% (10 μM)	-
Li *et al.* (2022)	132% (10 μM)	5.75	69.1% (10 μM)	879	-	-
Zhu *et al.* (2023)	132% (1 μM)	5.91	69.1% (1 μM)	159	-	-
Zhao *et al.* (2024)	-	-	-	-	-	19.6
Oliva *et al*. (2024)	18.9% (100 μM)	-	-	-	-	-
Eurofins	-36.6% (10 μM)	-	-2.40% (10 μM)	-	7.80% (10 μM)	-

[a]% inhibition = % of positive control (UDP)-only conditions; [b] 'McKenzie' refers to the experimental method developed by Mr Andre McKenzie within the Faculty of Medicine and Health at the University of Sydney. '-' infers that data were not presented in the corresponding literature.

Variability in the pharmacological profile of **37** amongst the laboratories discussed herein, could be rationalised by the differences in *in vitro* assay methodology. Of note, four key assay parameters were varied: cell-type, agonist concentration, agonist exposure time and antagonist pre-incubation. A comparison of the discussed parameters is supplied in appendix 15. Under specific conditions, variations to all four elements can result in off-target effects, thereby increasing the risk of false positives and negatives throughout the functional assays.

It is well documented that variation in basal expression of GPCR is present within non-genetically modified cell lines.[435] The three assays in agreeance (McKenzie, Oliva *et al.* and Eurofins) that antagonism is not reported, all utilised 132-1N1 cells. Whilst Zhu *et al.* and Zhao *et al*. utilised HEK-293 and CHO-cells respectively. 132-1N1 cells allow for the characterisation of compounds in a cellular background devoid of endogenous P2 receptor activity.[434,436,437] Whereas expression of other P2Y subtypes have been identified on both

HEK-293 and CHO cells, confirmed by an increase in Ca^{2+} signalling following addition of nucleotides.[435,438,439] Thus suggesting that the disparity of functional activity could be due to off-target effects at other P2-receptors. Further investigations should therefore include replication of the described Ca^{2+} flux assay in HEK-293 and CHO cell lines.

Additionally, concentration and exposure time to UDP agonist can greatly impact the response through off-target effects and non-antagonism mechanisms.[57,440] Upon glycosylation, UDP forms UDP-glucose, the endogenous ligand of P2Y14R. Lazarowski *et al.* identified that mechanical stimulation of a range of cell types, including 132-1N1 and CHO cells, observed an increase in extracellular UDP-glucose and ATP levels.[440] Selectivity data for other P2Y receptors is therefore imperative to confirm the antagonism pathway. Although, Zhu *et al*. and Zhao *et al*. both reported their lead structures **37** and **38**, respectively, to be selective amongst P2Y1-like receptors, individual assay details were unfortunately omitted.[170,257] Pre-longed exposure to UDP has been demonstrated to induce clathrin-dependent P2Y6R internalisation.[57] In HEK-293 cells, P2Y6R internalisation demonstrated a ligand-dependent and rapid-recyclizing process. The study also found some P2Y6 receptors to have transitioned to lysosomes and tagged for degradation.[57] Conversely, in astrocytoma 132-1N1 cells, recombinant P2Y6R were found not to internalise following activation by UDP.[57] Therefore, the extended exposure time (12 h) utilised by Zhu *et al.* could have led to compound-induced internalisation of the receptor rather than a reflection of true antagonism.

Pre-incubation of antagonists is a common method to account for potential slow kinetics of the antagonist in the *in vitro* assay.[441] Within Ca^{2+} assays the observed ligand pharmacology can vary significantly between early time points and after longer incubation times.[441] Within the compared methodology, pre-incubation times ranged from 0 – 45 min, with the variable omitted from the reported methodology by Zhao *et al.* and Eurofins (Appendix 15).[170] Our methodology excluded a pre-incubation to circumvent the concerns of false positives.[441] However, Oliva *et al.* reported a pre-incubation time of 45 min with no antagonism.[168] Thus, the effect of varied incubation time is inconclusive across the current data set.

Evidently, contrasting findings surrounding the functional activity of **37** have been reported. Considering similar data has been produced from three independent laboratories, considerable doubt on the utility of **37** as a P2Y6R antagonist is warranted.

5.2.3 *In Vitro* Evaluation of the Synthesised Compound Library

The compound library described in **Chapter 3** was evaluated for functional activity at the P2Y6R. At the time of writing some derivatives discussed in **Chapter 3**, and all those described in **Chapter 4**, have not been evaluated for functional activity at the hP2Y6R. *In vitro* data for the analysed compounds, presented in figure 5.4, will therefore be discussed independently.

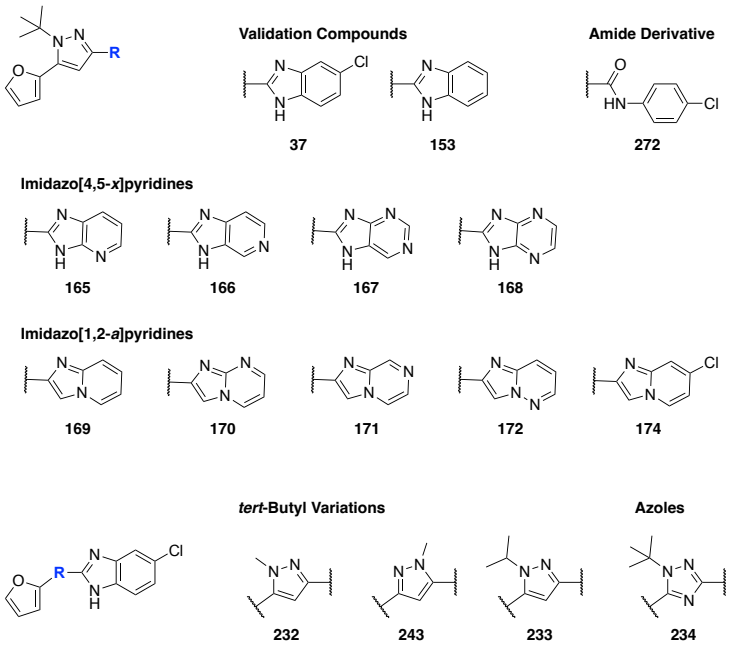

Figure 5.4 Compound library evaluated for activity at the hP2Y6R.

Compounds **165** – **172** and **174** described modifications to the 5,6-heterocycle motif through a nitrogen walk strategy. Varying the electronics around the heterocycle was unable to elicit P2Y6R antagonism, with no compound reporting significant reduction in UDP-stimulated F/F_0 signal (Figure 5.5). Of the 12 compounds analysed compounds **167** and **170** reported the greatest reduction in signal with 64.8% and 70.4% respectively (Figure 5.5). However, both compounds exhibited high levels of variation, preventing them from being considered statistically significant (Figure 5.5).

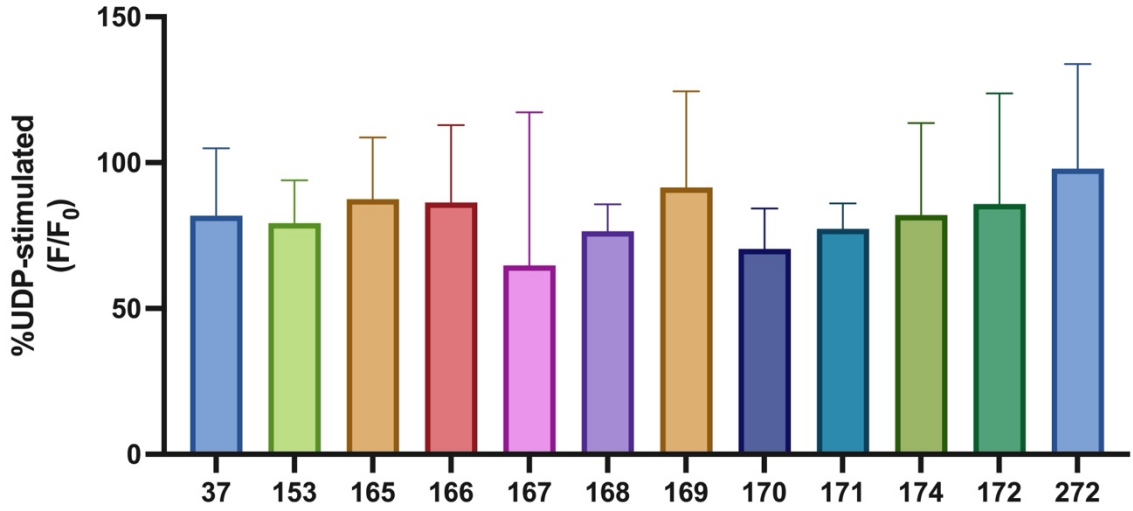

Figure 5.5 Modifications to the 5,6-heterocycle motif through a nitrogen-walk strategy demonstrated no antagonism of the P2Y6R. Antagonism was determined screening compounds at 10 μM in a Ca^{2+} flux assay in 132-1N1-hP2Y6 cells. Positive control (i.e. 100%) represent UDP (EC_{80})-only conditions. Experiments were performed in duplicate, and data is the mean percentage of positive control ± SD (n ≥ 3 experiments).

The pyrazole motif was then explored, including replacement of the *tert*-butyl group for sterically less hindered alkyl chains and varied electronics through the triazole analogue (Figure 5.6). Similarly, all compounds (**232** – **234** and **243**) failed to elicit antagonism of the hP2Y6R (Figure 5.6). Methyl derivative **232** reported a reduction of 50.9%, however it cannot be considered statistically significant due to the large standard deviation between repeats (Figure 5.6).

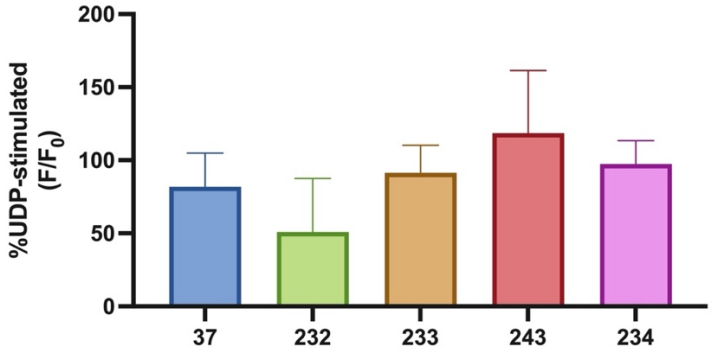

Figure 5.6 Modifications to the *tert*-butyl pyrazole motif demonstrated no antagonism of the P2Y6R. Antagonism was determined screening compounds at 10 μM in a Ca^{2+} flux assay in 132-1N1-hP2Y6 cells. Positive control (i.e.100%) represent UDP (EC_{80})-only conditions. Experiments were performed in duplicate, and data is the mean percentage of positive control ± SD (n ≥ 3 experiments).

5.3 *In Silico* Validation Experiments

The lead structure **37** was discovered *via* a structural-based virtual screening pipeline in which a P2Y6R homology model was generated using a template-based protein modeler RaptorX.[257] Additionally, this same homology model was then utilised by Zhao *et al.* in their hit identification workflow.[170] Molecular docking using homology models can offer valuable insights into molecular interactions; however, the accuracy of these predictions at the molecular level remains a subject of debate.[442,443] With multiple external groups now reporting replicability issues for both series of compounds, the validity of the homology model required further investigation.

With the P2Y6R crystal structure yet to be elucidated, the homology protein structure was constructed from a human P2Y1R template (PDB ID: 4XNV).[169] The structure was then minimised using molecular dynamic stimulations to obtain a more 'formal conformation' of the P2Y6R.[169] Homology models have played a central role in predicting protein structure, prior to formal elucidation.[442,444] In order to produce a successful homology model, two principles must be considered: the primary sequence of the amino acid determines the protein 3D structure, and the protein 3D structure is conserved in relation to the primary sequence.[445] Related proteins are considered to be eligible templates if the sequence-sequence alignment exceeds 35% sequence identity.[445] Throughout the P2Y receptors, the P2Y6 receptor shares the highest amino acid sequence identity (identical amino acid match) with the P2Y4R (33%) with only 28% shared identity with the P2Y1R (Table 5.2).[53] However, this is improved to 41% when considering sequence similarity (conservative substitutions) (Table 5.2).[53] This suggests that achieving a correct alignment would be difficult due to the number of required insertions and deletions.[444]

Table 5.2 Amino acid sequence similarity (entries in italics) and identity (entries in bold) (%) of P2Y1-like receptors following multiple sequence alignment performed by GPCRdb.[a]

	P2Y1	P2Y2	P2Y4	P2Y6	P2Y11
P2Y1		**28**	**32**	**28**	**25**
P2Y2	*44*		**48**	**31**	**22**
P2Y4	*47*	*61*		**33**	**25**
P2Y6	*41*	*41*	*43*		**19**
P2Y11	*42*	*35*	*38*	*30*	

[a]Reprinted (adapted) with permission from *WIREs Comput. Mol. Sci.* **2020**, 10, e1464. DOI: 10.1002/wcms/1464. Copyright 2025 John Wiley and Sons.

Additionally, the template crystal structure utilised (PDB ID: 4XNV) described the human P2Y1 receptor in complex with a non-nucleotide antagonist BPTU.[446] Identified to bind to the allosteric site on the external receptor interface with the lipid bilayer, the structure describes the first structurally characterised selective GPCR ligand located entirely outside of the helical bundle.[446] Allosteric modulators of GPCRs are often advantageous as they can convey selectivity due to the low degree of similarity amongst related subtypes.[110] Zhang *et al.* ascribed BPTU's selectivity for the P2Y1 receptor over other P2Y subtypes due to a key hydrophobic binding interaction with A106.[446] The amino acid A106 is unique to P2Y1, with other subtypes obtaining larger side chains in this location, therefore tolerating a very different steric allowance in the area.[446]

To overcome the limitations that accompany template-based methods, AI-based methods such as AlphaFold (AF), provide a far more accurate prediction of unknown protein structures.[447] AF utilises bioinformatic and physical approaches to predict protein structures.[448] Homology docking experiments were therefore repeated in the P2Y6R AF structure in parallel. In order to gain an accurate comparison, the defined ligand binding site remained constant to that reported by Zhu *et al*.[257]

5.3.1 Validation Compounds

Validation of the reported *in silico* model was achieved through the redocking of **37**, alongside reference compounds (**38 – 40**) from both scaffolds, including the hit and lead compounds identified in each study. Both tautomeric and enantiomeric forms of **37** and **38 – 40**, respectively, were assessed within the *in silico* model, as no discussion regarding the isolated derivative was reported in the corresponding articles.[170,257] Redocking experiments therefore refer to the compound form presented in the corresponding figures, although both analogues will be discussed in more depth in chapter **5.3.3**. To approximate the geometry of the ligand more accurately, ConfGen was utilised in the present study to generate up to 64 different conformations for each ligand.[449] By doing so, bias introduced by the configuration of the starting molecule is removed providing a good approximation of the bioactive geometry of the ligand. This is achieved by rejecting high energy or inactive conformers and identifying local torsional minima.[449]

RTD of compound *(R)*-**39** (hit compound identified by Zhu *et al*.) successfully emulated the hydrogen-bonding interactions between the carboxylate ion (predicted to be deprotonated at pH 7) and the amino acids Lys25 and Lys284 (Figure 5.7A).[257] However, it failed to predict the reported arene-H interaction between Tyr86 and the methyl group. On the contrary, several poses were generated for the benzimidazole ligand *5*-**37**, however all failed the redocking experiment with no pose able to replicate many of the reported interactions (Figure 5.7B).[257]

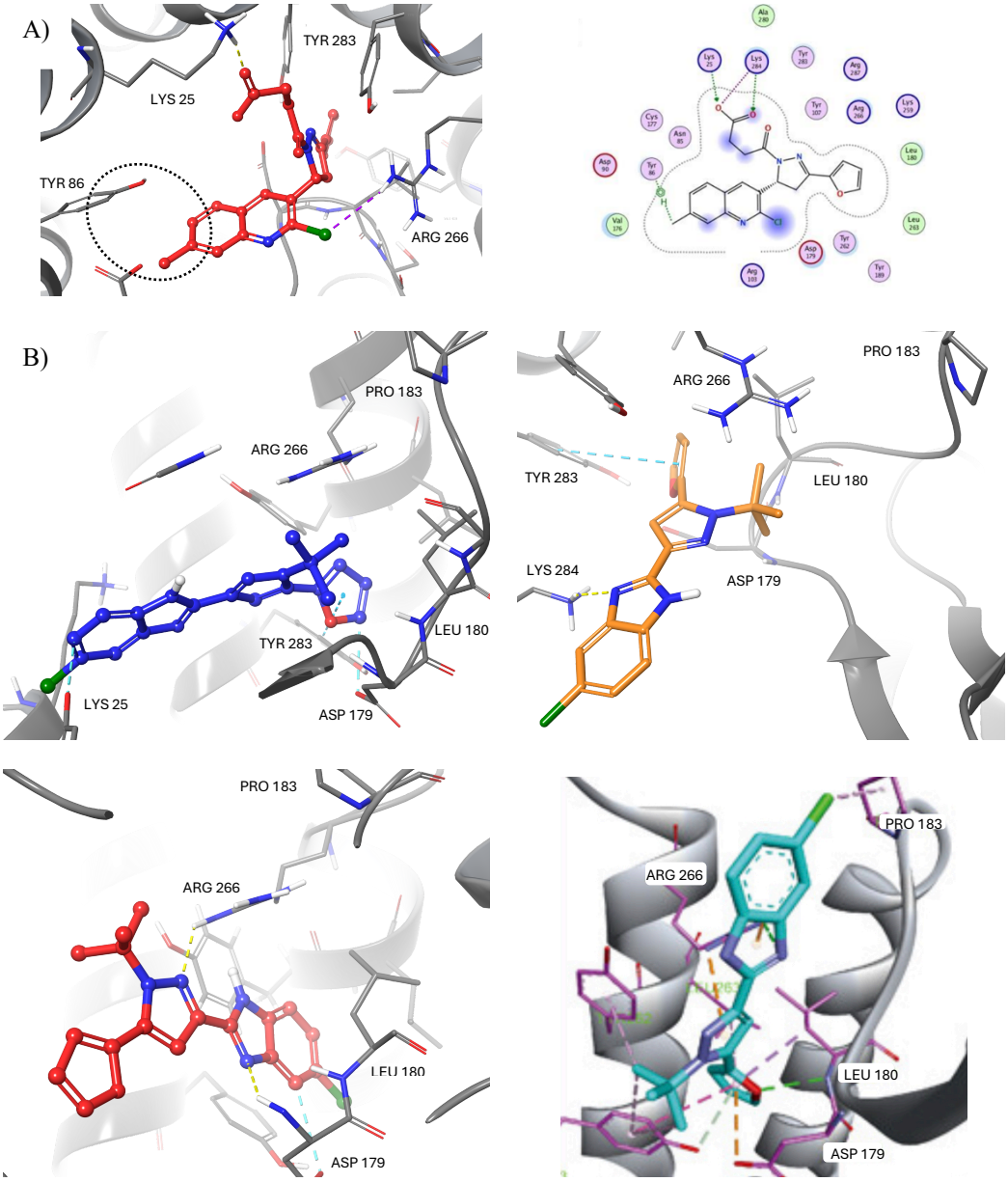

Figure 5.7 Re-docking of *(R)*-**39** (A) and *5*-**37** (B) in the P2Y6R homology models. A) Key arene-H interaction reported by Zhu *et al*. not observed (emphasised by dotted black circle) in re-docking experiment within the homology model. B) Re-docking of *5*-**37** in the P2Y6R templated homology model under RTD OPLS4 (blue), RTD OPLS2005 (orange) and IFD OPLS4 (red) methods, in comparison to the results published by Zhu *et al*. Reprinted (adapted) with permission from *J. Med. Chem.* **2023**, 66, 9, 6315-6332. DOI: 10.102/acs.jmedchem.3c00210. Copyright 2023 American Chemical Society.

Data obtained in docking studies is largely dependent on both algorithm and force field.[239,450] The current *in silico* study utilised the OPLS4 force field, whereas previous work by Zhu *et al.* applied the OLPS2005 force field. Zhao *et al.* failed to disclose what force field was applied in their molecular docking study.[170] The OPLS4 force field includes improvements to the representation of hydration, molecular ions, and sulfur interactions of the ligand within the

binding pocket leading to a more accurate depiction of binding.[239] Redocking and validation experiments were therefore repeated in the OPLS2005 force field to remove any variability. The top-scoring poses exhibited similar predicted binding interactions, and as a result, also failed the redocking process (Figure 5.7B). As no variation in predicted binding mode was observed for the validation compounds between force fields, the remaining experiments were thereby conducted with the OPLS4 force field due to the improved properties listed.[239]

As previously discussed in **Chapter 2** (**2.4.2.3**), misleading results in cross-docking studies within RTD methods are often observed as they do not take into account the movement of side-chains and the protein backbone when the ligand binds.[237] To overcome these limitations, compounds *(R)*-**39** and *5*-**37** were included in an IFD study. The compound library was initially restricted to those with described binding interactions by Zhu *et al*. to allow for a less computationally intensive experiment. Like the RTD study, redocking of *5*-**37** failed to adopt the binding interactions described within the original paper (Figure 5.7B). It is unclear why some protein crystal structures fail during redocking, and the corresponding implications it has on the reliability of future cross-docking experiments, however it is not uncommon.[237] Since the IFD results showed no significant improvement in validity, the more computationally efficient RTD approach was employed for the remaining literature compounds. Consequently, the RTD results for the benzimidazole and quinoline analogues will be discussed. Docking scores from both the rigid-target and induced-fit methods are provided in Appendix 17.

The three quinoline validation compounds (**38**, **40** and **281**) synthesised in **Chapter 4** were similarly subjected to redocking experiments in an effort to replicate the reported binding mode.[170] RTD experiments under both the OPLS4 and OPLS2005 force fields failed to replicate the aromatic interaction between Pro161 and the quinoline for compound *(R)*-**40**. Similarly, several poses were generated for *(R)*-**38**, however all failed the redocking experiment with no pose able to replicate the reported interactions.[170] However, both analogues successfully replicated the characteristic hydrogen bonding between the carboxylate ion and the amino acids Lys25 and Lys284 (Figure 5.7A). Docking scores suggest that this hydrogen bonding is beneficial for efficient binding with all carboxylate analogues reporting significantly better scores in comparison to the benzimidazole derivative **37**.

5.3.2 Molecular Modelling in a P2Y6R AlphaFold Model

AF predicts protein structures with a high level of accuracy through a deep-learning approach to homology modelling based on a trained neural network.[442] The P2Y6R AF sequence (AF-Q15077-F1) was generated by Dr Jonathan Du from the Sydney Pharmacy School, utilising localColabFold to complete the prediction model.[451] The docking process was then conducted in an identical manner to that of the template homology model, including definition of the receptor grid to allow for direct comparison between the two models. Validation compounds from both papers were prepared using the OPLS4 force field and all other parameters remained constant. Similar to that observed for the homology model, redocking of validation compounds failed to reproduce the binding poses previously described.

Distinct binding modes for *5*-**37** were observed between the homology and AF models (Figure 5.8). Both homology models predicted the benzimidazole motif to be pointing outwards from the receptor, however variation was observed in regards to the proximity of the furan to Pro183 (Figure 5.8). Within the AF model, the furan was depicted to be vertically parallel to Pro183, allowing for favourable π-π stacking interactions between the benzimidazole and pyrazole, with the amino acids Tyr178 and Tyr20 respectively (Figure 5.8B). Furthermore, stable interactions were also formed with Lys25, Tyr86, Gln171 and Arg266, resulting in an improved docking score to its homology counterpart (Appendix 17).

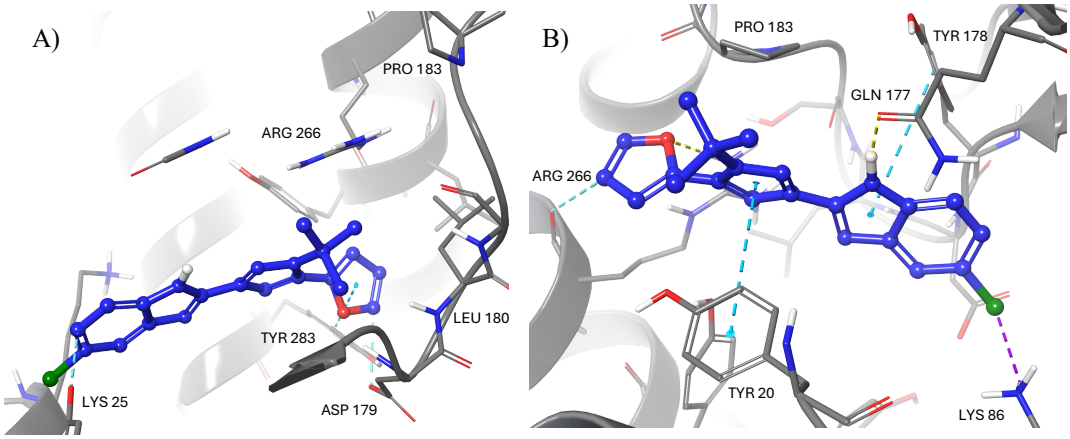

Figure 5.8 *5*-**37** displayed distinct binding modes in the template (A) and AlphaFold (B) homology models. Key binding interactions — e.g. hydrogen-bonds (yellow), π-π stacking (blue), arene-H interaction (cyan), halogen bond (purple) — denoted by the dotted coloured lines. Steric clashes with the surrounding protein (orange dotted lines) are predicted in both models for the *tert*-butyl motif.

5.3.3 Variability Between Tautomeric and Enantiomeric Forms

Interestingly, within the template homology model the two tautomers of *5(6)*-**37** adopted reverse orientations in the defined binding domain (Figure 5.9A). As reported, *5*-**37** was predicted to be positioned so that the furan ring is well docked into the binding pocket (Figure 5.9A). Conversely, the docking predicted *6*-**37** to bind with the benzimidazole motif inside the pocket (Figure 5.9A). Within the AF model, more similarity between the predicted binding interactions is observed for the pair of tautomers. For example, both tautomeric forms report a π-π stacking interaction between the benzimidazole and pyrazole motifs with Tyr178 and Tyr20, respectively (Figure 5.9B).

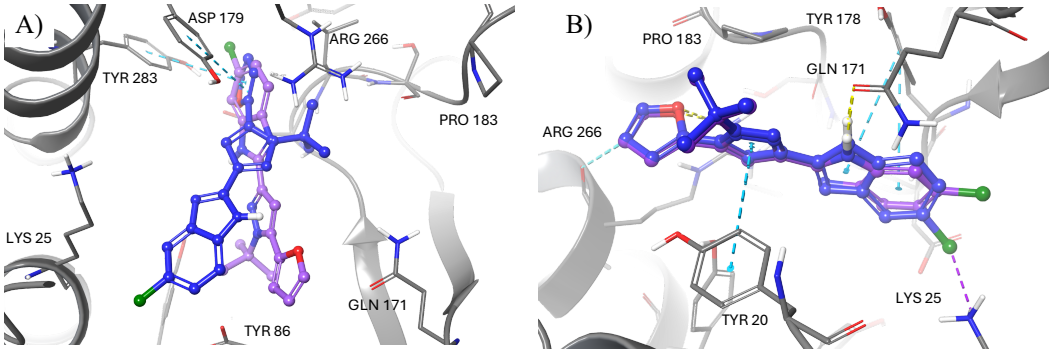

Figure 5.9 Comparison of predicted binding modes for **37** tautomers in the template (A) and AlphaFold (B) homology models. *5*-**37** is shown in dark blue, and *6*-**37** is displayed in purple.

Similarly, the two enantiomers of the dihydropyrazole quinoline compounds **38** and **40** produced different docking predictions. No trend was observed to predict the orientation of the dihydropyrazole motifs in either homology model. In the AF model, **38** described a common π-π stacking interaction with Tyr20, with subsequent variation in binding interactions clearly attributed to the chiral centre (Figure 5.10A). No common interaction was observed for **38** when docked in the homology model. Moreover, in the AF model **40** enantiomers adopted vertically opposite orientations (Figure 5.10B).

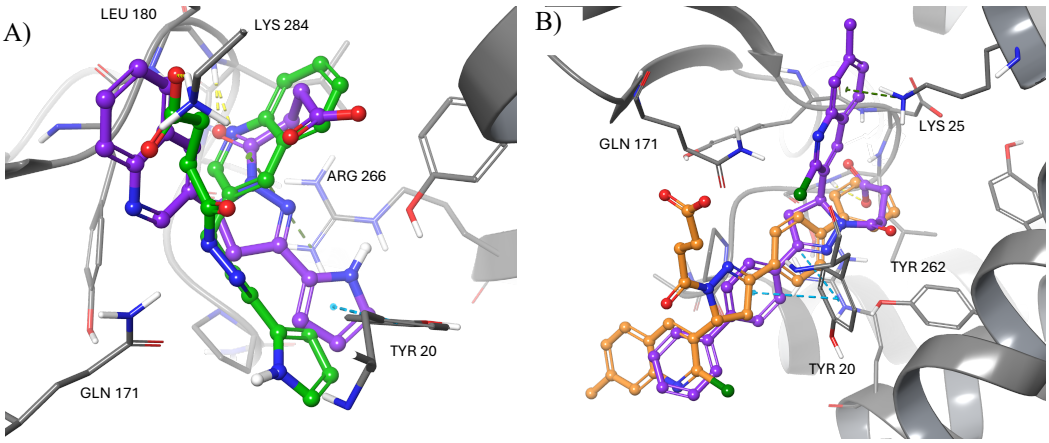

Figure 5.10 Predicting binding modes of **38** (A, *(R)*: green, *(S)*: purple) and **40** (B, *(R)*: orange, *(S)*: purple) enantiomers within the AlphaFold homology model.

Analysis of all the isomeric forms found them equally unsuccessful at replicating the reported docking figure interactions. Although both molecular models indicate that different binding modes of the tautomers/enantiomers do not significantly affect the compounds' ability to bind to the P2Y6R (as inferred from similar docking scores) they may influence the corresponding functional activity. This could, in turn, contribute to the variability observed across replicate *in vitro* studies.

5.4 Concluding Remarks

This chapter has outlined the biological assessment of the synthesised compound libraries presented in **Chapters 3** and **4**. The antagonist assay was developed by Mr André McKenzie as a tool to probe P2Y6R activity. Literature compounds, including both positive and negative controls were assessed to validate *a priori* results and our own SAR analysis. However, contrasting results were reported for the functional activity of reported P2Y6R antagonist chemotypes, bringing their validity into question. These observations were further supported through a third-party research centre and reported literature.[168] Ultimately, none of the modified benzimidazole structures tested demonstrated statistically significant inhibition of UDP-stimulated Ca^{2+} flux, and were therefore not deemed to be P2Y6R antagonists, providing no additional detail into the SAR surrounding the benzimidazole scaffold. *In silico* molecular modelling experiments similarly produced conflicting results to those conveyed in the published literature, with both leads **37** and **38** failing redocking experiments.[170,257] In addition, further disparity was observed between docking poses between the P2Y6R template and AF

homology models. The *in silico* study highlighted the vast difference in predicted binding modes for the tautomeric and enantiomeric forms of **37** and **38** respectively. Elucidation of the racemic ratio of the analysed dihydropyrazole quinoline compounds (**38** and **40**) within both the current study and that conducted by Zhao *et al.* is therefore required prior to further SAR on this scaffold. Additionally, assay variation between those that reported potent activity for **37** and those who did not could explain the discrepancy in results. Future work is required before any conclusions can be made about the reproducibility of the data produced in Zhu *et al.* and Zhao *et al*. Such includes analysis of the raw data and disclosure of detailed *in vitro* methodologies for replication under identical conditions. Furthermore, binding assays would provide critical data to rule out potential off-target effects and/or fluorescence interference.[49,441] Due to the corresponding uncertainty around published P2Y6R antagonist reproducibility, further investigation into the benzimidazole and quinoline scaffolds described herein is not warranted at this stage.

Chapter 6. Conclusions and Future Directions

6.1 P2X4R Focused Research

6.1.1 Summary and Conclusions of P2X4R Focused Research

The effect of adamantane on the selectivity and potency of known P2X4R antagonists was explored in **Chapter 2**. Through the introduction of adamantane, the exploratory study described, aimed to deepen our understanding of both the P2X4 and P2X7 receptor binding domain and provide a predictive framework for selective purinergic antagonists. Sourced from three structurally unique chemotypes, the chlorophenyl and adamantane derivatives of ten literature compounds (**25**, **51**, **52**, **81 – 88**, **113** – **118**, and **124** – **127**) were successfully synthesised (Figure 6.1). Incorporating a broad range of steric and electronic functionalities, the parent compounds selected from patent literature reported a range of functional activities to allow for a comprehensive assessment (Figure 6.1).

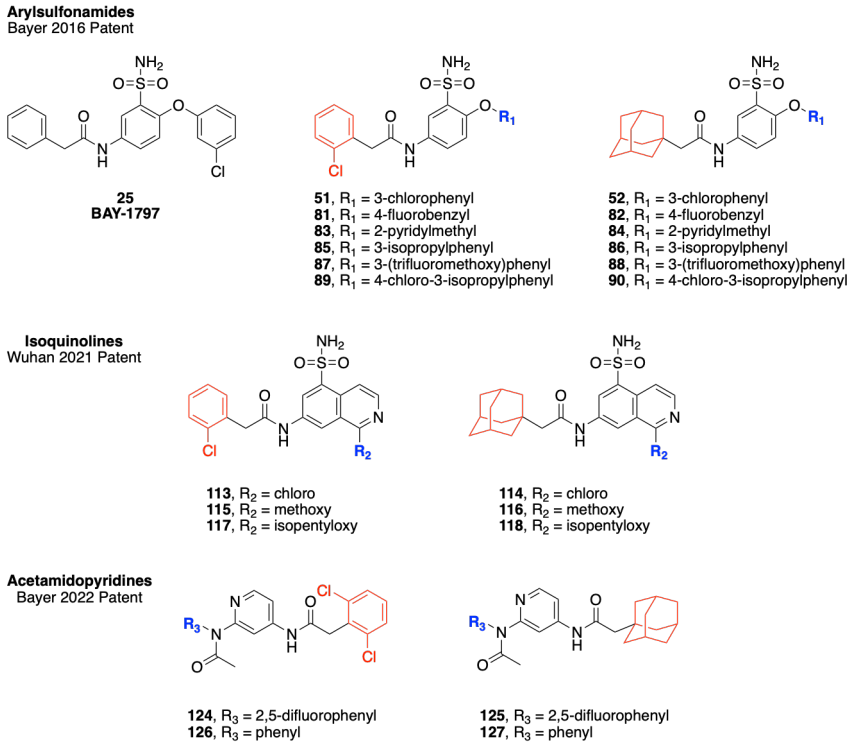

Figure 6.1 P2X4 compound library synthesised allowed for a comprehensive analysis of the effect of hydrophobic moieties on selectivity and potency.[142,148,149]

Analogues containing 3,5,7-trifluoroadamantane were also proposed to investigate whether increasing the electron density in the outermost portion of the polycyclic structure *via* a

hydrogen-to-fluorine replacement would influence binding site preference by altering the strength of hydrophobic interactions.[255] Due to the commercial cost, 2-(3,5,7-trifluoroadamantan-1-yl)acetic acid was required to be synthesised. However, despite extensive efforts (chapter **2.3**) a successful and scalable synthesis was not achieved.

Unfortunately, in the absence of P2X4R *in vitro* data no assertions can be made about the effects of adamantane on P2X4R antagonism. However, preliminary *in silico* analysis of the synthesised compound library (Figure 6.1) predicts detrimental steric clashes between the adamantane motif and surrounding protein and ligands. Removal of the aromatic motif, was shown to disrupt the stabilising aromatic interaction between the phenylacetamide motif and Trp84 reported by Shi *et al*.[8] This suggests that the recently elucidated trimeric binding pose of BAY-1797 in the P2X4R allosteric binding site cannot accommodate sterically complex 3D caged structures.

Whilst assessing for selectivity at the P2X7R, adamantyl-containing ligands within the acetamidopyridine chemotype demonstrated increased activity. In contrast, the arylsulfonamide and isoquinoline chemotypes exhibited varied activity, suggesting that incorporation of an adamantane motif alone is insufficient to confer P2X7R antagonist activity across these scaffolds. Furthermore, none of the synthesised analogues exhibited enhanced potency relative to previously reported P2X7R antagonists in the literature.

6.1.2 Future Directions of P2X4R Focused Research

Further *in vitro* analysis at the hP2X4R is required prior to evaluation of other hydrophobic groups. This will allow for quantitative comparison between the parent patent compounds and their adamantyl derivatives. Additionally, *in vitro* data at the P2X4R will provide potential validation data for the *in silico* methodology and docking study described in **Chapter 2** and thus evaluate its functionality as a triaging tool in future structure-based drug design.

Utilisation of the crystal structure in molecular docking experiments will provide invaluable information for future structure-based drug design. *In silico* structural data sets should be established from a range of library design techniques, including traditional SAR design, scaffold hopping and deconstruction/reconstruction approaches. The *in silico* study herein,

indicated that in order to adopt the mirrored homotrimer orientation, smaller polycycles or planar functional groups are required. Notably, the authors suggested that meta-substitution of the phenyl group may enhance specificity, citing vacant space in this area.[8] Thus, introduction of three-dimensional saturated C(sp^3)-rich phenyl bioisosteres such as bicyclo[1.1.1]pentane (BCP), cubane and norbornene into the three scaffolds represent two rational modifications for future compound design (Figure 6.2A).[452,453] The synthesis and subsequent evaluation of these compounds would provide valuable insights into the spatial and electronic parameters governing optimal P2X4R antagonistic activity (Figure 6.2B).[452] Moreover, with the extensive network of protected structural features present in current P2X4R antagonist patent literature, scaffold hopping provides an effective way to explore greater structural diversity. Ranging from simple heterocyclic replacements to topological structural overhauls, scaffold hopping has been employed extensively within CNS drug discovery to great success.[454]

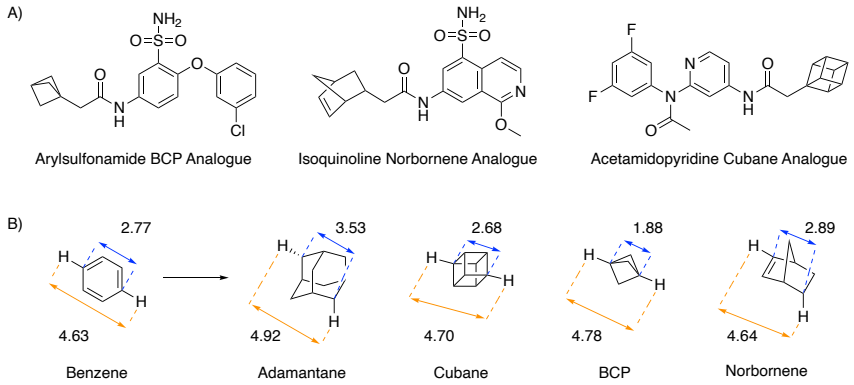

Figure 6.2 Example structures of substitution of the chlorophenyl motifs for saturated C(sp^3)-rich phenyl bioisosteres. B) Structural information of non-classical phenyl bioisosteres, highlighting the decrease in spatial size from adamantane. Data extracted from Tse *et al*. All distances are reported in Å.[452]

Furthermore, on-cell STD NMR spectroscopy could be utilised to aid binding mode determination and subsequent structural modifications of the isoquinoline and acetamidopyridine chemotypes. Recently demonstrated for the first time on membrane-embedded P2X7 ion channels, on-cell STD NMR in combination with molecular docking has been shown to successfully determine the ligand binding models for two P2X7R antagonists.[455]

The method offers a useful alternative for indicating binding in situations where experimental structural techniques such as X-ray crystallography and cryo-EM are challenging. Although unable to achieve the high-resolution and precision available in the former approaches, on-cell

STD NMR provides a higher throughput and less expensive alternative.[455] Within drug design efforts, on-cell STD NMR will provide an additional level of validation within SAR studies to guide next generation library design.

6.2 P2Y6R Focused Research

6.2.1 Summary and Conclusions of P2Y6R Focused Research

The work described in **Chapters 3** – **5** explored the synthesis and biological evaluation of a range of compounds centred around the diversification of compound **37**. Through the application of a range of small-molecule lead diversification and optimisation strategies, a diverse compound library of 27 novel ligands, describing modifications to all key structural components was achieved. A nitrogen walk strategy was initially employed to investigate the effect of hydrogen-bonding and electrostatic interactions within the binding site. Additionally, through substitution and isosteric replacement flexibility and steric contribution were also explored. Throughout **Chapter 4**, a hybrid strategy between the benzimidazole (**37**) and quinoline (**38**) chemotypes was employed to further broaden the chemical space and replace predicted metabolic soft spots. However, unexpected challenges and contradictory results throughout the biological evaluation of reported literature compounds have cast considerable doubt on the utility of **37** as a P2Y6R antagonist. Furthermore, no library compound assessed demonstrated inhibition of the P2Y6R.

6.2.2 Future Directions of P2Y6R Focused Research

The biological results of the benzimidazole (**37** and **153**) and quinoline (**38** and **40**) literature compounds were found to be contradictory to that reported.[170,257] Therefore, further investigations should focus on validating these results utilising identical cellular assay parameters, exploring potential biological consequences of isomeric forms, and confirming ligand binding at the P2Y6 receptor. Until the discrepancies surrounding the replicability of the published P2Y6R antagonists are addressed, further investigation into the SAR of these two chemotypes is not warranted. Crucially, before initiating any medicinal chemistry campaign, the development of a robust and reproducible functional assay is essential to enable meaningful progress in the area.

More broadly, the findings presented in this dissertation provide an interesting case study for the broader discussion of the reproducibility crisis being observed in modern day science.[454-457] With the breadth of scientific research expanding exponentially, and the overwhelming 'publish or perish' culture that dominates academia, reported examples of intra-laboratory data variability are only increasing.[457,458] In a recent survey conducted by *Nature*, more than 70% of 1576 researchers have failed to replicate another scientists experiments.[457] This observation is emphasised within preclinical models and pharmacological experiments more broadly.[459,460] Within a recent replication study of *in vitro* cancer experiments, 70.5% displayed a maximum change in values of greater than 1000 fold.[460] Although much of the data supporting the reproducibility crisis is anecdotal, it highlights the need to treat reported findings with the same level of thoroughness and scrutiny as the scientific experiments themselves.[456,461] Therefore, further emphasising the importance of incorporating validation compounds from literature within our own experiments.

Failure to provide raw data within scientific literature has been proposed to be one of the main causes of irreproducibility.[459] Thus, before any conclusions can be made on the reproducibility of the data presented by Zhu *et al.* and Zhao *et al.*, raw data and detailed methodologies should be provided to allow for replication under identical conditions. Furthermore, due to the complexity of biological systems, high level of data variability may just be an inherent feature.[460] Within the initial evaluation of the benzimidazole and quinoline compounds, neither study discussed the implication of the multiple isomeric forms. Different tautomers of drug candidates will adopt different interactions with the receptors, as seen in the *in silico* study in **Chapter 5**. Expanding on this, it has also been proposed that the time scale of the tautomeric equilibrium relative to that of the biological process can greatly affect the therapeutic result.[349] Both thermodynamic and kinetic factors must therefore be considered.[349] Depending on the relative time scales, both or only one tautomer may be the active species.[349] Further studies into the rate of interconversion between the benzimidazole tautomer's is therefore necessary. Additionally, it is well known that chirality can significantly affect a compounds biological activity.[462] Enantiomeric assignment of both the compounds analysed in both the Zhao *et al.* and current study should occur to ensure consistency and remove further variability.

Whilst there is significant conjecture about the functional activity of the benzimidazole (**37**) and quinoline (**38**) lead compounds explored throughout this dissertation, support for the

pharmacological role of the P2Y6R within inflammatory pathways is only growing.[56,59,463–465] Thus, the need for potent and selective drug like molecules is still pertinent. Significant SAR has been conducted by the Jacobson group on the 2*H*-chromene chemotype (Figure 6.3A).[165–168] The chemotype has reported a largely flat SAR profile, with no clear preference of positioning, chain length and terminal functionality of the ethynyl-linked substituent (Figure 6.3A).[168] However, the study did suggest that there is a hydrophobic receptor environment surrounding the pharmacophore.[168] Due to the corresponding limitations of poor potency and off-target inhibition at the adrenergic and dopamine receptors, further SAR investigation into the 2*H*-chromene chemotype is not recommended.[168]

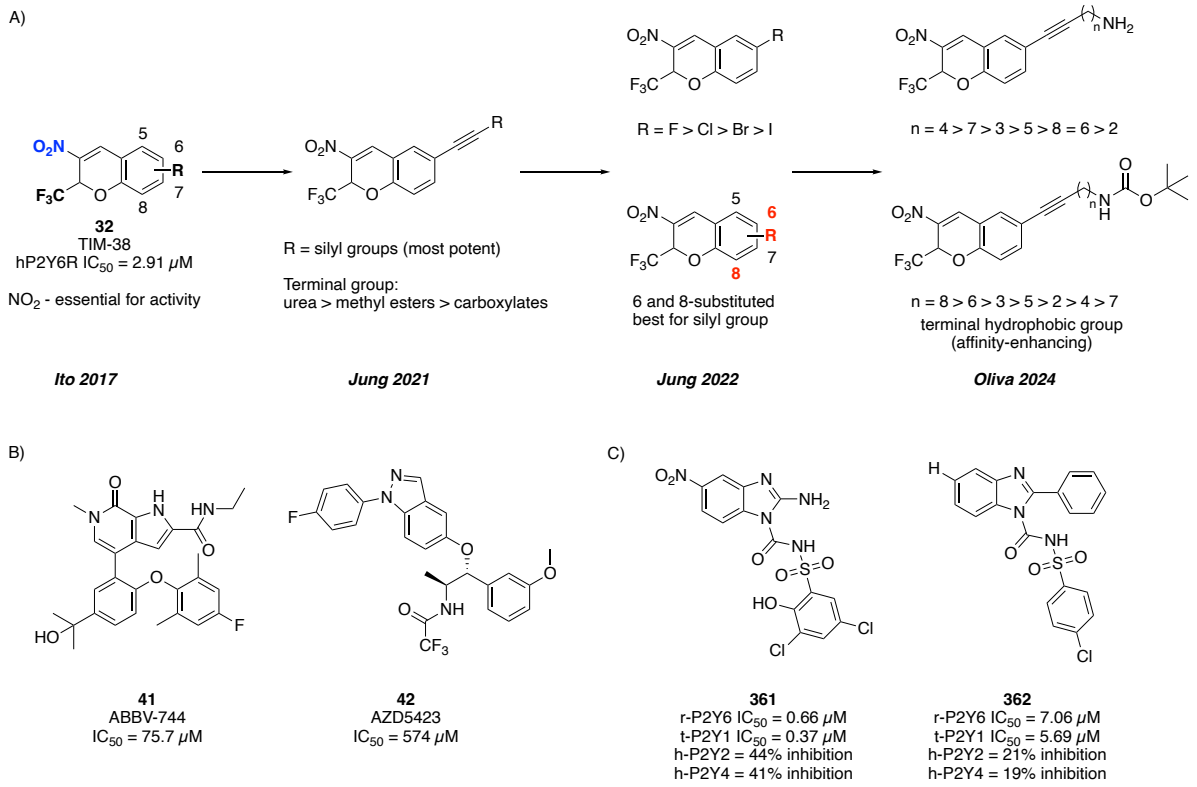

Figure 6.3 Search for novel P2Y6 antagonist chemotypes. A) Summary of the SAR conducted by the Jacobson group on the 2*H*-Chromene P2Y6 antagonist scaffold. B) Hit compounds from the machine learning-aided search for novel P2Y6 antagonists. Data extracted from Puhl *et al.*[173] C) Sulfonylurea analogues identified to have affinity for the P2Y6 receptor present as a potential opportunity for chemotype translation. Data extracted from Bano *et al.*[466]

Scaffold repurposing is a popular strategy used throughout drug discovery to identify new chemotypes.[467,468] In 2024, Puhl *et al*. performed a machine learning-aided search for P2Y6R ligands.[173] The study highlighted two structurally unique scaffolds (ABBV-744 and AZD5423) for further diversification (Figure 6.3B). Of the two, ABBV-744 (**41**), an experimental

anticancer drug, reported the most potent inhibition (IC_{50} = 75.7 μM).[173] Through the utilisation of both classical SAR, scaffold hopping techniques and early-stage PK modelling a diverse compound library could be constructed to deduce key pharmacophores. Additionally, as many P2Y receptors recognise similar nucleosides as their endogenous ligand, and appear in similar pharmacological pathways, antagonists could have translation potential. Thus, novel scaffolds could be identified through analysis of selectivity data of other P2Y antagonists. A series of benzimidazole derived sulfonylurea analogues (**361** and **362**) were identified as moderate inhibitors of *turkey*-P2Y1R, with off-target inhibition at the *rat*-P2Y6R (Figure 6.3C).[466] Investigation into whether these analogues share a similar activity relationship at the human receptors should be conducted. However, due to the structural similarity with **37** compounds **361** and **362** provide an interesting scaffold for further derivatisation.

6.3 Overall Concluding Remarks

The purinergic system is a key signalling pathway that plays a central role in regulating microglial behaviour across a broad range of (patho)physiological processes.[9] The work described in this dissertation details the exploration of purinergic receptor modulators and their effect on microglial function in the context of neuroinflammation. By advancing our understanding of the structural requirements for antagonising both P2X and P2Y receptors, this research provides foundational knowledge for modulating microglial function in pathological states, thereby offering critical insights for the development of therapeutic candidates for neurodegenerative disorders.

By employing a variety of compound library design approaches from both classical drug discovery and hybrid strategies, this work aimed to expand the pharmacophore models for the P2X4R and P2Y6R. An exploratory study investigating the effect of hydrophobic motifs on the selectivity and potency of known P2X4R antagonists was conducted through the introduction of adamantane. While definitive conclusions await hP2X4R *in vitro* data, preliminary *in silico* analysis suggests a steric limitation for effective P2X4R binding. Furthermore, although diversification of reported P2Y6R inhibitor scaffolds did not yield any new potent lead candidates, this research has identified discrepancies within the existing literature concerning P2Y6 antagonists. The necessary strategies and criteria for the continued evaluation of these candidates have been addressed throughout. However, more importantly,

for meaningful translation of P2Y6R antagonists towards clinical development there is an urgent need for robust, reproducible functional assays.

Overall, the research presented in this thesis contributes to the development of selective and potent purinergic receptor modulators through the investigation of pharmacophoric features. Through furthering our understanding of critical structural elements, this work will facilitate the discovery of drug-like purinergic receptor antagonists for studying microglial function in neuroinflammatory conditions.

Chapter 7. Experimental

7.1 General Information for Chemical Synthesis

Unless otherwise stated, reagents and solvents were sourced from commercial vendors and used without further purification. Anhydrous solvents were obtained from a PureSolv MD 7 solvent purification system (Innovative Technology, Inc.). Tetrahydrofuran and 1,4-dioxane were dried using 4 Å molecular sieves. All reagents were weighed out under ambient conditions. Unless otherwise states, reactions were conducted under a positive pressure of a dry nitrogen or argon atmosphere.

Analytical thin-layer chromatography (TLC) was conducted using Merck aluminum backed silica gel 60 F254 (0.2 mm) plates. For UV active compounds, shortwave (254 nM) and/or longwave (365 nM) ultraviolet (UV) light was used for visualization. Compounds without a UV active chromophore were visualised with potassium permanganate, vanillin, ninhydrin, bromocresol green, and cerium molybdate ("Goofy's Dip"). Flash column chromatography was performed using Merck© silica gel pore size 60 Å, 40-63 µM, 230-400 mesh. Additionally, flash chromatography purifications were also performed on a Biotage® Selekt flash purification system with a photo diode array detector and fraction collector. Velocity scientific solutions E series flash columns were used packed with silica gel (40 – 63 µM, 60 Å) sized 4 g, 12 g, 25 g, 40 g. Reverse phase columns were performed on Biotage® Sfär C18 Duo (30 µm, 100 Å), sized 6 g, 12 g. All isocratic solvent compositions are reported as their volume to volume (v/v) ratios, and gradients are reported as their percentages.

Nuclear magnetic resonance (NMR) spectra were recorded at 300 K unless stated otherwise, using either a Bruker© AVANCE DRX300 (300 MHz), DRX400 (400.1 MHz), AVANCE III DRX500 Ascend (500.1 MHz) or AVANCE NEO (500 MHz). NMR spectra were reported as a chemical shift (δ, ppm) with reference to the residual deuterated solvent peak, multiplicity (s = singlet, d = doublet, dd = doublet of doublets, dt = doublet of triplets, dq = doublet of quartets, ddd = doublet of doublet of doublets, ddt = doublet of doublet of triplets, dtd = doublet of triplet of doublets, dtt = doublet of triplet of triplets, t = triplet, td = triplet of doublets, tt = triplet of triplets, q = quartet, qd = quartet of doublets, p = pentet, h = heptet, m = multiplet), coupling constant (J, Hz), and relative integral. ^{13}C chemical shifts are expressed as parts per million

(ppm) with reference to the residual deuterated solvent and reported as chemical shift (δ, ppm); multiplicity (d = doublet, q = quartet); coupling constants (J, Hz). Proton decoupled ^{19}F chemical shifts are reported as parts per million (ppm). Nuclear assignments were performed with the aid of COSY, NOESY, HSQC and HMBC experiments where necessary.

Low-resolution mass spectrometry (LRMS) was performed using a Bruker© amaZon Speed-Ion Trap mass spectrometer using electrospray ionisation (ESI) or atmospheric pressure chemical ionization (APCI). Samples run by ESI were injected (20 µL) into a continuous flow of methanol or acetonitrile (0.3 mL/min) with an Alltech HPLS pump, and a direct probe injection method was utilised for APCI (corona current 4000 nA, vaporization temperature 400 °C). High resolution mass spectrometry (HRMS) was recorded on a Bruker 7T Apex Qe Fourier Transform Ion Cyclotron resonance mass spectrometer equipped with an Apollo II ESI/APCI/MALDI Dual source.

High-performance liquid chromatography (HPLC) purity analysis was performed with a Waters© 2695 Separations module equipped with Waters 2996 Photodiode Array detector, set at 254 nm. All samples were eluted through a Waters SunFire® C18 5 µM column (2.1 x 150 mm) using a flow rate of 0.2 mL/min of Solvent A: H_2O (+ 0.1% TFA) and Solvent B: CH_3CN (+ 0.1% TFA) with a gradient elution of 0-100% Solvent A:B over 30 min. HPLC data was acquired and processed using the Waters Empower 2 software and reported as a percentage purity and retention time (R_T) in minutes at 254 nm. Semi-preparative HPLC was performed with Waters© 2707 autosampler, 2735 gradient manager, 2489 UV/Vis detector and a Waters III fraction collector. Separations were performed with a SunFire® C18 OBDTM column (100 Å, 5 µm, 10 x 250 mm or 19 x 150 mm) using H_2O with 0.1% TFA (solvent A) and CH_3CN with 0.1% TFA (solvent B) at a flow rate of 4.0 or 7.0 mL/min. The semi-preparative method consisted of a gradient of 30–100% CH_3CN over 20 min with absorbance at 254 nm or 230 nm monitored for collection.

7.2 *In Silico* Studies

The following *in silico* molecular docking study was visualised, prepared, and calculated using Schrodinger Maestro v13.9 software (Schrodinger, LLC, New York USA).

7.2.1 P2X4 *In Silico* Study

7.2.1.1 Protein Preparation and Refinement of the P2X4R

The cryo-EM crystal structure of the human P2X4 receptor in complex with a P2X4R inhibitor, BAY-1797 (PDB ID: 9BQI) as reported by Shi *et al*, was retrieved from the RSCB Protein Data Bank.[8] Utilising the Protein Preparation Wizard embedded in Maestro v13.9 the protein was prepared for further analysis. This process includes assigning bond orders, adding hydrogens atoms, and creating zero order bonds to metals and disulphide bonds. Additionally, missing side chains were filled in using the PRIME feature and heteroatom states between pH 7 ± 2 were generated with Epik. [451,472,473] The hydrogen bond network was then optimised through the PROPKA function, using sample water orientations and the protonation state for each heteroatom as defined at pH 7. The protein was further optimised by removing any water molecules involved in hydrogen bonding further than 5Å from a heteroatom, and all but the co-cyrstallised ligand in Chain A. Finally, the total protein structure was energy minimised using the OPLS4 force field, and heavy atoms converged to a RMSD of 0.3 Å.[239]

7.2.1.2 Ligand Preparation

Compound structures were imported directly into the Maestro software from ChemDraw v23.1. All ligands were prepared using the LigPrep module to generate all potential ionisation states and tautomers at pH 7 ± 2.[239,469,470] Confgen was also used to generate up to 64 different conformations for each ligand.[449] By generating the conformations bias introduced by the configuration of the starting molecule is removed.[449] ConfGen provides a good approximation of the bioactive geometry of a ligand by rejecting high energy or inactive conformers and identifying local torsional minima.[449]

7.2.1.3 Receptor Grid Generation

The Receptor Grid Generation tool in Glide v9.1 was used to characterise the binding site for the docking studies.[238] The first binding site was defined by a 20 Å bounding box centred at the co-crystalised ligand within the allosteric site of chain A. A Coulomb-van der Waals scaling

factor of 1.0 for receptor van-der Waals radii was applied to protein atoms with a partial charge of less than 0.25 e and a similar factor of 0.8 was applied to ligand atoms with a partial charge cutoff of less than 0.15 e. Rotations of hydroxyl and thiol groups were not allowed.

7.2.1.4 Rigid Target Docking of P2X4 Ligands

The ligands (**25, 51, 52, 81, 82, 89, 90, 115 – 118, 124 – 127**) were docked into the receptor grids with Glide v9.1. All docking studies were carried out using the Extra Precision (XP) scoring function to refine binding energy estimates.[238] All ligands were docked with flexible states to allow sampling of the effect of nitrogen interconversion, changing ring conformations and non-planar amide functional groups penalised.[6]

7.2.1.5 Multi-Ligand Docking of P2X4 Ligands

The top scoring pose from the initial docking experiment was merged with the prepared protein. Subsequent binding sites (Chain B and C) were then defined by a 20 Å bounding box centred at around the key residues; A87, V90, D88 and K298. The ligands were then docked again into the receptor grid, using the XP scoring function. All other parameters stayed consistent to the initial screen.

7.2.2 P2Y6 *In Silico* Study

7.2.2.1 Protein Preparation and Refinement of the P2Y6 Template Homology Model

The P2Y6 templated homology model in complex with **1a** as reported by Zhu *et al*, was retrieved from the corresponding article. [251] Utilising the Protein Preparation Wizard embedded in Maestro v13.9 the protein was prepared for further analysis with those parameters described in **7.2.1.1**.

7.2.2.2 Protein Preparation and Refinement of the P2Y6 AlphaFold Homology Model

The P2Y6 AlphaFold homology model was generated by Dr Jonathan Du from the Sydney Pharmacy School, Faculty of Medicine and Health. The human P2Y6 amino acid sequence (uniprotKB: Q15077) was retrieved from UniProt and submitted as a full receptor into AlphaFold2. The prediction was generated using localColabfold. The protein was then prepared for further analysis utilizing the Protein Preparation Wizard in Maestro v13.9, *via* the methodology described in **7.2.1.1**.

7.2.2.3 Rigid Target Docking of P2Y6 Ligands

Compound structures were prepared in accordance with the methodology described in **7.2.1.2**. Confgen was only applied to literature validation compounds and not the compound library described in Chapters 3 and 4. Similarly a receptor gride was defined by a 20 Å bounding box centred at the co-crystalised ligand and residues listed by Zhu *et al.* for the template and AlphaFold homology models respectively. [257] All other parameters were kept consistent with those described in **7.2.1.3**. The ligands (**37 – 40, 281**) were docked into the respective receptor grides with Glide v9.1. All docking studies were carried out using the Extra Precision (XP) scoring function and identical parameters to **7.2.1.4**. Docking experiments were conducted with the OPLS4 and OPLS2005 force fields for both homology model types. Compounds were additionally sourced from the original paper to provide further validation.[257]

7.2.2.4 Induced Fit Docking of P2Y6 Ligands

The hit (*R*-**1a**) and lead (**5-37**) compound reported by Zhu *et al*. were docked into the receptor with Induced Fit Docking default settings.[257,471] Calculations were made using standard protocol and OPLS4 force field.[239] Initial ligand conformations for each compound were generated from the top ranked pose from the initial docking studies. Binding sites were defined by a 20 Å bounding box centred at the co-crystalised ligand within the P2Y6 active site. Receptor van der Waals scaling and Ligand van der Waals scaling was set to 0.50. Residues within 20 Å of ligand poses were refined, with optimisation of side chains. Ligands were redocked with Extra Precision (XP) to refine binding energy estimates.[238,472] All ligands were docked with flexible states to allow sampling of the effort of nitrogen interconversion, changing ring conformations and non-planar amide functional groups were penalised.[472]

7.3 General Synthetic Procedures

General Procedure A – Nucleophilic Aromatic Substitution of Aryl Fluoride

A solution of the respective 4-fluoronitrobenzene (1.0 eq) in acetonitrile (0.2 M) was treated with caesium carbonate (1.1 eq) and the relevant phenol (1.1 eq). The reaction was then stirred at 110 °C under a N_2 atmosphere for 6 hours, or until TLC confirmed consumption of starting material. The solvent was evaporated and the remaining solid was partitioned between EtOAc (25 mL/mmol) and H_2O (25 mL/mmol). The aqueous layer was extracted with EtOAc (3 x 25 mL/mmol), and pooled organic layers were washed with $NaHCO_3$ (1 x 25 mL/mmol) and brine

(1 x 25 mL/mmol). The organic fractions were dried over anhydrous $MgSO_4$ and solvent was removed *in vacuo*. The crude residue was purified by flash chromatography (EtOAc/Hex or MeOH/CH_2Cl_2 eluents).

General Procedure B – Béchamp Reduction with NH_4Cl

The nitroarene (1.0 eq) was dissolved in EtOH or THF/MeOH (1:1). $Fe_{(s)}$ (9.0 eq) and NH_4Cl (9.0 eq in H_2O) was added slowly to the stirring solution and heated to 75 °C for 3 h, or until TLC confirmed consumption of starting material. The reaction was cooled to rt and filtered over a pad of celite®. The celite® pad was washed with the EtOH and the subsequent filtrate concentrated. The resulting residue was partitioned between EtOAc (25 mL/mmol) and H_2O (25 mL/mmol). Aqueous layers were then washed with EtOAc (3 x 25 mL/mmol). The combined organic extracts were washed with brine (1 x 25 mL/mmol), dried over $MgSO_4$ and concentrated *in vacuo*. The crude residue was purified by flash chromatography (EtOAc/Hex or MeOH/CH_2Cl_2 eluents).

General Procedure C – Deprotection of 2,4-Dimethoxybenzyl Sulfonamides

The applicable 2,4-dimethoxybenzyl sulfonamide (1.0 eq) was dissolved in CH_2Cl_2 and treated dropwise with trifluoroacetic acid (50 eq). The 'purple' reaction mixture was stirred under N_2 at rt for an hour. Following consumption of starting material, the reaction was quenched with H_2O (2 mL). The aqueous layer was extracted with CH_2Cl_2 (3 x 25 mL/mmol). Pooled organic layers were washed with brine (1 x 25 mL/mmol), dried over $MgSO_4$ and concentrated *in vacuo*. The crude residue was purified by flash chromatography (EtOAc/Hex or MeOH/CH_2Cl_2 eluents).

General Procedure D – Acid Chloride Mediated Amide Coupling

Acid chloride was prepared by suspending the appropriate carboxylic acid (1.0 eq) in CH_2Cl_2 (0.1 M) at 0 °C and treating with oxalyl chloride (2.0 eq) in the presence of cat. DMF. The resultant solution was stirred at rt for 2 h and concentrated under a stream of N_2 to afford the required acid chloride. Crude acid chloride was then dissolved in CH_2Cl_2, and solvent was removed. This procedure was repeated 3 times to ensure removal of excess oxalyl chloride. The respective aniline (1.0 eq) was dissolved in CH_2Cl_2 at 0 °C. $^iPr_2NEt$ (4.0 eq) and solution of respective acid chloride (1.2 eq in CH_2Cl_2) were added dropwise to the solution. Reaction

mixture was allowed to come to rt and stirred under a N_2 atmosphere until TLC showed consumption of aniline. The reaction mixture was then washed with saturated $NaHCO_3$ (1 x 25 mL/mmol), and aqueous layers were extracted with CH_2Cl_2 (3 x 25 mL/mmol). Pooled organic layers were washed with brine, dried over $MgSO_4$ and concentrated *in vacuo*. The crude residue was purified by flash chromatography (EtOAc/Hex or MeOH/CH_2Cl_2 eluents).

General Procedure E – Buchwald-Hartwig Cross-Coupling

To a suspension of aniline/thiol (1.0 – 2.0 eq) and aryl halide (1.0 – 1.5 eq) in degassed 1,4-dioxane (0.2 M) was added $Pd_2(dba)_3$ or $Pd(dba)_2$ (5 mol%, w/w), Xantphos (10 mol%, w/w) and $^{i}Pr_2NEt$ (2.2 eq) or Cs_2CO_3 (1.6 eq). The reaction mixture was heated to 80 °C and stirred for 18 – 24 h, or until TLC confirmed consumption of starting material. The suspension was cooled to rt and catalyst was removed by filtering through celite®. The filtrate was concentrated and resulting residue portioned between EtOAc (25 mL/mmol) and H_2O (25 mL/mmol). The aqueous phase was then extracted with EtOAc (3 x 25 mL/mmol). The combined organic phases were then washed with brine (1 x 25 mL/mmol), dried over $MgSO_4$ and concentrated *in vacuo* to yield the desired product. The crude residue was purified by flash chromatography (EtOAc/Hex or MeOH/CH_2Cl_2 eluents).

General Procedure F – One-Pot Chlorooxidation and Amination

1,3-Dichloro-5,5-dimethylhydantoin (DCDMH) (1.0 – 2.0 eq) was added portion-wise to a stirring solution of the appropriate thioether (1.0 eq) in CH_3CN/THF/AcOH/H_2O (80:15:3:2) at 0 °C. The reaction was maintained at 0 °C for 2 hours before being concentrated to near dryness under a stream of N_2 gas. Whilst maintaining the temperature at <10 °C the residue was diluted with CH_2Cl_2 (25 mL/mmol) and washed with 5% $NaHCO_3$ (1 x 25 mL/mmol) and brine (1 x 25 mL/mmol). The organic layer was then dried over $MgSO_4$, filtered and evaporated to dryness. The residue was immediately used in the subsequent step where it was dissolved in NH_4OH and stirred at rt for 20 min. The reaction mixture was then heated to 50 °C and stirred for an additional 2 hours. Upon consumption of starting material, the solution was concentrated under a stream of N_2 overnight. The crude residue was purified by flash chromatography (EtOAc/Hex or MeOH/CH_2Cl_2 eluents).

General Procedure G – HATU of T_3P Mediated Amide Coupling

A solution of carboxylic acid (1.2 eq), coupling agent (HATU or T_3P 50% soln. in EtOAc, 1.0 –1.5 eq) and $^{i}Pr_2NEt$ or Et_3N (3.0 – 4.0 eq) in DMF (0.5 M) was stirred for 15 min at rt. The reaction mixture was then treated with corresponding amine (1.0 eq) and stirred for a further 3 h, or until TLC confirmed consumption of starting material. The reaction mixture was then diluted in H_2O (25 mL/mmol) and extracted with EtOAc (3 x 25 mL/mmol). The combined organic layers were further washed with sat. $NaHCO_3$ (1 x 25 mL/mmol), brine (1 x 25 mL/mmol), dried over $MgSO_4$ and concentrated *in vacuo*. The crude residue was purified by flash chromatography (EtOAc/Hex or MeOH/CH_2Cl_2 eluents).

General Procedure H – $LiAlH_4$ Reduction

A solution of starting material (1.0 eq) in anhydrous THF (0.2 M) under an inert atmosphere of N_2 was cooled to 0 °C. The reaction mixture was then treated portionwise with $LiAlH_4$ (1 – 3 eq). The reaction mixture was then stirred at 0 °C for 30 min and allowed to warm to rt over 1 h, followed by heating to reflux for 2 h. Following complete conversion of starting material by TLC, the reaction was cooled to 0 °C and quenched by sequential addition of H_2O (1 mL/g $LiAlH_4$), 4 M aq. NaOH (1 mL/g $LiAlH_4$) and H_2O (3 mL/g $LiAlH_4$). The crude mixture was filtered through a pad of celite® and washed with EtOAc (3 mL). Combined filtrates were concentrated *in vacuo*. The crude product was purified *via* flash chromatography (EtOAc/Hex or MeOH/CH_2Cl_2 eluents) to afford the desired alcohol.

General Procedure I – Paal-Knorr Pyrazole Formation

A solution of 1,3-dicarbonyl (1.0 eq) in EtOH (0.2 M) or HFIP (0.05 M) was treated with hydrazine (1.2 eq) at rt and stirred for 2 – 8 h. The solvent was evaporated and the residue taken up in EtOAc (1 x 25 mL/mmol), washed with H_2O (1 x 25 mL/mmol), brine (1 x 25 mL/mmol) dried over $MgSO_4$ and concentrated *in vacuo* to yield the desired product. The crude residue was purified by flash chromatography (EtOAc/Hex or MeOH/CH_2Cl_2 eluents).

General Procedure J – Base Catalysed Ester Hydrolysis

A solution of ester (1.0 eq) in MeOH/H_2O (3:1) solvent system was treated with $LiOH.H_2O$ (1.5 eq) and stirred at reflux for 2 h. The reaction mixture was concentrated *in vacuo* and the resultant residue diluted with H_2O (10 mL) and acidified *via* addition of 1 M aq. HCl. The

aqueous phase was then extracted with EtOAc (3 x 25 mL/mmol). The combined organic phases were then washed with brine (1 x 25 mL/mmol), dried over $MgSO_4$ and concentrated *in vacuo* to yield the desired carboxylic acid. Products were used without further purification.

General Procedure K – MW Assisted Benzimidazole Formation

A mixture of aldehyde (1.0 eq), the appropriate diamine (2.0 eq) and sodium metabisulfite (1.0 eq) in EtOH was irradiated for 5 min increments (x 4) at 140 °C in a microwave reactor. Reaction progress was monitored by TLC. The reaction mixture diluted with EtOAc (25 mL/mmol) and H_2O (25 mL/mmol). The aqueous phase was then extracted with EtOAc (3 x 25 mL/mmol). The combined organic phases were then washed with brine (1 x 25 mL/mmol), dried over $MgSO_4$ and concentrated *in vacuo* to yield the desired product. The crude residue was purified by flash chromatography (EtOAc/Hex or MeOH/CH_2Cl_2 eluents).

General Procedure L – Ortoleva King-like Reaction

To a solution of ketone (1.0 eq) and amine (1.0 eq) in EtOH (0.2 M), iodine (1.0 eq) and NH_4OAc (2.5 eq) was added at rt. The resulting mixture was heated to reflux and stirred for a subsequent 24 h open to air, or until TLC indicated conversion of starting material. The reaction was cooled to rt and diluted with H_2O (10 mL) and EtOAc (10 mL). The aqueous layer was extracted with EtOAc (3 x 25 mL/mmol). The combined organics were washed with brine (1 x 25 mL/mmol), dried over $MgSO_4$ and concentrated *in vacuo*. The crude product is purified *via* flash chromatography (EtOAc/Hex or MeOH/CH_2Cl_2 eluents) to afford the desired benzimidazole.

General Procedure M – Steglich Esterification

To a solution of carboxylic acid (1.0 eq) in CH_2Cl_2 (0.2 M) was added EtOH (1.0 eq) and DMAP (0.1 eq) at rt. The reaction mixture was cooled to 0 °C prior to addition of EDC.HCl (1.5 eq) portionwise. The reaction was warmed to rt and stirred for 3 h, or until TLC indicated consumption of starting material. After reaction completion, the reaction was dilute with CH_2Cl_2 (25 mL/mmol) and washed with sat. $NaHCO_{3\,(aq)}$ (1 x 25 mL/mmol). The organic layer was further washed with brine (1 x 25 mL/mmol), dried over $MgSO_4$ and concentrated *in vacuo*. Products were used without further purification.

General Procedure N – Benzimidazole Formation via the Cyclocondensation of Carboxylic Acid and Diamine Derivatives

$^{i}Pr_2NEt$ (4.0 eq) and HATU (1.2 eq) were added to a stirring solution of the appropriate carboxylic acid (1.0 eq) in DMF (0.5 M). Following 20 min of stirring at rt, 4-chlorobenzene-1,2-diamine (1.2 eq) was added to the solution. The solution was stirred at rt overnight, or until TLC confirmed consumption of starting material. The reaction mixture was then diluted in H_2O (25 mL/mmol) and extracted with EtOAc (3 x 25 mL/mmol). The combined organic layers were further washed with sat. $NaHCO_3$ (1 x 25 mL/mmol), brine (1 x 25 mL/mmol), dried over $MgSO_4$ and concentrated *in vacuo*. The crude residue was either partially purified by flash column chromatography or progressed without further purification. The residue was then dissolved in a AcOH/toluene (10:1) solvent mixture and stirred at 75 °C for 3 hours, followed by vacuum concentration. The crude mixture was partitioned between EtOAc (25 mL/mmol) and sat. aq. $NaHCO_3$ (25 mL/mmol). The aqueous phase was extracted with EtOAc (3 x 25 mL/mmol). The combined organic layers were further washed with brine (1 x 25 mL/mmol), dried over $MgSO_4$ and concentrated *in vacuo*. The crude residue was purified by flash chromatography (EtOAc/Hex or MeOH/CH_2Cl_2 eluents).

General Procedure O – Claisen-Schmidt Reaction to Yield α,β-Unsaturated Diketones

To a solution of aldehyde (1.0 eq) and ketone (1.0 eq) in EtOH (0.2 M) was added aq. NaOH (2.5 M, 2.0 eq). The reaction mixture was stirred at rt for 1 – 8 h, or until TLC confirmed consumption of starting material. The resulting precipitate was filtered, washed with EtOH, and dried to obtain the title compound. Products were used without further purification.

General Procedure P – Claisen Condensation with NaH

A solution of alkenone (1.0 eq) in THF or toluene (0.2 M) under an atmosphere of N_2 was cooled to 0 °C. The reaction mixture was then treated with NaH (60% Dispersion in mineral oil, 3.0 – 5.0 eq) and stirred at 0 °C for 15 min. The reaction mixture was then treated dropwise with a solution of ester or diethyl oxalate (2.0 – 2.5 eq) in toluene. The reaction mixture was stirred at 50 – 90 °C for 2 h. The reaction mixture was then diluted with ice-water (10 mL), acidified with 1M HCl (pH 1) and extracted with EtOAc (3 x 25 mL/mmol). The combined organic phases were then washed with brine (1 x 25 mL/mmol), dried over $MgSO_4$ and

concentrated *in vacuo* to yield the desired product. The crude residue was purified by flash chromatography (EtOAc/Hex or MeOH/CH_2Cl_2 eluents).

7.4 Chapter 2 Experimental and Characterisation

2-fluoro-5-nitrobenzenesulfonyl chloride (**43**)

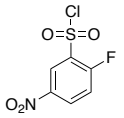

1-Fluoro-4-nitrobenzene (4.93 g, 34.9 mmol) was added dropwise to chlorosulfonic acid (23 mL, 349 mmol) at 0 °C. The reaction was then stirred at 100 °C with a $NaHCO_3$ bubbler system attached for 48 hours, or until TLC confirmed completion. The reaction mixture was cooled to 0 °C and quenched by slow addition to ice water (100 mL) with consistent stirring. The solution was extracted with EtOAc (2 x 100 mL) and the organic layers were pooled and washed with brine (2 x 50 mL). The organic layers were further dried over anhydrous $MgSO_4$, and solvent removed *in vacuo*. The crude residue was purified by flash chromatography (1:5 EtOAc/Hex) to yield compound **43** (5.78 g, 69%) as a dark brown oil. **^{1}H NMR** (500 MHz, $CDCl_3$) δ 8.85 (d, J = 2.8 Hz, 1H), 8.66 (dd, J = 8.8, 2.8 Hz, 1H), 7.60 (d, J = 8.8 Hz, 1H) ppm; **^{13}C NMR** (126 MHz, $CDCl_3$) δ 162.9, 160.7, 143.7, 132.7, 125.6, 119.8 ppm.

N-(2,4-dimethoxybenzyl)-2-fluoro-5-nitrobenzenesulfonamide (**45**)

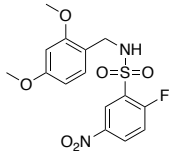

2-fluoro-5-nitrobenzenesulfonyl chloride (**43**) (3.54 g, 14.7 mmol) and $NaHCO_3$ (2.48 g, 29.6 mmol) are suspended in CH_2Cl_2 (20 mL). A solution of 1-(2,4-dimethoxyphenyl)methanamine (2.22 mL, 14.7 mmol) in CH_2Cl_2 (5 mL) is added dropwise. The reaction was stirred for 6 hours under N_2 at room temperature until TLC showed consumption of the sulfonyl chloride. The reaction mixture was then diluted with water and the aqueous components extracted with CH_2Cl_2 (2 x 30 mL). Organic extractions pooled and washed with brine (2 x 30 mL), then dried over $MgSO_4$ and concentrated *in vacuo*. Compound **45** was obtained as a yellow solid without further purification (2.80 g, 51%). **^{1}H NMR** (500 MHz, $CDCl_3$) δ 8.40 (d, J = 2.8 Hz, 1H), 8.24 (dd, J = 8.8, 2.8 Hz, 1H), 7.10 (t, J = 8.8 Hz, 1H), 6.87 (d, J = 8.2 Hz, 1H), 6.15 (dd, J = 8.2, 2.3 Hz, 1H), 6.09 (d, J = 2.3 Hz, 1H), 5.62 (t, J = 6.5 Hz, 1H), 4.25 (d, J = 6.3 Hz, 2H),

3.71 (s, 3H), 3.67 (s, 3H) ppm; **^{13}C NMR** (126 MHz, $CDCl_3$) δ 161.0, 158.1, 143.5, 131.2, 129.1, 126.5, 126.4, 117.4, 117.2, 115.5, 103.0, 98.4, 55.3, 55.1, 44.5 ppm; **LRMS (+ESI)** m/z: 393 ($[M+Na]^+$, 100); **(-ESI)** m/z: 369 ($[M-H]^-$, 100); **HRMS (+ESI)** Calc. for $C_{15}H_{15}FN_2NaO_6S$ $[M+Na]^+$: 393.05271, found: 393.05334; **(-ESI)** Calc. for $C_{15}H_{14}FN_2O_6S$ $[M-H]^-$: 369.05621, found: 369.05609.

2-(3-chlorophenoxy)-*N*-(2,4-dimethoxybenzyl)-5-nitrobenzenesulfonamide (**46**)

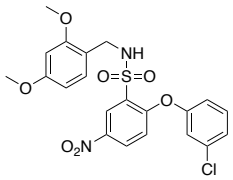

Compound **46** was synthesised from **45** (1.40 g, 3.78 mmol) and 3-chlorophenol (438 µL, 4.16 mmol) according to **General Procedure A** and was obtained as a yellow solid (1.63 g, 90%) following purification by flash chromatography (1:9 EtOAc:Hex).**^{1}H NMR** (500 MHz, $CDCl_3$) δ 8.66 (d, J = 2.8 Hz, 1H), 8.17 (dd, J = 9.1, 2.8 Hz, 1H), 7.37 (t, J = 8.1 Hz, 1H), 7.30 – 7.27 (m, 1H), 6.93 (t, J = 2.2 Hz, 1H), 6.91 – 6.85 (m, 2H), 6.74 (d, J = 9.1 Hz, 1H), 6.27 – 6.18 (td, 2H), 5.60 (t, J = 6.4 Hz, 1H), 4.26 (d, J = 6.3 Hz, 2H), 3.71 (s, 3H), 3.69 (s, 3H) ppm; **^{13}C NMR** (126 MHz, $CDCl_3$) δ 161.0, 158.7, 158.3, 154.4, 142.1, 135.9, 131.7, 131.3, 131.2, 128.7, 126.6, 126.5, 121.1, 118.9, 116.8, 116.3, 103.5, 98.6, 55.4, 44.0 ppm; **LRMS (+ESI)** m/z: 501/503 ($[M+Na]^+$, 100); **(-ESI)** m/z: 477/479 ($[M-H]^-$, 100); **HRMS (+ESI)** Calc. for $C_{21}H_{19}ClN_2NaO_7S$ $[M+Na]^+$: 501.04937/503.04627, found: 501.04992/503.04717; **(-ESI)** Calc. for $C_{21}H_{18}ClN_2O_7S$ $[M-H]^-$: 477.05287/479.04977, found: 477.05288/479.05006.

5-amino-2-(3-chlorophenoxy)-*N*-(2,4-dimethoxybenzyl)benzenesulfonamide (**47**)

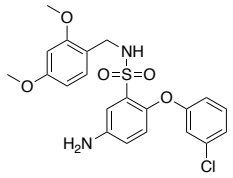

Compound **47** was synthesised from (1.36 g, 2.83 mmol) according to **General Procedure B** and was obtained as a brown crystalline solid (1.08 g, 73%) following purification by flash chromatography (1:99 EtOAc/CH_2Cl_2). **^{1}H NMR** (400 MHz, $CDCl_3$) δ 7.25 – 7.16 (m, 1H), 7.06 (dd, J = 8.0, 1.8 Hz, 1H), 6.93 (d, J = 8.6 Hz, 1H), 6.88 (t, J = 2.2 Hz, 1H), 6.77 (td, J = 8.6, 2.4 Hz, 2H), 6.65 (d, J = 8.6 Hz, 1H), 6.32 – 6.27 (m, 2H), 5.43 (t, J = 6.3 Hz, 1H), 5.29 (s, 2H)4.13 (d, J = 6.3 Hz, 2H), 3.76 (s, 3H), 3.72 (s, 3H) ppm; **^{13}C NMR** (101 MHz, $CDCl_3$)

δ 160.8, 158.4, 157.9, 145.4, 141.7, 135.1, 132.5, 130.7, 130.5, 123.8, 121.2, 120.3, 118.8, 116.8, 116.6, 116.5, 103.7, 98.3, 55.4, 55.2, 43.8 ppm; **LRMS (+ESI**) m/z: 471/473 ($[M+Na]^+$, 100); **(-ESI)** m/z: 447/449 ($[M-H]^-$, 100); **HRMS (+ESI)** Calc. for $C_{21}H_{21}ClN_2NaO_5S$ $[M+Na]^+$: 471.07519/473.07224, found: 471.07572/473.07295.

N-(4-(3-chlorophenoxy)-3-(*N*-(2,4-dimethoxybenzyl)sulfamoyl)phenyl)-2-phenylacetamide (**48**)

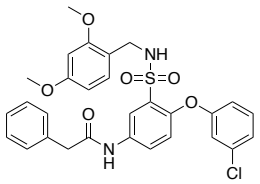

Compound **47** (200.2 mg, 0.44 mmol) was dissolved in CH_2Cl_2 at 0 °C. $^iPr_2NEt$ (388 µL, 2.23 mmol) and phenylacetyl chloride (80 µL, 0.61 mmol) were added dropwise to the solution. Reaction mixture was allowed to come to room temperature and stirred under a N_2 atmosphere until TLC showed consumption of aniline. The reaction mixture was then washed with saturated $NaHCO_3$, and aqueous layers were extracted with CH_2Cl_2. Pooled organic layers were washed with brine, dried over $MgSO_4$ and concentrated *in vacuo*. Compound **48** was obtained as a yellow crystalline solid (134.2 mg, 53%) following purification by flash chromatography (1:1 EtOAc:Hex). **^{1}H NMR** (300 MHz, $CDCl_3$) δ 8.10 (dd, J = 9.0, 2.7 Hz, 1H), 7.83 (s, 1H), 7.54 (d, J = 2.7 Hz, 1H), 7.40 – 7.38 (m, 1H), 7.36 – 7.29 (m, 3H), 7.26 (s, 1H), 7.22 (d, J = 8.1 Hz, 1H), 7.11 (ddd, J = 8.0, 2.0, 1.0 Hz, 1H), 6.89 (t, J = 2.2 Hz, 1H), 6.84 (d, J = 8.2 Hz, 1H), 6.79 (ddd, J = 8.2, 2.4, 1.0 Hz, 1H), 6.72 (d, J = 9.0 Hz, 1H), 6.25 (d, J = 2.3 Hz, 1H), 6.20 (dd, J = 8.2, 2.4 Hz, 1H), 5.54 (t, J = 6.3 Hz, 1H), 4.14 (d, J = 6.3 Hz, 2H), 3.72 (s, 2H), 3.68 (s, 3H), 3.68 (s, 3H) ppm; **^{13}C NMR** (75 MHz, $CDCl_3$) δ 169.7, 161.1, 158.4, 156.9, 149.5, 135.4, 134.4, 134.1, 131.2, 130.9, 130.8, 129.6, 129.3, 127.8, 125.7, 124.8, 121.1, 119.7, 117.5, 116.4, 104.0, 98.3, 55.5, 55.3, 44.7, 44.1 ppm; **LRMS (+ESI)** m/z: 589/591 ($[M+Na]^+$, 100), **(-ESI)** m/z: 565/567 ($[M-H]^-$, 100); **HRMS (+ESI)** Calc. for $C_{29}H_{27}ClN_2NaO_6S$ $[M+Na]^+$: 589.11706/591.11395, found 589.11756/591.11491.

N-(4-(3-chlorophenoxy)-3-sulfamoylphenyl)-2-phenylacetamide (**25**)

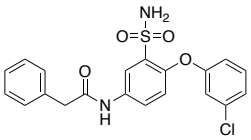

Compound **25** was synthesised from **48** (111.2 mg, 0.20 mmol) according to **General Procedure C** and was obtained as a white solid (57.2 mg, 70%) following purification by flash chromatography (1:4 EtOAc:Hex). **^{1}H NMR** (400 MHz, $CDCl_3$) δ 7.96 (dd, J = 8.9, 2.7 Hz, 1H), 7.69 (d, J = 2.7 Hz, 1H), 7.49 (s, 1H), 7.44 – 7.35 (m, 2H), 7.38 – 7.28 (m, 3H), 7.28 (s, 1H), 7.16 (ddd, J = 8.1, 2.0, 1.0 Hz, 1H), 7.05 (t, J = 2.1 Hz, 1H), 6.93 (ddd, J = 8.3, 2.4, 1.0 Hz, 1H), 6.87 (d, J = 8.9 Hz, 1H), 5.16 (s, 2H), 3.73 (s, 2H) ppm; **^{13}C NMR** (101 MHz, $CDCl_3$) δ 169.8, 156.8, 149.9, 135.6, 134.1, 133.8, 133.1, 131.0, 129.6, 129.5, 128.0, 126.3, 125.2, 120.3, 112.0, 117.7, 77.4, 44.7 ppm; **LRMS (+ESI)** m/z: 439/441 ($[M+Na]^+$, 100), **(-ESI)** m/z: 415/417 ($[M-H]^-$, 100); **HRMS (+ESI)** Calc. for $C_{20}H_{17}ClN_2O_4S$ $[M+H]^+$: 417.06703/419.06408, found 417.06722/419.06427; **HPLC** R_T = 24.34 min, 95.08% (254 nm).

N-(4-(3-chlorophenoxy)-3-(*N*-(2,4-dimethoxybenzyl)sulfamoyl)phenyl)-2-(2-chlorophenyl)acetamide (**49**)

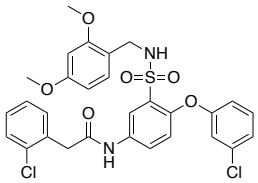

Compound **49** was prepared *via* an acid chloride amide coupling according to **General Procedure D** from **48 (**142 mg, 0.36 mmol) and 2-(2-chlorophenyl)acetic acid (72.1 mg, 0.42 mmol) and was obtained as a pale yellow solid (55.1 mg, 29%) following purification by flash chromatography (1:1 EtOAc:Hex). **^{1}H NMR** (500 MHz, $CDCl_3$) δ 7.99 (dd, J = 9.1, 2.5 Hz, 1H), 7.51 (d, J = 2.6 Hz, 1H), 7.49 – 7.46 (m, 1H), 7.44 – 7.40 (m, 2H), 7.34 – 7.31 (m, 2H), 7.22 (d, J = 8.1 Hz, 1H), 7.12 (d, J = 7.8 Hz, 1H), 6.88 (s, 1H), 6.86 (d, J = 8.1 Hz, 1H), 6.79 (d, J = 8.1 Hz, 1H), 6.72 (d, J = 8.9 Hz, 1H), 6.27 (d, J = 2.3 Hz, 1H), 6.21 (dd, J = 8.5, 2.2 Hz, 1H), 5.47 (t, J = 6.5 Hz, 1H), 4.14 (d, J = 5.9 Hz, 2H), 3.87 (s, 2H), 3.70 (s, 3H), 3.68 (s, 3H) ppm; **^{13}C NMR** (126 MHz, $CDCl_3$) δ 168.1, 161.0, 158.5, 156.8, 149.8, 135.4, 134.6, 133.6, 132.4, 132.0, 131.6, 130.9, 130.9, 130.2, 129.6, 127.8, 125.8, 124.8, 121.4, 119.8, 119.7, 117.6, 116.6, 104.0, 98.3, 55.5, 55.3, 44.0, 42.5 ppm; **LRMS (+ESI)** m/z: 623/625/627 ($[M+Na]^+$, 20), **(-ESI)** m/z: 599/601/603 ($[M-H]^-$, 80), 635/637/639 ($[M+Cl]^-$, 100); **HRMS**

(+ESI) Calc. for $C_{29}H_{26}Cl_2N_2NaO_6S$ $[M+Na]^+$: 623.07808/625.07505/627.07191, found 623.07842/625.07543/627.07282.

N-(4-(3-chlorophenoxy)-3-sulfamoylphenyl)-2-(2-chlorophenyl)acetamide (**51**)

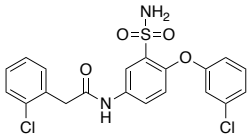

Compound **51** was synthesised from **49** (49.3 mg, 82.0 µmol) according to **General Procedure C** and was obtained as an off white solid (23.6 mg, 64%) following purification by flash chromatography (1:4 EtOAc:Hex). **^{1}H NMR** (400 MHz, DMSO-d_6) δ 10.52 (s, 1H), 8.22 (d, J = 2.7 Hz, 1H), 7.80 (dd, J = 8.9, 2.7 Hz, 1H), 7.44 (ddt, J = 10.2, 7.4, 2.4 Hz, 2H), 7.39 (d, J = 5.3 Hz, 3H), 7.35 – 7.28 (m, 2H), 7.19 (dd, J = 8.0, 2.0 Hz, 1H), 7.12 – 7.06 (m, 2H), 6.98 (dd, J = 8.3, 2.4 Hz, 1H), 3.85 (s, 2H) ppm; **^{13}C NMR** (101 MHz, DMSO-d_6) δ 168.1, 157.9, 147.5, 135.3, 135.2, 133.8, 133.7, 133.6, 132.2, 131.1, 129.0, 128.6, 127.1, 123.9, 123.3, 121.4, 118.7, 118.6, 117.0, 40.7 ppm; **LRMS (+ESI)** m/z: 473/475/477 ($[M+Na]^+$, 100), **(-ESI)** m/z: 449/451/453 ($[M-H]^-$, 100); **HRMS (+ESI)** Calc. for $C_{20}H_{16}Cl_2NaN_2O_4S$ $[M+Na]^+$: 473.01000/475.00705/477.00411, found 473.00932/475.00636/477.00348; **HPLC** R_T = 25.51 min, 97.63% (254 nm). Matched previously reported characterisation data.[141]

2-((3*r*,5*r*,7*r*)-adamantan-1-yl)-*N*-(4-(3-chlorophenoxy)-3-(*N*-(2,4-dimethoxybenzyl)sulfamoyl)phenyl)acetamide (**50**)

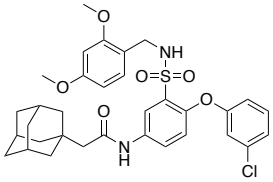

Compound **50** was prepared *via* an acid chloride amide coupling according to **General Procedure D** from **47 (**104 mg, 0.23 mmol) and 1-adamantaneacetic acid (55.5 mg, 0.29 mmol) and was obtained as a yellow crystalline solid (93.2 mg, 64%) following purification by flash chromatography (1:19 EtOAc:Hex). **^{1}H NMR** (300 MHz, $CDCl_3$) δ 8.22 (dd, J = 9.0, 2.7 Hz, 1H), 7.84 (s, 1H), 7.65 (d, J = 2.7 Hz, 1H), 7.23 (d, J = 8.2 Hz, 1H), 7.12 (ddd, J = 8.0, 1.9, 1.0 Hz, 1H), 6.92 (t, J = 2.2 Hz, 1H), 6.86 (d, J = 8.2 Hz, 1H), 6.82 (ddd, J = 8.2, 2.4, 1.0 Hz, 1H), 6.76 (d, J = 9.0 Hz, 1H), 6.29 (d, J = 2.3 Hz, 1H), 6.25 (dd, J = 8.2, 2.4 Hz, 1H), 5.55 (t, J = 6.3 Hz, 1H), 4.16 (d, J = 6.3 Hz, 2H), 3.73 (s, 3H), 3.71 (s, 3H), 2.13 (s, 2H), 2.02 – 1.95 (m, 3H), 1.76 – 1.63 (m, 12H); **^{13}C NMR** (75 MHz, $CDCl_3$) δ 169.9, 161.1, 158.5, 157.0, 149.3,

135.4, 134.4, 131.3, 130.9, 130.8, 125.5, 124.7, 120.9, 119.9, 119.7, 117.5, 116.4, 104.0, 98.4, 55.5, 55.3, 53.6, 52.7, 44.2, 42.7, 36.9, 33.5, 28.8 ppm; **LRMS (+ESI)** m/z: 647/649 ($[M+Na]^+$, 100), **(-ESI)** m/z: 623/625 ($[M-H]^-$, 100); **HRMS (+ESI)** Calc. for $C_{33}H_{37}ClN_2NaO_6S$ $[M+Na]^+$: 647.19531/649.19220, found 647.19552/649.19281.

2-((3*r*,5*r*,7*r*)-adamantan-1-yl)-*N*-(4-(3-chlorophenoxy)-3-sulfamoylphenyl)acetamide (**52**)

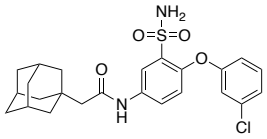

Compound **52** was synthesised from **50** (84.9 mg, 0.14 mmol) according to **General Procedure C** and was obtained as an off white solid (54.5 mg, 84.5%) following purification by flash chromatography (1:1 EtOAc:Hex). **^{1}H NMR** (400 MHz, $CDCl_3$) δ 8.10 (dd, J = 9.0, 2.7 Hz, 1H), 7.79 (d, J = 2.7 Hz, 1H), 7.69 (s, 1H), 7.29 (t, J = 8.2 Hz, 1H), 7.16 (dd, J = 7.9, 2.0 Hz, 1H), 7.07 (t, J = 2.3 Hz, 1H), 6.96 (dd, J = 8.2, 2.5 Hz, 1H), 6.91 (d, J = 8.9 Hz, 1H), 5.29 (s, 2H), 2.11 (s, 2H), 2.02 – 1.93 (m, 3H), 1.77 - 1.53 (m, 12H); **^{13}C NMR** (101 MHz, $CDCl_3$) δ 170.2, 156.9, 149.6, 135.6, 134.2, 133.1, 131.0, 126.1, 125.1, 120.5, 119.9, 119.7, 117.7, 52.7, 42.8, 36.8, 33.6, 28.8 ppm; **LRMS (+ESI)** m/z: 497/499 ($[M+Na]^+$, 100), **(-ESI)** m/z: 473/475 ($[M-H]^-$, 100); **HRMS (+ESI)** Calc. for $C_{24}H_{27}ClNaN_2O_4S$ $[M+Na]^+$: 497.12723/499.12412, found 497.12703/499.12410; **HPLC** R_T = 28.96 min, 98.01% (254 nm).

2-bromo-1-((4-fluorobenzyl)oxy)-4-nitrobenzene (**61**)

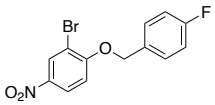

4-fluorobenzylbromide (320 µL, 2.57 mmol) and caesium carbonate (822 mg, 2.52 mmol) were added to a stirring solution of 2-bromo-4-nitrophenol (489 mg, 2.24 mmol) in acetonitrile (10 mL). The reaction was then stirred at 110 °C under a N_2 atmosphere for 2 hours, or until TLC confirmed consumption of starting material. The solvent was evaporated and the remaining solid was washed with EtOAc. Precipitate was collected via vacuum filtration and washed with EtOAc. The filtrate was then partitioned with H_2O and the aqueous layer was washed with $NaHCO_3$ and subsequent EtOAc. Pooled organic layers were then washed with brine and dried over anhydrous $MgSO_4$. Solvent was removed *in vacuo*. The crude residue was then washed with CH_2Cl_2 to yield compound **61** as a yellow solid (652 mg, 89%). **^{1}H NMR** (400 MHz, $CDCl_3$) δ 8.49 (d, J = 2.7 Hz, 1H), 8.19 (dd, J = 9.1, 2.7 Hz, 1H), 7.45 (dd, J = 8.8, 5.3 Hz, 2H), 7.15 – 7.08 (m, 2H), 6.99 (d, J = 9.1 Hz, 1H), 5.22 (s, 2H) ppm; **^{19}F NMR** (376 MHz,

$CDCl_3$) δ -113.1 ppm; **^{13}C NMR** (101 MHz, $CDCl_3$) δ 162.9 (d, J = 247.5 Hz), 160.0, 142.0, 130.9 (d, J = 3.3 Hz), 129.4, 129.1 (d, J = 8.4 Hz), 124.7, 116.0 (d, J = 21.8 Hz), 112.67, 112.3, 71.0 ppm; **LRMS (+APCI)** m/z: 325/327 ([M+H]$^+$, 100); **HRMS (+APCI)** for $C_{13}H_9BrFNO_3$ [M+H]$^+$: 325.98226/327.98021, found 325.98286/327.98083.

benzyl(2-((4-fluorobenzyl)oxy)-5-nitrophenyl)sulfane (**64**)

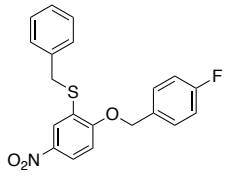

Compound **64** was synthesised from **61** (589 mg, 1.81 mmol) and benzyl mercaptan (430 µL, 3.68 mmol) according to **General Procedure E**. $Pd_2(dba)_3$ (85.5 mg, 0.09 mmol), Xantphos (115.1 mg, 0.20 mmol) and $^iPr_2NEt$ (705 µL, 4.05 mmol) were utilised as the Pd-catalyst, ligand and base respectively. Compound **A57** was obtained as a yellow solid (468 mg, 70%) following purification by flash chromatography (1:9 EtOAc/Hex). **^{1}H NMR** (400 MHz, $CDCl_3$) δ 8.13 (d, J = 2.7 Hz, 1H), 8.03 (dd, J = 8.9, 2.7 Hz, 1H), 7.43 (dd, J = 8.5, 5.4 Hz, 2H), 7.39 – 7.34 (m, 2H), 7.34 – 7.28 (m, 2H), 7.28 – 7.25 (m, 1H), 7.09 (t, J = 8.7 Hz, 2H), 6.91 (d, J = 9.0 Hz, 1H), 5.19 (s, 2H), 4.18 (s, 2H) ppm; **^{19}F NMR** (376 MHz, $CDCl_3$) δ -113.3 ppm; **^{13}C NMR** (101 MHz, $CDCl_3$) δ 162.9 (d, J = 247.2 Hz), 160.3, 142.1, 136.0, 131.2 (d, J = 3.5 Hz), 129.2 (d, J = 8.3 Hz), 129.1, 128.9, 128.6, 127.8, 123.4, 122.9, 115.9 (d, J = 21.7 Hz), 110.9, 70.7, 36.7 ppm; **LRMS (+APCI)** m/z: 370 ([M+H]$^+$, 100); **HRMS (+APCI)** for $C_{20}H_{16}FNO_3S$ [M+H]$^+$: 370.09077, found 370.09103.

3-(benzylthio)-4-((4-fluorobenzyl)oxy)aniline (**68**)

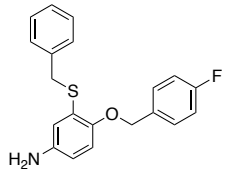

Compound **68** was synthesised from **64** (486.3 mg, 1.32 mmol) according to **General Procedure B** in a THF/MeOH solution (1:1 v/v, 10 mL) and was obtained as a brown solid (312.8 mg, 70%) following purification by flash chromatography (1:1 EtOAc:Hex). **^{1}H NMR** (400 MHz, $CDCl_3$) δ 7.43 (dd, J = 8.5, 5.6 Hz, 2H), 7.32 – 7.18 (m, 5H), 7.05 (t, J = 8.7 Hz, 2H), 6.72 (d, J = 8.4 Hz, 1H), 6.63 (d, J = 2.7 Hz, 1H), 6.47 (dd, J = 8.5, 2.8 Hz, 1H), 4.99 (s, 2H), 4.09 (s, 2H) ppm; **^{19}F NMR** (376 MHz, $CDCl_3$) δ -114.7 ppm; **^{13}C NMR** (101 MHz,

$CDCl_3$) δ 162.6 (d, J = 245.5 Hz), 149.8, 141.1, 137.6, 133.3 (d, J = 3.2 Hz), 129.3 (d, J = 8.1 Hz), 129.1, 128.6, 127.3, 127.1, 117.3, 115.5 (d, J = 21.5 Hz), 115.2, 113.9, 71.4, 37.4 ppm; **LRMS (+ESI)** m/z: 340 ([M+H]$^+$, 100); **HRMS (+ESI)** Calc. for $C_{20}H_{18}FNNaOS$ [M+Na]$^+$: 362.09853, found 362.09920; **HRMS (-ESI)** Calc. for $C_{20}H_{18}FNOS$.

N-(3-(benzylthio)-4-((4-fluorobenzyl)oxy)phenyl)-2-(2-chlorophenyl)acetamide (**72**)

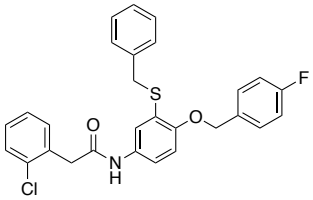

Compound **72** was synthesised from **68** (139.9 mg, 0.41 mmol) and 2-(2-chlorophenyl)acetic acid (90 mg, 0.53 mmol) according to **General Procedure D** and was obtained as an off white solid (75.6 mg, 37%) following purification by flash chromatography (1:9 EtOAc:Hex). **^{1}H NMR** (300 MHz, $CDCl_3$) δ 7.45 – 7.35 (m, 5H), 7.33 – 7.27 (m, 5H), 7.24 – 7.18 (m, 3H), 7.09 – 7.00 (m, 3H), 6.78 (d, J = 8.8 Hz, 1H), 5.04 (s, 2H), 4.08 (s, 2H), 3.82 (s, 2H) ppm; **^{19}F NMR** (282 MHz, $CDCl_3$) δ -114.2 ppm **^{13}C NMR** (75 MHz, $CDCl_3$) δ 167.8, 162.6 (d, J = 245.9 Hz), 153.1, 137.1, 134.5, 132.8, 132.6 (d, J = 3.0 Hz), 131.9, 131.7, 130.5, 130.1, 129.2, 129.2 (d, J = 8.1 Hz), 128.6, 127.7, 127.3, 126.9, 121.7, 119.1, 115.6 (d, J = 21.5 Hz), 112.9, 70.5, 42.6, 37.2 ppm; **LRMS (+ESI)** m/z: 514 ([M+Na]$^+$, 100) , **(-ESI)** m/z: 490 ([M-H]$^-$, 100); **HRMS (+ESI)** Calc. for $C_{28}H_{23}ClFNNaO_2S$ [M+Na]$^+$: 514.10143/516.09832, found 514.10207/516.09922.

2-(2-chlorophenyl)-*N*-(4-((4-fluorobenzyl)oxy)-3-sulfamoylphenyl)acetamide (**81**)

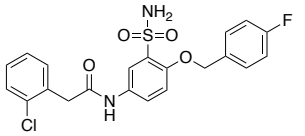

Compound **81** was synthesised from **72** (75.6 mg, 0.15 mmol) and DCDMH (61 mg, 0.31 mmol) according to **General Procedure F** and was obtained as an off white solid (34.3 mg, 50%) following purification by flash chromatography (1:19 EtOAc:Hex). **^{1}H NMR** (400 MHz, DMSO-d_6) δ 10.30 (s, 1H), 8.05 (d, J = 2.7 Hz, 1H), 7.69 (dd, J = 8.9, 2.7 Hz, 1H), 7.56 (dd, J = 8.5, 5.7 Hz, 2H), 7.46 – 7.38 (m, 2H), 7.33 – 7.26 (m, 2H), 7.19 (t, J = 8.9 Hz, 2H), 7.15 (d, J = 9.0 Hz, 1H), 7.08 (s, 2H), 5.30 (s, 2H), 3.80 (s, 2H) ppm; **^{19}F NMR** (376 MHz, DMSO-d_6) δ -114.7 ppm; **^{13}C NMR** (101 MHz, DMSO-d_6) δ 167.8, 161.6 (d, J = 243.3 Hz), 150.2, 133.8, 133.6, 132.9 (d, J = 3.0 Hz), 132.1, 131.9, 131.6, 129.3 (d, J = 8.2 Hz), 129.0, 128.6, 127.0,

123.9, 119.0, 115.1 (d, J = 21.4 Hz), 114.5, 68.9, 40.6 ppm; **LRMS (-ESI)** m/z: 448/450 ([M-H]$^-$, 100); **HRMS (+ESI)** Calc. for $C_{21}H_{18}ClFN_2NaO_4S$ [M+Na]$^+$: 471.05520/473.05225, found 471.05506/475.05211; **HPLC** R_T = 24.10 min, 95.95% (254 nm).

2-((3*r*,5*r*,7*r*)-adamantan-1-yl)-*N*-(3-(benzylthio)-4-((4-fluorobenzyl)oxy)phenyl)acetamide (**73**)

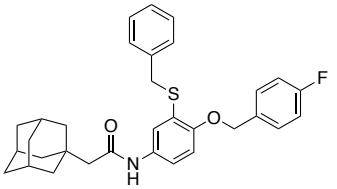

Compound **73** was synthesised from **68** (141.7 mg, 0.42 mmol) and 1-adamantaneacetic acid (100 mg, 0.51 mmol) according to **General Procedure D** and was obtained as an off white solid (177.5 mg, 82%) following purification by flash chromatography (1:9 EtOAc:Hex). **^{1}H NMR** (400 MHz, $CDCl_3$) δ 7.44 (d, J = 2.6 Hz, 1H), 7.41 (dd, J = 8.5, 5.6 Hz, 2H), 7.33 – 7.27 (m, 3H), 7.26 – 7.19 (m, 2H), 7.04 (t, J = 8.7 Hz, 1H), 6.94 (s, 1H), 6.80 (d, J = 8.7 Hz, 1H), 5.05 (s, 2H), 4.10 (s, 2H), 2.05 (s, 2H), 2.01 – 1.96 (m, 3H), 1.75 – 1.60 (m, 12H) ppm; **^{19}F NMR** (376 MHz, $CDCl_3$) δ -114.4 ppm; **^{13}C NMR** (101 MHz, $CDCl_3$) δ 169.3, 162.6 (d, J = 246.1 Hz), 153.0, 137.2, 132.7 (d, J = 3.0 Hz), 132.1, 129.21, 129.18 (d, J = 8.3 Hz), 128.6, 127.3, 126.8, 121.7, 118.9, 115.6 (d, J = 21.6 Hz), 113.1, 70.6, 52.9, 42.8, 37.2, 36.9, 33.4, 28.8 ppm; **LRMS (-ESI)** m/z: 514 ([M-H]$^-$, 100); **HRMS (+ESI)** Calc. for $C_{32}H_{34}FNNaO_2S$ [M+Na]$^+$: 538.21865, found 538.21893.

2-((3*r*,5*r*,7*r*)-adamantan-1-yl)-*N*-(4-((4-fluorobenzyl)oxy)-3-sulfamoylphenyl)acetamide (**82**)

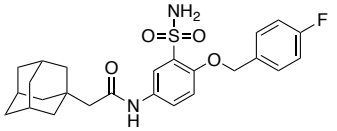

Compound **82** was synthesised from **73** (119 mg, 0.23 mmol) and DCDMH (90.9 mg, 0.46 mmol) according to **General Procedure F** and was obtained as a white solid (66.6 mg, 61%) following purification by flash chromatography (1:19 EtOAc:Hex). **^{1}H NMR** (400 MHz, DMSO-d_6) δ 9.83 (s, 1H), 8.06 (d, J = 2.7 Hz, 1H), 7.69 (dd, J = 9.0, 2.7 Hz, 1H), 7.60 – 7.52 (m, 2H), 7.24 – 7.14 (m, 2H), 7.12 (d, J = 9.0 Hz, 1H), 7.06 (s, 2H), 5.30 (s, 2H), 2.01 (s, 2H), 1.92 (s, 3H), 1.63 (dd, J = 22.4, 7.6 Hz, 12H) ppm; **^{19}F NMR** (376 MHz, DMSO-d_6) δ -114.72 ppm; **^{13}C NMR** (101 MHz, DMSO-d_6) δ 168.9, 161.6 (d, J = 243.1 Hz), 149.9, 133.0 (d, J = 2.8 Hz), 132.0, 131.5, 129.3 (d, J = 8.1 Hz), 123.8, 118.9, 115.1 (d, J = 21.3 Hz), 114.4, 68.9,

50.7, 42.1, 36.4, 32.7, 28.0 ppm; **LRMS (+ESI)** m/z: 495 ([M+Na]$^+$, 100), **(-ESI)** m/z: 471 ([M-H]$^-$, 100); **HRMS (+ESI)** Calc. for $C_{25}H_{29}FN_2NaO_4S$ [M+Na]$^+$: 495.17243, found 495.17240; **HPLC** R_T = 27.70 min, 95.99% (254 nm).

benzyl(2-fluoro-5-nitrophenyl)sulfane (**57**)

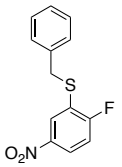

Compound **57** was synthesised from 2-bromo-1-fluoro-4-nitrobenzene (2.58 g, 11.7 mmol) and benzyl mercaptan (2.60 mL, 22.2 mmol) according to **General Procedure E**. $Pd_2(dba)_3$ (440 mg, 0.48 mmol), Xantphos (570 mg, 0.99 mmol) and $^iPr_2NEt$ (4.40 mL, 25.3 mmol) were utilised as the Pd-catalyst, ligand and base respectively. Compound **57** was obtained as a yellow solid (2.07 g, 67%) following purification by flash chromatography (1:99 EtOAc/Hex). **^{1}H NMR** (400 MHz, DMSO-*d*$_6$) δ 8.22 (dd, *J* = 6.5, 2.8 Hz, 1H), 8.14 – 8.08 (m, 1H), 7.39 (d, *J* = 7.5 Hz, 2H), 7.36 – 7.29 (m, 2H), 7.29 – 7.23 (m, 2H), 4.40 (s, 2H) ppm; **^{19}F NMR** (376 MHz, DMSO-*d*$_6$) δ -101.2 ppm; **^{13}C NMR** (101 MHz, DMSO-*d*$_6$) δ 162.8 (d, *J* = 252.8 Hz), 144.3 (d, *J* = 3.0 Hz), 136.1, 128.9, 128.5, 127.5, 126.1 (d, *J* = 19.9 Hz), 125.0 (d, *J* = 4.6 Hz), 123.5 (d, *J* = 10.1 Hz), 116.5 (d, *J* = 25.0 Hz), 41.6 ppm; **LRMS (+APCI)** m/z: 263 ([M+H]$^+$, 100); **HRMS (+APCI)** for $C_{13}H_{10}FNO_2S$ [M+H]$^+$: 263.04108, found 263.04139.

2-((2-(benzylthio)-4-nitrophenoxy)methyl)pyridine (**65**)

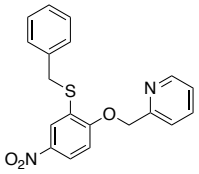

Prepared according to **General Procedure A** from **57** (876 mg, 3.33 mmol), 2-pyridinemethanol (350 µL, 3.66 mmol) and Cs_2CO_3 (1.19 g, 3.66 mmol) in CH_3CN (15 mL). Compound **65** was obtained as an off white solid (526 mg, 45%) following purification by flash chromatography (1:19 EtOAc:Hex). **^{1}H NMR** (300 MHz, $CDCl_3$) δ 8.60 (d, *J* = 4.8 Hz, 1H), 8.14 (d, *J* = 2.6 Hz, 1H), 8.03 (dd, *J* = 9.0, 2.7 Hz, 1H), 7.75 (td, *J* = 7.7, 1.8 Hz, 1H), 7.57 (d, *J* = 7.9 Hz, 1H), 7.44 – 7.35 (m, 2H), 7.38 – 7.25 (m, 4H), 6.95 (d, *J* = 9.0 Hz, 1H), 5.35 (s, 2H), 4.22 (s, 2H) ppm; **^{13}C NMR** (75 MHz, $CDCl_3$) δ 160.0, 155.8, 149.4, 142.2, 137.3, 136.0, 129.2, 128.9, 128.4, 127.8, 123.4, 123.3, 123.0, 121.4, 111.0, 71.8, 36.7 ppm; **LRMS (+ESI)** m/z 353 ([M+H]$^+$, 70), 375 ([M+Na]$^+$, 100); **HRMS (+ESI)** Calc. for $C_{19}H_{16}N_2NaO_3S$

[M+Na]$^+$: 375.07738, found 375.07796, **(-ESI)** Calc. for $C_{19}H_{16}N_2O_3S$ [M-H]$^-$: 351.08089, found 351.08068;

3-(benzylthio)-4-(pyridin-2-ylmethoxy)aniline (**69**)

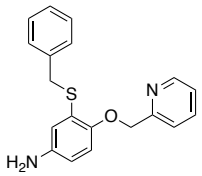

Compound **69** was synthesised from **65** (404 mg, 1.15 mmol) according to **General Procedure B** in THF/MeOH (1:1) and was obtained as a brown solid (225 mg, 61%) following purification by flash chromatography (1:19 EtOAc:Hex). **^{1}H NMR** (300 MHz, $CDCl_3$) δ 8.56 (d, J = 4.9 Hz, 1H), 7.69 (dd, J = 7.4, 1.8 Hz, 1H), 7.64 (d, J = 7.3 Hz, 1H), 7.37 – 7.27 (m, 4H), 7.24 – 7.16 (m, 2H), 6.73 (d, J = 8.5 Hz, 1H), 6.64 (d, J = 2.7 Hz, 1H), 6.47 (dd, J = 8.5, 2.8 Hz, 1H), 5.18 (s, 2H), 4.12 (s, 2H) ppm; **^{13}C NMR** (75 MHz, $CDCl_3$) δ 157.7, 149.4, 148.9, 140.8, 137.4, 136.9, 128.9, 128.5, 127.2, 126.5, 122.5, 121.3, 117.2, 113.9, 113.9, 71.9, 37.3 ppm; **LRMS (+ESI)** m/z: 323 ([M+H]$^+$, 100), 345 ([M+Na]$^+$, 75); **HRMS (+ESI)** Calc. for $C_{19}H_{18}N_2NaOS$ [M+Na]$^+$: 345.10321, found 345.10372, **(-ESI)** Calc. for $C_{19}H_{18}N_2OS$ [M-H]$^-$: 321.10671, found 321.10671.

N-(3-(benzylthio)-4-(pyridin-2-ylmethoxy)phenyl)-2-(2-chlorophenyl)acetamide (**74**)

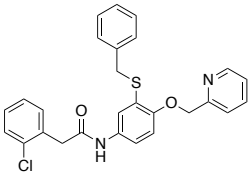

Compound **74** was synthesised from **69** (102.4 mg, 0.32 mmol) and 2-(2-chlorophenyl)acetic acid (64.6 mg, 0.38 mmol) according to **General Procedure D** and was obtained as a yellow solid (71.3 mg, 47%) following purification by flash chromatography (1:19 EtOAc:Hex). **^{1}H NMR** (300 MHz, $CDCl_3$) δ 8.55 (d, J = 4.3 Hz, 1H), 7.69 (td, J = 7.7, 1.8 Hz, 1H), 7.57 (d, J = 7.8 Hz, 1H), 7.45 (d, J = 2.9 Hz, 1H), 7.43 – 7.37 (m, 1H), 7.36 – 7.27 (m, 5H), 7.25 – 7.18 (m, 3H), 7.14 (dd, J = 8.7, 2.6 Hz, 1H), 7.06 (s, 1H), 6.79 (d, J = 8.8 Hz, 1H), 5.22 (s, 2H), 4.13 (s, 2H), 3.82 (s, 2H) ppm; **^{13}C NMR** (75 MHz, $CDCl_3$) δ 167.8, 157.2, 152.8, 149.2, 137.1, 134.5, 132.8, 131.9, 131.7, 130.1, 129.4, 129.2, 128.6, 127.7, 127.4, 126.6, 122.8, 121.7, 121.3, 119.1, 112.4, 71.4, 42.6, 37.2 ppm; **LRMS (-ESI)** m/z: 473/475 ([M-H]$^-$, 100; **HRMS (+ESI)** Calc. for $C_{27}H_{23}ClN_2NaO_2S$ [M+Na]$^+$: 497.10610/499.10299, found 497.10700/499.10411.

2-(2-chlorophenyl)-N-(4-(pyridin-2-ylmethoxy)-3-sulfamoylphenyl)acetamide **(83)**

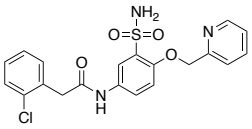

Compound **83** was synthesised from **74** (66.6 mg, 0.14 mmol) and DCDMH (55.3 mg, 0.28 mmol) according to **General Procedure F** and was obtained as a white powder (34 mg, 56%) following purification by flash chromatography (1:1 EtOAc:Hex). **^{1}H NMR** (400 MHz, DMSO-d_6) δ 10.33 (s, 1H), 8.58 (ddd, J = 4.9, 1.8, 0.9 Hz, 1H), 8.07 (d, J = 2.7 Hz, 1H), 7.84 (td, J = 7.7, 1.8 Hz, 1H), 7.74 (dd, J = 8.9, 2.7 Hz, 1H), 7.58 (d, J = 7.8 Hz, 1H), 7.47 – 7.38 (m, 2H), 7.40 – 7.32 (m, 3H), 7.34 – 7.27 (m, 2H), 7.21 (d, J = 9.0 Hz, 1H), 5.36 (s, 2H), 3.81 (s, 2H) ppm; **^{13}C NMR** (101 MHz, DMSO-d_6) δ 167.8, 156.1, 150.3, 149.0, 137.2, 133.8, 133.6, 132.2, 132.1, 131.8, 129.0, 128.6, 127.0, 123.9, 123.1, 121.6, 118.7, 114.5, 70.7, 40.6 ppm; **LRMS (+ESI)** m/z: 454/456 ([M+Na]$^+$, 100), **(-ESI)** m/z: 430/432 ([M-H]$^-$, 100); **HRMS (+ESI)** Calc. for $C_{20}H_{18}ClN_3O_4S$ [M+H]$^+$: 432.07793/434.07498, found 432.07813/434.07516; **HPLC** R_T = 17.10 min, 98.95% (254 nm).

2-((3r,5r,7r)-adamantan-1-yl)-N-(3-(benzylthio)-4-(pyridin-2-ylmethoxy)phenyl)acetamide (**75**)

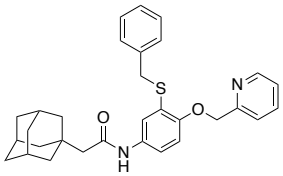

Compound **75** was synthesised from **69** (104.4 mg, 0.32 mmol) and 1-adamantaneacetic acid (75.6 mg, 0.39 mmol) according to **General Procedure D** and was obtained as an off white powder (125.1 mg, 77%) following purification by flash chromatography (1:1 EtOAc:Hex). **^{1}H NMR** (300 MHz, $CDCl_3$) δ 8.57 (d, J = 4.9 Hz, 1H), 7.71 (td, J = 7.7, 1.8 Hz, 1H), 7.60 (d, J = 7.8 Hz, 1H), 7.53 (d, J = 2.6 Hz, 1H), 7.38 – 7.33 (m, 2H), 7.34 – 7.25 (m, 2H), 7.23 (dd, J = 7.9, 2.5 Hz, 2H), 7.19 (d, J = 2.3 Hz, 1H), 6.88 (s, 1H), 6.82 (d, J = 8.8 Hz, 1H), 5.24 (s, 2H), 4.16 (s, 2H), 2.06 (s, 2H), 2.02 – 1.96 (m, 3H), 1.78 – 1.60 (m, 12H) ppm; **^{13}C NMR** (75 MHz, $CDCl_3$) δ 169.3, 157.3, 152.6, 149.2, 137.2, 137.1, 132.0, 129.3, 128.6, 127.3, 126.5, 122.8, 121.5, 121.3, 118.9, 112.5, 71.5, 53.0, 42.8, 37.2, 36.9, 33.4, 28.8 ppm; **LRMS (+ESI)** m/z: 499 ([M+H]$^+$, 100), **(-ESI)** m/z: 497 ([M-H]$^-$, 100); **HRMS (+ESI)** Calc. for $C_{31}H_{34}N_2NaO_2S$ [M+Na]$^+$: 521.22332, found 521.22372.

2-((3r,5r,7r)-adamantan-1-yl)-N-(4-(pyridin-2-ylmethoxy)-3-sulfamoylphenyl)acetamide **(84)**

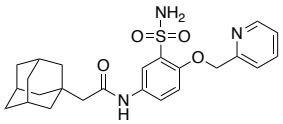

Compound **84** was synthesised from **75** (88.3 mg, 0.18 mmol) and DCDMH (70 mg, 0.35 mmol) according to **General Procedure F** and was obtained as a white powder (43.5 mg, 54%) following purification by flash chromatography (1:1 EtOAc:Hex). **^{1}H NMR** (400 MHz, DMSO-d_6) δ 9.87 (s, 1H), 8.58 (ddd, J = 4.8, 1.8, 0.9 Hz, 1H), 8.08 (d, J = 2.7 Hz, 1H), 7.84 (td, J = 7.7, 1.8 Hz, 1H), 7.73 (dd, J = 8.9, 2.7 Hz, 1H), 7.58 (d, J = 7.8 Hz, 1H), 7.39 – 7.33 (m, 3H), 7.18 (d, J = 9.0 Hz, 1H), 5.35 (s, 2H), 2.02 (s, 2H), 1.93 (s, 3H), 1.71 – 1.54 (m, 12H) ppm; **^{13}C NMR** (101 MHz, DMSO-d_6) δ 169.0, 156.1, 150.1, 149.0, 137.2, 132.3, 131.7, 123.9, 123.1, 121.6, 118.6, 114.4, 70.7, 50.7, 42.1, 36.4, 32.7, 28.0 ppm; **LRMS (+ESI)** m/z: 478 ([M+Na]$^+$, 100), **(-ESI)** m/z: 454 ([M-H]$^-$, 100); **HRMS (+ESI)** Calc. for $C_{24}H_{29}N_3O_4S$ [M+H]$^+$: 456.19515, found 456.19505; **HPLC** R_T = 20.74 min, 95.88% (254 nm).

2-bromo-1-(3-isopropylphenoxy)-4-nitrobenzene (**62**)

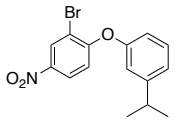

Prepared according to **General Procedure A** from 2-bromo-1-fluoro-4-nitrobenzene (509.1 mg, 2.31 mmol), 3-isopropylphenol (350 µL, 2.55 mmol) and Cs_2CO_3 (979.1 mg, 3.01 mmol) in CH_3CN (6 mL). Compound **62** was obtained as a white crystalline solid (689 mg, 90%) following purification by flash chromatography (1:99 EtOAc:Hex). **^{1}H NMR** (500 MHz, $CDCl_3$) δ 8.54 (d, J = 2.7 Hz, 1H), 8.08 (dd, J = 9.1, 2.7 Hz, 1H), 7.35 (t, J = 7.9 Hz, 1H), 7.15 (ddt, J = 7.8, 1.6, 0.8 Hz, 1H), 6.97 (t, J = 2.1 Hz, 1H), 6.89 (ddd, J = 8.0, 2.5, 1.0 Hz, 1H), 6.83 (d, J = 9.1 Hz, 1H), 2.94 (hept, J = 6.9 Hz, 1H), 1.26 (d, J = 6.9 Hz, 6H) ppm; **^{13}C NMR** (126 MHz, $CDCl_3$) δ 160.5, 154.7, 152.2, 142.8, 130.3, 129.7, 124.4, 124.2, 118.5, 117.7, 116.3, 113.0, 34.2, 24.0 ppm; **LRMS (+APCI)** m/z: 336/338 ([M+H]$^+$, 100); **HRMS (+APCI)** for $C_{15}H_{15}BrNO_3$ [M+H]$^+$: 336.02298/338.02094, found 336.02335/338.02129.

benzyl(2-(3-isopropylphenoxy)-5-nitrophenyl)sulfane (**66**)

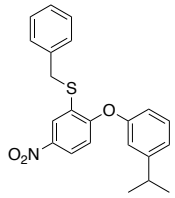

Method A: Prepared according to **General Procedure A** from **57** (493 mg, 1.87 mmol), 3-isopropylphenol (300 µL, 2.19 mmol) and Cs_2CO_3 (835 mg, 2.56 mmol) in CH_3CN (8 mL). Compound **66** was obtained as yellow solid (135 mg, 19%) following purification by flash chromatography (1:99 EtOAc:Hex).

Method B: Prepared according to **General Procedure E** from **62** (597 mg, 1.78 mmol), benzyl mercaptan (420 µL, 3.55 mmol), $Pd_2(dba)_3$ (81.4 mg, 0.089 mmol, 5 mol%), Xantphos (103 mg, 0.18 mmol, 10 mol%), $^iPr_2NEt$ (680 µL, 3.91 mmol) in 1,4-dioxane (10 mL). Compound **66** was obtained fluorescent yellow solid (602 mg, 89%) following purification by flash chromatography (100% Hex).

^{1}H NMR (500 MHz, $CDCl_3$) δ 8.22 (d, J = 2.7 Hz, 1H), 7.94 (dd, J = 9.0, 2.7 Hz, 1H), 7.44 – 7.38 (m, 2H), 7.36 – 7.30 (m, 4H), 7.14 – 7.10 (m, 1H), 6.94 (t, J = 2.1 Hz, 1H), 6.88 – 6.83 (m, 1H), 6.75 (d, J = 9.0 Hz, 1H), 4.25 (s, 2H), 2.93 (hept, J = 7.1 Hz, 1H), 1.26 (d, J = 6.9 Hz, 6H) ppm; **^{13}C NMR** (126 MHz, $CDCl_3$) δ 160.8, 154.9, 152.0, 142.9, 136.1, 130.1, 129.5, 129.1, 129.0, 127.8, 124.5, 123.8, 122.8, 118.5, 117.6, 115.3, 37.0, 34.2, 24.0 ppm; **LRMS (+APCI)** m/z: 380 ([M+H]$^+$, 100); **HRMS (+APCI)** for $C_{22}H_{21}NO_3S$ [M+H]$^+$: 380.13149, found 380.13169.

3-(benzylthio)-4-(3-isopropylphenoxy)aniline (**70**)

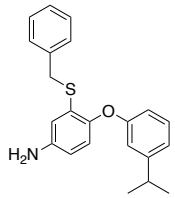

Compound **70** was synthesised from **66** (520 mg, 1.37 mmol) according to **General Procedure B** in MeOH:THF (1:1) and was obtained as a brown oil (364 mg, 76%) following purification by flash chromatography (1:19 EtOAc:Hex). **^{1}H NMR** (300 MHz, $CDCl_3$) δ 7.35 – 7.25 (m, 2H), 7.28 – 7.17 (m, 1H), 7.16 (d, J = 7.9 Hz, 1H), 6.89 (dt, J = 8.5, 1.6 Hz, 1H), 6.83 (t, J = 2.1 Hz, 1H), 6.80 (d, J = 8.5 Hz, 1H), 6.71 – 6.61 (m, 2H), 6.50 (dd, J = 8.5, 2.7 Hz, 1H), 4.08 (s, 2H), 2.86 (p, J = 6.8 Hz, 1H), 1.24 (s, 3H), 1.22 (s, 3H) ppm; **^{13}C NMR** (75 MHz, $CDCl_3$) δ 158.6, 150.9, 146.9, 143.2, 137.4, 129.9, 129.4, 129.1, 128.6, 127.3, 121.9, 120.4, 117.1,

115.3, 114.4, 113.9, 37.7, 34.2, 24.0 ppm; **LRMS (+ESI)** m/z: 350 ($[M+H]^+$, 70), 372 ($[M+Na]^+$, 100), **(-ESI)** m/z: 348 ($[M-H]^-$, 100); **HRMS (-ESI)** Calc. for $C_{22}H_{23}NOS$ $[M-H]^-$: 348.14276, found 348.14299.

N-(3-(benzylthio)-4-(3-isopropylphenoxy)phenyl)-2-(2-chlorophenyl)acetamide (**76**)

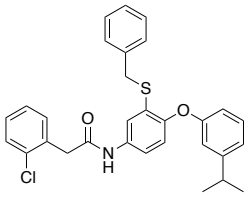

Compound **76** was prepared *via* an acid chloride amide coupling according to **General Procedure D** from **70** (127.3 mg, 0.36 mmol) and 2-(2-chlorophenyl)acetic acid (64.4 mg, 0.38 mmol). Compound **76** was obtained as a white solid (114 mg, 63%) following purification by flash chromatography (1:19 EtOAc:Hex). **^{1}H NMR** (500 MHz, $CDCl_3$) δ 7.49 (d, J = 2.6 Hz, 1H), 7.47 – 7.40 (m, 2H), 7.31 (dd, J = 6.4, 2.5 Hz, 3H), 7.25 (t, J = 7.2 Hz, 2H), 7.23 – 7.17 (m, 3H), 7.12 (s, 1H), 6.94 (d, J = 7.6 Hz, 1H), 6.82 (d, J = 8.7 Hz, 2H), 6.68 (dd, J = 8.2, 2.5 Hz, 1H), 4.11 (s, 2H), 3.84 (s, 2H), 2.85 (hept, J = 6.9 Hz, 1H), 1.22 (d, J = 6.9 Hz, 6H) ppm; **^{13}C NMR** (126 MHz, $CDCl_3$) δ 167.8, 157.4, 151.5, 151.2, 137.1, 134.5, 133.8, 132.7, 131.9, 130.1, 129.5, 129.4, 129.4, 129.2, 128.6, 127.8, 127.3, 121.9, 121.3, 119.8, 119.2, 116.3, 115.1, 42.6, 37.5, 34.2, 24.0 ppm; **LRMS (+ESI)** m/z: 524/526 ($[M+Na]^+$, 100), **(-ESI)** m/z: 500/502 ($[M-H]^-$, 100); **HRMS (+ESI)** Calc. for $C_{30}H_{28}ClNNaO_2S$ $[M+Na]^+$: 524.14215/526.13904, found 524.14290/526/14016.

2-(2-chlorophenyl)-N-(4-(3-isopropylphenoxy)-3-sulfamoylphenyl)acetamide (**85**)

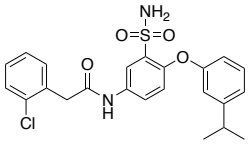

Compound **76** (63 mg, 0.13 mmol) was dissolved in CH_3CN/THF/AcOH/H_2O (80:15:3:2) solvent mixture. NCS (33.5 mg, 0.25 mmol) was added protionwise to the reaction mixture and stirred at rt for 5 h, until TLC indicated conversion of starting material. The reaction mixture was added to H2O, and extracted with EtOAc (3 x 5 mL). Pooled organic phases were washed with brine (1 x 5 mL), dried over $MgSO_4$ and concentrated *in vacuo*. The crude sulfonyl chloride was dissolved in THF (1 mL). $NH_4OH_{(aq)}$ (1 mL) was added dropwise and the reaction was stirred at rt for 1 hour. The reaction mixture was taken up in EtOAc then diluted into H_2O (5 mL) and extracted with EtOAc (3 x 10 mL). The combined organic layers were then washed

with brine (5 mL), dried over $MgSO_4$ and concentrated *in vacuo*. The crude product was purified by flash chromatography (1:4 EtOAc:Hex) to yield compound **85** as a white solid (24 mg, 42%). **^{1}H NMR** (400 MHz, $CDCl_3$) δ 7.91 (dd, J = 9.0, 2.7 Hz, 1H), 7.73 (d, J = 2.7 Hz, 1H), 7.71 (s, 1H), 7.44 – 7.36 (m, 2H), 7.30 – 7.23 (m, 3H), 7.06 (d, J = 7.7 Hz, 1H), 6.96 (t, J = 2.1 Hz, 1H), 6.86 – 6.80 (m, 2H), 5.25 (s, 2H), 3.84 (s, 2H), 2.88 (hept, J = 6.9 Hz, 1H), 1.22 (d, J = 6.9 Hz, 6H) ppm; **^{13}C NMR** (101 MHz, $CDCl_3$) δ 168.6, 155.6, 151.9, 151.2, 134.6, 132.8, 132.5, 132.1, 132.0, 130.1, 130.1, 129.4, 127.7, 126.5, 123.4, 120.1, 119.1, 118.3, 117.2, 42.3, 34.2, 24.0 ppm; **LRMS (+ESI)** m/z: 481/483 ([M+Na]$^+$, 100), **(-ESI)** m/z: 457/459 ([M-H]$^-$, 100); **HRMS (+ESI)** Calc. for $C_{23}H_{23}ClN_2NaO_4S$ [M+Na]$^+$: 481.09593/483.09298, found 481.09599/483.09302; **HPLC** R_T = 26.87 min, 97.02% (254 nm).

N-(4-(4-chloro-3-isopropylphenoxy)-3-sulfamoylphenyl)-2-(2-chlorophenyl)acetamide **(89)**

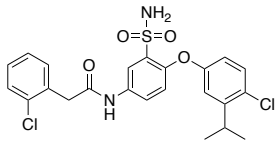

Compound **89** was synthesised from **76** (102.5 mg, 0.20 mmol) and DCDMH (80 mg, 0.41 mmol) according to **General Procedure F** and was obtained as an off white powder (31.2 mg, 31%) following purification by semi-preparative HPLC (30 – 100% v/v CH_3CN in H_2O, 0.1% TFA). **^{1}H NMR** (400 MHz, DMSO-d_6) δ 10.50 (s, 1H), 8.20 (d, J = 2.4 Hz, 1H), 7.76 (dd, J = 8.9, 2.4 Hz, 1H), 7.44 (t, J = 8.7 Hz, 2H), 7.39 (d, J = 8.7 Hz, 1H), 7.36 (s, 2H), 7.33 – 7.29 (m, 2H), 7.15 (d, J = 2.8 Hz, 1H), 6.99 (d, J = 8.9 Hz, 1H), 6.82 (dd, J = 8.7, 2.8 Hz, 1H), 3.84 (s, 2H), 3.30 - 3.23 (m, 1H), 1.19 (d, J = 6.8 Hz, 6H) ppm; **^{13}C NMR** (101 MHz, DMSO-d_6) δ 168.1, 155.8, 148.5, 146.6, 134.6, 134.5, 133.7, 133.7, 132.2, 130.2, 129.0, 128.6, 127.1, 126.7, 123.9, 120.3, 118.8, 117.9, 117.7, 40.7, 30.0, 22.2 ppm; **LRMS (+ESI)** m/z: 515/517/519 ([M+Na]$^+$, 60); **HRMS (+ESI)** Calc. for $C_{23}H_{22}Cl_2N_2NaO_4S$ [M+Na]$^+$: 515.05695/517.05392/519.05078, found 515.05768/517.05506/519.05255; **HPLC** R_T = 28.24 min, 97.07% (254 nm).

2-((3*r*,5*r*,7*r*)-adamantan-1-yl)-*N*-(3-(benzylthio)-4-(3-isopropylphenoxy)phenyl)acetamide (**77**)

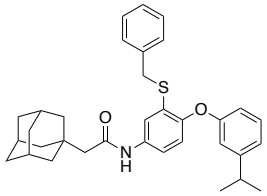

Compound **77** was prepared *via* an acid chloride amide coupling according to **General Procedure D** from **70** (79.9 mg, 0.23mmol) and 1-adamantaneacetic acid (55.4 mg, 0.29 mmol). Compound **77** was obtained as a white solid (94 mg, 78%) following purification by flash chromatography (1:4 EtOAc:Hex). **^{1}H NMR** (500 MHz, $CDCl_3$) δ 7.58 (d, J = 2.6 Hz, 1H), 7.35 – 7.29 (m, 2H), 7.29 – 7.23 (m, 3H), 7.23 – 7.17 (m, 2H), 7.00 (s, 1H), 6.97 – 6.91 (m, 1H), 6.88 – 6.82 (m, 2H), 6.70 (ddd, J = 8.1, 2.6, 0.9 Hz, 1H), 4.14 (s, 2H), 2.93 – 2.81 (m, J = 7.1 Hz, 1H), 2.08 (s, 2H), 2.06 – 1.98 (m, 3H), 1.77 – 1.61 (m, 12H), 1.23 (d, J = 6.9 Hz, 6H) ppm; **^{13}C NMR** (126 MHz, $CDCl_3$) δ 169.4, 157.5, 151.2, 151.2, 137.1, 134.1, 129.5, 129.3, 129.2, 128.6, 127.3, 121.7, 121.3, 119.9, 119.0, 116.3, 115.1, 53.0, 42.8, 37.5, 36.9, 34.2, 33.5, 28.8, 24.0 ppm; **LRMS (+ESI)** m/z: 548 ($[M+Na]^+$, 100), **(-ESI)** m/z: 524 ($[M-H]^-$, 100); **HRMS (+ESI)** Calc. for $C_{34}H_{39}NNaO_2S$ $[M+Na]^+$: 548.25937, found 548.26002.

2-((3*r*,5*r*,7*r*)-adamantan-1-yl)-*N*-(4-(3-isopropylphenoxy)-3-sulfamoylphenyl)acetamide (**86**) and 2-((3*r*,5*r*,7*r*)-adamantan-1-yl)-*N*-(4-(4-chloro-3-isopropylphenoxy)-3-sulfamoylphenyl)acetamide (**90**)

Compound **86** and **90** were synthesised from **77** (93.5 mg, 0.18 mmol) and DCDMH (66.3 mg, 0.34 mmol) according to **General Procedure F**. The two products were isolated following purification by semi-preparative HPLC (30 – 100% v/v CH_3CN in H_2O, 0.1% TFA).

2-((3*r*,5*r*,7*r*)-adamantan-1-yl)-*N*-(4-(3-isopropylphenoxy)-3-sulfamoylphenyl)acetamide (**86**)

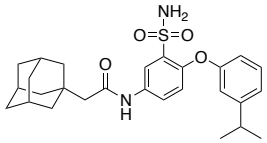

White solid (55.8 mg, 65%); **^{1}H NMR** (500 MHz, $CDCl_3$) δ 8.05 (dd, J = 9.0, 2.7 Hz, 1H), 7.79 (d, J = 2.7 Hz, 1H), 7.58 (s, 1H), 7.32 (d, J = 8.7 Hz, 1H), 7.06 (d, J = 2.9 Hz, 1H), 6.85 (d, J = 9.0 Hz, 1H), 6.79 (dd, J = 8.7, 2.9 Hz, 1H), 5.25 (s, 2H), 3.38 (hept, J = 7.0 Hz, 1H), 2.10 (s, 2H), 2.00 – 1.96 (m, 3H), 1.75 – 1.61 (m, 12H), 1.22 (d, J = 6.9 Hz, 6H) ppm; **^{13}C NMR** (126 MHz, $CDCl_3$) δ 170.1, 154.7, 150.4, 148.3, 133.6, 132.4, 131.0, 129.6, 126.2,

119.8, 119.3, 118.5, 118.2, 52.7, 42.8, 36.8, 33.5, 30.6, 28.8, 22.6 ppm; **LRMS (+ESI)** m/z: 505 ([M+Na]$^+$, 100), **(-ESI)** m/z: 481 ([M-H]$^-$, 100); **HRMS (+ESI)** Calc. for $C_{27}H_{34}N_2NaO_4S$ [M+Na]$^+$: 505.21315, found 505.21346; **HPLC** R_T = 28.97 min, 99.60% (254 nm).

2-((3*r*,5*r*,7*r*)-adamantan-1-yl)-*N*-(4-(4-chloro-3-isopropylphenoxy)-3-sulfamoylphenyl)acetamide (**90**)

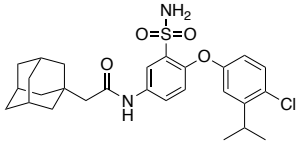

White solid (30.4 mg, 33%). Compound **90** was recrystallised in 2-propanol to yield a white crystalline solid for X-ray crystallography analysis. **^{1}H NMR** (500 MHz, DMSO-d_6) δ 10.02 (s, 1H), 8.21 (d, J = 2.6 Hz, 1H), 7.76 (dd, J = 8.9, 2.7 Hz, 1H), 7.39 (d, J = 8.7 Hz, 1H), 7.34 (s, 2H), 7.15 (d, J = 2.9 Hz, 1H), 6.97 (d, J = 8.9 Hz, 1H), 6.81 (dd, J = 8.7, 2.9 Hz, 1H), 3.28 (p, J = 6.9 Hz, 1H), 2.05 (s, 2H), 1.96 – 1.91 (m, 3H), 1.70 – 1.56 (m, 12H), 1.19 (d, J = 6.9 Hz, 6H) ppm; **^{13}C NMR** (126 MHz, DMSO-d_6) δ 169.3, 155.9, 148.3, 146.6, 134.7, 134.4, 130.2, 126.6, 123.9, 120.2, 118.7, 117.9, 117.6, 50.8, 42.1, 36.4, 32.7, 30.0, 28.0, 22.3 ppm; **LRMS (+ESI)** m/z: 539/541 ([M+Na]$^+$, 100), **(-ESI)** m/z: 515/517 ([M-H]$^-$, 100); **HRMS (+ESI)** Calc. for $C_{27}H_{33}ClN_2NaO_4S$ [M+Na]$^+$: 539.17418/541.17107, found 539.17388/541.17109; **HPLC** R_T = 30.21 min, 96.83% (254 nm). Structure confirmed by X-ray crystallography (Appendix 1).

2-bromo-4-nitro-1-(3-(trifluoromethoxy)phenoxy)benzene (**63**)

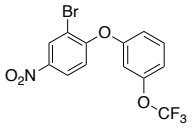

Prepared according to **General Procedure A** from 2-bromo-1-fluoro-4-nitrobenzene (511 mg, 2.32 mmol), 3-(trifluoromethoxy)phenol (340 µL, 2.63 mmol) and Cs_2CO_3 (863 mg, 2.65 mmol) in CH_3CN (7 mL). Compound **63** was obtained as yellow solid (765 mg, 87%) following purification by flash chromatography (1:9 EtOAc:Hex). **^{1}H NMR** (400 MHz, $CDCl_3$) δ 8.55 (d, J = 2.7 Hz, 1H), 8.14 (dd, J = 9.0, 2.7 Hz, 1H), 7.46 (t, J = 8.2 Hz, 1H), 7.13 (dt, J = 8.6, 1.3 Hz, 1H), 7.01 (dd, J = 8.2, 2.4 Hz, 1H), 6.97 (s, 1H), 6.95 (d, J = 9.1 Hz, 1H) ppm; **^{19}F NMR** (376 MHz, $CDCl_3$) δ -57.93 ppm; **^{13}C NMR** (101 MHz, $CDCl_3$) δ 159.1, 155.9, 150.6 (q, J = 1.9 Hz), 143.8, 131.4, 129.9, 124.5, 120.9 (q, J = 259.2 Hz), 118.0, 117.8, 117.7, 114.1, 113.0 ppm; **LRMS (+APCI)** m/z: 378/380 ([M+H]$^+$, 100), **(-APCI)** m/z: 377/379 ([M-H]$^-$,

100); **HRMS (+APCI)** for $C_{13}H_7BrF_3NO_4$ $[M+H]^+$: 377.95833/379.95628, found 377.95871/379.95668.

benzyl(5-nitro-2-(3-(trifluoromethoxy)phenoxy)phenyl)sulfane (**67**)

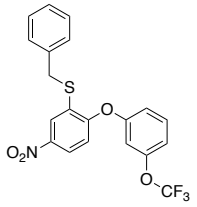

Compound **67** was synthesised from **63** (700 mg, 1.85 mmol) and benzyl mercaptan (450 µL, 3.84 mmol) according to **General Procedure E**. $Pd_2(dba)_3$ (96.5 mg, 0.11 mmol), Xantphos (121 mg, 0.21 mmol) and $^iPr_2NEt$ (700 µL, 4.07 mmol) were utilised as the Pd-catalyst, ligand and base respectively. Compound **67** was obtained as a yellow powder (562 mg, 72%) following purification by flash chromatography (1:99 EtOAc/Hex). **^{1}H NMR** (300 MHz, $CDCl_3$) δ 8.23 (d, J = 2.7 Hz, 1H), 7.98 (dd, J = 8.9, 2.7 Hz, 1H), 7.47 – 7.26 (m, 6H), 7.09 (d, J = 8.2 Hz, 1H), 6.94 (dd, J = 8.0, 2.3 Hz, 1H), 6.90 (s, 1H), 6.85 (d, J = 9.0 Hz, 1H), 4.23 (s, 2H) ppm; **^{19}F NMR** (282 MHz, $CDCl_3$) δ -57.88 ppm; **^{13}C NMR** (75 MHz, $CDCl_3$) δ 159.1, 156.2, 150.5 (q, J = 1.9 Hz), 143.9, 135.7, 131.2, 130.5, 129.1, 128.9, 127.9, 124.5, 122.7, 120.48 (d, J = 258.3 Hz), 117.8, 117.3, 117.0, 112.8, 37.1 ppm; **LRMS (+APCI)** m/z: 422 ($[M+H]^+$, 100); **HRMS (+APCI)** for $C_{20}H_{14}F_3NO_4S$ $[M+H]^+$: 422.06684, found 422.06758.

3-(benzylthio)-4-(3-(trifluoromethoxy)phenoxy)aniline (**71**)

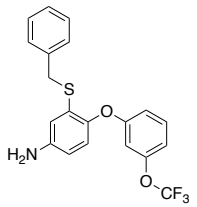

Compound **71** was synthesised from **67** (387 mg, 0.92 mmol) according to **General Procedure B** in MeOH:THF (1:1) and was obtained as an off-white solid (303 mg, 84%) following purification by flash chromatography (1:19 EtOAc:Hex). **^{1}H NMR** (300 MHz, $CDCl_3$) δ 7.31 – 7.20 (m, 6H), 6.89 – 6.84 (m, 1H), 6.82 (d, J = 8.5 Hz, 1H), 6.78 (ddd, J = 8.3, 2.4, 0.9 Hz, 1H), 6.72 (td, J = 2.4, 1.2 Hz, 1H), 6.66 (d, J = 2.7 Hz, 1H), 6.52 (dd, J = 8.5, 2.7 Hz, 1H), 4.05 (s, 2H), 3.59 (s, 2H) ppm; **^{19}F NMR** (282 MHz, $CDCl_3$) δ -57.72 ppm; **^{13}C NMR** (75 MHz, $CDCl_3$) δ 159.9, 150.2 (q, J = 1.5 Hz), 145.4, 144.1, 137.1, 130.5, 130.3, 129.0, 128.6, 127.4, 122.5, 120.55 (q, J = 257.5 Hz), 116.9, 114.6, 114.4, 114.1, 109.4, 37.7 ppm; **LRMS (+ESI)**

m/z: 392 ([M+H]$^+$, 100), **(-ESI)** m/z: 390 ([M-H]$^-$, 100); **HRMS (+ESI)** Calc. for $C_{20}H_{16}F_3NNaO_2S$ [M+Na]$^+$: 414.07461, found 414.07542, **(-ESI)** Calc. for $C_{20}H_{16}F_3NO_2S$ [M+H]$^-$: 390.07811, found 390.07803.

N-(3-(benzylthio)-4-(3-(trifluoromethoxy)phenoxy)phenyl)-2-(2-chlorophenyl)acetamide (**78**)

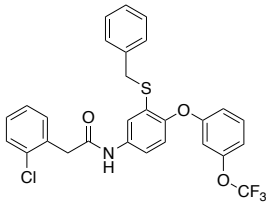

Compound **78** was prepared *via* an acid chloride amide coupling according to **General Procedure D** from **71** (145 mg, 0.37 mmol) and 2-(2-chlorophenyl)acetic acid (82.1 mg, 0.48 mmol). Compound **78** was isolated as a white solid (46.6 mg, 34%) following purification by flash chromatography (1:19 EtOAc:Hex). **^{1}H NMR** (500 MHz, DMSO-d_6) δ 10.35 (s, 1H), 7.88 (d, J = 2.5 Hz, 1H), 7.49 – 7.40 (m, 4H), 7.32 (ddd, J = 7.8, 4.4, 1.8 Hz, 4H), 7.30 – 7.21 (m, 3H), 7.08 – 7.03 (m, 2H), 6.82 (ddd, J = 8.4, 2.4, 0.8 Hz, 1H), 6.80 (d, J = 2.6 Hz, 1H), 4.15 (s, 2H), 3.86 (s, 2H) ppm; **^{19}F NMR** (471 MHz, DMSO-d_6) δ -56.8 ppm; **^{13}C NMR** (126 MHz, DMSO-d_6) δ 168.0, 158.7, 149.2 (q, J = 2.0 Hz), 146.8, 137.0, 136.6, 133.8, 133.7, 132.2, 131.3, 129.7, 129.0, 128.9, 128.6, 128.4, 127.2, 127.1, 121.6, 123.2 – 116.7 (m), 119.2, 117.8, 115.0, 114.5, 109.1, 40.8, 35.6 ppm; **LRMS (+ESI)** m/z: 566 ([M+Na]$^+$, 100), **(-ESI)** m/z: 542 ([M-H]$^-$, 100); **HRMS (+ESI)** Calc. for $C_{28}H_{21}F_3NNaO_3S$ [M+Na]$^+$: 566.07750/568.07439, found 566.07779/568.07506.

2-(2-chlorophenyl)-*N*-(3-sulfamoyl-4-(3-(trifluoromethoxy)phenoxy)phenyl)acetamide (**87**)

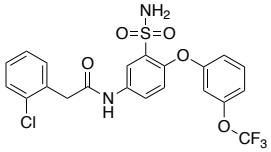

Compound **87** was synthesised from **78** (62.2 mg, 0.11 mmol) and DCDMH (26.0 mg, 0.31 mmol) according to **General Procedure F** and was obtained as a white powder (36.1 mg, 63%) following purification by flash chromatography (1:4 EtOAc:Hex). **^{1}H NMR** (500 MHz, DMSO-d_6) δ 10.53 (s, 1H), 8.23 (d, J = 2.7 Hz, 1H), 7.81 (dd, J = 8.9, 2.7 Hz, 1H), 7.49 (t, J = 8.3 Hz, 1H), 7.46 – 7.42 (m, 2H), 7.41 (s, 2H), 7.35 – 7.28 (m, 2H), 7.14 – 7.09 (m, 2H), 7.05 (td, J = 2.3, 1.1 Hz, 1H), 7.02 (ddd, J = 8.6, 2.3, 0.8 Hz, 1H), 3.85 (s, 2H) ppm; **^{19}F NMR**

(471 MHz, DMSO-d_6) δ -56.8 ppm; **^{13}C NMR** (126 MHz, DMSO-d_6) δ 168.2, 158.2, 149.0 (q, J = 1.8 Hz), 147.4, 135.4, 135.3, 133.7, 133.7, 132.2, 131.1, 129.0, 128.7, 127.1, 123.9, 121.5, 120.0 (dq, J = 9737.9, 256.6 Hz), 118.7, 117.1, 115.5, 111.5, 40.8 ppm; **LRMS (+ESI)** m/z: 523/525 ([M+Na]$^+$, 100), **(-ESI)** m/z: 499/501 ([M-H]$^-$, 100); **HRMS (+ESI)** Calc. for $C_{21}H_{16}ClF_3N_2NaO_5S$ [M+Na]$^+$: 523.03128/525.02817, found 523.03222/525.02940; **HPLC** R_T = 26.47 min, 98.24% (254 nm).

2-((3*r*,5*r*,7*r*)-adamantan-1-yl)-*N*-(3-(benzylthio)-4-(3-(trifluoromethoxy)phenoxy)phenyl)acetamide (**79**)

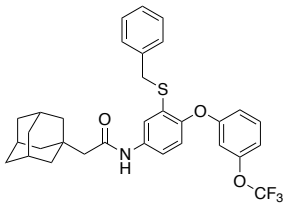

Compound **79** was prepared *via* an acid chloride amide coupling according to **General Procedure D** from **71** (103 mg, 0.26 mmol) and 1-adamantaneacetic acid (60.4 mg, 0.31 mmol). Compound **79** was isolated as a white powder (124 mg, 86%) following purification by flash chromatography (1:19 EtOAc:Hex). **^{1}H NMR** (500 MHz, DMSO-d_6) δ 9.87 (s, 1H), 7.86 (d, J = 2.5 Hz, 1H), 7.45 (dd, J = 8.7, 2.5 Hz, 1H), 7.42 (t, J = 8.2 Hz, 1H), 7.35 – 7.31 (m, 2H), 7.28 – 7.21 (m, 3H), 7.06 – 7.01 (m, 2H), 6.83 – 6.77 (m, 2H), 4.14 (s, 2H), 2.06 (s, 2H), 1.95 (t, J = 3.2 Hz, 3H), 1.72 – 1.57 (m, 12H) ppm; **^{19}F NMR** (471 MHz, DMSO-d_6) δ -56.8 ppm; **^{13}C NMR** (126 MHz, DMSO-d_6) δ 169.2, 158.7, 149.2 (q, J = 1.7 Hz), 146.6, 137.0, 136.7, 131.3, 129.5, 129.0, 128.3, 127.2, 121.5, 120.0 (q, J = 256.7 Hz), 119.3, 117.8, 115.0, 114.5, 109.1, 50.9, 42.1, 36.4, 35.5, 32.8, 28.0 ppm; **LRMS (+ESI)** m/z: 590 ([M+Na]$^+$, 100), **(-ESI)** m/z: 566 ([M-H]$^-$, 100); **HRMS (+ESI)** Calc. for $C_{32}H_{32}F_3NNaO_3S$ [M+Na]$^+$: 590.19472, found 590.19505.

2-((3*r*,5*r*,7*r*)-adamantan-1-yl)-*N*-(3-sulfamoyl-4-(3-(trifluoromethoxy)phenoxy)phenyl)acetamide (**88**)

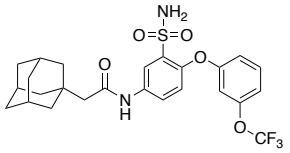

Compound **88** was synthesised from **79** (100 mg, 0.18 mmol) and DCDMH (68.5 mg, 0.35 mmol) according to **General Procedure F** and was obtained as a white powder (53.6 mg, 58%) following purification by flash chromatography (1:4 EtOAc:Hex). **^{1}H NMR** (500 MHz, $CDCl_3$) δ 8.14 (dd, J = 9.0, 2.7 Hz, 1H), 7.95 (s, 1H), 7.78 (d, J = 2.7 Hz, 1H), 7.37 (t, J = 8.2 Hz, 1H), 7.04 (dd, J = 8.1, 1.0 Hz, 1H), 6.98 – 6.94 (m, 2H), 6.89 (d, J = 8.9 Hz, 1H), 5.43 (s, 2H), 2.10 (s, 2H), 1.98 – 1.93 (m, 3H), 1.73 – 1.58 (m, 12H) ppm; **^{19}F NMR** (471 MHz, $CDCl_3$) δ -57.9 ppm; **^{13}C NMR** (126 MHz, $CDCl_3$) δ 170.5, 157.2, 150.4 (q, J = 2.0 Hz), 149.3, 134.3, 133.1, 131.1, 125.9, 120.5 (q, J = 258.3 Hz), 120.4, 119.7, 117.5, 116.9, 112.5, 52.6, 42.7, 36.8, 33.5, 28.8 ppm; **LRMS (+ESI)** m/z: 547 ($[M+Na]^+$, 100), **(-ESI)** m/z: 523 ($[M-H]^-$, 100); **HRMS (+ESI)** Calc. for $C_{25}H_{27}F_3N_2O_5S$ $[M+H]^+$: 525.16655, found 525.16652; **HPLC** R_T = 29.82 min, 98.16% (254 nm).

7-bromo-1-chloroisoquinoline-5-sulfonyl chloride (**96**)

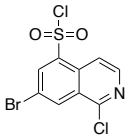

7-bromo-1-chloroisoquinoline (4.22 g, 17.4 mmol) was added was added dropwise to chlorosulfonic acid (11.6 mL, 174 mmol) at 0 °C. The reaction was then stirred at 100 °C with a $NaHCO_3$ bubbler system attached for 48 hours, or until TLC confirmed completion. The reaction mixture was cooled to 0 °C and quenched by slow addition to ice water (100 mL) with consistent stirring. The solution was extracted with EtOAc (2 x 25 mL/mmol) and the organic layers were pooled and washed with brine (1 x 25 mL/mmol). The organic layers were further dried over anhydrous $MgSO_4$, and solvent removed *in vacuo*. Compound **96** obtained as a bright yellow crystalline solid (3.03 g, 51%) following purification by flash chromatography (1:99 EtOAc:Hex). **^{1}H NMR** (300 MHz, $CDCl_3$) δ 8.94 (d, J = 1.0 Hz, 1H), 8.67 (d, J = 1.9 Hz, 1H), 8.59 (d, J = 6.1 Hz, 1H), 8.47 (dd, J = 6.0, 1.0 Hz, 1H) ppm; **^{13}C NMR** (75 MHz,

$CDCl_3$) δ 151.9, 145.0, 140.4, 136.9, 136.9, 131.3, 128.7, 120.5, 116.6 ppm; **LRMS (+APCI)** m/z: 340/342/344 ($[M+H]^+$, 100), **(-APCI)** m/z: 338/340/342 ($[M-H]^-$, 100).

7-bromo-1-chloroisoquinoline-5-sulfonamide (**97**)

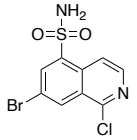

Compound **96** (376 mg, 1.10 mmol) was dissolved in the minimum volume of THF (1 mL). NH_4OH (1 mL, 25.1 mmol) was added dropwise, and the reaction was stirred at 50 °C for 3 h. The reaction was cooled to rt and concentrated under a stream of N_2. Compound **97** was isolated as a white powder (284 mg, 80%) following purification by flash chromatography (1:4 EtOAc:Hex). **^{1}H NMR** (400 MHz, CD_3OD) δ 8.79 – 8.75 (m, 1H), 8.56 (d, J = 1.9 Hz, 1H), 8.51 (dd, J = 6.0, 1.0 Hz, 1H), 8.44 (dd, J = 6.0, 1.2 Hz, 1H) ppm; **^{13}C NMR** (101 MHz, CD_3OD) δ 152.1, 144.2, 142.6, 136.1, 133.8, 133.3, 129.6, 122.0, 119.4 ppm; **LRMS (-ESI)** m/z: 319/321/323 ($[M-H]^-$, 100); **HRMS (+ESI)** Calc. for $C_9H_6BrClN_2O_2S$ $[M+H]^+$: 320.90947/322.90742/324.90447, found 320.90897/322.90692/324.90387.

(*E*)-*N*'-((7-bromo-1-chloroisoquinolin-5-yl)sulfonyl)-*N*,*N*-dimethylformimidamide (**95**)

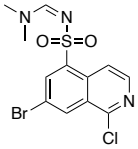

N,N-Dimethylformamide dimethyl acetal (1 mL, 0.91 mmol) was added dropwise to a stirring solution of **97** (243 mg, 0.75 mmol) in DMF (2 mL). Reaction was then stirred at 70 °C for 3 h. After cooling, the reaction was partitioned between H_2O (15 mL) and EtOAc (10 mL). The aqueous solution was extracted with EtOAc (3 x 25 mL/mmol) and the organic layers were pooled and washed with brine (1 x 25 mL/mmol). The organic layers were further dried over anhydrous $MgSO_4$, and solvent removed *in vacuo*. Compound **95** was isolated as a bright yellow crystalline solid (256 mg, 90%) following purification by flash chromatography (1:1 EtOAc:Hex). **^{1}H NMR** (500 MHz, $CDCl_3$) δ 8.69 (dd, J = 2.0, 0.9 Hz, 1H), 8.59 (dd, J = 6.0, 0.9 Hz, 1H), 8.53 (d, J = 2.0 Hz, 1H), 8.42 (d, J = 6.0 Hz, 1H), 8.15 (s, 1H), 3.15 (s, 3H), 3.01 (s, 3H) ppm; **^{13}C NMR** (126 MHz, $CDCl_3$) δ 159.4, 151.0, 143.3, 140.2, 134.4, 133.1, 132.7, 128.6, 120.9, 119.0, 41.8, 35.9 ppm; **LRMS (+ESI) m/z:** 397/399/401 ($[M+Na]^+$, 100);

HRMS (+ESI) Calc. for $C_{12}H_{11}BrClN_3NaO_2S$ $[M+Na]^+$: 397.93361/399.93134/401.92861, found 397/93332/399.93117/401.92835.

7-bromo-1-chloro-*N*-(2,4-dimethoxybenzyl)isoquinoline-5-sulfonamide (**99**)

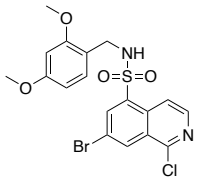

A solution of sulfonyl chloride **96** (1.2 g, 3.52 mmol) and $NaHCO_3$ (600 mg, 7.04 mmol) was suspended in CH_2Cl_2 (10 mL) under an atmosphere of N_2. The reaction mixture was then treated dropwise with a solution of 1-(2,4-dimethoxyphenyl)methanamine (0.53 mL, 3.52 mmol) in CH_2Cl_2 (3 mL). The reaction was stirred at rt for 6 h, or until TLC indicated conversion of starting material. The reaction mixture was diluted with H_2O, and the aqueous components extracted with CH_2Cl_2. The pooled organic extractions were washed with brine, dried over $MgSO_4$ and concentration *in vacuo*. Compound **99** was obtained as a yellow solid (1.03 g, 62%) following purification by flash chromatography (1:9 EtOAc:Hex). **^{1}H NMR** (500 MHz, $CDCl_3$) δ 8.53 (dd, J = 2.0, 0.9 Hz, 1H), 8.37 (d, J = 6.0 Hz, 1H), 8.25 (d, J = 2.0 Hz, 1H), 8.19 (dd, J = 6.0, 1.0 Hz, 1H), 6.64 (d, J = 8.2 Hz, 1H), 6.12 (dd, J = 8.2, 2.3 Hz, 1H), 5.78 (d, J = 2.4 Hz, 1H), 5.51 (t, J = 6.3 Hz, 1H), 4.16 (d, J = 6.4 Hz, 2H), 3.71 (s, 3H), 3.35 (s, 3H) ppm; **^{13}C NMR** (126 MHz, $CDCl_3$) δ 160.9, 157.6, 151.3, 143.2, 143.2, 138.0, 137.0, 134.6, 133.2, 131.8, 130.7, 129.9, 128.2, 121.1, 117.1, 115.0, 103.6, 97.8, 77.4, 77.2, 76.9, 55.4, 54.9, 44.7 ppm; **LRMS (+ESI)** m/z: 493/495/497 ($[M+Na]^+$, 100) , **(-ESI)** m/z: 469/471/473 ($[M-H]^-$, 100); **HRMS (+ESI)** Calc. for $C_{18}H_{16}BrClN_2NaO_4S$ $[M+Na]^+$: 492.95949/494.95722/496.95499, found 492.95994/494.95749/496.95499.

7-amino-1-chloro-*N*-(2,4-dimethoxybenzyl)isoquinoline-5-sulfonamide (**102**)

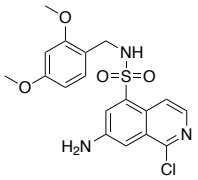

CuI (20.1 mg, 0.11 mmol), 4-OH-L-proline (13.8 mg, 0.11 mmol), Cs_2CO_3 (208 mg, 0.64 mmol) were added to a stirring solution of **99** (200 mg, 0.42 mmol) in DMSO (2 mL). NH_4OH (1.2 mL, 12.7 mmol) was added dropwise to the reaction mixture. The flask was tightly sealed with a Teflon screw cap and stirred at 140 °C for 18 h. Upon consumption of starting material, the reaction was cooled to rt and partitioned between EtOAc (10 mL) and H_2O (10 mL). The aqueous layer was extracted with EtOAc (3 x 25 mL/mmol). Combined organic layers were washed with brine (1 x 25 mL/mmol), dried and concentrated *in vacuo*. Compound **102** was isolated as a yellow solid (69.2 mg, 40%). **^{1}H NMR** (300 MHz, DMSO-d_6) δ 8.22 (s, 1H), 8.13 (d, J = 5.9 Hz, 1H), 7.97 (d, J = 5.9 Hz, 1H), 7.79 (d, J = 2.3 Hz, 1H), 7.29 (d, J = 2.3 Hz, 1H), 6.91 (d, J = 8.2 Hz, 1H), 6.33 (s, 2H), 6.19 (dd, J = 8.3, 2.4 Hz, 1H), 6.15 (d, J = 2.4 Hz, 1H), 3.92 (s, 2H), 3.65 (s, 3H), 3.42 (s, 3H) ppm; **^{13}C NMR** (75 MHz, DMSO-d_6) δ 159.9, 157.2, 147.9, 147.9, 137.2, 136.8, 129.8, 128.8, 125.1, 124.6, 117.9, 116.4, 106.1, 103.7, 97.5, 55.1, 54.8, 40.7 ppm; **LRMS (+ESI)** m/z: 430/432 ($[M+Na]^+$, 100), **(-ESI)** m/z: 406/408 ($[M-H]^-$, 100); **HRMS (+ESI)** Calc. for $C_{18}H_{18}ClN_3NaO_4S$ $[M+Na]^+$: 430.05988/432.05693, found 430.06044/432.05756.

N-(1-chloro-5-(*N*-(2,4-dimethoxybenzyl)sulfamoyl)isoquinolin-7-yl)-2-(2-chlorophenyl)acetamide (**107**)

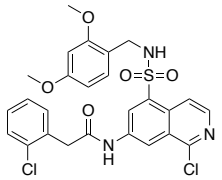

Compound **107** was prepared *via* a T_3P mediated amide coupling according to **General Procedure G** from **102** (82.2 mg, 202 µmol) and 2-(2-chlorophenyl)acetic acid (102 mg, 599 µmol). Compound **107** was isolated as an off white solid (62.6 mg, 55%) following purification by flash chromatography (3:7 EtOAc:Hex). **^{1}H NMR** (400 MHz, $CDCl_3$) δ 8.98 (dd, J = 2.3, 0.9 Hz, 1H), 8.25 (d, J = 6.0 Hz, 1H), 8.10 (dd, J = 6.0, 1.0 Hz, 1H), 8.04 (d, J = 2.3 Hz, 1H), 7.88 (s, 1H), 7.52 – 7.45 (m, 2H), 7.39 – 7.30 (m, 2H), 6.55 (d, J = 8.3 Hz, 1H), 5.98 (dd, J =

8.2, 2.3 Hz, 1H), 5.78 (d, *J* = 2.4 Hz, 1H), 5.49 (t, *J* = 6.4 Hz, 1H), 4.10 (d, *J* = 6.3 Hz, 2H), 3.97 (s, 2H), 3.62 (s, 3H), 3.33 (s, 3H) ppm; **^{13}C NMR** (101 MHz, $CDCl_3$) δ 168.6, 160.9, 157.7, 152.2, 141.9, 136.8, 136.4, 134.6, 132.2, 132.1, 130.5, 130.2, 129.9, 129.7, 128.3, 127.9, 127.6, 119.3, 116.6, 114.9, 104.0, 97.4, 55.4, 54.9, 44.6, 42.6 ppm; **LRMS (+ESI)** m/z: 582/584/586 ([M+Na]$^+$, 100), **(-ESI)** m/z: 558/560/562 ([M-H]$^-$, 100); **HRMS (+ESI)** Calc. for $C_{26}H_{23}Cl_2N_3NaO_5S$ [M+Na]$^+$: 582.06277/584.05974/586.05659, found 582.06385/ 584.06105/586.05811.

N-(1-chloro-5-sulfamoylisoquinolin-7-yl)-2-(2-chlorophenyl)acetamide (**113**)

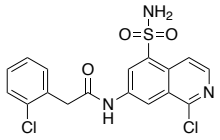

Compound **113** was synthesised from **107** (49.5 mg, 88.3 µmol) according to **General Procedure C** and was obtained as a white solid (22.1 mg, 61%) following purification by flash chromatography (3:7 EtOAc:Hex). **^{1}H NMR** (400 MHz, DMSO-d_6) δ 11.08 (s, 1H), 9.02 (d, *J* = 2.1 Hz, 1H), 8.67 (d, *J* = 2.2 Hz, 1H), 8.42 – 8.34 (m, 2H), 7.92 (s, 2H), 7.51 – 7.44 (m, 2H), 7.39 – 7.29 (m, 2H), 3.96 (s, 2H) ppm; **^{13}C NMR** (101 MHz, DMSO-d_6) δ 169.1, 150.3, 141.2, 140.2, 138.1, 133.7, 133.3, 132.3, 129.0, 128.8, 128.7, 127.5, 127.1, 125.0, 117.9, 115.9, 40.9 ppm; **LRMS (+ESI)** m/z: 431/433/436 ([M+Na]$^+$, 100), **(-ESI)** m/z: 408/410/412 ([M-H]$^-$, 100); **HRMS (+ESI)** Calc. for $C_{17}H_{13}Cl_2N_3NaO_3S$ [M+Na]$^+$: 431.99469/433.99174/ 435.98879, found 431.99451/433.99155/435.98853; **HPLC** R_T = 22.56 min, 96.26% (254 nm).

2-((3*r*,5*r*,7*r*)-adamantan-1-yl)-*N*-(1-chloro-5-(*N*-(2,4-dimethoxybenzyl)sulfamoyl)isoquinolin-7-yl)acetamide (**108**)

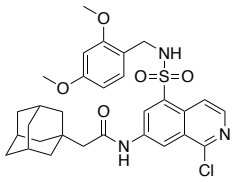

Compound **108** was prepared *via* a T_3P mediated amide coupling according to **General Procedure G** from **102** (29.3 mg, 71.8 μmol) and 1-adamantaneacetic acid (41.2 mg, 212 μmol). Compound **108** was isolated as a brown solid (17.2 mg, 41%) following purification by flash chromatography (1:4 EtOAc:Hex). **^{1}H NMR** (400 MHz, DMSO-d_6) δ 10.49 (s, 1H), 8.95 (d, J = 2.0 Hz, 1H), 8.48 – 8.37 (m, 1H), 8.35 (d, J = 2.1 Hz, 1H), 8.27 (s, 2H), 6.80 (d, J = 8.2 Hz, 1H), 6.05 (dd, J = 8.3, 2.3 Hz, 1H), 5.95 (d, J = 2.4 Hz, 1H), 3.97 (s, 2H), 3.59 (s, 3H), 3.27 (s, 3H), 2.16 (s, 2H), 1.99 – 1.94 (m, 3H), 1.73 – 1.58 (m, 12H) ppm; **^{13}C NMR** (101 MHz, DMSO-d_6) δ 170.2, 159.8, 157.0, 150.0, 140.7, 137.9, 136.9, 130.2, 128.7, 127.3, 126.9, 117.7, 115.8, 115.7, 103.7, 97.0, 54.9, 54.6, 50.9, 42.0, 41.8, 36.4, 36.3, 32.8, 28.0 ppm; **LRMS (+ESI)** m/z: 606/608 ([M+Na]$^+$, 100), **(-ESI)** m/z: 582/584 ([M-H]$^-$, 100); **HRMS (+ESI)** Calc. for $C_{30}H_{34}ClN_3NaO_5S$ [M+Na]$^+$: 606.17999/608.17689, found 606.18059/608.17765.

2-((3*r*,5*r*,7*r*)-adamantan-1-yl)-*N*-(1-chloro-5-sulfamoylisoquinolin-7-yl)acetamide (**114**)

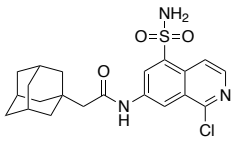

Compound **114** was synthesised from **107** (24.6 mg, 42.1 μmol) according to **General Procedure C** and was obtained as a white solid (12.1 mg, 66%) following purification by flash chromatography (3:7 EtOAc:Hex). **^{1}H NMR** (400 MHz, DMSO-d_6) δ 10.61 (s, 1H), 9.06 (d, J = 2.2 Hz, 1H), 8.67 (d, J = 2.1 Hz, 1H), 8.41 – 8.32 (m, 2H), 7.90 (s, 2H), 2.16 (s, 2H), 1.95 (s, 3H), 1.71 – 1.57 (m, 12H) ppm; **^{13}C NMR** (101 MHz, DMSO-d_6) δ 170.3, 150.3, 141.1, 140.0, 138.1, 128.6, 127.5, 125.1, 117.9, 115.6, 50.9, 42.0, 36.3, 32.8, 28.0 ppm; **LRMS (+ESI)** m/z: 456/458 ([M+Na]$^+$, 100), **(-ESI)** m/z: 432/434 ([M-H]$^-$, 100); **HRMS (+ESI)** Calc. for $C_{21}H_{24}ClN_3NaO_3S$ [M+Na]$^+$: 456.11191/458.10896, found 456.11178/458.10893; **HPLC** R_T = 27.04 min, 95.82% (254 nm).

7-bromo-*N*-(2,4-dimethoxybenzyl)-1-methoxyisoquinoline-5-sulfonamide (**103**)

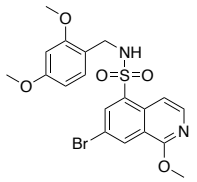

To a solution of **99** (326 mg, 0.69 mmol) in MeOH:CH_2Cl_2 (5:1, 6 mL) was slowly added NaOMe (668 mg, 12.4 mmol) in MeOH (2 mL) at 0 °C. The reaction was heated to reflux and stirred at this temperature for 18 h. The mixture was then allowed to cool to rt, and then 0 °C where it was quenched with H_2O (10 mL). The reaction was then diluted with CH_2Cl_2 (10 mL), and the aqueous phase was extracted (3 x 25 mL/mmol). Pooled organic layers were washed with brine (1 x 25 mL/mmol), dried and concentrated. Compound **103** (233 mg, 72%) was isolated as a white powder following purification by flash chromatography (1:4 EtOAc:Hex). **^{1}H NMR** (500 MHz, $CDCl_3$) δ 8.43 (dd, J = 2.1, 0.9 Hz, 1H), 8.16 (d, J = 2.1 Hz, 1H), 8.09 (d, J = 6.2 Hz, 1H), 7.70 (dd, J = 6.1, 0.9 Hz, 1H), 6.65 (d, J = 8.2 Hz, 1H), 6.12 (dd, J = 8.2, 2.3 Hz, 1H), 5.80 (d, J = 2.3 Hz, 1H), 5.46 (t, J = 6.4 Hz, 1H), 4.13 (d, J = 6.6 Hz, 3H), 4.12 (s, 3H), 3.71 (s, 3H), 3.35 (s, 3H) ppm; **^{13}C NMR (**126 MHz, $CDCl_3$) δ 160.7, 160.4, 157.7, 142.1, 136.8, 136.0, 131.9, 131.5, 130.5, 121.3, 118.7, 115.3, 111.0, 103.3, 98.0, 55.4, 54.8, 54.3, 44.7 ppm; **LRMS (+ESI)** m/z: 467/469 ([M+H]$^+$, 100); **HRMS (-ESI)** Calc. for $C_{19}H_{19}BrN_2O_5S$ [M-H]$^-$: 465.01253/467.01048, found 465.01243/467.01064.

7-amino-*N*-(2,4-dimethoxybenzyl)-1-methoxyisoquinoline-5-sulfonamide (**105**)

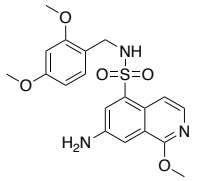

CuI (15.7 mg, 0.08 mmol), 4-OH-L-proline (20.4 mg, 0.16 mmol), Cs_2CO_3 (214 mg, 0.66 mmol) were added to a stirring solution of **103** (185 mg, 0.40 mmol) in DMSO (2 mL). NH_4OH (1.2 mL, 8.44 mmol) was added dropwise to the reaction mixture. The flask was tightly sealed with a Teflon screw cap and stirred at 140 °C for 18 h. Upon consumption of starting material, the reaction was cooled to rt and partitioned between EtOAc (10 mL) and H_2O (10 mL). The aqueous layer was extracted with EtOAc (3 x 25 mL/mmol). Combined organic layers were washed with brine (1 x 25 mL/mmol), dried and concentrated *in vacuo*. Compound **105** was isolated as a beige solid (128 mg, 80%) following purification by flash chromatography (1:4 EtOAc:Hex). **^{1}H NMR** (300 MHz, $CDCl_3$) δ 7.83 (d, J = 6.2 Hz, 1H), 7.62 (d, J = 2.5 Hz, 1H), 7.57 (d, J = 6.2 Hz, 1H), 7.43 (d, J = 2.5 Hz, 1H), 6.66 (d, J = 8.3 Hz, 1H), 6.11 (dd, J = 8.2,

2.4 Hz, 1H), 5.90 (d, *J* = 2.4 Hz, 1H), 5.40 (t, *J* = 6.4 Hz, 1H), 4.07 (s, 3H), 4.05 (d, *J* = 6.5 Hz, 2H), 3.69 (s, 3H), 3.40 (s, 3H) ppm; **^{13}C NMR** (75 MHz, $CDCl_3$) δ 160.6, 159.9, 157.8, 143.8, 137.7, 135.6, 130.3, 126.6, 124.1, 122.1, 115.7, 111.0, 109.8, 103.4, 97.8, 55.4, 54.8, 53.9, 44.5 ppm; **LRMS (+ESI)** m/z: 426 ($[M+Na]^+$, 100), **(-ESI)** m/z: 402 ($[M-H]^-$, 100); **HRMS (+ESI)** Calc. for $C_{98}H_{21}N_3NaO_5S$ $[M+Na]^+$: 426.10941, found 426.10909.

2-(2-chlorophenyl)-*N*-(5-(*N*-(2,4-dimethoxybenzyl)sulfamoyl)-1-methoxyisoquinolin-7-yl)acetamide (**109**)

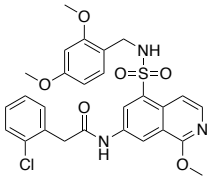

Compound **109** was prepared *via* a T_3P mediated amide coupling according to **General Procedure G** from **105** (40.1 mg, 99.4 µmol) and 2-(2-chlorophenyl)acetic acid (26.7 mg, 157 µmol). Compound **109** was isolated as an off white solid (27.2 mg, 49%) following purification by flash chromatography (1:4 EtOAc:Hex). **^{1}H NMR** (500 MHz, DMSO-d_6) δ 10.77 (s, 1H), 8.78 (d, *J* = 2.0 Hz, 1H), 8.32 (d, *J* = 2.3 Hz, 1H), 8.23 (s, 1H), 8.00 (d, *J* = 6.1 Hz, 1H), 7.84 (d, *J* = 6.3 Hz, 1H), 7.47 (dt, *J* = 6.7, 2.0 Hz, 2H), 7.37 – 7.31 (m, 2H), 6.89 (d, *J* = 8.2 Hz, 1H), 6.15 (dd, *J* = 8.3, 2.4 Hz, 1H), 6.07 (d, *J* = 2.3 Hz, 1H), 4.04 (s, 3H), 3.94 (s, 2H), 3.92 (s, 2H), 3.61 (s, 3H), 3.35 (s, 3H) ppm; **^{13}C NMR** (126 MHz, DMSO-d_6) δ 168.6, 159.9, 159.8, 157.1, 139.4, 136.3, 135.8, 133.7, 133.5, 132.3, 129.9, 129.0, 128.9, 128.8, 127.1, 125.6, 120.0, 116.3, 115.1, 111.6, 103.8, 97.3, 55.0, 54.7, 53.8, 40.8, 40.7, 40.1 ppm; **LRMS (+ESI)** m/z: 578/580 ($[M+Na]^+$, 100), **(-ESI)** m/z: 554/556 ($[M-H]^-$, 100); **HRMS (+ESI)** Calc. for $C_{27}H_{26}ClN_3NaO_6S$ $[M+Na]^+$: 578.11231/580.10920, found 578.11211/580.10933.

2-(2-chlorophenyl)-*N*-(1-methoxy-5-sulfamoylisoquinolin-7-yl)acetamide (**115**)

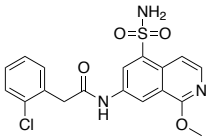

Compound **115** was synthesised from **109** (25.4 mg, 45.7 µmol) according to **General Procedure C** and was obtained as a white solid (10.2 mg, 55%) following purification by flash chromatography (3:7 EtOAc:Hex). **^{1}H NMR** (400 MHz, DMSO-d_6) δ 10.87 (s, 1H), 8.85 (d, *J* = 2.2 Hz, 1H), 8.54 (d, *J* = 2.3 Hz, 1H), 8.06 (d, *J* = 6.2 Hz, 1H), 7.90 (d, *J* = 6.2 Hz, 1H), 7.75 (s, 2H), 7.46 (dt, *J* = 7.0, 2.6 Hz, 2H), 7.37 – 7.29 (m, 2H), 4.06 (s, 3H), 3.92 (s, 2H)

ppm; **^{13}C NMR** (101 MHz, DMSO-d_6) δ 168.7, 160.1, 139.6, 139.2, 136.5, 133.7, 133.6, 132.3, 129.0, 128.8, 127.1, 123.8, 120.2, 115.0, 111.7, 53.9, 40.9 ppm; **LRMS (+ESI)** m/z: 428/430 ([M+Na]$^+$, 100), **(-ESI)** m/z: 404/406 ([M-H]$^-$, 100); **HRMS (+ESI)** Calc. for $C_{18}H_{16}ClN_3NaO_4S$ [M+Na]$^+$: 428.04423/430.04128, found 428.04429/430.04137; **HPLC** R_T = 22.04 min, 99.37% (254 nm).

2-((3*r*,5*r*,7*r*)-adamantan-1-yl)-*N*-(5-(*N*-(2,4-dimethoxybenzyl)sulfamoyl)-1-methoxyisoquinolin-7-yl)acetamide (**110**)

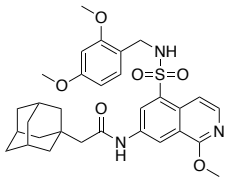

Compound **110** was prepared *via* a T_3P mediated amide coupling according to **General Procedure G** from **105** (50.9 mg, 126 µmol) and 1-adamantaneacetic acid (75.4 mg, 388 µmol). Compound **110** was isolated as an off white solid (44.1 mg, 60%) following purification by flash chromatography (1:4 EtOAc:Hex). **^{1}H NMR** (300 MHz, $CDCl_3$) δ 9.05 (d, J = 2.3 Hz, 1H), 8.06 (d, J = 2.3 Hz, 1H), 8.01 – 7.96 (m, 2H), 7.64 (d, J = 6.2 Hz, 1H), 6.55 (d, J = 8.2 Hz, 1H), 6.04 (dd, J = 8.2, 2.4 Hz, 1H), 5.85 (d, J = 2.4 Hz, 1H), 5.51 (t, J = 6.4 Hz, 1H), 4.11 (s, 3H), 4.07 (d, J = 6.3 Hz, 2H), 3.66 (s, 3H), 3.40 (s, 3H), 2.23 (s, 2H), 2.02 (s, 3H), 1.80 – 1.74 (m, 6H), 1.74 – 1.65 (m, 6H) ppm; **^{13}C NMR** (75 MHz, $CDCl_3$) δ 170.2, 161.2, 160.7, 157.7, 140.5, 135.4, 135.0, 130.3, 129.7, 126.5, 121.3, 117.9, 115.2, 110.5, 103.7, 97.8, 55.4, 54.9, 54.1, 52.8, 44.7, 42.7, 36.9, 33.6, 28.8 ppm; **LRMS (+ESI)** m/z: 602 ([M+Na]$^+$, 100), **(-ESI)** m/z: 578 ([M-H]$^-$, 100); **HRMS (+ESI)** Calc. for $C_{31}H_{37}N_3NaO_6S$ [M+Na]$^+$: 602.22953, found 602.23023.

2-((3*r*,5*r*,7*r*)-adamantan-1-yl)-*N*-(1-methoxy-5-sulfamoylisoquinolin-7-yl)acetamide (**116**)

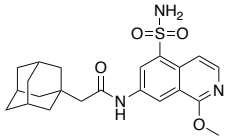

Compound **116** was synthesised from **110** (40.1 mg, 69.2 µmol) according to **General Procedure C** and was obtained as a pale yellow solid (17.8 mg, 60%) following purification by flash chromatography (3:7 EtOAc:Hex).**^{1}H NMR** (400 MHz, DMSO-d_6) δ 10.40 (s, 1H), 8.89 (dd, J = 2.3, 0.9 Hz, 1H), 8.53 (d, J = 2.2 Hz, 1H), 8.05 (d, J = 6.2 Hz, 1H), 7.90 (dd, J =

6.2, 0.9 Hz, 1H), 7.73 (s, 2H), 4.08 (s, 3H), 2.13 (s, 2H), 1.94 (s, 3H), 1.72 – 1.56 (m, 12H) ppm; **^{13}C NMR** (101 MHz, DMSO-d_6) δ 169.9, 160.0, 139.4, 139.0, 136.5, 128.6, 123.9, 120.2, 114.6, 111.7, 53.8, 50.9, 42.1, 36.4, 32.8, 28.0 ppm; **LRMS (+ESI)** m/z: 452 ([M+Na]$^+$, 100); **HRMS (+ESI)** Calc. for $C_{22}H_{27}N_3NaO_4S$ [M+Na]$^+$: 452.16145, found 452.16155; **HPLC** R_T = 26.39 min, 96.19% (254 nm).

7-bromo-*N*-(2,4-dimethoxybenzyl)-1-(isopentyloxy)isoquinoline-5-sulfonamide (**104**)

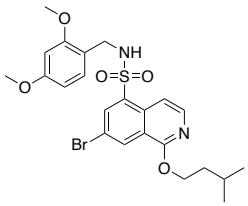

Compound **99** (313 mg, 0.66 mmol) was dissolved in DMF (2 mL), treated with NaH (60% mineral dispersion, 85.7 mg, 2.14 mmol) and isoamyl alcohol (100 µL, 0.92 mmol) at 0 °C. The reaction was allowed to come to rt over the next hour, and then stirred at 90 °C for 6 h. Following consumption of starting material as indicated by TLC, the reaction was cooled to rt, quenched with H_2O (10 mL) and the resulting aqueous was extracted with EtOAc (3 x 25 mL/mmol). Combined organic phases were washed with brine (1 x 25 mL/mmol), dried and concentrated *in vacuo*. Compound **104** was isolated as a white solid (257 mg, 74%) following purification by flash chromatography (1:4 EtOAc:Hex). **^{1}H NMR** (500 MHz, $CDCl_3$) δ 8.40 (d, J = 2.1 Hz, 1H), 8.16 (d, J = 2.1 Hz, 1H), 8.08 (d, J = 6.2 Hz, 1H), 7.68 (d, J = 6.2 Hz, 1H), 6.68 (d, J = 8.2 Hz, 1H), 6.14 (dd, J = 8.2, 2.4 Hz, 1H), 5.81 (d, J = 2.4 Hz, 1H), 5.44 (t, J = 6.4 Hz, 1H), 4.51 (t, J = 6.7 Hz, 2H), 4.13 (d, J = 6.4 Hz, 2H), 3.70 (s, 3H), 3.35 (s, 3H), 1.94 – 1.83 (m, 1H), 1.80 (q, J = 6.8 Hz, 2H), 1.03 (d, J = 6.4 Hz, 6H) ppm; **^{13}C NMR** (126 MHz, $CDCl_3$) δ 160.7, 160.2, 157.7, 142.3, 136.8, 135.9, 131.9, 131.5, 130.6, 121.5, 118.6, 115.4, 110.7, 103.3, 98.0, 65.8, 55.4, 54.8, 44.7, 37.8, 25.5, 22.8 ppm; **LRMS (+ESI)** m/z: 545/547 ([M+Na]$^+$, 100), **(-ESI)** m/z: 521/523 ([M-H]$^-$, 100); **HRMS (+ESI)** Calc. for $C_{23}H_{27}BrN_2NaO_5S$ [M+Na]$^+$: 545.07163/547.06958, found 545.07204/547.07007.

7-amino-*N*-(2,4-dimethoxybenzyl)-1-(isopentyloxy)isoquinoline-5-sulfonamide (**106**)

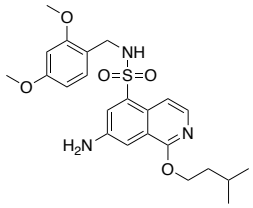

CuI (18.2 mg, 0.10 mmol), 4-OH-L-proline (16.2 mg, 0.12 mmol), Cs_2CO_3 (191 mg, 0.59 mmol) were added to a stirring solution of **104** (202 mg, 0.39 mmol) in DMSO (2 mL). NH_4OH (1 mL, 7.03 mmol) was added dropwise to the reaction mixture. The flask was tightly sealed with a Teflon screw cap and stirred at 140 °C for 18 h. Upon consumption of starting material, the reaction was cooled to rt and partitioned between EtOAc (10 mL) and H_2O (10 mL). The aqueous layer was extracted with EtOAc (3 x 25 mL/mmol). Combined organic layers were washed with brine (1 x 25 mL/mmol), dried and concentrated *in vacuo*. Compound **106** was isolated as a beige solid (128 mg, 72%) following purification by flash chromatography (1:4 EtOAc:Hex). **^{1}H NMR** (300 MHz, $CDCl_3$) δ 7.82 (d, J = 6.2 Hz, 1H), 7.62 (d, J = 2.6 Hz, 1H), 7.56 (d, J = 6.2 Hz, 1H), 7.43 (d, J = 2.6 Hz, 1H), 6.70 (d, J = 8.2 Hz, 1H), 6.13 (dd, J = 8.2, 2.3 Hz, 1H), 5.92 (d, J = 2.3 Hz, 1H), 5.38 (t, J = 6.3 Hz, 1H), 4.46 (t, J = 6.7 Hz, 2H), 4.04 (s, 2H), 3.68 (s, 3H), 3.39 (s, 3H), 1.95 – 1.81 (m, 1H), 1.77 (q, J = 6.7 Hz, 2H), 1.01 (d, J = 6.5 Hz, 6H) ppm; **^{13}C NMR** (75 MHz, $CDCl_3$) δ 160.6, 159.8, 157.9, 143.7, 137.9, 135.5, 130.4, 126.6, 124.0, 122.2, 115.7, 110.7, 109.8, 103.5, 97.8, 65.1, 55.4, 54.8, 44.5, 37.9, 25.5, 22.8 ppm; **LRMS (+ESI)** m/z: 482 ($[M+Na]^+$, 100), **(-ESI)** m/z: 458 ($[M-H]^-$, 100); **HRMS (+ESI)** Calc. for $C_{23}H_{29}N_3NaO_5S$ $[M+Na]^+$: 482.17201, found 482.17247.

2-(2-chlorophenyl)-*N*-(5-(*N*-(2,4-dimethoxybenzyl)sulfamoyl)-1-(isopentyloxy)isoquinolin-7-yl)acetamide (**111**)

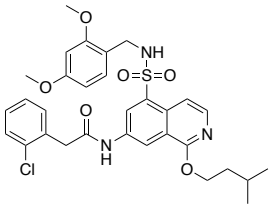

Compound **111** was prepared *via* a T_3P mediated amide coupling according to **General Procedure G** from **106** (39.8 mg, 86.6 µmol) and 2-(2-chlorophenyl)acetic acid (24.5 mg, 143 µmol). Compound **111** was isolated as a beige solid (24.4 mg, 46%) following purification by flash chromatography (1:4 EtOAc:Hex). **^{1}H NMR** (300 MHz, $CDCl_3$) δ 8.85 (d, J = 2.2 Hz, 1H), 7.97 (d, J = 6.4 Hz, 1H), 7.95 (d, J = 2.1 Hz, 1H), 7.87 (s, 1H), 7.61 (d, J = 6.2 Hz, 1H), 7.51 – 7.43 (m, 2H), 7.36 – 7.29 (m, 2H), 6.57 (d, J = 8.2 Hz, 1H), 5.99 (dd, J = 8.2, 2.3 Hz,

1H), 5.80 (d, *J* = 2.3 Hz, 1H), 5.50 (t, *J* = 6.4 Hz, 1H), 4.47 (t, *J* = 6.8 Hz, 2H), 4.06 (d, *J* = 6.3 Hz, 2H), 3.95 (s, 2H), 3.60 (s, 3H), 3.35 (s, 3H), 1.90 – 1.73 (m, 3H), 1.00 (d, *J* = 6.2 Hz, 6H) ppm; **^{13}C NMR** (75 MHz, $CDCl_3$) δ 168.3, 160.8, 160.5, 157.6, 140.7, 135.0, 134.7, 134.5, 132.3, 132.0, 130.3, 130.0, 129.9, 129.5, 127.7, 126.4, 121.1, 118.3, 115.0, 110.2, 103.5, 97.4, 65.5, 55.3, 54.7, 44.6, 42.5, 37.6, 25.4, 22.8 ppm; **LRMS (+ESI)** m/z: 634/636 ($[M+Na]^+$, 100), **(-ESI)** m/z: 610/612 ($[M-H]^-$, 100); **HRMS (+ESI)** Calc. for $C_{31}H_{34}ClN_3NaO_6S$ $[M+Na]^+$: 634.17491/636.17180, found 634.17572/636.17293.

2-(2-chlorophenyl)-*N*-(1-(isopentyloxy)-5-sulfamoylisoquinolin-7-yl)acetamide (**117**)

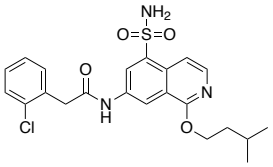

Compound **117** was synthesised from **111** (38.3 mg, 62.6 μmol) according to **General Procedure C** and was obtained as an off-white powder (22.4 mg, 77%) following purification by flash chromatography (3:7 EtOAc:Hex). **^{1}H NMR** (400 MHz, DMSO-d_6) δ 10.86 (s, 1H), 8.78 (d, *J* = 2.3 Hz, 1H), 8.62 (d, *J* = 2.2 Hz, 1H), 8.04 (d, *J* = 6.2 Hz, 1H), 7.89 (d, *J* = 6.3 Hz, 1H), 7.74 (s, 2H), 7.46 (dt, *J* = 6.8, 1.9 Hz, 2H), 7.37 – 7.30 (m, 2H), 4.50 (t, *J* = 6.7 Hz, 2H), 3.92 (s, 2H), 1.83 (dp, *J* = 13.2, 6.6 Hz, 1H), 1.72 (q, *J* = 6.7 Hz, 2H), 0.95 (d, *J* = 6.6 Hz, 6H) ppm; **^{13}C NMR** (101 MHz, DMSO-d_6) δ 168.7, 159.7, 139.6, 139.1, 136.5, 133.7, 133.6, 132.3, 129.0, 128.8, 128.7, 127.1, 123.8, 120.3, 114.9, 111.5, 64.6, 40.8, 37.2, 24.8, 22.5 ppm; **LRMS (+ESI)** m/z: 484 ($[M+Na]^+$, 100), **(-ESI)** m/z: 460 ($[M-H]^-$, 100); **HRMS (+ESI)** Calc. for $C_{22}H_{24}ClN_3NaO_4S$ $[M+Na]^+$: 484.10683/486.10388, found 484.10725/486.10458; **HPLC** R_T = 26.94 min, 97.63% (254 nm).

2-((3*r*,5*r*,7*r*)-adamantan-1-yl)-*N*-(5-(*N*-(2,4-dimethoxybenzyl)sulfamoyl)-1-(isopentyloxy)isoquinolin-7-yl)acetamide **(112)**

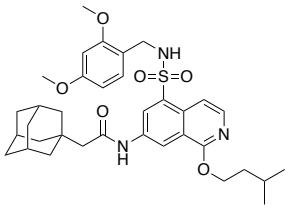

Compound **112** was prepared *via* a T_3P mediated amide coupling according to **General Procedure G** from **106** (56.7 mg, 123 µmol) and 1-adamantaneacetic acid (73.1 mg, 376 µmol). Compound **112** was isolated as an off white solid (38.7 mg, 49%) following purification by flash chromatography (1:4 EtOAc:Hex). **^{1}H NMR** (300 MHz, $CDCl_3$) δ 8.90 (d, J = 2.2 Hz, 1H), 8.09 (d, J = 2.3 Hz, 1H), 7.99 (d, J = 6.2 Hz, 1H), 7.68 (s, 1H), 7.64 (dd, J = 6.2, 0.9 Hz, 1H), 6.61 (d, J = 8.2 Hz, 1H), 6.06 (dd, J = 8.2, 2.3 Hz, 1H), 5.87 (d, J = 2.3 Hz, 1H), 5.46 (t, J = 6.4 Hz, 1H), 4.51 (t, J = 6.8 Hz, 2H), 4.08 (d, J = 6.3 Hz, 2H), 3.66 (s, 3H), 3.41 (s, 3H), 2.21 (s, 2H), 2.03 (s, 3H), 1.93 – 1.79 (m, 3H), 1.79 – 1.75 (m, 6H), 1.75 – 1.67 (m, 6H), 1.02 (d, J = 6.2 Hz, 6H) ppm; **^{13}C NMR** (75 MHz, $CDCl_3$) δ 169.9, 160.9, 160.8, 157.8, 140.7, 135.2, 135.2, 130.4, 129.9, 126.5, 121.4, 118.0, 115.3, 110.4, 103.8, 97.7, 65.6, 55.4, 54.9, 53.0, 44.7, 42.8, 37.8, 36.9, 33.6, 28.8, 25.6, 22.9 ppm; **LRMS (+ESI)** m/z: 636 ($[M+H]^+$, 90), 658 ($[M+Na]^+$, 100).

2-((3*r*,5*r*,7*r*)-adamantan-1-yl)-*N*-(1-(isopentyloxy)-5-sulfamoylisoquinolin-7-yl)acetamide (**118**)

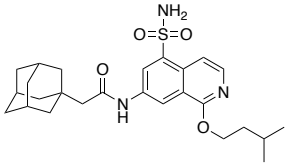

Compound **118** was synthesised from **112** (33.5 mg, 52.7 µmol) according to **General Procedure C** and was obtained as an off white solid (17.8 mg, 60%) following purification by flash chromatography (3:7 EtOAc:Hex). **^{1}H NMR** (400 MHz, DMSO-d_6) δ 10.39 (s, 1H), 8.77 (d, J = 1.7 Hz, 2H), 8.63 (d, J = 2.2 Hz, 1H), 8.02 (d, J = 6.2 Hz, 1H), 7.87 (d, J = 6.2 Hz, 1H), 7.72 (s, 2H), 4.52 (t, J = 6.7 Hz, 2H), 2.13 (s, 2H), 1.97 – 1.91 (m, 3H), 1.89 – 1.79 (m, 1H), 1.74 (q, J = 6.8 Hz, 2H), 1.70 – 1.57 (m, 12H), 0.98 (d, J = 6.5 Hz, 6H) ppm; **^{13}C NMR** (101 MHz, DMSO-d_6) δ 169.9, 159.7, 139.5, 139.0, 136.5, 128.7, 123.9, 120.3, 114.8, 111.5, 64.6, 50.9, 42.1, 37.2, 36.4, 32.8, 28.0, 24.9, 22.5 ppm; **LRMS (+ESI)** m/z: 508 ($[M+Na]^+$, 85),

(-ESI) m/z: 484 ([M-H]$^-$, 100); **HRMS (+ESI)** Calc. for $C_{26}H_{35}N_3NaO_4S$ [M+Na]$^+$: 508.22405, found 508.22348; **HPLC** R_T = 31.22 min, 95.28% (254 nm).

N-(3,5-difluorophenyl)-4-nitropyridin-2-amine (**130**)

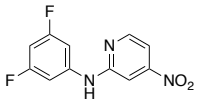

Compound **130** was synthesised from 3,5-difluoroaniline (509 mg, 3.94 mmol) and 2-bromo-4-nitropyridine (1.11 g, 5.47 mmol) according to **General Procedure E**. $Pd(dba)_2$ (67.1 mg, 0.12 mmol), Xantphos (149 mg, 0.26 mmol), Cs_2CO_3 (2.14 g, 6.57 mmol) were utilised as the Pd-catalyst, ligand and base respectively. Compound **130** was isolated as a yellow solid (812 mg, 82%) following purification by flash chromatography (1:9 EtOAc:Hex). **^{1}H NMR** (500 MHz, $CDCl_3$) δ 8.50 (d, J = 4.6 Hz, 1H), 7.52 – 7.48 (m, 2H), 7.09 (dd, J = 7.0, 1.5 Hz, 2H), 6.98 (s, 1H), 6.55 (ddt, J = 8.9, 6.6, 1.8 Hz, 1H) ppm; **^{19}F NMR** (471 MHz, $CDCl_3$) δ -108.5 ppm; **^{13}C NMR** (126 MHz, $CDCl_3$) δ 164.7 (d, J = 15.0 Hz), 162.7 (d, J = 15.1 Hz), 156.5, 155.6, 150.9, 141.7 (t, J = 13.2 Hz), 108.4, 102.9 (d, J = 7.6 Hz), 102.8, 102.7 (d, J = 7.6 Hz), 98.9 (t, J = 25.8 Hz) ppm; **LRMS (-ESI)** m/z: 250 ([M-H]$^-$, 100); **HRMS (-ESI)** Calc. for $C_{11}H_7F_2N_3O_2$ [M-H]$^-$: 250.04336, found 250.04329.

N-(3,5-difluorophenyl)-*N*-(4-nitropyridin-2-yl)acetamide (**131**)

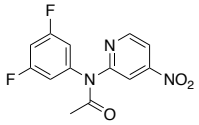

4-*N,N*-Dimethylaminopyridine (DMAP, 21.4 mg, 0.18 mmol) was added to a stirring solution of **130** (523 mg, 2.08 mmol) in acetic anhydride (10 mL). The reaction was heated to 110 °C for 4 h. After cooling to rt the mixture was concentrated to dryness *in vacuo*. The crude residue was partitioned between EtOAc (10 mL) and H_2O (10 mL). The aqueous layer was extracted with EtOAc (3 x 25 mL/mmol). The combined organic layer was washed with brine (1 x 25 mL/mmol), dried with $MgSO_4$ and concentrated *in vacuo*. Compound **131** was isolated as a white crystalline solid (610 mg, quant.) following purification by flash chromatography (1:4 EtOAc:Hex). **^{1}H NMR** (300 MHz, $CDCl_3$) δ 8.59 (d, J = 5.4 Hz, 1H), 8.51 (d, J = 1.7 Hz, 1H), 7.83 (dd, J = 5.4, 2.0 Hz, 1H), 6.97 – 6.79 (m, 3H), 2.17 (s, 3H) ppm; **^{19}F NMR** (282 MHz, $CDCl_3$) δ -107.37 ppm; **^{13}C NMR** (75 MHz, $CDCl_3$) δ 170.7, 165.1 (d, J = 14.0 Hz), 161.8 (d, J = 14.1 Hz), 156.1, 155.2, 150.3, 143.3 (t, J = 12.0 Hz), 113.7, 113.1 (d, J = 8.8 Hz), 113.1, 112.9 (d, J = 8.8 Hz), 104.8 (t, J = 25.3 Hz), 24.9 ppm; **LRMS (+ESI)** m/z: 294 ([M+H]$^+$,

100), **(-ESI)** m/z: 293 ([M-H]$^-$, 100); **HRMS (+ESI)** Calc. for $C_{13}H_9F_2N_3NaO_3$ [M+Na]$^+$: 316.05042, found 316.05012.

N-(4-aminopyridin-2-yl)-*N*-(3,5-difluorophenyl)acetamide (**132**)

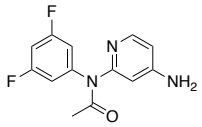

$Fe_{(s)}$ (203 mg, 3.64 mmol) was added slowly to a stirring solution of **131** (200 mg, 0.68 mmol) in glacial AcOH (1 mL). The reaction was stirred at rt for 3 h. After TLC demonstrated consumption of starting material, the reaction was filtered over a pad of celite. The celite pad was washed with EtOAc and the subsequent filtrate concentrated. The resulting residue was partitioned between EtOAc (10 mL) and H_2O (10 mL). Aqueous layers were then washed with EtOAc (3 x 25 mL/mmol). The combined organic extracts were washed with brine (1 x 25 mL/mmol), dried over $MgSO_4$ and concentrated *in vacuo*. The crude residue was purified by flash chromatography (1:9 EtOAc/Hex) to yield compound **132** (185 mg, 84%) as a beige solid. **^{1}H NMR** (300 MHz, $CDCl_3$) δ 8.10 (d, J = 6.2 Hz, 1H), 6.85 (dd, J = 8.1, 2.2 Hz, 2H), 6.68 (tt, J = 8.8, 2.3 Hz, 1H), 6.50 – 6.45 (m, 2H), 4.39 (s, 2H), 2.10 (s, 3H) ppm; **^{19}F NMR** (282 MHz, $CDCl_3$) δ -109.13 ppm; **^{13}C NMR** (75 MHz, $CDCl_3$) δ 170.6, 164.6 (d, J = 14.3 Hz), 161.4 (d, J = 14.3 Hz), 155.8, 155.2, 149.9, 144.0 (t, J = 12.5 Hz), 110.5 (d, J = 8.8 Hz), 110.2 (d, J = 8.7 Hz), 109.2, 107.3, 102.3 (t, J = 25.5 Hz), 24.1 ppm; **LRMS (+ESI)** m/z: 286 ([M+Na]$^+$, 100), **(-ESI)** m/z: 262 ([M-H]$^-$, 100); **HRMS (+ESI)** Calc. for $C_{13}H_{11}F_2N_3NaO$ [M+Na]$^+$: 286.07624, found 286.07586.

2-(2,6-dichlorophenyl)-*N*-(2-(*N*-(3,5-difluorophenyl)acetamido)pyridin-4-yl)acetamide (**124)**

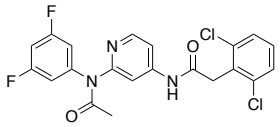

Compound **124** was prepared *via* a T_3P mediated amide coupling according to **General Procedure G** from **132** (30.9 mg, 0.12 mmol) and 2-(2,6-dichlorophenyl)acetic acid (26.4 mg, 0.13 mmol). Compound **124** was isolated as a white solid (8 mg, 19%) following purification by flash chromatography (1:1 EtOAc:Hex). **^{1}H NMR** (500 MHz, DMSO-d_6) δ 10.97 (s, 1H), 8.38 (d, J = 5.6 Hz, 1H), 7.76 (d, J = 2.0 Hz, 1H), 7.57 – 7.53 (m, 3H), 7.42 (dd, J = 8.6, 7.6 Hz, 1H), 7.27 (tt, J = 9.3, 2.4 Hz, 1H), 7.13 (dd, J = 8.0, 2.2 Hz, 2H), 4.15 (s, 2H), 2.08 (s, 3H) ppm; **^{19}F NMR** (471 MHz, DMSO-d_6) δ -109.5 ppm; **^{13}C NMR** (126 MHz, DMSO-d_6) δ 169.6,

167.9, 163.2 (d, J = 14.7 Hz), 161.3 (d, J = 14.9 Hz), 155.2, 149.6, 147.7, 144.3 (t, J = 12.1 Hz), 135.5, 131.5, 129.7, 128.2, 111.5 (d, J = 5.0 Hz), 111.4 (d, J = 5.1 Hz), 102.7 (t, J = 23.5 Hz), 38.7, 23.9 ppm; **LRMS (+ESI)** m/z: 472/474/476 ($[M+Na]^+$, 100), **(-ESI)** m/z: 448 ($[M-H]^-$, 100); **HRMS (+ESI)** Calc. for $C_{21}H_{15}Cl_2F_2N_3NaO_2$ $[M+Na]^+$: 472.04016/474.03721/476.03426, found 472.04026/474.03744/476.03464; **HPLC** R_T = 23.58 min, 98.63% (254 nm).

2-((3*r*,5*r*,7*r*)-adamantan-1-yl)-*N*-(2-(*N*-(3,5-difluorophenyl)acetamido)pyridin-4-yl)acetamide (**125**)

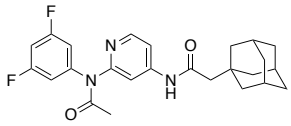

Compound **125** was prepared *via* an acid chloride amide coupling according to **General Procedure D** from **132** (150 mg, 0.46 mmol) and 1-adamantaneacetic acid (109 mg, 0.56 mmol). Compound **125** was isolated as a white solid (57.1 mg, 28%) following purification by flash chromatography (1:4 EtOAc:Hex). **^{1}H NMR** (500 MHz, DMSO-d_6) δ 10.31 (s, 1H), 8.29 (d, J = 5.6 Hz, 1H), 7.68 (s, 1H), 7.54 (dd, J = 5.6, 1.9 Hz, 1H), 7.20 (tt, J = 9.3, 2.4 Hz, 1H), 7.07 (dd, J = 8.2, 2.4 Hz, 2H), 2.09 (s, 2H), 2.02 (s, 3H), 1.92 (dd, J = 7.3, 4.1 Hz, 3H), 1.68 – 1.55 (m, 15H) ppm; **^{19}F NMR** (471 MHz, DMSO-d_6) δ -109.5 ppm; **^{13}C NMR** (126 MHz, DMSO-d_6) δ 170.6, 169.6, 163.2 (d, J = 14.8 Hz), 161.3 (d, J = 14.8 Hz), 155.1, 149.4, 147.8, 144.3 (t, J = 12.9 Hz), 112.0, 111.5 (d, J = 5.5 Hz), 111.3 (d, J = 5.2 Hz), 110.4, 102.6 (t, J = 25.9 Hz), 50.8, 42.0, 41.8, 36.3, 32.8, 28.0, 23.9 ppm; **LRMS (+ESI)** m/z: 462 ($[M+Na]^+$, 100), **(-ESI)** m/z: 438 ($[M-H]^-$, 100); **HRMS (+ESI)** Calc. for $C_{25}H_{27}F_2N_3O_2$ $[M+H]^+$: 440.21441, found 440.21443; **HPLC** R_T = 26.37 min, 97.78% (254 nm).

4-nitro-*N*-phenylpyridin-2-amine (**122**)

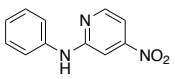

Compound **121** was synthesised from aniline (300 µL, 3.22 mmol) and 2-bromo-4-nitropyridine (910 mg, 4.48 mmol) according to **General Procedure E**. $Pd(dba)_2$ (52.1 mg, 0.09 mmol), Xantphos (125 mg, 0.22 mmol) and Cs_2CO_3 (1.56 g, 4.79 mmol) were utilised as the Pd-catalyst, ligand and base respectively. Compound **122** was isolated as a yellow solid (512 mg, 74%) following purification by flash chromatography (1:9 EtOAc:Hex). **^{1}H NMR** (500 MHz, $CDCl_3$) δ 8.41 (d, J = 5.5 Hz, 1H), 7.49 (d, J = 1.9 Hz, 1H), 7.41 (t, J = 7.7 Hz, 2H), 7.39 – 7.34 (m, 3H), 7.19 (t, J = 7.3 Hz, 1H), 7.07 (s, 1H) ppm; **^{13}C NMR** (126 MHz,

$CDCl_3$) δ 158.2, 155.8, 150.9, 138.9, 129.8, 124.9, 121.8, 107.1, 100.7 ppm; **LRMS (+ESI)** m/z: 216 ($[M+H]^+$, 100), **(-ESI)** m/z: 214 ($[M-H]^-$, 100); **HRMS (-ESI)** Calc. for $C_{11}H_9N_3O_2$ $[M-H]^-$: 214.06220, found 214.06189.

N-(4-nitropyridin-2-yl)-*N*-phenylacetamide (**121**)

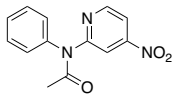

DMAP (21.4 mg, 0.18 mmol) was added to a stirring solution of **122** (407 mg, 1.89 mmol) in acetic anhydride (8 mL). The reaction was heated to 110 °C for 4 h. After cooling to rt the mixture was concentrated to dryness *in vacuo*. The crude residue was partitioned between EtOAc (10 mL) and H_2O (10 mL). The aqueous layer was extracted with EtOAc (3 x 25 mL/mmol). The combined organic layer was washed with brine (1 x 25 mL/mmol), dried with $MgSO_4$ and concentrated *in vacuo*. Compound **121** was isolated as an off white solid (456 mg, 94%) following purification by flash chromatography (1:9 EtOAc:Hex). **^{1}H NMR** (300 MHz, $CDCl_3$) δ 8.58 (d, J = 1.9 Hz, 1H), 8.55 (d, J = 5.4 Hz, 1H), 7.76 (dd, J = 5.4, 2.0 Hz, 1H), 7.56 – 7.39 (m, 3H), 7.34 – 7.25 (m, 2H), 2.11 (s, 3H) ppm; **^{13}C NMR** (75 MHz, $CDCl_3$) δ 171.6, 156.8, 155.0, 150.1, 141.3, 130.04, 129.3, 128.8, 113.0, 25.0 ppm; **LRMS (+ESI)** m/z: 280 ($[M+Na]^+$, 80); **HRMS (+ESI)** Calc. for $C_{13}H_{11}N_3NaO_3$ $[M+Na]^+$: 280.06926, found 280.06926.

N-(4-aminopyridin-2-yl)-*N*-phenylacetamide (**120**)

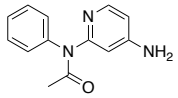

A solution of **121** (102 mg, 398 µmol) in EtOAc (3 mL) was purged under an atmosphere of N_2. The reaction mixture was then treated with Pd/C (10% w/w, 47.3 mg, 44.4 µmol) and put under an atmosphere of H_2 (balloon) at rt. The reaction mixture was then allowed to stir for 2 h, until TLC indicated conversion of starting material. The reaction mixture was then filtered through a pad of Celite® and concentrated *in vacuo* to yield compound **120** (90 mg, quant.) as a white solid. **^{1}H NMR** (300 MHz, $CDCl_3$) δ 8.01 (d, J = 5.6 Hz, 1H), 7.40 – 7.27 (m, 2H), 7.27 (s, 1H), 7.28 – 7.18 (m, 2H), 6.52 (d, J = 2.2 Hz, 1H), 6.35 (dd, J = 5.6, 2.2 Hz, 1H), 4.27 (s, 2H), 2.06 (s, 3H) ppm; **^{13}C NMR** (75 MHz, $CDCl_3$) δ 171.0, 156.4, 154.9, 149.4, 142.2, 129.4, 127.9, 127.3, 108.6, 106.9, 24.1 ppm; **LRMS (+ESI)** m/z: 228 ($[M+H]^+$, 100), 250

([M+Na]$^+$, 100), **(-ESI)** m/z: 226 ([M-H]$^-$, 100); **HRMS (+ESI)** Calc. for $C_{13}H_{13}N_3NaO$ [M+Na]$^+$: 250.09508, found 250.09486.

2-((3*r*,5*r*,7*r*)-adamantan-1-yl)-*N*-(2-(*N*-phenylacetamido)pyridin-4-yl)acetamide (**127**)

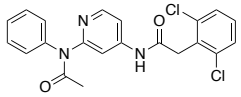

Compound **127** was prepared *via* an acid chloride amide coupling according to **General Procedure D** from **120** (40.4 mg, 0.18 mmol) and 1-adamantaneacetic acid (40.4 mg, 0.21 mmol). Compound **127** was isolated as a white solid (24.2 mg, 34%) following purification by flash chromatography (1:9 EtOAc:Hex). **^{1}H NMR** (500 MHz, DMSO-d_6) δ 10.25 (s, 1H), 8.25 (d, J = 5.6 Hz, 1H), 7.63 (d, J = 1.9 Hz, 1H), 7.49 (dd, J = 5.6, 1.9 Hz, 1H), 7.44 – 7.38 (m, 2H), 7.33 – 7.29 (m, 1H), 7.29 – 7.26 (m, 2H), 2.07 (s, 2H), 1.99 (s, 3H), 1.95 – 1.90 (m, 3H), 1.68 – 1.63 (m, 3H), 1.62 – 1.56 (m, 9H) ppm; **^{13}C NMR** (126 MHz, DMSO-d_6) δ 170.5, 169.7, 155.9, 149.1, 147.5, 142.0, 129.2, 128.0, 127.1, 111.6, 110.2, 50.8, 41.9, 36.3, 32.8, 28.0, 23.8 ppm; **LRMS (+ESI)** m/z: 404 ([M+H]$^+$, 30), 426 ([M+Na]$^+$, 100), **(-ESI)** m/z: 402 ([M-H]$^-$, 100); **HRMS (+ESI)** Calc. for $C_{25}H_{29}N_3O_2$ [M+H]$^+$: 404.23325, found 404.23342; **HPLC** R_T = 22.84 min, 98.92% (254 nm).

2-(2,6-dichlorophenyl)-*N*-(2-(*N*-phenylacetamido)pyridin-4-yl)acetamide (**126**)

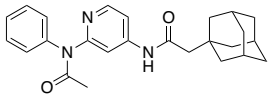

Compound **126** was prepared *via* an acid chloride amide coupling according to **General Procedure D** from **120** (39.9 mg, 0.18 mmol) and 2-(2,6-dichlorophenyl)acetic acid (34.3 mg, 0.17 mmol). Compound **126** was isolated as a white solid (21.8 mg, 30%) following purification by flash chromatography (1:1 EtOAc:Hex). **^{1}H NMR** (500 MHz, DMSO-d_6) δ 10.86 (s, 1H), 8.28 (d, J = 5.6 Hz, 1H), 7.65 (d, J = 2.0 Hz, 1H), 7.50 (s, 1H), 7.48 (s, 1H), 7.43 (dd, J = 5.7, 1.9 Hz, 1H), 7.40 (t, J = 7.7 Hz, 2H), 7.35 (dd, J = 8.6, 7.6 Hz, 1H), 7.30 (tt, J = 7.5, 1.9 Hz, 1H), 7.28 – 7.26 (m, 2H), 4.07 (s, 2H), 1.99 (s, 3H) ppm; **^{13}C NMR** (126 MHz, DMSO-d_6) δ 169.7, 167.9, 156.0, 149.3, 147.4, 142.0, 135.5, 131.6, 129.7, 129.2, 128.2, 128.0, 127.1, 111.5, 110.3, 38.6, 23.8 ppm; **LRMS (+ESI)** m/z: 436 ([M+Na]$^+$, 100), **(-ESI)** m/z: 412 ([M-H]$^-$, 100); **HRMS (+ESI)** Calc. for $C_{21}H_{17}Cl_2N_3O_2$ [M+H]$^+$: 414.07706/ 416.07411/418.07116, found 414.07720/416.07425/418.07127; **HPLC** R_T = 20.17 min, 98.36% (254 nm).

ethyl (3*s*,5*s*,7*s*)-3,5,7-trifluoroadamantane-1-carboxylate (**138)**

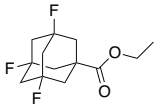

H_2SO_4 (catalytic amount) was added to a stirred solution of (3*s*,5*s*,7*s*)-3,5,7-trifluoroadamantane-1-carboxylic acid (999 mg, 4.27 mmol) in absolute EtOH (8 mL) and the resulting mixture brought to reflux for 2 hours upon which time the solvent was removed *in vacuo*. The residue was taken up in ether (15 mL) and washed subsequently with saturated $NaHCO_3$ (10 mL) and brine (10 mL), dried over $MgSO_4$, filtered and concentrated to give compound **138** as a white solid (840 mg, 75%) which was used in the next step without further purification. **^{1}H NMR** (400 MHz, $CDCl_3$) δ 4.18 (q, J = 7.1 Hz, 2H), 2.20 – 2.04 (m, 8H), 2.01 – 1.96 (m, 7H), 1.28 (t, J = 7.1 Hz, 3H) ppm; **^{19}F NMR** (376 MHz, $CDCl_3$) δ -143.3 ppm; **^{13}C NMR** (101 MHz, $CDCl_3$) δ 173.1 (q, J = 3.4 Hz), 92.9 (t, J = 15.2 Hz), 91.0 (t, J = 15.2 Hz), 61.7, 46.9 – 46.2 (m), 43.4 (q, J = 11.7 Hz), 42.4 – 41.9 (m), 14.2 ppm; **LRMS (+APCI)** m/z: 263 ($[M+H]^+$, 100); **HRMS (+APCI)** Calc. for $C_{13}H_{18}F_3O_2$ $[M+H]^+$: 263.12534, found 263.12519.

((3*s*,5*s*,7*s*)-3,5,7-trifluoroadamantan-1-yl)methanol (**137)**

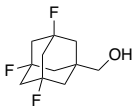

Compound **137** was prepared from **138** (809 mg, 3.08 mmol) according to **General Procedure H** to give compound **137** as a white crystalline solid (632 mg, 93%). **^{1}H NMR** (400 MHz, $CDCl_3$) δ 3.50 (s, 2H), 2.22 – 2.00 (m, 6H), 1.71 – 1.64 (m, 6H) ppm; **^{19}F NMR** (376 MHz, $CDCl_3$) δ -143.1 ppm; **^{13}C NMR** (101 MHz, $CDCl_3$) δ 93.3 (t, J = 15.0 Hz), 91.4 (t, J = 15.1 Hz), 70.1 (q, J = 2.3 Hz), 47.2 – 46.5 (m), 42.6 – 42.0 (m), 38.9 (q, J = 10.5 Hz) ppm; **LRMS (-ESI)** m/z: 219 ($[M-H]^-$, 100).

(3*s*,5*s*,7*s*)-3,5,7-trifluoroadamantane-1-carbaldehyde (**136)**

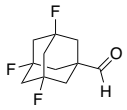

Method A: PCC (323 mg, 1.50 mmol) was added portionwise to a stirring solution of alcohol **137** (193 mg, 0.88 mmol) in CH_2Cl_2 (10 mL). The reaction was stirred at rt for 4 h. Upon full conversion of starting material as indicated by TLC, the reaction mixture was filtered over a bed of celite. The organic mixture was washed with H_2O (3 x 25 mL/mmol), brine (1 x 25 mL/mmol), dried and concentrated *in vacuo.* The resulting residue was redissolved in diethyl ether (5 mL) and filtered through celite to give compound **136** as an off-white oil (130 mg, 68%).

Method B: DMP (701 mg, 1.65 mmol) was added portion wise to a solution of alcohol **137** (302 mg, 1.37 mmol) in CH_2Cl_2 (4 mL) at 0 °C. The resultant slurry was stirred for 2 h at rt. Upon completion, the reaction contents were quenched with sat. aqueous $Na_2S_2O_3$ (5 mL) and sat. aqueous $NaHCO_3$ (5 mL). The resultant biphasic system was stirred vigorously for 5 min at rt, then filtered over a pad of celite. The filtrate was extracted with CH_2Cl_2, washed with brine, dried and concentrated. Compound **136** was isolated as an off-white oil (147 mg, 49%) following purification by flash chromatography (100% Hex).

Method C: A solution of alcohol **137** (103 mg, 0.47 mmol) and NMO (139 mg, 1.19 mmol) in CH_2Cl_2 (8 mL) was cooled to 0 °C under an atmosphere of N_2. The reaction mixture was then treated portionwise with TPAP (44.2 mg, 0.13 mmol) over a period of 10 min, and allowed to warm to rt. The reaction mixture was stirred at rt for 4 h, at which point TLC indicated conversion. The reaction mixture was then concentrated *in vacuo* directly purified by flash chromatography (100% Hex) to yield the corresponding aldehyde (**137**) (31.2 mg, 31%).

^{1}H NMR (400 MHz, $CDCl_3$) δ 9.48 (q, J = 1.6 Hz, 1H), 2.29 – 2.01 (m, 6H), 1.86 (q, J = 2.8 Hz, 6H) ppm; **^{19}F NMR** (376 MHz, $CDCl_3$) δ -143.1 ppm; **^{13}C NMR** (101 MHz, $CDCl_3$) δ 199.3 (q, J = 2.5 Hz), 93.2 (t, J = 14.8 Hz), 90.7 (t, J = 14.8 Hz), 48.1 (d, J = 10.3 Hz), 47.1 – 46.2 (m), 39.9 – 39.1 (m) ppm; **LRMS (+APCI)** m/z: 219 ($[M+H]^+$, 100); **HRMS (+APCI)** Calc. for $C_{11}H_{14}F_3O$ $[M+H]^+$: 219.09913, found 219.09951.

(3*r*,5*r*,7*r*)-1-(2,2-dibromovinyl)adamantane (**143)**

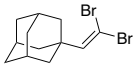

To an ice-cold stirred solution of (3*r*,5*r*,7*r*)-adamantane-1-carbaldehyde (155 mg, 0.94 mmol) and CBr_4 (648 mg, 1.95 mmol) in CH_2Cl_2 (3 mL) was added triphenylphosphine (952 mg, 3.63 mmol) in CH_2Cl_2 (2 mL). The reaction was stirred at rt for 2 h, at which point TLC indicated conversion. The reaction was quenched with hexane (5 mL) and filtered through celite. The resulting filtrate was concentrated *in vacuo* and purified *via* flash chromatography (100% Hex) to yield compound **143** as a white crystalline solid (196 mg, 65%). **^{1}H NMR** (300 MHz, $CDCl_3$) δ 6.38 (s, 1H), 1.99 (p, J = 3.2 Hz, 3H), 1.91 (d, J = 2.9 Hz, 6H), 1.69 (t, J = 3.1 Hz, 6H) ppm; **^{13}C NMR** (75 MHz, $CDCl_3$) δ 147.2, 84.3, 40.8, 38.4, 36.7, 28.6 ppm; **HRMS (+APCI)** Calc. for $C_{12}H_{16}Br_2$ $[M]^+$: 317.96133/319.95928/321.95723, found 317.96171/319.95964/ 321.95789.

2-((3*r*,5*r*,7*r*)-adamantan-1-yl)acetic acid (**145**)

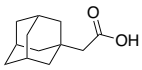

n-BuLi (2.5 M in hexane, 250 µL, 0.62 mmol) was added dropwise to a stirring solution of **143** (80 mg, 0.25 mmol) in THF (3 mL) at 0 °C, at stirred for 1 h. ^{i}PrOBpin (80 µL, 0.37 mmol) added to the reaction mixture and stirred for 2 h at 0 °C. Upon completion the reaction was quenched with HCl (4 M in 1,4-dioxane, 100 µL, 0.38 mmol). Then the reaction mixture was allowed to warm to room temperature and stirred for another 1 h. Solvent was then removed *in vacuo*, and the residue was diluted with diethyl ether (3 mL). Precipitate was removed by filtration, and the filtrate was washed H_2O (3 mL), and extracted with ether (10 mL). Combined organic layers were washed with brine (1 x 25 mL/mmol), dried and concentrated. The crude was used in the next step without further purification. To a solution of alkynyl boronate in acetone (1 mL) a solution of Oxone® (67.7 mg, 0.44 mmol) dissolved in H_2O (1 mL) was added dropwise. The reaction mixture was stirred for 12 h at 50 °C. Reaction was cooled to rt and extracted with EtOAc (3 x 25 mL/mmol). Combined organic layers were washed with brine (1 x 25 mL/mmol), dried and concentrated to give compound **145** as a white crystalline solid (23.8 mg, 49%). **^{1}H NMR** (500 MHz, $CDCl_3$) δ 2.10 (s, 2H), 1.98 (p, J = 3.2 Hz, 3H), 1.74 – 1.61 (m, 12H) ppm; **^{13}C NMR** (126 MHz, $CDCl_3$) δ 177.8, 48.8, 42.4, 36.8, 32.8, 28.8 ppm; **LRMS (-ESI)** m/z: 193 ($[M-H]^-$, 100). Matched previously reported characterisation data.[460]

(3*s*,5*s*,7*s*)-1-(2,2-dibromovinyl)-3,5,7-trifluoroadamantane (**146)**

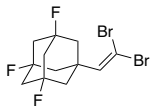

To an ice-cold stirred solution of **136** (80 mg, 0.54 mmol) and CBr_4 (383 mg, 1.15 mmol) in CH_2Cl_2 (1.5 mL) was added triphenylphosphine (570 mg, 2.17 mmol) in CH_2Cl_2 (500 µL). The reaction was stirred at rt for 2 h, at which point TLC indicated conversion. The reaction was quenched with hexane (5 mL) and filtered through celite. The resulting filtrate was concentrated *in vacuo* and purified *via* flash chromatography (100% Hex) to yield compound **146** as a white powder (90 mg, 52%). **^{1}H NMR** (400 MHz, $CDCl_3$) δ 6.48 (s, 1H), 2.18 – 2.05 (m, 6H), 2.03 (s, 6H) ppm; **^{19}F NMR** (376 MHz, $CDCl_3$) δ -143.1 ppm; **^{13}C NMR** (101 MHz, $CDCl_3$) δ 140.5 (q, J = 2.3 Hz), 92.5 (t, J = 15.6 Hz), 90.6 (t, J = 15.6 Hz), 89.0, 47.0 – 46.1 (m), 43.8 – 43.0 (m), 40.3 (q, J = 12.4 Hz) ppm; **HRMS (+APCI)** Calc. for $C_{12}H_{13}Br_2F_3$ $[M]^+$: 371.93306/373.93101/375.92897, found 371.93503/373.93291/375.93118.

2,2-dibromo-1-((3*s*,5*s*,7*s*)-3,5,7-trifluoroadamantan-1-yl)ethan-1-one (**148)**

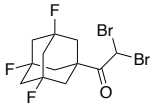

A solution of **138** (99.8 mg, 0.38 mmol) and dibromomethane (80 µL, 1.14 mmol) in THF (1 mL) was cooled to -78 °C. In a separate flask, a solution of TMP (180 µL, 1.06 mmol) in THF (500 µL) was cooled to 0 °C and treated with *n*-BuLi (2.5 M in hexanes, 360 µL, 0.90 mmol). The solution of LiTMP was immediately added dropwise to the ester solution over 15 min. After 20 min at -78 °C, the reaction mixture was added with caution to aq. HCl (1 M, 2 mL) and extracted with hexane (10 mL). Combined organic layers were washed with H_2O (1 x 25 mL/mmol), dried and concentrated *in vacuo*. Compound **148** was isolated as an off white solid (65 mg, 44%) following purification by flash chromatograpy (1:9 EtOAc:Hex). **^{1}H NMR** (400 MHz, $CDCl_3$) δ 6.24 (s, 1H), 2.26 – 2.02 (m, 12H) ppm; **^{19}F NMR** (376 MHz, $CDCl_3$) δ -143.1 ppm; **^{13}C NMR** (101 MHz, $CDCl_3$) δ 195.5, 93.0 (dt, J = 25.8, 15.2 Hz), 90.5 (dt, J = 27.2, 15.1 Hz), 48.0 (q, J = 11.1 Hz), 46.8 – 46.0 (m), 42.3 – 41.7 (m) ppm; **LRMS (+APCI)** m/z: 389/391/393 ($[M+H]^+$, 20); **HRMS (+APCI)** Calc. for $C_{12}H_{14}Br_2F_3O$ $[M+H]^+$: 388.93580/390.93375/392.93171, found 388.93615/390.93406/ 392.93230.

7.5 Chapter 3 Experimental and Characterisation

ethyl 4-(furan-2-yl)-2,4-dioxobutanoate (**157**)

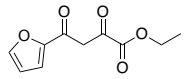

A suspension of *t*-BuOK (3.76 g, 33.0 mmol) in anhydrous THF (10 mL) was cooled to 0 °C. Commercially available 2-acetylfuran (1.88 g, 17.0 mmol) and diethyl oxalate (4.4 mL, 32.0 mmol) in 1,2-dimethoxyethane (10 mL) was added dropwise to the stirring suspension. The reaction was allowed to come to room temperature over the next hour, and a precipitate formed. Upon consumption of acetyl furan, confirmed via TLC, the mixture was quenched with 1M solution of HCl (17 mL, 17.0 mmol), dissolving the precipitate. The crude product was extracted with EtOAc (3 x 25 mL/mmol) and the pooled organic phase was washed with brine (1 x 25 mL/mmol) and dried over $MgSO_4$. Compound **157** was obtained as yellow crystals (2.98 g, 83%) following purification by flash chromatography (1:49 EtOAc:Hex). **^{1}H NMR** (400 MHz, $CDCl_3$) δ 14.45 (s, 1H), 7.67 (dd, J = 1.7, 0.8 Hz, 1H), 7.34 (dd, J = 3.7, 0.8 Hz, 1H), 6.93 (s, 1H), 6.61 (dd, J = 3.6, 1.7 Hz, 1H), 4.38 (q, J = 7.2 Hz, 2H), 1.40 (t, J = 7.1 Hz, 3H) ppm; **^{13}C NMR** (101 MHz, $CDCl_3$) δ 181.1, 166.3, 162.1, 151.1, 147.8, 118.5, 113.2, 99.1, 62.7, 14.2 ppm; **LRMS (+ESI)** m/z: 233 ($[M+Na]^+$, 100), **(-ESI)** m/z: 209 ($[M-H]^-$, 100); **HRMS (+ESI)** Calc. for $C_{10}H_{10}NaO_5$ $[M+Na]^+$: 233.04204, found 233.04207. Matched previously reported characterisation data.[263]

ethyl 1-(*tert*-butyl)-5-(furan-2-yl)-1H-pyrazole-3-carboxylate (**160**)

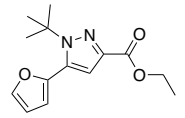

Compound **160** was synthesised from **157** (1.52 g, 7.23 mmol) and *tert*-butylhydrazine hydrochloride (1.24 g, 9.95 mmol) according to **General Procedure I** and was obtained as a yellow oil (1.78 g, 94%) following purification by flash chromatography (1:4 EtOAc:Hex). **^{1}H NMR** (500 MHz, $CDCl_3$) δ 7.55 (dd, J = 1.7, 0.7 Hz, 1H), 6.87 (s, 1H), 6.49 (dd, J = 3.3, 1.8 Hz, 1H), 6.47 (dd, J = 3.3, 0.7 Hz, 1H), 4.38 (q, J = 7.1 Hz, 2H), 1.55 (s, 9H), 1.38 (t, J = 7.1 Hz, 3H) ppm; **^{13}C NMR** (126 MHz, $CDCl_3$) δ 162.6, 143.9, 143.0, 140.7, 133.5, 113.9, 112.2, 111.5, 62.7, 60.9, 30.0, 14.5 ppm; **LRMS (+APCI)** m/z: 263 ($[M+H]^+$, 100); **LRMS (+ESI)** m/z: 285 ($[M+Na]^+$, 100); **HRMS (+ESI)** Calc. for $C_{14}H_{19}N_2O_3$ $[M+H]^+$: 263.13902, found 263.13932. Matched previously reported characterisation data.[263]

(1-(*tert*-butyl)-5-(furan-2-yl)-1H-pyrazol-3-yl) methanol (**161**)

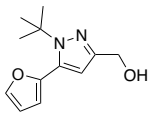

Compound **161** was prepared from **160** (1 g, 3.81 mmol) and treated with $LiAlH_4$ (1M in THF, 6.8 mL, 6.81 mmol) in THF (5 mL) according to **General Procedure H**. Compound **161** was isolated as a white solid (749 mg, 89%). **^{1}H NMR** (400 MHz, $CDCl_3$) δ 7.52 (dd, J = 1.9, 0.9 Hz, 1H), 6.47 (dd, J = 3.3, 1.9 Hz, 1H), 6.42 (dd, J = 3.3, 0.9 Hz, 1H), 6.34 (s, 1H), 4.67 (s, 2H), 1.49 (s, 9H) ppm, OH signal not observed; **^{13}C NMR** (101 MHz, $CDCl_3$) δ 148.9, 144.9, 142.6, 133.1, 111.6, 111.3, 109.3, 61.1, 59.2, 30.2 ppm; **LRMS (+APCI)** m/z: 221 ($[M+H]^+$, 100); **HRMS (+APCI)** Calc. for $C_{12}H_{17}N_2O_2$ $[M+H]^+$: 221.12845, found 221.12847.

1-(*tert*-butyl)-5-(furan-2-yl)-1H-pyrazole-3-carbaldehyde (**155**)

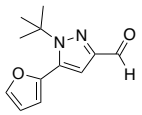

DMP (1.85 g, 4.36 mmol) was added portion wise to a solution of alcohol **161** (570 mg, 2.6 mmol) in CH_2Cl_2 (15 mL) at 0 °C. The resultant slurry was stirred for 1 h at rt. Upon completion, the reaction contents were quenched with sat. aqueous $Na_2S_2O_3$ (5 mL) and sat. aqueous $NaHCO_3$ (5 mL). The resultant biphasic system was stirred vigorously for 5 min at rt, then filtered over a pad of celite. The filtrate was extracted with CH_2Cl_2, washed with brine, dried and concentrated *in vacuo*. Compound **155** was isolated as a white solid (530 mg, 94%) following purification by flash chromatography (1:9 EtOAc:Hex). **^{1}H NMR** (400 MHz, $CDCl_3$) δ 9.96 (s, 1H), 7.56 (dd, J = 1.8, 0.9 Hz, 1H), 6.88 (s, 1H), 6.52 – 6.48 (m, 2H), 1.56 (s, 9H) ppm; **^{13}C NMR** (101 MHz, $CDCl_3$) δ 186.9, 148.5, 143.6, 143.2, 134.4, 112.5, 111.6, 110.7, 63.0, 30.0 ppm; **LRMS (+APCI)** m/z: 219 ($[M+H]^+$, 100) ppm; **HRMS (+APCI)** Calc. for $C_{12}H_{15}N_2O_2$ $[M+H]^+$: 219.11280, found 219.11288.

2-(1-(*tert*-butyl)-5-(furan-2-yl)-1H-pyrazol-3-yl)-5-chloro-1Hbenzo[d]imidazole (**37**)

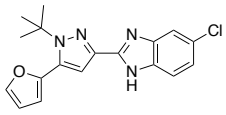

Compound **155** (40.2 mg, 184 µmol), 4-chlorobenzene-1,2-diamine (31.4 mg, 220 µmol) and sodium bisulfite (40.5 mg, 389 µmol) were dissolved in a solution of EtOH/H_2O (2:1, 2 mL) and refluxed for 1 h. The reaction solution was extracted with EtOAc (3 x 25 mL/mmol), dried with $MgSO_4$, concentrate *in vacuo*. Compound **37** was isolated as a white solid (47 mg, 75%) following purification by flash chromatography (1:4 EtOAc:Hex). Characterisation data is reported as a complex mix of tautomers. **^{1}H NMR** (500 MHz, DMSO-d_6) δ 12.94 – 12.70 (m, 1H), 7.91 (d, J = 1.7 Hz, 1H), 7.70 – 7.59 (m, 1H), 7.54 – 7.49 (m, 1H), 7.26 – 7.16 (m, 1H), 7.03 (s, 1H), 6.76 (d, J = 3.3 Hz, 1H), 6.67 (dd, J = 3.3, 1.9 Hz, 1H), 1.55 (s, 9H) ppm; **^{13}C NMR** (126 MHz, DMSO-d_6) δ 147.9, 147.5, 144.6, 143.9, 143.0, 142.5, 139.8, 135.2, 133.5, 133.3, 126.7, 125.9, 122.6, 121.9, 119.9, 118.1, 112.8, 112.5, 111.8, 111.2, 110.1, 61.8, 29.6 ppm; 2D Spectra available in Appendix 5; **LRMS (+ESI)** m/z: 341/343 ($[M+H]^+$, 100), 363/365 ($[M+Na]^+$, 100), **(-ESI)** m/z: 339/341 ($[M-H]^-$, 100); **HRMS (+ESI)** Calc. for $C_{18}H_{18}ClN_4O$ $[M+H]^+$: 341.11637/343.11342, found 341.11696/343.11421; **HPLC** R_T = 21.04 min, 99.70% (254 nm).

2-(1-(*tert*-butyl)-5-(furan-2-yl)-1H-pyrazol-3-yl)-1h-benzo[d]-imidazole (**153**).

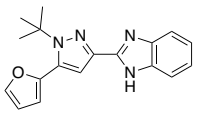

Compound **155** (29.1 mg, 133 µmol), *o*-phenyldiamine (23.4 mg, 216 µmol) and sodium bisulfite (55.5 mg, 533 µmol) were dissolved in a solution of EtOH/H_2O (2:1, 2 mL) and refluxed for 1 h. The reaction solution was extracted with EtOAc (3 x 25 mL/mmol), dried with $MgSO_4$, and concentrated *in vacuo*. Compound **153** was isolated as a white solid (26.5 mg, 65%) following purification by flash chromatography (1:4 EtOAc:Hex). **^{1}H NMR** (400 MHz, $CDCl_3$) δ 9.96 (s, 1H), 7.79 (s, 1H), 7.57 (t, J = 1.4 Hz, 1H), 7.46 (s, 1H), 7.27 (s, 1H), 7.25 (d, J = 3.2 Hz, 1H), 6.51 (d, J = 1.2 Hz, 2H), 1.59 (s, 9H) ppm; **^{13}C NMR** (101 MHz, $CDCl_3$) δ 147.2, 144.1, 142.9, 140.2, 134.2, 123.3, 122.3, 119.8, 112.2, 111.6, 110.7, 110.2, 62.1, 30.1 ppm; **LRMS (+ESI)** m/z: 307 ($[M+H]^+$, 100), **(-ESI)** m/z: 305 ($[M-H]^-$, 100); **HRMS (+ESI)** Calc. for $C_{18}H_{19}N_4O$ $[M+H]^+$: 307.15534, found 307.15540; **HPLC** R_T = 19.11 min, 99.5% (254 nm).

1-(*tert*-butyl)-5-(furan-2-yl)-1*H*-pyrazole-3-carboxylic acid (**163**)

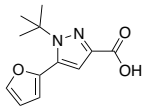

Prepared according to **General Procedure J** with **160** (1.51 g, 5.76 mmol) and $LiOH.H_2O$ (362 mg, 8.63 mmol). Compound **163** was obtained as a white solid (1.35 g, quant.) without need for further purification. **^{1}H NMR** (400 MHz, $CDCl_3$) δ 7.56 (dd, J = 5.9, 1.7 Hz, 1H), 6.96 (s, 1H), 6.52 – 6.49 (m, 2H), 1.56 (s, 9H) ppm, COOH signal not observed; **^{13}C NMR** (101 MHz, $CDCl_3$) δ 165.5, 143.5, 143.2, 139.7, 134.4, 114.2, 112.5, 111.6, 63.1, 30.0 ppm; **LRMS (+ESI)** m/z: 257 ($[M+Na]^+$, 70), **(-ESI)** m/z: 233 ($[M-H]^-$, 100); **HRMS (+ESI)** Calc. for $C_{12}H_{14}N_2NaO_3$ $[M+Na]^+$: 257.08966, found 257.08920.

2-(1-(*tert*-butyl)-5-(furan-2-yl)-1H-pyrazol-3-yl)benzo[d]oxazole (**154**)

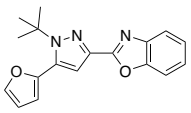

The aldehyde compound **155** (40.3 mg, 184 µmol) was added to a solution of *o*-aminophenol (21.8 mg, 200 µmol) in MeOH (1 mL). The resulting mixture was heated at 45 °C for 16 h and concentrated *in vacuo*. The residue was dissolved in CH_2Cl_2 (2 mL) and treated with 2,6-dimethyoxy-1,4-benzoquinone (DDQ, 50.7 mg, 223 µmol). The mixture was stirred at room temperature for 48 h. The resulting mixture was diluted with additional CH_2Cl_2 (5 mL) and washed with sat. aqueous $NaHCO_3$ (1 x 25 mL/mmol) and brine (1 x 25 mL/mmol). The crude product was purified by flash chromatography (1:49 EtOAc:Hex) to give compound **154** as an off-white powder (14.4 mg, 25%). **^{1}H NMR** (400 MHz, DMSO-d_6) δ 7.93 (dd, J = 1.9, 0.8 Hz, 1H), 7.84 – 7.75 (m, 2H), 7.48 – 7.37 (m, 2H), 7.18 (s, 1H), 6.81 (dd, J = 3.3, 0.8 Hz, 1H), 6.69 (dd, J = 3.3, 1.9 Hz, 1H), 1.55 (s, 9H) ppm; **^{13}C NMR** (101 MHz, DMSO-d_6) δ 157.6, 149.8, 144.0, 142.4, 141.2, 136.7, 133.8, 125.4, 124.8, 119.7, 112.8, 111.7, 111.7, 110.9, 62.3, 29.5 ppm; **LRMS (+ESI)** m/z: 308 ($[M+H]^+$, 50), 330 ($[M+Na]^+$, 100); **HRMS (+ESI)** Calc. for $C_{18}H_{18}N_3O_2$ $[M+H]^+$: 308.13935, found 308.13992; **HPLC** R_T = 27.74 min, 95.88% (254 nm).

2-(1-(*tert*-butyl)-5-(furan-2-yl)-1*H*-pyrazol-3-yl)-3*H*-imidazo[4,5-*b*]pyridine (**165**)

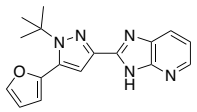

Compound **165** was synthesised from **155** (41.9 mg, 0.19 mmol) and pyridine-2,3-diamine (45.7 mg, 0.42 mmol) according to **General Procedure K** and was obtained as a yellow oil (19.0 mg, 32%) following purification by flash chromatography (1:49 MeOH/CH_2Cl_2). **^{1}H NMR** (400 MHz, $CDCl_3$) δ 11.19 (s, 1H), 8.42 (dd, J = 4.9, 1.5 Hz, 1H), 8.06 (dd, J = 8.0, 1.4 Hz, 1H), 7.58 (dd, J = 1.8, 1.0 Hz, 1H), 7.23 (dd, J = 8.0, 4.9 Hz, 1H), 7.13 (s, 1H), 6.57 – 6.50 (m, 2H), 1.61 (s, 9H) ppm; **^{13}C NMR** (101 MHz, $CDCl_3$) δ 148.3, 148.2, 144.1, 144.0, 143.0, 139.8, 136.4, 134.4, 127.1, 118.4, 112.3, 111.6, 110.4, 62.4, 30.2 ppm; **LRMS (+ESI)** m/z: 308 ($[M+H]^+$, 70), 330 ($[M+Na]^+$, 30), **(-ESI)** m/z: 306 ($[M-H]^-$, 100); **HRMS (+ESI)** Calc. for $C_{17}H_{18}N_5O$ $[M+H]^+$: 308.15059, found 308.15088; **HPLC** R_T = 18.03 min, 96.41% (254 nm).

2-(1-(*tert*-butyl)-5-(furan-2-yl)-1*H*-pyrazol-3-yl)-3*H*-imidazo[4,5-*c*]pyridine (**166**)

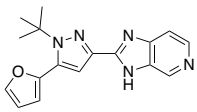

Compound **166** was synthesised from **155** (38.9 mg, 0.18 mmol) and pyridine-3,4-diamine (40.8 mg, 0.37 mmol) according to **General Procedure K** and was obtained as a yellow powder (19.6 mg, 35%) following purification by flash chromatography (1:99 MeOH:CH_2Cl_2). **^{1}H NMR** (500 MHz, DMSO-d_6) δ 13.08 (s, 1H), 8.91 (s, 1H), 8.31 (d, J = 5.5 Hz, 1H), 7.91 (d, J = 1.8 Hz, 1H), 7.55 (s, 1H), 7.09 (s, 1H), 6.78 (d, J = 3.2 Hz, 1H), 6.68 (dd, J = 3.2, 1.8 Hz, 1H), 1.55 (s, 9H) ppm; **^{13}C NMR** (126 MHz, DMSO-d_6) δ 147.9, 143.9, 142.9, 141.4, 141.3, 139.6, 133.6, 112.6, 111.7, 110.4, 107.0, 61.9, 29.5 ppm; 2 carbon peaks not observed due to peak broadening. Structure confirmed by 2D NMR experiments (Appendix 18). **LRMS (+ESI)** m/z: 308 ($[M+H]^+$, 100), **(-ESI)** m/z: 306 ($[M-H]^-$, 100); **HRMS (+ESI)** Calc. for $C_{17}H_{18}N_5O$ $[M+H]^+$: 308.15059, found 308.15064; **HPLC** R_T = 17.79 min, 97.75% (254 nm).

8-(1-(*tert*-butyl)-5-(furan-2-yl)-1*H*-pyrazol-3-yl)-7*H*-purine (**167**)

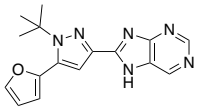

Compound **167** was synthesised from **155** (39.9 mg, 0.18 mmol) and pyrimidine-3,4-diamine (35.5 mg, 0.32 mmol) according to **General Procedure K** and was obtained as an off white powder (14.1 mg, 25%) following purification by flash chromatography (1:49 MeOH:CH_2Cl_2). **^{1}H NMR** (400 MHz, $CDCl_3$) δ 12.40 (s, 1H), 9.14 (s, 1H), 9.09 (s, 1H), 7.59 (s, 1H), 7.18 (s, 1H), 6.58 – 6.51 (m, 2H), 1.61 (s, 9H) ppm; **^{13}C NMR** (101 MHz, $CDCl_3$) δ 153.0, 152.3, 149.8, 147.4, 143.6, 143.2, 139.3, 135.3, 134.8, 112.5, 111.6, 111.1, 62.7, 30.2 ppm; **LRMS (+ESI)** m/z: 309 ($[M+H]^+$, 20), 331 ($[M+Na]^+$, 100), **(-ESI)** m/z: 307 ($[M-H]^-$, 100); **HRMS (+ESI)** Calc. for $C_{16}H_{17}N_6O$ $[M+H]^+$: 309.14584, found 309.14587; **HPLC** R_T = 18.87 min, 95.12% (254 nm).

2-(1-(*tert*-butyl)-5-(furan-2-yl)-1*H*-pyrazol-3-yl)-1*H*-imidazo[4,5-*b*]pyrazine (**168**)

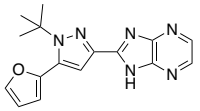

Compound **168** was synthesised from **155** (41.7 mg, 0.19 mmol) and pyrazine-2,3-diamine (40.2 mg, 0.37 mmol) according to **General Procedure K** and was obtained as an off white solid (17.7 mg, 30%) following purification by flash chromatography (1:4 EtOAc:Hex). **^{1}H NMR** (400 MHz, $CDCl_3$) δ 10.71 (s, 1H), 8.49 (d, J = 2.8 Hz, 1H), 8.30 (d, J = 2.8 Hz, 1H), 7.59 (s, 1H), 7.24 (s, 1H), 6.59 – 6.51 (m, 2H), 1.61 (s, 9H) ppm; **^{13}C NMR** (101 MHz, $CDCl_3$) δ 151.2, 150.3, 143.6, 143.2, 141.1, 140.0, 139.1, 138.2, 134.8, 112.5, 111.6, 111.6, 62.8, 30.1 ppm; **LRMS (+ESI)** m/z: 309 ($[M+H]^+$, 100), 331 ($[M+Na]^+$, 90), **(-ESI)** m/z: 307 ($[M-H]^-$, 100); **HRMS (+ESI)** Calc. for $C_{16}H_{17}N_6O$ $[M+H]^+$: 309.14584, found 309.14580; **HPLC** R_T = 21.52 min, 99.74% (254 nm).

1-(*tert*-butyl)-5-(furan-2-yl)-*N*-methoxy-*N*-methyl-1*H*-pyrazole-3-carboxamide (**187**)

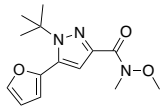

Compound **187** was prepared *via* a HATU mediated amide coupling according to **General Procedure G** from **163** (782 mg, 3.34 mmol) and *N*,*O*-dimethylhydroxylamine hydrochloride (408 mg, 4.18 mmol). Compound **187** was obtained as a yellow oil (870 mg, 94%) following purification by flash chromatography (1:4 EtOAc:Hex). **^{1}H NMR** (400 MHz, $CDCl_3$) δ 7.54 (dd, J = 1.9, 0.8 Hz, 1H), 6.87 (s, 1H), 6.51 – 6.45 (m, 2H), 3.83 (s, 3H), 3.47 (s, 3H), 1.54 (s, 9H) ppm; **^{13}C NMR** (101 MHz, $CDCl_3$) δ 144.1, 142.9, 142.2, 132.8, 114.0, 112.1, 111.4, 62.2, 61.7, 30.1 ppm; **LRMS (+ESI)** m/z: 300 ([M+Na]$^+$, 100); **HRMS (+ESI)** Calc. for $C_{14}H_{19}N_3NaO_3$ [M+Na]$^+$: 300.13186, found 300.13164.

1-(1-(*tert*-butyl)-5-(furan-2-yl)-1*H*-pyrazol-3-yl)ethan-1-one (**184)**

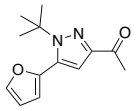

A solution of compound **187** (599 mg, 2.16 mmol) in anhydrous THF (10 mL) at 0 °C was treated dropwise with MeMgBr (3M in diethyl ether, 1.44 mL, 4.32 mmol). The reaction was slowly brought to rt over the next hour and stirred for a subsequent 2 h or until complete consumption of starting material by TLC. The reaction mixture was cooled to 0 °C and quenched with NH_4Cl (10 mL). The aqueous layer was extracted with EtOAc (3 x 25 mL/mmol). The combined organics were washed with brine (1 x 25 mL/mmol), dried over $MgSO_4$ and concentrated *in vacuo*. Compound **184** (482 mg, 96%) was isolated as a white solid following purification by flash chromatography (1:19 EtOAc in Hex). **^{1}H NMR** (400 MHz, $CDCl_3$) δ 7.54 (dd, J = 1.9, 0.8 Hz, 1H), 6.85 (s, 1H), 6.49 (dd, J = 3.3, 1.9 Hz, 1H), 6.46 (dd, J = 3.3, 0.9 Hz, 1H), 2.58 (s, 3H), 1.54 (s, 9H) ppm; **^{13}C NMR** (101 MHz, $CDCl_3$) δ 194.4, 148.3, 144.0, 143.0, 134.0, 112.2, 111.5, 111.3, 62.5, 30.0, 26.3 ppm; **LRMS (+ESI)** m/z: 255 ([M+Na]$^+$, 100); **HRMS (+ESI)** Calc. for $C_{13}H_{16}N_2NaO_2$ [M+Na]$^+$: 255.11040, found 255.11020.

2-bromo-1-(1-(*tert*-butyl)-5-(furan-2-yl)-1*H*-pyrazol-3-yl)ethan-1-one **(188)**

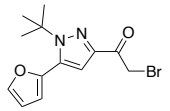

$^{i}Pr_2NEt$ (450 µL, 2.62 mmol) and trimethylsilyl trifluoromethanesulfonate (TMS-OTf, 350 µL, 1.96 mmol) were added sequentially to a stirring solution of **184** (152 mg, 0.65 mmol) in CH_2Cl_2 (1.5 mL) at 0 °C. The reaction mixture was stirred at rt for 5 h. Following consumption of starting material, the reaction was quenched with sat. aq. $NaHCO_3$ (5 mL). The mixed solution was extracted with CH_2Cl_2 (2 x 25 mL/mmol), and the combined organic phase was concentrated *in vacuo*. The resulting residue was dissolved in THF (1.5 mL) and cooled to 0 °C. NBS (112 mg, 0.63 mmol) was added portion wise to the reaction mixture, and stirred at rt for 6 h. After consumption of starting material, H_2O (10 mL) was added to the system to quench the reaction. The mixed solution was extracted with EtOAc (2 x 25 mL/mmol). The combined organic phase was first washed with brine (1 x 25 mL/mmol), then dried with $MgSO_4$, and concentrated *in vacuo*. Compound **188** was colourless oil (108 mg, 53%) following purification by flash chromatography (1:49 EtOAc:Hex). **^{1}H NMR** (300 MHz, $CDCl_3$) δ 7.56 (dd, J = 1.8, 0.9 Hz, 1H), 6.94 (s, 1H), 6.55 – 6.45 (m, 2H), 4.63 (s, 2H), 1.55 (s, 9H) ppm; **^{13}C NMR** (75 MHz, $CDCl_3$) δ 186.74, 145.32, 143.32, 143.04, 112.34, 112.11, 111.90, 111.44, 62.84, 31.96, 29.79 ppm; **LRMS (+APCI)** m/z: 311/313 ($[M+H]^+$, 50); **HRMS (+APCI)** Calc. for $C_{13}H_{16}BrN_2O_2$ $[M+H]^+$: 311.03897/313.03692, found 311.03866/313.03666.

2-(1-(*tert*-butyl)-5-(furan-2-yl)-1*H*-pyrazol-3-yl)imidazo[1,2-*a*]pyridine (**169**)

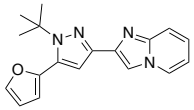

Method A: Compound **169** was synthesised from **184** (49.8 mg, 0.21 mmol) and 2-aminopyridine (22.6 mg, 0.24 mmol) according to **General Procedure L** under inert conditions. Compound **169** was isolated as a pale yellow solid (12.5 mg, 19%) following purification by flash chromatography (1:9 EtOAc:Hex).

Method B: **188** (33.7 mg, 108 µmol) and 2-aminopyridine (10.2 mg, 108 µmol) were dissolved in EtOH/H_2O (1:1 v/v, 1 mL). To this solution DBU (2 µL, 13.4 µmol) was added dropwise. The reaction mixture was stirred at rt then reflux for 20 h. The reaction mixture was diluted with H_2O (10 mL) and EtOAc (10 mL). The aqueous layer was extracted with EtOAc (3 x 25 mL/mmol). The combined organics were washed with brine (1 x 25 mL/mmol), dried over

$MgSO_4$ and concentrated *in vacuo*. Compound **169** was isolated as a pale yellow solid (12.5 mg, 19%) following purification by flash chromatography (1:4 EtOAc:Hex).

^{1}H NMR (400 MHz, $CDCl_3$) δ 8.11 (d, J = 6.6 Hz, 1H), 7.94 (s, 1H), 7.63 (d, J = 9.1 Hz, 1H), 7.55 (t, J = 1.2 Hz, 1H), 7.19 – 7.10 (m, 1H), 6.88 (s, 1H), 6.76 (t, J = 6.7 Hz, 1H), 6.49 (s, 2H), 1.58 (s, 9H) ppm; **^{13}C NMR** (101 MHz, $CDCl_3$) δ 145.6, 145.0, 143.6, 142.6, 140.8, 133.2, 125.6, 124.4, 117.8, 112.5, 111.6, 111.4, 109.4, 108.7, 61.42, 30.24 ppm; **LRMS (+ESI)** m/z: 307 ([M+H]$^+$, 100); **HRMS (+ESI)** Calc. for $C_{18}H_{19}N_4O$ [M+H]$^+$: 307.15534, found 307.15543; **HPLC** R_T = 18.91 min, 97.00% (254 nm).

2-(1-(*tert*-butyl)-5-(furan-2-yl)-1*H*-pyrazol-3-yl)imidazo[1,2-*a*]pyrimidine (**170**)

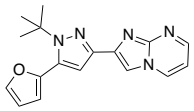

Method A: Compound **170** was synthesised from **184** (23.9 mg, 0.21 mmol) and pyrimidin-2-amine (10.1 mg, 0.11 mmol) according to **General Procedure L**. Compound **170** was isolated as an off white solid (7.0 mg, 22%) following purification by flash chromatography (1:9 EtOAc:Hex).

Method B: A solution of **188** (19.4 mg, 62.3 µmol) and pyrimidin-2-amine (7 mg, 73.6 µmol) in EtOH (1 mL) were stirred at 100 °C in a sealed tube for 24 h. Following consumption of starting material indicated by TLC, the reaction was cooled to rt and diluted with H_2O (10 mL) and EtOAc (10 mL). The aqueous layer was extracted with EtOAc (3 x 25 mL/mmol). The combined organics were washed with brine (1 x 25 mL/mmol), dried over $MgSO_4$ and concentrated *in vacuo*. Compound **170** was isolated as an off white solid (11.9 mg, 62%) following purification by flash chromatography (1:4 EtOAc:Hex).

^{1}H NMR (400 MHz, $CDCl_3$) δ 8.50 (dd, J = 4.1, 2.0 Hz, 1H), 8.42 (dd, J = 6.7, 2.0 Hz, 1H), 7.94 (s, 1H), 7.55 (t, J = 1.4 Hz, 1H), 7.01 (s, 1H), 6.85 (dd, J = 6.7, 4.1 Hz, 1H), 6.50 (d, J = 1.4 Hz, 2H), 1.57 (s, 9H) ppm; **^{13}C NMR** (101 MHz, $CDCl_3$) δ 149.5, 148.6, 144.8, 143.3, 142.6, 142.5, 133.3, 132.9, 111.8, 111.4, 110.1, 108.9, 106.6, 61.56, 30.21 ppm; **LRMS (+ESI)** m/z: 330 ([M+Na]$^+$, 100); **HRMS (+ESI)** Calc. for $C_{17}H_{18}N_5O$ [M+H]$^+$: 308.15059, found 308.15102; **HPLC** R_T = 18.06 min, 95.30% (254 nm).

2-(1-(*tert*-butyl)-5-(furan-2-yl)-1*H*-pyrazol-3-yl)imidazo[1,2-*a*]pyrazine (**171**)

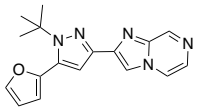

A solution of **188** (35.5 mg, 114 µmol) and pyridazin-3-amine (12.2 mg, 128 µmol) in EtOH (1 mL) were stirred at 100 °C in a sealed tube for 24 h. Following consumption of starting material indicated by TLC, the reaction was cooled to rt and diluted with H_2O (10 mL) and EtOAc (10 mL). The aqueous layer was extracted with EtOAc (3 x 25 mL/mmol). The combined organics were washed with brine (1 x 25 mL/mmol), dried over $MgSO_4$ and concentrated *in vacuo*. Compound **171** was isolated as a white solid (19.8 mg, 57%) following purification by flash chromatography (1:9 EtOAc:Hex). **^{1}H NMR** (500 MHz, $CDCl_3$) δ 9.09 (s, 1H), 8.06 (d, J = 4.7 Hz, 2H), 7.87 (d, J = 4.6 Hz, 1H), 7.56 (d, J = 1.4 Hz, 1H), 6.93 (s, 1H), 6.52 – 6.50 (m, 2H), 1.59 (s, 9H) ppm; **^{13}C NMR** (126 MHz, $CDCl_3$) δ 144.6, 143.6, 142.9, 142.8, 142.7, 140.9, 133.5, 129.8, 118.7, 111.8, 111.5, 109.9, 109.6, 61.72, 30.19 ppm; **LRMS (+ESI)** m/z: 330 ([M+H]$^+$, 90); **HRMS (+ESI)** Calc. for $C_{17}H_{18}N_5O$ [M+H]$^+$: 308.15059, found 308.15058; **HPLC** R_T = 19.12 min, 97.71% (254 nm).

2-(1-(*tert*-butyl)-5-(furan-2-yl)-1*H*-pyrazol-3-yl)imidazo[1,2-*b*]pyridazine (**172)**

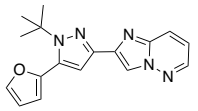

A solution of **188** (21.4 mg, 68.6 µmol) and pyridazin-3-amine (7.2 mg, 75.5 µmol) in EtOH (1 mL) were stirred at 100 °C in a sealed tube for 24 h. Following consumption of starting material indicated by TLC, the reaction was cooled to rt and diluted with H_2O (10 mL) and EtOAc (10 mL). The aqueous layer was extracted with EtOAc (3 x 25 mL/mmol). The combined organics were washed with brine (1 x 25 mL/mmol), dried over $MgSO_4$ and concentrated *in vacuo*. Compound **172** was isolated as an off white solid (11.9 mg, 62%) following purification by flash chromatography (1:4 EtOAc:Hex). **^{1}H NMR** (500 MHz, $CDCl_3$) δ 8.32 (s, 1H), 8.27 (dd, J = 4.6, 1.6 Hz, 1H), 7.95 (dd, J = 9.1, 1.8 Hz, 1H), 7.56 (s, 1H), 7.00 (dd, J = 9.2, 4.5 Hz, 1H), 6.89 (s, 1H), 6.51 – 6.48 (m, 2H), 1.59 (s, 9H) ppm; **^{13}C NMR** (126 MHz, $CDCl_3$) δ 144.8, 143.1, 143.0, 142.7, 140.9, 139.4, 133.3, 125.2, 116.7, 113.2, 111.7, 111.4, 109.4, 61.64, 30.2 ppm; **LRMS (+ESI)** m/z: 308 ([M+H]$^+$, 100); 330 ([M+Na]$^+$, 20); **HRMS (+ESI)** Calc. for $C_{17}H_{18}N_5O$ [M+H]$^+$: 308.15059, found 308.15120; **HPLC** R_T = 20.06 min, 97.30% (254 nm).

2-(1-(*tert*-butyl)-5-(furan-2-yl)-1*H*-pyrazol-3-yl)-7-chloroimidazo[1,2-*a*]pyridine (**174**)

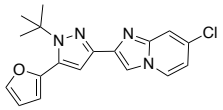

Compound **174** was synthesised from **184** (49.8 mg, 0.21 mmol) and 4-chloropyridin-2-amine (27.4 mg, 0.21 mmol) according to **General Procedure L**. Compound **174** was isolated as a yellow solid (17 mg, 26%) following purification by reverse flash chromatography (0 – 100% v/v CH_3CN in H_2O). **^{1}H NMR** (400 MHz, $CDCl_3$) δ 8.02 (d, J = 7.1 Hz, 1H), 7.91 (s, 1H), 7.63 (s, 1H), 7.55 (s, 1H), 6.86 (s, 1H), 6.76 (dd, J = 7.2, 2.1 Hz, 1H), 6.49 (s, 2H), 1.58 (s, 9H) ppm; **^{13}C NMR** (101 MHz, $CDCl_3$) δ 145.4, 144.9, 143.2, 142.6, 141.7, 133.3, 130.8, 125.8, 116.5, 114.2, 111.6, 111.4, 109.5, 108.8, 61.52, 30.21 ppm; **LRMS (+ESI)** m/z: 341/343 ($[M+H]^+$, 100), 363/365 ($[M+Na]^+$, 50); **HRMS (+ESI)** Calc. for $C_{18}H_{18}ClN_4O$ $[M+H]^+$: 341.11637/343.11342, found 341.11643/343.11355; **HPLC** R_T = 19.67 min, 97.53% (254 nm).

o-toluidine (**196)**

A solution of 4,4′-bipyridine (97.2 mg, 0.62 mmol) in DMF (2 mL) was cooled to 0 °C. *o*-nitrotoluene (150 µL, 1.24 mmol) and $B_2(OH)_4$ (320 mg, 3.57 mmol) were added to the reaction mixture slowly over 5 min. The reaction mixture was stirred at room temperature for 1 h. After complete consumption of the starting material as monitored by TLC, the reaction mixture was diluted with H_2O (10 mL) and EtOAc (10 mL). The aqueous layer was extracted with EtOAc (3 x 25 mL/mmol). The combined organics were washed with brine (1 x 25 mL/mmol), dried over $MgSO_4$ and concentrated *in vacuo*. Compound **196** was isolated as a yellow solid (86.3 mg, 65%) following purification by flash chromatography (1:9 EtOAc:Hex). **^{1}H NMR** (500 MHz, DMSO-d_6) δ 6.92 – 6.83 (m, 2H), 6.59 (dd, J = 7.9, 1.3 Hz, 1H), 6.45 (td, J = 7.3, 1.3 Hz, 1H), 4.74 (s, 2H), 2.04 (s, 3H) ppm; **^{13}C NMR** (126 MHz, DMSO-d_6) δ 146.5, 129.8, 126.4, 120.9, 116.0, 113.9, 17.4 ppm. Matched previously reported characterisation data.

1-(*tert*-butyl)-5-(furan-2-yl)-*N*-(*o*-tolyl)-1*H*-pyrazole-3-carboxamide **(197)**

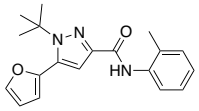

Compound **197** was prepared *via* a HATU mediated amide coupling according to **General Procedure G** from **163** (51.2 mg, 0.22 mmol) and *o*-toluidine **196** (28.1 mg, 0.26 mmol). The crude residue was purified by flash chromatography (1:9 EtOAc:Hex) to yield compound **197** as a white solid (61.5 mg, 87%). **^{1}H NMR** (500 MHz, $CDCl_3$) δ 8.82 (s, 1H), 8.20 (dd, J = 8.1, 1.4 Hz, 1H), 7.57 (t, J = 1.4 Hz, 1H), 7.32 – 7.22 (m, 2H), 7.21 (dd, J = 7.4, 1.5 Hz, 1H), 7.06 (td, J = 7.5, 1.4 Hz, 1H), 6.98 (s, 1H), 6.51 (d, J = 1.4 Hz, 1H), 2.38 (s, 3H), 1.58 (s, 9H) ppm; **^{13}C NMR** (126 MHz, $CDCl_3$) δ 159.8, 143.9, 143.6, 143.0, 136.3, 134.5, 130.5, 127.6, 127.1, 124.3, 121.6, 112.3, 111.7, 111.6, 62.4, 30.0, 17.6 ppm; **LRMS (+ESI)** m/z: 346 ([M+Na]$^+$, 100); **HRMS (+ESI)** Calc. for $C_{19}H_{21}N_3NaO_2$ [M+Na]$^+$: 346.15260, found 346.15233.

1-(phenylsulfonyl)-1*H*-indole **(210)**

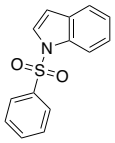

NaH (60% Dispersion in mineral oil, 93.8 mg, 2.35 mmol) was added portion wise to an ice-cold solution of indole (199 mg, 1.70 mmol) in DMF (3 mL). The solution was warmed to rt and stirred for 1 h before addition of phenylsulfonyl chloride (260 µL, 2.04 mmol). The solution was stirred for an additional 4 h and then slowly added to ice cold sat. aq. $NaHCO_3$ (10 mL). The aqueous layer was extracted with EtOAc (3 x 25 mL/mmol). The combined organics were washed with brine (1 x 25 mL/mmol), dried over $MgSO_4$ and concentrated *in vacuo*. Compound **210** was isolated as a white solid (409 mg, 94%) following purification by flash chromatography (1:49 EtOAc:Hex). **^{1}H NMR** (400 MHz, DMSO-d_6) δ 7.99 – 7.93 (m, 3H), 7.81 (d, J = 3.6 Hz, 1H), 7.70 – 7.65 (m, 1H), 7.59 (q, J = 7.8, 7.2 Hz, 3H), 7.34 (t, J = 7.8 Hz, 1H), 7.25 (t, J = 7.5 Hz, 1H), 6.85 (d, J = 3.7 Hz, 1H) ppm; **^{13}C NMR** (101 MHz, DMSO-d_6) δ 137.1, 134.6, 134.1, 130.4, 129.8, 126.9, 126.6, 124.7, 123.5, 121.6, 113.0, 109.5 ppm; **LRMS (+APCI)** m/z: 258 ([M+H]$^+$, 100); **HRMS (+APCI)** Calc. for $C_{14}H_{12}NO_2S$ [M+H]$^+$: 258.05833, found 258.05799.

1-(phenylsulfonyl)-1*H*-pyrrolo[2,3-*b*]pyridine (**211**)

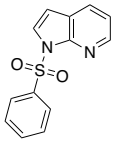

NaH (60% Dispersion in mineral oil, 105 mg, 2.57 mmol) was added portion wise to an ice-cold solution of 7-azaindole (203 mg, 1.72 mmol) in THF (2.5 mL). The solution was warmed to rt and stirred for 1 h before addition of phenylsulfonyl chloride (260 μL, 2.06 mmol). The solution was stirred for an additional 4 h and then slowly added to ice cold sat. aq. $NaHCO_3$ (10 mL). The aqueous layer was extracted with EtOAc (3 x 25 mL/mmol). The combined organics were washed with brine (1 x 25 mL/mmol), dried over $MgSO_4$ and concentrated *in vacuo*. Compound **211** was isolated as a white solid (401 mg, 91%) following purification by flash chromatography (1:49 EtOAc:Hex). **^{1}H NMR** (500 MHz, CD_3OD) δ 8.31 (d, J = 5.0 Hz, 1H), 8.11 (dd, J = 7.8, 1.0 Hz, 2H), 7.96 (d, J = 7.9 Hz, 1H), 7.81 (d, J = 4.1 Hz, 1H), 7.62 (t, J = 7.0 Hz, 1H), 7.52 (t, J = 7.6 Hz, 2H), 7.27 – 7.21 (m, 1H), 6.73 (d, J = 4.1 Hz, 1H) ppm; **^{13}C NMR** (126 MHz, CD_3OD) δ 148.4, 145.6, 139.6, 135.5, 131.4, 130.3, 128.8, 127.9, 124.7, 120.4, 107.1 ppm; **LRMS (+APCI)** m/z: 259 ($[M+H]^+$, 100); **HRMS (+APCI)** Calc. for $C_{13}H_{11}N_2O_2S$ $[M+H]^+$: 259.05358, found 259.05368.

(*E*)-3-(dimethylamino)-1-(furan-2-yl)prop-2-en-1-one (**204)**

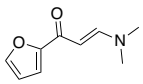

To a mixture of 2-acetylfuran (870 mg, 7.90 mmol) in DMF (2 mL) at rt was added DMF-DMA (5.2 mL, 39.5 mmol). The resulting mixture was heated to 80 °C and stirred for 2 h. The solvent was then evaporated *in vacuo* until DMF-DMA was fully removed. The crude product was purified by flash chromatography (1:19 MeOH:CH_2Cl_2) to give compound **204** as a bright yellow solid (657 mg, 50%). **^{1}H NMR** (400 MHz, DMSO-d_6) δ 7.80 – 7.76 (m, 1H), 7.67 (d, J = 12.4 Hz, 1H), 7.09 (d, J = 3.4 Hz, 1H), 6.62 – 6.56 (m, 1H), 5.64 (d, J = 12.4 Hz, 1H), 3.13 (s, 3H), 2.88 (s, 3H) ppm; **^{13}C NMR** (101 MHz, DMSO-d_6) δ 175.4, 154.5, 153.2, 144.8, 113.0, 111.8, 90.6, 44.4, 37.0 ppm; **LRMS (+ESI)** m/z: 166 ($[M+H]^+$, 100).

1-(*tert*-butyl)-5-(furan-2-yl)-1*H*-pyrazole (**205**)

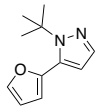

Compound **205** was prepared from **204** (101 mg, 0.61 mmol) and *tert*-butylhydrazine hydrochloride (93.8 mg, 0.75 mmol) in EtOH (1 mL) at reflux for 1 h according to **General Procedure I**. Compound **205** was isolated as a white solid (75.7 mg, 65%) following purification by flash chromatography (1:9 EtOAc:Hex). **^{1}H NMR** (400 MHz, $CDCl_3$) δ 7.54 (d, J = 1.9 Hz, 1H), 7.47 (d, J = 1.8 Hz, 1H), 6.48 (dd, J = 3.3, 1.9 Hz, 1H), 6.44 (d, J = 3.2 Hz, 1H), 6.36 (d, J = 1.8 Hz, 1H), 1.53 (s, 9H) ppm; **^{13}C NMR** (101 MHz, $CDCl_3$) δ 145.0, 142.6, 136.5, 132.0, 111.6, 111.3, 111.1, 61.1, 30.2 ppm; **LRMS (+APCI)** m/z: 191 ($[M+H]^+$, 100). Matched previously reported characterisation data.

ethyl furan-2-carboxylate (**220**)

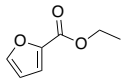

Prepared according to **General Procedure M** from 2-furoic acid (211 mg, 1.88 mmol), EtOH (440 µL, 7.53 mmol), DMAP (23 mg, 0.19 mmol) and EDC.HCl (364 mg, 1.90 mmol) in CH_2Cl_2 (3 mL). Compound **220** was obtained as a white solid (211 mg, 80%) following purification by flash chromatography (0 - 20% EtOAc in Hex). **^{1}H NMR** (500 MHz, $CDCl_3$) δ 7.55 (dd, J = 1.8, 0.9 Hz, 1H), 7.15 (dd, J = 3.5, 0.9 Hz, 1H), 6.48 (dd, J = 3.5, 1.7 Hz, 1H), 4.35 (q, J = 7.1 Hz, 2H), 1.36 (t, J = 7.1 Hz, 3H) ppm; **^{13}C NMR** (126 MHz, $CDCl_3$) δ 158.9, 146.3, 145.0, 117.8, 111.9, 61.1, 14.4 ppm; **LRMS (+ESI)** m/z: 163 ($[M+Na]^+$, 30). Matched previously reported characterisation data.[474]

3-(furan-2-yl)-3-oxopropanenitrile (**219**)

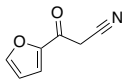

To a stirred solution of CH_3CN (250 µL, 4.79 mmol) and NaH (60% Dispersion in mineral oil, 247 mg, 6.18 mmol) in THF (1 mL) at 0 °C was added **220** (297 mg, 2.12 mmol) dropwise. The reaction was heated to reflux for 5 h. The mixture was cooled to 0 °C and the reaction was quenched with H_2O (5 mL) and neutralised with 1M HCl. The aqueous layer was extracted with EtOAc (3 x 25 mL/mmol). The combined organics were washed with brine (1 x 25 mL/mmol), dried over $MgSO_4$ and concentrated *in vacuo*. Compound **219** was isolated as a

white solid (152 mg, 53%) following purification by flash chromatography (1:4 EtOAc:Hex). **^{1}H NMR** (500 MHz, $CDCl_3$) δ 7.66 (dd, J = 1.7, 0.8 Hz, 1H), 7.39 (d, J = 3.7 Hz, 1H), 6.64 (dd, J = 3.7, 1.7 Hz, 1H), 3.96 (s, 2H) ppm; **^{13}C NMR** (126 MHz, $CDCl_3$) δ 175.9, 150.7, 147.9, 119.4, 113.5, 113.4, 28.3 ppm; **LRMS (+APCI)** m/z: 136 ($[M+H]^+$, 100), **(-APCI)** m/z: 134 ($[M-H]^-$, 100). Matched previously reported characterisation data.[475]

5-chloro-2-(5-(furan-2-yl)-1*H*-pyrazol-3-yl)-1*H*-benzo[*d*]imidazole (**231**)

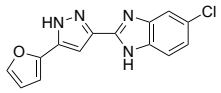

Compound **231** was synthesised via an acid deprotection of **37** (47 mg, 0.14 mmol) in toluene with trifluoroacetic acid (85 µL, 1.10 mmol). The reaction was heated in a sealed tube at 130°C for 12 h, or within a microwave at 160°C for 30 min. Upon competition, the reaction mixture was quenched with addition of H_2O, and the pH of the aqueous layer was adjusted to pH 7 with a sat. solution of $NaHCO_3$ (approx. 3 mL). The neutral aqueous layer was extracted with EtOAc (3 x 25 mL/mmol). Pooled organic layers were washed with brine (1 x 25 mL/mmol), dried with $MgSO_4$ and concentrated *in vacuo*. Compound **231** was obtained as a pale brown solid (27.5 mg, 70%) following purification by flash chromatography (3:7 EtOAc:Hex). **^{1}H NMR** (500 MHz, DMF-d_7) δ 7.83 (d, J = 1.2 Hz, 1H), 7.69 (d, J = 1.8 Hz, 1H), 7.66 (d, J = 8.5 Hz, 1H), 7.28 (dd, J = 8.5, 2.0 Hz, 1H), 7.25 (s, 1H), 6.99 (d, J = 3.4 Hz, 1H), 6.68 (dd, J = 3.4, 1.8 Hz, 1H) ppm, pyrazole N<u>H</u> and benzimidazole N<u>H</u> proton signal not observed; **^{13}C NMR** (126 MHz, DMF-d_7) δ 163.9, 163.7, 144.2, 128.0, 123.5, 112.8, 108.0, 101.9 ppm, 6 carbon peaks not observed due to broadening; **LRMS (+ESI)** m/z: 285/287 ($[M+H]^+$, 100); **HRMS (+ESI)** Calc. for $C_{14}H_{10}ClN_4O$ $[M+H]^+$: 285.05377/287.05081, found 285.05372/287.05078; **HPLC** R_T = 16.82 min, 99.62% (254 nm).

ethyl 5-(furan-2-yl)-1-methyl-1*H*-pyrazole-3-carboxylate (**236**)

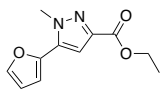

Compound **236** was synthesised from **157** (50.4 mg, 0.24 mmol) and methylhydrazine (20 µL, 0.38 mmol) in HFIP (500 µL) according to **General Procedure I** and was obtained as a yellow solid (45.2 mg, 86%) following purification by flash chromatography (1:9 EtOAc:Hex). **^{1}H NMR** (500 MHz, $CDCl_3$) δ 7.54 (s, 1H), 7.00 (s, 1H), 6.61 (d, J = 3.4 Hz, 1H), 6.53 (q, J = 1.6 Hz, 1H), 4.42 (q, J = 7.1 Hz, 2H), 4.12 (s, 3H), 1.41 (t, J = 7.1 Hz, 3H) ppm; **^{13}C NMR** (126 MHz, $CDCl_3$) δ 162.3, 144.0, 143.3, 142.8, 135.7, 111.7, 109.5, 107.8, 61.2, 39.6, 14.5 ppm;

LRMS (+ESI) m/z: 243 ([M+Na]$^+$, 100); **HRMS (+ESI)** Calc. for $C_{11}H_{12}N_2NaO_3$ [M+Na]$^+$: 243.07401, found 243.07361. Matched previously reported characterisation data.[350]

5-(furan-2-yl)-1-methyl-1*H*-pyrazole-3-carboxylic acid (**240**)

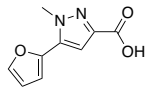

Prepared according to **General Procedure J** with **236** (49.2 mg, 0.22 mmol) and LiOH.H_2O (31.1 mg, 0.74 mmol). Compound **240** was obtained as a white solid (39.8 mg, 93%) without need for further purification. **^{1}H NMR** (500 MHz, $CDCl_3$) δ 7.55 (s, 1H), 7.06 (s, 1H), 6.64 (d, J = 3.4 Hz, 1H), 6.56 – 6.51 (m, 1H), 4.15 (s, 3H) ppm, COOH signal not observed; **^{13}C NMR** (126 MHz, $CDCl_3$) δ 166.1, 143.7, 143.5, 141.8, 136.2, 111.8, 109.8, 108.3, 39.8 ppm; **LRMS (+ESI)** m/z: 215 ([M+Na]$^+$, 100); **HRMS (+ESI)** Calc. for $C_9H_8N_2NaO_3$ [M+Na]$^+$: 215.04271, found 215.04234.

5-chloro-2-(5-(furan-2-yl)-1-methyl-1*H*-pyrazol-3-yl)-1*H*-benzo[*d*]imidazole (**232**)

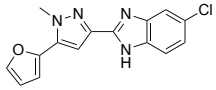

Prepared according to **General Procedure N** from **240** (30.2 mg, 0.16 mmol), 4-chlorobenzene-1,2-diamine (27.9 mg, 0.20 mmol), HATU (74.2 mg, 0.20 mmol) and ^{i}Pr$_2$NEt (120 µL, 0.69 mmol) in DMF (1 mL). Compound **232** was obtained as a white solid (18 mg, 38%) following purification by flash chromatography (1:3 EtOAc:Hex). Characterisation data is reported as a complex mix of tautomers. **^{1}H NMR** (500 MHz, DMSO-d_6) δ 13.07 – 12.96 (m, 1H), 7.91 (s, 1H), 7.69 – 7.61 (m, 1H), 7.50 – 7.44 (m, 1H), 7.25 – 7.16 (m, 1H), 7.15 (d, J = 2.9 Hz, 1H), 7.02 (d, J = 3.5 Hz, 1H), 6.72 (dt, J = 3.3, 1.5 Hz, 1H), 4.12 (s, 3H) ppm; **^{13}C NMR** (126 MHz, DMSO-d_6) δ 147.7, 147.3, 144.6, 144.0, 143.3, 142.4, 141.8, 135.4, 135.3, 133.3, 126.7, 125.9, 122.6, 121.8, 120.0, 118.1, 112.7, 112.0, 111.1, 109.9, 103.7, 103.6, 54.9 ppm; **LRMS (+ESI)** m/z: 299/301 ([M+H]$^+$, 75), 321/323 ([M+Na]$^+$, 100), **(-ESI)** m/z: 297/299 ([M-H]$^-$, 100); **HRMS (+ESI)** Calc. for $C_{15}H_{12}ClN_4O$ [M+H]$^+$: 299.06942/301.06647, found 299.06887/301.06594; **HPLC** R_T = 18.18 min, 98.11% (254 nm).

ethyl 3-(furan-2-yl)-1-methyl-1*H*-pyrazole-5-carboxylate (**238**)

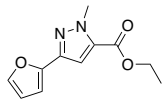

Compound **238** was synthesised from **157** (200 mg, 0.95 mmol) and methylhydrazine (100 µL, 1.90 mmol) in EtOH (3 mL) according to **General Procedure I** and was obtained as a white powder (74.2 mg, 35%) following purification by flash chromatography (1:24 EtOAc:Hex). **^{1}H NMR** (500 MHz, $CDCl_3$) δ 7.45 (dd, J = 1.8, 0.8 Hz, 1H), 7.02 (s, 1H), 6.66 (dd, J = 3.3, 0.8 Hz, 1H), 6.46 (dd, J = 3.4, 1.8 Hz, 1H), 4.36 (q, J = 7.1 Hz, 2H), 4.21 (s, 3H), 1.39 (t, J = 7.1 Hz, 3H) ppm; **^{13}C NMR** (126 MHz, $CDCl_3$) δ 159.8, 148.1, 142.5, 142.2, 133.7, 111.5, 107.7, 106.2, 61.3, 39.8, 14.4 ppm; **LRMS (+ESI)** m/z: 221 ($[M+H]^+$, 80), 243 ($[M+Na]^+$, 100); **HRMS (+ESI)** Calc. for $C_{11}H_{12}N_2NaO_3$ $[M+Na]^+$: 243.07401, found 243.07401. Matched previously reported characterisation data.[350]

3-(furan-2-yl)-1-methyl-1*H*-pyrazole-5-carboxylic acid (**241**)

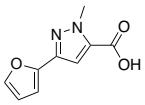

Prepared according to **General Procedure J** with **238** (70.8 mg, 0.32 mmol) and $LiOH.H_2O$ (47.8 mg, 1.14 mmol). Compound **241** was obtained as a white solid (57.5 mg, 93%) without need for further purification. **^{1}H NMR** (500 MHz, $CDCl_3$) δ 7.47 (s, 1H), 7.16 (s, 1H), 6.71 (d, J = 3.3 Hz, 1H), 6.49 – 6.46 (m, 1H), 4.25 (s, 3H) ppm, COO<u>H</u> signal not observed; **^{13}C NMR** (126 MHz, $CDCl_3$) δ 163.8, 147.7, 142.8, 142.4, 132.8, 111.5, 109.2, 106.6, 40.0 ppm; **LRMS (+ESI)** m/z: 215 ($[M+H]^+$, 100); **HRMS (+ESI)** Calc. for $C_9H_8N_2O_3Na$ $[M+H]^+$: 215.04271, found 215.04235.

5-chloro-2-(3-(furan-2-yl)-1-methyl-1*H*-pyrazol-5-yl)-1*H*-benzo[*d*]imidazole (**243)**

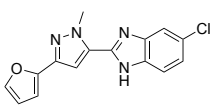

Prepared according to **General Procedure N** from **241** (36.6 mg, 0.19 mmol), 4-chlorobenzene-1,2-diamine (40.6 mg, 0.28 mmol), HATU (108 mg, 0.28 mmol) and ^{i}Pr$_2$NEt (150 µL, 0.86 mmol) in DMF (1 mL). Compound **243** was obtained as a white solid (18.2 mg, 32%) following purification by flash chromatography (1:3 EtOAc:Hex). Characterisation data is reported as a complex mix of tautomers. **^{1}H NMR** (500 MHz, DMSO-d_6) δ 13.22 (s, 1H),

7.75 (s, 1H), 7.72 – 7.60 (m, 2H), 7.28 (d, J = 8.9 Hz, 1H), 7.25 (s, 1H), 6.77 (d, J = 3.4 Hz, 1H), 6.60 (t, J = 2.5 Hz, 1H), 4.34 (s, 3H) ppm; **^{13}C NMR** (126 MHz, DMSO-d_6) δ 147.9, 144.2, 142.7, 142.1, 133.5, 123.1, 111.7, 105.9, 103.6, 48.6 ppm, 5 carbon peaks not observed due to peak broadening; **LRMS (+ESI)** m/z: 321/323 ([M+Na]$^+$, 100), **(-ESI)** m/z: 297/299 ([M-H]$^-$, 100); **HRMS (+ESI)** Calc. for $C_{15}H_{12}ClN_4O$ [M+H]$^+$: 299.06942/301.06647, found 299.06908/301.06615; **HPLC** R_T = 21.90 min, 98.36% (254 nm).

ethyl 5-(furan-2-yl)-1-isopropyl-1*H*-pyrazole-3-carboxylate (**237**)

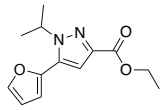

Compound **237** was synthesised from **157** (102 mg, 0.49 mmol) and isopropylhydrazine hydrochloride (67.7 mg, 0.61 mmol) according to **General Procedure I** and was obtained as a yellow oil (114.6 mg, 95%) following purification by flash chromatography (1:9 EtOAc:Hex). **^{1}H NMR** (500 MHz, $CDCl_3$) δ 7.53 (dd, J = 1.8, 0.8 Hz, 1H), 6.92 (s, 1H), 6.57 (d, J = 3.5 Hz, 1H), 6.51 (dd, J = 3.4, 1.8 Hz, 1H), 4.88 (hept, J = 6.6 Hz, 1H), 4.40 (q, J = 7.1 Hz, 2H), 1.56 (d, J = 6.6 Hz, 9H), 1.39 (t, J = 7.1 Hz, 3H) ppm; **^{13}C NMR** (126 MHz, $CDCl_3$) δ 162.5, 143.9, 143.3, 142.9, 134.3, 111.6, 110.0, 108.5, 61.0, 52.9, 22.7, 14.5 ppm; **LRMS (+ESI)** m/z: 271 ([M+Na]$^+$, 100); **HRMS (+ESI)** Calc. for $C_{13}H_{16}N_2NaO_3$ [M+Na]$^+$: 271.10531, found 271.10509.

5-(furan-2-yl)-1-isopropyl-1*H*-pyrazole-3-carboxylic acid (**242**)

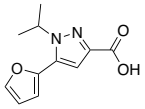

Prepared according to **General Procedure J** with **237** (29.5 mg, 0.12 mmol) and $LiOH.H_2O$ (17 mg, 0.41 mmol). Compound **242** was obtained as a white solid (25.4 mg, 97%) without need for further purification. **^{1}H NMR** (500 MHz, $CDCl_3$) δ 7.52 (s, 1H), 6.94 (s, 1H), 6.57 (d, J = 3.4 Hz, 1H), 6.52 – 6.49 (m, 1H), 4.88 (hept, J = 6.7 Hz, 1H), 1.54 (d, J = 6.6 Hz, 6H) ppm, COO<u>H</u> signal not observed; **^{13}C NMR** (126 MHz, $CDCl_3$) δ 164.1, 143.8, 143.3, 142.9, 134.7, 111.6, 110.1, 108.5, 52.8, 22.7 ppm; **LRMS (+ESI)** m/z: 243 ([M+Na]$^+$, 100); **HRMS (+ESI)** Calc. for $C_{11}H_{12}N_2NaO_3$ [M+Na]$^+$: 243.07401, found 243.07356.

5-chloro-2-(5-(furan-2-yl)-1-isopropyl-1*H*-pyrazol-3-yl)-1*H*-benzo[*d*]imidazole (**233**)

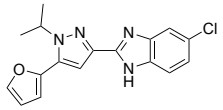

Prepared according to **General Procedure N** from **242** (25 mg, 0.11 mmol), 4-chlorobenzene-1,2-diamine (20.7 mg, 0.15 mmol), HATU (59.3 mg, 0.16 mmol) and $^{i}Pr_2NEt$ (80 µL, 0.45 mmol) in DMF (1 mL). Compound **233** was obtained as a white powder (13.8 mg, 37%) following purification by flash chromatography (1:4 EtOAc:Hex). Characterisation data is reported as a complex mix of tautomers. **^{1}H NMR** (500 MHz, DMSO-d_6) δ 12.91 – 12.80 (m, 1H), 7.90 (d, J = 1.8 Hz, 1H), 7.70 – 7.61 (m, 1H), 7.54 – 7.48 (m, 1H), 7.21 (ddd, J = 17.7, 8.6, 2.1 Hz, 1H), 7.11 (d, J = 2.9 Hz, 1H), 6.96 (d, J = 3.5 Hz, 1H), 6.71 (dt, J = 2.8, 1.3 Hz, 1H), 4.97 (hept, J = 6.5 Hz, 1H), 1.54 (d, J = 6.8 Hz, 6H) ppm; **^{13}C NMR** (126 MHz, DMSO-d_6) δ 147.9, 147.5, 144.6, 144.1, 143.1, 142.5, 142.0, 141.9, 135.3, 134.3, 133.3, 126.7, 125.9, 122.6, 121.9, 119.9, 118.1, 112.8, 112.0, 111.2, 110.3, 104.4, 104.3, 51.8, 22.6 ppm; **LRMS (+ESI)** m/z: 327/329 ([M+H]$^+$, 100), **(-ESI)** m/z: 325/327 ([M-H]$^-$, 100); **HRMS (+ESI)** Calc. for $C_{17}H_{16}ClN_4O$ [M+H]$^+$: 327.10072/329.09777, found 327.10015/329.09723; **HPLC** R_T = 19.83 min, 98.61% (254 nm).

ethyl 1-(*tert*-butyl)-5-(furan-2-yl)-1*H*-1,2,4-triazole-3-carboxylate **(245**)

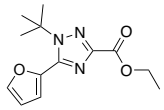

A suspension of *tert*-butylhydrazine hydrochloride (402 mg, 3.23 mmol) in THF (2 mL) was treated with Et_3N (450 µL, 3.23 mmol) before ethyl glyoxylate (50% *w/v* solution in toluene, 700 µL, 3.44 mmol) was added dropwise to the reaction mixture at 0 °C. The mixture was stirred at this temperature for 30 min and then for 7 h at reflux. Following consumption of ethyl glyoxylate indicated by TLC, the reaction mixture was concentrated under a stream of N_2 and carried through to the subsequent reaction without further purification. Ethyl (*E*)-2-(2-(*tert*-butyl)hydrazineylidene)acetate (**246**) was dissolved in CH_3CN (1 mL) and treated with freshly distilled furfurylamine (60 µL, 0.69 mmol). I_2 (19.6 mg, 77.2 µmol) and TBHP (70% aq., 100 µL, 0.76 mmol) was added slowly. The mixture was stirred at 90 °C under air for 4 h. The reaction was then cooled and diluted with H_2O (10 mL). The aqueous layer was extracted with EtOAc (3 x 25 mL/mmol). Pooled organic layers were washed with sodium thiosulfate (1 x 25 mL/mmol), brine (1 x 25 mL/mmol), dried with MgSO4 and concentrated *in vacuo*. Compound **245** was isolated as an off white solid (10 mg, 17% over two steps) following purification by

flash chromatography (1:9 Acetone:Hex). **^{1}H NMR** (500 MHz, $CDCl_3$) δ 7.60 (dd, J = 1.8, 0.8 Hz, 1H), 6.94 (dd, J = 3.4, 0.9 Hz, 1H), 6.57 (dd, J = 3.5, 1.8 Hz, 1H), 4.48 (q, J = 7.1 Hz, 2H), 1.63 (s, 9H), 1.43 (t, J = 7.1 Hz, 3H) ppm; **^{13}C NMR** (126 MHz, $CDCl_3$) δ 160.3, 152.1, 146.6, 143.9, 142.1, 114.6, 112.0, 62.8, 62.0, 29.9, 14.5 ppm; **LRMS (+ESI)** m/z: 286 ($[M+Na]^+$, 100).

methyl 1-(*tert*-butyl)-5-(furan-2-yl)-1*H*-1,2,4-triazole-3-carboxylate (**251**)

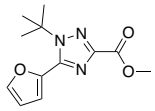

Methyl (*Z*)-2-amino-2-((furan-2-carbonyl)imino)acetate was prepared *via* a HATU mediated amide coupling according to **General Procedure G** from 2-furoic acid (304 mg, 2.71 mmol) and methyl 2-amino-2-iminoacetate hydrochloride (464 mg, 3.35 mmol). The reaction was stirred at rt for 12 h, or until TLC showed consumption of the carboxylic acid. *tert*-Butylhydrazine hydrochloride (510 mg, 4.09 mmol) and glacial AcOH (1.6 mL) were then added, and the reaction mixture was heated to 80 °C for a further 6 h. The reaction was then cooled to rt, diluted with EtOAc (15 mL) and extracted once with sat. $NaHCO_3$ (15 mL). The organic layer was dried with $MgSO_4$ and concentrated. The crude material was purified by flash chromatography (1:9 EtOAc:Hex) to afford compound **251** as a yellow oil (290 mg, 43%). **^{1}H NMR** (400 MHz, $CDCl_3$) δ 7.60 (s, 1H), 6.95 (d, J = 3.3 Hz, 1H), 6.59 – 6.55 (m, 1H), 3.99 (s, 3H), 1.64 (s, 9H) ppm; **^{13}C NMR** (101 MHz, $CDCl_3$) δ 160.6, 151.8, 146.7, 144.0, 142.1, 114.6, 112.0, 62.9, 52.3, 29.8 ppm; **LRMS (+ESI)** m/z: 272 ($[M+Na]^+$, 100); **HRMS (+ESI)** Calc. for $C_{12}H_{15}N_3NaO_3$ $[M+Na]^+$: 272.10056, found 272.10028.

1-(*tert*-butyl)-5-(furan-2-yl)-1*H*-1,2,4-triazole-3-carboxylic acid (**244**)

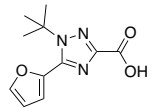

Prepared according to **General Procedure J** with **251** (109 mg, 0.44 mmol) and $LiOH.H_2O$ (51.1 mg, 1.22 mmol). Compound **244** was obtained as a white solid (81.8 mg, 80%) without need for further purification. **^{1}H NMR** (400 MHz, CD_3OD) δ 7.82 (d, J = 1.8 Hz, 1H), 6.98 (d, J = 3.4 Hz, 1H), 6.69 (dd, J = 3.7, 1.8 Hz, 1H), 1.63 (s, 9H) ppm, COO<u>H</u> signal not observed; **^{13}C NMR** (101 MHz, CD_3OD) δ 162.5, 153.2, 147.8, 145.8, 142.7, 115.8, 113.0,

64.2, 29.9 ppm; **LRMS (+ESI)** m/z: 258 ([M+Na]$^+$, 100), **(-ESI)** m/z: 234 ([M-H]$^-$, 100); **HRMS (+ESI)** Calc. for $C_{11}H_{13}N_3NaO_3$ [M+Na]$^+$: 258.08491, found 258.08490.

2-(1-(*tert*-butyl)-5-(furan-2-yl)-1*H*-1,2,4-triazol-3-yl)-5-chloro-1*H*-benzo[*d*]imidazole (**234**)

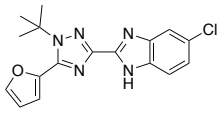

Prepared according to **General Procedure N** from **244** (80.6 mg, 0.34 mmol), 4-chlorobenzene-1,2-diamine (68.8 mg, 0.48 mmol), HATU (182 mg, 0.48 mmol) and ^{i}Pr$_2$NEt (240 µL, 1.38 mmol) in DMF (1 mL). Compound **234** was obtained as an orange crystalline solid (41.3 mg, 35%) following purification by flash chromatography (1:99 MeOH:CH_2Cl_2). Characterisation data is reported as a complex mix of tautomers. **^{1}H NMR** (500 MHz, DMSO-d_6) δ 13.38 – 13.18 (m, 1H), 8.03 (d, J = 1.2 Hz, 1H), 7.76 – 7.67 (m, 1H), 7.54 – 7.50 (m, 1H), 7.26 (ddd, J = 18.3, 8.6, 1.9 Hz, 2H), 7.06 (d, J = 3.4 Hz, 1H), 6.78 (dd, J = 3.4, 1.8 Hz, 1H), 1.60 (s, 9H) ppm; **^{13}C NMR** (126 MHz, DMSO-d_6) δ 151.7, 145.7, 145.3, 144.9, 144.5, 142.4, 141.4, 135.1, 133.2, 127.4, 126.3, 123.3, 122.3, 120.7, 118.7, 114.3, 113.2, 112.0, 111.5, 62.0, 29.3 ppm, 1 carbon peak not observed due to peak broadening; **LRMS (+ESI)** m/z: 364/366 ([M+Na]$^+$, 100), **(-ESI)** m/z: 340/342 ([M-H]$^-$, 100); **HRMS (+ESI)** Calc. for $C_{17}H_{17}ClN_5O$ [M+H]$^+$: 342.11161/344.10866, found 342.11141/344.10850; **HPLC** R_T 20.25 min, 97.48% (254 nm).

ethyl (*E*/*Z*)-3-(*tert*-butylamino)-2-nitroacrylate (**253**)

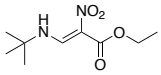

To a stirred solution of AcOH (1.5 mL) in EtOH (7.5 mL) was added appropriate *tert*-butylamine (3 mL, 28.6 mmol) and TOF (9.5 mL, 57.1 mmol). The reaction mixture was heated to reflux at 90 °C for 2 hours. The reaction mix was allowed to cool to room temperature and ethyl 2-nitroacetate (3.17 mL, 28.6 mmol) was added dropwise to the flask. The reaction mixture was again heated to reflux at 90 °C for 3 hours. Upon consumption of starting material indicated by TLC, the solution was concentrated under a stream of N_2. The crude residue was dissolved in a EtOAc (10 mL) and H_2O (10 mL). The aqueous layer was extracted with EtOAc (3 x 25 mL/mmol). The pooled organic layers were then washed with brine (1 x 25 mL/mmol), dried with $MgSO_4$ and concentrated. Compound **253** was isolated as pale yellow solid (1.95 g, 32%) following purification by flash chromatography (1:9 EtOAc:Hex). Characterisation data

is reported as a mixture of isomers with a ratio of approximately 1:1. **^{1}H NMR** (500 MHz, $CDCl_3$) δ 9.85 (s, 1H), 9.54 (s, 1H), 8.72 (d, J = 15.1 Hz, 1H), 8.16 (d, J = 15.4 Hz, 1H), 4.37 – 4.25 (m, 4H), 1.43 (s, 9H), 1.41 (s, 9H), 1.37 (t, J = 7.1 Hz, 3H), 1.33 (t, J = 7.1 Hz, 3H) ppm; **^{13}C NMR** (126 MHz, $CDCl_3$) δ 165.2, 161.9, 152.9, 148.7, 61.2, 55.4, 55.0, 29.8, 29.8, 14.5, 14.4 ppm; **LRMS (+ESI)** m/z: 239 ($[M+Na]^+$, 100); **HRMS (+ESI)** Calc. for $C_9H_{17}N_2O_4$ $[M+H]^+$: 217.11828, found 217.11820.

ethyl 1-(*tert*-butyl)-1*H*-imidazole-4-carboxylate (**252**)

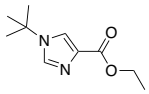

To a solution of AcOH (4 mL, 69.4 mmol) and TOF (5.80 mL, 34.7 mmol) was added compound **253** (1.50 g, 6.94 mmol) and Fe powder (1.94 g, 34.7 mmol). The reaction mix was refluxed at 85 °C and stirred under N_2 for 5 hrs. Over 5 hrs, 6 total eq. Fe and 6 total eq. TOF were added to the reaction mix as it continued to reflux. After 5 hrs, the reaction mix was concentrated *in vacuo*. The reaction mixture was dilute with H_2O (10 mL), and any remaining acetic acid was neutralised with NaOH. The aqueous layer was extracted with EtOAc (3 x 25 mL/mmol). The pooled organic layers were then washed with brine (1 x 25 mL/mmol), dried with $MgSO_4$ and concentrated. Compound **252** was isolated as an off white solid (1.02 g, 75%) following purification by flash chromatography (1:1 EtOAc:Hex). **^{1}H NMR** (500 MHz, $CDCl_3$) δ 7.74 (d, J = 1.5 Hz, 1H), 7.62 (d, J = 1.5 Hz, 1H), 4.36 (q, J = 7.1 Hz, 2H), 1.58 (s, 9H), 1.38 (t, J = 7.1 Hz, 3H) ppm; **^{13}C NMR** (126 MHz, $CDCl_3$) δ 163.3, 135.4, 133.9, 122.9, 60.6, 56.0, 30.7, 14.6 ppm; **LRMS (+APCI)** m/z: 197 ($[M+H]^+$, 100); **HRMS (+APCI)** Calc. for $C_{10}H_{17}N_2O_2$ $[M+H]^+$: 197.12845, found 197.12836.

ethyl 2-iodo-1-(*tert*-butyl)-1*H*-imidazole-4-carboxylate (**258**)

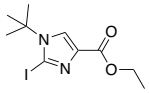

252 (40 mg, 0.20 mmol) was dissolved in THF (0.5 mL). *N*-Iodosuccinimide (NIS, 45.9 mg, 0.20 mmol) was added in one portion and the flask was covered with foil to exclude light. The mixture was heated to reflux for 24 h under argon. Additional NIS (45.9 mg, 0.20 mmol) was added at 12 h. The reaction was allowed to cool to room temperature, and saturated aq $NaHSO_3$ (5 mL) was added. The aqueous layer was extracted with EtOAc (3 x 25 mL/mmol). The pooled organic layers were then washed with brine (1 x 25 mL/mmol), dried with $MgSO_4$ and concentrated. Compound **258** was isolated as an off white solid (9.19 g, 40%) following

purification by flash chromatography (1:1 EtOAc:Hex). **^{1}H NMR** (500 MHz, $CDCl_3$) δ 7.78 (s, 1H), 4.36 (q, J = 7.1 Hz, 2H), 1.76 (s, 9H), 1.36 (t, J = 7.1 Hz, 3H) ppm; **^{13}C NMR** (126 MHz, $CDCl_3$) δ 162.2, 135.5, 127.0, 84.6, 60.9, 59.0, 30.4, 29.9, 14.6 ppm; **LRMS (+APCI)** m/z: 323 ($[M+H]^+$, 100); **HRMS (+APCI)** Calc. for $C_{10}H_{16}IN_2O_2$ $[M+H]^+$: 323.02510, found 323.02519.

ethyl 2-bromo-1-(*tert*-butyl)-1*H*-imidazole-4-carboxylate (**259**)

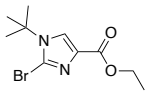

N-bromosuccinimide (NBS, 51.5 mg, 0.29 mmol) added to **252** (48.6 mg, 0.25 mmol) in DMF (1 mL) at 0°C. The reaction was brought to rt and stirred for 18 h. The reaction was diluted with ice-cold H_2O (5 mL) and extracted with EtOAc (3 x 25 mL/mmol). Combined organic layers were washed with brine (1 x 25 mL/mmol) and concentrated *in vacuo*. Compound **259** was isolated as an off-white solid (40.9 mg, 60%) following purification by flash chromatography (1:4 EtOAc:Hex). **^{1}H NMR** (500 MHz, $CDCl_3$) δ 7.77 (s, 1H), 4.36 (q, J = 7.1 Hz, 2H), 1.72 (s, 9H), 1.36 (t, J = 7.1 Hz, 3H) ppm; **^{13}C NMR** (126 MHz, $CDCl_3$) δ 162.3, 132.8, 126.1, 118.0, 60.9, 59.1, 29.8, 14.6 ppm; **LRMS (+ESI)** m/z: 297/299 ($[M+Na]^+$, 30); **HRMS (+APCI)** Calc. for $C_{10}H_{16}BrN_2O_2$ $[M+H]^+$: 275.03897/277.03692, found 275.03874/277.03672.

1-(*tert*-butyl)-1*H*-imidazole-4-carboxylic acid (**263**)

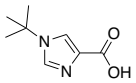

Prepared according to **General Procedure J** with **252** (179 mg, 0.91 mmol) and $LiOH.H_2O$ (46.1 mg, 1.10 mmol). Compound **263** was obtained as a white solid (152 mg, 99%) without need for further purification. **^{1}H NMR** (500 MHz, CD_3OD) δ 7.74 (d, J = 1.5 Hz, 1H), 7.64 (d, J = 1.5 Hz, 1H), 1.59 (s, 9H) ppm, COOH signal not observed; **^{13}C NMR** (126 MHz, CD_3OD) δ 171.3, 140.5, 135.5, 120.9, 56.8, 30.6 ppm; ; **LRMS (+ESI)** m/z: 181 ($[M+Na]^+$, 100), **(-ESI)** m/z: 167 ($[M-H]^-$, 70); **HRMS (+ESI)** Calc. for $C_8H_{11}N_2O_2$ $[M+H]^+$: 167.08260, found 167.08257.

2-(1-(*tert*-butyl)-1*H*-imidazol-4-yl)-5-chloro-1*H*-benzo[*d*]imidazole (**264**)

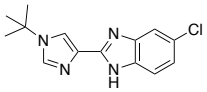

Prepared according to **General Procedure N** from **263** (123 mg, 0.73 mmol), 4-chlorobenzene-1,2-diamine (155 mg, 1.08 mmol), HATU (389 mg, 1.03 mmol) and $^{i}Pr_2NEt$ (500 µL, 2.87 mmol) in DMF (3 mL). Compound **264** was obtained as an off white solid (66.3 mg, 33%) following purification by flash chromatography (3:7 EtOAc:Hex). Characterisation data is reported as a complex mix of tautomers. **^{1}H NMR** (500 MHz, $CDCl_3$) δ 12.26 (s, 1H), 7.99 (d, J = 1.5 Hz, 1H), 7.75 (d, J = 1.5 Hz, 1H), 7.47 (s, 2H), 7.17 (dd, J = 8.5, 2.0 Hz, 1H), 1.65 (s, 9H) ppm; **^{13}C NMR** (126 MHz, $CDCl_3$) δ 149.3, 134.9, 133.3, 127.9, 122.9, 117.7, 56.4, 30.7 ppm; 4 carbon peaks not observed due to peak broadening; **LRMS (+ESI)** m/z: 274 ($[M+H]^+$, 100), 297 ($[M+Na]^+$, 40); **HRMS (+ESI)** Calc. for $C_{14}H_{16}N_4$ $[M+H]^+$: 275.10580, found 275.10530.

(*E*)-furan-2-carbaldehyde oxime (**266**)

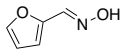

A solution of furfural (distilled, 500 µL, 6.04 mmol), hydroxylamine hydrochloride (835 mg, 12.0 mmol) and sodium hydroxide (473 mg, 11.8 mmol) in H_2O/EtOH (2:1, 3 mL) was stirred at r.t. for 1 h. The solution was evaporated, and the residue dissolved in EtOAc (10 mL). The organic layer was washed with H_2O (1 x 25 mL/mmol), dried with $MgSO_4$, filtered and evaporated to dryness. Compound **266** was isolated as a mixture (7:10) of oximes (536 mg, 80%). **^{1}H NMR** (500 MHz, $CDCl_3$) δ 9.47 (s, 1H), 8.85 (s, 0.7H), 8.02 (s, 0.7H), 7.52 (s, 1H), 7.49 (dd, J = 6.2, 1.7 Hz, 1H), 7.34 (d, J = 3.4 Hz, 0.7H), 6.64 (d, J = 3.4 Hz, 0.7H), 6.54 (dt, J = 3.2, 1.3 Hz, 1H), 6.46 (dt, J = 3.1, 1.4 Hz, 0.7H) ppm; **^{13}C NMR** (126 MHz, $CDCl_3$) δ 147.3, 145.2, 144.5, 143.5, 140.4, 137.3, 118.3, 112.8, 112.4, 111.7 ppm. Matched previously reported characterisation data.[476]

furan-2-carbonitrile (**267**)

Cupric acetate (100 mg, 0.55 mmol) was added to a stirring solution of **266** (613 mg, 5.52 mmol) in CH_3CN (5 mL). The mixture was heated to reflux for 1 h. After cooling to rt, the solution was directly evaporated to dryness, and the residue was purified by column chromatography (1:9 EtOAc:Hex) to yield compound **267** as colourless oil (205 mg, 40%). **^{1}H NMR** (500 MHz, $CDCl_3$) δ 7.59 (dd, J = 1.9, 0.8 Hz, 1H), 7.10 (dd, J = 3.6, 0.7 Hz, 1H), 6.53 (dd, J = 3.6, 1.8 Hz, 1H) ppm; **^{13}C NMR** (126 MHz, $CDCl_3$) δ 147.4, 126.5, 122.1, 111.6, 111.5 ppm. Matched previously reported characterisation data.[477]

N-(*tert*-butyl)furan-2-carboximidamide (**268**)

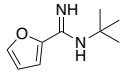

Under an air atmosphere, *tert*-butylamine (200 µL, 1.90 mmol) and the **267** (150 mg, 1.61 mmol) were added to a pressure flask (10 mL). $AlCl_3$ (87.3 mg, 0.65 mmol) was added in one portion while stirring the reaction. The flask was tightly sealed with a Teflon screw cap and stirred at room temperature for 1 h. Following this, ice-water (5 mL) was added to the mixture under vigorous stirring. Aqueous NaOH (2.5 M) was added until a pH of 14 was reached. The aqueous layer was extracted with CH_2Cl_2 (3 x 25 mL/mmol). The combined organic layers were washed with H_2O (1 x 25 mL/mmol) and then brine (1 x 25 mL/mmol), and dried over $MgSO_4$, filtered, and concentrated *in vacuo.* Compound **268** was isolated as white powder (88.4 mg, 33%) following purification by flash chromatography (1:19 MeOH:CH_2Cl_2). **^{1}H NMR** (500 MHz, DMSO-d_6) δ 8.97 (s, 2H), 8.13 (d, J = 1.6 Hz, 1H), 7.79 (d, J = 3.6 Hz, 1H), 6.82 (dd, J = 3.7, 1.8 Hz, 1H), 1.47 (s, 9H) ppm; **^{13}C NMR** (126 MHz, DMSO-d_6) δ 150.2, 148.0, 141.8, 118.3, 113.0, 53.8, 27.6 ppm; **LRMS (+ESI)** m/z: 167 ($[M+H]^+$, 100); **HRMS (+ESI)** Calc. for $C_9H_{15}N_2O$ $[M+H]^+$: 167.11789, found 167.11779.

2-(diethoxymethyl)furan (**271**)

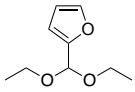

$Fe(OTs)_3.6H_2O$ (52.3 mg, 0.08 mmol) was added to a stirring solution of triethyl orthoformate (1.2 mL, 7.49 mmol) in EtOH (1 mL). Furfural (distilled, 200 µL, 2.5 mmol) was added dropwise, and the reaction was heated to 30 °C for 4 h. The reaction was cooled to rt and quench with sat. $NaHCO_3$ (3 mL), and stirred vigorously for 10 min. The aqueous layer was extracted with CH_2Cl_2 (3 x 25 mL/mmol). Pooled organic layers were washed with brine (1 x 25 mL/mmol) and dried over $MgSO_4$, filtered, and concentrated *in vacuo*. Compound **271** was isolated as a pale yellow oil (298 mg, 70%) and was stored at -8 °C in the absence of light. **^{1}H NMR** (500 MHz, $CDCl_3$) δ 7.40 (dd, J = 1.8, 0.9 Hz, 1H), 6.41 (dt, J = 3.3, 0.9 Hz, 1H), 6.35 (dd, J = 3.3, 1.8 Hz, 1H), 5.54 (s, 1H), 3.68 – 3.55 (m, 4H), 1.23 (t, J = 7.1 Hz, 6H) ppm; **^{13}C NMR** (126 MHz, $CDCl_3$) δ 152.0, 142.5, 110.2, 108.1, 96.5, 61.4, 15.3 ppm. Matched previously reported characterisation data.[478]

1-(*tert*-butyl)-*N*-(4-chlorophenyl)-5-(furan-2-yl)-1*H*-pyrazole-3-carboxamide (**272**)

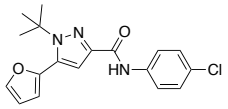

Compound **272** was prepared *via* a HATU mediated amide coupling according to **General Procedure G** from **163** (40.9 mg, 0.17 mmol) and 4-chloroaniline (32 mg, 0.24 mmol). Compound **272** was isolated as a white solid (49.1 mg, 82%) following purification by flash chromatography (1:49 EtOAc:Hex). **^{1}H NMR** (500 MHz, $CDCl_3$) δ 8.71 (s, 1H), 7.66 (d, J = 8.6 Hz, 2H), 7.56 (s, 1H), 7.32 (d, J = 8.6 Hz, 2H), 6.97 (s, 1H), 6.51 (s, 2H), 1.57 (s, 9H) ppm; **^{13}C NMR** (126 MHz, $CDCl_3$) δ 159.9, 143.7, 143.2, 143.1, 136.7, 134.6, 129.2, 129.0, 121.1, 112.4, 111.9, 111.6, 62.5, 30.0 ppm; **LRMS (+ESI)** m/z: 366/368 ($[M+Na]^+$, 100), **(-ESI)** m/z: 342/344 ($[M-H]^-$, 100); **HRMS (+ESI)** Calc. for $C_{18}H_{18}ClN_3NaO_2$ $[M+Na]^+$: 366.09798/368.09503, found 366.09751/368.09457; **HPLC** R_T = 28.96 min, 99.89% (254 nm).

N-methoxy-*N*-methylfuran-2-carboxamide (**276**)

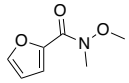

Compound **276** was prepared *via* a HATU mediated amide coupling according to **General Procedure G** from 2-furoic acid (248 mg, 2.21 mmol) and *N*,*O*-dimethylhydroxylamine (260 mg, 2.66 mmol). Compound **276** was isolated as a white solid (244 mg, 71%) following purification by flash chromatography (1:4 EtOAc:Hex). **^{1}H NMR** (500 MHz, $CDCl_3$) δ 7.57 (dd, J = 1.7, 0.8 Hz, 1H), 7.13 (dd, J = 3.4, 0.8 Hz, 1H), 6.49 (dd, J = 3.5, 1.8 Hz, 1H), 3.75 (s, 3H), 3.34 (s, 3H) ppm; **^{13}C NMR** (126 MHz, $CDCl_3$) δ 159.3, 145.8, 145.3, 117.5, 111.7, 61.5, 33.3 ppm; **LRMS (+ESI)** m/z: 178 ([M+Na]$^+$, 60); **HRMS (+ESI)** Calc. for $C_7H_9NNaO_3$ [M+Na]$^+$: 178.04746, found 178.04711.

5-furan-2-yl-5-hydroxy-3-oxo-pent-4-enoic acid ethyl ester (**277**)

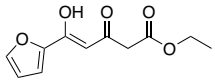

To a stirred suspension of NaH (60% Dispersion in oil, 113 mg, 2.84 mmol) in THF (2 mL) at 0 °C was added ethyl acetoacetate (180 µL, 1.42 mmol). This mixture was stirred for 30 min at which time the temperature of the reaction was further lowered to -78 °C. To this mixture was added *n*-BuLi (2.5 M solution in hexanes, 1.5 mL, 3 mmol) and the reaction was stirred for 10 min followed by addition of **276** (198 mg, 1.28 mmol). The reaction was stirred for an additional 30 min at -78 °C followed by warming up to 0 °C over 1 h. The reaction was quenched by addition of sat. aq. NH_4Cl, followed by extraction with EtOAc (3 x 25 mL/mmol). The combined organic phases were dried over $MgSO_4$, concentrated *in vacuo* to yield compound **277** (86 mg, 30%) following purification by flash chromatography (1:49 EtOAc:Hex). **^{1}H NMR** (500 MHz, $CDCl_3$) δ 15.21 (s, 1H), 7.58 (s, 1H), 7.18 (d, J = 3.5 Hz, 1H), 6.59 – 6.52 (m, 1H), 6.19 (s, 1H), 4.22 (q, J = 7.0 Hz, 2H), 3.42 (s, 2H), 1.29 (t, J = 7.2 Hz, 3H) ppm; **^{13}C NMR** (126 MHz, $CDCl_3$) δ 185.4, 175.2, 167.7, 150.0, 146.5, 116.4, 112.8, 96.6, 61.7, 44.9, 14.3 ppm; **LRMS (+ESI)** m/z: 247 ([M+Na]$^+$, 100); **HRMS (+ESI)** Calc. for $C_{11}H_{12}NaO_5$ [M+Na]$^+$: 247.05769, found 247.05747. Matched previously reported characterisation data.[377]

ethyl 2-(1-(*tert*-butyl)-5-(furan-2-yl)-1*H*-pyrazol-3-yl)acetate (**279**)

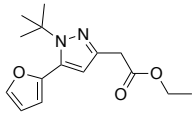

Compound **279** was synthesised from **277** (77.9 mg, 0.35 mmol) and *tert*-butylhydrazine hydrochloride (69.2 mg, 0.56 mmol) in EtOH (1.5 mL) according to **General Procedure I** and was obtained as a white powder (44.2 mg, 46%) following purification by flash chromatography (1:19 EtOAc:Hex). **^{1}H NMR** (500 MHz, $CDCl_3$) δ 7.51 (dd, J = 1.9, 0.9 Hz, 1H), 6.46 (dd, J = 3.3, 1.9 Hz, 1H), 6.43 (dd, J = 3.2, 0.9 Hz, 1H), 6.33 (s, 1H), 4.18 (q, J = 7.1 Hz, 2H), 3.67 (s, 3H), 1.49 (s, 9H), 1.28 (t, J = 7.1 Hz, 3H) ppm; **^{13}C NMR** (126 MHz, $CDCl_3$) δ 171.2, 145.1, 142.5, 142.2, 132.8, 111.4, 111.3, 110.6, 60.9, 60.9, 34.6, 30.2, 14.4 ppm; **LRMS (+ESI)** m/z: 299 ($[M+Na]^+$, 100).

2-(1-(*tert*-butyl)-5-(furan-2-yl)-1*H*-pyrazol-3-yl)acetic acid (**280)**

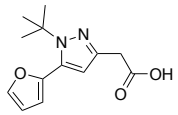

Prepared according to **General Procedure J** with **279** (44.2 mg, 0.16 mmol) and $LiOH.H_2O$ (10.1 mg, 0.24 mmol). Compound **280** was obtained as a white solid (28.6 mg, 72%) without need for further purification. **^{1}H NMR** (500 MHz, $CDCl_3$) δ 7.39 (d, J = 1.8 Hz, 1H), 6.35 (dd, J = 3.3, 1.9 Hz, 1H), 6.28 (d, J = 3.3 Hz, 1H), 6.18 (s, 1H), 4.04 (s, 1H), 3.39 (s, 2H), 1.35 (s, 9H) ppm, OH signal not observed; **^{13}C NMR** (126 MHz, $CDCl_3$) δ 178.7, 146.3, 145.1, 142.2, 132.5, 111.6, 111.5, 111.2, 60.7, 37.4, 30.1 ppm; **LRMS (+ESI)** m/z: 261 ($[M+Na]^+$, 100), **(-ESI)** m/z: 247 ($[M-H]^-$, 100); **HRMS (+ESI)** Calc. for $C_{13}H_{15}N_2O_3$ $[M+H]^+$: 247.10882, found 247.10882.

2-((1-(*tert*-butyl)-5-(furan-2-yl)-1*H*-pyrazol-3-yl)methyl)-5-chloro-1*H*-benzo[*d*]imidazole (**273**)

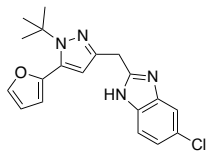

Prepared according to **General Procedure N** from **280** (28.6 mg, 0.12 mmol), 4-chlorobenzene-1,2-diamine (24.0 mg, 0.17 mmol), HATU (65.3 mg, 0.17 mmol) and $^{i}Pr_2NEt$ (80 µL, 0.46 mmol) in DMF (1 mL). Compound **273** was obtained as a white solid (11.4 mg, 28%) following purification by flash chromatography (3:7 EtOAc:Hex). **^{1}H NMR** (500 MHz, DMSO-d_6) δ 12.46 (s, 1H), 7.82 (s, 1H), 7.53 (s, 1H), 7.48 (d, J = 8.7 Hz, 1H), 7.15 (dd, J = 8.5, 2.0 Hz, 1H), 6.59 (s, 1H), 6.32 (s, 1H), 4.14 (s, 2H), 1.43 (s, 9H) ppm; **^{13}C NMR** (126 MHz, DMSO-d_6) δ 154.1, 144.3, 143.9, 143.4, 132.3, 125.8, 121.6, 111.7, 111.6, 110.1, 60.4, 29.7, 28.4 ppm, 4 carbon peaks not observed due to peak broadening; **LRMS (+ESI)** m/z: 355/357 ($[M+H]^+$, 100), 377/379 ($[M+Na]^+$, 90), **(-ESI)** m/z: 353/355 ($[M-H]^-$, 100); **HRMS (+ESI)** Calc. for $C_{19}H_{20}ClN_4O$ $[M+H]^+$: 355.13202/357.12907, found 355.13246/357.12967; **HPLC** R_T = 20.52 min, 96.49% (254 nm).

7.6 Chapter 4 Experimental and Characterisation

(*E*)-1-(1*H*-pyrrol-2-yl)-3-(quinolin-3-yl)prop-2-en-1-one (**282**)

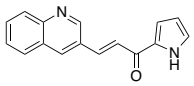

Prepared according to **General Procedure O** from quinoline-3-carbaldehyde (200 mg, 1.27 mmol), 2-acetylpyrrole (142 mg, 1.30 mmol) and aq. NaOH (2.5 M, 1 mL, 2.54 mmol) in EtOH (2 mL). Compound **282** was obtained as a pale yellow powder (218 mg, 69%) following filtration. **^{1}H NMR** (500 MHz, DMSO-d_6) δ 12.05 (s, 1H), 9.41 (d, J = 2.2 Hz, 1H), 8.78 (d, J = 2.1 Hz, 1H), 8.06 (dd, J = 8.4, 1.1 Hz, 1H), 8.01 (dd, J = 8.2, 1.4 Hz, 1H), 8.00 (d, J = 15.7 Hz, 1H), 7.84 (d, J = 15.7 Hz, 1H), 7.82 – 7.79 (m, 1H), 7.67 (ddd, J = 8.1, 6.8, 1.2 Hz, 1H), 7.46 (dd, J = 3.8, 1.4 Hz, 1H), 7.21 (dd, J = 2.4, 1.4 Hz, 1H), 6.31 (dd, J = 3.8, 2.4 Hz, 1H) ppm; **^{13}C NMR** (126 MHz, DMSO-d_6) δ 177.4, 150.2, 147.8, 137.4, 135.6, 133.0, 130.4, 128.9, 128.6, 128.2, 127.5, 127.3, 126.8, 124.9, 117.9, 110.3 ppm; **LRMS (-ESI)** m/z: 247 ($[M-H]^-$, 100); **HRMS (+ESI)** Calc. for $C_{16}H_{12}N_2NaO$ $[M+Na]^+$: 271.08418, found 271.08371.

4-(3-(1*H*-pyrrol-2-yl)-5-(quinolin-3-yl)-4,5-dihydro-1*H*-pyrazol-1-yl)-4-oxobutanoic acid (**38**)

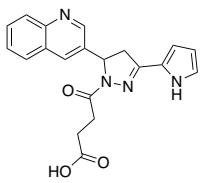

To a solution of **282** (50.3 mg, 0.20 mmol) in EtOH (1 mL) was added hydrazine monohydrate (50 µL, 1.01 mmol). The reaction was stirred at 80 °C for 2 h. Following consumption of starting material as indicated by TLC, the reaction was added to ice H_2O. The resulting precipitate was filtered, washed with EtOH and dried to obtain the dihydropyrazole analogue **287**. The residue was dissolved in $CHCl_3$ (2 mL) and treated with succinic anhydride (39.2 mg, 0.39 mmol). The reaction was stirred at reflux 4 h. The precipitate was filtered and washed with EtOAc to yield compound **38** as a grey solid (30.3 mg, 41% over two steps). **^{1}H NMR** (500 MHz, DMSO-*d*$_6$) δ 12.09 (s, 1H), 11.58 (s, 1H), 8.81 (d, J = 2.2 Hz, 1H), 8.08 (d, J = 2.4 Hz, 1H), 8.00 (d, J = 8.5 Hz, 1H), 7.95 (d, J = 8.2 Hz, 1H), 7.73 (t, J = 7.7 Hz, 1H), 7.59 (t, J = 7.5 Hz, 1H), 6.98 (d, J = 3.3 Hz, 1H), 6.56 – 6.51 (m, 1H), 6.15 (q, J = 2.8 Hz, 1H), 5.72 (dd, J = 11.7, 4.7 Hz, 1H), 3.86 (dd, J = 17.8, 11.8 Hz, 1H), 3.22 (dd, J = 17.8, 4.7 Hz, 1H), 3.09 (dt, J = 16.9, 6.9 Hz, 1H), 2.91 (dt, J = 17.0, 6.6 Hz, 1H), 2.58 – 2.43 (m, 2H) (overlapping with solvent peak) ppm; **^{13}C NMR** (126 MHz, DMSO-*d*$_6$) δ 173.9, 168.6, 149.5, 148.2, 146.9, 135.0, 131.9, 129.3, 128.6, 128.1, 127.4, 126.8, 123.4, 122.7, 112.8, 109.3, 57.0, 41.8, 28.7, 28.5 ppm; **LRMS (+ESI)** m/z: 385 ($[M+Na]^+$, 100), **(-ESI)** m/z: 361 ($[M-H]^-$, 100); **HRMS (+ESI)** Calc. for $C_{20}H_{19}N_4O_3$ $[M+H]^+$: 363.14517, found 363.14450; **HPLC** R_T = 8.41 min, 99.47% (254 nm). Matched previously reported characterisation data.[170]

(*E*)-1-([1,1'-biphenyl]-4-yl)-3-(2-chloro-7-methylquinolin-3-yl)prop-2-en-1-one (**283**)

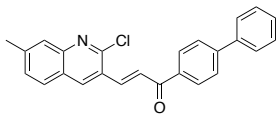

Prepared according to **General Procedure O** from 2-chloro-7-methylquinoline-3-carbaldehyde (200 mg, 0.97 mmol), 4-acetylbiphenyl (190 mg, 0.97 mmol) and aq. NaOH (2.5 M, 0.8 mL, 1.95 mmol) in EtOH (2 mL). Compound **283** was obtained as a pale yellow powder (265 mg, 71%) following filtration. **^{1}H NMR** (500 MHz, $CDCl_3$) δ 8.47 (s, 1H), 8.23 (d, J = 15.7 Hz, 1H), 8.14 (dt, J = 8.4, 2.0 Hz, 2H), 7.81 (q, J = 1.1 Hz, 1H), 7.79 (d, J = 8.4 Hz, 1H), 7.76 (dt, J = 8.4, 2.0 Hz, 2H), 7.66 (dd, J = 8.3, 1.3 Hz, 2H), 7.63 (d, J = 15.4 Hz,

1H), 7.52 – 7.47 (m, 2H), 7.46 – 7.40 (m, 2H), 2.58 (s, 3H) ppm; **^{13}C NMR** (126 MHz, $CDCl_3$) δ 189.5, 150.6, 148.4, 146.1, 142.8, 140.0, 139.7, 136.5, 136.1, 130.2, 129.5, 129.5, 129.1, 129.1, 128.5, 127.8, 127.7, 127.5, 127.5, 127.4, 127.3, 126.0, 125.2, 22.3 ppm; **LRMS (+ESI)** m/z: 406/408 ([M+Na]$^+$, 100); **HRMS (+ESI)** Calc. for $C_{25}H_{18}ClNNaO_2$ [M+Na]$^+$: 406.09691/408.09396, found 406.09748/408.09456.

4-(3-([1,1'-biphenyl]-4-yl)-5-(2-chloro-7-methylquinolin-3-yl)-4,5-dihydro-1*H*-pyrazol-1-yl)-4-oxobutanoic acid (**40**)

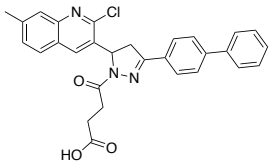

To a solution of **283** (104 mg, 0.27 mmol) in EtOH (2 mL) was added hydrazine monohydrate (70 µL, 1.44 mmol). The reaction was stirred at 80 °C for 2 h. Following consumption of starting material as indicated by TLC, the reaction was added to ice H_2O. The resulting precipitate was filtered, washed with EtOH and dried to obtain the dihydropyrazole analogue **288**. The residue was dissolved in $CHCl_3$ (2 mL) and treated with succinic anhydride (51.5 mg, 0.51 mmol). The reaction was stirred at reflux 4 h. The precipitate was filtered and washed with EtOAc to yield compound **40** as a grey solid (51.3 mg, 38% over two steps). **^{1}H NMR** (500 MHz, DMSO-d_6) δ 12.15 (s, 1H), 8.05 (s, 1H), 7.92 – 7.86 (m, 3H), 7.79 (s, 1H), 7.76 (d, J = 7.9 Hz, 2H), 7.72 (d, J = 7.7 Hz, 2H), 7.51 – 7.46 (m, 3H), 7.40 (t, J = 7.4 Hz, 1H), 5.86 (dd, J = 12.0, 5.1 Hz, 1H), 4.06 (dd, J = 18.0, 12.0 Hz, 1H), 3.42 – 3.23 (m, 2H) (overlapping with H_2O peak), 2.94 (dt, J = 17.1, 6.4 Hz, 1H), 2.61 – 2.54 (m, 2H), 2.52 (s, 3H) ppm; **^{13}C NMR** (126 MHz, DMSO-d_6) δ 173.9, 169.3, 154.2, 147.9, 146.5, 141.8, 140.9, 139.1, 134.9, 131.4, 129.9, 129.5, 129.0, 128.0, 127.8, 127.4, 126.9, 126.7, 126.3, 125.1, 57.4, 40.7, 28.6, 28.5, 21.4 ppm; **LRMS (+ESI)** m/z: 520/522 ([M+Na]$^+$, 100), **(-ESI)** m/z: 496/498 ([M-H]$^-$, 100); **HRMS (+ESI)** Calc. for $C_{29}H_{24}ClN_3NaO_3$ [M+Na]$^+$: 520.13984/522.13689, found 520.13977/522.13694; **HPLC** R_T = 28.90 min, 96.01% (254 nm). Matched previously reported characterisation data.[170]

(*E*)-3-(2-chloro-7-methylquinolin-3-yl)-1-(4-hydroxyphenyl)prop-2-en-1-one (**284**)

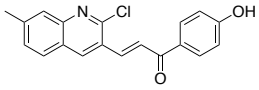

Prepared according to **General Procedure O** from 2-chloro-7-methylquinoline-3-carbaldehyde (205 mg, 0.99 mmol), 4-hydroxyacetophenone (138 mg, 1.01 mmol) and aq. NaOH (2.5 M, 0.8 mL, 1.99 mmol) in EtOH (2 mL). Compound **284** was obtained as a white powder (255 mg, 79%) following purification by flash chromatography (0 – 100% v/v EtOAc in Hex). **^{1}H NMR** (500 MHz, DMSO-d_6) δ 9.17 (s, 1H), 8.12 (d, J = 8.8 Hz, 2H), 8.09 (s, 1H), 8.00 (s, 1H), 7.96 (d, J = 8.7 Hz, 1H), 7.77 (s, 1H), 7.56 (dd, J = 8.4, 1.6 Hz, 1H), 6.93 (d, J = 8.7 Hz, 2H), 2.55 (s, 3H) ppm; **^{13}C NMR** (126 MHz, DMSO-d_6) δ 186.5, 162.6, 149.7, 147.4, 142.5, 137.1, 136.6, 131.4, 130.1, 128.7, 128.2, 126.7, 126.3, 126.0, 125.1, 115.5, 21.6 ppm; **LRMS (-ESI)** m/z: 322/324 ([M-H]$^-$, 100); **HRMS (+ESI)** Calc. for $C_{19}H_{14}ClNNaO_2$ [M+Na]$^+$: 346.06053/348.05758, found 346.06053/348.05760.

(*E*)-1-(4-(benzyloxy)phenyl)-3-(2-chloro-7-methylquinolin-3-yl)prop-2-en-1-one (**289**)

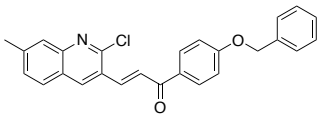

To a suspended solution of **284** (50.1 mg, 0.15 mmol) and NaH (60% Dispersion in mineral oil, 7.2 mg, 0.18 mmol) in DMF/THF (2:1 v/v, 1.5 mL) at 0 °C, was added benzyl bromide (25 µL, 0.21 mmol). The reaction mixture was brought to rt, with stirring over 3 h. The solution was cooled to 0 °C and quenched with 1M HCl (1 mL) followed by addition of H_2O (3 mL) and EtOAc (10 mL). The layers were separated, and the aqueous layer (pH > 4) was extracted with EtOAc (3 x 25 mL/mmol). The combined organic layers were washed with brine (1 x 25 mL/mmol), dried with $MgSO_4$ and concentrated *in vacuo*. Compound **289** was isolated as a white solid (57.4 mg, 90%) following purification by flash chromatography (0 – 30% v/v EtOAc in Hex). **^{1}H NMR** (500 MHz, $CDCl_3$) δ 8.44 (s, 1H), 8.18 (d, J = 15.6 Hz, 1H), 8.10 – 8.05 (m, 2H), 7.81 (s, 1H), 7.77 (d, J = 8.3 Hz, 1H), 7.60 (d, J = 15.7 Hz, 1H), 7.47 – 7.39 (m, 6H), 7.38 – 7.33 (m, 1H), 7.11 – 7.06 (m, 2H), 5.17 (s, 2H), 2.58 (s, 3H) ppm; **^{13}C NMR** (126 MHz, $CDCl_3$) δ 188.3, 163.0, 150.6, 148.3, 142.6, 139.0, 136.3, 136.0, 131.2, 131.0, 130.1, 128.9, 128.5, 127.8, 127.7, 127.7, 127.5, 126.0, 125.3, 115.0, 70.4, 22.3 ppm; **LRMS (+APCI)** m/z: 414/416 ([M+H]$^+$, 50); **HRMS (+ESI)** Calc. for $C_{26}H_{20}ClNNaO_2$ [M+Na]$^+$: 436.10748/438.10453, found 436.10742/438.10448.

4-(3-(4-(benzyloxy)phenyl)-5-(2-chloro-7-methylquinolin-3-yl)-4,5-dihydro-1*H*-pyrazol-1-yl)-4-oxobutanoic acid (**290**)

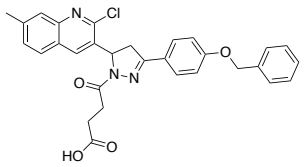

To a solution of **289** (49.8 mg, 0.12 mmol) in EtOH (1 mL) was added hydrazine monohydrate (40 µL, 0.82 mmol). The reaction was stirred at 80 °C for 2 h. Following consumption of starting material as indicated by TLC. The reaction mixture was diluted with H_2O (3 mL) and EtOAc (10 mL). The layers were separated, and the aqueous layer (pH > 8) was extracted with EtOAc (3 x 25 mL/mmol). The combined organic layers were washed with brine (1 x 25 mL/mmol), dried with $MgSO_4$ and concentrated *in vacuo* to yield the dihydropyrazole analogue (**291**). The residue was dissolved in $CHCl_3$ (2 mL) and treated with succinic anhydride (26.7 mg, 0.27 mmol). The reaction was stirred at reflux 4 h. The precipitate was filtered and washed with EtOAc to yield compound **290** as a grey solid (50 mg, 81% over two steps). **^{1}H NMR** (500 MHz, DMSO-d_6) δ 8.01 (s, 1H), 7.89 (d, J = 8.4 Hz, 1H), 7.76 – 7.71 (m, 3H), 7.47 (dd, J = 8.4, 1.7 Hz, 1H), 7.45 (d, J = 1.7 Hz, 1H), 7.44 (s, 1H), 7.38 (dd, J = 8.4, 6.6 Hz, 2H), 7.35 – 7.30 (m, 1H), 7.09 (d, J = 8.9 Hz, 2H), 5.80 (dd, J = 11.9, 5.0 Hz, 1H), 5.16 (s, 2H), 4.06 – 3.94 (m, 1H), 3.31 – 3.20 (m, 2H) (overlapping with H_2O peak), 2.89 (dt, J = 17.2, 6.4 Hz, 1H), 2.65 – 2.52 (m, 2H), 2.51 (s, 3H) (overlapped with solvent peak) ppm; **^{13}C NMR** (126 MHz, DMSO-d_6) δ 173.9, 169.1, 160.1, 155.2, 154.3, 148.0, 146.5, 140.9, 136.7, 131.5, 129.5, 128.4, 127.9, 127.8, 127.7, 126.3, 125.1, 123.6, 118.1, 115.1, 79.2, 69.3, 40.8, 28.6, 28.6, 21.4 ppm; **LRMS (+ESI)** m/z: 550/552 ($[M+Na]^+$, 100); **HRMS (+ESI)** Calc. for $C_{30}H_{26}ClN_3NaO_4$ $[M+Na]^+$: 550.15040/552.14745, found 550.15050/552.14756.

4-(5-(2-chloro-7-methylquinolin-3-yl)-3-(4-hydroxyphenyl)-4,5-dihydro-1*H*-pyrazol-1-yl)-4-oxobutanoic acid diTFA salt (**281**)

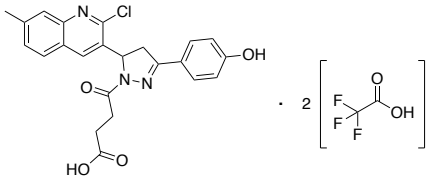

A suspension of **290** (50 mg, 94.7 μmol) in CH_2Cl_2 (1 mL) was treated with BBr_3 (1M in CH_2Cl_2, 190 μL, 189 μmol) at 0 °C before stirring at rt for 1 h. Solvent was removed under a stream of N_2. The reaction was taken up in CH_2Cl_2 and concentrated 2 more times. Compound **290** was isolated as the di-TFA salt (10.9 mg, 17%) following purification by reverse phase chromatography (0 – 100% v/v CH_3CN in H_2O, 0.1% TFA). **^{1}H NMR** (400 MHz, DMSO-d_6) δ 12.12 (s, 1H), 9.99 (s, 1H), 8.00 (s, 1H), 7.88 (d, J = 8.3 Hz, 1H), 7.74 (s, 1H), 7.63 (d, J = 8.6 Hz, 2H), 7.47 (dd, J = 8.4, 1.7 Hz, 1H), 6.82 (d, J = 8.8 Hz, 2H), 5.78 (dd, J = 11.8, 4.9 Hz, 1H), 3.96 (dd, J = 17.9, 11.9 Hz, 1H), 3.29 – 3.19 (m, 2H), 2.89 (dt, J = 17.0, 6.3 Hz, 1H), 2.59 – 2.52 (m, 2H), 2.51 (s, 3H) (overlapped with solvent peak) ppm; **^{19}F NMR** (376 MHz, DMSO-d_6) δ -73.4 ppm; **^{13}C NMR** (101 MHz, DMSO-d_6) δ 173.9, 168.9, 159.6, 154.5, 148.0, 146.5, 140.8, 134.8, 131.5, 129.5, 128.5, 127.7, 126.3, 125.0, 121.7, 115.5, 57.1, 40.8, 28.5, 28.5, 21.3 ppm; **LRMS (+ESI)** m/z: 460/462 ([M+Na]$^+$, 100) , **(-ESI)** m/z: 436/438 ([M-H]$^-$, 100); **HRMS (+ESI)** Calc. for $C_{23}H_{20}ClN_3NaO_4$ [M+Na]$^+$: 460.10345/462.10050, found 460.10356/462.10072; **HPLC** R_T = 20.72 min, 95.10% (254 nm). Matched previously reported characterisation data.[170]

ethyl 2,4-dioxo-4-(thiophen-2-yl)butanoate (**308**)

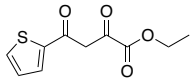

Prepared according to **General Procedure P** from 2-acetylthiophene (171 μL, 1.59 mmol), diethyl oxalate (320 μL, 2.38 mmol) and NaH (123 mg, 3.08 mmol) in toluene (3 mL). Compound **308** was obtained an orange solid (304 mg, 85%) following purification by flash chromatography (1:49 EtOAc:Hex). **^{1}H NMR** (500 MHz, $CDCl_3$) δ 14.61 (s, 1H), 7.85 (dd, J = 3.9, 1.2 Hz, 1H), 7.74 (dd, J = 4.9, 1.1 Hz, 1H), 7.19 (dd, J = 4.9, 3.8 Hz, 1H), 6.91 (s, 1H), 4.39 (q, J = 7.2 Hz, 2H), 1.40 (t, J = 7.2 Hz, 3H) ppm; **^{13}C NMR** (126 MHz, $CDCl_3$) δ 186.2, 165.0, 162.3, 142.3, 135.3, 132.7, 128.8, 99.6, 62.7, 14.2 ppm; **LRMS (-ESI)** m/z: 255 ([M-H]$^-$, 100); **HRMS (+ESI)** Calc. for $C_{10}H_{10}NaO_4S$ [M+Na]$^+$: 249.01920, found 249.01909.

ethyl 1-(*tert*-butyl)-5-(thiophen-2-yl)-1*H*-pyrazole-3-carboxylate (**314**)

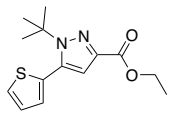

Compound **314** was synthesised from **308** (251 mg, 1.11 mmol) and *tert*-butylhydrazine hydrochloride (225 mg, 1.81 mmol) according to **General Procedure I** and was obtained as a white solid (277 mg, 90%) following purification by flash chromatography (1:19 EtOAc:Hex). **^{1}H NMR** (500 MHz, $CDCl_3$) δ 7.45 (dd, J = 5.1, 1.3 Hz, 1H), 7.10 (dd, J = 3.5, 1.2 Hz, 1H), 7.06 (dd, J = 5.2, 3.5 Hz, 1H), 6.81 (s, 1H), 4.38 (q, J = 7.1 Hz, 2H), 1.57 (s, 9H), 1.38 (t, J = 7.1 Hz, 3H) ppm; **^{13}C NMR** (126 MHz, $CDCl_3$) δ 162.7, 140.6, 136.1, 132.4, 130.4, 127.8, 126.9, 114.6, 63.2, 60.9, 30.8, 14.5 ppm; **LRMS (+ESI)** m/z: 301 ([M+Na]$^+$, 100); **HRMS (+ESI)** Calc. for $C_{14}H_{18}N_2NaO_2S$ [M+Na]$^+$: 301.09812, found 301.09805**.**

1-(*tert*-butyl)-5-(thiophen-2-yl)-1*H*-pyrazole-3-carboxylic acid (**320**)

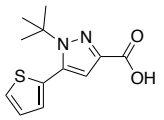

Prepared according to **General Procedure J** with **314** (147 mg, 0.53 mmol) and $LiOH.H_2O$ (12.3 mg, 0.29 mmol). Compound **320** was obtained as a white solid (81 mg, 61%) without need for further purification. **^{1}H NMR** (500 MHz, DMSO-d_6) δ 12.71 (s, 1H), 7.77 (dd, J = 5.2, 1.0 Hz, 1H), 7.28 (dd, J = 3.5, 1.2 Hz, 1H), 7.16 (dd, J = 5.2, 3.5 Hz, 1H), 6.73 (s, 1H), 1.48 (s, 9H) ppm; **^{13}C NMR** (126 MHz, DMSO-d_6) δ 163.0, 140.6, 135.6, 131.3, 130.8, 128.7, 127.2, 113.9, 62.6, 30.2 ppm; **LRMS (+ESI)** m/z: 273 ([M+Na]$^+$, 100); **HRMS (+ESI)** Calc. for $C_{12}H_{14}N_2NaO_2S$ [M+Na]$^+$: 273.06682, found 273.06682.

2-(1-(*tert*-butyl)-5-(thiophen-2-yl)-1*H*-pyrazol-3-yl)-5-chloro-1*H*-benzo[*d*]imidazole (**292**)

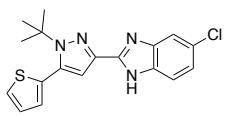

Prepared according to **General Procedure N** from **314** (50.1 mg, 0.20 mmol), 4-chlorobenzene-1,2-diamine (37.3 mg, 0.26 mmol), HATU (91.3 mg, 0.24 mmol) and ^{i}Pr$_2$NEt (140 µL, 0.80 mmol) in DMF (2 mL). Compound **292** was obtained as an off white solid (23 mg, 32%) following purification by flash chromatography (1:9 EtOAc:Hex). Characterisation data is reported as a complex mix of tautomers. **^{1}H NMR** (500 MHz, DMSO-d_6) δ 12.79 (s,

1H), 7.79 (dd, *J* = 5.2, 1.2 Hz, 1H), 7.71 – 7.46 (m, 2H), 7.33 (dd, *J* = 3.5, 1.2 Hz, 1H), 7.25 – 7.16 (m, 2H), 6.91 (s, 1H), 1.56 (s, 9H) ppm; **^{13}C NMR** (126 MHz, DMSO-d_6) δ 147.8, 144.6, 142.6, 139.7, 136.1, 135.3, 133.3, 131.5, 130.7, 128.6, 127.3, 126.6, 125.8, 122.3, 121.9, 119.9, 118.0, 112.7, 111.1, 110.7, 62.3, 30.3 ppm, 1 carbon peak not observed due to peak broadening; **LRMS (+ESI)** m/z: 357/359 ($[M+H]^+$, 100), **(-ESI)** m/z: 355/357 ($[M-H]^-$, 100); **HRMS (+ESI)** Calc. for $C_{18}H_{18}ClN_4S$ $[M+H]^+$: 357.09352/359.09057, found 357.09286/359.09007; **HPLC** R_T = 20.94 min, 97.64% (254 nm).

ethyl 4-(4-methoxyphenyl)-2,4-dioxobutanoate (**309**)

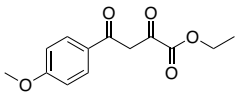

Prepared according to **General Procedure P** from 4-methoxyacetophenone (105 mg, 0.70 mmol), diethyl oxalate (188 µL, 1.39 mmol) and NaH (83.6 mg, 2.09 mmol) in toluene (2 mL). Compound **309** was obtained an orange solid (94.2 mg, 54%) following purification by flash chromatography (1:9 EtOAc:Hex). **^{1}H NMR** (500 MHz, $CDCl_3$) δ 15.45 (s, 1H), 7.99 (d, *J* = 8.5 Hz, 2H), 7.03 (s, 1H), 6.98 (d, *J* = 8.5 Hz, 2H), 4.40 (q, *J* = 7.1 Hz, 2H), 3.89 (s, 3H), 1.41 (t, *J* = 7.1 Hz, 3H) ppm; **^{13}C NMR** (126 MHz, $CDCl_3$) δ 190.5, 168.3, 164.5, 162.6, 130.5, 127.9, 114.4, 97.9, 62.7, 55.7, 14.3 ppm; **LRMS (+ESI)** m/z: 273 ($[M+Na]^+$), **(-ESI)** m/z: 249 ($[M-H]^-$); **HRMS (+ESI)** Calc. for $C_{13}H_{14}NaO_5$ $[M+Na]^+$: 273.07334, found 273.07304.

ethyl 1-(*tert*-butyl)-5-(4-methoxyphenyl)-1*H*-pyrazole-3-carboxylate (**315**)

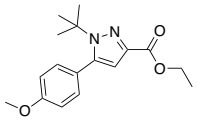

Compound **315** was synthesised from **309** (77.3 mg, 0.31 mmol) and *tert*-butylhydrazine hydrochloride (61.6 mg, 0.49 mmol) according to **General Procedure I** and was obtained as a white solid (71.6 mg, 77%) following purification by flash chromatography (1:9 EtOAc:Hex). **^{1}H NMR** (500 MHz, $CDCl_3$) δ 7.25 – 7.21 (m, 2H), 6.94 – 6.89 (m, 2H), 6.64 (s, 1H), 4.38 (q, *J* = 7.1 Hz, 2H), 3.85 (s, 3H), 1.49 (s, 9H), 1.38 (t, *J* = 7.1 Hz, 3H) ppm; **^{13}C NMR** (126 MHz, $CDCl_3$) δ 163.0, 160.1, 144.1, 140.6, 131.9, 125.3, 113.5, 112.4, 62.74, 60.8, 55.5, 31.2, 14.6 ppm; **LRMS (+ESI)** m/z: 325 ($[M+Na]^+$, 100); **HRMS (+ESI)** Calc. for $C_{17}H_{22}N_2NaO_3$ $[M+Na]^+$: 325.15226, found 352.15166.

1-(*tert*-butyl)-5-(4-methoxyphenyl)-1*H*-pyrazole-3-carboxylic acid (**321**)

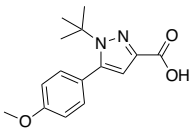

Prepared according to **General Procedure J** with **315** (58.9 mg, 0.19 mmol) and $LiOH.H_2O$ (12.3 mg, 0.29 mmol). Compound **321** was obtained as a white solid (43.4 mg, 81%) without need for further purification. **^{1}H NMR** (500 MHz, CD_3OD) δ 7.30 – 7.24 (m, 2H), 7.02 – 6.96 (m, 2H), 6.58 (s, 1H), 3.85 (s, 3H), 1.48 (s, 9H) ppm, COOH proton signal not observed; **^{13}C NMR** (126 MHz, CD_3OD) δ 166.1, 161.7, 145.9, 141.8, 132.9, 126.2, 114.5, 113.0, 63.9, 55.8, 31.3 ppm; **LRMS (+ESI)** m/z: 297 ($[M+Na]^+$, 70), **(-ESI)** m/z: 273 ($[M-H]^-$, 30); **HRMS (+ESI)** Calc. for $C_{15}H_{18}N_2NaO_3$ $[M+Na]^+$: 297.12096, found 297.12040.

2-(1-(*tert*-butyl)-5-(4-methoxyphenyl)-1*H*-pyrazol-3-yl)-5-chloro-1*H*-benzo[*d*]imidazole (**293**)

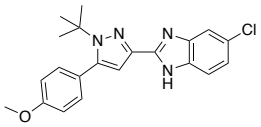

Prepared according to **General Procedure N** from **321** (39.1 mg, 0.14 mmol), 4-chlorobenzene-1,2-diamine (24.4 mg, 0.17 mmol), HATU (65.1 mg, 0.17 mmol) and $^iPr_2NEt$ (100 µL, 0.57 mmol) in DMF (2 mL). Compound **293** was obtained as a white solid (16.8 mg, 31%) following purification by flash chromatography (1:9 EtOAc:Hex). Characterisation data is reported as a complex mix of tautomers. **^{1}H NMR** (500 MHz, DMSO-d_6) δ 12.74 (s, 1H), 7.68 – 7.48 (m, 2H), 7.37 (d, J = 8.1 Hz, 2H), 7.19 (d, J = 8.5 Hz, 1H), 7.03 (d, J = 8.1 Hz, 2H), 6.71 (s, 1H), 3.82 (s, 3H), 1.49 (s, 9H) ppm; **^{13}C NMR** (126 MHz, DMSO-d_6) δ 159.6, 148.4, 148.0, 144.7, 144.1, 142.6, 139.5, 135.3, 133.3, 131.6, 126.5, 125.7, 124.7, 122.3, 121.6, 119.8, 118.0, 113.5, 112.6, 111.1, 108.5, 61.8, 55.2, 30.7 ppm; **LRMS (+ESI)** m/z: 381/383 ($[M+H]^+$, 100), **(-ESI)** m/z: 379/381 ($[M-H]^-$, 100); **HRMS (+ESI)** Calc. for $C_{21}H_{22}ClN_4O$ $[M+H]^+$: 381.14767/383.14472, found 381.14727/383.14447; **HPLC** R_T = 21.45 min, 98.20% (254 nm).

ethyl 4-(3-methoxyphenyl)-2,4-dioxobutanoate (**310**)

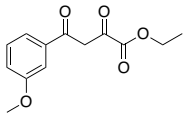

Prepared according to **General Procedure P** from 3-methoxyacetophenone (200 µL, 1.46 mmol), diethyl oxalate (280 µL, 2.07 mmol) and NaH (135 mg, 3.37 mmol) in toluene (2 mL). Compound **310** was obtained as a yellow solid (337 mg, 92%) following purification by flash chromatography (1:9 EtOAc:Hex). **^{1}H NMR** (500 MHz, $CDCl_3$) δ 15.24 (s, 1H), 7.56 (dt, J = 7.7, 1.3 Hz, 1H), 7.50 (dd, J = 2.7, 1.7 Hz, 1H), 7.39 (t, J = 8.0 Hz, 1H), 7.14 (ddd, J = 8.2, 2.6, 0.9 Hz, 1H), 7.04 (s, 1H), 4.39 (q, J = 7.1 Hz, 2H), 3.86 (s, 3H), 1.40 (t, J = 7.2 Hz, 3H) ppm; **^{13}C NMR** (126 MHz, $CDCl_3$) δ 190.9, 169.5, 162.3, 160.1, 136.5, 123.0, 120.6, 120.3, 112.4, 98.3, 62.7, 55.6, 14.2 ppm; **LRMS (+APCI)** m/z: 251 ($[M+H]^+$, 100) , **(-APCI)** m/z: 249 ($[M-H]^-$, 100); **HRMS (+APCI)** Calc. for $C_{13}H_{15}O_5$ $[M+H]^+$: 251.09140, found 251.09115.

ethyl 1-(*tert*-butyl)-5-(3-methoxyphenyl)-1*H*-pyrazole-3-carboxylate (**316**)

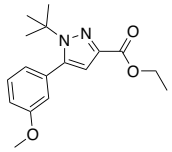

Compound **316** was synthesised from **310** (200 mg, 0.80 mmol) and *tert*-butylhydrazine hydrochloride (152 mg, 1.22 mmol) according to **General Procedure I** and was obtained as a pale yellow solid (198 mg, 82%) following purification by flash chromatography (10 – 20% v/v EtOAc in Hex). **^{1}H NMR** (500 MHz, $CDCl_3$) δ 7.30 (t, J = 8.4 Hz, 1H), 6.96 (ddd, J = 8.3, 2.6, 1.0 Hz, 1H), 6.92 (dt, J = 7.6, 1.3 Hz, 1H), 6.86 (dd, J = 2.6, 1.5 Hz, 1H), 6.66 (s, 1H), 4.38 (q, J = 7.1 Hz, 2H), 3.81 (s, 3H), 1.51 (s, 9H), 1.37 (t, J = 7.1 Hz, 3H) ppm; **^{13}C NMR** (126 MHz, $CDCl_3$) δ 162.9, 159.1, 144.0, 140.7, 134.5, 129.1, 123.2, 116.4, 114.4, 112.0, 62.9, 60.8, 55.4, 31.1, 14.5 ppm; **LRMS (+ESI)** m/z: 303 ($[M+H]^+$, 30), 325 ($[M+Na]^+$, 100); **HRMS (+ESI)** Calc. for $C_{17}H_{22}N_2NaO_3$ $[M+Na]^+$: 325.15226, found 325.15254.

1-(*tert*-butyl)-5-(3-methoxyphenyl)-1*H*-pyrazole-3-carboxylic acid **(322)**

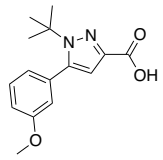

Prepared according to **General Procedure J** with **316** (148 mg, 0.49 mmol) and $LiOH.H_2O$ (35.3 mg, 0.84 mmol). Compound **322** was obtained as a white solid (122 mg, 91%) without need for further purification. **^{1}H NMR** (500 MHz, $CDCl_3$) δ 7.31 (t, J = 7.9 Hz, 1H), 6.98 (ddd, J = 8.4, 2.6, 1.0 Hz, 1H), 6.93 (dt, J = 7.6, 1.2 Hz, 1H), 6.88 (dd, J = 2.7, 1.5 Hz, 1H), 6.74 (s, 1H), 3.82 (s, 3H), 1.52 (s, 9H) ppm, COOH proton signal not observed; **^{13}C NMR** (126 MHz, $CDCl_3$) δ 165.9, 159.2, 144.9, 139.7, 134.1, 129.2, 123.1, 116.4, 114.6, 112.3, 63.3, 55.5, 31.1 ppm; **LRMS (+ESI)** m/z: 297 ($[M+Na]^+$, 90); **HRMS (+ESI)** Calc. for $C_{15}H_{18}N_2NaO_3$ $[M+Na]^+$: 297.12096, found 297.12119.

2-(1-(*tert*-butyl)-5-(3-methoxyphenyl)-1*H*-pyrazol-3-yl)-5-chloro-1*H*-benzo[*d*]imidazole (**294**)

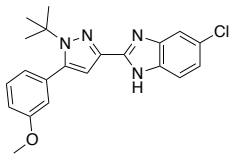

Prepared according to **General Procedure N** from **322** (81.8 mg, 0.30 mmol), 4-chlorobenzene-1,2-diamine (55.4 mg, 0.39 mmol), HATU (134 mg, 0.35 mmol) and ^{i}Pr$_2$NEt (200 µL, 1.19 mmol) in DMF (1 mL). Compound **294** was obtained as a white solid (43 mg, 38%) following purification by reverse phase chromatography (0 – 100% v/v CH_3CN in H_2O). **^{1}H NMR** (400 MHz, DMSO-d_6) δ 7.59 (d, J = 1.2 Hz, 1H), 7.56 (d, J = 8.5 Hz, 1H), 7.40 (t, J = 7.9 Hz, 1H), 7.20 (dd, J = 8.4, 2.1 Hz, 1H), 7.07 (ddd, J = 8.4, 2.7, 0.9 Hz, 1H), 7.03 (dt, J = 7.5, 1.2 Hz, 1H), 7.02 – 7.00 (m, 1H), 6.74 (s, 1H), 3.80 (s, 3H), 1.50 (s, 9H) ppm, benzimidazole NH proton signal not observed; **^{13}C NMR** (101 MHz, DMSO-d_6) δ 158.7, 148.2, 144.0, 139.7, 134.2, 129.2, 126.1, 122.7, 122.0, 116.1, 114.5, 108.3, 62.1, 55.3, 30.7 ppm, 4 carbon peaks not observed due to peak broadening; **LRMS (+ESI)** m/z: 381/383 ($[M+H]^+$, 100), **(-ESI)** m/z: 379/381 ($[M-H]^-$, 100); **HRMS (+ESI)** Calc. for $C_{21}H_{22}ClN_4O$ $[M+H]^+$: 381.14767/383.14472, found 381.14766/383.14475; **HPLC** R_T = 21.15 min, 97.19% (254 nm).

ethyl 2,4-dioxo-4-(*m*-tolyl)butanoate (**311**)

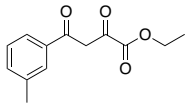

Prepared according to **General Procedure P** from 1-(*m*-tolyl)ethan-1-one (200 µL, 1.49 mmol), diethyl oxalate (300 µL, 2.24 mmol) and NaH (148 mg, 3.70 mmol) in toluene (2 mL). Compound **311** was obtained as a yellow oil (307 mg, 88%) following purification by flash chromatography (1:9 EtOAc:Hex). **^{1}H NMR** (500 MHz, $CDCl_3$) δ 15.32 (s, 1H), 7.83 – 7.77 (m, 2H), 7.45 – 7.37 (m, 2H), 7.07 (s, 1H), 4.41 (q, J = 7.1 Hz, 2H), 2.44 (s, 3H), 1.42 (t, J = 7.1 Hz, 3H) ppm; **^{13}C NMR** (126 MHz, $CDCl_3$) δ 191.1, 169.8, 162.4, 138.9, 135.1, 134.8, 128.9, 128.6, 125.3, 98.2, 62.7, 21.5, 14.3 ppm; **LRMS (+APCI)** m/z: 235 ($[M+H]^+$, 100), **(-APCI)** m/z: 233 ($[M-H]^-$, 100); **HRMS (+APCI)** Calc. for $C_{13}H_{15}O_4$ $[M+H]^+$: 235.09649, found 235.09630.

ethyl 1-(*tert*-butyl)-5-(*m*-tolyl)-1*H*-pyrazole-3-carboxylate (**317**)

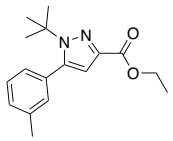

Compound **317** was synthesised from **311** (300 mg, 1.28 mmol) and *tert*-butylhydrazine hydrochloride (239 mg, 1.92 mmol) according to **General Procedure I** and was obtained as a white solid (308 mg, 84%) following purification by flash chromatography (1:49 EtOAc:Hex). **^{1}H NMR** (500 MHz, $CDCl_3$) δ 7.30 – 7.27 (m, 1H), 7.25 – 7.21 (m, 1H), 7.15 – 7.11 (m, 2H), 6.65 (s, 1H), 4.38 (q, J = 7.1 Hz, 2H), 2.38 (s, 3H), 1.50 (s, 9H), 1.38 (t, J = 7.1 Hz, 3H) ppm; **^{13}C NMR** (126 MHz, $CDCl_3$) δ 163.0, 144.4, 140.6, 137.8, 133.2, 131.3, 129.6, 127.9, 127.8, 112.1, 62.9, 60.8, 31.2, 21.5, 14.5 ppm; **LRMS (+ESI)** m/z: 287 ($[M+H]^+$, 80); **HRMS (+ESI)** Calc. for $C_{17}H_{22}N_2NaO_2$ $[M+Na]^+$: 309.15735, found 309.15753.

1-(*tert*-butyl)-5-(*m*-tolyl)-1*H*-pyrazole-3-carboxylic acid (**323**)

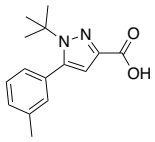

Prepared according to **General Procedure J** with **317** (303 mg, 1.06 mmol) and $LiOH.H_2O$ (68.8 mg, 1.64 mmol). Compound **323** was obtained as a white solid (268 mg, 98%) without need for further purification. **^{1}H NMR** (500 MHz, $CDCl_3$) δ 7.32 – 7.27 (m, 1H), 7.26 – 7.23 (m, 1H), 7.17 – 7.12 (m, 2H), 6.72 (s, 1H), 2.39 (s, 3H), 1.50 (s, 9H) ppm, COOH proton signal not observed; **^{13}C NMR** (126 MHz, $CDCl_3$) δ 165.1, 145.4, 139.6, 137.9, 132.8, 131.3, 129.9, 128.0, 127.7, 112.2, 63.2, 31.1, 21.5 ppm; **LRMS (+ESI)** m/z: 281 ($[M+Na]^+$, 100); **HRMS (+ESI)** Calc. for $C_{15}H_{18}N_2NaO_2$ $[M+Na]^+$: 281.12605, found 281.12619.

2-(1-(*tert*-butyl)-5-(*m*-tolyl)-1*H*-pyrazol-3-yl)-5-chloro-1*H*-benzo[*d*]imidazole (**295**)

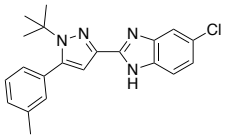

Prepared according to **General Procedure N** from **323** (155 mg, 0.60 mmol), 4-chlorobenzene-1,2-diamine (98.0 mg, 0.69 mmol), HATU (266 mg, 0.70 mmol) and ^{i}Pr$_2$NEt (420 µL, 2.41 mmol) in DMF (2 mL). Compound **295** was obtained as a white solid (113 mg, 52%) following purification by reverse phase chromatography (0 – 100% v/v CH_3CN in H_2O). **^{1}H NMR** (500 MHz, DMSO-d_6) δ 7.59 (d, J = 2.0 Hz, 1H), 7.56 (d, J = 8.5 Hz, 1H), 7.36 (t, J = 7.5 Hz, 1H), 7.32 – 7.29 (m, 1H), 7.29 – 7.27 (m, 1H), 7.25 (dd, J = 7.3, 1.6 Hz, 1H), 7.19 (dd, J = 8.5, 2.1 Hz, 1H), 6.72 (s, 1H), 2.37 (s, 3H), 1.48 (s, 9H) ppm, benzimidazole NH proton signal not observed; **^{13}C NMR** (126 MHz, DMSO-d_6) δ 148.3, 144.4, 139.7, 137.4, 132.9, 130.8, 129.6, 128.0, 127.5, 126.1, 122.0, 108.3, 62.0, 30.7, 20.9 ppm, 4 carbon peaks not observed due to peak broadening; **LRMS (+ESI)** m/z: 365/367 ($[M+H]^+$, 100), **(-ESI)** m/z: 363/365 ($[M-H]^-$, 100); **HRMS (+ESI)** Calc. for $C_{21}H_{22}ClN_4$ $[M+H]^+$: 365.15275/167.14980, found 365.15280/367.14998; **HPLC** R_T = 21.91 min, 98.07% (254 nm).

ethyl 4-(4-(*tert*-butyl)phenyl)-2,4-dioxobutanoate (**312**)

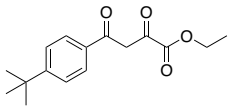

Prepared according to **General Procedure P** from 1-(4-(*tert*-butyl)phenyl)ethan-1-one (200 µL, 1.11 mmol), diethyl oxalate (220 µL, 1.66 mmol) and NaH (103 mg, 2.57 mmol) in toluene (2 mL). Compound **312** was obtained as an off white solid (250 mg, 82%) following purification by flash chromatography (1:9 EtOAc:Hex). **^{1}H NMR** (500 MHz, $CDCl_3$) δ 15.38 (s, 1H), 7.93 (dt, J = 8.7, 2.2 Hz, 2H), 7.51 (dt, J = 8.5, 2.3 Hz, 2H), 7.06 (s, 1H), 4.40 (q, J = 7.2 Hz, 2H), 1.41 (t, J = 7.1 Hz, 3H), 1.35 (s, 9H) ppm; **^{13}C NMR** (126 MHz, $CDCl_3$) δ 190.7, 169.6, 162.5, 158.0, 132.4, 128.0, 126.0, 98.0, 62.7, 35.4, 31.2, 14.2 ppm; **LRMS (+ESI)** m/z: 299 ($[M+Na]^+$, 100); **HRMS (+ESI)** Calc. for $C_{16}H_{21}O_4$ $[M+H]^+$: 277.14344, found 277.14371.

ethyl 1-(*tert*-butyl)-5-(4-(*tert*-butyl)phenyl)-1*H*-pyrazole-3-carboxylate (**318**)

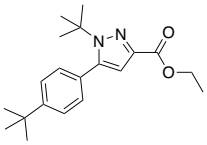

Compound **318** was synthesised from **312** (207 mg, 0.75 mmol) and *tert*-butylhydrazine hydrochloride (138 mg, 1.11 mmol) according to **General Procedure I** and was obtained as a white solid (203 mg, 82%) following purification by flash chromatography (0 – 20% v/v EtOAc in Hex). **^{1}H NMR** (400 MHz, $CDCl_3$) δ 7.40 (dt, J = 8.4, 2.2 Hz, 2H), 7.25 (dt, J = 8.4, 1.9 Hz, 2H), 6.66 (s, 1H), 4.38 (q, J = 7.1 Hz, 2H), 1.50 (s, 9H), 1.41 – 1.34 (m, 12H) ppm; **^{13}C NMR** (101 MHz, $CDCl_3$) δ 163.0, 152.2, 144.4, 140.6, 130.3, 130.2, 124.9, 112.3, 62.8, 60.8, 34.9, 31.5, 31.2, 14.5 ppm; **LRMS (+ESI)** m/z: 351 ($[M+Na]^+$, 100); **HRMS (+ESI)** Calc. for $C_{20}H_{29}N_2O_2$ $[M+H]^+$: 329.22235, found 329.22284.

1-(*tert*-butyl)-5-(4-(*tert*-butyl)phenyl)-1*H*-pyrazole-3-carboxylic acid **(324)**

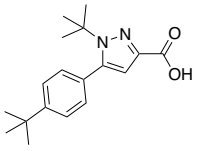

Prepared according to **General Procedure J** with **318** (150 mg, 0.46 mmol) and $LiOH.H_2O$ (32.4 mg, 0.77 mmol). Compound **324** was obtained as a white solid (121 mg, 88%) without need for further purification. **^{1}H NMR** (500 MHz, $CDCl_3$) δ 7.41 (dt, J = 8.4, 2.3 Hz, 2H), 7.26 (dt, J = 8.3, 2.3 Hz, 2H), 6.72 (s, 1H), 1.49 (s, 9H), 1.36 (s, 9H) ppm, COOH proton signal not observed; **^{13}C NMR** (126 MHz, $CDCl_3$) δ 178.2, 164.0, 152.4, 145.6, 139.6, 130.3, 129.7, 125.1, 112.1, 63.1, 34.9, 31.4, 31.1 ppm; **LRMS (+ESI)** m/z: 323 ($[M+Na]^+$, 90), **(-ESI)** m/z: 299 ($[M-H]^-$, 100); **HRMS (+ESI)** Calc. for $C_{18}H_{25}N_2O_2$ $[M+H]^+$: 301.19105, found 301.19154.

2-(1-(*tert*-butyl)-5-(4-(*tert*-butyl)phenyl)-1*H*-pyrazol-3-yl)-5-chloro-1*H*-benzo[*d*]imidazole (**296**)

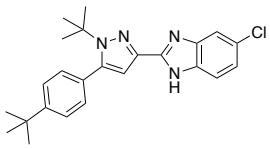

Prepared according to **General Procedure N** from **324** (78.9 mg, 0.26 mmol), 4-chlorobenzene-1,2-diamine (46.2 mg, 0.32 mmol), HATU (120 mg, 0.31 mmol) and $^iPr_2NEt$ (180 µL, 1.05 mmol) in DMF (2 mL). Compound **296** was obtained as a white solid (40 mg, 38%) following purification by flash chromatography (1:9 EtOAc:Hex). **^{1}H NMR** (400 MHz, DMSO-d_6) δ 12.74 (s, 1H), 7.65 – 7.52 (m, 2H), 7.49 (d, J = 8.1 Hz, 2H), 7.38 (d, J = 8.0 Hz, 2H), 7.20 (d, J = 8.5 Hz, 1H), 6.72 (s, 1H), 1.48 (s, 9H), 1.33 (s, 9H) ppm; **^{13}C NMR** (101 MHz, DMSO-d_6) δ 151.5, 148.2, 144.2, 139.6, 130.0, 129.9, 124.8, 122.0, 117.7, 108.4, 61.9, 34.4, 31.0, 30.7 ppm, 4 carbon peaks not observed due to peak broadening; **LRMS (+ESI)** m/z: 407/409 ($[M+H]^+$, 100), **(-ESI)** m/z: 405/407 ($[M-H]^-$, 100); **HRMS (+ESI)** Calc. for $C_{24}H_{28}ClN_4$ $[M+H]^+$: 407.19970/409.19675, found 407.19974/409.19684; **HPLC** R_T = 20.92 min, 99.01% (254 nm).

ethyl 4-(1*H*-indol-3-yl)-2,4-dioxobutanoate (**313**)

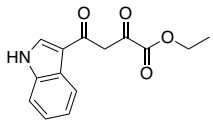

Prepared according to **General Procedure P** from 3-acetylindole (162 mg, 1.02 mmol), diethyl oxalate (200 μL, 1.53 mmol) and NaH (102 mg, 2.55 mmol) in THF/toluene (1:1, 4 mL). Compound **313** was obtained as a yellow solid (142 mg, 54%) following purification by flash chromatography (1:9 EtOAc:Hex).**^{1}H NMR** (500 MHz, DMSO-d_6) δ 12.42 (s, 1H), 8.73 (d, J = 3.2 Hz, 1H), 8.25 – 8.19 (m, 1H), 7.54 – 7.49 (m, 1H), 7.31 – 7.22 (m, 2H), 7.03 (s, 1H), 4.31 (q, J = 7.1 Hz, 2H), 1.32 (t, J = 7.1 Hz, 3H) ppm; **^{13}C NMR** (126 MHz, DMSO-d_6) δ 189.2, 162.3, 162.0, 137.1, 136.0, 125.1, 123.6, 122.6, 121.5, 114.7, 112.6, 100.5, 61.8, 13.9 ppm; **LRMS (+APCI)** m/z: 260 ([M+H]$^+$, 100), **(-APCI)** m/z: 258 ([M-H]$^-$, 100); **HRMS (+APCI)** Calc. for $C_{14}H_{14}NO_4$ [M+H]$^+$: 260.09173, found 260.09146.

ethyl 1-(*tert*-butyl)-5-(1*H*-indol-3-yl)-1*H*-pyrazole-3-carboxylate (**319**)

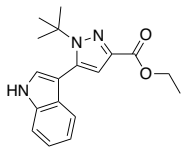

Compound **319** was synthesised from **313** (72.3 mg, 0.28 mmol) and *tert*-butylhydrazine hydrochloride (52.1 mg, 0.42 mmol) according to **General Procedure I** and was obtained as a white solid (63.4 mg, 73%) following purification by flash chromatography (1:4 EtOAc:Hex). **^{1}H NMR** (500 MHz, DMSO-d_6) δ 11.49 (s, 1H), 7.52 (d, J = 2.4 Hz, 1H), 7.45 (dt, J = 8.1, 0.9 Hz, 1H), 7.19 (d, J = 7.9 Hz, 1H), 7.15 (ddd, J = 8.1, 6.9, 1.2 Hz, 1H), 7.04 (ddd, J = 7.9, 7.0, 1.0 Hz, 1H), 6.63 (s, 1H), 4.28 (q, J = 7.1 Hz, 2H), 1.43 (s, 9H), 1.29 (t, J = 7.1 Hz, 3H) ppm; **^{13}C NMR** (126 MHz, DMSO-d_6) δ 162.0, 139.7, 137.3, 135.4, 128.0, 126.6, 121.7, 119.8, 118.7, 113.3, 111.8, 105.5, 61.9, 59.9, 30.1, 14.3 ppm; **LRMS (+ESI)** m/z: 334 ([M+Na]$^+$, 100), **(-ESI)** m/z: 310 ([M-H]$^-$, 100); **HRMS (+ESI)** Calc. for $C_{18}H_{22}N_3O_2$ [M+H]$^+$: 312.17065, found 312.17119.

1-(*tert*-butyl)-5-(1*H*-indol-3-yl)-1*H*-pyrazole-3-carboxylic acid (**325**)

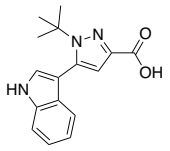

Prepared according to **General Procedure J** with **319** (49.3 mg, 0.16 mmol) and $LiOH.H_2O$ (10.5 mg, 0.25 mmol). Compound **325** was obtained as a white solid (41.5 mg, 93%) without need for further purification. **^{1}H NMR** (500 MHz, CD_3OD) δ 7.44 (dt, J = 8.2, 0.9 Hz, 1H), 7.32 (s, 1H), 7.23 (dt, J = 8.0, 1.0 Hz, 1H), 7.17 (ddd, J = 8.2, 7.0, 1.2 Hz, 1H), 7.06 (ddd, J = 8.0, 7.0, 1.0 Hz, 1H), 6.68 (s, 1H), 1.50 (s, 9H) ppm, indole NH and COOH proton signal not observed; **^{13}C NMR** (126 MHz, CD_3OD) δ 166.2, 141.8, 139.4, 137.2, 129.8, 127.0, 123.1, 121.1, 120.0, 114.8, 112.6, 107.8, 63.5, 30.9 ppm; **LRMS (+ESI)** m/z: 306 ($[M+Na]^+$, 100), **(-ESI)** m/z: 282 ($[M-H]^-$, 100); **HRMS (+ESI)** Calc. for $C_{16}H_{17}N_3NaO_2$ $[M+Na]^+$: 306.12130, found 306.12131.

2-(1-(*tert*-butyl)-5-(1H-indol-3-yl)-1H-pyrazol-3-yl)-5-chloro-1H-benzo[d]imidazole (**297**)

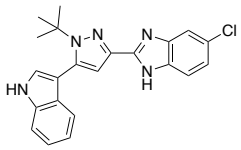

Prepared according to **General Procedure N** from **325** (34.7 mg, 0.12 mmol), 4-chlorobenzene-1,2-diamine (21.9 mg, 0.15 mmol), HATU (60.2 mg, 0.16 mmol) and $^iPr_2NEt$ (85 µL, 0.49 mmol) in DMF (1 mL). Compound **297** was obtained as a white solid (15.8 mg, 33%) following purification by flash chromatography (1:9 EtOAc:Hex). **^{1}H NMR** (400 MHz, DMSO-d_6) δ 12.75 (s, 1H), 11.52 (s, 1H), 7.58 (d, J = 10.9 Hz, 3H), 7.48 (d, J = 8.1 Hz, 1H), 7.26 (d, J = 7.9 Hz, 1H), 7.19 (dd, J = 8.5, 1.9 Hz, 1H), 7.16 (d, J = 7.0 Hz, 1H), 7.05 (t, J = 7.4 Hz, 1H), 6.78 (s, 1H), 1.51 (s, 9H) ppm; **^{13}C NMR** (101 MHz, DMSO-d_6) δ 148.5, 139.7, 137.5, 135.4, 128.1, 126.4, 126.0, 121.9, 121.6, 119.7, 118.7, 111.8, 110.1, 105.9, 61.4, 30.3 ppm, 4 carbon peaks not observed due to peak broadening; **LRMS (+ESI)** m/z: 390/392 ($[M+H]^+$, 100), 412/414 ($[M+Na]^+$, 80), **(-ESI)** m/z: 388/390 ($[M-H]^-$, 100); **HRMS (+ESI)** Calc. for $C_{22}H_{21}ClN_5$ $[M+H]^+$: 390.14800/392.14505, found 390.14807/392.14523; **HPLC** R_T = 20.92 min, 99.01% (254 nm).

ethyl 2,4-dioxo-4-(pyridin-3-yl)butanoate (**328**)

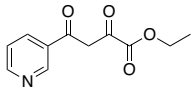

Prepared according to **General Procedure P** from 3-acetylpyridine (210 mg, 1.73 mmol), diethyl oxalate (470 μL, 3.47 mmol) and NaH (208 mg, 5.20 mmol) in THF (3 mL). Compound **328** was obtained an orange solid (142 mg, 37%) following purification by flash chromatography (1:4 EtOAc:Hex).**^{1}H NMR** (500 MHz, $CDCl_3$) δ 9.20 (dd, J = 2.3, 0.9 Hz, 1H), 8.82 (dd, J = 4.8, 1.7 Hz, 1H), 8.26 (dt, J = 8.1, 2.0 Hz, 1H), 7.46 (ddd, J = 8.0, 4.8, 0.9 Hz, 1H), 7.07 (s, 1H), 4.41 (q, J = 7.1 Hz, 2H), 1.42 (t, J = 7.2 Hz, 3H) ppm; **^{13}C NMR** (126 MHz, $CDCl_3$) δ 188.7, 171.0, 161.9, 154.1, 149.3, 135.2, 130.7, 123.9, 98.1, 63.0, 14.2 ppm; **LRMS (+APCI)** m/z: 222 ($[M+H]^+$, 100) , **(-APCI)** m/z: 220 ($[M-H]^-$, 100); **HRMS (+APCI)** Calc. for $C_{11}H_{12}NO_4$ $[M+H]^+$: 222.07608, found 222.07594.

ethyl 1-(*tert*-butyl)-5-(pyridin-3-yl)-1*H*-pyrazole-3-carboxylate (**326**)

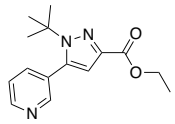

Compound **326** was synthesised from **328** (119 mg, 0.54 mmol) and *tert*-butylhydrazine hydrochloride (100 mg, 0.81 mmol) according to **General Procedure I** and was obtained as a white solid (98.8 mg, 67%) following purification by flash chromatography (1:9 EtOAc:Hex). **^{1}H NMR** (500 MHz, $CDCl_3$) δ 8.68 (dd, J = 4.9, 1.7 Hz, 1H), 8.60 (dd, J = 2.3, 0.9 Hz, 1H), 7.67 (dt, J = 7.8, 2.0 Hz, 1H), 7.36 (ddd, J = 7.8, 4.9, 0.9 Hz, 1H), 6.72 (s, 1H), 4.39 (q, J = 7.1 Hz, 2H), 1.50 (s, 9H), 1.38 (t, J = 7.1 Hz, 3H) ppm; **^{13}C NMR** (126 MHz, $CDCl_3$) δ 162.7, 150.8, 150.2, 141.1, 140.5, 137.8, 129.6, 122.9, 113.1, 63.1, 61.0, 31.3, 14.5 ppm; **LRMS (+ESI)** m/z: 296 ($[M+Na]^+$, 100); **HRMS (+ESI)** Calc. for $C_{15}H_{20}N_3O_2$ $[M+H]^+$: 274.15500, found 274.15464.

(1-(*tert*-butyl)-5-(pyridin-3-yl)-1*H*-pyrazol-3-yl)methanol (**329**)

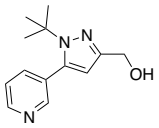

Compound **329** was synthesised from **326** (91.9 mg, 0.34 mmol) and $LiAlH_4$ (23 mg, 0.61 mmol) in THF (3 mL) according to **General Procedure H** and was obtained as a white solid (61.3 mg, 79%) following purification by flash chromatography (2:3 EtOAc:Hex). **^{1}H NMR** (500 MHz, $CDCl_3$) δ 8.65 (dd, J = 5.0, 1.8 Hz, 1H), 8.59 (d, J = 2.1 Hz, 1H), 7.66 (dt, J = 7.8, 2.0 Hz, 1H), 7.34 (ddd, J = 7.7, 4.8, 0.9 Hz, 1H), 6.18 (s, 1H), 4.70 (s, 2H), 1.45 (s, 9H) ppm, O<u>H</u> proton signal not observed; **^{13}C NMR** (126 MHz, $CDCl_3$) δ 150.7, 149.7, 149.2, 140.2, 137.7, 130.6, 122.9, 108.6, 61.6, 59.3, 31.5 ppm; **LRMS (+ESI)** m/z: 254 ($[M+Na]^+$, 100); **HRMS (+ESI)** Calc. for $C_{13}H_{17}N_3NaO$ $[M+Na]^+$: 254.12638, found 254.12638.

1-(*tert*-butyl)-5-(pyridin-3-yl)-1*H*-pyrazole-3-carbaldehyde (**330**)

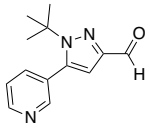

DMP (79.6 mg, 0.19 mmol) was added portionwise to a stirring solution of **329** (28.3 mg, 0.12 mmol) in CH_2Cl_2 (1 mL). The reaction was stirred at rt for 1 hour or until TLC indicated complete consumption of starting material. The reaction was then quenched with a 1:1 solution of sat. $Na_2S_2O_3$ and sat. $NaHCO_3$, and stirred vigorously for 5 min. The aqueous solution was then extracted with CH_2Cl_2 (3 x 25 mL/mmol). The organic layers were pooled, washed with brine (1 x 25 mL/mmol), dried over $MgSO_4$ and concentrated *in vacuo* to yield the desired aldehyde **330** as a white powder (19.1 mg, 68%) following purification by flash chromatography (1:4 EtOAc:Hex). **^{1}H NMR** (500 MHz, $CDCl_3$) δ 9.98 (s, 1H), 8.71 – 8.67 (m, 1H), 8.61 (s, 1H), 7.67 (dt, J = 7.8, 2.0 Hz, 1H), 7.38 (ddd, J = 7.8, 4.9, 0.9 Hz, 1H), 6.72 (s, 1H), 1.51 (s, 9H) ppm; **^{13}C NMR** (126 MHz, $CDCl_3$) δ 187.0, 150.7, 150.4, 148.8, 141.4, 137.8, 129.3, 123.0, 110.0, 63.4, 31.2 ppm; **LRMS (+APCI)** m/z: 230 ($[M+H]^+$, 100); **HRMS (+APCI)** Calc. for $C_{13}H_{16}N_3O$ $[M+H]^+$: 230.12879, found 230.12911.

2-(1-(*tert*-butyl)-5-(pyridin-3-yl)-1*H*-pyrazol-3-yl)-5-chloro-1*H*-benzo[*d*]imidazole (**298**)

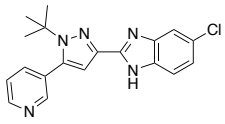

Compound **330** (17.3 mg, 75.5 μmol) was added to a stirring solution of 4-chlorobenzene-1,2-diamine (12.9 mg, 90.5 μmol) and $NaHSO_3$ (15.7 mg, 0.15 mmol) in EtOH/H_2O (2:1, 1.5 mL) solvent mixture. The reaction was heated to reflux for 2 hours. Following consumption of starting material, the reaction was cooled to room temperature and concentrated under a stream of N_2. Compound **298** was obtained as an off white solid (19.8 mg, 75%) following purification by flash chromatography (1:4 EtOAc:Hex). Characterisation data is reported as a complex mix of tautomers. **^{1}H NMR** (400 MHz, Acetone-d_6) δ 12.10 (s, 1H), 8.70 (dd, J = 4.8, 1.6 Hz, 1H), 8.69 (d, J = 2.3 Hz, 2H), 7.92 (dt, J = 7.9, 2.0 Hz, 1H), 7.69 – 7.54 (m, 2H), 7.52 (ddd, J = 7.8, 4.9, 0.9 Hz, 1H), 7.21 (dd, J = 8.5, 2.0 Hz, 1H), 6.89 (s, 1H), 1.51 (s, 9H) ppm; **^{13}C NMR** (101 MHz, Acetone-d_6) δ 151.4, 150.9, 149.2, 146.3, 144.2, 142.2, 141.5, 138.6, 136.1, 134.1, 130.5, 128.4, 127.6, 123.9, 123.6, 122.9, 121.0, 119.4, 113.2, 112.0, 110.2, 63.2, 31.4 ppm, 1 carbon peak not observed due to peak broadening; **LRMS (+ESI)** m/z: 352/354 ($[M+H]^+$, 60), 374/376 ($[M+Na]^+$, 100), **(-ESI)** m/z: 350/352 ($[M-H]^-$, 100); **HRMS (+ESI)** Calc. for $C_{19}H_{19}ClN_5$ $[M+H]^+$: 352.13235/354.12940, found 352.13229/354.12966; **HPLC** R_T = 16.21 min, 99.69% (254 nm).

1-(furan-2-yl)-3-(quinolin-3-yl)propane-1,3-dione (**333**)

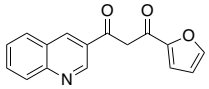

Prepared according to **General Procedure P** from 2-acetylfuran (103 mg, 0.94 mmol), ethyl quinoline-3-carboxylate (452 mg, 2.25 mmol) and NaH (188 mg, 4.68 mmol) in THF (3 mL). Compound **333** was obtained a yellow solid (122 mg, 49%) following purification by flash chromatography (10 – 25% v/v EtOAc in Hex). **^{1}H NMR** (500 MHz, $CDCl_3$) δ 9.39 (d, J = 2.3 Hz, 1H), 8.76 (dd, J = 2.3, 0.8 Hz, 1H), 8.17 (d, J = 8.5 Hz, 1H), 7.96 (dd, J = 8.2, 1.4 Hz, 1H), 7.83 (ddd, J = 8.5, 6.9, 1.5 Hz, 1H), 7.32 (dd, J = 3.5, 0.8 Hz, 1H), 6.92 (s, 1H), 6.63 (dd, J = 3.5, 1.7 Hz, 1H) ppm; **^{13}C NMR** (126 MHz, $CDCl_3$) δ 179.9, 178.2, 151.0, 149.7, 148.1, 146.7, 135.6, 131.7, 129.6, 129.2, 127.7, 127.6, 127.3, 116.7, 113.0, 93.6 ppm; **LRMS (+APCI)** m/z: 266 ($[M+H]^+$, 100), **(-APCI)** m/z: 264 ($[M-H]^-$, 100).

3-(1-(*tert*-butyl)-5-(furan-2-yl)-1*H*-pyrazol-3-yl)quinoline (**299)**

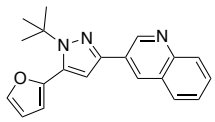

Compound **299** was synthesised from **333** (65 mg, 0.25 mmol) and *tert*-butylhydrazine hydrochloride (45.8 mg, 0.37 mmol) according to **General Procedure I** at reflux. Compound **299** was obtained as a white solid (17.9 mg, 23%) following purification by flash chromatography (10 – 50% v/v EtOAc in Hex). **^{1}H NMR** (400 MHz, $CDCl_3$) δ 9.40 (d, J = 2.1 Hz, 1H), 8.51 (d, J = 2.1 Hz, 1H), 8.11 (d, J = 8.5 Hz, 1H), 7.87 (d, J = 8.3 Hz, 1H), 7.68 (ddd, J = 8.5, 6.8, 1.5 Hz, 1H), 7.58 (t, J = 1.4 Hz, 1H), 7.54 (t, J = 7.5 Hz, 1H), 6.83 (s, 1H), 6.55 – 6.51 (m, 2H), 1.61 (s, 9H) ppm; **^{13}C NMR** (101 MHz, $CDCl_3$) δ 149.2, 147.7, 145.3, 144.6, 142.8, 133.7, 131.2, 129.4, 129.1, 128.3, 128.1, 126.9, 111.9, 111.4, 108.5, 61.8, 30.2 ppm; **LRMS (+ESI)** m/z 318 ([M+H]$^+$, 100), 332 ([M+Na]$^+$, 40); **HRMS (+ESI)** Calc. for $C_{20}H_{20}N_3O$ [M+H]$^+$: 318.16009, found 318.16001; **HPLC** R_T = 21.63 min, 98.88% (254 nm).

ethyl 3-oxo-3-(*m*-tolylamino)propanoate (**338**)

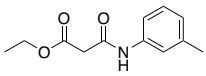

Compound **338** was prepared *via* an acid chloride amide coupling according to **General Procedure D** from 3-ethoxy-3-oxopropanoic acid (440 µL, 3.33 mmol) and *m*-toluidine (300 µL, 2.80 mmol). The crude residue was purified by flash chromatography (1:9 EtOAc:Hex) to yield compound **338** as an orange oil (322 mg, 52%). **^{1}H NMR** (500 MHz, $CDCl_3$) δ 9.13 (s, 1H), 7.40 – 7.37 (m, 1H), 7.34 (dd, J = 8.1, 2.2 Hz, 1H), 7.21 (t, J = 7.8 Hz, 1H), 6.94 (d, J = 7.5 Hz, 1H), 4.26 (q, J = 7.1 Hz, 2H), 3.46 (s, 2H), 2.34 (s, 3H), 1.32 (t, J = 7.1 Hz, 3H) ppm; **^{13}C NMR** (126 MHz, $CDCl_3$) δ 170.2, 162.9, 139.1, 137.5, 129.0, 125.5, 120.9, 117.3, 62.0, 41.7, 21.6, 14.2 ppm; **LRMS (+ESI)** m/z: 244 ([M+Na]$^+$, 100), **(-ESI)** m/z: 220 ([M-H]$^-$,100); **HRMS (+ESI)** Calc. for $C_{12}H_{16}NO_3$ [M+H]$^+$: 222.11247, found 222.11207.

2-chloro-7-methylquinoline-3-carboxylic acid (**344**)

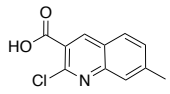

2-chloro-7-methylquinoline-3-carbaldehyde (506 mg, 2.46 mmol) was dissolved in warm *t*-BuOH (9 mL), cooled to room temperature and 2-methylbut-2-ene (3 mL, 28.3 mmol) was added dropwise. A solution of sodium chlorite (1.42 g, 15.7 mmol) and sodium dihydrogen phosphate (1.47 g, 12.3 mmol) in H_2O (3 mL) was added dropwise with stirring over 10 min. The reaction was stirred at room temperature for a further 3 h. Most of the solvent was removed at reduced pressure, H_2O (10 mL) was added, and the solution was acidified with conc. HCl. The precipitate was collected by filtration and washed with H_2O to give the carboxylic acid **344** as a pale yellow solid (465 mg, 85%). **^{1}H NMR** (500 MHz, DMSO-d_6) δ 8.86 (s, 1H), 8.05 (d, J = 8.4 Hz, 1H), 7.79 (s, 1H), 7.57 (dd, J = 8.3, 1.6 Hz, 1H), 2.55 (s, 3H) ppm, COOH proton signal not observed; **^{13}C NMR** (126 MHz, DMSO-d_6) δ 165.7, 147.7, 146.5, 143.3, 141.0, 130.1, 128.6, 126.6, 124.5, 123.9, 21.5 ppm; **LRMS (-ESI)** m/z: 219/221 ([M-H]$^-$, 100); **HRMS (+ESI)** Calc. for $C_{11}H_8ClNNaO_2$ $[M+Na]^+$: 244.01358/246.01063, found 244.01354/246.01063.

ethyl 2-chloro-7-methylquinoline-3-carboxylate (**341**)

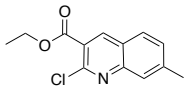

Prepared according to **General Procedure M** from **344** (250 mg, 1.13 mmol), EtOH (70 µL, 1.2 mmol), DMAP (16 mg, 0.13 mmol) and EDC.HCl (239 mg, 1.25 mmol) in CH_2Cl_2 (2.5 mL). Compound **341** was obtained as a white solid (211 mg, 75%) following purification by flash chromatography (0 - 5% EtOAc in Hex). **^{1}H NMR** (500 MHz, $CDCl_3$) δ 8.63 (s, 1H), 7.82 (s, 1H), 7.78 (d, J = 8.3 Hz, 1H), 7.45 (dd, J = 8.3, 1.7 Hz, 1H), 4.46 (q, J = 7.1 Hz, 1H), 2.58 (s, 3H), 1.45 (t, J = 7.2 Hz, 3H) ppm; **^{13}C NMR** (126 MHz, $CDCl_3$) δ 164.9, 148.7, 147.9, 143.8, 141.4, 130.2, 128.1, 127.7, 124.1, 123.8, 62.2, 22.3, 14.4 ppm; **LRMS (+APCI)** m/z: 250/252 ([M+H]$^+$, 100); **HRMS (+ESI)** Calc. for $C_{13}H_{12}ClNNaO_2$ $[M+Na]^+$: 272.04488/274.04193, found 272.04494/274.04208.

2-chloro-8-methylquinoline-3-carboxylic acid (**345**)

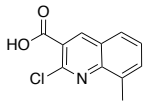

2-chloro-8-methylquinoline-3-carbaldehyde (496 mg, 2.41 mmol) was dissolved in warm *t*-BuOH (9 mL), cooled to room temperature and 2-methylbut-2-ene (3 mL, 28.9 mmol) was added dropwise. A solution of sodium chlorite (1.42 g, 15.7 mmol) and sodium dihydrogen phosphate (1.47 g, 12.1 mmol) in H_2O (3 mL) was added dropwise with stirring over 10 min.

The reaction was stirred at room temperature for a further 3 h. Most of the solvent was removed at reduced pressure, H_2O (10 mL) was added, and the solution was acidified with conc. HCl. The precipitate was collected by filtration and washed with H_2O to give the carboxylic acid **345** as a yellow solid (502 mg, 94%). **^{1}H NMR** (500 MHz, DMSO-d_6) δ 8.88 (s, 1H), 7.99 (dd, J = 8.3, 1.5 Hz, 1H), 7.77 (dt, J = 7.0, 1.3 Hz, 1H), 7.61 (dd, J = 8.2, 7.1 Hz, 1H), 2.67 (s, 3H) ppm, COOH proton signal not observed; **^{13}C NMR** (126 MHz, DMSO-d_6) δ 165.8, 146.4, 145.5, 141.4, 135.5, 132.5, 127.7, 126.7, 126.0, 125.4, 17.2 ppm; **LRMS (-ESI)** m/z: 219/221 ([M-H]$^-$, 100); **HRMS (+ESI)** Calc. for $C_{11}H_8ClNNaO_2$ [M+Na]$^+$: 244.01358/246.01063, found 244.01357/246.01067.

ethyl 2-chloro-8-methylquinoline-3-carboxylate (**346**)

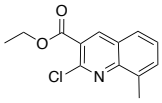

Prepared according to **General Procedure M** from **346** (265 mg, 1.2 mmol), EtOH (70 µL, 1.2 mmol), DMAP (15.8 mg, 0.13 mmol) and EDC.HCl (240 mg, 1.25 mmol) in CH_2Cl_2 (2.5 mL). Compound **345** was obtained as a white solid (172 mg, 58%) following purification by flash chromatography (0 - 10% EtOAc in Hex). **^{1}H NMR** (500 MHz, $CDCl_3$) δ 8.62 (s, 1H), 7.72 (dd, J = 8.1, 1.4 Hz, 1H), 7.66 (dt, J = 7.0, 1.3 Hz, 1H), 7.50 (dd, J = 8.1, 7.1 Hz, 1H), 4.47 (q, J = 7.1 Hz, 2H), 2.78 (s, 2H), 1.46 (t, J = 7.2 Hz, 3H) ppm; **^{13}C NMR** (126 MHz, $CDCl_3$) δ 165.1, 147.6, 146.6, 141.8, 137.0, 132.7, 127.7, 126.3, 126.1, 124.5, 62.2, 17.9, 14.4 ppm; **LRMS (+APCI)** m/z: 250/252 ([M+H]$^+$, 100) **HRMS (+ESI)** Calc. for $C_{13}H_{12}ClNNaO_2$ [M+Na]$^+$: 272.04488/274.04193, found 272.04500/274.04221.

2-chloro-*N*-methoxy-*N*,8-dimethylquinoline-3-carboxamide (**352**)

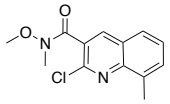

Compound **352** was prepared *via* a HATU mediated amide coupling according to **General Procedure G** from **345** (103 mg, 0.46 mmol) and *N*,*O*-dimethylhydroxylamine hydrochloride (54.1 mg, 0.55 mmol). Compound **352** was obtained as a white solid (96.3 mg, 78%) following purification by flash chromatography (0 - 20% EtOAc in Hex). **^{1}H NMR** (500 MHz, $CDCl_3$) δ 8.12 (s, 1H), 7.68 (d, J = 8.1 Hz, 1H), 7.63 (d, J = 7.1 Hz, 1H), 7.49 (t, J = 7.6 Hz, 1H), 3.46 (d, J = 18.2 Hz, 6H), 2.78 (s, 3H) ppm; **^{13}C NMR** (126 MHz, $CDCl_3$) δ 167.2, 146.9, 145.5, 137.0, 136.8, 131.5, 129.2, 127.5, 126.3, 125.8, 61.6, 32.7, 17.9 ppm; **LRMS (+APCI)** m/z: 265/267 ($[M+H]^+$, 100); **HRMS (+APCI)** Calc. for $C_{13}H_{14}ClN_2O_2$ $[M+H]^+$: 265.07383/267.07088, found 265.07368/267.07080.

1-(2-chloro-8-methylquinolin-3-yl)ethan-1-one (**351**)

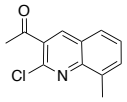

A solution of compound **352** (89.4 mg, 0.34 mmol) in anhy. THF (1 mL) at -78 °C was treated dropwise with MeMgBr (3M in diethyl ether, 220 µL, 0.68 mmol). The reaction was slowly brought to rt over the next hour and stirred for a subsequent 2 h or until complete consumption of starting material by TLC. The reaction mixture was cooled to 0 °C and quenched with NH_4Cl (2 eq). The aqueous layer (pH > 4) was extracted with EtOAc (3 x 25 mL/mmol). The combined organics were washed with brine (1 x 25 mL/mmol), dried over $MgSO_4$ and concentrated *in vacuo*. Compound **351** (42.3 mg, 57%) was isolated as a white solid following purification by flash chromatography (0 – 20% v/v EtOAc in Hex). **^{1}H NMR** (500 MHz, $CDCl_3$) δ 8.35 (s, 1H), 7.72 (d, J = 8.2 Hz, 1H), 7.66 (dt, J = 7.1, 1.2 Hz, 1H), 7.50 (dd, J = 8.1, 7.1 Hz, 1H), 2.78 (s, 3H), 2.77 (s, 3H) ppm; **^{13}C NMR** (126 MHz, $CDCl_3$) δ 199.1, 147.5, 145.0, 139.8, 137.0, 133.0, 132.5, 127.8, 126.5, 126.4, 30.8, 17.9 ppm; **LRMS (+APCI)** m/z: 220/222 ($[M+H]^+$, 100); **HRMS (+APCI)** Calc. for $C_{12}H_{11}ClNO$ $[M+H]^+$: 220.05237/222.04942, found 220.05214/222.04921.

(*E*)-3-(2-chloro-7-methylquinolin-3-yl)-1-(furan-2-yl)prop-2-en-1-one (**353**)

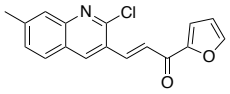

Prepared according to **General Procedure O** from 2-chloro-7-methylquinoline-3-carbaldehyde (302 mg, 1.47 mmol), 2-acetylfuran (164 mg, 1.49 mmol) and aq. NaOH (2.5 M, 1.2 mL, 2.94 mmol) in EtOH (3 mL). Compound **353** was obtained as a pale yellow powder (324 mg, 74%) following purification by flash chromatography (0 – 30% v/v EtOAc in Hex). **^{1}H NMR** (500 MHz, DMSO-d_6) δ 9.10 (s, 1H), 8.13 (d, J = 1.7 Hz, 1H), 8.02 (d, J = 15.6 Hz, 1H), 7.97 (d, J = 8.4 Hz, 1H), 7.89 (d, J = 15.6 Hz, 1H), 7.86 (d, J = 3.8 Hz, 1H), 7.78 – 7.75 (m, 1H), 7.56 (dd, J = 8.4, 1.7 Hz, 1H), 6.84 (dd, J = 3.6, 1.7 Hz, 1H), 2.54 (s, 3H) ppm; **^{13}C NMR** (126 MHz, DMSO-d_6) δ 175.9, 152.7, 149.6, 148.9, 147.5, 142.7, 137.2, 136.7, 130.2, 128.3, 126.7, 125.8, 125.7, 125.0, 120.3, 113.0, 21.6 ppm; **LRMS (+ESI)** m/z: 298/300 ($[M+H]^+$, 70), 320/322 ($[M+Na]^+$, 60). **HRMS (+ESI)** Calc. for $C_{17}H_{12}ClNNaO_2$ $[M+Na]^+$: 320.04488/322.04193, found 320.04493/322.04200.

2-chloro-3-(5-(furan-2-yl)-1*H*-pyrazol-3-yl)-7-methylquinoline (**357**)

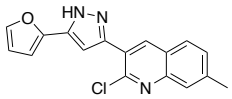

Hydrazine monohydrate (60 µL, 1.23 mmol) was added dropwise to a stirring solution of **350** (249 mg, 0.84 mmol) in EtOH (3 mL). The reaction was stirred at reflux for 1 h. The reaction mixture was then cooled to rt, and the resulting precipitate was filtered, and washed with EtOH. The corresponding solid was dried *in vacuo* for 2 h, before being dissolved in DMSO (2.5 mL) with cat. I_2 and stirred at 140 °C for 2 h. Following complete consumption of starting material as indicated by TLC, the reaction was cooled to rt and poured into ice H_2O. The aqueous layer was adjusted to pH 5 and extracted with EtOAc (3 x 25 mL/mmol). The combined organics were washed with brine (1 x 25 mL/mmol), dried over $MgSO_4$ and concentrated *in vacuo*. Compound **357** (207 mg, 79%) was isolated as a brown solid following purification by flash chromatography (0 – 50% v/v EtOAc in Hex). Characterisation data is reported as a complex mix of tautomers. **^{1}H NMR** (500 MHz, DMSO-d_6) δ 13.74 (s, 1H), 13.48 (s, 1H), 8.78 – 8.59 (m, 1H), 8.06 – 7.93 (m, 2H), 7.85 – 7.68 (m, 3H), 7.61 – 7.47 (m, 2H), 7.13 – 6.95 (m, 1H), 6.95 – 6.73 (m, 1H), 6.70 – 6.55 (m, 2H), 2.54 (s, 5H) ppm; **^{13}C NMR** (126 MHz, DMSO-d_6) δ 148.7, 147.7, 147.5, 146.5, 144.4, 143.7, 143.1, 142.3, 142.0, 141.3, 138.9, 138.6, 138.4,

134.7, 130.1, 127.9, 126.5, 125.8, 125.0, 124.5, 121.9, 111.9, 111.6, 107.1, 105.7, 103.7, 102.6, 21.5 ppm; **LRMS (+ESI)** m/z: 310/312 ($[M+H]^+$, 100), 332/334 ($[M+Na]^+$, 80), **(-ESI)** m/z: 308/310 ($[M-H]^-$, 100); **HRMS (+ESI)** Calc. for $C_{17}H_{13}ClN_3O$ $[M+H]^+$: 310.07417/312.07122, found 310.07420/312.07126.

3-(1-(*tert*-butyl)-5-(furan-2-yl)-1*H*-pyrazol-3-yl)-2-chloro-7-methylquinoline (**300**) and

3-(1-(*tert*-butyl)-3-(furan-2-yl)-1*H*-pyrazol-5-yl)-2-chloro-7-methylquinoline (**359**)

2-chloro-3-(5-(furan-2-yl)-1*H*-pyrazol-3-yl)-7-methylquinoline (24.8 mg, 0.08 mmol) and $Cu(OTf)_2$ (1.6 mg, 5 mol%) were combined in a round bottom flask and purged with N_2. CH_2Cl_2 (0.5 mL) and *tert*-butyl 2,2,2-trichloroacetimidate (40 µL, 0.22 mmol) were added, then stirred at rt for 16 – 24 h. The reaction was diluted with CH_2Cl_2 (25 mL/mmol) and washed with 1M NaOH (10 mL/mmol), then H_2O (10 mL/mmol). The combined aqueous layers were extracted with CH_2Cl_2 (3 x 25 mL/mmol), dried over $MgSO_4$ and concentrated *in vacuo*. The crude product was purified *via* column chromatography (0 – 30% v/v EtOAc in Hex) to yield both regioisomers (**300** and **359**).

3-(1-(*tert*-butyl)-5-(furan-2-yl)-1*H*-pyrazol-3-yl)-2-chloro-7-methylquinoline (**300**)

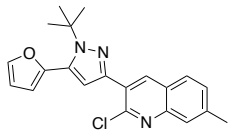

White powder (5.3 mg, 18%); **^{1}H NMR** (500 MHz, $CDCl_3$) δ 8.62 (s, 1H), 7.79 (s, 1H), 7.78 (d, J = 8.4 Hz, 1H), 7.57 (dd, J = 1.9, 0.9 Hz, 1H), 7.39 (dd, J = 8.3, 1.7 Hz, 1H), 7.02 (s, 1H), 6.55 – 6.50 (m, 2H), 2.56 (s, 3H), 1.61 (s, 9H) ppm; **^{13}C NMR** (126 MHz, $CDCl_3$) δ 148.8, 147.2, 144.6, 144.2, 142.8, 141.0, 138.0, 132.9, 129.5, 127.6, 127.4, 126.3, 125.6, 112.3, 111.9, 111.4, 61.8, 30.2, 22.1 ppm; **LRMS (+ESI)** m/z: 366/368 ($[M+H]^+$, 100); **HRMS (+ESI)** Calc. for $C_{21}H_{21}ClN_3O$ $[M+H]^+$: 366.13677/368.13382, found 366.13687/368.13396; **HPLC** R_T = 31.24 min, 95.31% (254 nm).

3-(1-(*tert*-butyl)-3-(furan-2-yl)-1*H*-pyrazol-5-yl)-2-chloro-7-methylquinoline (**359**)

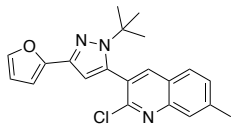

White solid (2.9 mg, 9.9%); **^{1}H NMR** (500 MHz, $CDCl_3$) δ 8.11 (s, 1H), 7.87 (s, 1H), 7.74 (d, J = 8.3 Hz, 1H), 7.49 – 7.45 (m, 2H), 6.68 – 6.66 (m, 1H), 6.46 (q, J = 1.9 Hz, 2H), 2.60 (s, 3H), 1.53 (s, 9H) ppm; **^{13}C NMR** (126 MHz, $CDCl_3$) δ 150.7, 149.2, 148.0, 142.4, 141.9, 141.8, 140.2, 138.5, 130.1, 127.8, 127.5, 126.5, 124.4, 111.3, 107.4, 105.8, 62.3, 30.9, 22.2 ppm; **LRMS (+ESI)** m/z: 366/368 ($[M+H]^+$, 100); **HRMS (+ESI)** Calc. for $C_{21}H_{21}ClN_3O$ $[M+H]^+$: 366.13677/368.13382, found 366.13687/368.13394; **HPLC** R_T = 29.11 min, 96.58% (254 nm).

(*E*)-3-(2-chloro-8-methylquinolin-3-yl)-1-(furan-2-yl)prop-2-en-1-one (**354**)

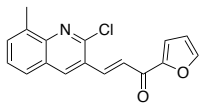

Prepared according to **General Procedure O** from 2-chloro-8-methylquinoline-3-carbaldehyde (303 mg, 1.47 mmol), 2-acetylfuran (160 mg, 1.45 mmol) and aq. NaOH (2.5 M, 1.2 mL, 2.95 mmol) in EtOH (3 mL). Compound **354** was obtained as an off white powder (311 mg, 71%) following purification by flash chromatography (0 – 30% v/v EtOAc in Hex). **^{1}H NMR** (500 MHz, DMSO-d_6) δ 9.14 (s, 1H), 8.13 (d, J = 1.7 Hz, 1H), 8.05 (d, J = 15.7 Hz, 1H), 7.93 (d, J = 15.6 Hz, 1H), 7.92 (dd, J = 8.4, 1.4 Hz, 1H), 7.87 (d, J = 3.5 Hz, 1H), 7.74 (dt, J = 7.1, 1.3 Hz, 1H), 7.61 (dd, J = 8.1, 7.0 Hz, 1H), 6.85 (dd, J = 3.6, 1.7 Hz, 1H), 2.67 (s, 3H) ppm; **^{13}C NMR (**126 MHz, DMSO-d_6) δ 175.9, 152.7, 149.0, 148.7, 146.3, 137.8, 136.6, 135.6, 132.0, 127.8, 127.0, 126.5, 126.1, 120.4, 113.0, 17.3 ppm; **LRMS (+ESI)** m/z: 298/300 ($[M+H]^+$, 20), 320/322 ($[M+Na]^+$, 60); **HRMS (+ESI)** Calc. for $C_{17}H_{12}ClNNaO_2$ $[M+Na]^+$: 320.04488/322.04193, found 320.04504/322.04211.

2-chloro-3-(5-(furan-2-yl)-1*H*-pyrazol-3-yl)-8-methylquinoline (**358**)

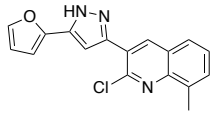

Hydrazine monohydrate (80 µL, 1.67 mmol) was added dropwise to a stirring solution of **354** (249 mg, 0.84 mmol) in EtOH (3 mL). The reaction was stirred at reflux for 1 h. The reaction mixture was then cooled to rt, and the resulting precipitate was filtered, and washed with EtOH. The corresponding solid was dried *in vacuo* for 2 h, before being dissolved in DMSO (2 mL) with cat. I_2 and stirred at 140 °C for 2 h. Following complete consumption of starting material as indicated by TLC, the reaction was cooled to rt and poured into ice H_2O. The aqueous layer was adjusted to pH 5 and extracted with EtOAc (3 x 25 mL/mmol). The combined organics were washed with brine (1 x 25 mL/mmol), dried over $MgSO_4$ and concentrated *in vacuo*. Compound **358** (133 mg, 53%) was isolated as a brown solid following purification by flash chromatography (0 – 50% v/v EtOAc in Hex). Characterisation data is reported as a complex mix of tautomers. **^{1}H NMR** (500 MHz, DMSO-d_6) δ 13.87 – 13.44 (m, 1H), 8.84 – 8.63 (m, 1H), 8.01 – 7.88 (m, 1H), 7.86 – 7.65 (m, 2H), 7.65 – 7.50 (m, 1H), 7.15 – 6.97 (m, 1H), 6.97 – 6.75 (m, 1H), 6.71 – 6.53 (m, 1H), 2.70 (s, 3H) ppm; **^{13}C NMR** (126 MHz, DMSO-d_6) δ 145.3, 143.2, 142.3, 139.5, 138.9, 135.3, 134.6, 131.4, 130.9, 127.7, 127.3, 126.1, 111.9, 107.1, 103.8, 102.6, 40.1, 40.0, 39.9, 39.9, 39.8, 39.7, 39.6, 39.5, 39.4, 39.2, 39.0, 17.3 ppm; **LRMS (+ESI)** m/z: 310/312 ($[M+H]^+$, 100), **(-ESI)** m/z: 308/310 ($[M-H]^-$, 100); **HRMS (+ESI)** Calc. for $C_{17}H_{13}ClN_3O$ $[M+H]^+$: 310.07417/312.07122, found 310.07426/312.07132.

3-(1-(*tert*-butyl)-5-(furan-2-yl)-1*H*-pyrazol-3-yl)-2-chloro-8-methylquinoline (**301**) and

3-(1-(*tert*-butyl)-3-(furan-2-yl)-1*H*-pyrazol-5-yl)-2-chloro-8-methylquinoline (**360**)

2-chloro-3-(5-(furan-2-yl)-1*H*-pyrazol-3-yl)-8-methylquinoline (40.8 mg, 0.13 mmol) and $Cu(OTf)_2$ (4.8 mg, 10 mol%) were combined in a round bottom flask and purged with N_2. CH_2Cl_2 (0.7 mL) and *tert*-butyl 2,2,2-trichloroacetimidate (60 µL, 0.33 mmol) were added, then stirred at rt for 16 – 24 h. The reaction was diluted with CH_2Cl_2 (25 mL/mmol) and washed with 1M NaOH (10 mL/mmol), then H_2O (10 mL/mmol). The combined aqueous layers were extracted with CH_2Cl_2 (3 x 25 mL/mmol), dried over $MgSO_4$ and concentrated *in vacuo*. The crude product was purified *via* column chromatography (0 – 30% v/v EtOAc in Hex) to yield both regioisomers (**301** and **360**).

3-(1-(*tert*-butyl)-5-(furan-2-yl)-1*H*-pyrazol-3-yl)-2-chloro-8-methylquinoline (**301**)

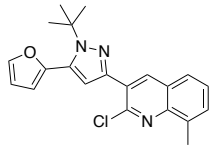

White crystalline solid (12.1 mg, 25%); **^{1}H NMR** (400 MHz, $CDCl_3$) δ 8.64 (s, 1H), 7.72 (d, J = 8.1 Hz, 1H), 7.58 (d, J = 1.8 Hz, 1H), 7.55 (d, J = 7.0 Hz, 1H), 7.44 (t, J = 7.6 Hz, 1H), 7.05 (s, 1H), 6.56 – 6.51 (m, 2H), 2.79 (s, 3H), 1.61 (s, 9H) ppm; **^{13}C NMR** (101 MHz, $CDCl_3$) δ 147.8, 146.2, 144.7, 144.2, 142.8, 138.4, 136.5, 132.9, 130.4, 127.6, 126.9, 126.9, 125.9, 112.4, 111.9, 111.4, 61.8, 30.3, 17.9 ppm; **LRMS (+ESI)** m/z: 366/368 ($[M+H]^+$, 100); **HRMS (+ESI)** Calc. for $C_{21}H_{21}ClN_3O$ $[M+H]^+$: 366.13677/368.13382, found 366.13699/368.13409; **HPLC** R_T = 32.75 min, 98.16% (254 nm).

3-(1-(*tert*-butyl)-3-(furan-2-yl)-1*H*-pyrazol-5-yl)-2-chloro-8-methylquinoline (**360**)

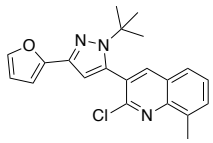

White powder (8.1 mg, 17%); **^{1}H NMR** (400 MHz, $CDCl_3$) δ 8.13 (s, 1H), 7.67 (t, J = 8.7 Hz, 2H), 7.52 (t, J = 7.6 Hz, 1H), 7.47 – 7.45 (m, 1H), 6.68 (d, J = 3.4 Hz, 1H), 6.47 (d, J = 1.9 Hz, 1H), 6.46 (s, 1H), 2.82 (s, 3H), 1.54 (s, 9H) ppm; **^{13}C NMR** (101 MHz, $CDCl_3$) δ 149.7, 149.2, 147.0, 141.9, 141.8, 140.7, 138.6, 137.1, 131.6, 127.6, 127.2, 126.4, 125.7, 111.3, 107.4, 105.8, 62.3, 30.9, 17.9 ppm; **LRMS (+ESI)** m/z: 366/368 ($[M+H]^+$, 100); **HRMS (+ESI)** Calc. for $C_{21}H_{21}ClN_3O$ $[M+H]^+$: 366.13677/368.13382, found 366.13702/368.13413; **HPLC** R_T = 31.60 min, 95.81% (254 nm).

7.7 Biological Assay Details

7.7.1 P2X4R Cell Culture

HEK293 cells stably expressing human P2X4R (HEK-hP2X4R) and mitochondrially-targeted Photina photoprotein (Revvity, 2025a) were cultured in minimum essential medium with Earle's salt (MEM; Sigma-Aldrich) supplemented with 10% heated-inactivated FBS, Geneticin (400 μg mL-1, Roche), puromycin (0.2 μg mL-1: Sigma-Aldrich) and penicillin-streptomycin (100 IU mL-1, Thermo Scientific) as per the manufacturer's protocol. Cells were

incubated at 37 °C and 5% CO_2 in a humidified CO_2 incubator. They were fed every 2 – 3 days and passaged using trypsin (0.25%, Sigma-Aldrich)/EDTA (0.53 mM, Sigma-Aldrich) (5 min).

7.7.2 P2X4R Photoscreen Assay

HEK-hP2X4R cells were detached using trypsin (0.25%)/EDTA (0.53 mM) collected via centrifuge (150 g, 5 min) and resuspended in culture media. Resuspended cells were plated at 5 x104 cells/well into 96-well black-walled CellBIND plates (Corning) coated with poly-L-lysine (100 µg mL^{-1}; Sigma-Aldrich) and incubated for 24 h (37 °C, 5% CO_2). Utilising the stably-expressed Photina protein, a Photoscreen assay was conducted as per the manufacturer's protocol (Revvity, 2025a). Following incubation, cell culture media was replaced with 50 µL modified HBSS ($CaCl_2$ 1.26 mM, $MgCl_2$ 0.49 mM, $MgSO_4$ 0.41 mM, KCl 5.33 mM, KH_2PO_4 0.44 mM, $NaHCO_3$ 4.17 mM, NaCl 138 mM, Na_2HPO_4 0.34 mM, glucose 5.56 mM, HEPES 20 mM) supplemented with native coelenterazine (10 µM, Promega) and incubated at room temperature (RT) for 4 h in the dark. For the agonist assay, CTP (Sigma-Aldrich) was serially diluted in modified HBSS in a range of 0.001 µM – 1000 µM. Fifty microlitres of serial dilutions were injected onto cells as per settings outlined in Table 5.1 using a Flexstation 3 Multi-Mode Microplate Reader (Molecular Devices). Collected luminescence data was normalised by subtracting baseline signal (0 - 21 s) and then the area under the curve was calculated for 0 – 31 s after injection of conditions for each well to allow for detection of the peak signal and return to baseline as per manufacturer's protocol (Revvity, 2025a). Normalised agonist data was analysed by a 4-paramter sigmoidal dose-response (agonist) fit in GraphPad 10.0.

7.7.3 P2X4R Ca^{2+} Flux Assay

HEK-hP2X4R cells were collected as mentioned in Section 5.3.3. Resuspended cells were plated at 5 x104 cells/well into 96-well black-walled CellBIND plates (Corning) coated with poly-L-lysine (100 µg mL^{-1}; Sigma-Aldrich) and incubated for 24 h (37 °C, 5% CO_2). Utilising the downstream accumulation of Ca^{2+} following P2X4R activation, the Ca^{2+} flux Fluo-4 NW dye (Invitrogen) was utilised as per the manufacturer's protocol. After incubation, culture media was replaced with 80 µL dye solution containing Fluo-4 NW (1x, Invitrogen), probenecid (5mM Invitrogen) and modified HBSS assay buffer (KCl 5.37 mM, KH_2PO_4 0.44 mM, NaCl 137 mM, NaH_2PO_4 0.337 mM, glucose 5.56 mM, $CaCl_2$ 1.26 mM, HEPES

20 mM, $MgCl_2$ 0.5 mM, $MgSO_4$ 0.41 mM, $NaHCO_3$ 4.17 mM, pH 7.4) and incubated for 0.5 h at 37 °C. For the agonist assay, CTP and ATP (Sigma-Aldrich) were serially diluted in modified HBSS in a range of 0.001 μM – 100 μM, to directly compare to the Photoscreen assay. For the antagonist assay, compounds were made up at the same concentration range with the addition of agonist ATP (1 μM) and treated onto cells as mentioned above. Twenty microlitres of serial dilutions were injected onto cells as per the settings outlined in Table 5.2 using a Flexstation 3 Multi-Mode Microplate Reader (Molecular Devices). Collected luminescence data was normalised by subtracting baseline signal (0 - 30 s) and then the area under the curve was calculated for 0 – 90s after injection of conditions for each well to allow for detection of the peak signal and return to baseline. Normalised agonist data was analysed by a 4-paramter sigmoidal dose-response (agonist) fit in GraphPad 10.0.

7.7.4 P2X7R Cell Culture

Human THP-1 cells were cultured in RPMI-1640 medium (with ATCC modification; Gibco) supplemented with 10% heated inactivated foetal bovine serum (FBS; Gibco). Cells were incubated at 37 °C and 5% CO_2 in a humidified CO_2 incubator.

7.7.5 P2X7R YO-PRO®-1 Assay

THP-1 cells were collected via centrifuge (125 g, 5 min) and resuspended in RPMI-1640 media supplemented with 5% FBS, lipopolysaccharide (from *E. coli* strain 0111:B4; Sigma-Aldrich; 100 ng mL^{-1}) and recombinant human IFN-γ (R&D Systems; 10 ng mL^{-1}). Resuspended cells were seeded at a density of 1.5 x 105 cells per well into 96-well black-walled CellBIND plates (Corning) and allowed to differentiate during an incubation of 24 h (37 °C, 5% CO_2). The supernatant was then removed, and the cells washed with 150 μL Hank's Balanced Salt Solution containing low Ca^{2+} (HBSS; KCl 5.37 mM, KH_2PO_4 0.44 mM, NaCl 136.89 mM, Na_2HPO_4 0.34 mM, glucose 5.55 mM, $NaHCO_3$ 4.17 mM, $CaCl_2$ 0.1 mM, pH 7.4). Cells were then treated in 100 μL of warmed HBSS containing YO-PRO®-1Iodide (Invitrogen; 1 μM) and BzATP (Sigma Aldrich: 100 μM) or vehicle 1 (ultrapure water; 0.4% v/v) and test compounds or vehicle 2 (DMSO; 0.1% v/v). Fluorescence of each well was then recorded every 30 s for 1.5 h at 37 °C using a BMG POLARstar Omega (λ_{ex} = 485-12, λ_{em} = 520) plate reader. To determine the IC_{50} for each experiment, the recorded data at the 1 h mark was collected and fitted using a 4-parameter sigmoidal dose-response (inhibition) fit in GraphPad Prism 10.0

(GraphPad software). Each compound was tested in technical duplicate with a minimum of three independent repetitions completed. The calculated IC_{50} for each assay was then used to determine the average and standard deviation (SD).

7.7.6 P2Y6R Cell Culture

Human 132-1N1 astrocytoma cells stably transfected with the human P2Y6R (132-1N1-hP2Y6R) receptor (132-1N1-hP2Y6R; Revvity) were cultured in Dulbecco's Modified Eagle Medium (DMEM; Gibco) supplemented with 10% heated-inactivated FBS, sodium pyruvate (1 mM, Gibco) and geneticin (0.4 mg mL-1, Roche) as per the manufacturer's protocol. Cells were incubated at 37 °C and 5% CO_2 in a humidified CO_2 incubator. Cells were fed every 2 – 3 days and passaged using trypsin (0.25%, Sigma-Aldrich)/EDTA (0.53 mM, Sigma-Aldrich) (5 min).

7.7.7 P2Y6R IP-one Gq Detection Assay

132-1N1-hP2Y6R cells were detached using trypsin/EDTA, collected via centrifuge (150 g, 5 min) and resuspended in culture media. Resuspended cells were seeded at three densities (4.375 x103, 8.375 x103 or 10.375 x103 cells/well) into a 384-well plate (Corning) coated with poly-L-lysine (100 µg mL^{-1}; Sigma-Aldrich) and incubated for 24 h (37 °C, 5% CO_2). The HTRF IP-One Gq Detection Kit (Revvity) was utilised as a P2Y6R agonist assay to measure IP1 accumulation, according to the manufacturer's protocol. Stock solution of uridine 5'-diphosphate disodium salt hydrate (Sigma-Aldrich) was made up at 1000x the final concentration in ultra-pure water. Stock solution was then diluted 1000x in stimulation buffer and serially diluted further in stimulation buffer (HEPES 10 mM, $CaCl_2$ 1 mM, $MgCl_2$ 0.5 mM, KCl 4.2 mM, NaCl 146 mM, glucose 5.5 mM, LiCl 50 mM, pH 7.4). The final serial dilutions spanned a range of 0.01 – 100 µM. Media was removed from cells, and they were treated with 14 µL of serially-diluted UDP and incubated for 1 h at 37 °C. Following incubation, IP1-d2 reagent (3 µL) and IP1-Tb cryptate (3 µL) antibody diluted in kit lysis & detection buffer was added and incubated for a further 1 h at RT. After incubation, 15 µL was transferred to a 384-well white ProxiPlate (Revvity) and fluorescence recorded (665 nM and 620 nM) using a PHERAstar microplate reader (BMG Labtech).

Raw fluorescence was converted to a ratio (Ratio=(665 nm)/(620 nm)×10^4). To determine the EC_{50} for each experiment, fluorescence ratio from unknown samples were interpolated to the standard curve of each experiment using a 4-parameter sigmoidal fit in GraphPad Prism 10.0, to obtain IP1 values. A concentration-response curve was then constructed using these values via a 4-paramter sigmoidal dose-response (agonist) fit in GraphPad 10.0. Each compound was tested in technical duplicate with a minimum of three independent repetitions completed. The data from each assay was then used to determine the average and standard deviation (SD) EC_{50} for each compound.

7.7.8 P2Y6R Ca^{2+} Flux Assay

Cells were collected as mentioned in Section 6.3.3. Resuspended cells were plated at 2 x104 cells/well into 96-well black-walled CellBIND plates (Corning) and incubated for 24 h (37 °C, 5% CO_2). To measure the downstream accumulation of Ca^{2+} following P2Y6R activation, the Ca^{2+} flux Fluo-4 NW (Invitrogen) was utilised as per manufactures protocol. After incubation, culture media was replaced with 80 µL dye solution containing Fluo-4 NW (1x, Invitrogen), probenecid (5 mM, Invitrogen) dissolved in modified HBSS assay buffer (KCl 5.37 mM, KH_2PO_4 0.44 mM, NaCl 137 mM, NaH_2PO_4 0.337 mM, glucose 5.5 mM, $CaCl_2$ 1.26 mM, HEPES 20 mM, $MgCl_2$ 0.5 mM, $MgSO_4$ 0.41 mM, $NaHCO_3$ 4.17 mM, pH 7.4) and incubated for 0.5 h at 37 °C. Working agonist concentrations ranging from ranged from 0.001 µM – 100 µM were made up as per Section 6.3.3,. Fluorescence (λEx=494 nm, λEm=516 nm) was recorded for 31 s for a baseline and then 20 µL was injected onto cells at 3 μLs^{-1} with fluorescence recorded for a further 150 s using a Flexstation 3 Multi-Mode Microplate Reader (Molecular Devices) using the same instrument settings as outlined in Table 5.2. For the antagonist assay, compounds were made up in the same concentration range with the addition of an EC_{80} concentration of agonist UDP (0.075 µM) and treated onto cells as mentioned above.

Collected fluorescence data was normalised by dividing peak levels (F1) by the average signal of 0 – 31 s before injection of agonist (F0) for each well. Normalised agonist data was analysed as per Section 6.3.3 by a 4-parameter sigmoidal dose-response (agonist) fit in GraphPad 10.0. Mean Ca^{2+} flux signal of antagonists were used to compare differences to mean-agonist only conditions, using a one-way analysis of variance (ANOVA) with a Dunnett's post-hoc test.

Chapter 8. References

(1) Burnstock, G. Introduction to Purinergic Signaling. In *Purinergic Signaling: Methods and Protocols*; Pelegrín, P., Ed.; Springer: New York, NY, 2020; pp 1–15. https://doi.org/10.1007/978-1-4939-9717-6_1.

(2) Burnstock, G. Purine and Purinergic Receptors. *Brain and Neuroscience Advances* **2018**, *2*, 2398212818817494. https://doi.org/10.1177/2398212818817494.

(3) Burnstock, G. Purinergic Nerves. *Pharmacological Reviews* **1972**, *24* (3), 509–581.

(4) Burnstock, G. Purinergic Receptors. *Journal of Theoretical Biology* **1976**, *62* (2), 491–503. https://doi.org/10.1016/0022-5193(76)90133-8.

(5) *Purinergic Signaling in Neuroinflammation*; Illes, P., Ed.; MDPI - Multidisciplinary Digital Publishing Institute, 2023. https://doi.org/10.3390/books978-3-0365-7686-2.

(6) Woods, L. T.; Forti, K. M.; Shanbhag, V. C.; Camden, J. M.; Weisman, G. A. P2Y Receptors for Extracellular Nucleotides: Contributions to Cancer Progression and Therapeutic Implications. *Biochemical Pharmacology* **2021**, *187*, 114406. https://doi.org/10.1016/j.bcp.2021.114406.

(7) Oken, A. C.; Krishnamurthy, I.; Savage, J. C.; Lisi, N. E.; Godsey, M. H.; Mansoor, S. E. Molecular Pharmacology of P2X Receptors: Exploring Druggable Domains Revealed by Structural Biology. *Frontiers in Pharmacology* **2022**, *13*, 925880. https://doi.org/10.3389/fphar.2022.925880.

(8) Shi, H.; Ditter, I. A.; Oken, A. C.; Mansoor, S. E. Human P2X4 Receptor Gating Is Modulated by a Stable Cytoplasmic Cap and a Unique Allosteric Pocket. *Science Advances* **2025**, *11* (3), eadr3315. https://doi.org/10.1126/sciadv.adr3315.

(9) Illes, P.; Rubini, P.; Ulrich, H.; Zhao, Y.; Tang, Y. Regulation of Microglial Functions by Purinergic Mechanisms in the Healthy and Diseased CNS. *Cells* **2020**, *9* (5), 1108. https://doi.org/10.3390/cells9051108.

(10) McCarthy, A. E.; Yoshioka, C.; Mansoor, S. E. Full-Length P2X7 Structures Reveal How Palmitoylation Prevents Channel Desensitization. *Cell* **2019**, *179* (3), 659-670.e13. https://doi.org/10.1016/j.cell.2019.09.017.

(11) Nagel, J.; Bous, C.; Abdelrahman, A.; Schiedel, A. C.; Müller, C. E. Species Differences of P2X4 Receptor Modulators. *ACS Pharmacology & Translational Science* **2025**, *8* (5), 1320–1332. https://doi.org/10.1021/acsptsci.4c00688.

(12) Sluyter, R.; Adriouch, S.; Fuller, S. J.; Nicke, A.; Sophocleous, R. A.; Watson, D. Animal Models for the Investigation of P2X7 Receptors. *International Journal of Molecular Sciences* **2023**, *24* (9), 8225. https://doi.org/10.3390/ijms24098225.

(13) Fortuny-Gomez, A.; Fountain, S. J. Pharmacological Differences between Human and Mouse P2X4 Receptor Explored Using Old and New Tools. *Purinergic Signalling* **2024**, *20* (6), 659–667. https://doi.org/10.1007/s11302-024-10018-x.

(14) Pegoraro, A.; Grignolo, M.; Ruo, L.; Ricci, L.; Adinolfi, E. P2X7 Variants in Pathophysiology. *International Journal of Molecular Sciences* **2024**, *25* (12), 6673. https://doi.org/10.3390/ijms25126673.

(15) Burnstock, G. P2X Ion Channel Receptors and Inflammation. *Purinergic Signalling* **2016**, *12* (1), 59–67. https://doi.org/10.1007/s11302-015-9493-0.

(16) Kanellopoulos, J. M.; Almeida-da-Silva, C. L. C.; Rüütel Boudinot, S.; Ojcius, D. M. Structural and Functional Features of the P2X4 Receptor: An Immunological Perspective. *Frontiers in Immunology* **2021**, *12*, 645834. https://doi.org/10.3389/fimmu.2021.645834.

(17) Sophocleous, R. A.; Ooi, L.; Sluyter, R. The P2X4 Receptor: Cellular and Molecular Characteristics of a Promising Neuroinflammatory Target. *International Journal of Molecular Sciences* **2022**, *23* (10), 5739. https://doi.org/10.3390/ijms23105739.

(18) Xu, J.; Chai, H.; Ehinger, K.; Egan, T. M.; Srinivasan, R.; Frick, M.; Khakh, B. S. Imaging P2X4 Receptor Subcellular Distribution, Trafficking, and Regulation Using P2X4-pHluorin. *Journal of General Physiology* **2014**, *144* (1), 81–104. https://doi.org/10.1085/jgp.201411169.

(19) Qureshi, O. S.; Paramasivam, A.; Yu, J. C. H.; Murrell-Lagnado, R. D. Regulation of P2X4 Receptors by Lysosomal Targeting, Glycan Protection and Exocytosis. *Journal of Cell Science* **2007**, *120* (21), 3838–3849. https://doi.org/10.1242/jcs.010348.

(20) Suurväli, J.; Boudinot, P.; Kanellopoulos, J.; Rüütel Boudinot, S. P2X4: A Fast and Sensitive Purinergic Receptor. *Biomedical Journal* **2017**, *40* (5), 245–256. https://doi.org/10.1016/j.bj.2017.06.010.

(21) Ulmann, L.; Hirbec, H.; Rassendren, F. P2X4 Receptors Mediate PGE2 Release by Tissue-Resident Macrophages and Initiate Inflammatory Pain. *The EMBO Journal* **2010**, *29* (14), 2290–2300. https://doi.org/10.1038/emboj.2010.126.

(22) Ulmann, L.; Hatcher, J. P.; Hughes, J. P.; Chaumont, S.; Green, P. J.; Conquet, F.; Buell, G. N.; Reeve, A. J.; Chessell, I. P.; Rassendren, F. Up-Regulation of P2X4 Receptors in Spinal Microglia after Peripheral Nerve Injury Mediates BDNF Release and Neuropathic Pain. *The Journal of Neuroscience* **2008**, *28* (44), 11263–11268. https://doi.org/10.1523/JNEUROSCI.2308-08.2008.

(23) Castillo, C.; Saez-Orellana, F.; Godoy, P. A.; Fuentealba, J. Microglial Activation Modulated by P2X4R in Ischemia and Repercussions in Alzheimer's Disease. *Frontiers in Physiology* **2022**, *13*, 814999. https://doi.org/10.3389/fphys.2022.814999.

(24) Kawate, T.; Michel, J. C.; Birdsong, W. T.; Gouaux, E. Crystal Structure of the ATP-Gated P2X4 Ion Channel in the Closed State. *Nature* **2009**, *460* (7255), 592–598. https://doi.org/10.1038/nature08198.

(25) Hattori, M.; Gouaux, E. Molecular Mechanism of ATP Binding and Ion Channel Activation in P2X Receptors. *Nature* **2012**, *485* (7397), 207–212. https://doi.org/10.1038/nature11010.

(26) Khakh, B. S.; Proctor, W. R.; Dunwiddie, T. V.; Labarca, C.; Lester, H. A. Allosteric Control of Gating and Kinetics at P2X4Receptor Channels. *Journal of Neuroscience* **1999**, *19* (17), 7289–7299. https://doi.org/10.1523/JNEUROSCI.19-17-07289.1999.

(27) Nicke, A.; Kerschensteiner, D.; Soto, F. Biochemical and Functional Evidence for Heteromeric Assembly of P2X1 and P2X4 Subunits. *Journal of Neurochemistry* **2005**, *92* (4), 925–933. https://doi.org/10.1111/j.1471-4159.2004.02939.x.

(28) Illes, P.; Müller, C. E.; Jacobson, K. A.; Grutter, T.; Nicke, A.; Fountain, S. J.; Kennedy, C.; Schmalzing, G.; Jarvis, M. F.; Stojilkovic, S. S.; et al. Update of P2X Receptor Properties and Their Pharmacology: IUPHAR Review 30. *British Journal of Pharmacology* **2021**, *178* (3), 489–514. https://doi.org/10.1111/bph.15299.

(29) Sluyter, R. The P2X7 Receptor. In *Protein Reviews: Volume 19*; Atassi, M. Z., Ed.; Springer: Singapore, 2017; pp 17–53. https://doi.org/10.1007/5584_2017_59.

(30) Liu, X.; Li, Y.; Huang, L.; Kuang, Y.; Wu, X.; Ma, X.; Zhao, B.; Lan, J. Unlocking the Therapeutic Potential of P2X7 Receptor: A Comprehensive Review of Its Role in Neurodegenerative Disorders. *Frontiers in Pharmacology* **2024**, *15*, 1450704. https://doi.org/10.3389/fphar.2024.1450704.

(31) Illes, P. P2X7 Receptors Amplify CNS Damage in Neurodegenerative Diseases. *International Journal of Molecular Sciences* **2020**, *21* (17), 5996. https://doi.org/10.3390/ijms21175996.

(32) Campagno, K. E.; Mitchell, C. H. The P2X7 Receptor in Microglial Cells Modulates the Endolysosomal Axis, Autophagy, and Phagocytosis. *Frontiers in Cellular Neuroscience* **2021**, *15*, 645244. https://doi.org/10.3389/fncel.2021.645244.

(33) Craigie, E.; Birch, R. E.; Unwin, R. J.; Wildman, S. S. The Relationship between P2X4 and P2X7: A Physiologically Important Interaction? *Frontiers in Physiology* **2013**, *4*, 00216. https://doi.org/10.3389/fphys.2013.00216.

(34) Boumechache, M.; Masin, M.; Edwardson, J. M.; Górecki, D. C.; Murrell-Lagnado, R. Analysis of Assembly and Trafficking of Native P2X4 and P2X7 Receptor Complexes in Rodent Immune Cells. *The Journal of Biological Chemistry* **2009**, *284* (20), 13446–13454. https://doi.org/10.1074/jbc.M901255200.

(35) Ma, W.; Korngreen, A.; Weil, S.; Cohen, E. B.-T.; Priel, A.; Kuzin, L.; Silberberg, S. D. Pore Properties and Pharmacological Features of the P2X Receptor Channel in Airway Ciliated Cells. *The Journal of Physiology* **2006**, *571* (3), 503–517. https://doi.org/10.1113/jphysiol.2005.103408.

(36) Sakaki, H.; Fujiwaki, T.; Tsukimoto, M.; Kawano, A.; Harada, H.; Kojima, S. P2X4 Receptor Regulates P2X7 Receptor-Dependent IL-1β and IL-18 Release in Mouse Bone Marrow-Derived Dendritic Cells. *Biochemical and Biophysical Research Communications* **2013**, *432* (3), 406–411. https://doi.org/10.1016/j.bbrc.2013.01.135.

(37) Hung, S.-C.; Choi, C. H.; Said-Sadier, N.; Johnson, L.; Atanasova, K. R.; Sellami, H.; Yilmaz, Ö.; Ojcius, D. M. P2X4 Assembles with P2X7 and Pannexin-1 in Gingival Epithelial Cells and Modulates ATP-Induced Reactive Oxygen Species Production and Inflammasome Activation. *PLOS ONE* **2013**, *8* (7), e70210. https://doi.org/10.1371/journal.pone.0070210.

(38) Kawano, A.; Tsukimoto, M.; Mori, D.; Noguchi, T.; Harada, H.; Takenouchi, T.; Kitani, H.; Kojima, S. Regulation of P2X7-Dependent Inflammatory Functions by P2X4 Receptor in Mouse Macrophages. *Biochemical and Biophysical Research Communications* **2012**, *420* (1), 102–107. https://doi.org/10.1016/j.bbrc.2012.02.122.

(39) Guo, C.; Masin, M.; Qureshi, O. S.; Murrell-Lagnado, R. D. Evidence for Functional P2X4/P2X7 Heteromeric Receptors. *Molecular Pharmacology* **2007**, *72* (6), 1447–1456. https://doi.org/10.1124/mol.107.035980.

(40) Antonio, L.; Stewart, A.; Xu, X.; Varanda, W.; Murrell-Lagnado, R.; Edwardson, J. P2X4 Receptors Interact with Both P2X2 and P2X7 Receptors in the Form of Homotrimers. *British Journal of Pharmacology* **2011**, *163* (5), 1069–1077. https://doi.org/10.1111/j.1476-5381.2011.01303.x.

(41) Trang, M.; Schmalzing, G.; Müller, C. E.; Markwardt, F. Dissection of P2X4 and P2X7 Receptor Current Components in BV-2 Microglia. *International Journal of Molecular Sciences* **2020**, *21* (22), 8489. https://doi.org/10.3390/ijms21228489.

(42) Jacobson, K. A.; Delicado, E. G.; Gachet, C.; Kennedy, C.; von Kügelgen, I.; Li, B.; Miras-Portugal, M. T.; Novak, I.; Schöneberg, T.; Perez-Sen, R.; et al. Update of P2Y

Receptor Pharmacology: IUPHAR Review 27. *British Journal of Pharmacology* **2020**, *177* (11), 2413–2433. https://doi.org/10.1111/bph.15005.

(43) Conroy, S.; Kindon, N.; Kellam, B.; Stocks, M. J. Drug-like Antagonists of P2Y Receptors—From Lead Identification to Drug Development. *Journal of Medicinal Chemistry* **2016**, *59* (22), 9981–10005. https://doi.org/10.1021/acs.jmedchem.5b01972.

(44) von Kügelgen, I.; Hoffmann, K. Pharmacology and Structure of P2Y Receptors. *Neuropharmacology* **2016**, *104*, 50–61. https://doi.org/10.1016/j.neuropharm.2015.10.030.

(45) Müller, C. E.; Namasivayam, V. Recommended Tool Compounds and Drugs for Blocking P2X and P2Y Receptors. *Purinergic Signalling* **2021**, *17* (4), 633–648. https://doi.org/10.1007/s11302-021-09813-7.

(46) Pasternack, S. M.; von Kügelgen, I.; Aboud, K. A.; Lee, Y.-A.; Rüschendorf, F.; Voss, K.; Hillmer, A. M.; Molderings, G. J.; Franz, T.; Ramirez, A.; et al. G Protein–Coupled Receptor P2Y5 and Its Ligand LPA Are Involved in Maintenance of Human Hair Growth. *Nature Genetics* **2008**, *40* (3), 329–334. https://doi.org/10.1038/ng.84.

(47) Yanagida, K.; Masago, K.; Nakanishi, H.; Kihara, Y.; Hamano, F.; Tajima, Y.; Taguchi, R.; Shimizu, T.; Ishii, S. Identification and Characterization of a Novel Lysophosphatidic Acid Receptor, P2y5/LPA6. *The Journal of Biological Chemistry* **2009**, *284* (26), 17731–17741. https://doi.org/10.1074/jbc.M808506200.

(48) Lovászi, M.; Branco Haas, C.; Antonioli, L.; Pacher, P.; Haskó, G. The Role of P2Y Receptors in Regulating Immunity and Metabolism. *Biochemical Pharmacology* **2021**, *187*, 114419. https://doi.org/10.1016/j.bcp.2021.114419.

(49) Puthanveedu, M.; Knight, R.; Stocks, M. J. Drug-like Antagonists of P2Y Receptor Subtypes: An Update. *Journal of Medicinal Chemistry* **2025**, *68* (9), 9057–9083. https://doi.org/10.1021/acs.jmedchem.5c00249.

(50) Kim, H. S.; Ohno, M.; Xu, B.; Kim, H. O.; Choi, Y.; Ji, X. D.; Maddileti, S.; Marquez, V. E.; Harden, T. K.; Jacobson, K. A. 2-Substitution of Adenine Nucleotide Analogues Containing a Bicyclo[3.1.0]Hexane Ring System Locked in a Northern Conformation: Enhanced Potency as P2Y1 Receptor Antagonists. *Journal of Medicinal Chemistry* **2003**, *46* (23), 4974–4987. https://doi.org/10.1021/jm030127+.

(51) Chen, X.-Q.; Stefanski, K.; Shen, H.; Huang, C.; Caporuscio, C.; Yang, W.; Lam, P.; Su, C.; Gudmundsson, O.; Hageman, M. Oral Delivery of Highly Lipophilic Poorly Water-Soluble Drugs: Spray-Dried Dispersions to Improve Oral Absorption and Enable High-Dose Toxicology Studies of a P2Y1 Antagonist. *Journal of Pharmaceutical Sciences* **2014**, *103* (12), 3924–3931. https://doi.org/10.1002/jps.24199.

(52) Kindon, N.; Davis, A.; Dougall, I.; Dixon, J.; Johnson, T.; Walters, I.; Thom, S.; McKechnie, K.; Meghani, P.; Stocks, M. J. From UTP to AR-C118925, the Discovery of a Potent Non Nucleotide Antagonist of the P2Y2 Receptor. *Bioorganic & Medicinal Chemistry Letters* **2017**, *27* (21), 4849–4853. https://doi.org/10.1016/j.bmcl.2017.09.043.

(53) Neumann, A.; Müller, C. E.; Namasivayam, V. P2Y1-like Nucleotide Receptors—Structures, Molecular Modeling, Mutagenesis, and Oligomerization. *WIREs Computational Molecular Science* **2020**, *10* (4), e1464. https://doi.org/10.1002/wcms.1464.

(54) Robichaud, J.; Fournier, J.-F.; Gagné, S.; Gauthier, J. Y.; Hamel, M.; Han, Y.; Hénault, M.; Kargman, S.; Levesque, J.-F.; Mamane, Y.; et al. Applying the Pro-Drug

Approach to Afford Highly Bioavailable Antagonists of P2Y14. *Bioorganic & Medicinal Chemistry Letters* **2011**, *21* (14), 4366–4368. https://doi.org/10.1016/j.bmcl.2010.12.113.

(55) Anwar, S.; Pons, V.; Rivest, S. Microglia Purinoceptor P2Y6: An Emerging Therapeutic Target in CNS Diseases. *Cells* **2020**, *9* (7), 1595. https://doi.org/10.3390/cells9071595.

(56) Dundee, J. M.; Brown, G. C. The Microglial P2Y6 Receptor as a Therapeutic Target for Neurodegenerative Diseases. *Translational Neurodegeneration* **2024**, *13* (1), 47. https://doi.org/10.1186/s40035-024-00438-5.

(57) Girard, M.; Bellefeuille, S. D.; Eiselt, É.; Arguin, G.; Longpré, J.-M.; Sarret, P.; Gendron, F.-P. Ligand-Dependent Intracellular Trafficking of the G Protein-Coupled P2Y6 Receptor. *Biochimica et Biophysica Acta (BBA) - Molecular Cell Research* **2023**, *1870* (5), 119476. https://doi.org/10.1016/j.bbamcr.2023.119476.

(58) Puigdellívol, M.; Milde, S.; Vilalta, A.; Cockram, T. O. J.; Allendorf, D. H.; Lee, J. Y.; Dundee, J. M.; Pampuščenko, K.; Borutaite, V.; Nuthall, H. N.; et al. The Microglial P2Y6 Receptor Mediates Neuronal Loss and Memory Deficits in Neurodegeneration. *Cell Reports* **2021**, *37* (13), 110148. https://doi.org/10.1016/j.celrep.2021.110148.

(59) Umpierre, A. D.; Li, B.; Ayasoufi, K.; Simon, W. L.; Zhao, S.; Xie, M.; Thyen, G.; Hur, B.; Zheng, J.; Liang, Y.; et al. Microglial P2Y6 Calcium Signaling Promotes Phagocytosis and Shapes Neuroimmune Responses in Epileptogenesis. *Neuron* **2024**, *112* (12), 1959-1977.e10. https://doi.org/10.1016/j.neuron.2024.03.017.

(60) Ivanov, A. A.; Costanzi, S.; Jacobson, K. A. Defining the Nucleotide Binding Sites of P2Y Receptors Using Rhodopsin-Based Homology Modeling. *Journal of Computer-Aided Molecular Design* **2006**, *20* (7), 417–426. https://doi.org/10.1007/s10822-006-9054-2.

(61) Gao, C.; Jiang, J.; Tan, Y.; Chen, S. Microglia in Neurodegenerative Diseases: Mechanism and Potential Therapeutic Targets. *Signal Transduction and Targeted Therapy* **2023**, *8* (1), 359. https://doi.org/10.1038/s41392-023-01588-0.

(62) Kim, S. U.; de Vellis, J. Microglia in Health and Disease. *Journal of Neuroscience Research* **2005**, *81* (3), 302–313. https://doi.org/10.1002/jnr.20562.

(63) Muzio, L.; Viotti, A.; Martino, G. Microglia in Neuroinflammation and Neurodegeneration: From Understanding to Therapy. *Frontiers in Neuroscience* **2021**, *15*, 742065. https://doi.org/10.3389/fnins.2021.742065.

(64) Bachiller, S.; Jiménez-Ferrer, I.; Paulus, A.; Yang, Y.; Swanberg, M.; Deierborg, T.; Boza-Serrano, A. Microglia in Neurological Diseases: A Road Map to Brain-Disease Dependent-Inflammatory Response. *Frontiers in Cellular Neuroscience* **2018**, *12*, 00488. https://doi.org/10.3389/fncel.2018.00488.

(65) Biswas, K. Microglia Mediated Neuroinflammation in Neurodegenerative Diseases: A Review on the Cell Signaling Pathways Involved in Microglial Activation. *Journal of Neuroimmunology* **2023**, *383*, 578180. https://doi.org/10.1016/j.jneuroim.2023.578180.

(66) Smolders, S. M.-T.; Kessels, S.; Vangansewinkel, T.; Rigo, J.-M.; Legendre, P.; Brône, B. Microglia: Brain Cells on the Move. *Progress in Neurobiology* **2019**, *178*, 101612. https://doi.org/10.1016/j.pneurobio.2019.04.001.

(67) Franco-Bocanegra, D. K.; McAuley, C.; Nicoll, J. A. R.; Boche, D. Molecular Mechanisms of Microglial Motility: Changes in Ageing and Alzheimer's Disease. *Cells* **2019**, *8* (6), 639. https://doi.org/10.3390/cells8060639.

(68) Paolicelli, R. C.; Sierra, A.; Stevens, B.; Tremblay, M.-E.; Aguzzi, A.; Ajami, B.; Amit, I.; Audinat, E.; Bechmann, I.; Bennett, M.; et al. Microglia States and Nomenclature: A Field at Its Crossroads. *Neuron* **2022**, *110* (21), 3458–3483. https://doi.org/10.1016/j.neuron.2022.10.020.

(69) Li, Z.; Li, W.; Li, Q.; Tang, M. Extracellular Nucleotides and Adenosine Regulate Microglial Motility and Their Role in Cerebral Ischemia. *Acta Pharmaceutica Sinica B* **2013**, *3* (4), 205–212. https://doi.org/10.1016/j.apsb.2013.06.003.

(70) Hong, S.; Dissing-Olesen, L.; Stevens, B. New Insights on the Role of Microglia in Synaptic Pruning in Health and Disease. *Current Opinion in Neurobiology* **2016**, *36*, 128–134. https://doi.org/10.1016/j.conb.2015.12.004.

(71) Faust, T. E.; Gunner, G.; Schafer, D. P. Mechanisms Governing Activity-Dependent Synaptic Pruning in the Developing Mammalian CNS. *Nature Reviews Neuroscience* **2021**, *22* (11), 657–673. https://doi.org/10.1038/s41583-021-00507-y.

(72) Hong, S.; Beja-Glasser, V. F.; Nfonoyim, B. M.; Frouin, A.; Li, S.; Ramakrishnan, S.; Merry, K. M.; Shi, Q.; Rosenthal, A.; Barres, B. A.; et al. Complement and Microglia Mediate Early Synapse Loss in Alzheimer Mouse Models. *Science* **2016**, *352* (6286), 712–716. https://doi.org/10.1126/science.aad8373.

(73) Andrews, S. J.; Renton, A. E.; Fulton-Howard, B.; Podlesny-Drabiniok, A.; Marcora, E.; Goate, A. M. The Complex Genetic Architecture of Alzheimer's Disease: Novel Insights and Future Directions. *eBioMedicine* **2023**, *90*, 104511. https://doi.org/10.1016/j.ebiom.2023.104511.

(74) Zhang, W.; Phillips, K.; Wielgus, A. R.; Liu, J.; Albertini, A.; Zucca, F. A.; Faust, R.; Qian, S. Y.; Miller, D. S.; Chignell, C. F.; et al. Neuromelanin Activates Microglia and Induces Degeneration of Dopaminergic Neurons: Implications for Progression of Parkinson's Disease. *Neurotoxicity Research* **2011**, *19* (1), 63–72. https://doi.org/10.1007/s12640-009-9140-z.

(75) Carracedo, S.; Launay, A.; Dechelle-Marquet, P.-A.; Faivre, E.; Blum, D.; Delarasse, C.; Boué-Grabot, E. Purinergic-Associated Immune Responses in Neurodegenerative Diseases. *Progress in Neurobiology* **2024**, *243*, 102693. https://doi.org/10.1016/j.pneurobio.2024.102693.

(76) Burnstock, G.; Krügel, U.; Abbracchio, M. P.; Illes, P. Purinergic Signalling: From Normal Behaviour to Pathological Brain Function. *Progress in Neurobiology* **2011**, *95* (2), 229–274. https://doi.org/10.1016/j.pneurobio.2011.08.006.

(77) Shieh, C.-H.; Heinrich, A.; Serchov, T.; van Calker, D.; Biber, K. P2X7-Dependent, but Differentially Regulated Release of IL-6, CCL2, and TNF-α in Cultured Mouse Microglia. *Glia* **2014**, *62* (4), 592–607. https://doi.org/10.1002/glia.22628.

(78) Haynes, S. E.; Hollopeter, G.; Yang, G.; Kurpius, D.; Dailey, M. E.; Gan, W.-B.; Julius, D. The P2Y12 Receptor Regulates Microglial Activation by Extracellular Nucleotides. *Nature Neuroscience* **2006**, *9* (12), 1512–1519. https://doi.org/10.1038/nn1805.

(79) Davalos, D.; Grutzendler, J.; Yang, G.; Kim, J. V.; Zuo, Y.; Jung, S.; Littman, D. R.; Dustin, M. L.; Gan, W.-B. ATP Mediates Rapid Microglial Response to Local Brain Injury in Vivo. *Nature Neuroscience* **2005**, *8* (6), 752–758. https://doi.org/10.1038/nn1472.

(80) Illes, P.; Rubini, P.; Ulrich, H.; Zhao, Y.; Tang, Y. Regulation of Microglial Functions by Purinergic Mechanisms in the Healthy and Diseased CNS. *Cells* **2020**, *9* (5), 1108. https://doi.org/10.3390/cells9051108.

(81) Burnstock, G.; Knight, G. E. The Potential of P2X7 Receptors as a Therapeutic Target, Including Inflammation and Tumour Progression. *Purinergic Signalling* **2018**, *14* (1), 1–18. https://doi.org/10.1007/s11302-017-9593-0.

(82) Li, F.; Wang, L.; Li, J.-W.; Gong, M.; He, L.; Feng, R.; Dai, Z.; Li, S.-Q. Hypoxia Induced Amoeboid Microglial Cell Activation in Postnatal Rat Brain Is Mediated by ATP Receptor P2X4. *BMC Neuroscience* **2011**, *12* (1), 111. https://doi.org/10.1186/1471-2202-12-111.

(83) He, W.; Wang, Q.; Sha, W.; Wang, L.; Li, D.; Chen, G. P2X4 Inhibition Reduces Microglia Inflammation and Apoptosis by NLRP3 and Improves Nervous System Defects in Rat Brain Trauma Model. *Journal of Clinical Neuroscience* **2022**, *99*, 224–232. https://doi.org/10.1016/j.jocn.2022.03.009.

(84) Zhang, T.; Zhang, M.; Cui, S.; Liang, W.; Jia, Z.; Guo, F.; Ou, W.; Wu, Y.; Zhang, S. The Core of Maintaining Neuropathic Pain: Crosstalk between Glial Cells and Neurons (Neural Cell Crosstalk at Spinal Cord). *Brain and Behavior* **2023**, *13* (2), e2868. https://doi.org/10.1002/brb3.2868.

(85) Hua, J.; Garcia de Paco, E.; Linck, N.; Maurice, T.; Desrumaux, C.; Manoury, B.; Rassendren, F.; Ulmann, L. Microglial P2X4 Receptors Promote ApoE Degradation and Contribute to Memory Deficits in Alzheimer's Disease. *Cellular and Molecular Life Sciences* **2023**, *80* (5), 138. https://doi.org/10.1007/s00018-023-04784-x.

(86) Ma, J.; Gao, J.; Niu, M.; Zhang, X.; Wang, J.; Xie, A. P2X4R Overexpression Upregulates Interleukin-6 and Exacerbates 6-OHDA-Induced Dopaminergic Degeneration in a Rat Model of PD. *Frontiers in Aging Neuroscience* **2020**, *12*. https://doi.org/10.3389/fnagi.2020.580068.

(87) Montilla, A.; Mata, G. P.; Matute, C.; Domercq, M. Contribution of P2X4 Receptors to CNS Function and Pathophysiology. *International Journal of Molecular Sciences* **2020**, *21* (15), 5562. https://doi.org/10.3390/ijms21155562.

(88) Zabala, A.; Vazquez-Villoldo, N.; Rissiek, B.; Gejo, J.; Martin, A.; Palomino, A.; Perez-Samartín, A.; Pulagam, K. R.; Lukowiak, M.; Capetillo-Zarate, E.; et al. P2X4 Receptor Controls Microglia Activation and Favors Remyelination in Autoimmune Encephalitis. *EMBO Molecular Medicine* **2018**, *10* (8), e8743. https://doi.org/10.15252/emmm.201708743.

(89) Varma, R.; Chai, Y.; Troncoso, J.; Gu, J.; Xing, H.; Stojilkovic, S. S.; Mattson, M. P.; Haughey, N. J. Amyloid-β Induces a Caspase-Mediated Cleavage of P2X4 to Promote Purinotoxicity. *NeuroMolecular Medicine* **2009**, *11* (2), 63–75. https://doi.org/10.1007/s12017-009-8073-2.

(90) Sharp, A. J.; Polak, P. E.; Simonini, V.; Lin, S. X.; Richardson, J. C.; Bongarzone, E. R.; Feinstein, D. L. P2x7 Deficiency Suppresses Development of Experimental Autoimmune Encephalomyelitis. *Journal of Neuroinflammation* **2008**, *5* (1), 33. https://doi.org/10.1186/1742-2094-5-33.

(91) Carmo, M. R. S.; Menezes, A. P. F.; Nunes, A. C. L.; Pliássova, A.; Rolo, A. P.; Palmeira, C. M.; Cunha, R. A.; Canas, P. M.; Andrade, G. M. The P2X7 Receptor Antagonist Brilliant Blue G Attenuates Contralateral Rotations in a Rat Model of Parkinsonism through a Combined Control of Synaptotoxicity, Neurotoxicity and

Gliosis. *Neuropharmacology* **2014**, *81*, 142–152. https://doi.org/10.1016/j.neuropharm.2014.01.045.

(92) Rampe, D.; Wang, L.; Ringheim, G. E. P2X7 Receptor Modulation of β-Amyloid- and LPS-Induced Cytokine Secretion from Human Macrophages and Microglia. *Journal of Neuroimmunology* **2004**, *147* (1), 56–61. https://doi.org/10.1016/j.jneuroim.2003.10.014.

(93) McLarnon, J. G.; Ryu, J. K.; Walker, D. G.; Choi, H. B. Upregulated Expression of Purinergic P2X7 Receptor in Alzheimer Disease and Amyloid-β Peptide-Treated Microglia and in Peptide-Injected Rat Hippocampus. *Journal of Neuropathology & Experimental Neurology* **2006**, *65* (11), 1090–1097. https://doi.org/10.1097/01.jnen.0000240470.97295.d3.

(94) Vázquez-Villoldo, N.; Domercq, M.; Martín, A.; Llop, J.; Gómez-Vallejo, V.; Matute, C. P2X4 Receptors Control the Fate and Survival of Activated Microglia. *Glia* **2014**, *62* (2), 171–184. https://doi.org/10.1002/glia.22596.

(95) Toulme, E.; Khakh, B. S. Imaging P2X4 Receptor Lateral Mobility in Microglia. *Journal of Biological Chemistry* **2012**, *287* (18), 14734–14748. https://doi.org/10.1074/jbc.M111.329334.

(96) Tsuda, M.; Shigemoto-Mogami, Y.; Koizumi, S.; Mizokoshi, A.; Kohsaka, S.; Salter, M. W.; Inoue, K. P2X4 Receptors Induced in Spinal Microglia Gate Tactile Allodynia after Nerve Injury. *Nature* **2003**, *424* (6950), 778–783. https://doi.org/10.1038/nature01786.

(97) Miyanishi, M.; Tada, K.; Koike, M.; Uchiyama, Y.; Kitamura, T.; Nagata, S. Identification of Tim4 as a Phosphatidylserine Receptor. *Nature* **2007**, *450* (7168), 435–439. https://doi.org/10.1038/nature06307.

(98) Domercq, M.; Matute, C. Targeting P2X4 and P2X7 Receptors in Multiple Sclerosis. *Current Opinion in Pharmacology* **2019**, *47*, 119–125. https://doi.org/10.1016/j.coph.2019.03.010.

(99) Savio, L. E. B.; de Andrade Mello, P.; da Silva, C. G.; Coutinho-Silva, R. The P2X7 Receptor in Inflammatory Diseases: Angel or Demon? *Frontiers in Pharmacology* **2018**, *9*, 52. https://doi.org/10.3389/fphar.2018.00052.

(100) Oliveira-Giacomelli, Á.; Petiz, L. L.; Andrejew, R.; Turrini, N.; Silva, J. B.; Sack, U.; Ulrich, H. Role of P2X7 Receptors in Immune Responses During Neurodegeneration. *Frontiers in Cellular Neuroscience* **2021**, *15*, 662935. https://doi.org/10.3389/fncel.2021.662935.

(101) Fan, X.; Ma, W.; Zhang, Y.; Zhang, L. P2X7 Receptor (P2X7R) of Microglia Mediates Neuroinflammation by Regulating (NOD)-Like Receptor Protein 3 (NLRP3) Inflammasome-Dependent Inflammation After Spinal Cord Injury. *Medical Science Monitor : International Medical Journal of Experimental and Clinical Research* **2020**, *26*, e925491. https://doi.org/10.12659/MSM.925491.

(102) He, Y.; Taylor, N.; Fourgeaud, L.; Bhattacharya, A. The Role of Microglial P2X7: Modulation of Cell Death and Cytokine Release. *Journal of Neuroinflammation* **2017**, *14* (1), 135. https://doi.org/10.1186/s12974-017-0904-8.

(103) Tewari, M.; Michalski, S.; Egan, T. M. Modulation of Microglial Function by ATP-Gated P2X7 Receptors: Studies in Rat, Mice and Human. *Cells* **2024**, *13* (2), 161. https://doi.org/10.3390/cells13020161.

(104) Langfelder, A.; Okonji, E.; Deca, D.; Wei, W.-C.; Glitsch, M. D. Extracellular Acidosis Impairs P2Y Receptor-Mediated Ca2+ Signalling and Migration of Microglia. *Cell Calcium* **2015**, *57* (4), 247–256. https://doi.org/10.1016/j.ceca.2015.01.004.

(105) Koizumi, S.; Shigemoto-Mogami, Y.; Nasu-Tada, K.; Shinozaki, Y.; Ohsawa, K.; Tsuda, M.; Joshi, B. V.; Jacobson, K. A.; Kohsaka, S.; Inoue, K. UDP Acting at P2Y6 Receptors Is a Mediator of Microglial Phagocytosis. *Nature* **2007**, *446* (7139), 1091–1095. https://doi.org/10.1038/nature05704.

(106) Inoue, K. UDP Facilitates Microglial Phagocytosis Through P2Y6 Receptors. *Cell Adhesion & Migration* **2007**, *1* (3), 131–132. https://doi.org/10.4161/cam.1.3.4937.

(107) Yang, X.; Lou, Y.; Liu, G.; Wang, X.; Qian, Y.; Ding, J.; Chen, S.; Xiao, Q. Microglia P2Y6 Receptor Is Related to Parkinson's Disease through Neuroinflammatory Process. *Journal of Neuroinflammation* **2017**, *14* (1), 38. https://doi.org/10.1186/s12974-017-0795-8.

(108) Neher, J. J.; Neniskyte, U.; Hornik, T.; Brown, G. C. Inhibition of UDP/P2Y6 Purinergic Signaling Prevents Phagocytosis of Viable Neurons by Activated Microglia in Vitro and in Vivo. *Glia* **2014**, *62* (9), 1463–1475. https://doi.org/10.1002/glia.22693.

(109) Dane, C.; Stokes, L.; Jorgensen, W. T. P2X Receptor Antagonists and Their Potential as Therapeutics: A Patent Review (2010-2021). *Expert Opinion on Therapeutic Patents* **2022**, *32* (7), 769–790. https://doi.org/10.1080/13543776.2022.2069010.

(110) Abdel-Magid, A. F. Allosteric Modulators: An Emerging Concept in Drug Discovery. *ACS Medicinal Chemistry Letters* **2015**, *6* (2), 104–107. https://doi.org/10.1021/ml5005365.

(111) Jacobson, K. A.; Müller, C. E. Medicinal Chemistry of Adenosine, P2Y and P2X Receptors. *Neuropharmacology* **2016**, *104*, 31–49. https://doi.org/10.1016/j.neuropharm.2015.12.001.

(112) Stokes, L.; Bidula, S.; Bibič, L.; Allum, E. To Inhibit or Enhance? Is There a Benefit to Positive Allosteric Modulation of P2X Receptors? *Frontiers in Pharmacology* **2020**, *11*, 627. https://doi.org/10.3389/fphar.2020.00627.

(113) Müller, C. E.; Namasivayam, V. Agonists, Antagonists, and Modulators of P2X7 Receptors. In *The P2X7 Receptor: Methods and Protocols*; Nicke, A., Ed.; Springer US: New York, NY, 2022; pp 31–52. https://doi.org/10.1007/978-1-0716-2384-8_2.

(114) Abdelrahman, A.; Namasivayam, V.; Hinz, S.; Schiedel, A. C.; Köse, M.; Burton, M.; El-Tayeb, A.; Gillard, M.; Bajorath, J.; de Ryck, M.; et al. Characterization of P2X4 Receptor Agonists and Antagonists by Calcium Influx and Radioligand Binding Studies. *Biochemical Pharmacology* **2017**, *125*, 41–54. https://doi.org/10.1016/j.bcp.2016.11.016.

(115) Tang, M.; Hu, X.; Wang, Y.; Yao, X.; Zhang, W.; Yu, C.; Cheng, F.; Li, J.; Fang, Q. Ivermectin, a Potential Anticancer Drug Derived from an Antiparasitic Drug. *Pharmacological Research* **2021**, *163*, 105207. https://doi.org/10.1016/j.phrs.2020.105207.

(116) Csóka, B.; Németh, Z. H.; Szabó, I.; Davies, D. L.; Varga, Z. V.; Pálóczi, J.; Falzoni, S.; Di Virgilio, F.; Muramatsu, R.; Yamashita, T.; et al. Macrophage P2X4 Receptors Augment Bacterial Killing and Protect against Sepsis. *JCI Insight* **2018**, *3* (11), e99431. https://doi.org/10.1172/jci.insight.99431.

(117) Csóka, B.; Németh, Z. H.; Törő, G.; Idzko, M.; Zech, A.; Koscsó, B.; Spolarics, Z.; Antonioli, L.; Cseri, K.; Erdélyi, K.; et al. Extracellular ATP Protects against Sepsis through Macrophage P2X7 Purinergic Receptors by Enhancing Intracellular Bacterial Killing. *The FASEB Journal* **2015**, *29* (9), 3626–3637. https://doi.org/10.1096/fj.15-272450.

(118) Draganov, D.; Gopalakrishna-Pillai, S.; Chen, Y.-R.; Zuckerman, N.; Moeller, S.; Wang, C.; Ann, D.; Lee, P. P. Modulation of P2X4/P2X7/Pannexin-1 Sensitivity to Extracellular ATP via Ivermectin Induces a Non-Apoptotic and Inflammatory Form of Cancer Cell Death. *Scientific Reports* **2015**, *5* (1), 16222. https://doi.org/10.1038/srep16222.

(119) Bidula, S.; Dhuna, K.; Helliwell, R.; Stokes, L. Positive Allosteric Modulation of P2X7 Promotes Apoptotic Cell Death over Lytic Cell Death Responses in Macrophages. *Cell Death & Disease* **2019**, *10* (12), 882. https://doi.org/10.1038/s41419-019-2110-3.

(120) Mehta, N.; Kaur, M.; Singh, M.; Chand, S.; Vyas, B.; Silakari, P.; Bahia, M. S.; Silakari, O. Purinergic Receptor P2X7: A Novel Target for Anti-Inflammatory Therapy. *Bioorganic & Medicinal Chemistry* **2014**, *22* (1), 54–88. https://doi.org/10.1016/j.bmc.2013.10.054.

(121) Ali, Z.; Laurijssens, B.; Ostenfeld, T.; McHugh, S.; Stylianou, A.; Scott-Stevens, P.; Hosking, L.; Dewit, O.; Richardson, J. C.; Chen, C. Pharmacokinetic and Pharmacodynamic Profiling of a P2X7 Receptor Allosteric Modulator GSK1482160 in Healthy Human Subjects. *British Journal of Clinical Pharmacology* **2013**, *75* (1), 197–207. https://doi.org/10.1111/j.1365-2125.2012.04320.x.

(122) Recourt, K.; van der Aart, J.; Jacobs, G.; de Kam, M.; Drevets, W.; van Nueten, L.; Kanhai, K.; Siebenga, P.; Zuiker, R.; Ravenstijn, P.; et al. Characterisation of the Pharmacodynamic Effects of the P2X7 Receptor Antagonist JNJ-54175446 Using an Oral Dexamphetamine Challenge Model in Healthy Males in a Randomised, Double-Blind, Placebo-Controlled, Multiple Ascending Dose Trial. *Journal of Psychopharmacology* **2020**, *34* (9), 1030–1042. https://doi.org/10.1177/0269881120914206.

(123) Zarrinmayeh, H.; Territo, P. R. Purinergic Receptors of the Central Nervous System: Biology, PET Ligands, and Their Applications. *Molecular Imaging* **2020**, *19*, 1536012120927609. https://doi.org/10.1177/1536012120927609.

(124) Janssen, B.; Vugts, D. J.; Wilkinson, S. M.; Ory, D.; Chalon, S.; Hoozemans, J. J. M.; Schuit, R. C.; Beaino, W.; Kooijman, E. J. M.; van den Hoek, J.; et al. Identification of the Allosteric P2X7 Receptor Antagonist [11C]SMW139 as a PET Tracer of Microglial Activation. *Scientific Reports* **2018**, *8* (1), 6580. https://doi.org/10.1038/s41598-018-24814-0.

(125) Berdyyeva, T.; Xia, C.; Taylor, N.; He, Y.; Chen, G.; Huang, C.; Zhang, W.; Kolb, H.; Letavic, M.; Bhattacharya, A.; et al. PET Imaging of the P2X7 Ion Channel with a Novel Tracer [18F]JNJ-64413739 in a Rat Model of Neuroinflammation. *Molecular Imaging and Biology* **2019**, *21* (5), 871–878. https://doi.org/10.1007/s11307-018-01313-2.

(126) Mikkelsen, J. D.; Aripaka, S. S.; Kaad, S.; Pazarlar, B. A.; Pinborg, L.; Finsen, B.; Varrone, A.; Bang-Andersen, B.; Bastlund, J. F. Characterization of the Novel P2X7 Receptor Radioligand [3H]JNJ-64413739 in Human Brain Tissue. *ACS Chemical Neuroscience* **2023**, *14* (1), 111–118. https://doi.org/10.1021/acschemneuro.2c00561.

(127) Wang, Y.; Liao, W.; Wang, L.; Li, J.; Huang, D.; Cheng, W.; Tian, J.; Luan, P. Advance and Prospect of Positron Emission Tomography in Alzheimer's Disease Research. *Molecular Psychiatry* **2025**, 1–11. https://doi.org/10.1038/s41380-025-03081-2.

(128) Hagens, M. H. J.; Golla, S. S. V.; Janssen, B.; Vugts, D. J.; Beaino, W.; Windhorst, A. D.; O'Brien-Brown, J.; Kassiou, M.; Schuit, R. C.; Schwarte, L. A.; et al. The P2X7 Receptor Tracer [11C]SMW139 as an in Vivo Marker of Neuroinflammation in Multiple Sclerosis: A First-in Man Study. *European Journal of Nuclear Medicine and Molecular Imaging* **2020**, *47* (2), 379–389. https://doi.org/10.1007/s00259-019-04550-x.

(129) Alzghool, O. M.; Aarnio, R.; Helin, J. S.; Wahlroos, S.; Keller, T.; Matilainen, M.; Solis, J.; Danon, J. J.; Kassiou, M.; Snellman, A.; et al. Glial Reactivity in a Mouse Model of Beta-Amyloid Deposition Assessed by PET Imaging of P2X7 Receptor and TSPO Using [11C]SMW139 and [18F]F-DPA. *EJNMMI Research* **2024**, *14* (1), 25. https://doi.org/10.1186/s13550-024-01085-7.

(130) Baxter, A.; Bent, J.; Bowers, K.; Braddock, M.; Brough, S.; Fagura, M.; Lawson, M.; McInally, T.; Mortimore, M.; Robertson, M.; et al. Hit-to-Lead Studies: The Discovery of Potent Adamantane Amide P2X7 Receptor Antagonists. *Bioorganic & Medicinal Chemistry Letters* **2003**, *13* (22), 4047–4050. https://doi.org/10.1016/j.bmcl.2003.08.034.

(131) O'Brien-Brown, J.; Jackson, A.; Reekie, T. A.; Barron, M. L.; Werry, E. L.; Schiavini, P.; McDonnell, M.; Munoz, L.; Wilkinson, S.; Noll, B.; et al. Discovery and Pharmacological Evaluation of a Novel Series of Adamantyl Cyanoguanidines as P2X7 Receptor Antagonists. *European Journal of Medicinal Chemistry* **2017**, *130*, 433–439. https://doi.org/10.1016/j.ejmech.2017.02.060.

(132) Donnelly-Roberts, D. L.; Namovic, M. T.; Surber, B.; Vaidyanathan, S. X.; Perez-Medrano, A.; Wang, Y.; Carroll, W. A.; Jarvis, M. F. [3H]A-804598 ([3H]2-Cyano-1-[(1S)-1-Phenylethyl]-3-Quinolin-5-Ylguanidine) Is a Novel, Potent, and Selective Antagonist Radioligand for P2X7 Receptors. *Neuropharmacology* **2009**, *56* (1), 223–229. https://doi.org/10.1016/j.neuropharm.2008.06.012.

(133) Dane, C.; Cumbers, G. A.; Allen, B.; Montgomery, A. P.; Danon, J. J.; Kassiou, M. Unlocking Therapeutic Potential: The Role of Adamantane in Drug Discovery. *Australian Journal of Chemistry* **2024**, *77* (8), CH24075. https://doi.org/10.1071/CH24075.

(134) Nelson, D. W.; Sarris, K.; Kalvin, D. M.; Namovic, M. T.; Grayson, G.; Donnelly-Roberts, D. L.; Harris, R.; Honore, P.; Jarvis, M. F.; Faltynek, C. R.; et al. Structure−Activity Relationship Studies on N′-Aryl Carbohydrazide P2X7 Antagonists. *Journal of Medicinal Chemistry* **2008**, *51* (10), 3030–3034. https://doi.org/10.1021/jm701516f.

(135) Kelly, M. G.; Kincaid, J. Bicycloheteroaryl Compounds as P2X7 Modulators and Uses Thereof. US7297700B2, 2007.

(136) Tsuzuki, N.; Hama, T.; Hibi, T.; Konishi, R.; Futaki, S.; Kitagawa, K. Adamantane as a Brain-Directed Drug Carrier for Poorly Absorbed Drug: Antinociceptive Effects of [D-Ala2]Leu-Enkephalin Derivatives Conjugated with the 1-Adamantane Moiety. *Biochemical Pharmacology* **1991**, *41* (4), R5-8. https://doi.org/10.1016/0006-2952(91)90616-d.

(137) Tsuzuki, N.; Hama, T.; Kawada, M.; Hasui, A.; Konishi, R.; Shiwa, S.; Ochi, Y.; Futaki, S.; Kitagawa, K. Adamantane as a Brain-Directed Drug Carrier for Poorly Absorbed Drug. 2. AZT Derivatives Conjugated with the 1-Adamantane Moiety. *Journal of Pharmaceutical Sciences* **1994**, *83* (4), 481–484. https://doi.org/10.1002/jps.2600830407.

(138) Dane, C.; Montgomery, A. P.; Kassiou, M. The Adamantane Scaffold: Beyond a Lipophilic Moiety. *European Journal of Medicinal Chemistry* **2025**, *291*, 117592. https://doi.org/10.1016/j.ejmech.2025.117592.

(139) Jacobson, K. A.; Giancotti, L. A.; Lauro, F.; Mufti, F.; Salvemini, D. Treatment of Chronic Neuropathic Pain: Purine Receptor Modulation. *Pain* **2020**, *161* (7), 1425–1441. https://doi.org/10.1097/j.pain.0000000000001857.

(140) Matsumura, Y.; Yamashita, T.; Sasaki, A.; Nakata, E.; Kohno, K.; Masuda, T.; Tozaki-Saitoh, H.; Imai, T.; Kuraishi, Y.; Tsuda, M.; et al. A Novel P2X4 Receptor-Selective Antagonist Produces Anti-Allodynic Effect in a Mouse Model of Herpetic Pain. *Scientific Reports* **2016**, *6*, 32461. https://doi.org/10.1038/srep32461.

(141) Werner, S.; Mesch, S.; Hillig, R. C.; ter Laak, A.; Klint, J.; Neagoe, I.; Laux-Biehlmann, A.; Dahllöf, H.; Bräuer, N.; Puetter, V.; et al. Discovery and Characterization of the Potent and Selective P2X4 Inhibitor N-[4-(3-Chlorophenoxy)-3-Sulfamoylphenyl]-2-Phenylacetamide (BAY-1797) and Structure-Guided Amelioration of Its CYP3A4 Induction Profile. *Journal of Medicinal Chemistry* **2019**, *62* (24), 11194–11217. https://doi.org/10.1021/acs.jmedchem.9b01304.

(142) Werner, S.; Mesch, S.; Bräuer, N.; Pook, E.; Dahllöf, H.; Nubbemeyer, R.; Osmers, M.; Kalthof, B. Aromatic Sulfonamide Derivatives. WO2016198374, 2016.

(143) Werner, S.; Mesch, S.; Cleve, A.; Bräuer, N.; Herbert, S.; Koch, M.; Dahllöf, H.; Osmers, M.; Hardaker, E.; Lishchynskyi, A. Aromatic Sulfonamide Derivatives. WO2017191000, 2017.

(144) Werner, S.; Mesch, S.; Osmers, M.; Nubbemeyer, R. Field of Application of the Invention. WO2018104305, 2018.

(145) Werner, S.; Mesch, S.; Braeuer, N. Aromatic Sulfonamide Derivatives and Their Use as Anatagonists or Negative Allosteric Modulators of P2x4. WO2018104307, 2018.

(146) Werner, S.; Cleve, A. Aromatic Sulfonamide Derivatives as Antagonists or Negative Allosteric Modulators of P2x4 Receptor. WO2018210729, 2018.

(147) Erlitz, K. S.; Siutkina, A. I.; Prinz, A.-K.; Koch, O.; Kalinin, D. V.; Junker, A. Piperazine-Based P2X4 Receptor Antagonists. *Archiv der Pharmazie* **2025**, *358* (1), e2400860. https://doi.org/10.1002/ardp.202400860.

(148) Bäurle, S.; Ring, S.; Nagel, J.; Laux-Biehlmann, A.; Nubbemeyer, R.; Pook, E.; Wittrock, S.; Walter, D.; Scott, R. Substituted N-Phenylacetamides Having P2x4 Receptor Antagonistic Activity. WO2022002859, 2022.

(149) Lou, J.; Chen, Y.; Zhang, Y.; Guo, X.; Qian, L.; Liu, L.; Peng, W.; Rong, F.; Wang, C. Fused Ring Compound and Application Thereof. WO2021136238, 2021.

(150) Sakuma, S.; Kobayashi, K.; Ushioda, M.; Imai, T.; Inoue, K. P2X4 Receptor Antagonist. WO2015005467, 2015.

(151) Ushioda, M.; Kobayashi, K.; Saito, D.; Sakuma, S.; Imai, T.; Inoue, K. P2X4 Receptor Antagonist, 2013.

(152) Sakuma, S.; Endo, T.; Kanakubo, N.; Arai, M.; Takahashi, T.; Imai, T.; Taguchi, K.; Nakata, E.; Mochiduki, N.; Ushioda, M.; et al. $P2x_4$ Receptor Antagonist. WO2009022731, 2009.

(153) Bäurle, S.; Ring, S.; Nagel, J.; Laux-Biehlmann, A.; Nubbemeyer, R.; Pook, E.; Walter, D.; Scott, J. Substituted N-Heteroaryl-N-Pyridinylacetamides as P2x4 Modulators, 2022.

(154) Lou, J.; Chen, Y.; Zhang, Y.; Guo, X.; Liu, L.; Peng, W.; Rong, F.; Wu, W.; Wang, C. Aromatic Compound, and Preparation Method Therefor and Application Thereof. WO2022161416, 2022.

(155) Toshiyasu, I.; Junzo, K. Drug for Treating Cough. WO2019177117, 2019.

(156) Maruoka, H.; Barrett, M. O.; Ko, H.; Tosh, D. K.; Melman, A.; Burianek, L. E.; Balasubramanian, R.; Berk, B.; Costanzi, S.; Harden, T. K.; et al. Pyrimidine Ribonucleotides with Enhanced Selectivity as P2Y6 Receptor Agonists: Novel 4-Alkyloxyimino, (S)-Methanocarba, and 5′-Triphosphate γ-Ester Modifications. *Journal of Medicinal Chemistry* **2010**, *53* (11), 4488–4501. https://doi.org/10.1021/jm100287t.

(157) Ginsburg-Shmuel, T.; Haas, M.; Schumann, M.; Reiser, G.; Kalid, O.; Stern, N.; Fischer, B. 5-OMe-UDP Is a Potent and Selective P2Y6-Receptor Agonist. *Journal of Medicinal Chemistry* **2010**, *53* (4), 1673–1685. https://doi.org/10.1021/jm901450d.

(158) Chetty, A.; Sharda, A.; Warburton, R.; Weinberg, E. O.; Dong, J.; Fang, M.; Sahagian, G. G.; Chen, T.; Xue, C.; Castellot, J. J.; et al. A Purinergic P2Y6 Receptor Agonist Prodrug Modulates Airway Inflammation, Remodeling, and Hyperreactivity in a Mouse Model of Asthma. *Journal of Asthma and Allergy* **2018**, *11*, 159–171. https://doi.org/10.2147/JAA.S151849.

(159) Ginsburg-Shmuel, T.; Haas, M.; Grbic, D.; Arguin, G.; Nadel, Y.; Gendron, F.-P.; Reiser, G.; Fischer, B. UDP Made a Highly Promising Stable, Potent, and Selective P2Y6-Receptor Agonist upon Introduction of a Boranophosphate Moiety. *Bioorganic & Medicinal Chemistry* **2012**, *20* (18), 5483–5495. https://doi.org/10.1016/j.bmc.2012.07.042.

(160) Jacob, T. F.; Singh, V.; Dixit, M.; Ginsburg-Shmuel, T.; Fonseca, B.; Pintor, J.; Youdim, M. B. H.; Major, D. T.; Weinreb, O.; Fischer, B. A Promising Drug Candidate for the Treatment of Glaucoma Based on a P2Y6-Receptor Agonist. *Purinergic Signalling* **2018**, *14* (3), 271–284. https://doi.org/10.1007/s11302-018-9614-7.

(161) Haas, M.; Ginsburg-Shmuel, T.; Fischer, B.; Reiser, G. 5-OMe-Uridine-5′-*O*-(α-Boranodiphosphate), a Novel Nucleotide Derivative Highly Active at the Human P2Y6 Receptor Protects against Death-Receptor Mediated Glial Apoptosis. *Neuroscience Letters* **2014**, *578*, 80–84. https://doi.org/10.1016/j.neulet.2014.06.030.

(162) Puhl, A. C.; Lewicki, S. A.; Gao, Z.-G.; Pramanik, A.; Makarov, V.; Ekins, S.; Jacobson, K. A. Machine Learning-Aided Search for Ligands of P2Y6 and Other P2Y Receptors. *Purinergic Signalling* **2024**. https://doi.org/10.1007/s11302-024-10003-4.

(163) Meltzer, D.; Ethan, O.; Arguin, G.; Nadel, Y.; Danino, O.; Lecka, J.; Sévigny, J.; Gendron, F.-P.; Fischer, B. Synthesis and Structure–Activity Relationship of Uracil Nucleotide Derivatives towards the Identification of Human P2Y6 Receptor Antagonists. *Bioorganic & Medicinal Chemistry* **2015**, *23* (17), 5764–5773. https://doi.org/10.1016/j.bmc.2015.07.004.

(164) Mamedova, L. K.; Joshi, B. V.; Gao, Z.-G.; von Kügelgen, I.; Jacobson, K. A. Diisothiocyanate Derivatives as Potent, Insurmountable Antagonists of P2Y6

Nucleotide Receptors. *Biochemical Pharmacology* **2004**, *67* (9), 1763–1770. https://doi.org/10.1016/j.bcp.2004.01.011.

(165) Ito, M.; Egashira, S.; Yoshida, K.; Mineno, T.; Kumagai, K.; Kojima, H.; Okabe, T.; Nagano, T.; Ui, M.; Matsuoka, I. Identification of Novel Selective P2Y6 Receptor Antagonists by High-Throughput Screening Assay. *Life Sciences* **2017**, *180*, 137–142. https://doi.org/10.1016/j.lfs.2017.05.017.

(166) Jung, Y.-H.; Jain, S.; Gopinatth, V.; Phung, N. B.; Gao, Z.-G.; Jacobson, K. A. Structure Activity Relationship of 3-Nitro-2-(Trifluoromethyl)-2*H*-Chromene Derivatives as P2Y6 Receptor Antagonists. *Bioorganic & Medicinal Chemistry Letters* **2021**, *41*, 128008. https://doi.org/10.1016/j.bmcl.2021.128008.

(167) Jung, Y.-H.; Shah, Q.; Lewicki, S. A.; Pramanik, A.; Gopinatth, V.; Pelletier, J.; Sévigny, J.; Iqbal, J.; Jacobson, K. A. Synthesis and Pharmacological Characterization of Multiply Substituted 2*H*-Chromene Derivatives as P2Y6 Receptor Antagonists. *Bioorganic & Medicinal Chemistry Letters* **2022**, *75*, 128981. https://doi.org/10.1016/j.bmcl.2022.128981.

(168) Oliva, P.; Pramanik, A.; Jung, Y.-H.; Lewicki, S. A.; Mwendwa, J. M.; Park, J. H.; Jacobson, K. A. Functionalized Congeners of 2H-Chromene P2Y6 Receptor Antagonists. *Cells* **2024**, *13* (16), 1366. https://doi.org/10.3390/cells13161366.

(169) Zhu, Y.; Zhou, M.; Cheng, X.; Wang, H.; Li, Y.; Guo, Y.; Wang, Y.; Tian, S.; Mao, T.; Zhang, Z.; et al. Discovery of Selective P2Y6R Antagonists with High Affinity and In Vivo Efficacy for Inflammatory Disease Therapy. *Journal of Medicinal Chemistry* **2023**, *66* (9), 6315–6332. https://doi.org/10.1021/acs.jmedchem.3c00210.

(170) Zhao, Y.; Han, B.; Wei, Z.; Li, Y.; Yao, Y.; Song, C.; Duan, Y. Discovery of a Potent, Highly Selective, and In *Vivo* Anti-Inflammatory Efficacious, P2Y6R Antagonist with a Novel Quinoline-Pyrazole Scaffold. *European Journal of Medicinal Chemistry* **2024**, *279*, 116890. https://doi.org/10.1016/j.ejmech.2024.116890.

(171) Alberto, A. V. P.; Santos, L. H. S.; Ferreira, R.; Ferreira, D. N. M.; Alves, L. A. A Brief View of Molecular Modeling Approaches to P2 Receptors. In *Receptors P1 and P2 as Targets for Drug Therapy in Humans*; IntechOpen, 2019. https://doi.org/10.5772/intechopen.86862.

(172) Nguyen, A. T. N.; Nguyen, D. T. N.; Koh, H. Y.; Toskov, J.; MacLean, W.; Xu, A.; Zhang, D.; Webb, G. I.; May, L. T.; Halls, M. L. The Application of Artificial Intelligence to Accelerate G Protein-Coupled Receptor Drug Discovery. *British Journal of Pharmacology* **2024**, *181* (14), 2371–2384. https://doi.org/10.1111/bph.16140.

(173) Puhl, A. C.; Lewicki, S. A.; Gao, Z.-G.; Pramanik, A.; Makarov, V.; Ekins, S.; Jacobson, K. A. Machine Learning-Aided Search for Ligands of P2Y6 and Other P2Y Receptors. *Purinergic Signalling* **2024**, *20* (6), 617–627. https://doi.org/10.1007/s11302-024-10003-4.

(174) Peterson, S. M.; Hutchings, C. J.; Hu, C. F.; Mathur, M.; Salameh, J. W.; Axelrod, F.; Sato, A. K. Discovery and Design of G Protein-Coupled Receptor Targeting Antibodies. *Expert Opinion on Drug Discovery* **2023**, *18* (4), 417–428. https://doi.org/10.1080/17460441.2023.2193389.

(175) Yu, W.; Hill, W. G. Lack of Specificity Shown by P2Y6 Receptor Antibodies. *Naunyn-Schmiedeberg's Archives of Pharmacology* **2013**, *386* (10), 885–891. https://doi.org/10.1007/s00210-013-0894-8.

(176) Burnstock, G.; Boeynaems, J.-M. Purinergic Signalling and Immune Cells. *Purinergic Signalling* **2014**, *10* (4), 529–564. https://doi.org/10.1007/s11302-014-9427-2.

(177) Kohno, K.; Tsuda, M. Role of Microglia and P2X4 Receptors in Chronic Pain. *Pain Reports* **2021**, *6* (1), e864. https://doi.org/10.1097/PR9.0000000000000864.

(178) Thomas, A. Design and Synthesis of P2X4 Ion Channel Inhibitors for the Treatment of Neuropathic and Inflammatory Pain. Honours Thesis, The University of Sydney, 2020.

(179) Hauff, P.; Werner, S. Aromatic Sulfonamide Derivatives for the Treatment of Ischemic Stroke. WO2019081573, May 2, 2019.

(180) Evano, G.; Nitelet, A.; Thilmany, P.; Dewez, D. F. Metal-Mediated Halogen Exchange in Aryl and Vinyl Halides: A Review. *Frontiers in Chemistry* **2018**, *6*, 114. https://doi.org/10.3389/fchem.2018.00114.

(181) Forero-Cortés, P. A.; Haydl, A. M. The 25th Anniversary of the Buchwald–Hartwig Amination: Development, Applications, and Outlook. *Organic Process Research & Development* **2019**, *23* (8), 1478–1483. https://doi.org/10.1021/acs.oprd.9b00161.

(182) Veisi, H. Convenient One-Pot Synthesis of Sulfonamides from Thiols and Disulfides Using 1,3-Dichloro-5,5-Dimethylhydantoin (DCH). *Bulletin of the Korean Chemical Society* **2012**, *33* (2), 383–386. https://doi.org/10.5012/bkcs.2012.33.2.383.

(183) Pu, Y.-M.; Christesen, A.; Ku, Y.-Y. A Simple and Highly Effective Oxidative Chlorination Protocol for the Preparation of Arenesulfonyl Chlorides. *Tetrahedron Letters* **2010**, *51* (2), 418–421. https://doi.org/10.1016/j.tetlet.2009.11.047.

(184) Chen, Z.; Zhou, B.; Cai, H.; Zhu, W.; Zou, X. Simple and Efficient Methods for Selective Preparation of α-Mono or α,α-Dichloro Ketones and β-Ketoesters by Using DCDMH. *Green Chemistry* **2009**, *11* (2), 275–278. https://doi.org/10.1039/B815169E.

(185) Yan, J.; Ni, T.; Yan, F. Simple and Efficient Procedures for Selective Preparation of 3-Haloindoles and 2,3-Dihaloindoles by Using 1,3-Dibromo-5,5-Dimethylhydantoin and 1,3-Dichloro-5,5-Dimethylhydantoin. *Tetrahedron Letters* **2015**, *56* (9), 1096–1098. https://doi.org/10.1016/j.tetlet.2015.01.080.

(186) Walker, M. D.; Andrews, B. I.; Burton, A. J.; Humphreys, L. D.; Kelly, G.; Schilling, M. B.; Scott, P. W. The Development of a New Manufacturing Route to the Novel Anticonvulsant, SB-406725A. *Organic Process Research & Development* **2010**, *14* (1), 108–113. https://doi.org/10.1021/op9002054.

(187) Nishiguchi, A.; Maeda, K.; Miki, S. Sulfonyl Chloride Formation from Thiol Derivatives by N-Chlorosuccinimide Mediated Oxidation. *Synthesis* **2006**, *24*, 4131–4134. https://doi.org/10.1055/s-2006-950353.

(188) Chen, R.; Xu, S.; Shen, F.; Xu, C.; Wang, K.; Wang, Z.; Liu, L. Facile Synthesis of Sulfonyl Chlorides/Bromides from Sulfonyl Hydrazides. *Molecules* **2021**, *26* (18), 5551. https://doi.org/10.3390/molecules26185551.

(189) García-Domínguez, A.; West, N. M.; Hembre, R. T.; Lloyd-Jones, G. C. Thiol Chlorination with N-Chlorosuccinimide: HCl-Catalyzed Release of Molecular Chlorine and the Dichotomous Effects of Water. *ACS Catalysis* **2023**, *13* (14), 9487–9494. https://doi.org/10.1021/acscatal.3c02380.

(190) Finley, K. T. Quinolines and Isoquinolines. In *Kirk-Othmer Encyclopedia of Chemical Technology*; John Wiley & Sons, Ltd, 2005. https://doi.org/10.1002/0471238961.1721091406091412.a01.pub2.

(191) Buskes, M. J.; Blanco, M.-J. Impact of Cross-Coupling Reactions in Drug Discovery and Development. *Molecules* **2020**, *25* (15), 3493. https://doi.org/10.3390/molecules25153493.

(192) Hesp, K. D.; Genovino, J. Palladium- and Copper-Catalysed C–N Cross-Coupling in Drug Discovery. In *Synthetic Methods in Drug Discovery: Volume 1*; Drug Discovery Series; The Royal Society of Chemistry, 2016; Vol. 1, pp 170–241.

(193) Surry, D. S.; Buchwald, S. L. Dialkylbiaryl Phosphines in Pd-Catalyzed Amination: A User's Guide. *Chemical Science* **2010**, *2* (1), 27–50. https://doi.org/10.1039/C0SC00331J.

(194) Bhagwanth, S.; Waterson, A. G.; Adjabeng, G. M.; Hornberger, K. R. Room-Temperature Pd-Catalyzed Amidation of Aryl Bromides Using Tert-Butyl Carbamate. *The Journal of Organic Chemistry* **2009**, *74* (12), 4634–4637. https://doi.org/10.1021/jo9004537.

(195) Qin, L.; Cui, H.; Zou, D.; Li, J.; Wu, Y.; Zhu, Z.; Wu, Y. Pd-Catalyzed Amidation of Aryl(Het) Halides with *Tert*-Butyl Carbamate. *Tetrahedron Letters* **2010**, *51* (33), 4445–4448. https://doi.org/10.1016/j.tetlet.2010.06.083.

(196) Surry, D. S.; Buchwald, S. L. Biaryl Phosphane Ligands in Palladium-Catalyzed Amination. *Angewandte Chemie International Edition* **2008**, *47* (34), 6338–6361. https://doi.org/10.1002/anie.200800497.

(197) Wolfe, J. P.; Åhman, J.; Sadighi, J. P.; Singer, R. A.; Buchwald, S. L. An Ammonia Equivalent for the Palladium-Catalyzed Amination of Aryl Halides and Triflates. *Tetrahedron Letters* **1997**, *38* (36), 6367–6370. https://doi.org/10.1016/S0040-4039(97)01465-2.

(198) Kondo, Y.; Morimoto, H.; Ohshima, T. Recent Progress towards the Use of Benzophenone Imines as an Ammonia Equivalent. *Chemistry Letters* **2020**, *49* (5), 497–504. https://doi.org/10.1246/cl.200099.

(199) Ruiz-Castillo, P.; Buchwald, S. L. Applications of Palladium-Catalyzed C–N Cross-Coupling Reactions. *Chemical Reviews* **2016**, *116* (19), 12564–12649. https://doi.org/10.1021/acs.chemrev.6b00512.

(200) Ma, D.; Jiang, Y. Cu(I)/Amino Acid Catalyzed Coupling Reactions of Aryl Halides and Nucleophiles: Applications in Large-Scale Production. *Chimia* **2011**, *65* (12), 914–918. https://doi.org/10.2533/chimia.2011.914.

(201) Cai, Q.; Zhang, H.; Zou, B.; Xie, X.; Zhu, W.; He, G.; Wang, J.; Pan, X.; Chen, Y.; Yuan, Q.; et al. Amino Acid-Promoted Ullmann-Type Coupling Reactions and Their Applications in Organic Synthesis. *Pure and Applied Chemistry* **2009**, *81* (2), 227–234. https://doi.org/10.1351/PAC-CON-08-08-19.

(202) Liu, W.; Han, L.-Y.; Liu, R.-L.; Xu, L.-G.; Bi, Y.-L. Copper-Catalyzed *N*-Arylation of 2-Arylindoles with Aryl Halides. *Chinese Chemical Letters* **2014**, *25* (9), 1240–1243. https://doi.org/10.1016/j.cclet.2014.04.021.

(203) Xu, H.; Wolf, C. Efficient Copper-Catalyzed Coupling of Aryl Chlorides, Bromides and Iodides with Aqueous Ammonia. *Chemical Communications* **2009**, 3035–3037. https://doi.org/10.1039/B904188E.

(204) Jiang, L.; Lu, X.; Zhang, H.; Jiang, Y.; Ma, D. CuI/4-Hydro-l-Proline as a More Effective Catalytic System for Coupling of Aryl Bromides with N-Boc Hydrazine and Aqueous Ammonia. *The Journal of Organic Chemistry* **2009**, *74* (12), 4542–4546. https://doi.org/10.1021/jo9006738.

(205) Thomas, A. D.; Josemin; Asokan, C. V. Vilsmeier–Haack Reactions of Carbonyl Compounds: Synthesis of Substituted Pyrones and Pyridines. *Tetrahedron* **2004**, *60* (23), 5069–5076. https://doi.org/10.1016/j.tet.2004.04.017.

(206) Bergman, J.; Stålhandske, C. Cyclization of *N*-Acylanthranilic Acids with Vilsmeier Reagents. Chemical and Structural Studies. *Tetrahedron* **1996**, *52* (3), 753–770. https://doi.org/10.1016/0040-4020(95)01035-1.

(207) Al Musaimi, O.; Wisdom, R.; Talbiersky, P.; De La Torre, B. G.; Albericio, F. Propylphosphonic Anhydride (T3P®) as Coupling Reagent for Solid-Phase Peptide Synthesis. *ChemistrySelect* **2021**, *6* (11), 2649–2657. https://doi.org/10.1002/slct.202100123.

(208) Wanka, L.; Iqbal, K.; Schreiner, P. R. The Lipophilic Bullet Hits the Targets: Medicinal Chemistry of Adamantane Derivatives. *Chemical Reviews* **2013**, *113* (5), 3516–3604. https://doi.org/10.1021/cr100264t.

(209) Lamoureux, G.; Artavia, G. Use of the Adamantane Structure in Medicinal Chemistry. *Current Medicinal Chemistry* **2010**, *17* (26), 2967–2978. https://doi.org/10.2174/092986710792065027.

(210) Meanwell, N. A. The Influence of Bioisosteres in Drug Design: Tactical Applications to Address Developability Problems. *Tactics in Contemporary Drug Design* **2014**, *9*, 283. https://doi.org/10.1007/7355_2013_29.

(211) *2237221-72-4|2-(3,5,7-Trifluoroadamantan-1-yl)acetic acid| Ambeed*. https://www.ambeed.com/products/2237221-72-4.html (accessed 2025-08-08).

(212) Sebastian, S.; Monika; Khatana, A. K.; Yadav, E.; Gupta, M. K. Recent Approaches towards One-Carbon Homologation–Functionalization of Aldehydes. *Organic & Biomolecular Chemistry* **2021**, *19* (14), 3055–3074. https://doi.org/10.1039/D1OB00135C.

(213) *828-51-3|Adamantane-1-carboxylic acid*. Ambeed. https://www.ambeed.com/products/828-51-3.html (accessed 2025-08-08).

(214) *214557-89-8|3,5,7-Trifluoroadamantane-1-carboxylic acid| Ambeed*. https://www.ambeed.com/products/214557-89-8.html (accessed 2025-08-08).

(215) O'Brien-Brown, J. Novel P2X7 Receptor Ligands. PhD Thesis, The University of Sydney, Sydney, Australia, 2018.

(216) Garrett, T. Identification of Novel Modulators for Neurodegenerative Disease States. PhD Thesis, The University of Sydney, 2025.

(217) Huh, D. H.; Jeong, J. S.; Lee, H. B.; Ryu, H.; Kim, Y. G. An Efficient Method for One-Carbon Elongation of Aryl Aldehydes via Their Dibromoalkene Derivatives. *Tetrahedron* **2002**, *58* (50), 9925–9932. https://doi.org/10.1016/S0040-4020(02)01324-8.

(218) Shen, W.; Kunzer, A. A Facile One-Carbon Homologation of Aryl Aldehydes to Amides. *Organic Letters* **2002**, *4* (8), 1315–1317. https://doi.org/10.1021/ol025608m.

(219) Tao, L.; Yang, W.; Zhao, W. Synthesis of Carboxylic Acids, Esters, and Amides from 1,1-Dibromoalkenes via Oxidation of Alkynyl Boronate Intermediates. *ChemistrySelect* **2021**, *6* (33), 8532–8536. https://doi.org/10.1002/slct.202102150.

(220) Li, C.; Zhao, P.; Li, R.; Zhang, B.; Zhao, W. Oxidation of Alkynyl Boronates to Carboxylic Acids, Esters, and Amides. *Angewandte Chemie International Edition* **2020**, *59* (27), 10913–10917. https://doi.org/10.1002/anie.202000988.

(221) Haggett, J. G.; Domaille, D. W. Ortho-Boronic Acid Carbonyl Compounds and Their Applications in Chemical Biology. *Chemistry – A European Journal* **2024**, *30* (7), e202302485. https://doi.org/10.1002/chem.202302485.

(222) Aggarwal, V. K.; Mereu, A. Amidine-Promoted Addition of Chloroform to Carbonyl Compounds. *The Journal of Organic Chemistry* **2000**, *65* (21), 7211–7212. https://doi.org/10.1021/jo000584n.

(223) Chambers, R. D.; Hutchinson, J. 6.01 - Trihalides. In *Comprehensive Organic Functional Group Transformations*; Katritzky, A. R., Meth-Cohn, O., Rees, C. W., Eds.; Elsevier Science: Oxford, 1995; pp 1–33. https://doi.org/10.1016/B0-08-044705-8/00219-3.

(224) Taylor, J. E.; Bull, S. D.; Williams, J. M. J. Amidines, Isothioureas, and Guanidines as Nucleophilic Catalysts. *Chemical Society Reviews* **2012**, *41* (6), 2109–2121. https://doi.org/10.1039/C2CS15288F.

(225) Li, Z.; Gupta, M. K.; Snowden, T. S. One-Carbon Homologation of Primary Alcohols and the Reductive Homologation of Aldehydes Involving a Jocic-Type Reaction. *European Journal of Organic Chemistry* **2015**, *2015* (32), 7009–7019. https://doi.org/10.1002/ejoc.201501089.

(226) Kowalski, C. J.; Reddy, R. E. Ester Homologation Revisited: A Reliable, Higher Yielding and Better Understood Procedure. *The Journal of Organic Chemistry* **1992**, *57* (26), 7194–7208. https://doi.org/10.1021/jo00052a038.

(227) Wlochal, J.; Davies, R. D. M.; Burton, J. Cubanes in Medicinal Chemistry: Synthesis of Functionalized Building Blocks. *Organic Letters* **2014**, *16* (16), 4094–4097. https://doi.org/10.1021/ol501750k.

(228) Gunosewoyo, H. Polycarbocyclic Compounds as Novel P2X7 Receptor Ligands. PhD Thesis, The University of Sydney, 2009.

(229) Joyce, J. Cubane as a 3D Scaffold for Fragment Library Construction. PhD Thesis, The University of Sydney, 2025.

(230) Wang, Z. Fritsch-Buttenberg-Wiechell Rearrangement. In *Comprehensive Organic Name Reactions and Reagents*; John Wiley & Sons, Ltd, 2010; pp 1151–1154. https://doi.org/10.1002/9780470638859.conrr252.

(231) Liu, H.; Tian, Y.; Lee, K.; Krishnan, P.; Wang, M. K.-M.; Whelan, S.; Mevers, E.; Soloveva, V.; Dedic, B.; Liu, X.; et al. Identification of Potent Ebola Virus Entry Inhibitors with Suitable Properties for in Vivo Studies. *Journal of Medicinal Chemistry* **2018**, *61* (14), 6293–6307. https://doi.org/10.1021/acs.jmedchem.8b00704.

(232) Augustine, J. K.; Bombrun, A.; Atta, R. N. A Practical and Cost-Efficient, One-Pot Conversion of Aldehydes into Nitriles Mediated by 'Activated DMSO.' *Synlett* **2011**, *2011*, 2223–2227. https://doi.org/10.1055/s-0030-1261181.

(233) Yan, G.; Zhang, Y.; Wang, J. Recent Advances in the Synthesis of Aryl Nitrile Compounds. *Advanced Synthesis & Catalysis* **2017**, *359* (23), 4068–4105. https://doi.org/10.1002/adsc.201700875.

(234) Eaton, P. E.; Yip, Y. C. The Preparation and Fate of Cubylcarbinyl Radicals. *Journal of the American Chemical Society* **1991**, *113* (20), 7692–7697. https://doi.org/10.1021/ja00020a035.

(235) Kumar, S. Chapter 12 - Diazomethane: Risk Assessment, Environmental, and Health Hazard. In *Hazardous Gases*; Singh, J., Kaushik, R. D., Chawla, M., Eds.; Academic Press, 2021; pp 141–152. https://doi.org/10.1016/B978-0-323-89857-7.00018-9.

(236) Pinzi, L.; Rastelli, G. Molecular Docking: Shifting Paradigms in Drug Discovery. *International Journal of Molecular Sciences* **2019**, *20* (18), 4331. https://doi.org/10.3390/ijms20184331.

(237) Ramírez, D.; Caballero, J. Is It Reliable to Take the Molecular Docking Top Scoring Position as the Best Solution without Considering Available Structural Data? *Molecules : A Journal of Synthetic Chemistry and Natural Product Chemistry* **2018**, *23* (5), 1038. https://doi.org/10.3390/molecules23051038.

(238) Friesner, R. A.; Murphy, R. B.; Repasky, M. P.; Frye, L. L.; Greenwood, J. R.; Halgren, T. A.; Sanschagrin, P. C.; Mainz, D. T. Extra Precision Glide: Docking and Scoring Incorporating a Model of Hydrophobic Enclosure for Protein−Ligand Complexes. *Journal of Medicinal Chemistry* **2006**, *49* (21), 6177–6196. https://doi.org/10.1021/jm051256o.

(239) Lu, C.; Wu, C.; Ghoreishi, D.; Chen, W.; Wang, L.; Damm, W.; Ross, G. A.; Dahlgren, M. K.; Russell, E.; Von Bargen, C. D.; et al. OPLS4: Improving Force Field Accuracy on Challenging Regimes of Chemical Space. *Journal of Chemical Theory and Computation* **2021**, *17* (7), 4291–4300. https://doi.org/10.1021/acs.jctc.1c00302.

(240) Tsujimura, M.; Ishikita, H.; Saito, K. Determinants of Hydrogen Bond Distances in Proteins. *Physical Chemistry Chemical Physics* **2025**, *27* (18), 9794–9805. https://doi.org/10.1039/D5CP00511F.

(241) Anjana, R.; Vaishnavi, M. K.; Sherlin, D.; Kumar, S. P.; Naveen, K.; Kanth, P. S.; Sekar, K. Aromatic-Aromatic Interactions in Structures of Proteins and Protein-DNA Complexes: A Study Based on Orientation and Distance. *Bioinformation* **2012**, *8* (24), 1220–1224. https://doi.org/10.6026/97320630081220.

(242) Arcon, J. P.; Turjanski, A. G.; Martí, M. A.; Forli, S. Biased Docking for Protein-Ligand Pose Prediction. *Methods in molecular biology* **2021**, *2266*, 39–72. https://doi.org/10.1007/978-1-0716-1209-5_3.

(243) Ma, X.; Idle, J. R.; Gonzalez, F. J. The Pregnane X Receptor: From Bench to Bedside. *Expert opinion on drug metabolism & toxicology* **2008**, *4* (7), 895–908. https://doi.org/10.1517/17425255.4.7.895.

(244) Lynch, T.; Price, A. The Effect of Cytochrome P450 Metabolism on Drug Response, Interactions, and Adverse Effects. *American Family Physician* **2007**, *76* (3), 391–396.

(245) Dane, C. Design and Synthesis of P2X4 Receptor Inhibitors for the Treatment of Chronic Pain. Honours Thesis, The University of Sydney, 2021.

(246) Miller, E. B.; Murphy, R. B.; Sindhikara, D.; Borrelli, K. W.; Grisewood, M. J.; Ranalli, F.; Dixon, S. L.; Jerome, S.; Boyles, N. A.; Day, T.; et al. Reliable and Accurate Solution to the Induced Fit Docking Problem for Protein–Ligand Binding. *Journal of Chemical Theory and Computation* **2021**, *17* (4), 2630–2639. https://doi.org/10.1021/acs.jctc.1c00136.

(247) McKenzie, A. Investigation of Novel Purinergic Therapeutics for the Treatment of Alzheimer's Disease and Amyotrophic Lateral Sclerosis. PhD Thesis, The University of Sydney, Sydney, Australia, 2025.

(248) Sluyter, R.; McEwan, T. B.-D.; Sophocleous, R. A.; Stokes, L. Methods for Studying P2X4 Receptor Ion Channels in Immune Cells. *Journal of Immunological Methods* **2024**, *526*, 113626. https://doi.org/10.1016/j.jim.2024.113626.

(249) Gee, K. R.; Brown, K. A.; Chen, W.-N. U.; Bishop-Stewart, J.; Gray, D.; Johnson, I. Chemical and Physiological Characterization of Fluo-4 Ca2+-Indicator Dyes. *Cell Calcium* **2000**, *27* (2), 97–106. https://doi.org/10.1054/ceca.1999.0095.

(250) Cordero-Sánchez, C.; Mudarra-Fraguas, I.; Fernández-Carvajal, A. Fluorescence-Based Functional Assays for Ca2+-Permeable ThermoTRP Channels. In *TRP Channels: Methods and Protocols*; Ferrer-Montiel, A., Hucho, T., Eds.; Springer: New York, NY, 2019; pp 99–110. https://doi.org/10.1007/978-1-4939-9446-5_7.

(251) Ase, A. R.; Honson, N. S.; Zaghdane, H.; Pfeifer, T. A.; Séguéla, P. Identification and Characterization of a Selective Allosteric Antagonist of Human P2X4 Receptor Channels. *Molecular Pharmacology* **2015**, *87* (4), 606–616. https://doi.org/10.1124/mol.114.096222.

(252) Sophocleous, R. A.; Berg, T.; Finol-Urdaneta, R. K.; Sluyter, V.; Keshiya, S.; Bell, L.; Curtis, S. J.; Curtis, B. L.; Seavers, A.; Bartlett, R.; et al. Pharmacological and Genetic Characterisation of the Canine P2X4 Receptor. *British Journal of Pharmacology* **2020**, *177* (12), 2812–2829. https://doi.org/10.1111/bph.15009.

(253) Schneider, M.; Prudic, K.; Pippel, A.; Klapperstück, M.; Braam, U.; Müller, C. E.; Schmalzing, G.; Markwardt, F. Interaction of Purinergic P2X4 and P2X7 Receptor Subunits. *Frontiers in Pharmacology* **2017**, *8*. https://doi.org/10.3389/fphar.2017.00860.

(254) Garrett, T.; Gilchrist, J.; McKenzie, A.; Larik, F. A.; Danon, J.; Werry, E.; Kassiou, M. An Investigation on Linker Modifications of Cyanoguanidine-Based P2X7 Receptor Antagonists. *ChemMedChem* **2024**, e202400163. https://doi.org/10.1002/cmdc.202400163.

(255) Aravindhan, R.; Ummal Momeen, M.; Hu, J. Halogenation Effects on the Bridgehead Position of the Adamantane Molecule. *Chemical Physics Letters* **2023**, *829*, 140746. https://doi.org/10.1016/j.cplett.2023.140746.

(256) Biffinger, J. C.; Kim, H. W.; DiMagno, S. G. The Polar Hydrophobicity of Fluorinated Compounds. *ChemBioChem* **2004**, *5* (5), 622–627. https://doi.org/10.1002/cbic.200300910.

(257) Zhu, Y.; Zhou, M.; Cheng, X.; Wang, H.; Li, Y.; Guo, Y.; Wang, Y.; Tian, S.; Mao, T.; Zhang, Z.; et al. Discovery of Selective P2Y6R Antagonists with High Affinity and In Vivo Efficacy for Inflammatory Disease Therapy. *Journal of Medicinal Chemistry* **2023**, *66* (9), 6315–6332. https://doi.org/10.1021/acs.jmedchem.3c00210.

(258) Li, Huanqiu; Hu, Qinghua; Zhu, Yifan; Wang, Hui; Wei, Ruonan; Zhou, Mengze. 2-Pyrazole-3-Benzimidazole Derivative as Well as Preparation Method and Application Thereof. CN114276338, 2022.

(259) Hu, Qinghua; Li, Huanqiu; Leng, Haifeng; Zhou, Mengze. Benzoxazole Compound as Well as Preparation Method, Pharmaceutical Composition and Application Thereof. CN114478511, 2022.

(260) Claramunt, R. M.; López, C.; Santa María, M. D.; Sanz, D.; Elguero, J. The Use of NMR Spectroscopy to Study Tautomerism. *Progress in Nuclear Magnetic Resonance Spectroscopy* **2006**, *49* (3), 169–206. https://doi.org/10.1016/j.pnmrs.2006.07.001.

(261) Hansen, P. E. Structural Studies of β-Diketones and Their Implications on Biological Effects. *Pharmaceuticals* **2021**, *14* (11), 1189. https://doi.org/10.3390/ph14111189.

(262) Nonhebel, D. C. NMR Spectra of Intramolecularly Hydrogen-Bonded Compound—I: β-Diketones, o-Hydroxyaldehydes and o-Hydroxyketones. *Tetrahedron* **1968**, *24* (4), 1869–1874. https://doi.org/10.1016/S0040-4020(01)82493-5.

(263) Ruatta, S. M.; Murguía, M. C.; Ramírez de Arellano, C.; Fustero, S. Regio-Specific Synthesis of New 1-(*Tert*-Butyl)-1*H*-Pyrazolecarboxamide Derivatives. *Tetrahedron Letters* **2017**, *58* (25), 2441–2444. https://doi.org/10.1016/j.tetlet.2017.05.029.

(264) Semenov, S. G.; Makarova, M. V. On the Degenerate Tautomerism. *Russian Journal of General Chemistry* **2013**, *83* (12), 2331–2333. https://doi.org/10.1134/S1070363213120189.

(265) Martin, Y. C. Let's Not Forget Tautomers. *Journal of Computer-Aided Molecular Design* **2009**, *23* (10), 693–704. https://doi.org/10.1007/s10822-009-9303-2.

(266) Su, F.; Sun, Z.; Su, W.; Liang, X. NMR Investigation and Theoretical Calculations on the Tautomerism of Benzimidazole Compounds. *Journal of Molecular Structure* **2018**, *1173*, 690–696. https://doi.org/10.1016/j.molstruc.2018.07.038.

(267) García-Báez, E. V.; Padilla-Martínez, I. I.; Cruz, A.; Rosales-Hernández, M. C. 13C-NMR Chemical Shifts in 1,3-Benzazoles as a Tautomeric Ratio Criterion. *Molecules* **2022**, *27* (19), 6268. https://doi.org/10.3390/molecules27196268.

(268) Minkin, V. I.; Garnovskii, A. D.; Elguero, J.; Katritzky, A. R.; Denisko, O. V. The Tautomerism of Heterocycles: Five-Membered Rings with Two or More Heteroatoms. In *Advances in Heterocyclic Chemistry*; Katritzky, A. R., Ed.; Academic Press, 2000; Vol. 76, pp 157–323. https://doi.org/10.1016/S0065-2725(00)76005-3.

(269) Wilson, C. G. M.; Arkin, M. R. Chapter 5 - Screening and Biophysics in Small Molecule Discovery. In *Small Molecule Drug Discovery*; Trabocchi, A., Lenci, E., Eds.; Elsevier, 2020; pp 127–161. https://doi.org/10.1016/B978-0-12-818349-6.00005-4.

(270) Mayer, M.; Meyer, B. Characterization of Ligand Binding by Saturation Transfer Difference NMR Spectroscopy. *Angewandte Chemie International Edition* **1999**, *38* (12), 1784–1788. https://doi.org/10.1002/(SICI)1521-3773(19990614)38:12%253C1784::AID-ANIE1784%253E3.0.CO;2-Q.

(271) Angulo, J.; Nieto, P. M. STD-NMR: Application to Transient Interactions between Biomolecules—a Quantitative Approach. *European Biophysics Journal* **2011**, *40* (12), 1357–1369. https://doi.org/10.1007/s00249-011-0749-5.

(272) Quirós, M. T.; Macdonald, C.; Angulo, J.; Muñoz, M. P. Spin Saturation Transfer Difference NMR (SSTD NMR): A New Tool to Obtain Kinetic Parameters of Chemical Exchange Processes. *Journal of Visualized Experiments : JoVE* **2016**, No. 117, 54499. https://doi.org/10.3791/54499.

(273) Spingler, B.; Schnidrig, S.; Todorova, T.; Wild, F. Some Thoughts about the Single Crystal Growth of Small Molecules. *CrystEngComm* **2012**, *14* (3), 751–757. https://doi.org/10.1039/C1CE05624G.

(274) Bachhav, H. M.; Bhagat, S. B.; Telvekar, V. N. Efficient Protocol for the Synthesis of Quinoxaline, Benzoxazole and Benzimidazole Derivatives Using Glycerol as Green Solvent. *Tetrahedron Letters* **2011**, *52* (43), 5697–5701. https://doi.org/10.1016/j.tetlet.2011.08.105.

(275) Bui, H. T. B.; Ha, Q. T. K.; Oh, W. K.; Vo, D. D.; Chau, Y. N. T.; Tu, C. T. K.; Pham, E. C.; Tran, P. T.; Tran, L. T.; Mai, H. V. Microwave Assisted Synthesis and

Cytotoxic Activity Evaluations of New Benzimidazole Derivatives. *Tetrahedron Letters* **2016**, *57* (8), 887–891. https://doi.org/10.1016/j.tetlet.2016.01.042.

(276) Praveen, C.; Nandakumar, A.; Dheenkumar, P.; Muralidharan, D.; Perumal, P. T. Microwave-Assisted One-Pot Synthesis of Benzothiazole and Benzoxazole Libraries as Analgesic Agents. *Journal of Chemical Sciences* **2012**, *124* (3), 609–624. https://doi.org/10.1007/s12039-012-0251-3.

(277) Patel, S. R.; Patil, R. V.; Chavan, J. U.; Beldar, A. G. Nanocatalyzed Synthesis of Benzoxazoles. *ChemistrySelect* **2023**, *8* (35), e202301972. https://doi.org/10.1002/slct.202301972.

(278) Kumar, D.; Rudrawar, S.; Chakraborti, A. K. One-Pot Synthesis of 2-Substituted Benzoxazoles Directly from Carboxylic Acids. *Australian Journal of Chemistry* **2008**, *61* (11), 881–887. https://doi.org/10.1071/CH08193.

(279) Kumar, R.; Selvam, C.; Kaur, G.; Chakraborti, A. K. Microwave-Assisted Direct Synthesis of 2-Substituted Benzoxazoles from Carboxylic Acids under Catalyst and Solvent-Free Conditions. *Synlett* **2005**, *2005*, 1401–1404. https://doi.org/10.1055/s-2005-868509.

(280) Wang, R.; Kang, R.; Yang, X.; Cheng, Y.; Bai, H.; Du, Z. Design, Synthesis, and Anti-Fungal Evaluation of Heterocyclic Benzoxazole Derivatives. *Molecules* **2022**, *27* (23), 8375. https://doi.org/10.3390/molecules27238375.

(281) Dev, D.; Chandra, J.; Palakurthy, N. B.; Thalluri, K.; Kalita, T.; Mandal, B. Benzoxazole and Benzothiazole Synthesis from Carboxylic Acids in Solution and on Resin by Using Ethyl 2-Cyano-2-(2-nitrobenzenesulfonyloxyimino)Acetate and para-Toluenesulfonic Acid. *Asian Journal of Organic Chemistry* **2016**, *5* (5), 663–675. https://doi.org/10.1002/ajoc.201500527.

(282) Chang, J.; Zhao, K.; Pan, S. Synthesis of 2-Arylbenzoxazoles via DDQ Promoted Oxidative Cyclization of Phenolic Schiff Bases—a Solution-Phase Strategy for Library Synthesis. *Tetrahedron Letters* **2002**, *43* (6), 951–954. https://doi.org/10.1016/S0040-4039(01)02302-4.

(283) Vitaku, E.; Smith, D. T.; Njardarson, J. T. Analysis of the Structural Diversity, Substitution Patterns, and Frequency of Nitrogen Heterocycles among U.S. FDA Approved Pharmaceuticals. *Journal of Medicinal Chemistry* **2014**, *57* (24), 10257–10274. https://doi.org/10.1021/jm501100b.

(284) Pennington, L. D.; Moustakas, D. T. The Necessary Nitrogen Atom: A Versatile High-Impact Design Element for Multiparameter Optimization. *Journal of Medicinal Chemistry* **2017**, *60* (9), 3552–3579. https://doi.org/10.1021/acs.jmedchem.6b01807.

(285) Mallo-Abreu, A.; Prieto-Díaz, R.; Jespers, W.; Azuaje, J.; Majellaro, M.; Velando, C.; García-Mera, X.; Caamaño, O.; Brea, J.; Loza, M. I.; et al. Nitrogen-Walk Approach to Explore Bioisosteric Replacements in a Series of Potent A2B Adenosine Receptor Antagonists. *Journal of Medicinal Chemistry* **2020**, *63* (14), 7721–7739. https://doi.org/10.1021/acs.jmedchem.0c00564.

(286) Garai, S.; Kulkarni, P. M.; Schaffer, P. C.; Leo, L. M.; Brandt, A. L.; Zagzoog, A.; Black, T.; Lin, X.; Hurst, D. P.; Janero, D. R.; et al. Application of Fluorine- and Nitrogen-Walk Approaches: Defining the Structural and Functional Diversity of 2-Phenylindole Class of Cannabinoid 1 Receptor Positive Allosteric Modulators. *Journal of Medicinal Chemistry* **2020**, *63* (2), 542–568. https://doi.org/10.1021/acs.jmedchem.9b01142.

(287) Ma, H.; Wang, H.; Gillespie, J. C.; Mendez, R. E.; Selley, D. E.; Zhang, Y. Exploring Naltrexamine Derivatives Featuring Azaindole Moiety via Nitrogen-Walk Approach to Investigate Their in Vitro Pharmacological Profiles at the Mu Opioid Receptor. *Bioorganic & Medicinal Chemistry Letters* **2021**, *41*, 127953. https://doi.org/10.1016/j.bmcl.2021.127953.

(288) Bagdi, A. K.; Santra, S.; Monir, K.; Hajra, A. Synthesis of Imidazo[1,2-a]Pyridines: A Decade Update. *Chemical Communications* **2015**, *51* (9), 1555–1575. https://doi.org/10.1039/C4CC08495K.

(289) Deep, A.; Bhatia, R. K.; Kaur, R.; Kumar, S.; Jain, U. K.; Singh, H.; Batra, S.; Kaushik, D.; Deb, P. K. Imidazo[1,2-a]Pyridine Scaffold as Prospective Therapeutic Agents. *Current Topics in Medicinal Chemistry* **2017**, *17* (2), 238–250. https://doi.org/10.2174/1568026616666160530153233.

(290) Panda, J.; Raiguru, B. P.; Mishra, M.; Mohapatra, S.; Nayak, S. Recent Advances in the Synthesis of Imidazo[1,2-a]Pyridines: A Brief Review. *ChemistrySelect* **2022**, *7* (3), e202103987. https://doi.org/10.1002/slct.202103987.

(291) Mahurkar, N. D.; Gawhale, N. D.; Lokhande, M. N.; Uke, S. J.; Kodape, M. M. Benzimidazole: A Versatile Scaffold for Drug Discovery and beyond – A Comprehensive Review of Synthetic Approaches and Recent Advancements in Medicinal Chemistry. *Results in Chemistry* **2023**, *6*, 101139. https://doi.org/10.1016/j.rechem.2023.101139.

(292) Kumar, M.; Pandey, S. K.; Chaudhary, N.; Mishra, A.; Gupta, D. Highly Efficient Method for the Synthesis of Substituted Benzimidazoles Using Sodium Metabisulfite Adsorbed on Silica Gel. *Results in Chemistry* **2022**, *4*, 100403. https://doi.org/10.1016/j.rechem.2022.100403.

(293) Xing, Y.-Y.; Liu, C.; Wu, F. Efficient Synthesis of Substituted Imidazo[4,5-b]Pyridines. *Heterocyclic Communications* **2013**, *19* (5), 327–330. https://doi.org/10.1515/hc-2013-0059.

(294) Yamani, A.; Zdżalik-Bielecka, D.; Lipner, J.; Stańczak, A.; Piórkowska, N.; Stańczak, P. S.; Olejkowska, P.; Hucz-Kalitowska, J.; Magdycz, M.; Dzwonek, K.; et al. Discovery and Optimization of Novel Pyrazole-Benzimidazole CPL304110, as a Potent and Selective Inhibitor of Fibroblast Growth Factor Receptors FGFR (1–3). *European Journal of Medicinal Chemistry* **2021**, *210*, 112990. https://doi.org/10.1016/j.ejmech.2020.112990.

(295) Kallinen, A.; Boyd, R.; Lane, S.; Bhalla, R.; Mardon, K.; Stimson, D. H. R.; Werry, E. L.; Fulton, R.; Connor, M.; Kassiou, M. Synthesis and in Vitro Evaluation of Fluorine-18 Benzimidazole Sulfones as CB2 PET-Radioligands. *Organic & Biomolecular Chemistry* **2019**, *17* (20), 5086–5098. https://doi.org/10.1039/C9OB00656G.

(296) Abdullah, I.; Chee, C. F.; Lee, Y.-K.; Thunuguntla, S. S. R.; Satish Reddy, K.; Nellore, K.; Antony, T.; Verma, J.; Mun, K. W.; Othman, S.; et al. Benzimidazole Derivatives as Potential Dual Inhibitors for PARP-1 and DHODH. *Bioorganic & Medicinal Chemistry* **2015**, *23* (15), 4669–4680. https://doi.org/10.1016/j.bmc.2015.05.051.

(297) Akande, A. A.; Salar, U.; Khan, K. M.; Syed, S.; Aboaba, S. A.; Chigurupati, S.; Wadood, A.; Riaz, M.; Taha, M.; Bhatia, S.; et al. Substituted Benzimidazole Analogues as Potential α-Amylase Inhibitors and Radical Scavengers. *ACS Omega* **2021**, *6* (35), 22726–22739. https://doi.org/10.1021/acsomega.1c03056.

(298) Huynh, T.-K.-C.; Nguyen, T.-H.-A.; Nguyen, T.-C.-T.; Hoang, T.-K.-D. Synthesis and Insight into the Structure–Activity Relationships of 2-Phenylbenzimidazoles as

Prospective Anticancer Agents. *RSC Advances* **2020**, *10* (35), 20543–20551. https://doi.org/10.1039/D0RA02282A.

(299) Pham, E. C.; Le, T. V. T.; Truong, T. N. Design, Synthesis, Bio-Evaluation, and in Silico Studies of Some N-Substituted 6-(Chloro/Nitro)-1H-Benzimidazole Derivatives as Antimicrobial and Anticancer Agents. *RSC Advances* **2022**, *12* (33), 21621–21646. https://doi.org/10.1039/D2RA03491C.

(300) Yonetoku, Y.; Kubota, H.; Okamoto, Y.; Toyoshima, A.; Funatsu, M.; Ishikawa, J.; Takeuchi, M.; Ohta, M.; Tsukamoto, S. Novel Potent and Selective Calcium-Release-Activated Calcium (CRAC) Channel Inhibitors. Part 1: Synthesis and Inhibitory Activity of 5-(1-Methyl-3-Trifluoromethyl-1*H*-Pyrazol-5-Yl)-2-Thiophenecarboxamides. *Bioorganic & Medicinal Chemistry* **2006**, *14* (14), 4750–4760. https://doi.org/10.1016/j.bmc.2006.03.024.

(301) Khademi, Z.; Heravi, M. M. Applications of Claisen Condensations in Total Synthesis of Natural Products. An Old Reaction, a New Perspective. *Tetrahedron* **2022**, *103*, 132573. https://doi.org/10.1016/j.tet.2021.132573.

(302) Ashok, D.; Ram Reddy, M.; Ramakrishna, K.; Nagaraju, N.; Dharavath, R.; Sarasija, M. Iodine Mediated Synthesis of Some New Imidazo[1,2-a]Pyridine Derivatives and Evaluation of Their Antimicrobial Activity. *Journal of Heterocyclic Chemistry* **2020**, *57* (6), 2528–2534. https://doi.org/10.1002/jhet.3967.

(303) Jahan, K.; Sofi, F. A.; Salim, S. A.; Bharatam, P. V. NIS Mediated Dehydrogenative-Cyclocondensation in Aqueous Medium towards the Synthesis of 2-Arylimidazo[1,2-a]Pyridines and Their 3-Formylated Derivatives. *Tetrahedron* **2022**, *112*, 132715. https://doi.org/10.1016/j.tet.2022.132715.

(304) Veer, B.; Singh, R. Facile Synthesis of 2-Arylimidazo[1,2-a]Pyridines Catalysed by DBU in Aqueous Ethanol. *Proceedings of the Royal Society* **2019**, *475* (2230), 20190238. https://doi.org/10.1098/rspa.2019.0238.

(305) Cosimelli, B.; Laneri, S.; Ostacolo, C.; Sacchi, A.; Severi, E.; Porcù, E.; Rampazzo, E.; Moro, E.; Basso, G.; Viola, G. Synthesis and Biological Evaluation of Imidazo[1,2-*a*]Pyrimidines and Imidazo[1,2-*a*]Pyridines as New Inhibitors of the Wnt/β-Catenin Signaling. *European Journal of Medicinal Chemistry* **2014**, *83*, 45–56. https://doi.org/10.1016/j.ejmech.2014.05.071.

(306) Raczyńska, E. D.; Kolczyńska, K.; Stępniewski, T. M. Consequences of One-Electron Oxidation and One-Electron Reduction for 4-Aminopyrimidine—DFT Studies. *Journal of Molecular Modeling* **2012**, *18* (8), 3523–3533. https://doi.org/10.1007/s00894-012-1358-7.

(307) Naoum, J. N.; Chandra, K.; Shemesh, D.; Gerber, R. B.; Gilon, C.; Hurevich, M. DMAP-Assisted Sulfonylation as an Efficient Step for the Methylation of Primary Amine Motifs on Solid Support. *Beilstein Journal of Organic Chemistry* **2017**, *13*, 806–816. https://doi.org/10.3762/bjoc.13.81.

(308) Rodriguez, J.; Maldonado, R.; Ramirez-Garcia, G.; Cervantes, E.; Cruz, F. Microwave-assisted Synthesis and Luminescent Activity of Imidazo[1,2-a]Pyridine Derivatives - Rodríguez - 2020 - Journal of Heterocyclic Chemistry - Wiley Online Library. *Journal of Heterocyclic Chemistry 57* (5), 2063–2296. https://doi.org/10.1098/rspa.2019.0238.

(309) Santra, S.; Mitra, S.; Bagdi, A. K.; Majee, A.; Hajra, A. Iron(III)-Catalyzed Three-Component Domino Strategy for the Synthesis of Imidazo[1,2-*a*]Pyridines. *Tetrahedron Letters* **2014**, *55* (37), 5151–5155. https://doi.org/10.1016/j.tetlet.2014.07.094.

(310) Katritziky, A.R.; Pozharskii, A.F. *Handbook of Heterocyclic Chemistry*, 2nd ed.; Pergamon: Oxford, 2000.

(311) McDonald, I. M.; Peese, K. M. General Method for the Preparation of Electron-Deficient Imidazo[1,2-a]Pyridines and Related Heterocycles. *Organic Letters* **2015**, *17* (24), 6002–6005. https://doi.org/10.1021/acs.orglett.5b02966.

(312) Humphrey, G. R.; Kuethe, J. T. Practical Methodologies for the Synthesis of Indoles. *Chemical Reviews* **2006**, *106* (7), 2875–2911. https://doi.org/10.1021/cr0505270.

(313) Taber, D. F.; Tirunahari, P. K. Indole Synthesis: A Review and Proposed Classification. *Tetrahedron* **2011**, *67* (38), 7195–7210. https://doi.org/10.1016/j.tet.2011.06.040.

(314) Chandra, A.; Yadav, S. C.; Cheekatla, S. R.; Kumar, A. A Review on Indole Synthesis from Nitroarenes: Classical to Modern Approaches. *Organic & Biomolecular Chemistry* **2025**, *23*, 6853–6887. https://doi.org/10.1039/D5OB00338E.

(315) Siddalingamurthy, E.; Mahadevan, K. M.; Masagalli, J. N.; Harishkumar, H. N. Mild, Efficient Fischer Indole Synthesis Using 2,4,6-Trichloro-1,3,5-Triazine (TCT). *Tetrahedron Letters* **2013**, *54* (41), 5591–5596. https://doi.org/10.1016/j.tetlet.2013.07.157.

(316) Lipińska, T. M.; Czarnocki, S. J. A New Approach to Difficult Fischer Synthesis: The Use of Zinc Chloride Catalyst in Triethylene Glycol under Controlled Microwave Irradiation. *Organic Letters* **2006**, *8* (3), 367–370. https://doi.org/10.1021/ol052255t.

(317) Gribble, Gordon. Madelung Indole Synthesis. In *Indole Ring Synthesis*; John Wiley & Sons, Ltd, 2016; pp 147–155. https://doi.org/10.1002/9781118695692.ch8.

(318) Da Settimo, F.; Simorini, F.; Taliani, S.; La Motta, C.; Marini, A. M.; Salerno, S.; Bellandi, M.; Novellino, E.; Greco, G.; Cosimelli, B.; et al. Anxiolytic-like Effects of N,N-Dialkyl-2-Phenylindol-3-Ylglyoxylamides by Modulation of Translocator Protein Promoting Neurosteroid Biosynthesis. *Journal of Medicinal Chemistry* **2008**, *51* (18), 5798–5806. https://doi.org/10.1021/jm8003224.

(319) Schirok, H.; Paulsen, H.; Kroh, W.; Chen, G.; Gao, P. Improved Synthesis of the Selective Rho-Kinase Inhibitor 6-Chloro-N4-{3,5-Difluoro-4-[(3-Methyl-1H-Pyrrolo[2,3-b]Pyridin-4-Yl)Oxy]Phenyl}pyrimidin-2,4-Diamine. *Organic Process Research & Development* **2010**, *14* (1), 168–173. https://doi.org/10.1021/op900260k.

(320) Chen, C.; Lieberman, D. R.; Larsen, R. D.; Verhoeven, T. R.; Reider, P. J. Syntheses of Indoles via a Palladium-Catalyzed Annulation between Iodoanilines and Ketones. *The Journal of Organic Chemistry* **1997**, *62* (9), 2676–2677. https://doi.org/10.1021/jo970278i.

(321) Jia, Y.; Zhu, J. Palladium-Catalyzed, Modular Synthesis of Highly Functionalized Indoles and Tryptophans by Direct Annulation of Substituted o-Haloanilines and Aldehydes. *The Journal of Organic Chemistry* **2006**, *71* (20), 7826–7834. https://doi.org/10.1021/jo061471s.

(322) Gopalsamy, A.; Yang, H.; Ellingboe, J. W.; Tsou, H.-R.; Zhang, N.; Honores, E.; Powell, D.; Miranda, M.; McGinnis, J. P.; Rabindran, S. K. Pyrazolo[1,5-*a*]Pyrimidin-7-Yl Phenyl Amides as Novel Anti-Proliferative Agents: Parallel Synthesis for Lead Optimization of Amide Region. *Bioorganic & Medicinal Chemistry Letters* **2005**, *15* (6), 1591–1594. https://doi.org/10.1016/j.bmcl.2005.01.066.

(323) Bergman, J.; Venemalm, L. Efficient Synthesis of 2-Chloro-, 2-Bromo-, and 2-Iodoindole. *The Journal of Organic Chemistry* **1992**, *57* (8), 2495–2497. https://doi.org/10.1021/jo00034a058.

(324) Ketcha, D. M.; Lieurance, B. A.; Homan, D. F. J.; Gribble, G. W. Synthesis of Alkyl-Substituted N-Protected Indoles via Acylation and Reductive Deoxygenation. *The Journal of Organic Chemistry* **1989**, *54* (18), 4350–4356. https://doi.org/10.1021/jo00279a023.

(325) Kondo, Y.; Yoshida, A.; Sakamoto, T. Magnesiation of Indoles with Magnesium Amide Bases. *Journal of the Chemical Society, Perkin Transactions 1* **1996**, No. 19, 2331–2332. https://doi.org/10.1039/P19960002331.

(326) Zeng, X.-X.; Zheng, R.-L.; Zhou, T.; He, H.-Y.; Liu, J.-Y.; Zheng, Y.; Tong, A.-P.; Xiang, M.-L.; Song, X.-R.; Yang, S.-Y.; et al. Novel Thienopyridine Derivatives as Specific Anti-Hepatocellular Carcinoma (HCC) Agents: Synthesis, Preliminary Structure–Activity Relationships, and in Vitro Biological Evaluation. *Bioorganic & Medicinal Chemistry Letters* **2010**, *20* (21), 6282–6285. https://doi.org/10.1016/j.bmcl.2010.08.088.

(327) Frizzo, C. P.; Marzari, M. R. B.; Buriol, L.; Moreira, D. N.; Rosa, F. A.; Vargas, P. S.; Zanatta, N.; Bonacorso, H. G.; Martins, M. A. P. Ionic Liquid Effects on the Reaction of β-Enaminones and *Tert*-Butylhydrazine and Applications for the Synthesis of Pyrazoles. *Catalysis Communications* **2009**, *10* (15), 1967–1970. https://doi.org/10.1016/j.catcom.2009.07.005.

(328) Negri, G.; Kascheres, C. Study of the Reactivity of α-Acylenaminoketones. Synthesis of Pyrazoles. *Journal of Heterocyclic Chemistry* **2001**, *38* (1), 109–123. https://doi.org/10.1002/jhet.5570380116.

(329) Onodera, S.; Kochi, T.; Kakiuchi, F. Synthesis of N-Arylpyrazoles by Palladium-Catalyzed Coupling of Aryl Triflates with Pyrazole Derivatives. *The Journal of Organic Chemistry* **2019**, *84* (10), 6508–6515. https://doi.org/10.1021/acs.joc.9b00673.

(330) Kang, E.; Kim, H. T.; Joo, J. M. Transition-Metal-Catalyzed C–H Functionalization of Pyrazoles. *Organic & Biomolecular Chemistry* **2020**, *18* (32), 6192–6210. https://doi.org/10.1039/D0OB01265C.

(331) Qiu, D.; Jin, L.; Zheng, Z.; Meng, H.; Mo, F.; Wang, X.; Zhang, Y.; Wang, J. Synthesis of Pinacol Arylboronates from Aromatic Amines: A Metal-Free Transformation. *The Journal of Organic Chemistry* **2013**, *78* (5), 1923–1933. https://doi.org/10.1021/jo3018878.

(332) Qiu, D.; Zhang, Y.; Wang, J. Direct Synthesis of Arylboronic Pinacol Esters from Arylamines. *Organic Chemistry Frontiers* **2014**, *1* (4), 422–425. https://doi.org/10.1039/C4QO00009A.

(333) Secrieru, A.; O'Neill, P. M.; Cristiano, M. L. S. Revisiting the Structure and Chemistry of 3(5)-Substituted Pyrazoles. *Molecules* **2020**, *25* (1), 42. https://doi.org/10.3390/molecules25010042.

(334) Gao, Y.; Wang, H.; Xu, M.; Lian, H.; Pan, Y.; Shi, Y. Addition of Acetonitrile Anions to Unsaturated Systems Under Ultrasonically Dispersed Potassium System. *Organic Preparations and Procedures International* **2001**, *33* (4), 351–356. https://doi.org/10.1080/00304940109356599.

(335) Fandrick, D. R.; Sanyal, S.; Kaloko, J.; Mulder, J. A.; Wang, Y.; Wu, L.; Lee, H.; Roschangar, F.; Hoffmann, M.; Senanayake, C. H. A Michael Equilibration Model To

Control Site Selectivity in the Condensation toward Aminopyrazoles. *Organic Letters* **2015**, *17* (12), 2964–2967. https://doi.org/10.1021/acs.orglett.5b01248.

(336) Fichez, J.; Busca, P.; Prestat, G. Recent Advances in Aminopyrazoles Synthesis and Functionalisation. *Targets Heterocycl. Syst.* **2017**, *21*, 322–347. https://doi.org/10.17374/targets.2018.21.322.

(337) Ghosh, A. K.; Brindisi, M.; Sarkar, A. The Curtius Rearrangement: Applications in Modern Drug Discovery and Medicinal Chemistry. *ChemMedChem* **2018**, *13* (22), 2351–2373. https://doi.org/10.1002/cmdc.201800518.

(338) Thomas, J. B.; Giddings, A. M.; Olepu, S.; Wiethe, R. W.; Warner, K. R.; Sarret, P.; Longpre, J.-M.; Runyon, S. P.; Gilmour, B. P. The Amide Linker in Nonpeptide Neurotensin Receptor Ligands Plays a Key Role in Calcium Signaling at the Neurotensin Receptor Type 2. *Bioorganic & Medicinal Chemistry Letters* **2015**, *25* (10), 2060–2064. https://doi.org/10.1016/j.bmcl.2015.03.083.

(339) Lebel, H.; Leogane, O. Boc-Protected Amines via a Mild and Efficient One-Pot Curtius Rearrangement. *Organic Letters* **2005**, *7* (19), 4107–4110. https://doi.org/10.1021/ol051428b.

(340) Yasuhara, A.; Sakamoto, T. Deprotection of *N*-Sulfonyl Nitrogen-Heteroaromatics with Tetrabutylammonium Fluoride. *Tetrahedron Letters* **1998**, *39* (7), 595–596. https://doi.org/10.1016/S0040-4039(97)10653-0.

(341) Clemens, J.; Bell, E. L.; Londregan, A. T. Selective N2-Alkylation of 1H-Indazoles and 1H-Azaindazoles. *Synthesis* **2022**, *54*, 3215–3226. https://doi.org/10.1055/s-0040-1719917.

(342) Kumar, D.; Kaur, G.; Negi, A.; Kumar, S.; Singh, S.; Kumar, R. Synthesis and Xanthine Oxidase Inhibitory Activity of 5,6-Dihydropyrazolo/Pyrazolo[1,5-*c*]Quinazoline Derivatives. *Bioorganic Chemistry* **2014**, *57*, 57–64. https://doi.org/10.1016/j.bioorg.2014.08.007.

(343) Schofield, K.; Grimmett, M. R.; Grimmett, M. R.; Keene, B. R. T. *Heteroaromatic Nitrogen Compounds: The Azoles*; CUP Archive, 1976.

(344) Katritzky, A. R.; Ramsden, C. A.; Joule, J. A.; Zhdankin, V. V. *Handbook of Heterocyclic Chemistry*; Elsevier, 2010.

(345) Couto Rodrigues, S.; Silva Moratório de Moraes, R.; Tavares de Almeida Pinto, G.; Miranda Martins, M. T.; Antunes do Nascimento, P.; Alves Soares, D. L.; Mestre Botelho, A. B.; Cardoso Cruz, C.; Cunha, A. C. A Review on Chemistry and Methods of Synthesis of 1,2,4-Triazole Derivatives. *The Chemical Record* **2025**, *25* (1), e202400190. https://doi.org/10.1002/tcr.202400190.

(346) Lazzara, P. R.; Moore, T. W. Scaffold-Hopping as a Strategy to Address Metabolic Liabilities of Aromatic Compounds. *RSC Medicinal Chemistry* **2019**, *11* (1), 18–29. https://doi.org/10.1039/c9md00396g.

(347) Assandri, A.; Tarzia, G.; Bellasio, E.; Ciabatti, R.; Tuan, G.; Ferrari, P.; Zerilli, L.; Lanfranchi, M.; Pelizzi, G. Metabolic Oxidation of the Pyrrole Ring: Structure and Origin of Some Urinary Metabolites of the Anti-Hypertensive Pyrrolylpyridazinamine, Mopidralazine.: III: Studies with the 13C-Labelled Drug. *Xenobiotica* **1987**, *17* (5), 559–573. https://doi.org/10.3109/00498258709043963.

(348) Pollock, P. M.; Cole, K. P. T-Butyl as a Pyrazole Protecting Group: Preparation and Use of 1-Tert-Butyl-3-Methyl-1H-Pyrazole-5-Amine. In *Organic Syntheses*; John Wiley & Sons, Ltd, 2014; pp 537–548. https://doi.org/10.1002/0471264229.os089.52.

(349) Larina, L. I. Chapter Five - Tautomerism and Structure of Azoles: Nuclear Magnetic Resonance Spectroscopy. In *Advances in Heterocyclic Chemistry*; Scriven, E. F. V., Ramsden, C. A., Eds.; Academic Press, 2018; Vol. 124, pp 233–321. https://doi.org/10.1016/bs.aihch.2017.06.003.

(350) Fustero, S.; Román, R.; Sanz-Cervera, J. F.; Simón-Fuentes, A.; Cuñat, A. C.; Villanova, S.; Murguía, M. Improved Regioselectivity in Pyrazole Formation through the Use of Fluorinated Alcohols as Solvents: Synthesis and Biological Activity of Fluorinated Tebufenpyrad Analogs. *The Journal of Organic Chemistry* **2008**, *73* (9), 3523–3529. https://doi.org/10.1021/jo800251g.

(351) Fustero, S.; Román, R.; Sanz-Cervera, J. F.; Simón-Fuentes, A.; Bueno, J.; Villanova, S. Synthesis of New Fluorinated Tebufenpyrad Analogs with Acaricidal Activity Through Regioselective Pyrazole Formation. *The Journal of Organic Chemistry* **2008**, *73* (21), 8545–8552. https://doi.org/10.1021/jo801729p.

(352) Motiwala, H. F.; Armaly, A. M.; Cacioppo, J. G.; Coombs, T. C.; Koehn, K. R. K.; Norwood, V. M. I.; Aubé, J. HFIP in Organic Synthesis. *Chemical Reviews* **2022**, *122* (15), 12544–12747. https://doi.org/10.1021/acs.chemrev.1c00749.

(353) Zabaleta, N.; Uria, U.; Reyes, E.; Carrillo, L.; Vicario, J. L. Ion-Pairing Catalysis in the Enantioselective Addition of Hydrazones to N-Acyldihydropyrrole Derivatives. *Chemical Communications* **2018**, *54* (64), 8905–8908. https://doi.org/10.1039/C8CC05311A.

(354) Zhang, X.-H.; Kang, H.-Q.; Tao, Y.-Y.; Li, Y.-H.; Zhao, J.-R.; Ya-Gao; Ma, L.-Y.; Liu, H.-M. Identification of Novel 1,3-Diaryl-1,2,4-Triazole-Capped Histone Deacetylase 6 Inhibitors with Potential Anti-Gastric Cancer Activity. *European Journal of Medicinal Chemistry* **2021**, *218*, 113392. https://doi.org/10.1016/j.ejmech.2021.113392.

(355) Chen, Z.; Li, H.; Dong, W.; Miao, M.; Ren, H. I2-Catalyzed Oxidative Coupling Reactions of Hydrazones and Amines and the Application in the Synthesis of 1,3,5-Trisubstituted 1,2,4-Triazoles. *Organic Letters* **2016**, *18* (6), 1334–1337. https://doi.org/10.1021/acs.orglett.6b00277.

(356) Dai, J.; Tian, S.; Yang, X.; Liu, Z. Synthesis Methods of 1,2,3-/1,2,4-Triazoles: A Review. *Frontiers in Chemistry* **2022**, *10*. https://doi.org/10.3389/fchem.2022.891484.

(357) Castanedo, G. M.; Seng, P. S.; Blaquiere, N.; Trapp, S.; Staben, S. T. Rapid Synthesis of 1,3,5-Substituted 1,2,4-Triazoles from Carboxylic Acids, Amidines, and Hydrazines. *The Journal of Organic Chemistry* **2011**, *76* (4), 1177–1179. https://doi.org/10.1021/jo1023393.

(358) Lafferty, Tyler. Synthesis of a 1,2,4-Substituted Imidazole for a Fragment-Based Drug Discovery Library. Honours Thesis, Rollins College, Winter Park, FL, 2017.

(359) Blakemore, D. Suzuki–Miyaura Coupling. **2016**, 1–69. https://doi.org/10.1039/9781782622086.

(360) Bellina, F.; Rossi, R. Regioselective Functionalization of the Imidazole Ring via Transition Metal-Catalyzed C-N and C-C Bond Forming Reactions. *Advanced Synthesis & Catalysis* **2010**, *352* (8), 1223–1276. https://doi.org/10.1002/adsc.201000144.

(361) Bellina, F.; Rossi, R. Regioselective Functionalization of the Imidazole Ring via Transition Metal-Catalyzed C□N and C□C Bond Forming Reactions. *Advanced Synthesis & Catalysis* **2010**, *352* (8), 1223–1276. https://doi.org/10.1002/adsc.201000144.

(362) Joo, J. M.; Touré, B. B.; Sames, D. C–H Bonds as Ubiquitous Functionality: A General Approach to Complex Arylated Imidazoles via Regioselective Sequential Arylation of All Three C–H Bonds and Regioselective N-Alkylation Enabled by SEM-Group Transposition. *The Journal of Organic Chemistry* **2010**, *75* (15), 4911–4920. https://doi.org/10.1021/jo100727j.

(363) Whitten, J. P.; Matthews, D. P.; McCarthy, J. R. [2-(Trimethylsilyl)Ethoxy]Methyl (SEM) as a Novel and Effective Imidazole and Fused Aromatic Imidazole Protecting Group. *The Journal of Organic Chemistry* **1986**, *51* (10), 1891–1894. https://doi.org/10.1021/jo00360a044.

(364) Grimmett, M. R. Halogenation of Heterocycles: I. Five-Membered Rings. In *Advances in Heterocyclic Chemistry*; Katritzky, A. R., Ed.; Academic Press, 1993; Vol. 57, pp 291–411. https://doi.org/10.1016/S0065-2725(08)60890-9.

(365) Causey, C. P.; Allen, W. E. Anion Binding by Fluorescent Biimidazole Diamides. *The Journal of Organic Chemistry* **2002**, *67* (17), 5963–5968. https://doi.org/10.1021/jo020098v.

(366) Allen, W. E.; Fowler, C. J.; Lynch, V. M.; Sessler, J. L. Self-Assembled Helices from 2,2′-Biimidazoles. *Chemistry – A European Journal* **2001**, *7* (3), 721–729. https://doi.org/10.1002/1521-3765(20010202)7:3%253C721::AID-CHEM721%253E3.0.CO;2-1.

(367) Tang, R.-J.; Milcent, T.; Crousse, B. Regioselective Halogenation of Arenes and Heterocycles in Hexafluoroisopropanol. *The Journal of Organic Chemistry* **2018**, *83* (2), 930–938. https://doi.org/10.1021/acs.joc.7b02920.

(368) Furet, P.; Guagnano, V.; Holzer, P.; Kallen, J.; Mah, R.; Masuya, K.; Schlapbach, A.; Vaupel, A. Substituted Purinone Compounds. WO2014115077, 2014.

(369) Bellina, F.; Calandri, C.; Cauteruccio, S.; Rossi, R. Efficient and Highly Regioselective Direct C-2 Arylation of Azoles, Including Free (NH)-Imidazole, -Benzimidazole and -Indole, with Aryl Halides. *Tetrahedron* **2007**, *63* (9), 1970–1980. https://doi.org/10.1016/j.tet.2006.12.068.

(370) Li, J.-H.; Zhu, Q.-M.; Xie, Y.-X. Pd(OAc)2/DABCO-Catalyzed Suzuki–Miyaura Cross-Coupling Reaction in DMF. *Tetrahedron* **2006**, *62* (47), 10888–10895. https://doi.org/10.1016/j.tet.2006.08.103.

(371) Messina, C.; Douglas, L. Z.; Liu, J. T.; Forgione, P. Successive Pd-Catalyzed Decarboxylative Cross-Couplings for the Modular Synthesis of Non-Symmetric Di-Aryl-Substituted Thiophenes. *European Journal of Organic Chemistry* **2020**, *2020* (32), 5182–5191. https://doi.org/10.1002/ejoc.202000780.

(372) Lu, P.; Sanchez, C.; Cornella, J.; Larrosa, I. Silver-Catalyzed Protodecarboxylation of Heteroaromatic Carboxylic Acids. *Organic Letters* **2009**, *11* (24), 5710–5713. https://doi.org/10.1021/ol902482p.

(373) Dhanush, P. C.; Saranya, P. V.; Anilkumar, G. Microwave Assisted C-H Activation Reaction: An Overview. *Tetrahedron* **2022**, *105*, 132614. https://doi.org/10.1016/j.tet.2021.132614.

(374) Copin, C.; Henry, N.; Buron, F.; Routier, S. Palladium-Catalyzed Direct Arylation of 2,6-Disubstituted Imidazo[2,1-b][1,3,4]Thiadiazoles. *Synlett* **2016**, *27*, 1091–1095. https://doi.org/10.1055/s-0035-1561317.

(375) Bellina, F.; Calandri, C.; Cauteruccio, S.; Rossi, R. Efficient and Highly Regioselective Direct C-2 Arylation of Azoles, Including Free (NH)-Imidazole, -

Benzimidazole and -Indole, with Aryl Halides. *Tetrahedron* **2007**, *63* (9), 1970–1980. https://doi.org/10.1016/j.tet.2006.12.068.

(376) Bi, F.; Song, D.; Zhang, N.; Liu, Z.; Gu, X.; Hu, C.; Cai, X.; Venter, H.; Ma, S. Design, Synthesis and Structure-Based Optimization of Novel Isoxazole-Containing Benzamide Derivatives as FtsZ Modulators. *European Journal of Medicinal Chemistry* **2018**, *159*, 90–103. https://doi.org/10.1016/j.ejmech.2018.09.053.

(377) Wang, G.; Chen, R.; Zhao, S.; Yang, L.; Guo, H.; Sun, S.; Wang, J.; Domena, J.; Xing, Y. Efficient Synthesis of 1,2,4-Oxadiazine-5-Ones via [3+3] Cycloaddition of in Situ Generated Aza-Oxyallylic Cations with Nitrile Oxides. *Tetrahedron Letters* **2018**, *59* (21), 2018–2020. https://doi.org/10.1016/j.tetlet.2018.04.025.

(378) Debnath, P.; Baeten, M.; Lefèvre, N.; Daele, S. V.; Maes, B. U. W. Synthesis of Secondary Amides from N-Substituted Amidines by Tandem Oxidative Rearrangement and Isocyanate Elimination. *Advanced Synthesis & Catalysis* **2015**, *357* (1), 197–209. https://doi.org/10.1002/adsc.201400648.

(379) Rauws, T. R. M.; Maes, B. U. W. Transition Metal-Catalyzed N-Arylations of Amidines and Guanidines. *Chemical Society Reviews* **2012**, *41* (6), 2463–2497. https://doi.org/10.1039/C1CS15236J.

(380) Garigipati, R. S. An Efficient Conversion of Nitriles to Amidines. *Tetrahedron Letters* **1990**, *31* (14), 1969–1972. https://doi.org/10.1016/S0040-4039(00)88891-7.

(381) Li, Bryan; Chiu, Charles; Hank, Richard; Murry, Jerry; Roth, Joshua; Tobiassen, Harry. An Optimized Process for Formation of 2,4-Disubstituted Imidazoles from Condensation of Amidines and α-Haloketones. *Organic Process Research & Development* **2002**, *6* (5), 682–683.

(382) Uphade, M.; Katritch, V.; Cherezov, V.; Sadybekov, A.; Nazarova, A. L.; Shaye, H.; Zarzycka, B.; Majumdar, S.; Varga, B. R.; Shepherd, A.; et al. At2 Antagonists for Non-Addictive Pain Relief, 2024.

(383) Mansilla, H.; Afonso, M. M. Iron(III) Tosylate in the Preparation of Dimethyl and Diethyl Acetals from Ketones and β -Keto Enol Ethers from Cyclic β -Diketones. *Synthetic Communications* **2008**, *38* (15), 2607–2618. https://doi.org/10.1080/00397910802219361.

(384) Do, H.-Q.; Khan, R. M. K.; Daugulis, O. A General Method for Copper-Catalyzed Arylation of Arene C−H Bonds. *Journal of the American Chemical Society* **2008**, *130* (45), 15185–15192. https://doi.org/10.1021/ja805688p.

(385) Knapp, D. M.; Gillis, E. P.; Burke, M. D. A General Solution for Unstable Boronic Acids: Slow-Release Cross-Coupling from Air-Stable MIDA Boronates. *Journal of the American Chemical Society* **2009**, *131* (20), 6961–6963. https://doi.org/10.1021/ja901416p.

(386) Fu, H. Y.; Doucet, H. Methyl 2-Furoate: An Alternative Reagent to Furan for Palladium-Catalysed Direct Arylation. *European Journal of Organic Chemistry* **2011**, *2011* (35), 7163–7173. https://doi.org/10.1002/ejoc.201101102.

(387) Knapp, D. M.; Gillis, E. P.; Burke, M. D. A General Solution for Unstable Boronic Acids: Slow-Release Cross-Coupling from Air-Stable MIDA Boronates. *Journal of the American Chemical Society* **2009**, *131* (20), 6961–6963. https://doi.org/10.1021/ja901416p.

(388) Lennox, A.; Lloyd-Jones, Guy. Selection of Boron Reagents for Suzuki–Miyaura Coupling. *Chemical Society Reviews* **2014**, *43*, 412–443. https://doi.org/10.1039/C3CS60197H.

(389) Huggins, D. J.; Sherman, W.; Tidor, B. Rational Approaches to Improving Selectivity in Drug Design. *Journal of Medicinal Chemistry* **2012**, *55* (4), 1424–1444. https://doi.org/10.1021/jm2010332.

(390) Fang, Z.; Song, Y.; Zhan, P.; Zhang, Q.; Liu, X. Conformational Restriction: An Effective Tactic in 'Follow-On'-Based Drug Discovery. *Future Medicinal Chemistry* **2014**, *6* (8), 885–901. https://doi.org/10.4155/fmc.14.50.

(391) Wipf, P.; Skoda, E. M.; Mann, A. Chapter 11 - Conformational Restriction and Steric Hindrance in Medicinal Chemistry. In *The Practice of Medicinal Chemistry (Fourth Edition)*; Wermuth, C. G., Aldous, D., Raboisson, P., Rognan, D., Eds.; Academic Press: San Diego, 2015; pp 279–299. https://doi.org/10.1016/B978-0-12-417205-0.00011-0.

(392) Tang, K.; Wang, S.; Gao, W.; Song, Y.; Yu, B. Harnessing the Cyclization Strategy for New Drug Discovery. *Acta Pharmaceutica Sinica B* **2022**, *12* (12), 4309–4326. https://doi.org/10.1016/j.apsb.2022.09.022.

(393) Kumari, S.; Carmona, A. V.; Tiwari, A. K.; Trippier, P. C. Amide Bond Bioisosteres: Strategies, Synthesis, and Successes. *Journal of Medicinal Chemistry* **2020**, *63* (21), 12290–12358. https://doi.org/10.1021/acs.jmedchem.0c00530.

(394) Li, H.; Mattingly, A. E.; Jania, L. A.; Smith, R.; Melander, R. J.; Ernst, R. K.; Koller, B. H.; Melander, C. Benzimidazole Isosteres of Salicylanilides Are Highly Active Colistin Adjuvants. *ACS Infectious Diseases* **2021**, *7* (12), 3303–3313. https://doi.org/10.1021/acsinfecdis.1c00463.

(395) Wurtz, N. R.; Johnson, J. A.; Viet, A.; Shirude, P. S.; Baligar, V.; Madduri, S.; Cheney, D. L.; Park, H.; Lupisella, J. A.; Hsu, M.-Y.; et al. Discovery of Heteroaryl Urea Isosteres for Formyl Peptide Receptor 2 Agonists. *ACS Medicinal Chemistry Letters* **2022**, *13* (6), 943–948. https://doi.org/10.1021/acsmedchemlett.2c00079.

(396) Im, D.; Moon, H.; Kim, J.; Oh, Y.; Jang, M.; Hah, J.-M. Conformational Restriction of a Type II FMS Inhibitor Leading to Discovery of 5-Methyl-N-(2-Aryl-1H-Benzo[d]Imidazo-5-Yl)Isoxazole-4-Carboxamide Analogues as Selective FLT3 Inhibitors. *Journal of Enzyme Inhibition and Medicinal Chemistry* **2019**, *34* (1), 1716–1721. https://doi.org/10.1080/14756366.2019.1671837.

(397) Schmidt, D.; Conrad, J.; Klaiber, I.; Beifuss, U. Synthesis of the Bis-Potassium Salts of 5-Hydroxy-3-Oxopent-4-Enoic Acids and Their Use for the Efficient Preparation of 4-Hydroxy-2H-Pyran-2-Ones and Other Heterocycles. *Chemical Communications* **2006**, 4732–4734. https://doi.org/10.1039/B611105J.

(398) Huckin, S. N.; Weiler, L. Alkylation of Dianions of .Beta.-Keto Esters. *Journal of the American Chemical Society* **1974**, *96* (4), 1082–1087. https://doi.org/10.1021/ja00811a023.

(399) Hanamoto, T.; Hiyama, T. A Facile Entry to β,δ-Diketo and *Syn*-β,δ-Dihydroxy Esters. *Tetrahedron Letters* **1988**, *29* (49), 6467–6470. https://doi.org/10.1016/S0040-4039(00)82375-8.

(400) Ren, H.-C.; Zhu, X.; Hao, K.; Le, S.-Y. Editorial: Application of PKPD Modeling in Drug Discovery and Development. *Frontiers in Pharmacology* **2025**, *16*. https://doi.org/10.3389/fphar.2025.1614689.

(401) Davies, M.; Jones, R. D. O.; Grime, K.; Jansson-Löfmark, R.; Fretland, A. J.; Winiwarter, S.; Morgan, P.; McGinnity, D. F. Improving the Accuracy of Predicted Human Pharmacokinetics: Lessons Learned from the AstraZeneca Drug Pipeline Over Two Decades. *Trends in Pharmacological Sciences* **2020**, *41* (6), 390–408. https://doi.org/10.1016/j.tips.2020.03.004.

(402) Gallo, J. M. Pharmacokinetic/Pharmacodynamic-Driven Drug Development. *Mount Sinai Journal of Medicine* **2010**, *77* (4), 381–388. https://doi.org/10.1002/msj.20193.

(403) Tian, M.; Peng, Y.; Zheng, J. Metabolic Activation and Hepatotoxicity of Furan-Containing Compounds. *Drug Metabolism and Disposition: The Biological Fate of Chemicals* **2022**, *50* (5), 655–670. https://doi.org/10.1124/dmd.121.000458.

(404) St. Jean, D. J. Jr.; Fotsch, C. Mitigating Heterocycle Metabolism in Drug Discovery. *Journal of Medicinal Chemistry* **2012**, *55* (13), 6002–6020. https://doi.org/10.1021/jm300343m.

(405) Wishart, D. S.; Tian, S.; Allen, D.; Oler, E.; Peters, H.; Lui, V. W.; Gautam, V.; Djoumbou-Feunang, Y.; Greiner, R.; Metz, T. O. BioTransformer 3.0—a Web Server for Accurately Predicting Metabolic Transformation Products. *Nucleic Acids Research* **2022**, *50* (W1), W115–W123. https://doi.org/10.1093/nar/gkac313.

(406) de Bruyn Kops, C.; Šícho, M.; Mazzolari, A.; Kirchmair, J. GLORYx: Prediction of the Metabolites Resulting from Phase 1 and Phase 2 Biotransformations of Xenobiotics. *Chemical Research in Toxicology* **2021**, *34* (2), 286–299. https://doi.org/10.1021/acs.chemrestox.0c00224.

(407) Šícho, M.; Stork, C.; Mazzolari, A.; de Bruyn Kops, C.; Pedretti, A.; Testa, B.; Vistoli, G.; Svozil, D.; Kirchmair, J. FAME 3: Predicting the Sites of Metabolism in Synthetic Compounds and Natural Products for Phase 1 and Phase 2 Metabolic Enzymes. *Journal of Chemical Information and Modeling* **2019**, *59* (8), 3400–3412. https://doi.org/10.1021/acs.jcim.9b00376.

(408) Matlock, M. K.; Hughes, T. B.; Swamidass, S. J. XenoSite Server: A Web-Available Site of Metabolism Prediction Tool. *Bioinformatics* **2015**, *31* (7), 1136–1137. https://doi.org/10.1093/bioinformatics/btu761.

(409) Sampath Kumar, H. M.; Herrmann, L.; Tsogoeva, S. B. Structural Hybridization as a Facile Approach to New Drug Candidates. *Bioorganic & Medicinal Chemistry Letters* **2020**, *30* (23), 127514. https://doi.org/10.1016/j.bmcl.2020.127514.

(410) Conradie, J. A Frontier Orbital Energy Approach to Redox Potentials. *Journal of Physics: Conference Series* **2015**, *633* (1), 012045. https://doi.org/10.1088/1742-6596/633/1/012045.

(411) Rojas, D. M. S.; Maggio, R. M.; Kaufman, T. S. A Nuclear Magnetic Resonance-Based Study of the Behavior of the Tautomers of Triclabendazole in DMSO-*d*6, in the Presence of Water. *Journal of Molecular Structure* **2023**, *1283*, 135315. https://doi.org/10.1016/j.molstruc.2023.135315.

(412) Gale, P. A.; Hiscock, J. R.; Lalaoui, N.; Light, M. E.; Wells, N. J.; Wenzel, M. Benzimidazole-Based Anion Receptors: Tautomeric Switching and Selectivity. *Organic & Biomolecular Chemistry* **2012**, *10* (30), 5909–5915. https://doi.org/10.1039/C1OB06800H.

(413) Kereselidze, J. A.; Zarqua, T. S.; Kikalishvili, T. J.; Churgulia, E. J.; Makaridze, M. S. Some New Views on the Tautomerisation Mechanism. *Russian Chemical Reviews* **2002**, *71* (12), 993–1003. https://doi.org/10.1070/RC2002v071n12ABEH000727.

(414) Asif Iqbal, M.; Raza Shah, A.; Hua, R. Base-Promoted Synthesis of 3-Arylquinolines Using DMSO as C1 Source. *Tetrahedron Letters* **2024**, *140*, 155044. https://doi.org/10.1016/j.tetlet.2024.155044.

(415) Li, X.; Wu, C.; Lin, X.; Cai, X.; Liu, L.; Luo, G.; You, Q.; Xiang, H. Synthesis and Biological Evaluation of 3-Aryl-Quinolin Derivatives as Anti-Breast Cancer Agents Targeting ERα and VEGFR-2. *European Journal of Medicinal Chemistry* **2019**, *161*, 445–455. https://doi.org/10.1016/j.ejmech.2018.10.045.

(416) Meth-Cohn, O.; Taylor, D. L. The Reverse Vilsmeier Approach to the Synthesis of Quinolines, Quinolinium Salts and Quinolones. *Tetrahedron* **1995**, *51* (47), 12869–12882. https://doi.org/10.1016/0040-4020(95)00729-R.

(417) Sharma, S.; Singh, V.; Vaishali; Kumar, R.; Jamra, R.; Banyal, N.; Jyoti. From 2011 to 2022: The Development of Pyrazole Derivatives through the α,β-Unsaturated Carbonyl Compounds. *Journal of Heterocyclic Chemistry* **2024**, *61* (2), 232–284. https://doi.org/10.1002/jhet.4758.

(418) Hockstedler, A. N.; Edjah, B. A.; Azhar, S. Z.; Mendoza, H.; Brown, N. A.; Arrowood, H. B.; Clay, A. C.; Shah, A. B.; Duffek, G. M.; Cui, J.; et al. 13C NMR Spectroscopy of Heterocycles: 1-Phenyl-3-Aryl/t-Butyl-5-Arylpyrazoles. *Heterocyclic Communications* **2017**, *23* (2), 125–131. https://doi.org/10.1515/hc-2017-0034.

(419) Pratt, B. A.; Mohan, R. Fused Bicyclic Compounds for the Treatment of Disease. WO2016081918, 2016.

(420) Ulomskiy, E. N.; Lyapustin, D. N.; Mukhin, E. M.; Voinkov, E. K.; Fedotov, V. V.; Savateev, K. V.; Eltsov, O. S.; Gorbunov, E. B.; Drokin, R. A.; Rusinov, V. L.; et al. ANRORC Process in 1-Alkylazolo[5,1-c][1,2,4]Triazin-4(1H)-Ones. *Chemistry of Heterocyclic Compounds* **2018**, *54* (1), 63–69. https://doi.org/10.1007/s10593-018-2231-0.

(421) Huang, A.; Wo, K.; Lee, S. Y. C.; Kneitschel, N.; Chang, J.; Zhu, K.; Mello, T.; Bancroft, L.; Norman, N. J.; Zheng, S.-L. Regioselective Synthesis, NMR, and Crystallographic Analysis of N1-Substituted Pyrazoles. *The Journal of Organic Chemistry* **2017**, *82* (17), 8864–8872. https://doi.org/10.1021/acs.joc.7b01006.

(422) Meador, R. I. L.; Mate, N. A.; Chisholm, J. D. Acid Catalyzed N-Alkylation of Pyrazoles with Trichloroacetimidates. *Organics* **2022**, *3* (2), 111–121. https://doi.org/10.3390/org3020009.

(423) Cran, J. W.; Vidhani, D. V.; Krafft, M. E. Copper-Catalyzed N-Tert-Butylation of Aromatic Amines under Mild Condi-tions Using Tert-Butyl 2,2,2-Trichloroacetimidate. *Synlett* **2014**, *25*, 1550–1554. https://doi.org/10.1055/s-0033-1339107.

(424) Sweis, R. F. Target (In)Validation: A Critical, Sometimes Unheralded, Role of Modern Medicinal Chemistry. *ACS Medicinal Chemistry Letters* **2015**, *6* (6), 618–621. https://doi.org/10.1021/acsmedchemlett.5b00183.

(425) Garbison, K. E.; Heinz, B. A.; Lajiness, M. E. IP-3/IP-1 Assays. In *Assay Guidance Manual*; Markossian, S., Grossman, A., Baskir, H., Arkin, M., Auld, D., Austin, C., Baell, J., Brimacombe, K., Chung, T. D. Y., Coussens, N. P., et al., Eds.; Eli Lilly & Company and the National Center for Advancing Translational Sciences: Bethesda (MD), 2004.

(426) Wang, S; Alousi, A; Thompson, A. The Lifetime of Inositol 1,4,5-Trisphosphate in Single Cells. *The Journal of General Physiology* **1995**, *105* (1), 149–171. https://doi.org/10.1085/jgp.105.1.149.

(427) Jamaluddin, A. Quantifying Gq Signaling Using the IP1 Homogenous Time-Resolved Fluorescence (HTRF) Assay. In *Calcium Signaling: Methods and Protocols*; Gorvin, C. M., Ed.; Springer US: New York, NY, 2025; pp 23–32. https://doi.org/10.1007/978-1-0716-4164-4_2.

(428) Abbracchio, M. P.; Burnstock, G.; Boeynaems, J.-M.; Barnard, E. A.; Boyer, J. L.; Kennedy, C.; Knight, G. E.; Fumagalli, M.; Gachet, C.; Jacobson, K. A.; et al. International Union of Pharmacology LVIII: Update on the P2Y G Protein-Coupled Nucleotide Receptors: From Molecular Mechanisms and Pathophysiology to Therapy. *Pharmacological Reviews* **2006**, *58* (3), 281–341. https://doi.org/10.1124/pr.58.3.3.

(429) Govindan, S.; Taylor, E. J.; Taylor, C. W. Ca2+ Signalling by P2Y Receptors in Cultured Rat Aortic Smooth Muscle Cells. *British Journal of Pharmacology* **2010**, *160* (8), 1953–1962. https://doi.org/10.1111/j.1476-5381.2010.00763.x.

(430) Lee, C. R.; Guivarch, F.; Dau, C. N. V.; Tessier, D.; Krstulovic, A. M. Determination of Polar Alkylating Agents as Thiocyanate/Isothiocyanate Derivatives by Reaction Headspace Gas Chromatography. *Analyst* **2003**, *128* (7), 857–863. https://doi.org/10.1039/B300721A.

(431) Joseph, V. B.; Satchell, D. P. N.; Satchell, R. S.; Wassef, W. N. Hydrolysis of Aryl and Alkyl Isothiocyanates in Aqueous Perchloric Acid. *Journal of the Chemical Society, Perkin Transactions 2* **1992**, 339–341. https://doi.org/10.1039/P29920000339.

(432) Robaye, B.; Boeynaems, J.-M.; Communi, D. Slow Desensitization of the Human P2Y6 Receptor. *European Journal of Pharmacology* **1997**, *329* (2), 231–236. https://doi.org/10.1016/S0014-2999(97)89184-4.

(433) Southey, M. W. Y.; Brunavs, M. Introduction to Small Molecule Drug Discovery and Preclinical Development. *Frontiers in Drug Discovery* **2023**, *3*, 1314077. https://doi.org/10.3389/fddsv.2023.1314077.

(434) Dunker, C.; Vinnenberg, L.; Isaak, A.; Karabatak, E.; Hundehege, P.; Budde, T.; Murakami, K.; Junker, A. Exploring P2X Receptor Activity: A Journey from Cellular Impact to Electrophysiological Profiling. *Biochemical Pharmacology* **2024**, *229*, 116543. https://doi.org/10.1016/j.bcp.2024.116543.

(435) Atwood, B. K.; Lopez, J.; Wager-Miller, J.; Mackie, K.; Straiker, A. Expression of G Protein-Coupled Receptors and Related Proteins in HEK293, AtT20, BV2, and N18 Cell Lines as Revealed by Microarray Analysis. *BMC Genomics* **2011**, *12*, 14. https://doi.org/10.1186/1471-2164-12-14.

(436) Bianchi, B. R.; Lynch, K. J.; Touma, E.; Niforatos, W.; Burgard, E. C.; Alexander, K. M.; Park, H. S.; Yu, H.; Metzger, R.; Kowaluk, E.; et al. Pharmacological Characterization of Recombinant Human and Rat P2X Receptor Subtypes. *European Journal of Pharmacology* **1999**, *376* (1), 127–138. https://doi.org/10.1016/S0014-2999(99)00350-7.

(437) Schachter, J. B.; Li, Q.; Boyer, J. L.; Nicholas, R. A.; Harden, T. K. Second Messenger Cascade Specificity and Pharmacological Selectivity of the Human P2Y1-Purinoceptor. *British Journal of Pharmacology* **1996**, *118* (1), 167–173. https://doi.org/10.1111/j.1476-5381.1996.tb15381.x.

(438) Werry, T. D.; Christie, M. I.; Dainty, I. A.; Wilkinson, G. F.; Willars, G. B. Ca2+ Signalling by Recombinant Human CXCR2 Chemokine Receptors Is Potentiated by P2Y Nucleotide Receptors in HEK Cells. *British Journal of Pharmacology* **2002**, *135* (5), 1199–1208. https://doi.org/10.1038/sj.bjp.0704566.

(439) Iredale, P. A.; Hill, S. J. Increases in Intracellular Calcium via Activation of an Endogenous P2-Purinoceptor in Cultured CHO-K1 Cells. *British Journal of Pharmacology* **1993**, *110* (4), 1305–1310. https://doi.org/10.1111/j.1476-5381.1993.tb13960.x.

(440) Lazarowski, E. R.; Shea, D. A.; Boucher, R. C.; Harden, T. K. Release of Cellular UDP-Glucose as a Potential Extracellular Signaling Molecule. *Molecular Pharmacology* **2003**, *63* (5), 1190–1197. https://doi.org/10.1124/mol.63.5.1190.

(441) Charlton, S. J.; Vauquelin, G. Elusive Equilibrium: The Challenge of Interpreting Receptor Pharmacology Using Calcium Assays. *British Journal of Pharmacology* **2010**, *161* (6), 1250–1265. https://doi.org/10.1111/j.1476-5381.2010.00863.x.

(442) Plonski, A. P.; Reed, S. M. Assessing Protein Homology Models with Docking Reproducibility. *Journal of Molecular Graphics and Modelling* **2023**, *121*, 108430. https://doi.org/10.1016/j.jmgm.2023.108430.

(443) Cavasotto, C. N. Homology Models in Docking and High-Throughput Docking. *Current Topics in Medicinal Chemistry* **2011**, *11* (12), 1528–1534. https://doi.org/10.2174/156802611795860951.

(444) Xiang, Z. Advances in Homology Protein Structure Modeling. *Current Protein & Peptide Science* **2006**, *7* (3), 217–227. https://doi.org/10.2174/138920306777452312.

(445) Hameduh, T.; Haddad, Y.; Adam, V.; Heger, Z. Homology Modeling in the Time of Collective and Artificial Intelligence. *Computational and Structural Biotechnology Journal* **2020**, *18*, 3494–3506. https://doi.org/10.1016/j.csbj.2020.11.007.

(446) Zhang, D.; Gao, Z.-G.; Zhang, K.; Kiselev, E.; Crane, S.; Wang, J.; Paoletta, S.; Yi, C.; Ma, L.; Zhang, W.; et al. Two Disparate Ligand Binding Sites in the Human P2Y1 Receptor. *Nature* **2015**, *520* (7547), 317–321. https://doi.org/10.1038/nature14287.

(447) Binbay, F. A.; Rathod, D. C.; George, A. A. P.; Imhof, D. Quality Assessment of Selected Protein Structures Derived from Homology Modeling and AlphaFold. *Pharmaceuticals* **2023**, *16* (12), 1662. https://doi.org/10.3390/ph16121662.

(448) Jumper, J.; Evans, R.; Pritzel, A.; Green, T.; Figurnov, M.; Ronneberger, O.; Tunyasuvunakool, K.; Bates, R.; Žídek, A.; Potapenko, A.; et al. Highly Accurate Protein Structure Prediction with AlphaFold. *Nature* **2021**, *596* (7873), 583–589. https://doi.org/10.1038/s41586-021-03819-2.

(449) Shelley, J. C.; Cholleti, A.; Frye, L. L.; Greenwood, J. R.; Timlin, M. R.; Uchimaya, M. Epik: A Software Program for pK(a) Prediction and Protonation State Generation for Drug-like Molecules. *Journal of Computer-Aided Molecular Design* **2007**, *21* (12), 681–691. https://doi.org/10.1007/s10822-007-9133-z.

(450) Cross, J. B.; Thompson, D. C.; Rai, B. K.; Baber, J. C.; Fan, K. Y.; Hu, Y.; Humblet, C. Comparison of Several Molecular Docking Programs: Pose Prediction and Virtual Screening Accuracy. *Journal of Chemical Information and Modeling* **2009**, *49* (6), 1455–1474. https://doi.org/10.1021/ci900056c.

(451) Mirdita, M.; Schutze, K.; Moriwaki, Y.; Heo, L.; Ovchinnikov, S.; Steinegger, M. ColabFold: Making Protein Folding Accessible to All | Nature Methods. *Nature Methods* **2022**, *19*, 679–682.

(452) Tse, E. G.; Houston, S. D.; Williams, C. M.; Savage, G. P.; Rendina, L. M.; Hallyburton, I.; Anderson, M.; Sharma, R.; Walker, G. S.; Obach, R. S.; et al. Nonclassical Phenyl Bioisosteres as Effective Replacements in a Series of Novel

Open-Source Antimalarials. *Journal of Medicinal Chemistry* **2020**, *63* (20), 11585–11601. https://doi.org/10.1021/acs.jmedchem.0c00746.

(453) Tsien, J.; Hu, C.; Merchant, R. R.; Qin, T. Three-Dimensional Saturated C(Sp3)-Rich Bioisosteres for Benzene. *Nature Reviews Chemistry* **2024**, *8* (8), 605–627. https://doi.org/10.1038/s41570-024-00623-0.

(454) Callis, T. B.; Garrett, T. R.; Montgomery, A. P.; Danon, J. J.; Kassiou, M. Recent Scaffold Hopping Applications in Central Nervous System Drug Discovery. *Journal of Medicinal Chemistry* **2022**, *65* (20), 13483–13504. https://doi.org/10.1021/acs.jmedchem.2c00969.

(455) Monaco, S.; Browne, J.; Wallace, M.; Angulo, J.; Stokes, L. On-Cell Saturation Transfer Difference NMR Spectroscopy on Ion Channels: Characterizing Negative Allosteric Modulator Binding Interactions of P2X7. *Journal of the American Chemical Society* **2025**, *147* (36). https://doi.org/10.1021/jacs.5c02985.

(456) Pethick, S.; Wass, M. N.; Michaelis, M. Is There a Reproducibility Crisis? On the Need for Evidence-Based Approaches. *International Studies in the Philosophy of Science* **2025**, 1–17. https://doi.org/10.1080/02698595.2025.2538937.

(457) Baker, M. 1,500 Scientists Lift the Lid on Reproducibility. *Nature* **2016**, *533* (7604), 452–454. https://doi.org/10.1038/533452a.

(458) Udesky, L. 'Publish or Perish' Culture Blamed for Reproducibility Crisis. *Nature* **2025**. https://doi.org/10.1038/d41586-024-04253-w.

(459) Miyakawa, T. No Raw Data, No Science: Another Possible Source of the Reproducibility Crisis. *Molecular Brain* **2020**, *13* (1), 24. https://doi.org/10.1186/s13041-020-0552-2.

(460) Reddin, I. G.; Fenton, T. R.; Wass, M. N.; Michaelis, M. Large Inherent Variability in Data Derived from Highly Standardised Cell Culture Experiments. *Pharmacological Research* **2023**, *188*, 106671. https://doi.org/10.1016/j.phrs.2023.106671.

(461) Calnan, M.; Kirchin, S.; Roberts, D. L.; Wass, M. N.; Michaelis, M. Understanding and Tackling the Reproducibility Crisis – Why We Need to Study Scientists' Trust in Data. *Pharmacological Research* **2024**, *199*, 107043. https://doi.org/10.1016/j.phrs.2023.107043.

(462) McVicker, R. U.; O'Boyle, N. M. Chirality of New Drug Approvals (2013–2022): Trends and Perspectives. *Journal of Medicinal Chemistry* **2024**, *67* (4), 2305–2320. https://doi.org/10.1021/acs.jmedchem.3c02239.

(463) Li, L.; Lai, L.; Qiu, D.; Ding, Y.; Yu, M.; Zhang, T.; Wang, Z.; Wang, S. P2Y6 Receptor: A Promising Therapeutic Target for Atherosclerosis. *European Journal of Pharmacology* **2025**, *998*, 177513. https://doi.org/10.1016/j.ejphar.2025.177513.

(464) Daghbouche-Rubio, N.; Álvarez-Miguel, I.; Flores, V. A.; Rojo-Mencía, J.; Navedo, M.; Nieves-Citrón, M.; Cidad, P.; Pérez-García, M. T.; López-López, J. R. The P2Y6 Receptor as a Potential Keystone in Essential Hypertension. *Function* **2024**, *5* (6), zqae045. https://doi.org/10.1093/function/zqae045.

(465) Xu, Y.; Li, W.; Zhang, J.; Gao, W.; Zhang, T.; Chen, Q.; Wang, N.; Zhou, Y.; Zhang, F.; Qin, J. Inhibition of P2Y6 Receptor-Mediated Microglia Phagocytosis Aggravates Brain Injury in Mice of Intracerebral Hemorrhage. *Cellular and Molecular Neurobiology* **2025**, *45* (1), 67. https://doi.org/10.1007/s10571-025-01573-x.

(466) Bano, S.; Hussain, Z.; Langer, P.; Weisman, G. A.; Iqbal, J. Synthesis, Structure-Activity Relationships and Biological Evaluation of Benzimidazole Derived

Sulfonylurea Analogues as a New Class of Antagonists of P2Y1 Receptor. *Frontiers in Pharmacology* **2023**, *14*, 1217315. https://doi.org/10.3389/fphar.2023.1217315.

(467) Pinzi, L.; Bisi, N.; Rastelli, G. How Drug Repurposing Can Advance Drug Discovery: Challenges and Opportunities. *Frontiers in Drug Discovery* **2024**, *4*, 1460100. https://doi.org/10.3389/fddsv.2024.1460100.

(468) Chen, H.; Wu, J.; Gao, Y.; Chen, H.; Zhou, J. Scaffold Repurposing of Old Drugs Towards New Cancer Drug Discovery. *Current Topics in Medicinal Chemistry* **2016**, *16* (19), 2107–2114. https://doi.org/10.2174/1568026616666160216155556.

(469) Jacobson, M. P.; Friesner, R. A.; Xiang, Z.; Honig, B. On the Role of the Crystal Environment in Determining Protein Side-Chain Conformations. *Journal of Molecular Biology* **2002**, *320* (3), 597–608. https://doi.org/10.1016/S0022-2836(02)00470-9.

(470) Jacobson, M. P.; Pincus, D. L.; Rapp, C. S.; Day, T. J. F.; Honig, B.; Shaw, D. E.; Friesner, R. A. A Hierarchical Approach to All-Atom Protein Loop Prediction. *Proteins: Structure, Function, and Bioinformatics* **2004**, *55* (2), 351–367. https://doi.org/10.1002/prot.10613.

(471) Sherman, W.; Day, T.; Jacobson, M. P.; Friesner, R. A.; Farid, R. Novel Procedure for Modeling Ligand/Receptor Induced Fit Effects. *Journal of Medicinal Chemistry* **2006**, *49* (2), 534–553. https://doi.org/10.1021/jm050540c.

(472) Friesner, R. A.; Banks, J. L.; Murphy, R. B.; Halgren, T. A.; Klicic, J. J.; Mainz, D. T.; Repasky, M. P.; Knoll, E. H.; Shelley, M.; Perry, J. K.; et al. Glide: A New Approach for Rapid, Accurate Docking and Scoring. 1. Method and Assessment of Docking Accuracy. *Journal of Medicinal Chemistry* **2004**, *47* (7), 1739–1749. https://doi.org/10.1021/jm0306430.

(473) Wheatley, E.; Melnychenko, H.; Silvi, M. Iterative One-Carbon Homologation of Unmodified Carboxylic Acids. *Journal of the American Chemical Society* **2024**, *146* (50), 34285–34291. https://doi.org/10.1021/jacs.4c13630.

(474) Liang, A.; Han, S.; Wang, L.; Li, J.; Zou, D.; Wu, Y.; Wu, Y. Palladium-Catalyzed Carbonylations of Arylboronic Acids: Synthesis of Arylcarboxylic Acid Ethyl Esters. *Advanced Synthesis & Catalysis* **2015**, *357* (14–15), 3104–3108. https://doi.org/10.1002/adsc.201500521.

(475) Mamuye, A. D.; Castoldi, L.; Azzena, U.; Holzer, W.; Pace, V. Chemoselective Efficient Synthesis of Functionalized β-Oxonitriles through Cyanomethylation of Weinreb Amides. *Organic & Biomolecular Chemistry* **2015**, *13* (7), 1969–1973. https://doi.org/10.1039/C4OB02398F.

(476) Urquilla, A.; Merrer, D. C.; Sumner, R.; Denton, R. W. Synthesis and Biological Activity of 2-(2-Amino-2-Phenylethyl)-5-Oxotetrahydrofuran-2-Carboxylic Acid: A Microwave-Assisted 1,3-Dipolar Cycloaddition Approach. *Synlett* **2021**, *32*, 1735–1740. https://doi.org/10.1055/a-1560-1767.

(477) Wang, L.; Wang, Y.; Shen, J.; Chen, Q.; He, M.-Y. Nickel-Catalyzed Cyanation of Phenol Derivatives Activated by 2,4,6-Trichloro-1,3,5-Triazine. *Organic & Biomolecular Chemistry* **2018**, *16* (26), 4816–4820. https://doi.org/10.1039/C8OB01034J.

(478) Wang, D.; Cao, F.-R.; Lu, G.; Ren, J.; Zeng, B.-B. Practical Acetalization and Transacetalization of Carbonyl Compounds Catalyzed by Recyclable PVP-I. *Tetrahedron* **2021**, *92*, 132250. https://doi.org/10.1016/j.tet.2021.132250.

Appendix

Appendix 1. Crystal Structure of Compound 90

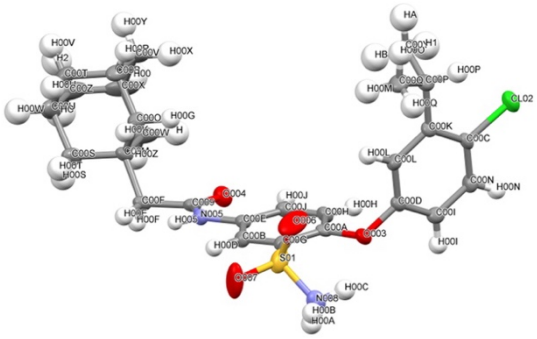

≡

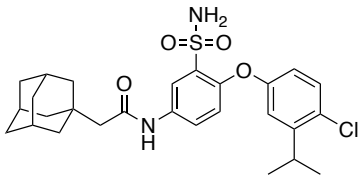

Table 1. Crystal data and structure refinement for 23bh004.

Identification code	shelx
Empirical formula	C27 H33 Cl N2 O4 S
Formula weight	517.06
Temperature	150(2) K
Wavelength	0.71073 Å
Crystal system	Triclinic
Space group	P -1
Unit cell dimensions	a = 8.0355(5) Å; a= 89.577(5)°. b = 11.1161(7) Å; b= 83.738(5)°. c = 15.0561(9) Å; g = 79.054(5)°.
Volume	1312.39(14) $Å^3$
Z	2
Density (calculated)	1.308 Mg/m^3
Absorption coefficient	0.261 mm^{-1}
F(000)	548
Crystal size	0.310 x 0.110 x 0.080 mm^3
Theta range for data collection	2.722 to 26.370°.
Index ranges	-8<=h<=10, -13<=k<=12, -18<=l<=18
Reflections collected	8998
Independent reflections	5296 [R(int) = 0.0955]
Completeness to theta = 25.242°	99.1 %
Absorption correction	None
Refinement method	Full-matrix least-squares on F^2
Data / restraints / parameters	5296 / 0 / 330
Goodness-of-fit on F^2	1.036
Final R indices [I>2sigma(I)]	R1 = 0.0595, wR2 = 0.1217
R indices (all data)	R1 = 0.1013, wR2 = 0.1452
Extinction coefficient	n/a
Largest diff. peak and hole	0.368 and -0.363 $e.Å^{-3}$

Table 2. Atomic coordinates (x 10^4) and equivalent isotropic displacement parameters ($Å^2$x 10^3) for 23bh004. U(eq) is defined as one third of the trace of the orthogonalised U^{ij} tensor.

Atom	x	y	z	U(eq)
C(1)	2451(4)	5027(2)	6444(2)	25(1)
C(2)	3773(4)	5246(2)	6894(2)	24(1)
C(3)	4861(4)	5982(2)	6524(2)	28(1)
C(4)	4596(4)	6530(2)	5704(2)	28(1)
C(5)	3267(4)	6325(2)	5251(2)	23(1)
C(6)	2206(4)	5552(2)	5616(2)	27(1)
C(7)	3799(4)	7550(2)	3889(2)	26(1)
C(8)	3011(4)	7987(2)	3052(2)	28(1)
C(9)	2343(4)	9390(2)	3035(2)	26(1)
C(10)	1188(4)	9847(2)	3882(2)	31(1)
C(11)	485(4)	11229(3)	3827(2)	38(1)
C(12)	-563(4)	11467(3)	3035(2)	47(1)
C(13)	575(6)	11027(3)	2186(2)	55(1)
C(14)	1289(5)	9656(3)	2242(2)	47(1)
C(15)	3804(4)	10100(2)	2915(3)	50(1)
C(16)	3093(5)	11473(3)	2844(3)	62(1)
C(17)	1973(5)	11907(3)	3711(3)	51(1)
C(18)	2023(6)	11717(3)	2060(3)	74(2)
C(19)	4588(4)	5326(2)	8362(2)	25(1)
C(20)	6261(4)	5026(2)	8520(2)	29(1)
C(21)	6820(4)	5665(2)	9179(2)	30(1)
C(22)	5663(4)	6571(2)	9660(2)	24(1)
C(23)	3944(4)	6869(2)	9527(2)	25(1)
C(24)	3434(4)	6223(2)	8849(2)	26(1)
C(25)	2719(4)	7864(2)	10069(2)	35(1)
C(26)	2822(5)	9120(3)	9655(2)	51(1)
C(27)	889(4)	7651(3)	10200(2)	40(1)
N(1)	2896(3)	6861(2)	4420(2)	25(1)
N(2)	2003(4)	2858(2)	7248(2)	35(1)
O(1)	3992(3)	4661(2)	7707(1)	29(1)
O(2)	5151(3)	7803(2)	4071(1)	36(1)
O(3)	83(3)	4777(2)	7708(2)	61(1)
O(4)	56(3)	3871(2)	6216(2)	64(1)
S(1)	987(1)	4139(1)	6925(1)	38(1)

Cl(1)	6459(1)	7363(1)	10478(1)	39(1)

Table 3. Bond lengths [Å] and angles [°] for 23bh004.

Atom-Atom	Length/Å	Atom-Atom	Length/Å
C(1)-C(2)	1.380(4)	C(15)-H(15A)	0.9900
C(1)-C(6)	1.390(4)	C(15)-H(15B)	0.9900
C(1)-S(1)	1.768(3)	C(16)-C(17)	1.527(5)
C(2)-C(3)	1.378(4)	C(16)-C(18)	1.528(6)
C(2)-O(1)	1.394(3)	C(16)-H(16)	1.0000
C(3)-C(4)	1.392(4)	C(17)-H(17A)	0.9900
C(3)-H(3)	0.9500	C(17)-H(17B)	0.9900
C(4)-C(5)	1.383(4)	C(18)-H(18A)	0.9900
C(4)-H(4)	0.9500	C(18)-H(18B)	0.9900
C(5)-C(6)	1.392(4)	C(19)-C(20)	1.369(4)
C(5)-N(1)	1.418(3)	C(19)-C(24)	1.380(4)
C(6)-H(6)	0.9500	C(19)-O(1)	1.413(3)
C(7)-O(2)	1.232(3)	C(20)-C(21)	1.385(4)
C(7)-N(1)	1.353(4)	C(20)-H(20)	0.9500
C(7)-C(8)	1.507(4)	C(21)-C(22)	1.383(4)
C(8)-C(9)	1.551(3)	C(21)-H(21)	0.9500
C(8)-H(8A)	0.9900	C(22)-C(23)	1.394(4)
C(8)-H(8B)	0.9900	C(22)-Cl(1)	1.761(3)
C(9)-C(10)	1.523(4)	C(23)-C(24)	1.393(4)
C(9)-C(15)	1.529(4)	C(23)-C(25)	1.510(4)
C(9)-C(14)	1.533(4)	C(24)-H(24)	0.9500
C(10)-C(11)	1.538(4)	C(25)-C(27)	1.525(4)
C(10)-H(10A)	0.9900	C(25)-C(26)	1.537(4)
C(10)-H(10B)	0.9900	C(25)-H(25)	1.0000
C(11)-C(17)	1.524(5)	C(26)-H(26A)	0.9800
C(11)-C(12)	1.527(4)	C(26)-H(26B)	0.9800
C(11)-H(11)	1.0000	C(26)-H(26C)	0.9800
C(12)-C(13)	1.516(5)	C(27)-H(27A)	0.9800
C(12)-H(12A)	0.9900	C(27)-H(27B)	0.9800
C(12)-H(12B)	0.9900	C(27)-H(27C)	0.9800
C(13)-C(18)	1.505(6)	N(1)-H(01)	0.85(3)
C(13)-C(14)	1.528(4)	N(2)-S(1)	1.602(3)
C(13)-H(13)	1.0000	N(2)-H(02)	0.82(3)

C(14)-H(14A)	0.9900	N(2)-H(03)	0.87(4)
C(14)-H(14B)	0.9900	O(3)-S(1)	1.431(2)
C(15)-C(16)	1.532(4)	O(4)-S(1)	1.432(2)

Atom-Atom-Atom	Length/Å	Atom-Atom-Atom	Length/Å
C(2)-C(1)-C(6)	120.0(3)	H(15A)-C(15)-H(15B)	108.2
C(2)-C(1)-S(1)	121.1(2)	C(17)-C(16)-C(18)	109.2(3)
C(6)-C(1)-S(1)	118.8(2)	C(17)-C(16)-C(15)	108.5(3)
C(3)-C(2)-C(1)	120.3(3)	C(18)-C(16)-C(15)	110.5(3)
C(3)-C(2)-O(1)	122.2(3)	C(17)-C(16)-H(16)	109.5
C(1)-C(2)-O(1)	117.5(2)	C(18)-C(16)-H(16)	109.5
C(2)-C(3)-C(4)	119.8(3)	C(15)-C(16)-H(16)	109.5
C(2)-C(3)-H(3)	120.1	C(11)-C(17)-C(16)	109.2(3)
C(4)-C(3)-H(3)	120.1	C(11)-C(17)-H(17A)	109.8
C(5)-C(4)-C(3)	120.4(3)	C(16)-C(17)-H(17A)	109.8
C(5)-C(4)-H(4)	119.8	C(11)-C(17)-H(17B)	109.8
C(3)-C(4)-H(4)	119.8	C(16)-C(17)-H(17B)	109.8
C(4)-C(5)-C(6)	119.5(3)	H(17A)-C(17)-H(17B)	108.3
C(4)-C(5)-N(1)	124.0(3)	C(13)-C(18)-C(16)	109.7(3)
C(6)-C(5)-N(1)	116.6(2)	C(13)-C(18)-H(18A)	109.7
C(1)-C(6)-C(5)	120.0(3)	C(16)-C(18)-H(18A)	109.7
C(1)-C(6)-H(6)	120.0	C(13)-C(18)-H(18B)	109.7
C(5)-C(6)-H(6)	120.0	C(16)-C(18)-H(18B)	109.7
O(2)-C(7)-N(1)	123.0(3)	H(18A)-C(18)-H(18B)	108.2
O(2)-C(7)-C(8)	122.6(3)	C(20)-C(19)-C(24)	122.3(3)
N(1)-C(7)-C(8)	114.4(3)	C(20)-C(19)-O(1)	119.3(2)
C(7)-C(8)-C(9)	114.1(2)	C(24)-C(19)-O(1)	118.3(3)
C(7)-C(8)-H(8A)	108.7	C(19)-C(20)-C(21)	118.7(3)
C(9)-C(8)-H(8A)	108.7	C(19)-C(20)-H(20)	120.6
C(7)-C(8)-H(8B)	108.7	C(21)-C(20)-H(20)	120.6
C(9)-C(8)-H(8B)	108.7	C(22)-C(21)-C(20)	118.8(3)
H(8A)-C(8)-H(8B)	107.6	C(22)-C(21)-H(21)	120.6
C(10)-C(9)-C(15)	108.9(2)	C(20)-C(21)-H(21)	120.6
C(10)-C(9)-C(14)	108.0(2)	C(21)-C(22)-C(23)	123.4(2)
C(15)-C(9)-C(14)	108.7(3)	C(21)-C(22)-Cl(1)	116.6(2)
C(10)-C(9)-C(8)	111.7(2)	C(23)-C(22)-Cl(1)	120.0(2)
C(15)-C(9)-C(8)	111.7(2)	C(24)-C(23)-C(22)	116.2(2)

C(14)-C(9)-C(8)	107.8(2)
C(9)-C(10)-C(11)	110.4(2)
C(9)-C(10)-H(10A)	109.6
C(11)-C(10)-H(10A)	109.6
C(9)-C(10)-H(10B)	109.6
C(11)-C(10)-H(10B)	109.6
H(10A)-C(10)-H(10B)	108.1
C(17)-C(11)-C(12)	110.3(3)
C(17)-C(11)-C(10)	109.0(3)
C(12)-C(11)-C(10)	109.3(2)
C(17)-C(11)-H(11)	109.4
C(12)-C(11)-H(11)	109.4
C(10)-C(11)-H(11)	109.4
C(13)-C(12)-C(11)	108.9(3)
C(13)-C(12)-H(12A)	109.9
C(11)-C(12)-H(12A)	109.9
C(13)-C(12)-H(12B)	109.9
C(11)-C(12)-H(12B)	109.9
H(12A)-C(12)-H(12B)	108.3
C(18)-C(13)-C(12)	109.7(3)
C(18)-C(13)-C(14)	109.5(3)
C(12)-C(13)-C(14)	109.8(3)
C(18)-C(13)-H(13)	109.3
C(12)-C(13)-H(13)	109.3
C(14)-C(13)-H(13)	109.3
C(13)-C(14)-C(9)	110.7(2)
C(13)-C(14)-H(14A)	109.5
C(9)-C(14)-H(14A)	109.5
C(13)-C(14)-H(14B)	109.5
C(9)-C(14)-H(14B)	109.5
H(14A)-C(14)-H(14B)	108.1
C(9)-C(15)-C(16)	110.1(3)
C(9)-C(15)-H(15A)	109.6
C(16)-C(15)-H(15A)	109.6
C(9)-C(15)-H(15B)	109.6
C(16)-C(15)-H(15B)	109.6
C(24)-C(23)-C(25)	122.0(3)
C(22)-C(23)-C(25)	121.8(2)
C(19)-C(24)-C(23)	120.5(3)
C(19)-C(24)-H(24)	119.7
C(23)-C(24)-H(24)	119.7
C(23)-C(25)-C(27)	113.8(2)
C(23)-C(25)-C(26)	109.8(3)
C(27)-C(25)-C(26)	111.6(2)
C(23)-C(25)-H(25)	107.0
C(27)-C(25)-H(25)	107.0
C(26)-C(25)-H(25)	107.0
C(25)-C(26)-H(26A)	109.5
C(25)-C(26)-H(26B)	109.5
H(26A)-C(26)-H(26B)	109.5
H(26B)-C(26)-H(26C)	109.5
C(25)-C(27)-H(27A)	109.5
C(25)-C(27)-H(27B)	109.5
H(27A)-C(27)-H(27B)	109.5
C(25)-C(27)-H(27C)	109.5
H(27A)-C(27)-H(27C)	109.5
H(27B)-C(27)-H(27C)	109.5
C(7)-N(1)-C(5)	128.6(3)
C(7)-N(1)-H(01)	115.0(17)
C(5)-N(1)-H(01)	116.4(17)
S(1)-N(2)-H(02)	116(2)
S(1)-N(2)-H(03)	109(2)
H(02)-N(2)-H(03)	105(3)
C(2)-O(1)-C(19)	115.91(19)
O(3)-S(1)-O(4)	119.38(17)
O(3)-S(1)-N(2)	106.92(16)
O(4)-S(1)-N(2)	107.06(16)
O(3)-S(1)-C(1)	107.78(14)
O(4)-S(1)-C(1)	105.83(14)
N(2)-S(1)-C(1)	109.66(14)

Table 4. Anisotropic displacement parameters ($Å^2 x\ 10^3$)for 23bh004. The anisotropic displacement factor exponent takes the form: $-2p^2[\ h^2 a^{*2} U^{11} + ... + 2\ h\ k\ a^*\ b^*\ U^{12}\ ]$

Atom	U^{11}	U^{22}	U^{33}	U^{23}	U^{13}	U^{12}
C(1)	22(2)	25(1)	27(2)	1(1)	3(1)	-3(1)
C(2)	32(2)	19(1)	19(2)	-7(1)	2(1)	-2(1)
C(3)	29(2)	27(2)	29(2)	-5(1)	-2(1)	-9(1)
C(4)	33(2)	26(1)	27(2)	-2(1)	4(1)	-12(1)
C(5)	25(2)	22(1)	21(2)	-5(1)	2(1)	-4(1)
C(6)	25(2)	28(2)	27(2)	-1(1)	-2(1)	-4(1)
C(7)	31(2)	21(1)	25(2)	-5(1)	2(1)	-5(1)
C(8)	39(2)	24(1)	23(2)	-4(1)	4(1)	-10(1)
C(9)	38(2)	21(1)	21(2)	-3(1)	1(1)	-9(1)
C(10)	37(2)	30(2)	24(2)	2(1)	5(1)	-2(1)
C(11)	48(2)	32(2)	26(2)	-2(1)	11(2)	5(1)
C(12)	48(2)	33(2)	55(2)	8(2)	-12(2)	3(2)
C(13)	102(3)	33(2)	28(2)	4(1)	-15(2)	-3(2)
C(14)	87(3)	27(2)	26(2)	2(1)	-12(2)	-3(2)
C(15)	48(2)	24(2)	75(3)	-8(2)	23(2)	-13(1)
C(16)	60(3)	26(2)	96(3)	-10(2)	27(2)	-21(2)
C(17)	63(3)	27(2)	63(3)	-14(2)	-7(2)	-4(2)
C(18)	128(4)	25(2)	53(3)	9(2)	39(3)	-1(2)
C(19)	35(2)	24(1)	17(2)	1(1)	-2(1)	-8(1)
C(20)	31(2)	28(2)	24(2)	-1(1)	5(1)	-3(1)
C(21)	27(2)	34(2)	30(2)	5(1)	-4(1)	-8(1)
C(22)	30(2)	28(1)	18(2)	-1(1)	-2(1)	-10(1)
C(23)	30(2)	27(1)	19(2)	3(1)	-1(1)	-4(1)
C(24)	26(2)	28(1)	23(2)	1(1)	-3(1)	-1(1)
C(25)	38(2)	36(2)	28(2)	-7(1)	-3(2)	0(1)
C(26)	62(3)	33(2)	54(2)	-8(2)	-3(2)	-3(2)
C(27)	35(2)	44(2)	34(2)	-6(1)	3(2)	7(1)
N(1)	25(2)	28(1)	24(1)	0(1)	-3(1)	-10(1)
N(2)	37(2)	38(2)	33(2)	6(1)	-2(2)	-17(1)
O(1)	38(1)	28(1)	23(1)	-2(1)	-5(1)	-10(1)
O(2)	37(1)	41(1)	31(1)	2(1)	-2(1)	-16(1)
O(3)	39(2)	63(2)	66(2)	10(1)	32(1)	5(1)
O(4)	54(2)	92(2)	67(2)	46(1)	-35(2)	-52(1)
S(1)	25(1)	49(1)	41(1)	16(1)	-1(1)	-13(1)

Cl(1)	47(1)	45(1)	30(1)	-2(1)	-10(1)	-18(1)

Table 5. Hydrogen coordinates (x 10^4) and isotropic displacement parameters (Å^{2}x 10^3) for 23bh004.

Atom	x	y	z	U(eq)
H(3)	5788	6113	6827	34
H(4)	5333	7049	5455	34
H(6)	1315	5382	5299	32
H(8A)	2052	7562	2989	34
H(8B)	3872	7751	2530	34
H(10A)	1840	9685	4406	38
H(10B)	230	9399	3962	38
H(11)	-257	11516	4391	45
H(12A)	-1528	11025	3115	56
H(12B)	-1032	12354	2998	56
H(13)	-107	11177	1665	66
H(14A)	2015	9371	1681	57
H(14B)	337	9201	2311	57
H(15A)	4567	9807	2367	60
H(15B)	4479	9955	3431	60
H(16)	4057	11929	2758	74
H(17A)	2652	11743	4224	62
H(17B)	1537	12800	3690	62
H(18A)	1564	12605	2024	89
H(18B)	2744	11450	1494	89
H(20)	7025	4392	8184	34
H(21)	7977	5483	9298	36
H(24)	2281	6400	8722	31
H(25)	3116	7871	10675	42
H(26A)	3985	9272	9652	76
H(26B)	2025	9761	10009	76
H(26C)	2523	9128	9041	76
H(27A)	429	7691	9622	60
H(27B)	191	8284	10604	60
H(27C)	871	6842	10460	60
H(01)	1990(30)	6730(20)	4220(17)	10(7)
H(02)	2700(40)	2470(30)	6870(20)	30(10)

H(03)	2600(50)	2990(30)	7670(30)	64(13)

Table 6. Torsion angles [°] for 23bh004.

A-B-C-D	**Angle/°**
C(6)-C(1)-C(2)-C(3)	-0.2(4)
S(1)-C(1)-C(2)-C(3)	-177.4(2)
C(6)-C(1)-C(2)-O(1)	-177.8(2)
S(1)-C(1)-C(2)-O(1)	5.0(3)
C(1)-C(2)-C(3)-C(4)	1.7(4)
O(1)-C(2)-C(3)-C(4)	179.1(2)
C(2)-C(3)-C(4)-C(5)	-1.2(4)
C(3)-C(4)-C(5)-C(6)	-0.8(4)
C(3)-C(4)-C(5)-N(1)	179.1(2)
C(2)-C(1)-C(6)-C(5)	-1.7(4)
S(1)-C(1)-C(6)-C(5)	175.5(2)
C(4)-C(5)-C(6)-C(1)	2.2(4)
N(1)-C(5)-C(6)-C(1)	-177.7(2)
O(2)-C(7)-C(8)-C(9)	-68.2(4)
N(1)-C(7)-C(8)-C(9)	111.7(3)
C(7)-C(8)-C(9)-C(10)	-50.9(3)
C(7)-C(8)-C(9)-C(15)	71.4(3)
C(7)-C(8)-C(9)-C(14)	-169.3(3)
C(15)-C(9)-C(10)-C(11)	58.6(3)
C(14)-C(9)-C(10)-C(11)	-59.2(3)
C(8)-C(9)-C(10)-C(11)	-177.5(2)
C(9)-C(10)-C(11)-C(17)	-59.6(3)
C(9)-C(10)-C(11)-C(12)	60.9(3)
C(17)-C(11)-C(12)-C(13)	59.6(3)
C(10)-C(11)-C(12)-C(13)	-60.2(4)
C(11)-C(12)-C(13)-C(18)	-60.5(3)
C(11)-C(12)-C(13)-C(14)	59.9(4)
C(18)-C(13)-C(14)-C(9)	60.4(4)
C(12)-C(13)-C(14)-C(9)	-60.1(4)
C(10)-C(9)-C(14)-C(13)	58.8(4)
C(15)-C(9)-C(14)-C(13)	-59.2(4)
C(8)-C(9)-C(14)-C(13)	179.6(3)
C(10)-C(9)-C(15)-C(16)	-59.6(4)

C(14)-C(9)-C(15)-C(16)	57.8(3)
C(8)-C(9)-C(15)-C(16)	176.5(3)
C(9)-C(15)-C(16)-C(17)	61.3(4)
C(9)-C(15)-C(16)-C(18)	-58.5(4)
C(12)-C(11)-C(17)-C(16)	-59.0(3)
C(10)-C(11)-C(17)-C(16)	60.9(3)
C(18)-C(16)-C(17)-C(11)	58.8(3)
C(15)-C(16)-C(17)-C(11)	-61.8(4)
C(12)-C(13)-C(18)-C(16)	61.3(4)
C(14)-C(13)-C(18)-C(16)	-59.3(4)
C(17)-C(16)-C(18)-C(13)	-60.3(4)
C(15)-C(16)-C(18)-C(13)	59.0(4)
C(24)-C(19)-C(20)-C(21)	-1.5(4)
O(1)-C(19)-C(20)-C(21)	-178.4(2)
C(19)-C(20)-C(21)-C(22)	0.8(4)
C(20)-C(21)-C(22)-C(23)	1.0(4)
C(20)-C(21)-C(22)-Cl(1)	-179.1(2)
C(21)-C(22)-C(23)-C(24)	-2.0(4)
Cl(1)-C(22)-C(23)-C(24)	178.16(19)
C(21)-C(22)-C(23)-C(25)	179.8(3)
Cl(1)-C(22)-C(23)-C(25)	-0.1(4)
C(20)-C(19)-C(24)-C(23)	0.4(4)
O(1)-C(19)-C(24)-C(23)	177.4(2)
C(22)-C(23)-C(24)-C(19)	1.2(4)
C(25)-C(23)-C(24)-C(19)	179.5(3)
C(24)-C(23)-C(25)-C(27)	31.8(4)
C(22)-C(23)-C(25)-C(27)	-150.1(3)
C(24)-C(23)-C(25)-C(26)	-94.2(3)
C(22)-C(23)-C(25)-C(26)	83.9(3)
O(2)-C(7)-N(1)-C(5)	0.7(4)
C(8)-C(7)-N(1)-C(5)	-179.2(2)
C(4)-C(5)-N(1)-C(7)	6.4(4)
C(6)-C(5)-N(1)-C(7)	-173.7(3)
C(3)-C(2)-O(1)-C(19)	36.4(3)
C(1)-C(2)-O(1)-C(19)	-146.0(2)
C(20)-C(19)-O(1)-C(2)	-103.1(3)
C(24)-C(19)-O(1)-C(2)	79.9(3)

C(2)-C(1)-S(1)-O(3)	63.9(2)
C(6)-C(1)-S(1)-O(3)	-113.2(2)
C(2)-C(1)-S(1)-O(4)	-167.3(2)
C(6)-C(1)-S(1)-O(4)	15.5(3)
C(2)-C(1)-S(1)-N(2)	-52.1(3)
C(6)-C(1)-S(1)-N(2)	130.7(2)

Appendix 2. 2D NMR Characterisation of Compound 97

97 – ^{1}H NMR (CD_3OD, 400 MHz, 298 K) and ^{13}C NMR

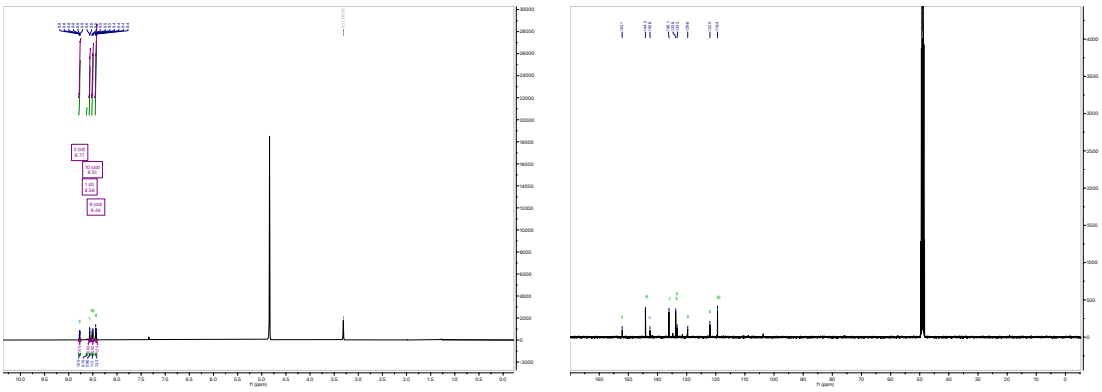

97 – ^{1}H NMR

(8.2 – 9.0 ppm)

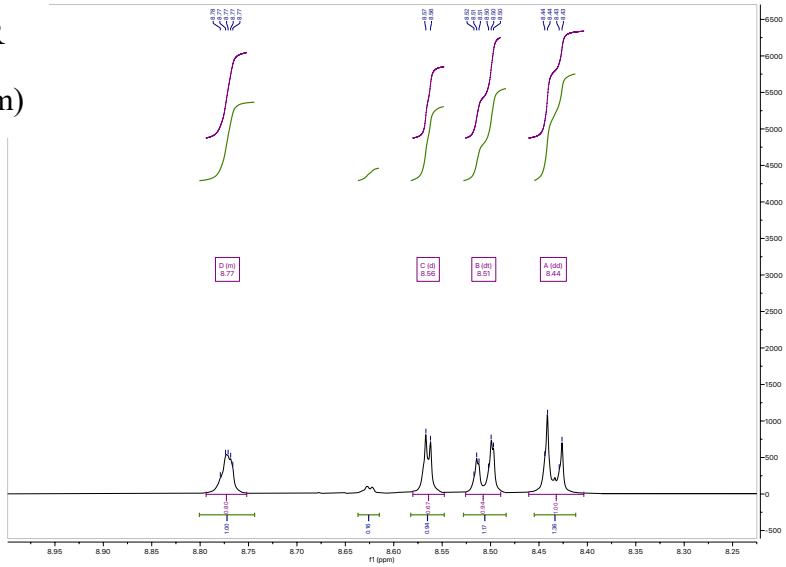

97 – ^{13}C NMR

(115 – 155 ppm)

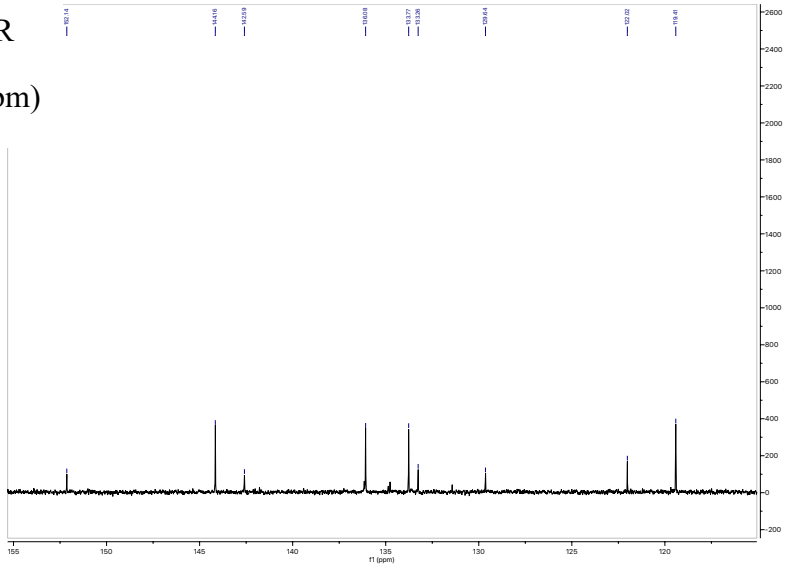

97 – COSY

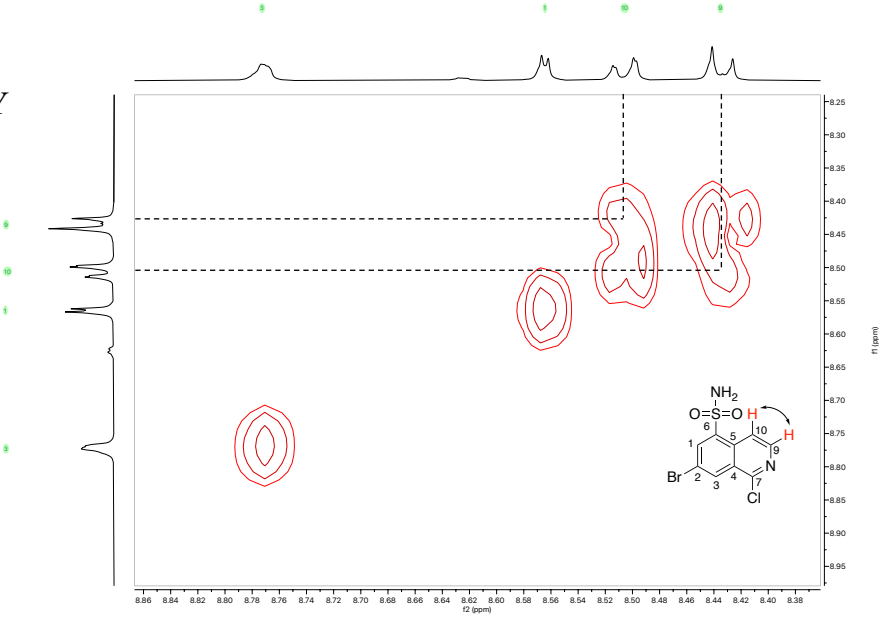

97 – HMBC

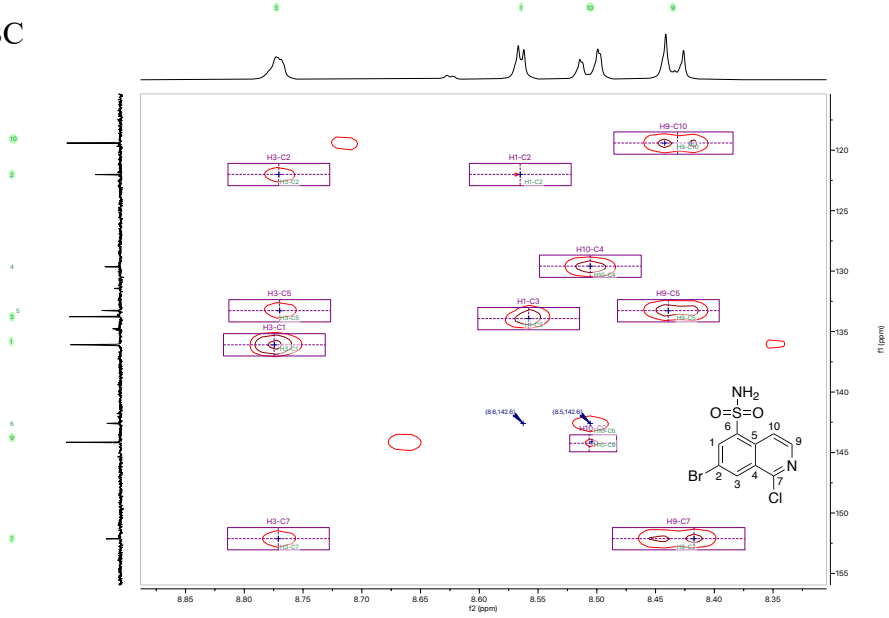

Appendix 3. Characterisation Data of Compound 133

Compound **133** was isolated as an off white crystalline solid (11.3 mg, 16%) following recrystallisation in 2-propanol. **^{1}H NMR** (500 MHz, $CDCl_3$) δ 8.26 (d, J = 5.7 Hz, 1H), 7.76 (s, 1H), 7.48 (d, J = 1.9 Hz, 1H), 7.46 (d, J = 8.1 Hz, 2H), 7.31 (dd, J = 8.5, 7.6 Hz, 1H), 7.18 (dd, J = 5.7, 2.1 Hz, 1H), 6.87 – 6.80 (m, 2H), 6.68 (tt, J = 8.9, 2.3 Hz, 1H), 6.55 (s, 1H), 2.76 (s, 6H), 2.08 (s, 3H) ppm; **^{19}F NMR** (471 MHz, $CDCl_3$) δ -109.1 ppm; **^{13}C NMR** (126 MHz, $CDCl_3$) δ 170.5, 166.1, 164.0 (d, J = 14.2 Hz), 162.0 (d, J = 14.3 Hz), 155.5, 150.5, 149.8, 148.7, 143.9 (t, J = 12.7 Hz), 139.1, 133.7, 130.7, 128.5, 113.1, 111.8, 110.9 – 110.2 (m), 110.7 (d, J = 24.7 Hz), 102.5 (t, J = 24.9 Hz), 95.2, 24.2 ppm; **LRMS (+ESI)** m/z: 505/507/509 ($[M+H]^+$, 50), 527/529/531 ($[M+Na]^+$, 100) , **(-ESI)** m/z: 503/505/507 ($[M-H]^-$, 100); **HRMS (+ESI)** Calc. for $C_{24}H_{21}Cl_2F_2N_4O_2$ $[M+H]^+$: 505.10041/507.09746/509.09451, found 505.10072/507.09776/509.09477.

X-ray Crystallography:

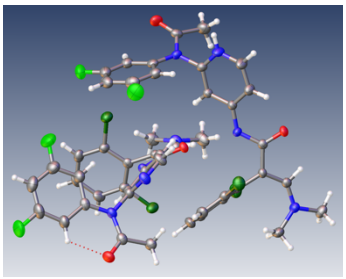

≡

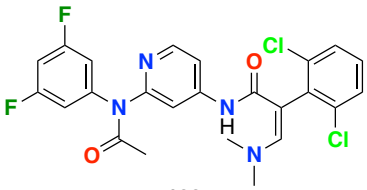

133

Table 1. Crystal data and structure refinement for 22BH044-CDB22_2f_10 (**133**)

Identification Code	22BH044-CDB22_2f_10
Empirical Formula	$C_{48}H_{39}Cl_4F_4N_8O_4$
Formula Weight	1007.67
Temperature	150.00(14) K
Crystal system	Monoclinic
Space group	P 21/n
Unit cell dimensions	a = 10.0373(2) Å b = 20.7621(5) Å c = 22.5505(4) Å α = 90° β = 93.127(2)° γ = 90°
Volume	4692.42(17) $Å^3$
Z	4
Calculated density	1.426 g/cm^3
Absorption coefficient	2.882 mm^{-1}
F(000)	2072.0
Crystal size	0.356 x 0.096 x 0.043 mm^3
Radiation	Cu Ka (λ = 1.54184)
Theta range for data collection	5.79 to 117.864°
Index ranges	$-10 \leq h \leq 11$, $-23 \leq k \leq 23$, $-25 \leq l \leq 25$
Reflections collected	37438
Independent reflections	6731 [R_{int} = 0.0722, R_{sigma} = 0.0424]
Data/restraints/parameters	6731/0/619
Goodness-of-fit on F^2	1.026
Final R indexes [I>=2 σ(I)]	R_1 = 0.0408, wR_2 = 0.0958
Final R indexes [all data]	R_1 = 0.0620, wR_2 = 0.1076
Largest diff. peak/hole	0.54/-0.47 e $Å^{-3}$

Table 2. Fractional Atomic Coordinates (x10^4) and Equivalent Isotropic Displacement Parameters (Å^2 x 10^3) for 22BH044-CDB22_2f_10. U_{eq} is defined as 1/3 of the trace of the orthogonalised U_{IJ} tensor.

Atom	*x*	*y*	*z*	U(eq)
Cl01	5709.6(8)	4228.2(4)	538.1(3)	38.8(2)
Cl02	5639.3(8)	5423.1(4)	2675.7(3)	39.1(2)
Cl03	11116.5(8)	2270.6(4)	2583.2(3)	41.5(2)
Cl04	9956.4(8)	3766.5(4)	650.0(3)	41.8(2)
O005	8760.2(19)	4148.4(9)	2247.9(8)	26.9(4)
O006	13716.5(18)	3650.8(9)	2161.0(8)	28.3(5)
F007	5667.8(19)	5636.8(10)	4232.1(9)	58.6(6)
O008	9757(2)	6620.4(10)	3863.9(10)	41.9(6)
F009	8376(2)	3921.4(10)	4908.4(9)	66.5(6)
O00A	4265(2)	999.5(10)	3204.2(9)	41.8(6)
N00B	6604(2)	3852.9(10)	2380.7(9)	23.9(5)
N00C	11595(2)	3892.1(11)	2411.2(9)	25.4(5)
F00	836(2)	1751.1(12)	4324.3(11)	78.8(7)
F00E	3571(3)	3505.5(12)	4838.7(11)	80.7(8)
N00F	10258(2)	5557.6(11)	3742.6(10)	30.0(6)
N00G	5065(2)	2006.4(11)	3436.8(10)	28.6(6)
N00H	12593(2)	2657.1(12)	675.5(10)	32.1(6)
N00I	7885(2)	5488.2(12)	989.2(10)	32.9(6)
N00J	7199(2)	2424.3(12)	3700.3(11)	33.9(6)
N00K	12364(3)	5064.3(13)	3910.6(11)	39.1(7)
C00L	11908(3)	3179.1(13)	1592.9(12)	24.1(6)
C00M	7042(3)	4713.6(13)	1700.5(11)	23.0(6)
C00N	5887(3)	2925.2(13)	2903.9(12)	25.2(6)
C00O	7555(3)	4230.4(13)	2124.9(11)	23.4(6)
C00P	6870(3)	3387.7(13)	2820.4(11)	23.6(6)
C00Q	10968(3)	4726.7(13)	3073.3(12)	25.8(6)
C00R	5585(3)	4819.9(13)	1607.5(12)	25.0(6)
C00S	11915(3)	4275.9(13)	2911.2(12)	25.2(6)
C00T	12498(3)	3578.0(13)	2069.6(12)	25.1(6)
C00U	10479(3)	2982.2(13)	1597.0(11)	24.5(6)
C00V	6104(3)	2470.7(13)	3339.6(12)	27.4(7)
C00W	7989(3)	5000.4(13)	1376.3(11)	26.3(6)
C00X	12743(3)	3030.2(13)	1154.2(12)	27.2(7)
C00Y	11243(3)	5098.3(13)	3572.0(12)	28.7(7)
C00Z	9144(3)	5308.9(14)	4030.4(12)	29.3(7)
C010	4833(3)	5136.2(13)	2023.9(12)	28.4(7)
C011	9507(3)	3200.2(14)	1176.4(12)	28.0(7)
C012	8031(3)	3355.0(14)	3190.9(12)	30.2(7)
C013	10016(3)	2553.0(13)	2014.7(12)	28.1(7)
C014	4069(3)	2197.6(14)	3828.5(12)	30.2(7)
C015	4874(3)	4613.9(14)	1094.3(12)	28.9(7)
C016	5098(3)	1422.4(15)	3142.6(13)	31.6(7)
C017	10487(3)	6211.5(14)	3671.9(13)	32.3(7)
C018	7907(3)	5613.8(15)	3992.4(13)	35.9(8)
C019	13095(3)	4233.9(15)	3262.9(13)	35.3(7)
C01A	8204(3)	2984.5(15)	1147.5(13)	35.3(7)
C01B	3481(3)	5240.8(14)	1940.2(14)	35.1(7)

Table 3. Anisotropic Displacement Parameters ($Å^2$ x 10^3) for 22BH044-CDB22_2f_10. The Anisotropic displacement factor exponent takes the form: $-2\pi^2[h^2a^{*2}U_{11}+2hka^*b^*U_{12}+\ldots]$.

Atom	U_{11}	U_{22}	U_{33}	U_{23}	U_{13}	U_{12}
Cl01	38.8(5)	43.3(5)	33.6(4)	-9.4(3)	-5.4(3)	5.2(4)
Cl02	41.7(5)	41.1(4)	34.6(4)	-9.1(3)	3.2(3)	0.8(4)
Cl03	43.4(5)	42.4(5)	38.7(4)	13.2(3)	2.7(4)	4.2(4)
Cl04	41.4(5)	47.8(5)	36.5(4)	13.6(4)	3.2(3)	3.7(4)
O005	18.5(11)	30.2(11)	31.8(10)	2.2(8)	-0.1(8)	-1.3(9)
O006	17.4(11)	32.2(11)	35.3(11)	-1.0(9)	0.3(9)	1.0(9)
F007	31.0(12)	72.1(15)	73.1(14)	-14.8(11)	7.4(10)	1.6(10)
O008	41.1(14)	25.5(12)	58.5(14)	-7.7(10)	-2.1(11)	5.1(10)
F009	82.0(17)	51.1(13)	67.8(14)	20.0(11)	18.8(12)	-7.5(12)
O00A	38.7(14)	38.0(13)	49.6(13)	-3.8(10)	10.6(11)	-14.6(11)
N00B	23.2(13)	20.2(12)	28.4(12)	4.2(10)	1.6(10)	-2.2(10)
N00C	23.7(13)	25.3(13)	27.3(12)	-5.6(10)	2.8(10)	1.6(10)
F00	49.4(14)	82.8(17)	108.5(19)	-15.0(14)	41.9(13)	-20.9(13)
F00E	80.2(18)	80.2(17)	84.5(16)	-42.2(14)	32.1(14)	-12.8(14)
N00F	32.6(15)	24.8(13)	32.5(13)	-6.9(11)	2.6(11)	-0.2(11)
N00G	25.7(14)	27.2(13)	33.0(13)	5.8(11)	2.5(11)	-4.9(11)
N00H	31.4(15)	33.5(14)	32.1(13)	-6.2(11)	7.0(11)	-2.0(11)
N00I	34.4(15)	35.7(15)	28.4(13)	9.0(11)	0.4(11)	-6.9(12)
N00J	28.9(15)	35.4(15)	36.8(14)	9.6(11)	-3.5(12)	-2.6(12)
N00K	38.7(17)	42.5(16)	34.9(14)	-15.4(12)	-8.5(13)	2.6(13)
C00L	21.2(16)	24.6(15)	26.8(14)	1.1(12)	3.7(12)	-0.5(12)
C00M	23.7(16)	22.3(15)	23.1(14)	-1.8(11)	0.9(12)	-0.4(12)
C00N	23.0(16)	24.8(15)	28.0(14)	0.1(12)	2.3(12)	1.1(12)
C00O	25.6(17)	23.0(15)	21.7(13)	-4.6(11)	1.4(12)	-2.1(12)
C00P	22.1(16)	23.8(15)	25.3(14)	0.1(12)	3.7(12)	2.2(12)
C00Q	24.8(16)	25.7(15)	26.9(14)	-0.7(12)	1.3(12)	-0.9(12)
C00R	27.5(17)	18.4(14)	28.8(15)	6.8(12)	0.5(13)	-1.9(12)
C00S	23.6(16)	24.1(15)	27.9(15)	-0.6(12)	1.1(12)	-0.5(12)
C00T	26.3(18)	21.5(15)	27.4(14)	3.1(12)	0.5(13)	0.5(12)
C00U	23.8(16)	21.9(15)	28.0(14)	-7.0(12)	3.8(12)	-0.4(12)
C00V	25.5(17)	26.0(16)	30.9(15)	1.7(13)	4.4(13)	-0.3(13)
C00W	26.8(17)	29.2(16)	22.8(14)	-2.0(12)	0.0(12)	-2.0(13)
C00X	25.8(17)	23.4(15)	32.4(16)	0.5(13)	2.4(13)	-0.2(12)
C00Y	31.6(18)	24.0(15)	30.5(16)	-3.4(12)	2.2(14)	-2.2(13)
C00Z	35.2(18)	28.9(16)	23.8(14)	-7.1(12)	1.1(13)	-2.8(14)
C010	30.3(18)	24.0(15)	30.9(15)	0.0(12)	1.0(13)	1.9(13)
C011	27.9(17)	27.9(16)	28.3(15)	-3.4(12)	3.2(13)	1.0(13)
C012	25.5(17)	32.4(17)	32.3(16)	4.3(13)	-1.9(13)	-6.4(13)
C013	30.6(18)	22.6(15)	31.4(15)	-0.4(12)	3.6(13)	0.2(13)
C014	27.0(17)	34.9(17)	28.8(15)	11.0(13)	2.5(13)	1.0(14)
C015	30.7(17)	24.6(15)	31.1(15)	-1.2(12)	-0.1(13)	2.2(13)
C016	28.6(18)	33.8(18)	32.3(16)	7.7(13)	1.2(13)	-2.3(15)
C017	33.8(18)	28.4(17)	33.7(16)	-3.0(14)	-6.6(14)	-3.7(14)
C018	37(2)	36.7(18)	33.3(16)	-7.8(14)	-0.7(14)	0.3(15)
C019	30.5(18)	39.3(18)	35.5(17)	-4.4(14)	-3.6(14)	8.0(14)
C01A	29.1(18)	41.5(19)	34.8(17)	-10.9(15)	-2.7(14)	2.1(15)
C01B	33.6(19)	26.7(16)	45.8(18)	4.5(14)	9.0(15)	6.0(14)

Atom	U_{11}	U_{22}	U_{33}	U_{23}	U_{13}	U_{12}
C01C	30.7(19)	32.6(17)	44.9(18)	1.4(15)	-12.6(15)	4.8(14)
C01D	23.3(17)	35.4(18)	60(2)	6.1(16)	-4.4(16)	5.1(14)
C01E	43(2)	33.7(18)	34.0(17)	-4.7(14)	4.6(15)	-1.4(15)
C01F	28.9(18)	38.4(18)	36.7(17)	10.0(14)	-7.8(14)	-7.2(15)
C01G	39(2)	30.4(17)	43.7(18)	0.2(14)	12.7(15)	-9.0(15)
C01H	26.7(18)	40.4(19)	51(2)	-10.0(16)	6.4(15)	-12.0(15)
C01I	38.5(19)	34.7(18)	36.1(17)	3.2(14)	7.3(14)	-5.4(15)
C01J	36(2)	49(2)	39.3(18)	-13.4(16)	2.4(15)	-2.3(16)
C01K	31.8(19)	40.0(19)	46.5(19)	4.2(15)	10.5(15)	-2.4(15)
C01L	47(2)	36.6(18)	33.1(16)	-0.5(14)	14.2(15)	3.4(15)
C01M	45(2)	32.2(18)	43.5(18)	12.7(14)	-8.5(16)	-2.4(15)
C01N	37(2)	40.5(19)	43.1(18)	-16.3(15)	3.7(15)	-1.0(15)
C01O	31.7(19)	53(2)	40.1(18)	-13.5(16)	-10.9(15)	8.9(16)
C01P	34(2)	56(2)	59(2)	9.2(19)	13.8(17)	-5.0(18)
C01Q	40(2)	48(2)	42.1(18)	-4.1(16)	10.4(16)	-5.5(16)
C01R	43(2)	56(2)	39.3(18)	-10.1(17)	9.9(16)	-13.0(18)
C01S	48(2)	60(2)	35.6(17)	8.7(16)	6.5(16)	-18.5(18)
C01T	61(3)	38.2(19)	36.2(18)	1.4(15)	7.8(17)	-9.5(18)
C01U	49(2)	34.9(19)	54(2)	-3.1(16)	6.3(17)	-10.4(16)
C01V	46(2)	61(2)	47(2)	6.4(19)	17.4(17)	10.9(19)
C01W	55(3)	52(2)	42.9(19)	-7.0(17)	9.6(18)	-2.4(19)

Table 4. Bond Lengths for 22BH044-CDB22_2f_10.

Atom	Atom	Length/Å	Atom	Atom	Length/Å
Cl01	C015	1.741(3)	C00M	C00R	1.482(4)
Cl02	C010	1.744(3)	C00M	C00W	1.367(4)
Cl03	C013	1.748(3)	C00N	C00P	1.397(4)
Cl04	C011	1.747(3)	C00N	C00V	1.371(4)
O005	C00O	1.238(3)	C00P	C012	1.398(4)
O006	C00T	1.239(3)	C00Q	C00S	1.396(4)
F007	C01J	1.365(4)	C00Q	C00Y	1.379(4)
O008	C017	1.217(4)	C00R	C010	1.400(4)
F009	C01T	1.363(4)	C00R	C015	1.393(4)
O00A	C016	1.225(3)	C00S	C019	1.392(4)
N00B	C00O	1.385(3)	C00U	C011	1.399(4)
N00B	C00P	1.399(3)	C00U	C013	1.395(4)
N00C	C00S	1.404(3)	C00Z	C018	1.392(4)
N00C	C00T	1.384(4)	C00Z	C01E	1.393(4)
F00	C01P	1.368(4)	C010	C01B	1.377(4)
F00E	C01W	1.348(4)	C011	C01A	1.381(4)
N00F	C00Y	1.441(4)	C012	C01F	1.378(4)
N00F	C00Z	1.420(4)	C013	C01G	1.376(4)
N00F	C017	1.388(4)	C014	C01K	1.401(4)
N00G	C00V	1.445(4)	C014	C01Q	1.386(4)
N00G	C014	1.426(4)	C015	C01C	1.386(4)
N00G	C016	1.383(4)	C016	C01I	1.501(4)
N00H	C00X	1.331(4)	C017	C01U	1.508(4)
N00H	C01L	1.461(4)	C018	C01J	1.366(5)
N00H	C01N	1.457(4)	C019	C01O	1.375(4)
N00I	C00W	1.337(4)	C01A	C01H	1.374(4)
N00I	C01M	1.455(4)	C01B	C01D	1.381(4)
N00I	C01S	1.460(4)	C01C	C01D	1.375(4)
N00J	C00V	1.335(4)	C01E	C01T	1.364(5)
N00J	C01F	1.345(4)	C01G	C01H	1.380(4)
N00K	C00Y	1.327(4)	C01J	C01R	1.374(5)
N00K	C01O	1.335(4)	C01K	C01P	1.368(5)
C00L	C00T	1.457(4)	C01P	C01V	1.359(5)
C00L	C00U	1.491(4)	C01Q	C01W	1.375(5)
C00L	C00X	1.367(4)	C01R	C01T	1.368(5)
C00M	C00O	1.461(4)	C01V	C01W	1.368(5)

Table 5. Bond Angles for 22BH044-CDB22_2f_10.

Atom	Atom	Atom	Angle/°	Atom	Atom	Atom	Angle/°
C00O	N00B	C00P	125.2(2)	C018	C00Z	C01E	119.4(3)
C00T	N00C	C00S	125.9(2)	C01E	C00Z	N00F	118.6(3)
C00Z	N00F	C00Y	116.8(2)	C00R	C010	Cl02	118.9(2)
C017	N00F	C00Y	119.7(2)	C01B	C010	Cl02	118.0(2)
C017	N00F	C00Z	123.2(2)	C01B	C010	C00R	123.1(3)
C014	N00G	C00V	116.4(2)	C00U	C011	Cl04	118.8(2)
C016	N00G	C00V	118.4(2)	C01A	C011	Cl04	117.7(2)
C016	N00G	C014	125.2(2)	C01A	C011	C00U	123.4(3)
C00X	N00H	C01L	120.0(3)	C01F	C012	C00P	118.4(3)
C00X	N00H	C01N	125.1(3)	C00U	C013	Cl03	119.3(2)
C01N	N00H	C01L	115.0(2)	C01G	C013	Cl03	117.6(2)
C00W	N00I	C01M	124.9(3)	C01G	C013	C00U	123.2(3)
C00W	N00I	C01S	119.2(3)	C01K	C014	N00G	123.2(3)
C01M	N00I	C01S	115.4(3)	C01Q	C014	N00G	118.0(3)
C00V	N00J	C01F	114.6(2)	C01Q	C014	C01K	118.9(3)
C00Y	N00K	C01O	116.2(3)	C00R	C015	Cl01	119.6(2)
C00T	C00L	C00U	120.2(2)	C01C	C015	Cl01	117.6(2)
C00X	C00L	C00T	115.0(3)	C01C	C015	C00R	122.8(3)
C00X	C00L	C00U	124.8(2)	O00A	C016	N00G	122.7(3)
C00O	C00M	C00R	120.3(2)	O00A	C016	C01I	120.6(3)
C00W	C00M	C00O	114.7(2)	N00G	C016	C01I	116.7(3)
C00W	C00M	C00R	124.7(2)	O008	C017	N00F	122.3(3)
C00V	C00N	C00P	118.9(3)	O008	C017	C01U	122.2(3)
O005	C00O	N00B	121.1(2)	N00F	C017	C01U	115.4(3)
O005	C00O	C00M	123.2(2)	C01J	C018	C00Z	118.3(3)
N00B	C00O	C00M	115.8(2)	C01O	C019	C00S	118.5(3)
C00N	C00P	N00B	117.5(2)	C01H	C01A	C011	118.9(3)
C00N	C00P	C012	117.2(2)	C010	C01B	C01D	119.0(3)
C012	C00P	N00B	125.3(3)	C01D	C01C	C015	119.2(3)
C00Y	C00Q	C00S	118.7(3)	C01C	C01D	C01B	120.6(3)
C010	C00R	C00M	122.6(2)	C01T	C01E	C00Z	118.4(3)
C015	C00R	C00M	121.9(3)	N00J	C01F	C012	125.4(3)
C015	C00R	C010	115.5(3)	C013	C01G	C01H	119.4(3)
C00Q	C00S	N00C	117.5(2)	C01A	C01H	C01G	120.2(3)
C019	C00S	N00C	124.9(3)	F007	C01J	C018	118.0(3)
C019	C00S	C00Q	117.6(3)	F007	C01J	C01R	117.7(3)
O006	C00T	N00C	121.4(2)	C018	C01J	C01R	124.3(3)
O006	C00T	C00L	123.4(3)	C01P	C01K	C014	117.8(3)
N00C	C00T	C00L	115.2(2)	N00K	C01O	C019	124.7(3)
C011	C00U	C00L	122.9(2)	F00	C01P	C01K	117.1(3)
C013	C00U	C00L	122.4(3)	C01V	C01P	F00	117.6(3)
C013	C00U	C011	114.7(3)	C01V	C01P	C01K	125.2(3)
N00J	C00V	N00G	115.9(2)	C01W	C01Q	C014	119.2(3)
N00J	C00V	C00N	125.4(3)	C01T	C01R	C01J	115.1(3)
C00N	C00V	N00G	118.7(2)	F009	C01T	C01E	117.4(3)
N00I	C00W	C00M	130.3(3)	F009	C01T	C01R	118.2(3)
N00H	C00X	C00L	132.2(3)	C01E	C01T	C01R	124.4(3)
N00K	C00Y	N00F	117.0(2)	C01P	C01V	C01W	115.2(3)
N00K	C00Y	C00Q	124.4(3)	F00E	C01W	C01Q	117.6(3)
C00Q	C00Y	N00F	118.6(3)	F00E	C01W	C01V	118.8(3)
C018	C00Z	N00F	121.9(3)	C01V	C01W	C01Q	123.6(3)

Table 6. Torsion Angles for 22BH044-CDB22_2f_10.

A	B	C	D	Angle/°	A	B	C	D	Angle/°
Cl01	C015	C01C	C01D	-178.8(2)	C00X	C00L	C00T	N00C	161.1(2)
Cl02	C010	C01B	C01D	179.5(2)	C00X	C00L	C00U	C011	-64.8(4)
Cl03	C013	C01G	C01H	179.4(2)	C00X	C00L	C00U	C013	113.7(3)
Cl04	C011	C01A	C01H	-179.4(2)	C00Y	N00F	C00Z	C018	-152.0(3)
F007	C01J	C01R	C01T	179.0(3)	C00Y	N00F	C00Z	C01E	25.7(4)
N00B	C00P	C012	C01F	179.1(3)	C00Y	N00F	C017	O008	-172.2(3)
N00C	C00S	C019	C01O	-178.9(3)	C00Y	N00F	C017	C01U	9.6(4)
F00	C01P	C01V	C01W	-179.1(3)	C00Y	N00K	C01O	C019	-0.5(5)
N00F	C00Z	C018	C01J	178.7(3)	C00Y	C00Q	C00S	N00C	178.3(2)
N00F	C00Z	C01E	C01T	-178.3(3)	C00Y	C00Q	C00S	C019	-0.7(4)
N00G	C014	C01K	C01P	-178.7(3)	C00Z	N00F	C00Y	N00K	-102.9(3)
N00G	C014	C01Q	C01W	178.6(3)	C00Z	N00F	C00Y	C00Q	77.2(3)
C00L	C00U	C011	Cl04	-4.1(4)	C00Z	N00F	C017	O008	1.5(4)
C00L	C00U	C011	C01A	174.9(3)	C00Z	N00F	C017	C01U	-176.6(3)
C00L	C00U	C013	Cl03	4.0(4)	C00Z	C018	C01J	F007	-179.9(3)
C00L	C00U	C013	C01G	-174.9(3)	C00Z	C018	C01J	C01R	-0.6(5)
C00M	C00R	C010	Cl02	0.5(4)	C00Z	C01E	C01T	F009	-179.6(3)
C00M	C00R	C010	C01B	179.6(3)	C00Z	C01E	C01T	C01R	-0.4(5)
C00M	C00R	C015	Cl01	-0.8(4)	C010	C00R	C015	Cl01	178.8(2)
C00M	C00R	C015	C01C	179.9(3)	C010	C00R	C015	C01C	-0.5(4)
C00N	C00P	C012	C01F	0.4(4)	C010	C01B	C01D	C01C	-0.5(5)
C00O	N00B	C00P	C00N	-161.4(2)	C011	C00U	C013	Cl03	-177.4(2)
C00O	N00B	C00P	C012	19.8(4)	C011	C00U	C013	C01G	3.7(4)
C00O	C00M	C00R	C010	73.6(4)	C011	C01A	C01H	C01G	0.8(5)
C00O	C00M	C00R	C015	-106.9(3)	C013	C00U	C011	Cl04	177.3(2)
C00O	C00M	C00W	N00I	-174.3(3)	C013	C00U	C011	C01A	-3.7(4)
C00P	N00B	C00O	O005	4.8(4)	C013	C01G	C01H	C01A	-0.8(5)
C00P	N00B	C00O	C00M	-176.3(2)	C014	N00G	C00V	N00J	92.2(3)
C00P	C00N	C00V	N00G	178.0(2)	C014	N00G	C00V	C00N	-86.3(3)
C00P	C00N	C00V	N00J	-0.4(4)	C014	N00G	C016	O00A	-1.7(4)
C00P	C012	C01F	N00J	-1.0(5)	C014	N00G	C016	C01I	178.1(2)
C00Q	C00S	C019	C01O	0.0(4)	C014	C01K	C01P	F00	179.5(3)
C00R	C00M	C00O	O005	-175.4(2)	C014	C01K	C01P	C01V	-0.2(5)
C00R	C00M	C00O	N00B	5.7(4)	C014	C01Q	C01W	F00E	178.8(3)
C00R	C00M	C00W	N00I	11.4(5)	C014	C01Q	C01W	C01V	0.4(6)
C00R	C010	C01B	C01D	0.4(5)	C015	C00R	C010	Cl02	-179.0(2)
C00R	C015	C01C	C01D	0.5(5)	C015	C00R	C010	C01B	0.1(4)
C00S	N00C	C00T	O006	-5.1(4)	C015	C01C	C01D	C01B	0.1(5)
C00S	N00C	C00T	C00L	176.6(2)	C016	N00G	C00V	N00J	-88.6(3)
C00S	C00Q	C00Y	N00F	-179.2(2)	C016	N00G	C00V	C00N	92.8(3)
C00S	C00Q	C00Y	N00K	0.9(4)	C016	N00G	C014	C01K	-10.3(4)
C00S	C019	C01O	N00K	0.6(5)	C016	N00G	C014	C01Q	171.2(3)
C00T	N00C	C00S	C00Q	158.0(3)	C017	N00F	C00Y	N00K	71.3(4)
C00T	N00C	C00S	C019	-23.1(4)	C017	N00F	C00Y	C00Q	-108.6(3)
C00T	C00L	C00U	C011	113.0(3)	C017	N00F	C00Z	C018	34.1(4)
C00T	C00L	C00U	C013	-68.5(4)	C017	N00F	C00Z	C01E	-148.2(3)
C00T	C00L	C00X	N00H	175.8(3)	C018	C00Z	C01E	C01T	-0.5(4)
C00U	C00L	C00T	O006	164.9(3)	C018	C01J	C01R	C01T	-0.3(5)
C00U	C00L	C00T	N00C	-16.9(4)	C01E	C00Z	C018	C01J	1.0(4)
C00U	C00L	C00X	N00H	-6.3(5)	C01F	N00J	C00V	N00G	-178.6(3)

A	B	C	D	Angle/°
C00U	C011	C01A	C01H	1.6(4)
C00U	C013	C01G	C01H	−1.6(5)
C00V	N00G	C014	C01K	168.8(3)
C00V	N00G	C014	C01Q	−9.7(4)
C00V	N00G	C016	O00A	179.2(3)
C00V	N00G	C016	C01I	−1.0(4)
C00V	N00J	C01F	C012	0.8(5)
C00V	C00N	C00P	N00B	−178.6(2)
C00V	C00N	C00P	C012	0.2(4)
C00W	C00M	C00O	O005	10.1(4)
C00W	C00M	C00O	N00B	−168.9(2)
C00W	C00M	C00R	C010	−112.4(3)
C00W	C00M	C00R	C015	67.1(4)
C00X	C00L	C00T	O006	−17.2(4)

A	B	C	D	Angle/°
C01F	N00J	C00V	C00N	−0.1(4)
C01J	C01R	C01T	F009	179.9(3)
C01J	C01R	C01T	C01E	0.8(5)
C01K	C014	C01Q	C01W	0.0(5)
C01K	C01P	C01V	C01W	0.6(6)
C01L	N00H	C00X	C00L	173.0(3)
C01M	N00I	C00W	C00M	6.8(5)
C01N	N00H	C00X	C00L	−7.4(5)
C01O	N00K	C00Y	N00F	179.8(3)
C01O	N00K	C00Y	C00Q	−0.3(5)
C01P	C01V	C01W	F00E	−179.1(3)
C01P	C01V	C01W	C01Q	−0.7(6)
C01Q	C014	C01K	C01P	−0.2(5)
C01S	N00I	C00W	C00M	−165.0(3)

Table 7. Hydrogen Atom Coordinates (Å x 10^4) and Isotropic Displacement Parameters (Å^2 x 10^3) for 22BH044-CDB22_2f_10.

Atom	*x*	*y*	*z*	U(eq)
H00K	12507.36	5310.62	4225.21	47
H00N	5080.83	2925.65	2662.71	30
H00Q	10151.24	4776.41	2844.73	31
H00W	8860.34	4825.23	1435.47	32
H00X	13592.63	3231.35	1199.74	33
H012	8729.35	3658.89	3155.26	36
H018	7780.92	6004.73	3777.57	43
H019	13769.8	3934.69	3170.94	42
H01A	7582.73	3138.39	847.63	42
H01N	3006.98	5460.26	2232.36	42
H01P	3058.87	4558.22	645.18	44
H01Q	1891.22	5087.9	1363.64	48
H01E	10123.29	4513.23	4369.6	44
H01S	8937.47	2851.38	3853.12	42
H01G	8457.6	2027.68	2286.28	45
H01H	6930.82	2386.64	1541.98	47
H01T	6103.82	1622.97	2398.42	54
H01U	6195.37	880.77	2587.77	54
H01V	7068.83	1407.98	2951.48	54
H01W	2709.13	1466.15	3675.17	47
H01B	14316.37	2961.48	354.94	58
H01C	13223.85	2752.15	-151.92	58
H01D	14020.15	2214.47	232.53	58
H01X	6128.08	5676.06	556.37	61
H01Y	6950.6	6309.63	748.74	61
H	6198.84	5906.35	1234.61	61
H01F	11044.21	2116.02	905.33	60
H01I	11754.79	1849.22	336.45	60
H01J	10798.87	2465.32	276.23	60
H01O	14077.22	4604.45	3980.21	50
H01Z	5073.62	3001.77	4116.68	52
H01R	6244.94	4589.23	4777.41	55
H01	9772.06	5380.75	747.91	72
HA	9138.53	6065.83	569.75	72
HB	8705.52	5437.21	196.43	72
H01K	12497.88	6251.86	3549.37	69
H01L	11693.57	6846.26	3253.52	69
H01M	11619.78	6153.52	2942.29	69
H1	1513.74	2783.17	4861.27	61

Appendix 4. P2X4 *In Silico* Docking Scores

Table 1. *In silico* hP2X4 rigid-target docking (RTD) scores of arylsulfonamide compounds (**25**, **51**, **52**, **85** and **86**). A more negative score denotes a stronger binding affinity. Ligands were docked sequentially into the protein chains A – C, with top scoring pose merged.

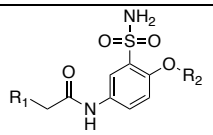

Compound	R_1	R_2	Chain	Docking score (kcal/mol)
25 (BAY-1797)	phenyl	3-chlorophenyl	A	-10.522
			B	-11.405
			C	**-12.260**
51	2-chlorophenyl	3-chlorophenyl	A	-9.459
			B	-10.165
			C	**-10.565**
52	adamantyl	3-chlorophenyl	A	-2.880
			B	-6.372
			C	**-4.038**
81	2-chlorophenyl	4-fluorobenzyl	A	-11.040
			B	-10.391
			C	**-9.790**
82	adamantyl	4-fluorobenzyl	A	-6.084
			B	-3.397
			C	**-8.101**
85	2-chlorophenyl	3-isopropylphenyl	A	-10.275
			B	-10.425
			C	**-9.867**
86	adamantyl	3-isopropylphenyl	A	-6.049
			B	-7.247
			C	—[a]

[a]Grid-energy minimum failed.

Table 2. *In silico* hP2X4 rigid-target docking (RTD) scores of isoquinoline compounds (**115** – **118**). A more negative score denotes a stronger binding affinity. Ligands were docked sequentially into the protein chains A – C, with top scoring pose merged.

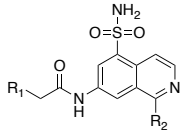

Compound	R_1	R_2	Chain	Docking score (kcal/mol)
115	2-chlorophenyl	methoxy	A	-8.001
			B	-8.266
			C	**-8.062**
116	adamantyl	methoxy	A	-4.274
			B	-5.402
			C	**-6.137**
117	2-chlorophenyl	isopentyloxy	A	-7.141
			B	-6.505
			C	**-8.577**
118	adamantyl	isopentyloxy	A	-4.224
			B	-7.163
			C	**-1.013**

Table 3. *In silico* hP2X4 rigid-target docking (RTD) scores of acetamidopyridine compounds **124** – **127**). A more negative score denotes a stronger binding affinity. Ligands were docked sequentially into the protein chains A – C, with top scoring pose merged. H^+ compounds refer to the protonated species of the ligand predicted by LigPrep.

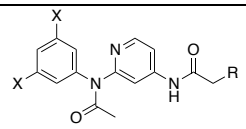

Compound	R	X	Chain	Docking score (kcal/mol)
124	2,6-dichlorophenyl	F	A	-8.835
			B	-6.463
			C	**-9.147**
125	adamantyl	F	A	-5.104
			B	-5.379
			C	**-0.212**
126	2,6-dichlorophenyl	H	A	-7.501
			B	-7.841
			C	**-5.558**
127	adamantyl	H	A	1.1629
			B	-6.583
			C	**-3.887**
124 H^+	2,6-dichlorophenyl	F	A	-1.870
			B	-3.194
			C	**-0.128**
125 H^+	adamantyl	F	A	1.161
			B	-0.120
			C	**1.815**
126 H^+	2,6-dichlorophenyl	H	A	-6.600
			B	-3.711
			C	**-4.052**
127 H^+	adamantyl	H	A	-1.244
			B	5.087
			C	**-1.160**

Appendix 5. 2D NMR Characterisation of Compound 37

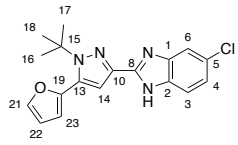

37 - ^{1}H NMR (DMSO-d_6, 500 MHz, 298 K)

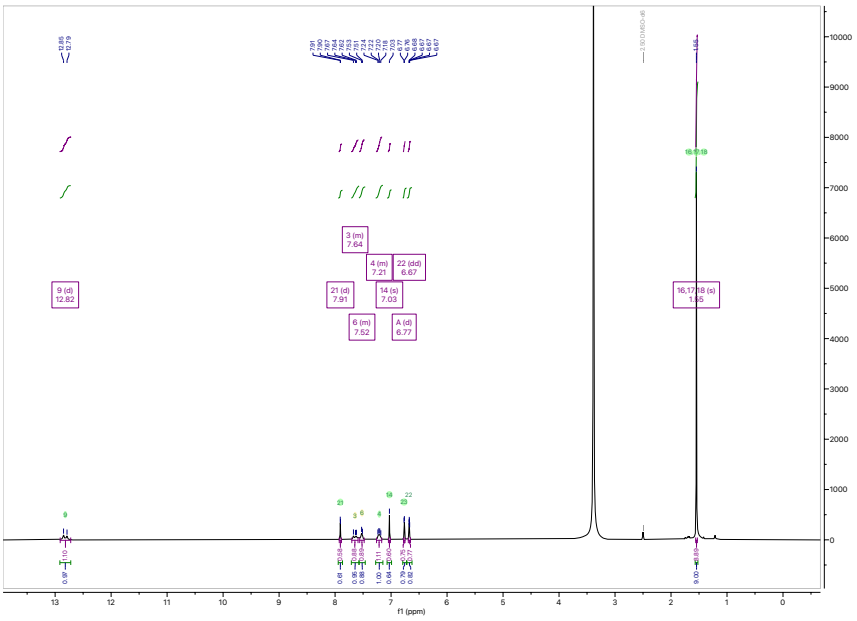

37 – ^{13}C NMR (DMSO-d_6, 126 MHz, 298 K)

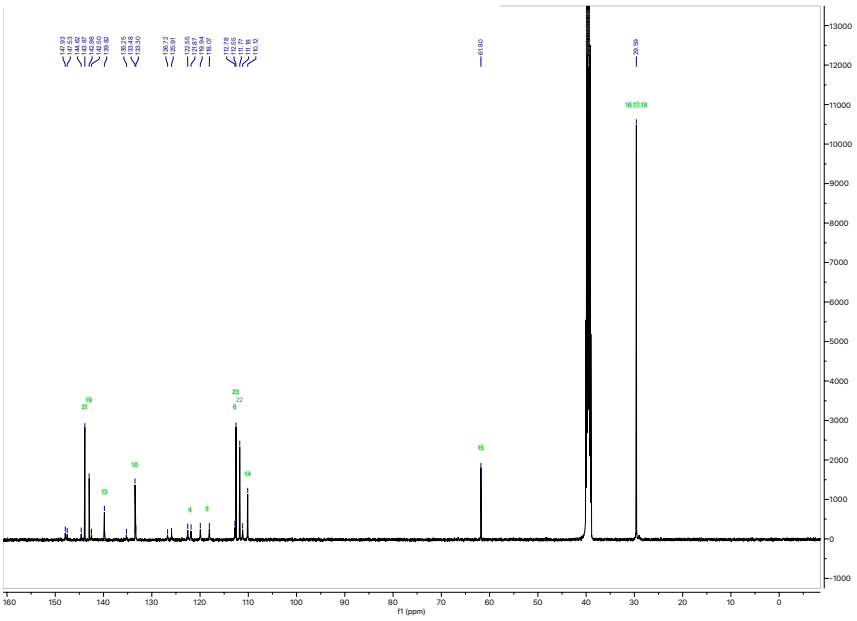

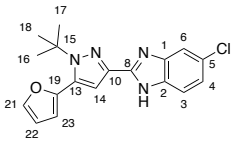

37 – COSY

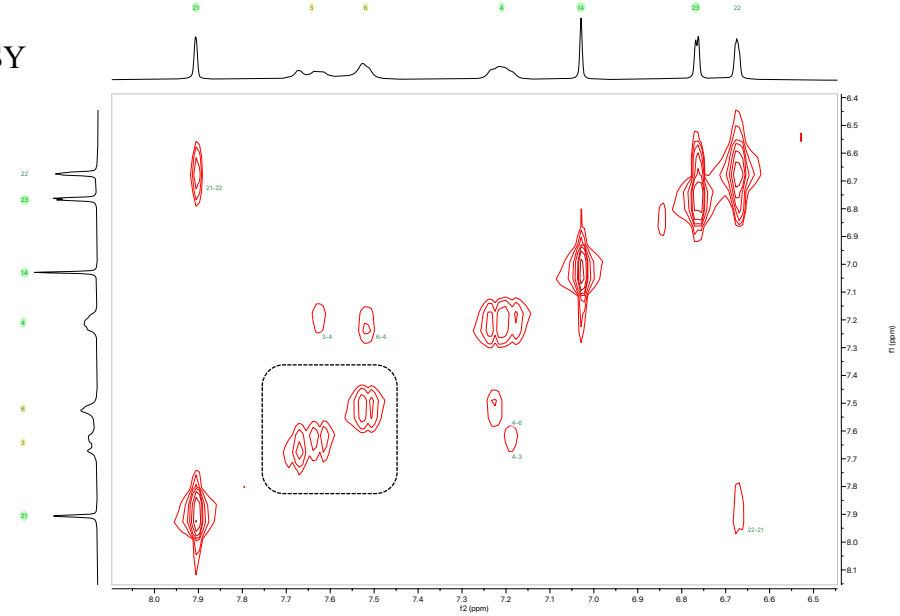

37 – NOESY

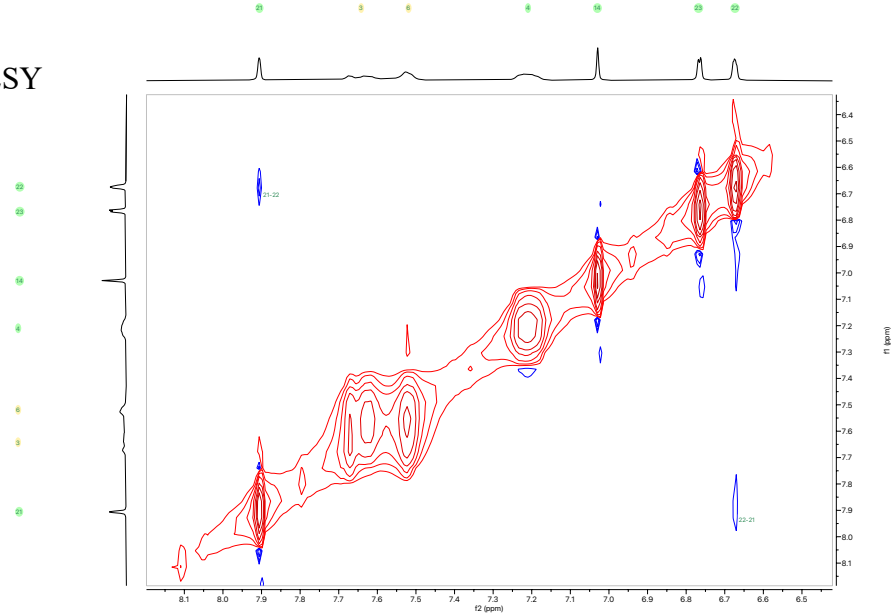

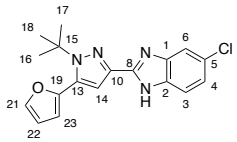

37 – HSQC

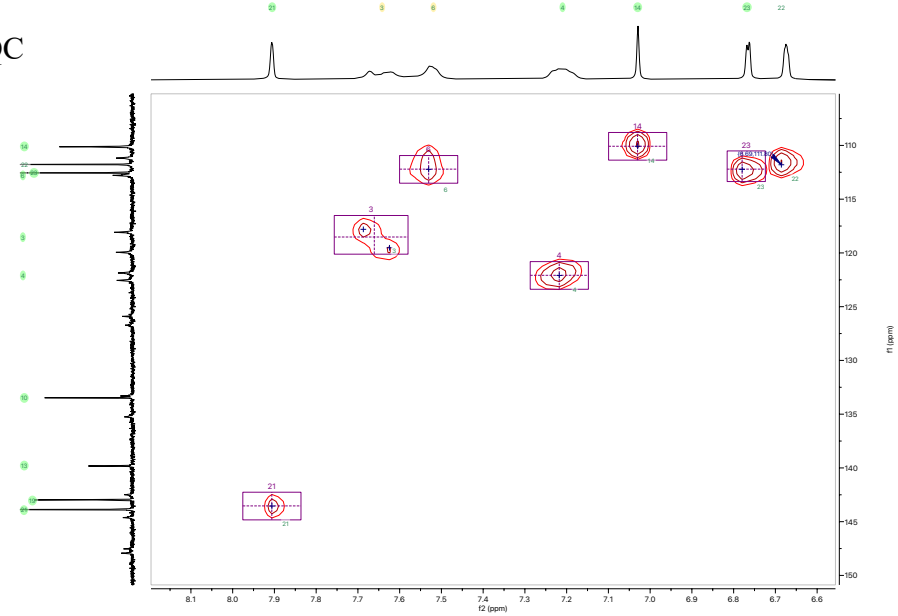

37 – HMBC

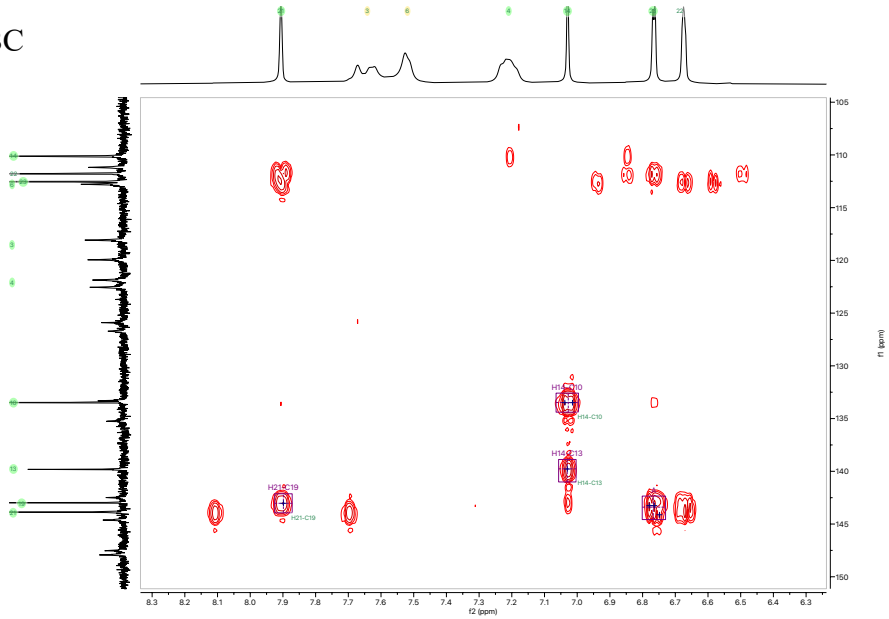

Appendix 6. **Characterisation of Side Products Formed in Synthetic Attempts to Access the Imidazo[1,2-*c*]pyrimidine (173) Analogue (Table 3.8)**

Entry 4: 1-(5-(5-bromofuran-2-yl)-1-(*tert*-butyl)-1*H*-pyrazol-3-yl)ethan-1-one (**192**)

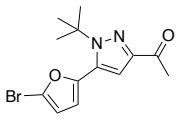

White solid (19.9 mg, 48%); **^{1}H NMR** (400 MHz, $CDCl_3$) δ 6.86 (s, 1H), 6.46 – 6.39 (m, 2H), 2.58 (s, 3H), 1.57 (s, 9H) ppm; **^{13}C NMR** (101 MHz, $CDCl_3$) δ 194.3, 148.3, 145.9, 132.9, 122.8, 114.6, 113.2, 111.7, 62.8, 30.1, 26.4 ppm; **LRMS (+ESI)** m/z: 333/335 ($[M+Na]^+$, 100).

192 - ^{1}H NMR ($CDCl_3$, 400 MHz, 298 K)

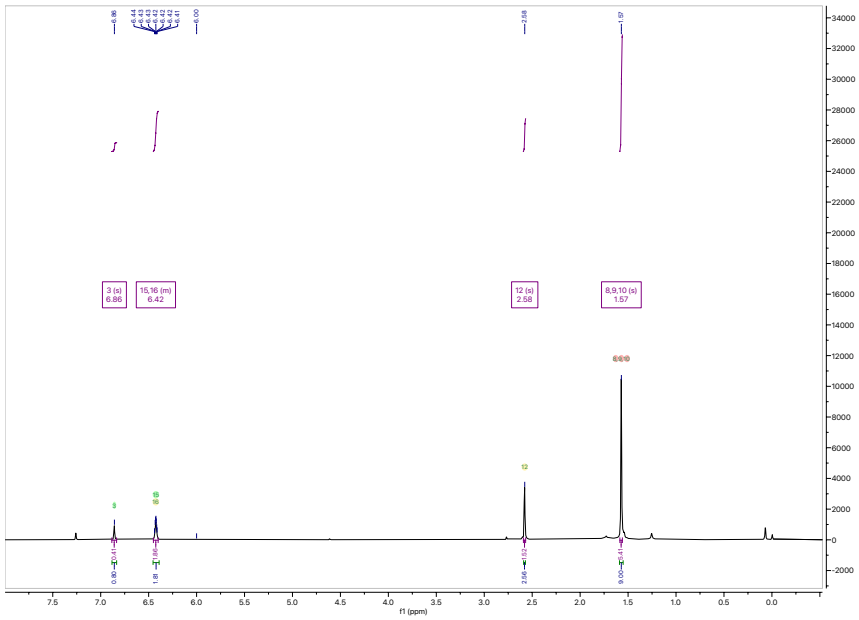

192 - ^{13}C NMR ($CDCl_3$, 101 MHz, 298 K)

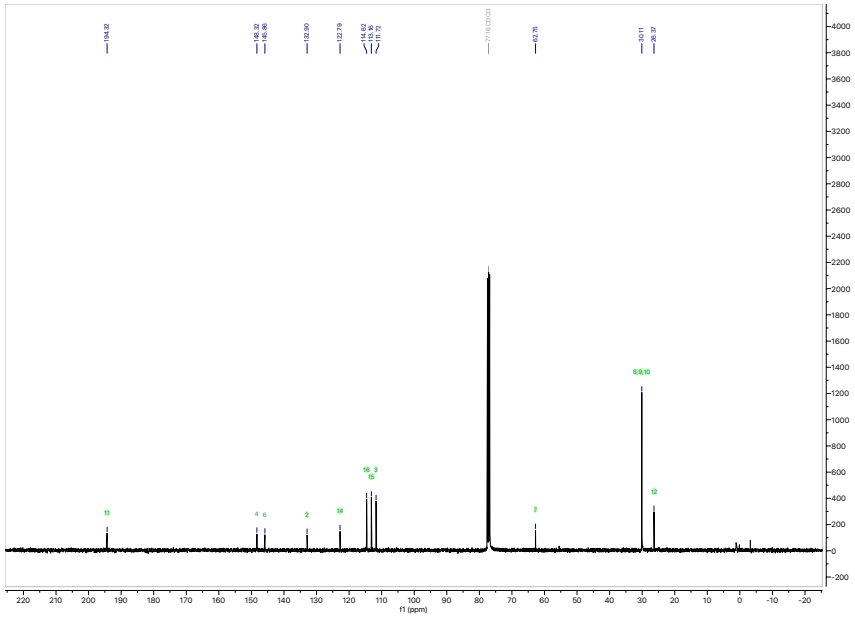

192 - HMBC

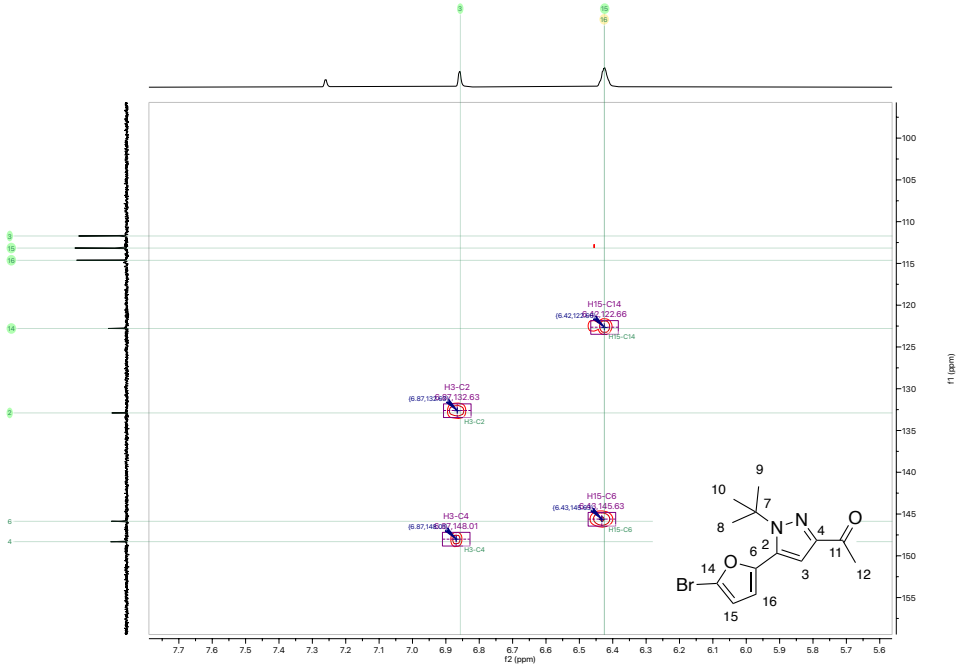

Entries 5 and 6:

1-(1-(*tert*-butyl)-5-(furan-2-yl)-1*H*-pyrazol-3-yl)-2-nitroethan-1-ol (**193**)

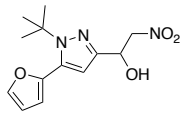

Off-white powder (22 mg, 68%); **^{1}H NMR** (400 MHz, DMSO-d_6) δ 7.85 (t, J = 1.1 Hz, 1H), 6.63 (d, J = 1.0 Hz, 2H), 6.48 (s, 1H), 6.03 (d, J = 6.0 Hz, 1H), 5.24 (ddd, J = 9.6, 5.9, 3.5 Hz, 1H), 4.92 (dd, J = 12.6, 3.5 Hz, 1H), 4.70 (dd, J = 12.6, 9.9 Hz, 1H), 1.42 (s, 9H) ppm; **^{13}C NMR** (101 MHz, DMSO-d_6) δ 148.0, 143.7, 143.5, 132.3, 111.8, 111.5, 108.8, 80.5, 65.2, 60.6, 29.6 ppm; **LRMS (+ESI)** m/z: 302 ([M+Na]$^{+}$, 80).

Appendix 7. Characterisation of Compound 216

5-(5-bromofuran-2-yl)-1-(*tert*-butyl)-1*H*-pyrazole (**216**)

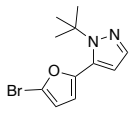

n-BuLi (2.5M solution in hexanes, 100 µL, 0.25 mmol) was added dropwise to a solution of **205** (39.9 mg, 0.21 mmol) in THF (1 mL) at -40 °C. The reaction was cooled to -78 °C, and carbon tetrabromide (181 mg, 0.55 mmol) in THF (1 mL) solution was added dropwise to the mixture. The reaction was then stirred for 1 h at -78 °C, and then for an additional hour at rt. Following consumption of starting material as indicated by TLC, the reaction was cooled to 0 °C and quenched with H_2O (5 mL). The aqueous phase was extracted with diethyl ether (3 x 25 mL/mmol). The combined organics were washed with brine (1 x 25 mL/mmol), dried over $MgSO_4$ and concentrated *in vacuo*. The titled compound was isolated as an off white solid (30.2 mg, 53%) following purification by flash chromatography (100% CH_2Cl_2). **^{1}H NMR** (500 MHz, $CDCl_3$) δ 7.47 (d, J = 1.8 Hz, 1H), 6.42 – 6.38 (m, 2H), 6.36 (d, J = 1.8 Hz, 1H), 1.55 (s, 9H) ppm; **^{13}C NMR** (126 MHz, $CDCl_3$) δ 146.9, 136.6, 130.9, 122.3, 114.1, 113.0, 111.5, 61.3, 30.3 ppm; **LRMS (+APCI)** m/z: 269/271 ($[M+H]^+$, 100).

216 - ^{1}H NMR ($CDCl_3$, 500 MHz, 298 K)

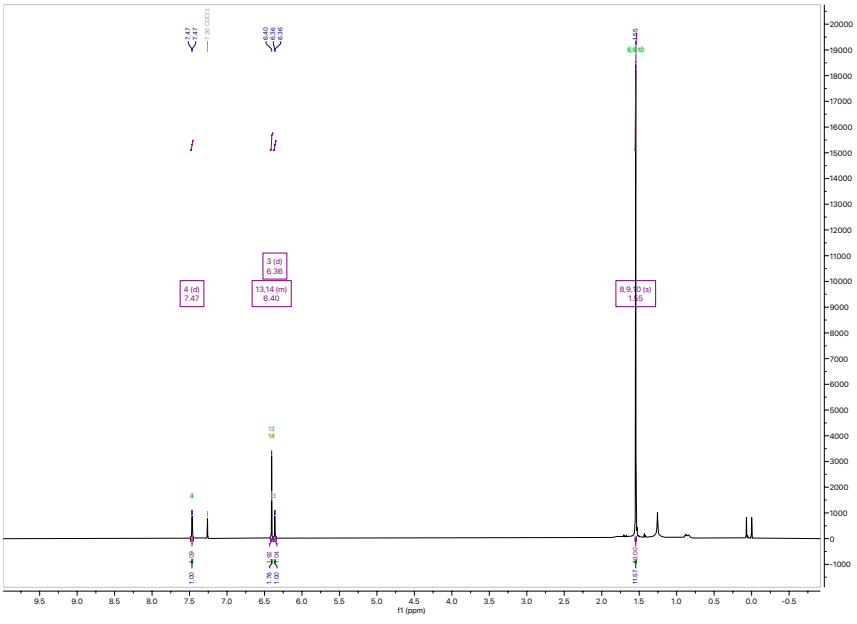

216 – ^{13}C NMR ($CDCl_3$, 126 MHz, 298 K)

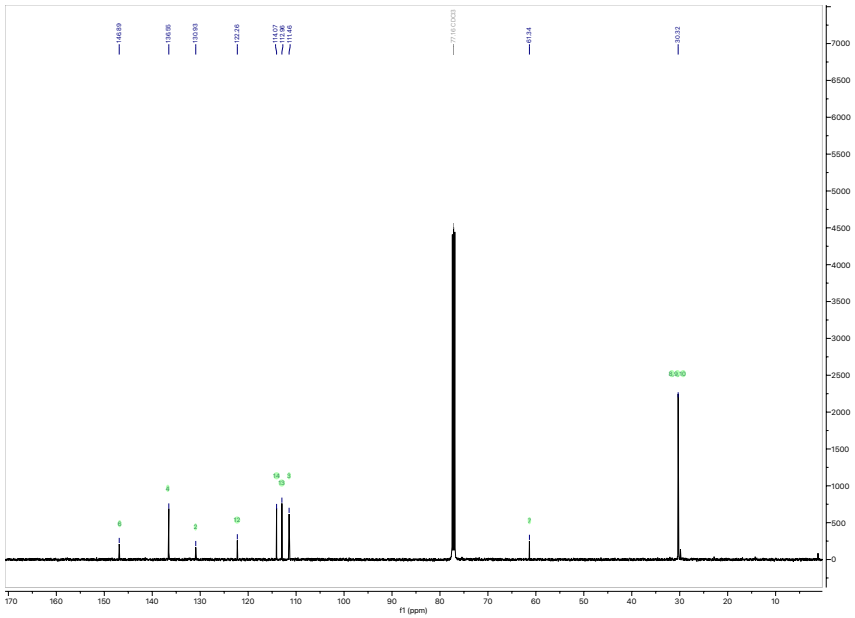

216 - COSY

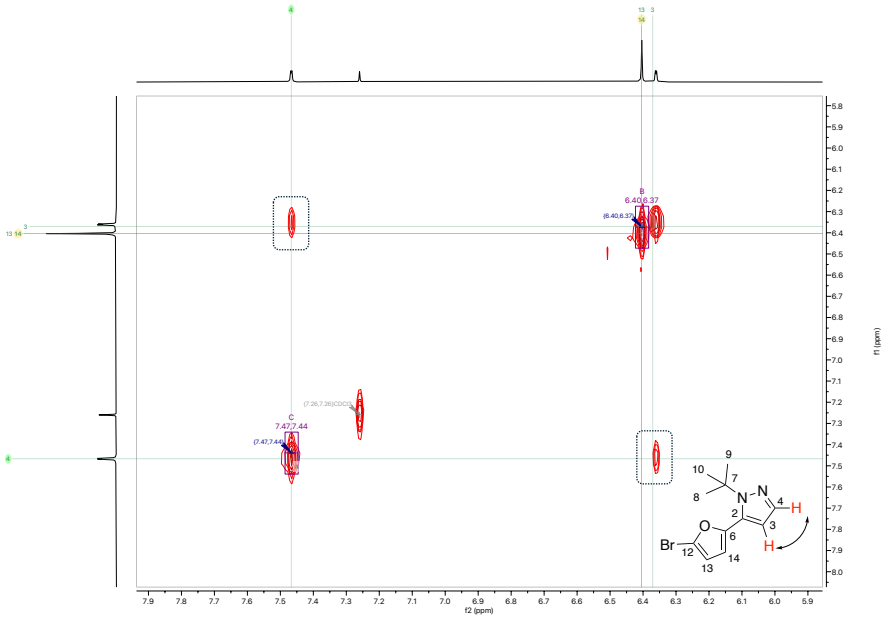

216 - HMBC

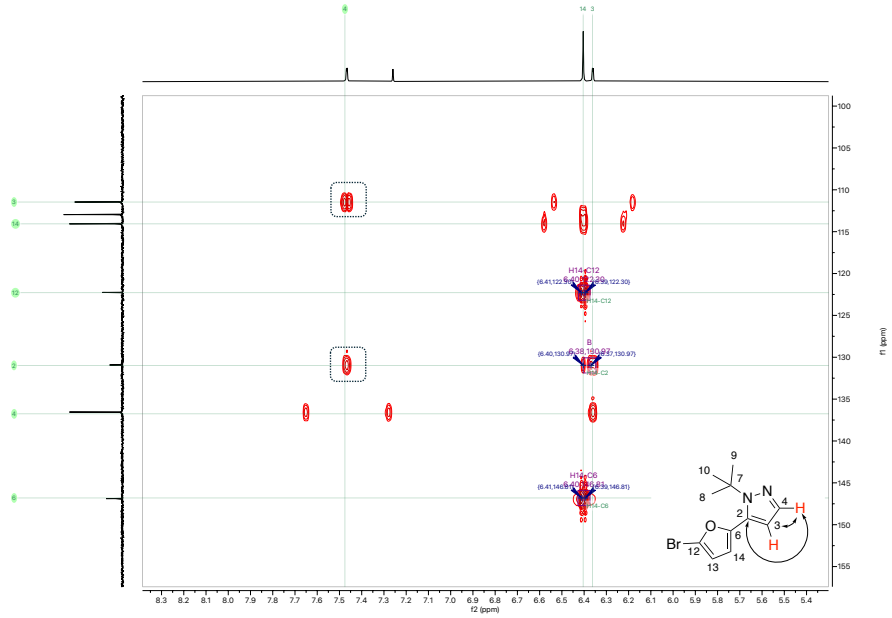

Appendix 8. In Silico Docking of Compound 272

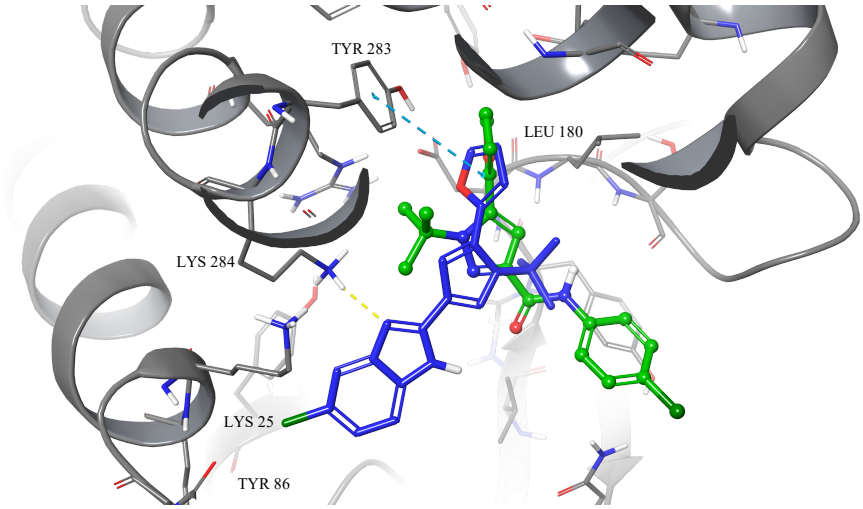

Figure 1. Predicted binding mode of **37** (blue) and amide derivative **272** (green) in the P2Y6 template homology model. Alternate orientations are observed for the two molecules.

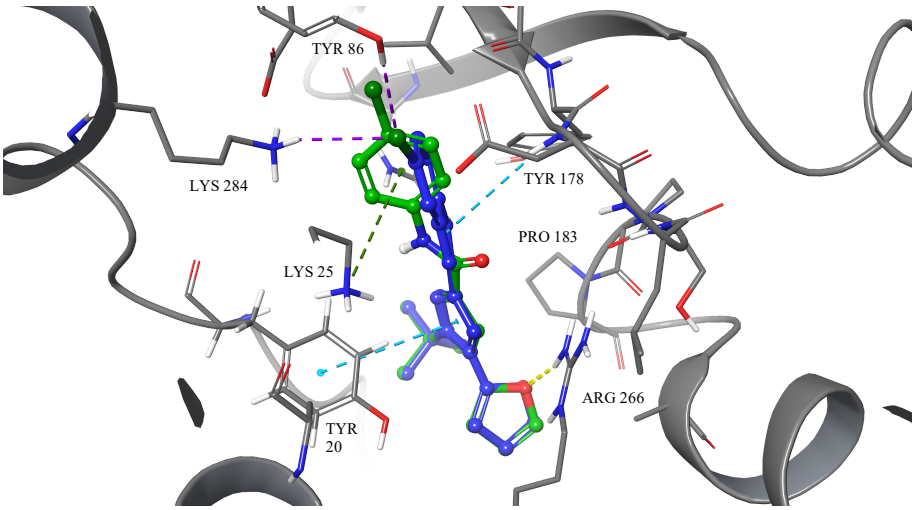

Figure 2. Lead compound **37** (blue) and amide derivative **272** (green) demonstrates a similar binding mode with the AlphaFold P2Y6 homology model. Key hydrogen-bonding (yellow dotted lines) and π-π stacking (blue dotted lines) interactions are observed between the furan and pyrazole with Arg266 and Tyr20 respectively.

Appendix 9. 2D NMR Characterisation of Compound 279

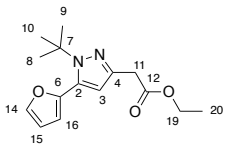

279 – ^{1}H NMR ($CDCl_3$, 500 MHz, 298 K)

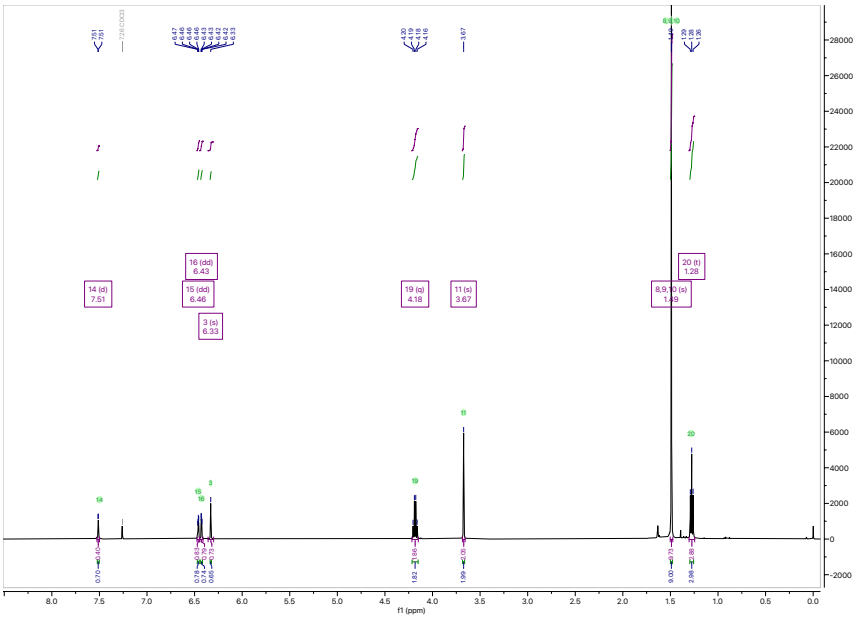

279 –^{13}C NMR ($CDCl_3$, 126 MHz, 298 K)

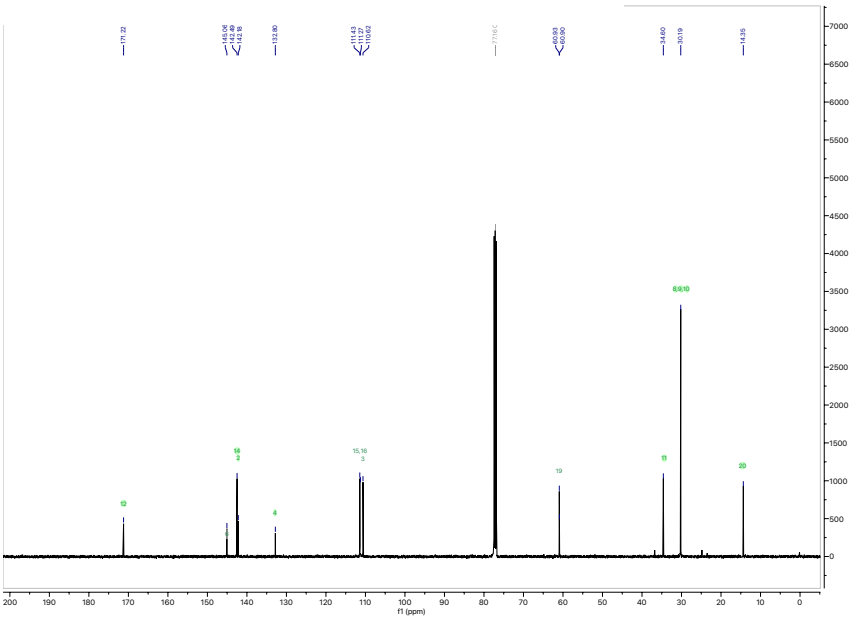

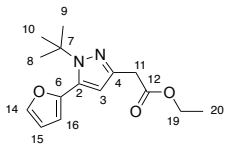

279 – COSY

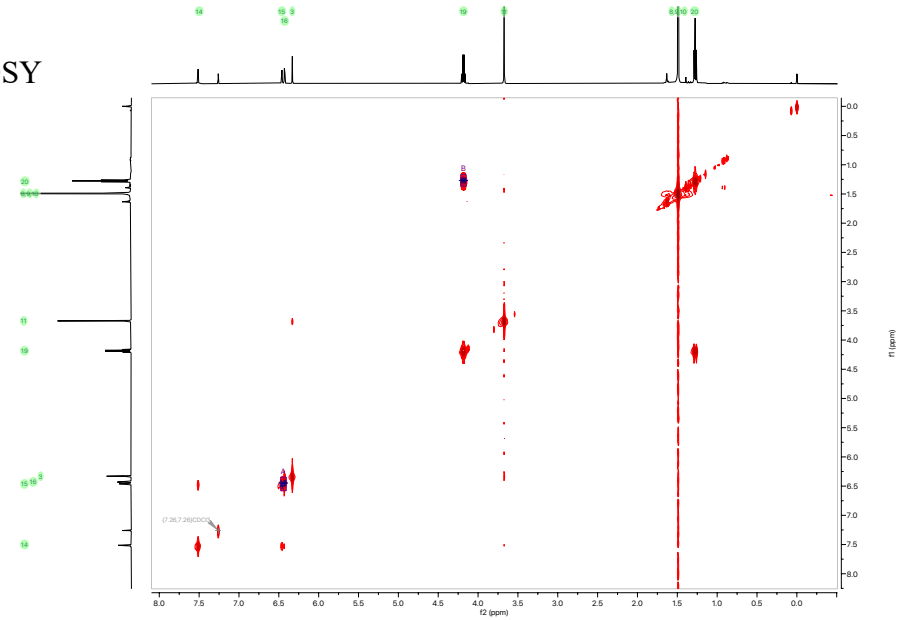

279 – NOESY

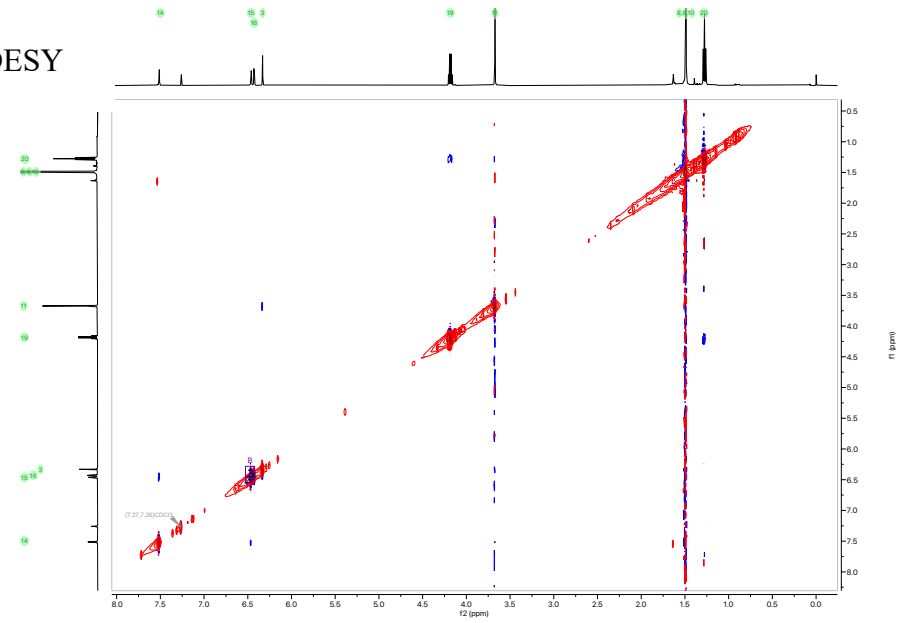

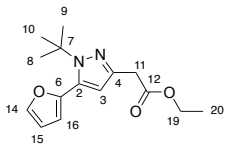

279 – HSQC

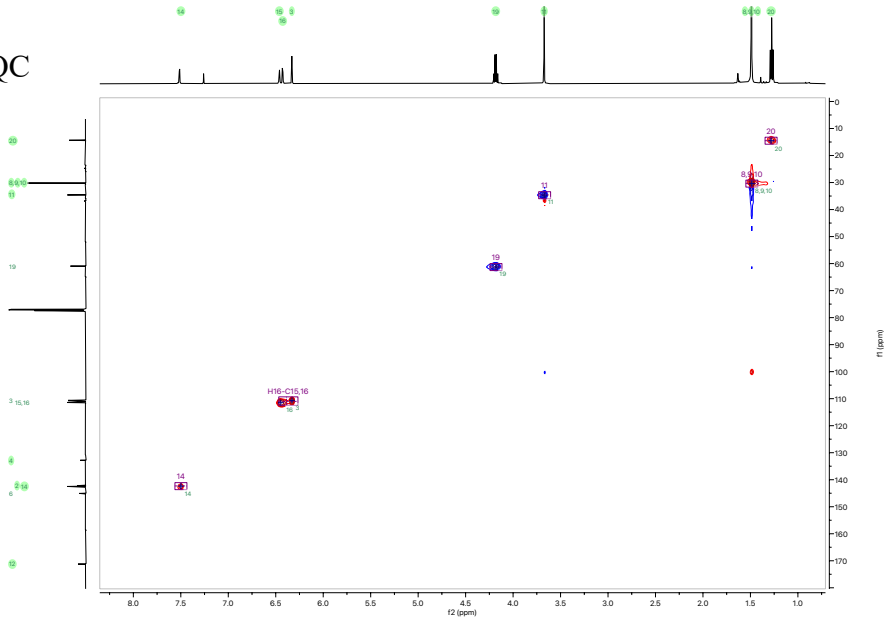

279– HMBC

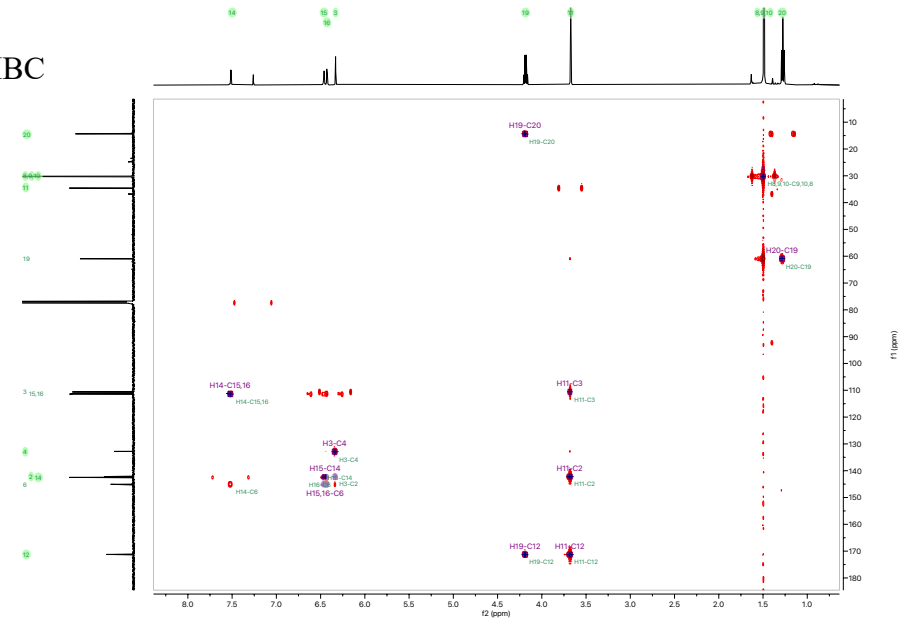

Appendix 10. Computational Metabolism Analysis of Lead Compound 37

Table 1. Predicted ADME properties of **37** and **154** by QikProp (Schrodinger) software.

ADME Property	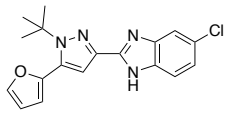 **37**	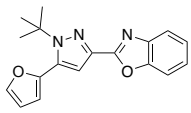 **154**
Metabolism likely	Furan epoxidation	Furan epoxidation
Molecular Weight	340.811	307.351
cLogP	4.928	4.272
Log BB (brain/blood) (-3 / 1.2)	0.295	0.249
Predicted CNS activity (-- to ++)	+	+
Herg K^+ channel blockage: log IC_{50} (concern below -5)	-5.585	-5.640

Table 2. Potential phase 1 and/or phase 2 metabolism of **37** as predicted by machine learning models. Potential positions of metabolism are ranked by reaction rule sets and listed in order of probability reported by the respective software tool. Data extracted from listed software tools.

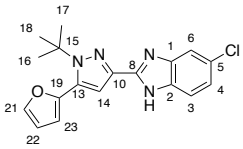

Software	Type of Metabolism	Position
BioTransformer 3	Hydroxylation by CYP1A2	C4, C6 C16 – 18 C21
FAME3	Site of Metabolism	C21
GLORYx	Hydroxylation	C21, C22 C4, C3
XenoSite	Epoxidation	C21-22 C3-5
	Quinonation	C13, C10, C1, C2

Appendix 11. 2D NMR Characterisation of Compound 298

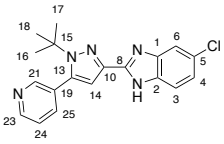

298 – ^{1}H NMR (Acetone-d_6, 400 MHz, 298 K)

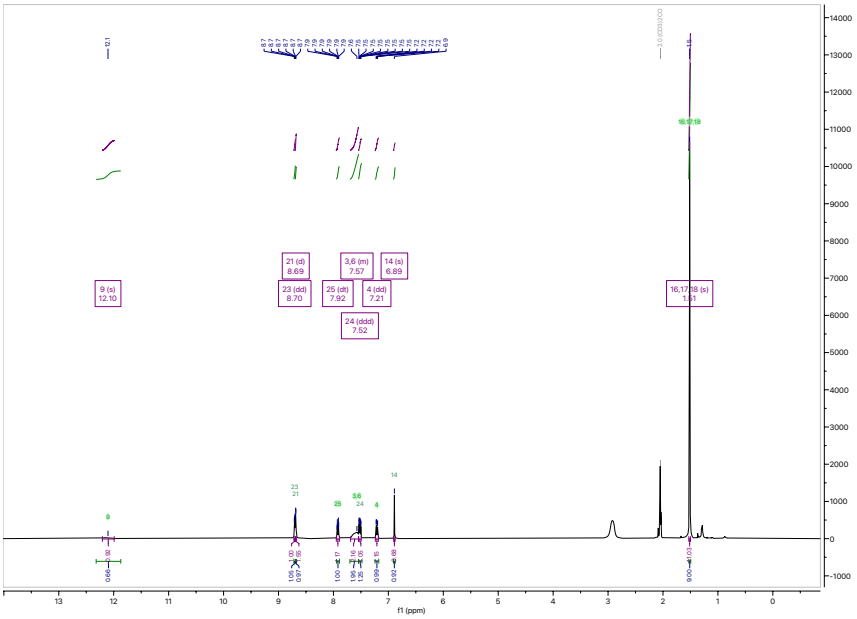

298 –^{13}C NMR (Acetone-d_6, 101 MHz, 298 K)

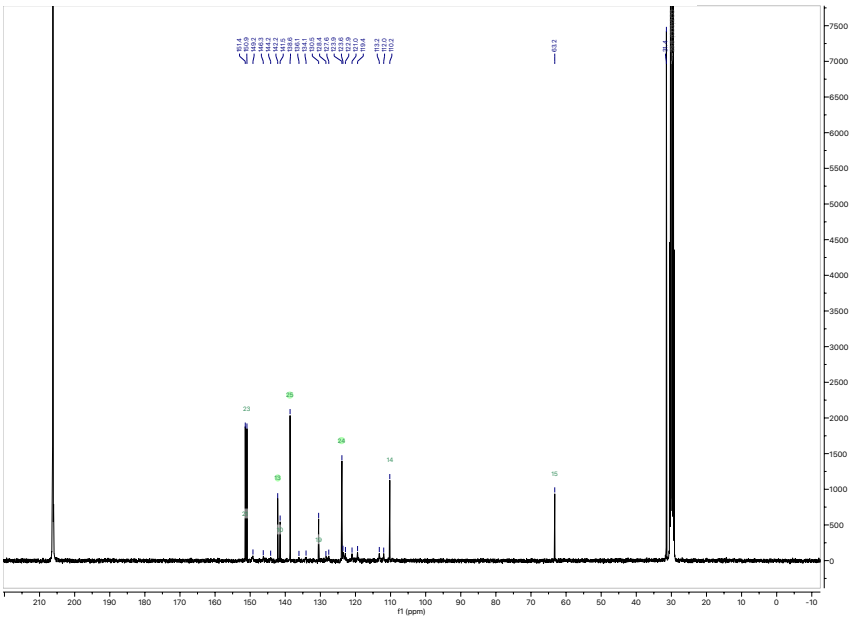

298 – COSY

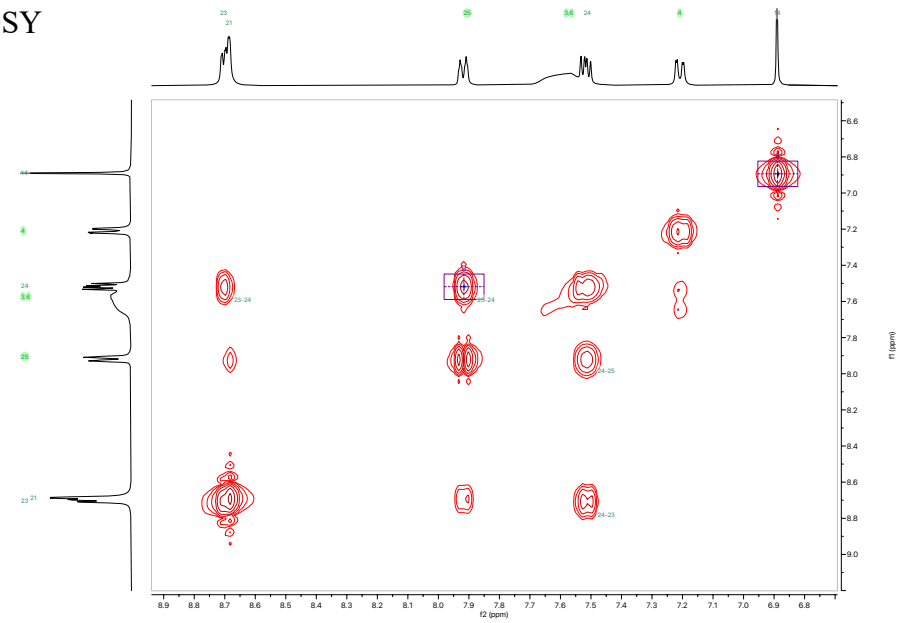

298 – NOESY

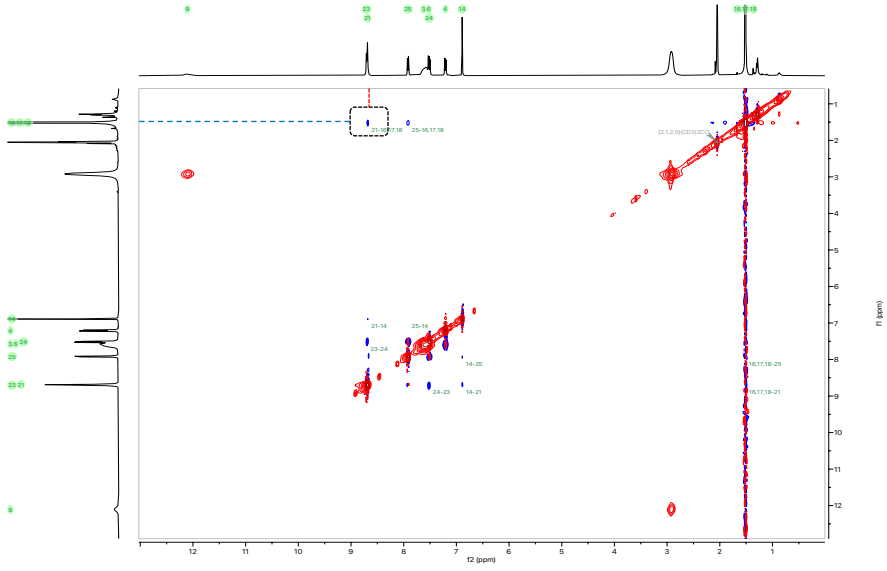

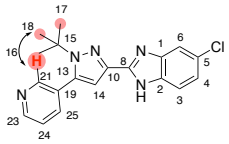

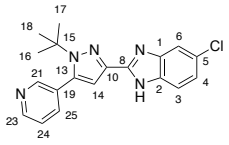

298 – HSQC

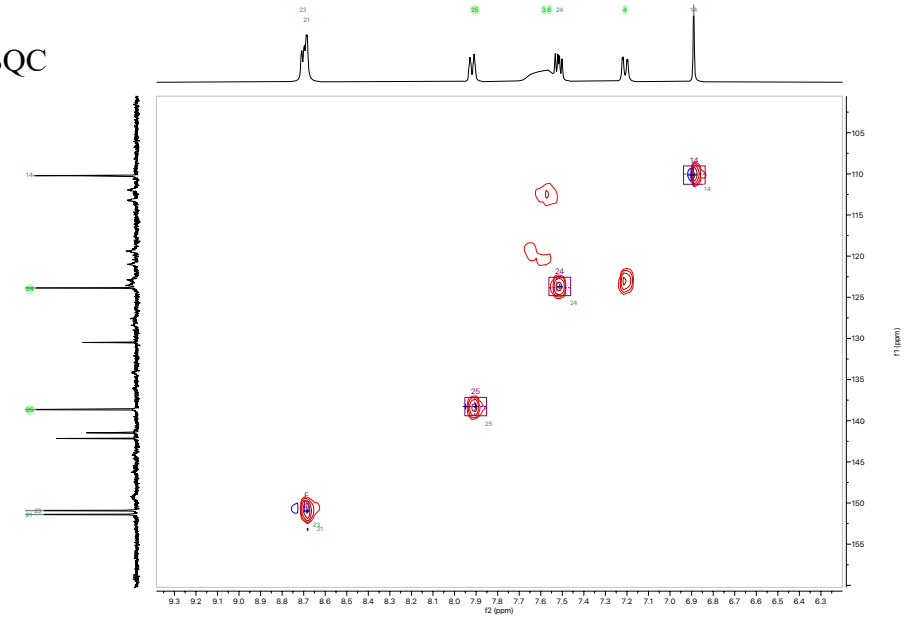

298 – HMBC

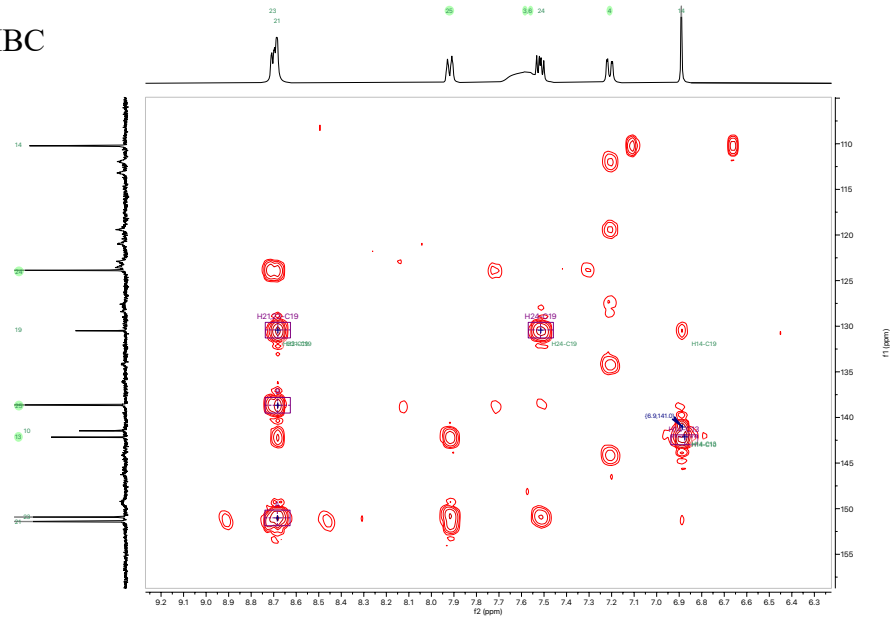

Appendix 12. 2D NMR Characterisation of Compound 299

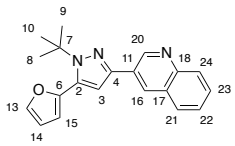

299 – ^{1}H NMR ($CDCl_3$, 400 MHz, 298 K)

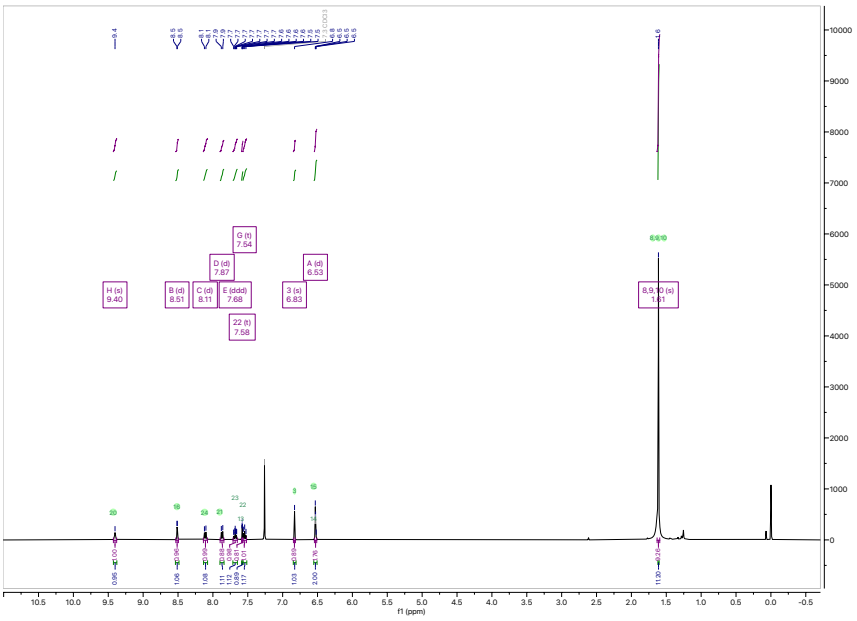

299 – ^{13}C NMR ($CDCl_3$, 101 MHz, 298 K)

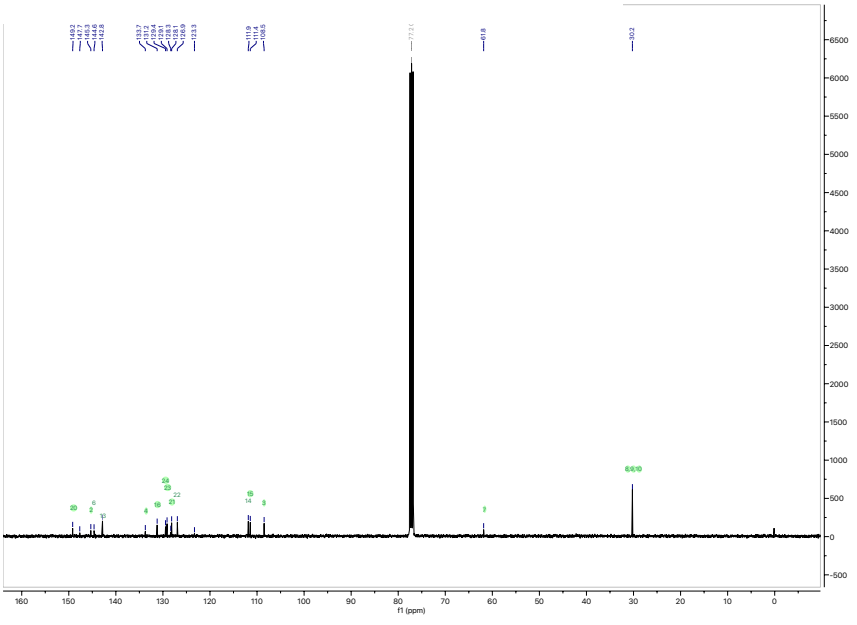

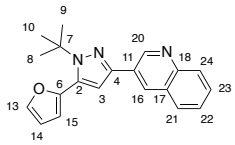

299 – COSY

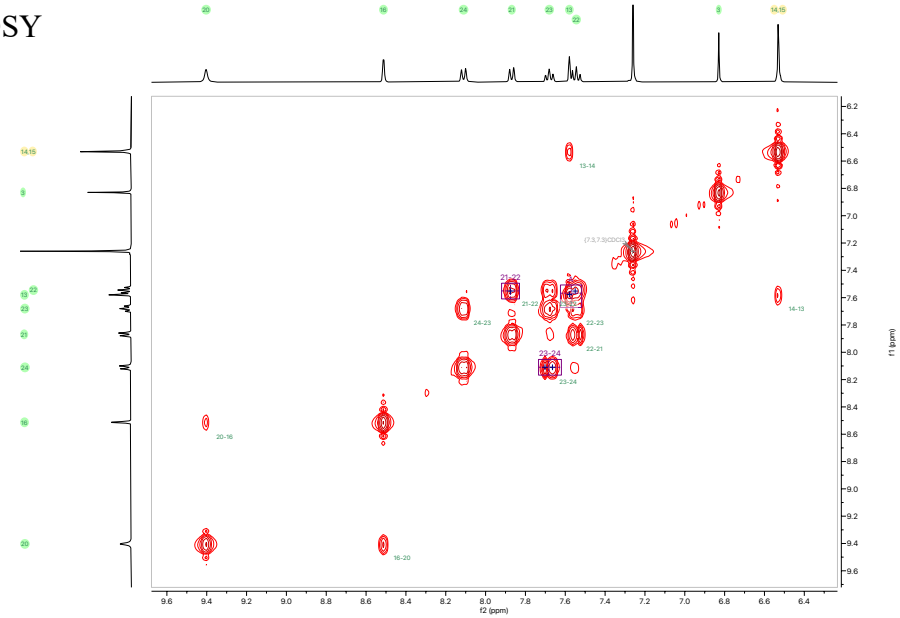

299 – NOESY

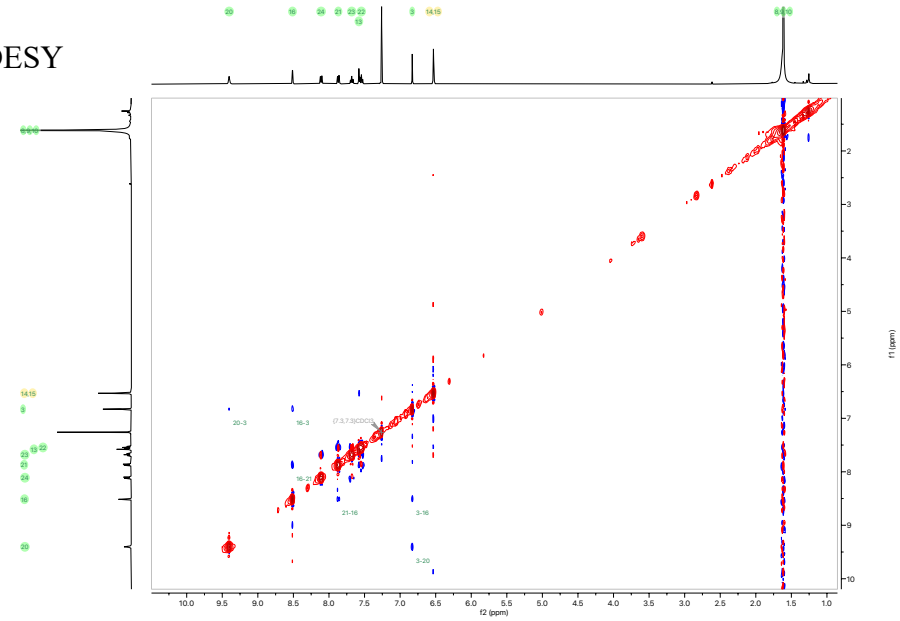

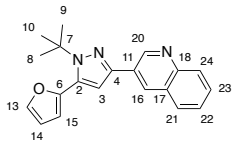

299 – HSQC

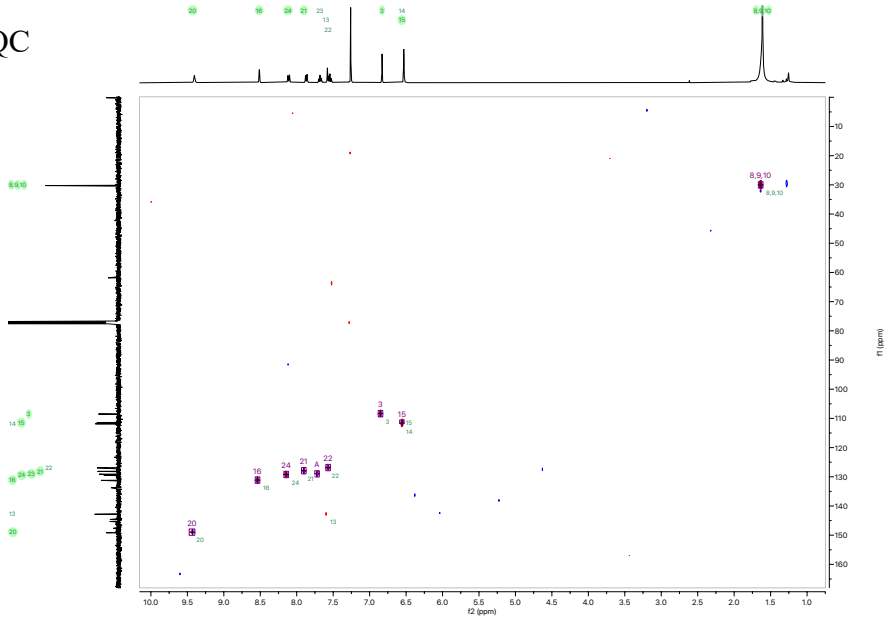

299 – HMBC

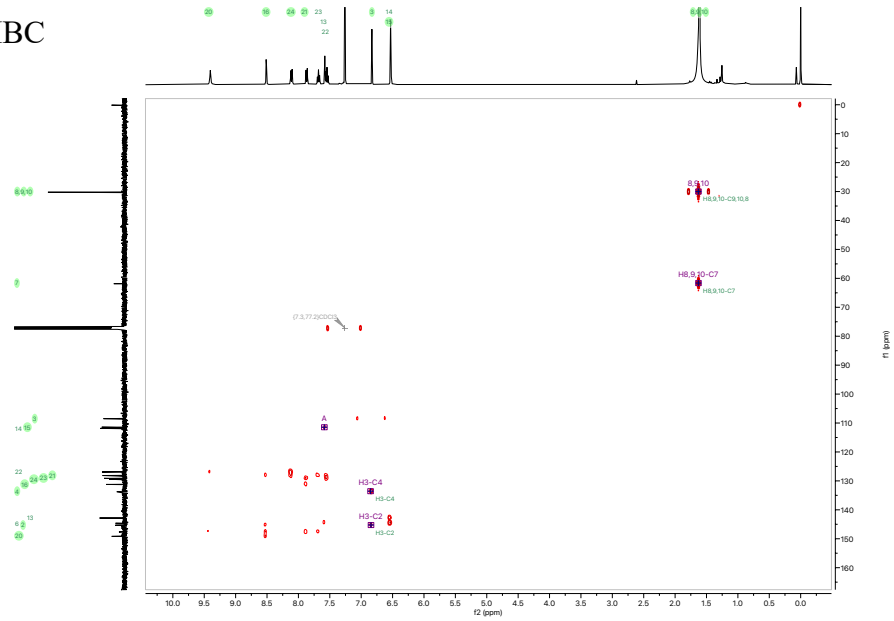

Appendix 13. Characterisation of Esterification Side Products 347 and 348

ethyl 2-ethoxy-7-methylquinoline-3-carboxylate (**347**)

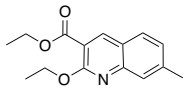

^{1}H NMR (500 MHz, $CDCl_3$) δ 8.54 (s, 1H), 7.66 (d, J = 8.2 Hz, 1H), 7.63 – 7.60 (m, 1H), 7.23 (dd, J = 8.2, 1.7 Hz, 1H), 4.60 (q, J = 7.1 Hz, 2H), 4.41 (q, J = 7.1 Hz, 2H), 2.53 (s, 3H), 1.48 (t, J = 7.1 Hz, 3H), 1.42 (t, J = 7.1 Hz, 3H) ppm; **^{13}C NMR** (126 MHz, $CDCl_3$) δ 165.4, 159.7, 148.3, 142.5, 142.1, 128.3, 126.8, 126.5, 121.9, 115.5, 62.5, 61.3, 22.1, 14.6, 14.4 ppm; **LRMS (+ESI)** m/z: 282 ($[M+Na]^+$, 100).

ethyl 2-ethoxy-8-methylquinoline-3-carboxylate (**348**)

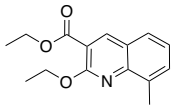

^{1}H NMR (500 MHz, $CDCl_3$) δ 8.56 (s, 1H), 7.62 (dd, J = 8.1, 1.5 Hz, 1H), 7.55 (dt, J = 7.1, 1.4 Hz, 1H), 7.29 (dd, J = 8.0, 7.1 Hz, 1H), 4.64 (q, J = 7.0 Hz, 2H), 4.42 (q, J = 7.1 Hz, 2H), 2.68 (s, 3H), 1.51 (t, J = 7.1 Hz, 3H), 1.43 (t, J = 7.1 Hz, 3H) ppm; **^{13}C NMR** (126 MHz, $CDCl_3$) δ 165.4, 158.5, 146.9, 142.7, 135.4, 131.8, 126.4, 124.3, 123.8, 115.9, 62.5, 61.4, 17.7, 14.5, 14.4 ppm; **LRMS (+ESI)** m/z: 282 ($[M+Na]^+$, 70).

Appendix 14. Assignment of Chloroquinoline Hybrid Analogue Regioisomers

Assignment of chloroquinoline hybrid analogue (**300**, **301**, **359**, **360**) regioisomers was achieved through observed NOE correlations.

^{1}H NMR: $CDCl_3$, 400 MHz, 298 K

300

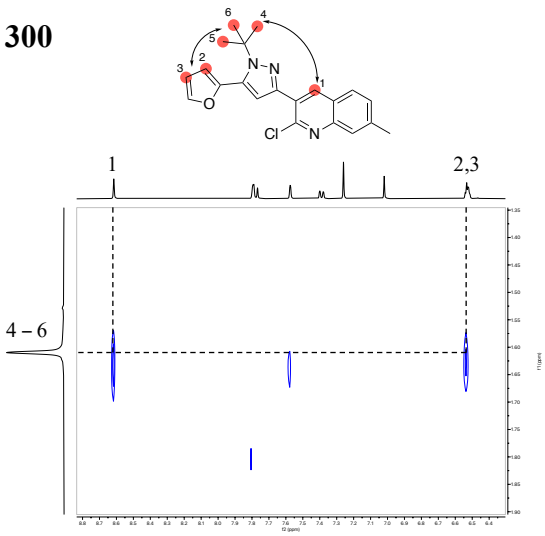

359

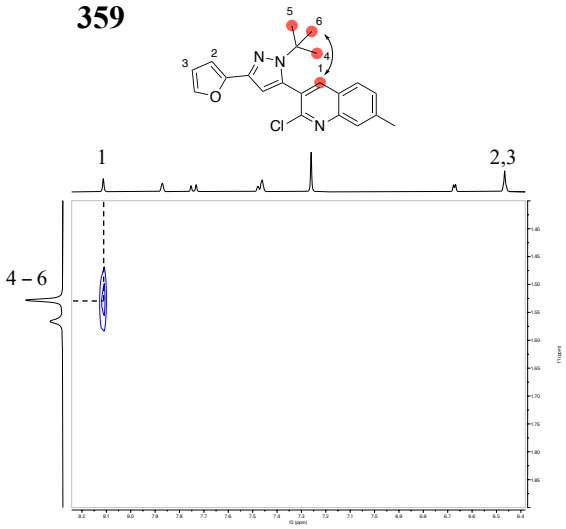

301

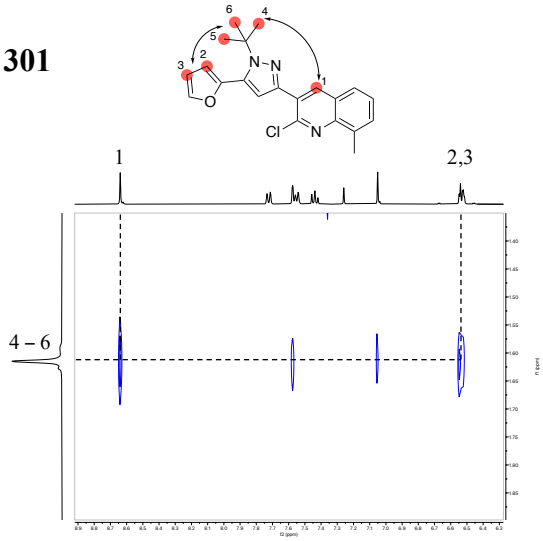

360

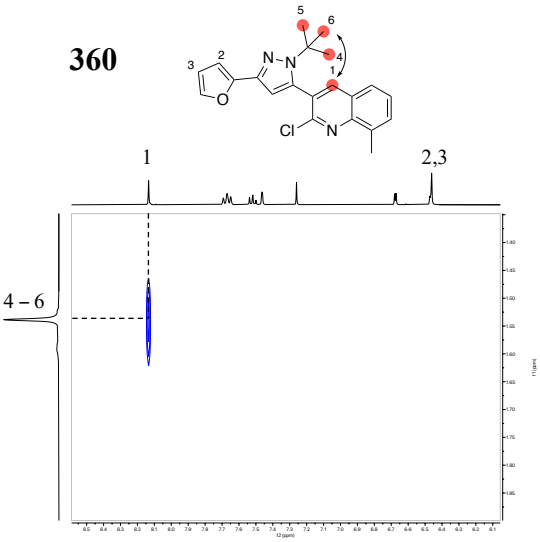

Source	Cell Type	Assay	Kit (Company)	Detection	[UDP] nM	UDP Exposure	Pre-Incubation
McKenzie[a]	132-1N1-hP2Y6R	Ca^{2+} Flux	Fluo-4 NW (Invitrogen)	Fluorescence	75	1 – 3 min	0
Li *et al.* (2022)	HEK293-hP2Y6R	IP_3 accumulation	IP_3 ELISA (Elabscience)	Absorbance	10000	12 h	30
Zhu *et al.* (2023)	HEK293-hP2Y6R	IP_3 accumulation	IP_3 ELISA (Elabscience)	Absorbance	10000	12 h	30
Zhao *et al.* (2024)	CHO-hP2Y6R	Ca^{2+} Flux	FLIPR Calcium 6 (Molecular Devices)	Fluorescence	N/R[b]	1 – 3 min	N/R[b]
Oliva *et al.* (2024)	132-1N1-hP2Y6R	Ca^{2+} Flux	FLIPR Calcium 6 (Molecular Devices)	Fluorescence	100	1 – 3 min	45
Eurofins	132-1N1-hP2Y6R	Ca^{2+} Flux	Proprietary	Fluorimetry	10	N/R[b]	N/R[b]

[a] ‘ McKenzie’ refers to the experimental method developed by Mr Andre McKenzie with the Faculty of Medicine and Health at the University of Sydney; [b]N/R = not reported. 132-1N1: human astrocytoma cells; HEK: human embryonic kidney cells; CHO:

Appendix 16. Stability Study of MRS2578 (31)

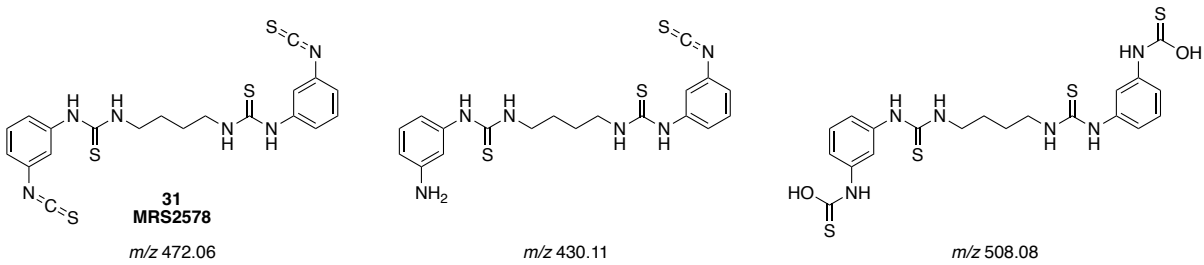

Figure 1. Potential degradation products of MRS2578 observed by NMR and LR ESI-MS.

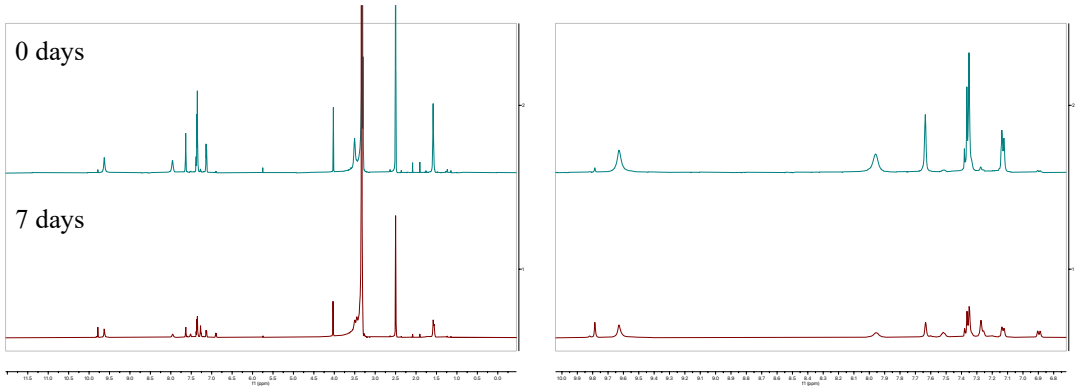

Figure 2. ^{1}H NMR (DMSO-d_6, 500 MHz, 298 K) spectra of MRS2578 acquired 7 days apart. Sample was stored at ambient temperature.

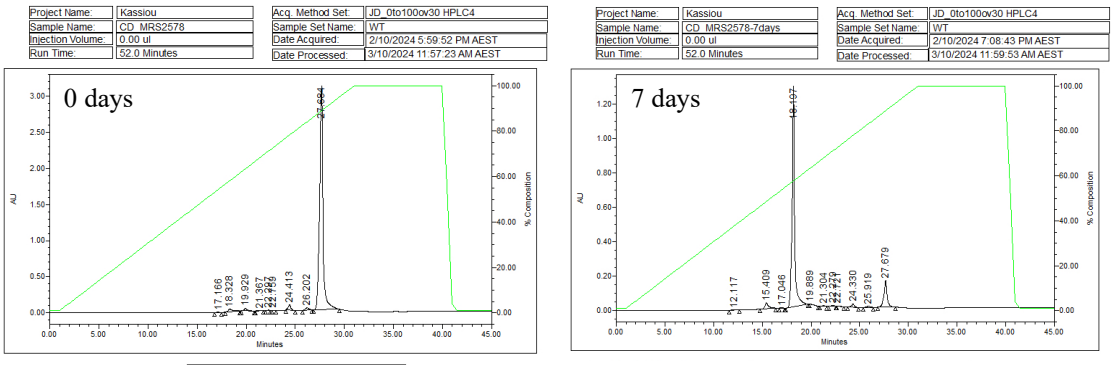

Figure 3. Analytical HPLC (0 – 100% MeCN:H_2O) trace of MRS2578 samples stored at ambient temperature for 0 and 7 days.

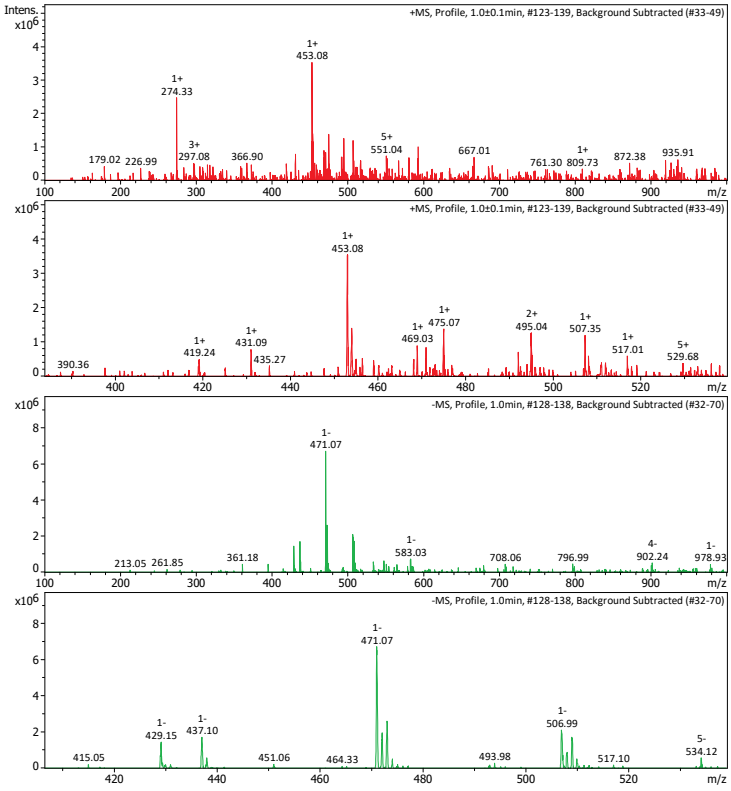

Figure 4. LRMS (+ESI) and (-ESI) of MRS2578 dissolved in DMSO (diluted 1 x 10^{-3} fold MeOH) at 0 days.

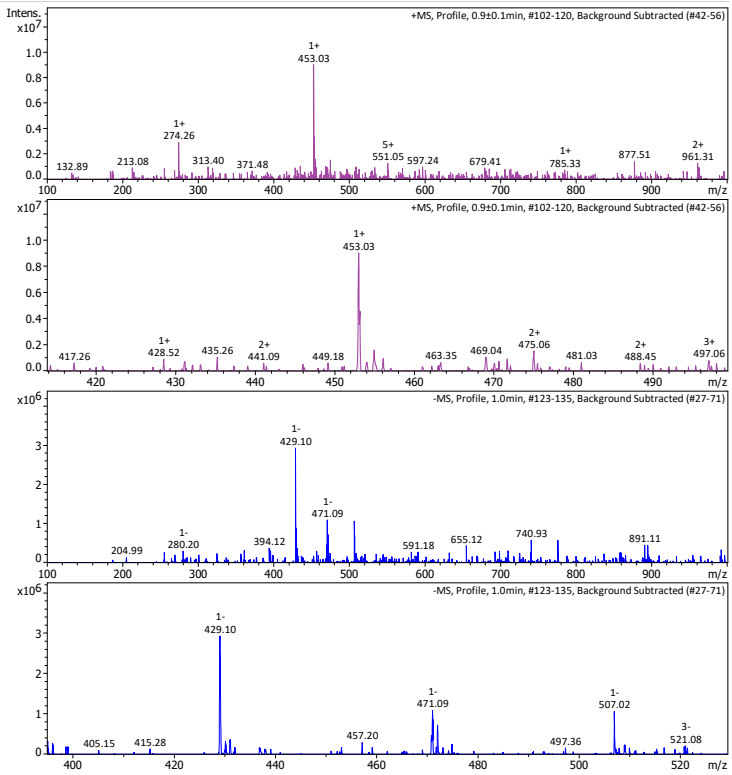

Figure 5. LRMS (+ESI) and (-ESI) of MRS2578 dissolved in DMSO (diluted 1 x 10^{-3} fold MeOH) after being stored at ambient temperature for 7 days.

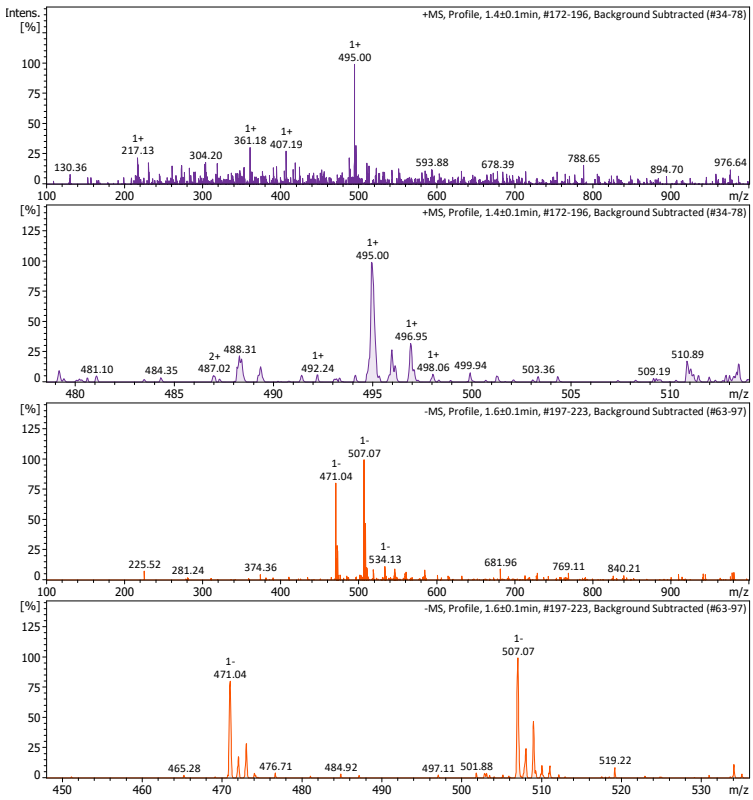

Figure 6. LRMS (+ESI) and (-ESI) of MRS2578 dissolved in DMSO (diluted 1 x 10^{-3} fold MeOH) after being stored at -8 °C for 7 days.

Appendix 17. P2Y6 *In Silico* Docking Scores

Table 1. *In silico* hP2Y6 induced-fit docking (IFD) and rigid-target docking (RTD) scores of reference compounds. A more negative score denotes a stronger binding affinity.

Compound	Template Homology			AlphaFold
	IFD Score (kcal/mol)	RTD Score (kcal/mol)		RTD Score (kcal/mol)
	OPLS4	OPLS4	OPLS2005	OPLS4
(*R*)-39	-12.58	-4.64	-8.22	-7.19
(*S*)-39		-8.22	-7.16	-7.57
***5*-37**	-7.96	-2.22	-2.22	-4.63
***6*-37**		-2.31	-2.31	-4.90
153		-2.53	-4.17	-5.10
154		-4.25	-4.24	-4.44
(*R*)-38		-6.39	-6.39	-8.20
(*S*)-38		-6.04	-6.04	-9.21
(*R*)-40		-6.47	-6.47	-6.90
(*S*)-40		-5.88	-5.52	-8.61
(*R*)-281		-4.44	-4.44	-9.39
(*S*)-281		-4.81	-4.83	-8.66

Appendix 18. 2D NMR Characterisation of Compound 166

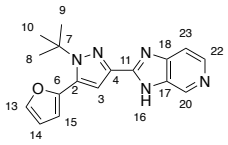

166 – ^{1}H NMR (DMSO-d_6, 400 MHz, 298 K)

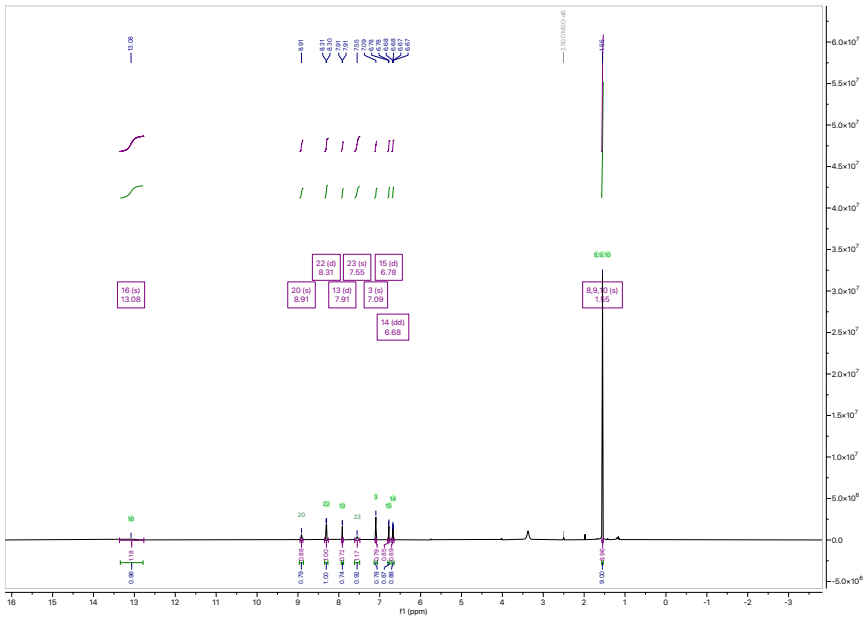

166 –^{13}C NMR (DMSO-d_6, 101 MHz, 298 K)

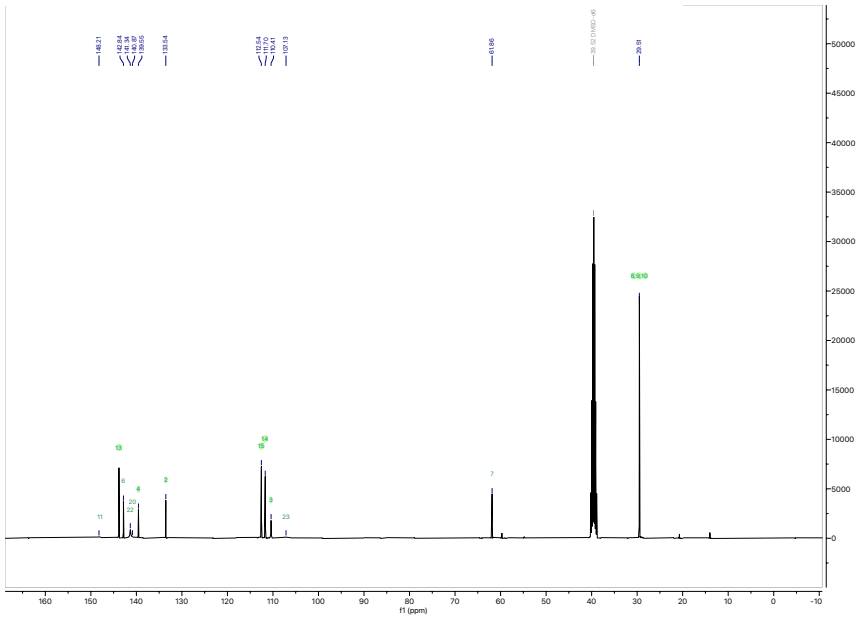

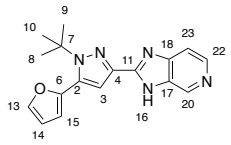

166 – COSY

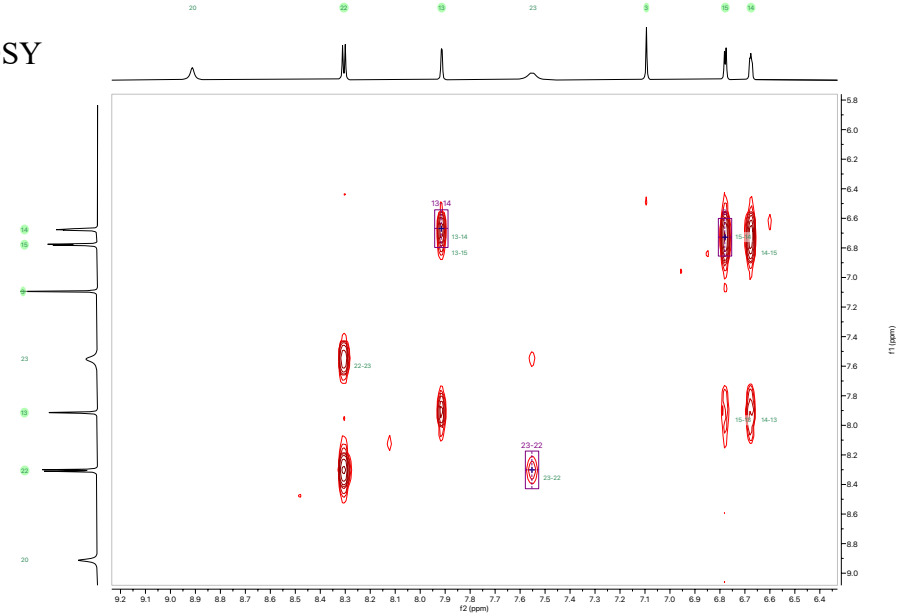

166 – NOESY

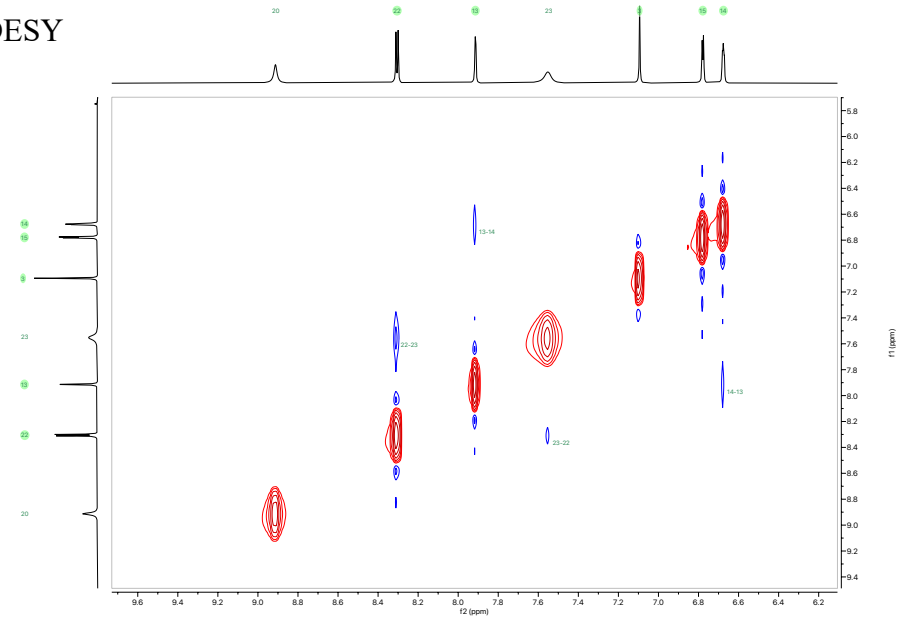

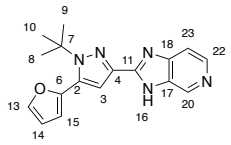

166 – HSQC

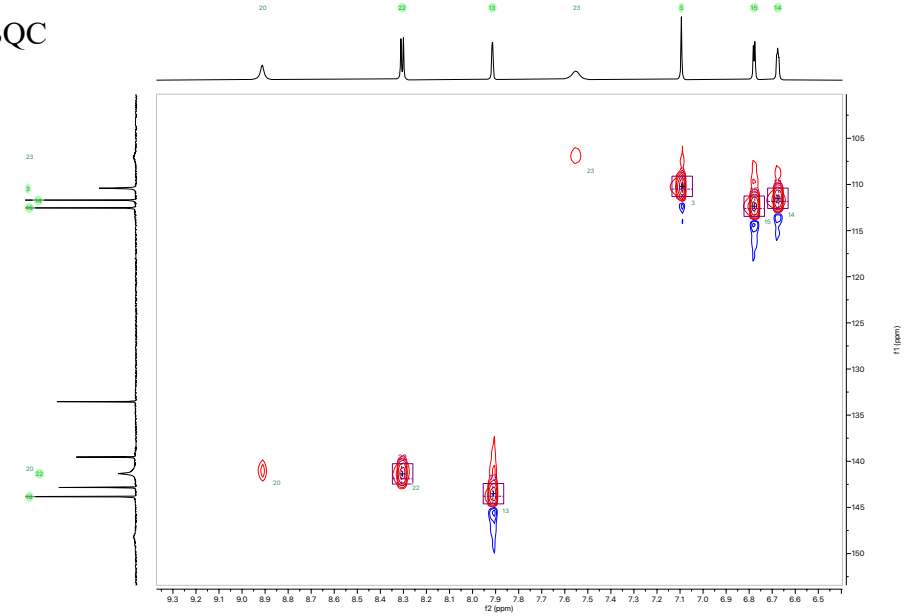

166 – HMBC